Interplanetary Mission Analysis and Design

Stephen Kemble

EXTRA MATERIALS
extras.springer.com

Springer

PRAXIS

Interplanetary Mission Analysis and Design

Stephen Kemble

Interplanetary Mission Analysis and Design

Published in association with
Praxis Publishing
Chichester, UK

Mr Stephen Kemble
Consultant
EADS Astrium
Stevenage
Hertfordshire
UK

SPRINGER–PRAXIS BOOKS IN ASTRONAUTICAL ENGINEERING
SUBJECT *ADVISORY EDITOR:* John Mason M.Sc., B.Sc., Ph.D.

ISBN 10: 3-540-29913-0 Springer-Verlag Berlin Heidelberg New York

Springer is part of Springer-Science + Business Media (springeronline.com)

Bibliographic information published by Die Deutsche Bibliothek

Die Deutsche Bibliothek lists this publication in the Deutsche Nationalbibliografie; detailed bibliographic data are available from the Internet at http://dnb.ddb.de

Library of Congress Control Number: 2005935455

Printed in Germany

Cover design: Jim Wilkie
Project copy editor: Bob Marriott
Project management: Originator Publishing Services, Gt Yarmouth, Norfolk, UK

Printed on acid-free paper

Contents

Preface

One of the enduring legacies of the twentieth century will be the advent of space travel. This achievement has changed the way we think about our presence in the Universe and now offers the possibility to explore beyond our own world. Nobody experiencing the Apollo missions of the 1960s and 70s could be unaffected by the magnitude of those achievements. Now, nearly forty years later, space travel is almost commonplace, although man's personal presence in space is still limited.

The pioneering edge of space exploration now lies beyond Earth and its moon, as numerous spacecraft over the last thirty years have visited most of the planets of the Solar System. Mars remains the focus of many such missions and is likely to be the first planet that man visits personally, not just through robotic craft. Perhaps the most fascinating interplanetary missions to date have been the Voyagers. Launched in the late 1970s, these spacecraft were flung out of the Solar System after flying by the outer planets. They have now passed far beyond Pluto as they leave the Sun's domain behind.

These technical achievements have inspired numerous science fiction stories, which in turn have themselves perhaps influenced the drive for new space missions and exploration. Although 'warp drives' remain for the present in the realm of science fiction, more adventurous missions to explore our Solar System are being planned. These include an initiative to place a man on Mars and also for a detailed robotic exploration of Jupiter and its family of moons. This later system has already been inspected by the Galileo spacecraft and revealed a fascinating 'micro solar system' with a rich variety of features. Also, both current (Messenger) and planned future missions (Bepi–Colombo) to Mercury will undertake the difficult route to the innermost planet of the Solar System. In addition to the planets, the minor bodies of the Solar System are being explored. A challenging example is ESA's Rosetta mission, following a complex route to achieve a rendez-vous with a comet.

MISSION ANALYSIS AND DESIGN

This diverse range of missions require numerous techniques for their analysis and design. These aspects will be considered in this book, including the key issues of escaping from a planet, interplanetary transfer, and capture at a target planet. Certain 'classical' methods for the design of such trajectories have been employed for many years. As missions became more demanding, then new techniques were developed to enable more efficient designs to be realised. These allow the efficient utilisation of newly evolving propulsion technologies. This theme is continuing, as both new mathematical and computational ideas are considered for the solution of these problems.

The objective of this book is to describe a selection of techniques that may be applied to the analysis and design of interplanetary missions. The focus is on methods that enable the efficient solution of the problems considered. Details of the methods are given. However, this text is not intended as a reference on astrodynamics. Summaries of key derivations are included.

The terms 'mission analysis' and 'mission design' can have several meanings. The one taken here is that of the analysis and design of spacecraft transfers. Therefore, the focus is on techniques in orbital mechanics and trajectory optimisation that may be applied to the objective. The aspects of mission analysis particularly relevant to interplanetary missions are considered here.

This book is divided into five major chapters. The first chapter focuses on 'conventional' analysis and design techniques for interplanetary missions. This includes the basic ideas of Hohmann transfers, the solution of Lambert's problem and the fundamentals of planetary escape and capture. These basic ideas of interplanetary transfers are then extended to consider return missions to the planets. The issue of escape from Earth is also considered in more detail, in the context of the efficient utilisation of launch vehicle capabilities. This subject is also further expanded in Appendix 4.

The second chapter briefly considers aspects of spacecraft propulsion systems. These systems are a fundamental factor in the nature of interplanetary mission designs and therefore warrant some consideration in a book such as this.

The third chapter focuses on optimisation. In particular, methods for obtaining solutions to local optimisation problems are considered. These generally require gradient evaluations and are often called 'gradient based' methods. These methods are essential for the efficient design of interplanetary missions. As more complex propulsion system types are considered, so the complexity of the optimisation problems increases. Many developments are taking place in this area. Only gradient-based methods are considered here. However, it should be noted that alternative techniques such as evolutionary computing offer very interesting prospects for the identification of globally optimal solutions. In addition to trajectory optimisation problems, the nature of spacecraft optimisation is discussed, where the design of the propulsion installation may be optimised together with the transfer trajectory.

The fourth chapter considers a range of 'special' methods that may be employed

for mission analysis and design. These methods allow the planning of more efficient transfers. A consequence of the improved efficiency is the increased complexity of the transfer routes. Some of these methods take advantage of interesting features of astrodynamics. A good example of this is the phenomenon of gravitational escape or capture at a planet, which has been observed for comets in the Solar System. Consequently, this chapter contains an outline description of the three-body problem and mission designs that can utilise three-body effects. Many of the techniques considered in this chapter allow the efficient utilisation of advanced propulsion system concepts. This is particularly true for low-thrust systems. The effect of low thrust systems on orbit evolution is considered via the application of perturbation equations. Considerable attention is paid to 'gravity assist'. This technique allows the utilisation of combined gravity fields to enable a spacecraft to significantly modify its orbital energy, without the need for manoeuvre.

The final chapter describes a series of mission examples that utilise the methods described in the previous sections. These include missions using gravity assist, low-thrust propulsion, gravitational escape and capture. Many of the examples are generic, in that they consider typical transfers between planets. However, certain examples are relevant to actual missions, either past, current, or future.

The appendices describe the basics of orbital mechanics, orbital reference frames, and also the properties of the planets. The data is intended as a source of reference for the material in the book.

A CD is included to give some examples of interplanetary missions. A simulation tool is included. This is used to generate animated sequences that show interplanetary transfers. The missions illustrated include both transfers to the inner and outer planets. Instructions for use are contained on the CD. The software runs on Windows based PC systems.

Although every effort has been made to eliminate mathematical and factual errors in the material in this book, complete accuracy cannot be guaranteed. Please send any errors found and suggested corrections to the author.

Acknowledgements

I would like to thank numerous groups and individuals. First, project teams within the European Space Agency (ESA), with whom I have worked. This work has provided much of the background for the material in this text, particularly through the diverse series of projects undertaken. Specifically, the Bepi–Colombo project led by J. Van Casteran with lead mission analyst R. Jehn, the Science Payloads and Advanced Concepts, planetary exploration studies team led by P. Falkner, the Lisa–Pathfinder project led by G.Racca with lead mission analyst M. Landgraf, the SOLO project led by N. Rando with lead mission analyst G. Janin and also M. Hechler, J. Rodriguez Canabal, and W. Flury on a wide range of projects. I would like to thank the many colleagues at EADS Astrium with whom I work, particularly those with whom I regularly work (or have worked) directly on mission analysis topics, including C. Warren, M.J. Taylor, A. Povoleri, and G. Hughes.

I would also like to specifically thank R.C. Parkinson, for support and always asking the most interesting questions!

Also many thanks to Clive Horwood at Praxis and Neil Shuttlewood at Originator.

Figures

Tables

Nomenclature

COMMONLY USED TERMS

The following lists a series of acronyms, mathematical symbols, and phrases frequently used in this text. This is not a comprehensive list and details of further terms used are given in the appropriate sections.

COMMON ACRONYMS

ΔV Delta-V
EGA Earth Gravity Assist
GA Gravity Assist
Isp Specific Impulse
JGA Jupiter Gravity Assist
LGA Lunar Gravity assist
MGA Mercury Gravity Assist
NEP Nuclear Electric Propulsion
SEP Solar Electric Propulsion
SGA Saturn Gravity Assist
VGA Venus Gravity Assist
V_∞ Excess hyperbolic speed

GRAVITY ASSIST SEQUENCE LABELLING

E Earth
J Jupiter

L Moon (Earth's)
M Mercury
S Saturn
V Venus

Example: V–E–E = Venus, Earth, Earth gravity assist sequence

COMMON SUBSCRIPTS TO MATHEMATICAL TERMS

C Denotes term relative to central body
I Denotes a vector expressed in an inertially oriented frame
p Denotes term relative to major body

COMMON MATHEMATICAL SYMBOLS

a Semi-major axis of ellipse
α Velocity vector deflection angle (in gravity assist description)
Thrust vector azimuth angle in low-thrust vector modelling
A_X^Y Transformation matrix from Y to X frame
b Semi-minor axis of ellipse
β Angle describing the location of the intersection of the approaching asymptotic excess hyperbolic velocity vector with the B plane (in gravity assist description)
Thrust vector elevation angle in low-thrust vector modelling
e Eccentricity
C Jacobi constant (in three-body problem)
Constraint (in optimisation problems)
d Distance
ΔV Delta-V
E Eccentric anomaly (in ephemeris elements)
Energy (usually per unit mass)
F Hyperbolic anomaly
Γ Flight path angle
h Angular momentum (usually per unit mass)
i Inclination
J Objective function
λ Lagrange multiplier (in non-linear programming methods)
Longitude (in orbit kinematics)
m Mass
M Mean anomaly
μ Gravitational parameter (in gravitational acceleration terms)
Mass ratio (in three-body problem)
p Orbit semi-latus rectum

P	Adjoint vector (in indirect optimisation)
r	Spacecraft position (may be used as vector or magnitude)
r_{planet}	Major body position (may be used as vector or magnitude)
t	Elapsed time
T	Thrust (often per unit mass)
τ	Orbit period
θ	True anomaly (in ephemeris elements) Angle between approaching relative velocity vector and major body velocity vector in gravity assist
u	Control vector
U	Potential
V	Spacecraft velocity (may be used as vector or magnitude)
V_{planet}	Major body velocity (may be used as vector or magnitude)
ω	Angular velocity (of major body) (may be used as vector or magnitude)
Ω	Right ascension of ascending node
X	State vector
V_∞	Excess hyperbolic speed
V_{rel}	Velocity relative to major body (used in two-body approximation)

NOTATION

$\sum_{i}^{N}$ Summation abbreviated form of $\sum_{i=1}^{i=N}$

COMMONLY USED TERMINOLOGY

Term	*Description*
Aerobraking	The process of utilisation of a pericentre passage (or multiple passages) through a major body's atmosphere with the objective of reducing the apocentre.
Aerocapture	The process of utilisation of a pericentre passage through a major body's atmosphere with the objective of reducing the energy of an approaching spacecraft in an initially unbound orbit to reach a bound orbit.
Approach plane	In a gravity assist, the plane containing the velocity of the major body and the asymptotic excess hyperbolic velocity vector.
Asymptotic excess hyperbolic velocity vector	The velocity vector whose magnitude is equal to the excess hyperbolic speed and direction defined by the asymptotes of the hyperbola when either approaching or departing from a major body.
B plane	The plane normal to an approaching asymptotic excess hyperbolic velocity vector and passing through the centre of the major body.

Central body	The primary body with the dominant gravity field in a system. Examples are the Sun for transfers in the Solar System, or Jupiter for transfers to the Jovian moons.
ΔV or Delta-V	The speed change effected by propulsive force to implement a change in orbit. Includes the inefficiency arising from non-impulsive manoeuvres. Implemented by a spacecraft propulsion system or environmental perturbation to the orbit.
Direct optimisation method	Method to determine the optimal control solution that minimises or maximises an objective using the approximation of a parameterisation of a continuously variable control function.
Escape orbit	An unbound orbit (energy > 0), resulting in a hyperbola.
Excess hyperbolic vector	The speed remaining at infinite distance (when in a hyperbolic orbit). In practice, approximated by the speed after leaving the sphere of influence.
Fly-by	A passage close to a major body during the course of a trajectory about a central body.
Gravity assist	The process of utilisation of the gravity field of a major body, during the course of a trajectory about the central body, with the result of energy and angular momentum modification with respect to the central body.
Gravitational escape (or capture) (or gravity assisted escape or capture)	The process of achieving an escape orbit from an initial bound orbit under the influence of the gravity fields of a major and central body. (Reverse for capture.)
Halo orbit	An 'orbit' about a collinear Lagrange libration point whose periods in and out of ecliptic are equal.
Hohmann transfer	A two-impulse transfer over half of an ellipse. Optimal transfer between coplanar, circular orbits.
Indirect optimisation method	Method to determine the optimal control solution that minimises or maximises an objective using variational calculus methods. Pontryagin's maximum (or minimum) principle is employed.
Invariant manifold	A constrained trajectory in phase space describing both the position and velocity vectors. Used in the context of the three-body problem to describe the evolution of a spacecraft trajectory under the influence of combined gravity fields (and neglecting non-gravitational perturbations).
Keplerian orbit	An orbit that is the solution of the two-body problem. Solutions are conic sections: ellipse, parabola or hyperbola.

Lagrange libration point	A point of equilibrium in the three-body problem, considering the gravity fields of two bodies and the centrigugal force term. Five points exist, lying in the orbit plane of the major body about the central body. Three lie along the line passing through the central to major body.
Lambert's problem	The problem of finding an orbit connecting two positions over a particular time interval.
Lissajous orbit	An 'orbit' about a collinear Lagrange libration point whose periods in and out of ecliptic are unequal.
Low thrust	A propulsive force producing a small resultant acceleration on the spacecraft ($\ll 1$ g). Examples are electric propulsion systems and solar sails.
Major body	The secondary body with the locally dominant gravity field in a particular mission phase, such as a fly-by. Examples are a planet encountered during the course of a trajectory about the Sun or a moon during the course of a trajectory about a planet.
Non-gravitational perturbation	A small acceleration term (compared with the gravity field of the central body) applied to an orbiting object, arising from non-gravitational sources (e.g., low-thrust propulsion, solar radiation pressure, atmospheric drag).
Non-linear programming	A iterative method to determine the solution of an optimisation problem by using gradient information regarding the objective and constraints.
Patch conic	The method of approximating the motion of a spacecraft under the influence of the gravity fields of a central and major body by using a sequence of conic sections (each of which is a solution to a two-body problem).
Resonant orbit	An orbit whose period may be expressed as an integer ratio with the period of the orbit of the major body to which it relates.
Secular perturbation	A perturbing term that effects a net orbit change after a complete revolution. When considered over multiple revolutions the mean ephemeris of the orbit undergoes a progressive evolution.
Specific impulse	Impulse delivered per unit mass of propellant.
Sphere of influence	Locus of points around a major body obtained by considering the perturbing gravitational acceleration of the central body compared with the gravitational acceleration for the central body.
Synodic period	Repeat period when considering the re-occurrence of relative longitudes of two major bodies. Assumes coplanar, circular orbits.

Three-body problem	The problem of motion of a spacecraft under the combined influence of the gravity fields of two massive bodies.
Two-body problem	The problem of motion of a spacecraft under the influence of the gravity field of a single massive body.
Weak stability boundary	Term sometimes used to describe a region under the influence of combined gravity fields (of a major and central body).

AXES SYSTEMS USED IN ILLUSTRATIONS

The figures illustrating transfer trajectories are often drawn over a reference grid. The scaling of the grid is detailed for each plot. It is generally 1 AU from centre to edge with a sub-grid size of 0.1 AU.

The grid lies in the ecliptic and the conventional X axis direction (i.e., to the first point in Aries) is in a vertical direction (i.e., to the top of the page). Details of axes and reference systems are given in Appendix 2.

1

Interplanetary missions

A series of well-established methods may be used for the design of interplanetary missions. Basic tools are used to generate transfers between the planets, but the nature of these transfers reveals a rich set of trajectory types that are available to the mission designer. The issue of leaving a planetary orbit and capture at the target planet must also be considered. Finally, the implications of return missions can be considered, both in the context of robotic exploration and manned missions.

1.1 FUNDAMENTALS OF INTERPLANETARY MISSIONS

In this section, the issues of transferring from planet to another will be considered. This includes the nature of the transfers themselves and Lambert's problem, which is a key aspect of such transfers.

1.1.1 Interplanetary transfers

The planets of the Solar System mostly move in near-circular orbits, remaining close to the plane of the ecliptic. The major exception is Pluto, which not only moves in a significantly elliptical orbit, but also has an orbital plane that is inclined to the ecliptic by more than 10°.

When considering transfers between the planets, it would be tempting to consider their orbits as co-planer and circular. Indeed, such approximations yield a rough order of magnitude results. However, because the planets' heliocentric velocities are very high, any deviation in their direction from the assumed circular tangents can strongly influence the final ΔV required for a transfer between planets.

The properties of the planets' orbits are shown in Table 1.1.1.

Table 1.1.2 shows the orbital energy relative to the Sun as the central body. This energy can be expressed as energy compared with Earth's energy relative to the Sun,

Table 1.1.1. Planet orbit properties.

	sma (AU)	sma (km)	Energy	Period (days)	Eccentricity	Mu	Energy rel Earth
Mercury	0.38709893	5.79E+07	−1.14E+09	87.97	0.20563069	2.22E+13	−6.99E+08
Venus	0.72333199	1.08E+08	−6.10E+08	224.70	0.00677323	3.25E+14	−1.69E+08
Earth	1.00000011	1.50E+08	−4.41E+08	365.26	0.01671022	3.99E+14	0.00E+00
Mars	1.52366231	2.28E+08	−2.90E+08	686.96	0.09341233	4.28E+13	1.52E+08
Jupiter	5.20336301	7.78E+08	−8.48E+07	4,335.36	0.04839266	1.27E+17	3.56E+08
Saturn	9.53707032	1.43E+09	−4.63E+07	10,757.76	0.0541506	3.79E+16	3.95E+08
Uranus	19.1912639	2.87E+09	−2.30E+07	30,708.22	0.04716771	5.83E+15	4.18E+08
Neptune	30.0689635	4.50E+09	−1.47E+07	60,225.02	0.00858587	6.86E+15	4.27E+08
Pluto	39.4816868	5.91E+09	−1.12E+07	90,613.48	0.24880766	4.42E+13	4.30E+08

Table 1.1.2. Planet orbital velocities.

	R_{min} (km)	V at R_{min} (km/s)	R_{max} (km)	V at R_{max}
Mercury	46,001,448	58.976	69,817,246	38.858
Venus	107,474,994	35.259	108,942,304	34.784
Earth	147,096,623	30.287	152,099,177	29.291
Mars	206,655,710	26.498	249,225,938	21.972
Jupiter	741,096,388	13.699	815,828,797	12.444
Saturn	1,348,673,598	10.193	1,508,110,731	9.115
Uranus	2,733,511,855	7.123	2,991,539,939	6.509
Neptune	4,440,286,960	5.497	4,538,878,194	5.378
Pluto	4,433,588,797	6.106	7,321,604,748	3.698

and is shown in Figure 1.1.1. The plot shows that a mission to Mercury requires a greater energy change than missions to the distant outer planets.

The fundamental mechanism of an interplanetary transfer can be best understood by firstly using the co-planar, circular orbit approximation and the application of a Hohmann transfer. The Hohmann transfer is the well-known optimal elliptical transfer technique between two circular orbits. Such a transfer is half of an ellipse, whose perihelion lies at the radius of the inner planet and aphelion at the radius of the outer planet.

The ΔV for the transfer may be evaluated by the following:

$$\Delta V = (V_{pe} - V_{P1}) + (V_{P2} - V_{ap}) \tag{1.1.1}$$

where an outward transfer is assumed from planet 1 to 2, V_{p1} and V_{p2} being the respective planet circular orbit speeds and V_{pe} and V_{ap} being the transfer orbit speeds at perihelion and aphelion.

Figure 1.1.2 shows the mechanism. The Hohmann transfer is used because it is the minimum ΔV transfer, which in turn minimises fuel use.

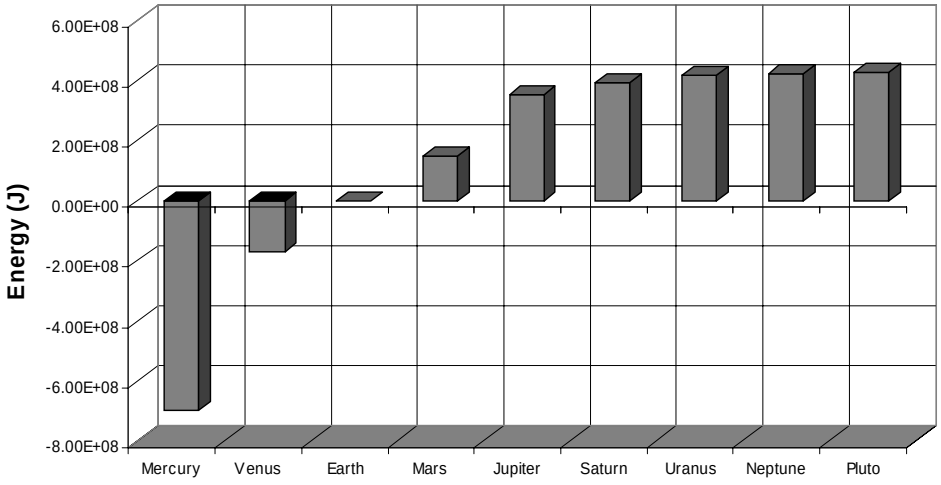

Figure 1.1.1. Planetary orbital energy with respect to the Sun relative to Earth's energy with respect to the Sun.

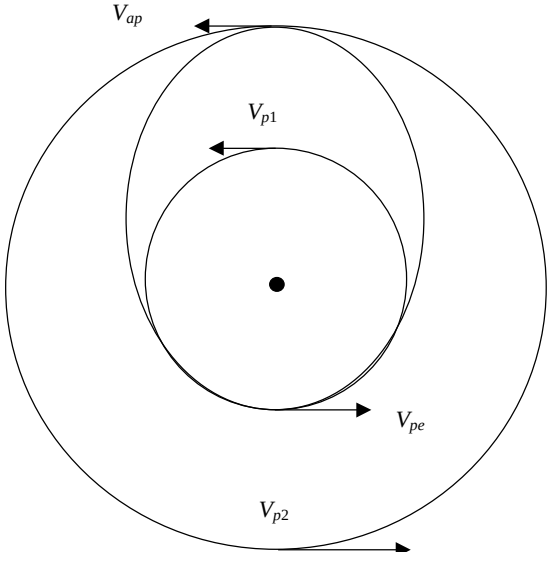

Figure 1.1.2. Hohmann transfer between circular planetary orbits.

The period is determined by the planets defining the transfer; that is, if a is the semi-major axis, $(r_{p1} + r_{p2})/2$, then the duration of the transfer (half a revolution) is expressed by:

$$\frac{\tau}{2} = \pi\sqrt{\frac{a^3}{\mu}} \tag{1.1.2}$$

where r_{p1} is the radius of the orbit of planet 1 and r_{p2} is the radius of the orbit of planet 2. μ is the Sun's gravitational parameter.

The total ΔV is then:

$$\Delta V = \left(\sqrt{2\mu\left(\frac{1}{r_{p1}} - \frac{1}{2a}\right)} - \sqrt{\frac{\mu}{r_{p1}}}\right) + \left(\sqrt{\frac{\mu}{r_{p2}}} - \sqrt{2\mu\left(\frac{1}{r_{p2}} - \frac{1}{2a}\right)}\right) \tag{1.1.3}$$

In this context, ΔV is the sum of speed changes that the spacecraft must undergo from a state co-orbiting the Solar System with the first planet to a state where it co-orbits with the second planet, but neglecting the effects of the gravity fields of both planets. In fact, for small objects in the Solar System, with relatively weak gravity fields, such as asteroids, then this calculation is very close to the actual total ΔV.

The previous discussion is idealistic in several respects, In practice, the transfer problem is more complex, but this type of analysis is generally a very good starting point in assessing the manoeuvre requirements for a planet-to-planet transfer.

When the complete problem is considered, then the following factors must be taken into consideration:

- The planets move in elliptical orbits which therefore effect the relative velocity at departure and arrival.
- The planets all possess some degree of orbital inclination with respect to the ecliptic, and some out-of-ecliptic velocity component is therefore needed.
- The actual locations of the planets must be considered; that is, the previously assumed geometry that planet 2 will be at for the desired true anomaly to rendezvous with the spacecraft.
- For transfers between large objects (any of the nine planets), this ΔV calculation will not in general be the full speed change required. This is because the spacecraft will generally start its journey from an orbit bound to the first planet and end its journey in an orbit bound to the second planet.

These factors are expanded in the following sections. This type of optimum transfer described here is sometimes referred to as a 'conjunction class' transfer. This term arises from the geometry of the location of planet 1 which is in conjunction with planet 2's location at arrival, although there is no true conjunction at either departure or arrival.

Other transfer types beyond this conjunction category will also be considered.

1.1.2 Lambert's problem

One of the fundamental problems of interplanetary missions is to devise a trajectory for a spacecraft that leaves one planet at a certain epoch and then arrives at a second planet at a later epoch. In principle, these departure and arrival epochs may be chosen at will, but not without a significant implication for the ΔV required to implement such a transfer.

This is a manifestation of Lambert's problem, which may stated as follows: given an initial and final position, together with a time of flight between these

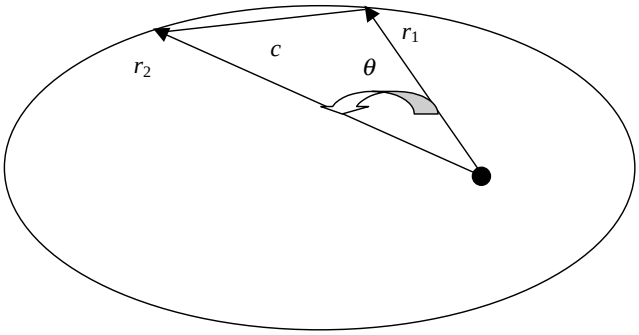

Figure 1.1.3. Lambert's problem.

positions, determine the connecting orbit. This is shown diagrammatically in Figure 1.1.3, where a closed orbit is assumed to link the initial position at planet 1 to the final position at planet 2, where once again r_1 is the radial distance in the spacecraft's orbit when leaving planet 1 and r_2 is the radial distance in the spacecraft's orbit when arriving at planet 2.

Lambert stated that the time of flight between two such positions depends upon three quantities, all defined in the diagram. These are:

- The semi-major axis of the connecting ellipse, 'a'.
- The chord length, c.
- The sum of the position radii from the focus or the connecting ellipse.

The basis of this statement can be obtained from the following analysis. The following derivation was first performed by Lagrange and is described more fully in Battin (see references). Firstly, consider the connecting orbit where the time of flight defines the difference in mean anomalies:

$$M_2 - M_1 = n(t_2 - t_1) = \sqrt{\frac{\mu}{a^3}}(t_2 - t_1) \tag{1.1.4}$$

where M_1 and M_2 are the mean anomalies at points 1 and 2 and n is the mean motion of the connecting orbit. Then, using the relationship between mean and eccentric anomalies given by Kepler's equation:

$$\begin{aligned}(t_2 - t_1) &= \sqrt{\frac{a^3}{\mu}}(E_2 - E_1 - e(\sin E_2 - \sin E_1)) \\ &= 2\sqrt{\frac{a^3}{\mu}}\left(\left(\frac{E_2 - E_1}{2}\right) - e\left(\sin\left(\frac{E_2 - E_1}{2}\right)\cos\left(\frac{E_2 + E_1}{2}\right)\right)\right)\end{aligned} \tag{1.1.5}$$

Using intermediate variables, A, B, where

$$A = \frac{E_2 - E_1}{2} \qquad \text{and} \qquad \cos B = e\cos\frac{E_2 + E_1}{2}$$

$$(t_2 - t_1) = 2\sqrt{\frac{a^3}{\mu}}(A - \sin A\cos B) \tag{1.1.6}$$

The triangle in Figure 1.1.3 can now be considered. The length of the chord connecting the two positions is given by:

$$c^2 = r_1^2 + r_2^2 - 2r_1 r_2\cos\theta \tag{1.1.7}$$

Using the relationships $r_1 = a(1 - e\cos E_1)$ and $r_2 = a(1 - e\cos E_2)$, the following relationships can be found:

$$r_1 + r_2 = 2a(1 - \cos A\cos B) \tag{1.1.8}$$

It may be shown that:

$$c = 2a\sin A\sin B \tag{1.1.9}$$

By definition, the semi-perimeter is:

$$s = \frac{r_1 + r_2 + c}{2} \tag{1.1.10}$$

where s is the semi-perimeter of the connecting triangle between the focus and the two points.

Then, using the intermediate variables α and β, where $\alpha = A + B$ and $\beta = B - A$, Equations 1.1.8, 1.1.9 and 1.1.10 plus some manipulation yields:

$$\sin^2\frac{\alpha}{2} = \frac{s}{2a} \qquad \text{and} \qquad \sin^2\frac{\beta}{2} = \frac{s - c}{2a} \tag{1.1.11}$$

Using these definitions in Equation 1.1.6, the following expression is derived:

$$(t_2 - t_1) = \sqrt{\frac{a^3}{\mu}}((\alpha - \sin\alpha) - (\beta - \sin\beta)) \tag{1.1.12}$$

The solution of the above equation is potentially subject to difficulties in determination of α and β from Equation 1.1.11. Certain ancillary calculations may be made to resolve this. The 'minimum energy' semi-major axis and related variables are defined as:

$$a_m = \frac{s}{2} = \frac{r_1 + r_2 + c}{4} \qquad \sin\frac{\beta_m}{2} = \sqrt{\frac{s - c}{s}} \qquad t_m = \sqrt{\frac{a_m^3}{\mu}}(\pi - \beta_m + \sin\beta_m)$$

Then

$$\beta' = \beta, \pi > \theta > 0 \qquad \alpha' = \alpha, t_m > (t_2 - t_1)$$

$$\beta' = -\beta, 2\pi > \theta > \pi' \qquad \alpha' = 2\pi - \alpha, (t_2 - t_1) > t_m$$

This applies for the case of an elliptical orbit. In certain cases, such as where the transfer time is short, the connecting orbit may be hyperbolic. In this case, the

solution becomes modified to:

$$(t_2 - t_1) = \sqrt{\frac{-a^3}{\mu}}((\sinh\alpha - \alpha) - (\sinh\beta - \beta)) \tag{1.1.13}$$

where

$$\sinh^2\frac{\alpha}{2} = -\frac{s}{2a} \qquad \text{and} \qquad \sinh^2\frac{\beta}{2} = -\frac{s-c}{2a} \tag{1.1.14}$$

noting 'a' is negative in the hyperbolic case.

This confirms the original theorem regarding the relationship between the time difference, the semi-major axis, the sum of the radii and the chord length.

The semi-major axis is now evaluated iteratively from the relationship given in Equation 1.1.12 or 1.1.13. The eccentricity of the transfer orbit may be found after calculating the semi-latus rectum, p:

$$p = \frac{4a(s-r_1)(s-r_2)}{c^2}\sin^2\left(\frac{\alpha+\beta}{2}\right) \tag{1.1.15}$$

or alternatively,

$$p = \frac{4ar_1r_2}{c^2}\sin^2\frac{\theta}{2}\sin^2\left(\frac{\alpha+\beta}{2}\right)$$

and in the hyperbolic case,

$$p = -\frac{4ar_1r_2}{c^2}\sin^2\frac{\theta}{2}\sinh^2\left(\frac{\alpha+\beta}{2}\right)$$

The eccentricity may then be found using $p = a(1-e^2)$.

Equation 1.1.12 can be solved in several ways, but all require an iterative process. To illustrate the nature of the problem, a transfer from Earth to Mars can be considered. The spacecraft leaves Earth on 23 October 2011, and transfer durations of 150, 180 and 200 days are then investigated by varying the arrival epoch at Mars. These two epochs (departure and arrival) specify two radius vectors, from which the quantities 'c' and 's' may be calculated.

Figure 1.1.4 illustrates the highly non-linear nature of the error function. In principle, methods such as Newton–Raphson can be employed to find the solution, but will not always converge, the behaviour depending on the initial estimate of the semi-major axis. Some specialised algorithms have been developed and are described definitively in Battin (see references for this section). Also, multi-revolution transfers may be solved within this problem context and are also described in the references.

The transfer orbit

Having found the semi-major axis and eccentricity of the transfer orbit, the full ephemeris may be derived, so that the initial and final velocities may be calculated. This allows the calculation of the change in the heliocentric velocity vector required when departing from the first planet and then arriving at the second planet.

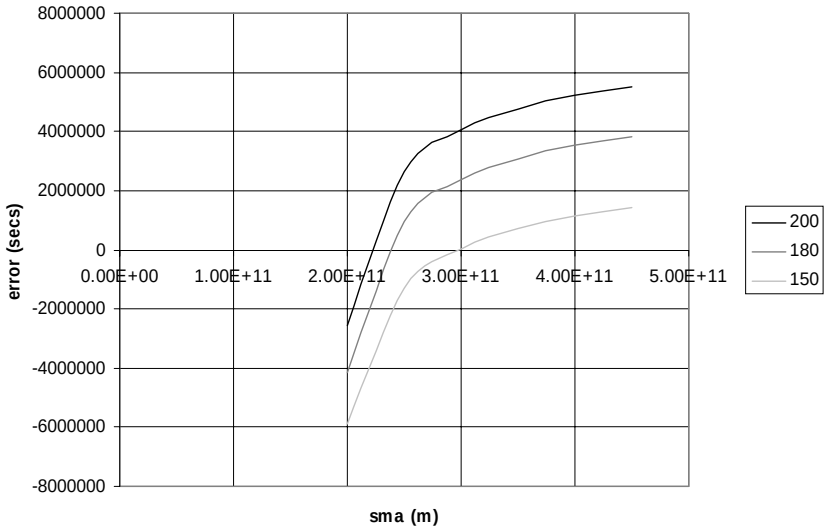

Figure 1.1.4. Error function versus sma. An estimate at the value of semi-major axis solving the equation can be made and substituted into the right-hand side of Equation 1.1.12. Then a plot of error between the left-hand and right-hand sides versus the semi-major axis can be obtained. The solution lies where the error equals zero.

Firstly, consider that the two positions described in the previous section as scalar radii, are in fact vector positions. These correspond to the location of the planetary bodies in question at the epoch of departure and arrival. Therefore r_1 and r_2 will now be denoted as the heliocentric position vectors, $\underline{r}_1$ and $\underline{r}_2$. The transfer orbit is contained within the plane defined by these two vectors. The velocity at these two radii and the full ephemeris of the connecting orbit may be calculated using the following process.

The speed at each position is given by the classical relationship derived from orbital energy:

$$V = \sqrt{2\mu\left(\frac{1}{r} - \frac{1}{2a}\right)} \tag{1.1.16}$$

where μ is the central body gravitational parameter. This is obtained for r_1 and r_2 respectively.

The cosine of the true anomaly (f) at each of the two positions is obtained by:

$$\cos f = \frac{1}{e}\left(\frac{a(1-e^2)}{r} - 1\right)$$

This is evaluated at each of the two radii, yielding $\cos(f_1)$ and $\cos(f_2)$. The sine of the true anomaly at each of the two radii is obtained via the trigonometric identities:

$$\cos(f_1 + \vartheta) = \cos f_1 \cos\theta - \sin f_1 \sin\vartheta = \cos f_2$$

$$\cos(f_2 - \vartheta) = \cos f_2 \cos\theta + \sin f_2 \sin\vartheta = \cos f_1$$

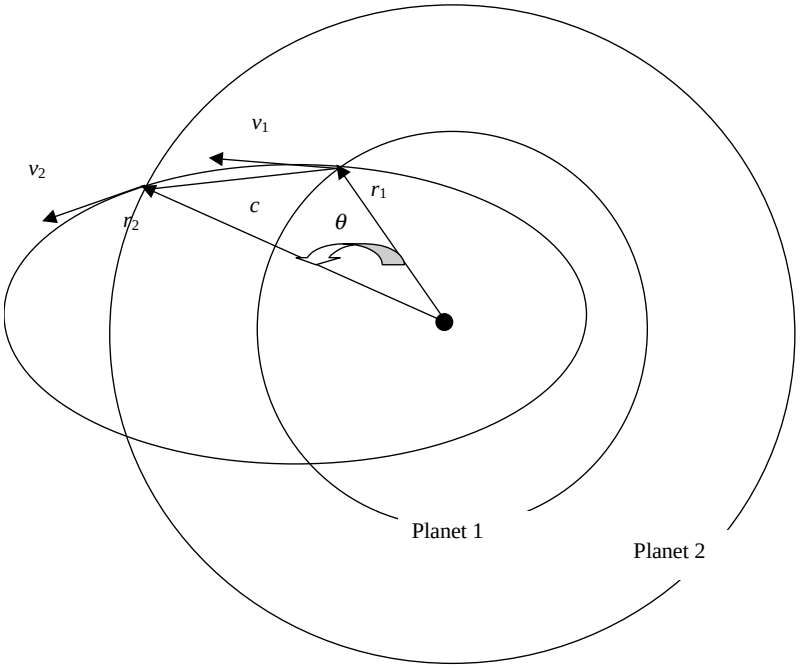

Figure 1.1.5. Lambert's problem for a transfer between two planetary orbits.

The flight path angle (the angle between the velocity vector and the normal to the radius vector in the orbit plane) at each of the two radii (sine and cosine) is given by:

$$V \sin\Gamma = \left(e \sin f \sqrt{\frac{\mu}{a(1-e^2)}} \right) \tag{1.1.17}$$

and also:

$$V \cos\Gamma = \left(\frac{1}{1 + e\cos f} \sqrt{\frac{\mu}{a(1-e^2)}} \right)$$

The Cartesian frame velocity components may now be evaluated as follows. Firstly calculate the normal to the orbit plane (which also contains the angular momentum vector direction, which in turn defines the inclination vector) by:

$$\hat{n} = \frac{\underline{r_1} \wedge \underline{r_2}}{|\underline{r_1} \wedge \underline{r_2}|}$$

The forwards normal to the radius vector, contained within the orbit plane, is then given by (at the two positions):

$$\hat{n}_{F1} = \frac{\underline{n} \wedge \underline{r_1}}{|r_1|} \qquad \text{and} \qquad \hat{n}_{F2} = \frac{\underline{n} \wedge \underline{r_2}}{|r_2|}$$

The velocity vector is then constructed as follows:

$$\underline{V_1} = V_1 \cos\Gamma_1 \hat{n}_{F1} + V_1 \sin\Gamma_1 \hat{r}_1 \quad \text{and} \quad \underline{V_2} = V_2 \cos\Gamma_2 \hat{n}_{F2} + V_2 \sin\Gamma_2 \hat{r}_2 \tag{1.1.18}$$

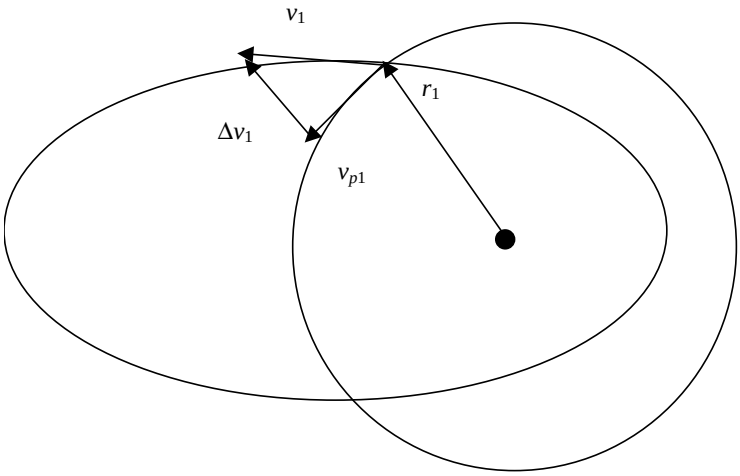

Figure 1.1.6. The velocity change required when departing the first planet.

The velocity change is obtained from a vector subtraction of the transfer orbit velocity at the planet and the planet's velocity.

$$\underline{\Delta V_1} = \underline{V_1} = \underline{V_{p1}} \qquad \text{and} \qquad \underline{\Delta V_2} = \underline{V_2} = \underline{V_{p2}} \tag{1.1.19}$$

where V_{p1} is the velocity vector of planet 1 at departure, V_{p2} is the velocity vector of planet 2 at arrival, ΔV_1 is the velocity vector increment needed to leave planet 1, and ΔV_2 is the velocity vector increment needed to rendezvous with planet 2.

The magnitude of this velocity change is very well approximated by the excess hyperbolic speed of the spacecraft with respect to the planet. (A more detailed description of the motion between planet and Sun-centred motion is included in Chapter 4).

1.1.3 Solutions to Lambert's problem for an interplanetary transfer

The solution of Lambert's problem is illustrated for the example of a transfer from Earth to Mars. The transfer is approached in a series of stages. In this first illustration, it is assumed that both Earth and Mars lie in circular orbits with zero inclination with respect to the ecliptic. This means that the relative orbital phasing between Earth and Mars is retained (the longitude of perihelion and mean anomaly at any reference epoch are unchanged).

Figure 1.1.7 shows contours of constant excess hyperbolic speed V_∞ for transfers from Earth to Mars, over a two year period, starting in 2008. The plot shows the effect of a range of launch epochs and transfer durations. The V_∞ values shown are the sum of V_∞ departing Earth and V_∞ approaching Mars. The contours use steps of 2,000 m/s in the V_∞ total, with the minimum value lying in the 5,000–7,000 m/s range.

The plot clearly shows the presence of a minimum with respect to both transfer duration and launch date. This can be interpreted as the condition where it is

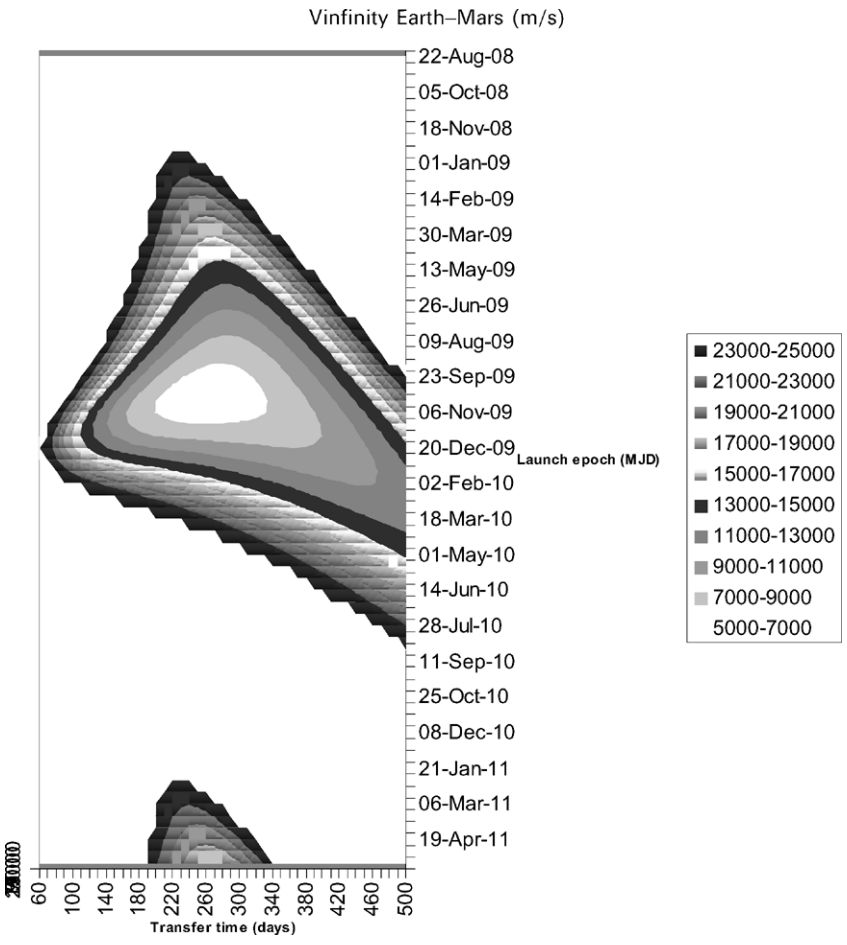

Figure 1.1.7. Transfer V_∞ contours for a transfer from an idealised circular Earth orbit to an idealised Mars circular orbit at zero inclinations.

possible to execute a Hohmann transfer between the two circular orbits. The planets possess the correct relative orbital locations to enable such a transfer for the launch epoch where the minimum occurs. The optimum transfer period is approximately 260 days. This corresponds to the prediction obtained using the methods of the previous sections for a Hohmann transfer. The V_∞ total is 5.7 km/sec, consisting of 3.04 km/sec leaving Earth and 2.68 km/sec approaching Mars. This result will repeat at a later launch date, when Earth and Mars once again reach the required relative orbital geometry at launch. This interval is related to the synodic period of the two planets (discussed later in this chapter).

The second stage of the analysis is to introduce the eccentricities of the orbits of Earth and Mars. The major effect will be due to the eccentricity of Mars' orbit (more than 0.09), as that of Earth is 0.0167.

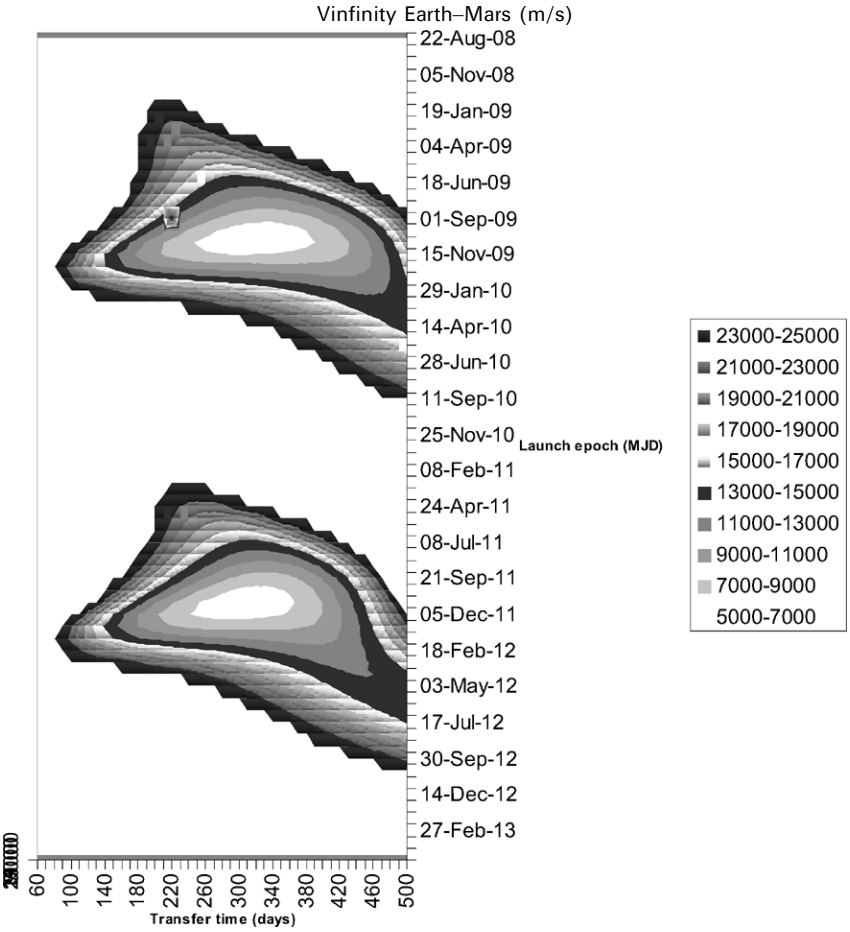

Figure 1.1.8. Transfer V_∞ contours for a transfer from Earth orbit to an idealised Mars orbit possessing zero inclination, but with normal eccentricity.

The period of launch dates is extended to four years in this second example seen in Figure 1.1.8. The main features seen in Figure 1.1.7 are still present. Two local minima are seen, the second corresponding to a later launch case, over two years later, when the favourable Earth–Mars geometry repeats. However, the transfer duration for the first minimum is longer, at approximately 320 days. The second local minimum feature is not an exact repeat of the first, earlier launch date's pattern. This is because although the same favourable transfer relative geometry is obtained, the actual positions of Earth and Mars are changed, so that rendezvous with Mars takes place at a different true anomaly. In this case the optimum transfer duration is approximately 300 days.

The third stage of the analysis is to represent the full martian orbit ephemeris, by now including the inclination. This is approximately 1.85° with respect to the

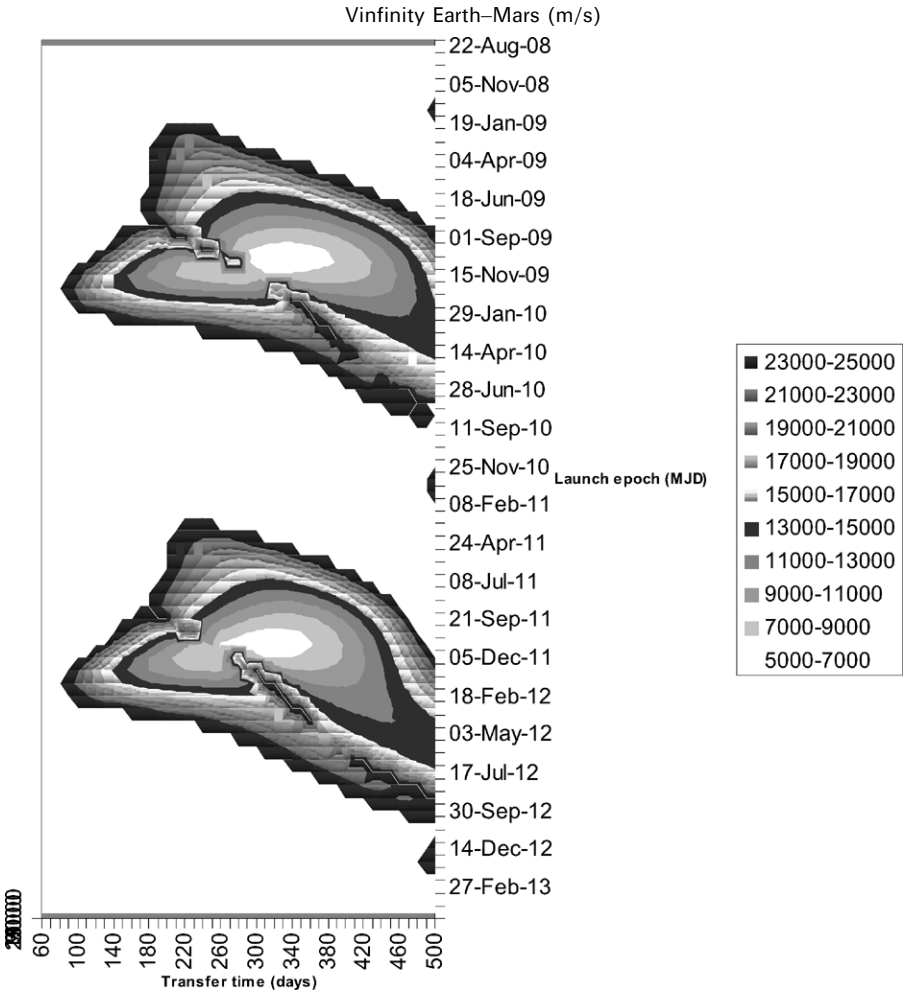

Figure 1.1.9. Transfer V_∞ contours for a transfer from Earth to Mars.

ecliptic. The nature of the local minima now possesses a new feature and may be seen in Figure 1.1.9. This is the occurrence of two minima at similar launch epochs, with different transfer durations. That is, at each occurrence of favourable transfer geometry, two local minimum solutions exist. In the examples shown, the longer transfers have better performance than the shorter ones, but this is not always the case, depending on the precise transfer opportunity under consideration.

This phenomenon of the two local minima can be examined in greater detail. An example launch date is taken that lies close to the second local minimum in 2011. The date is 23 October 2011. From Figure 1.1.9, two minima are expected as the transfer duration evolves. Figure 1.1.10 shows the presence of these minima.

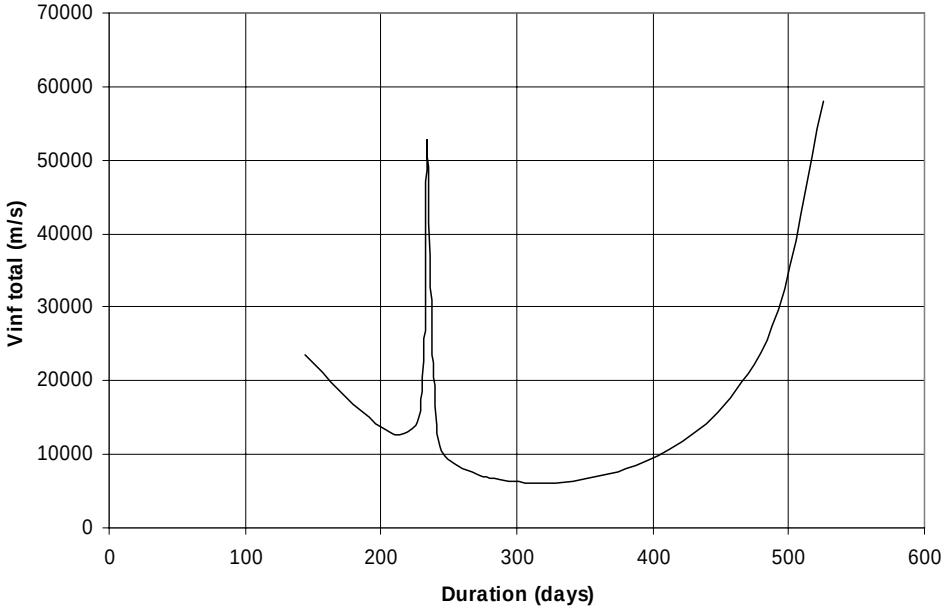

Figure 1.1.10. Total Vinfinity (leaving Earth and approaching Mars) versus transfer duration for a launch on 23 October 2011.

The second minimum is the lower of the two. This is expected, as the optimal launch dates for the two local minima in Figure 1.1.9 are different. However, these minima are separated by a sharp rise in the V_∞ total. This effect arises from the inclination of the Martian orbit. As the transfer approaches a conjunction-type transfer, with aphelion close to the orbital radius of Mars at the rendezvous, it becomes increasingly difficult to achieve the out-of-plane component of the rendezvous position. The solution is to increase the heliocentric inclination of the transfer orbit. This effect is illustrated in Figure 1.1.11, which details a range of transfer trajectories corresponding to different durations in Figure 1.1.10.

Transfers with durations less than the first minimum may be seen as well as transfers in the vicinity of the central maximum. As this maximum is approached, the transfers acquire progressively higher and higher inclinations, until a point is reached where they switch to a near-180-degree change in the location of the transfer orbit ascending node. Therefore, northerly transfers switch to southerly transfers. The upper plot in Figure 1.1.11 shows only the in-ecliptic components and the orbits of Earth and Mars (thick lines). The very short and very long transfers are apparent, corresponding to early and late rendezvous cases. The lower plot in Figure 1.1.11 shows the three-dimensional motion, where the extensive out-of-ecliptic motion can be seen for transfer durations close to the central maximum V_∞ case. The orbits of Earth and Mars are shown by the thicker lines.

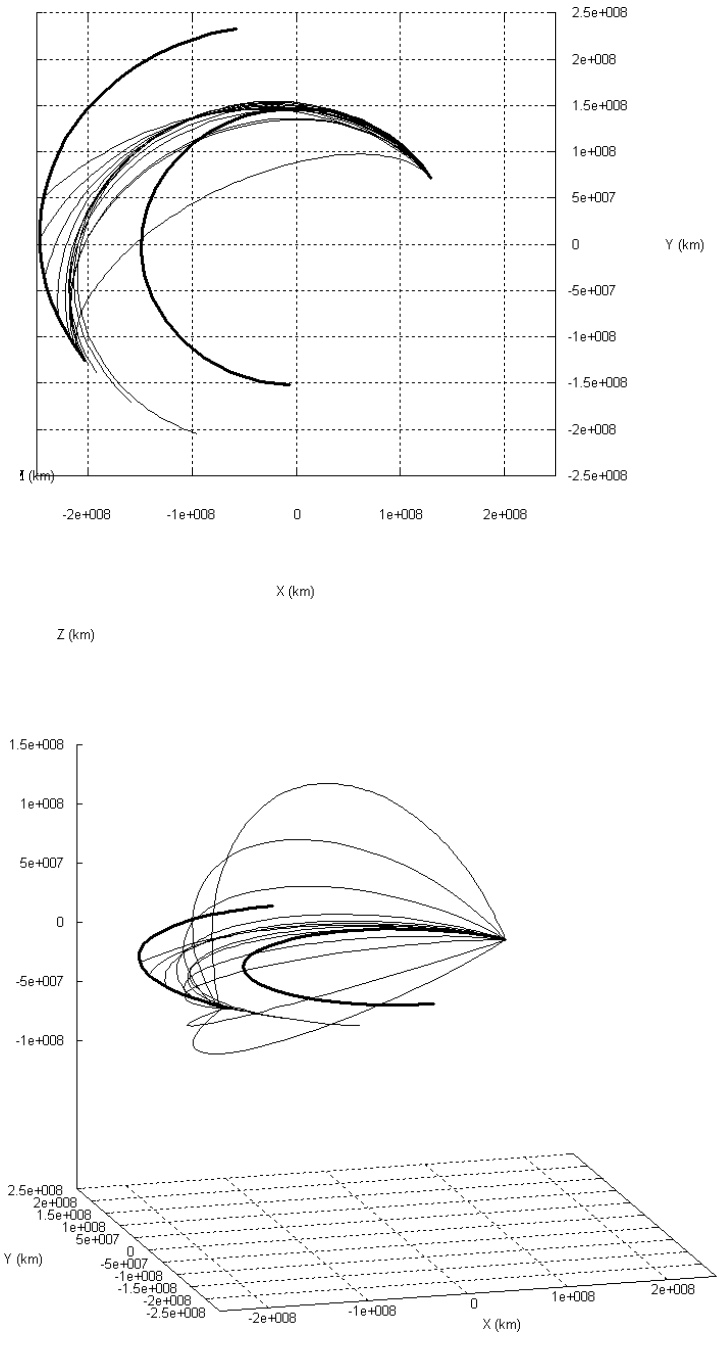

Figure 1.1.11. Transfers from Earth to Mars for a launch on 23 October 2011, for a range of transfer durations spanning the two minima and the central maximum in V_∞.

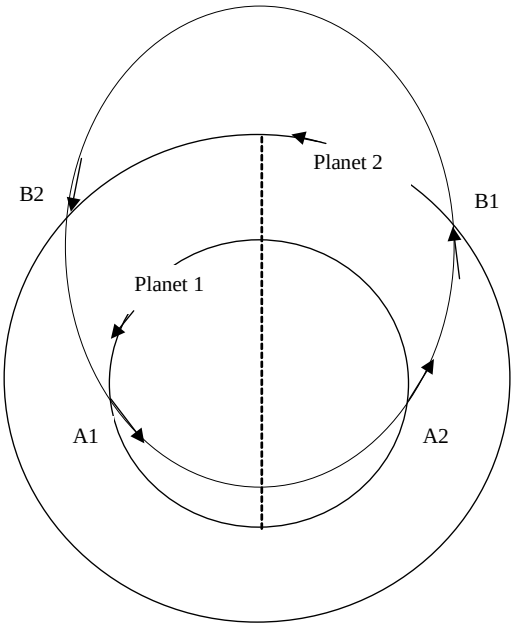

Figure 1.1.12. Transfer types between planets.

1.1.4 Transfer types

If a general transfer ellipse is considered, with spacecraft and planets all rotating about the Sun in the same direction, then four transfer options between two circular orbits may be identified, as shown in Figure 1.1.12.

(a) Route A2 to B1 is initially radially outward bound and arrives in an outwards radial direction at the second planet.
(b) Route A2 to B2 is initially radially outward bound and arrives in an inwards radial direction at the second planet. This route is longer than a).
(c) Route A1 to B1 is initially radially inward bound and arrives in an outwards radial direction at the second planet.
(d) Route A1 to B2 is initially radially inward bound and arrives in an inwards radial direction at the second planet. This route is longer than c).

This does not mean that these transfers are available via the same revolution of the ellipse, as could be inferred from Figure 1.1.12, as the actual phasing of the planets must be considered. It is an illustration of the possible types of transfer between two circular orbits.

Transfer types are sometimes classified. The previous section has demonstrated results for the case of circular planetary orbits where the minimum V_∞ case is a Hohmann transfer with perihelion at Earth and Aphelion at Mars. The change in true anomaly of the transferring spacecraft is 180°. It is possible to achieve transfers

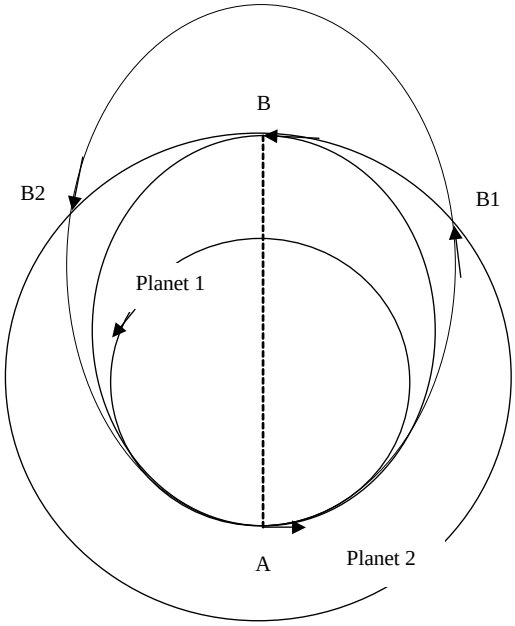

Figure 1.1.13. Optimum transfer between planets and accelerated and delayed arrival.

that use less than or greater than 180° in true anomaly, and these could for example lie on either side of the local minimum shown in Figure 1.1.7.

In Figure 1.1.13, a transfer from A to B is the minimum Vinfinity transfer case, and is the minimum seen in Figure 1.1.7. When compared with the general options discussed previously, then this is the limiting case where A1 and A2 merge for the case of a tangential departure and B1 and B2 merge for the case of a tangential approach. If a horizontal line (a line of constant launch dates) is considered at this optimal epoch in Figure 1.1.6, then variation in the transfer duration means that the spacecraft arrives at planet 2 either before or after the optimum. This is analogous to arrival at B1 or B2, respectively, in Figure 1.1.13, although once again not both through the same elliptical orbit as illustrated, as the phasing of the planet's orbits must be considered. Therefore, arrival at B1 would be via a different elliptical orbit than arrival at B2. The change in true anomaly of the spacecraft transfer orbit is then either less than or greater than 180°. These transfers, categorised by change in true anomaly, are sometimes labelled type 1 and type 2 transfers. This need not correspond to only the tangential departure case, but may be applied to any general departure case.

When the full details of the planet's orbits are considered – in particular its inclination – it is found that there are two local optima, neither of which experiences a 180-degree change in true anomaly for the transfer. The shorter transfer minimum discussed will generally have a true anomaly change of less than 180° and the longer a true anomaly change greater than 180°. Therefore, according to the previous classification, these are type 1 and type 2 transfers respectively.

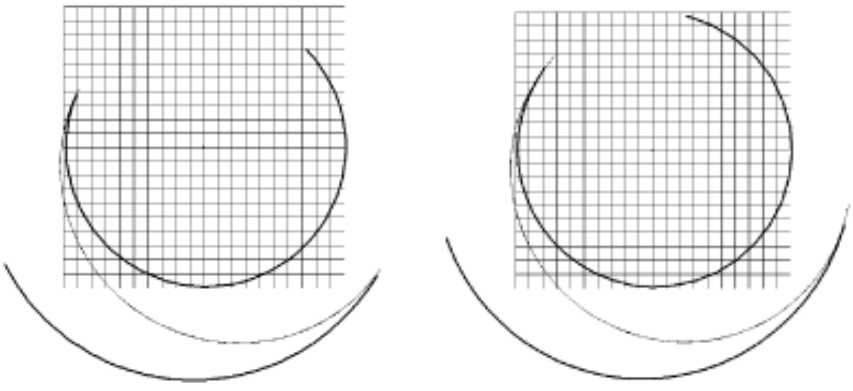

Figure 1.1.14. 2011 transfers from Earth to Mars.

The results in the previous illustrations show that for launches in late 2009 and late 2011 the two local minima with respect to transfer duration have durations of typically 250 and 310 days. Figure 1.1.14 shows the actual minimum V_∞ transfers for launch in 2011. The half grid size is 1 AU, and the dark lines are sections of Earth (inner orbit) and Martian orbits. The dashed lines show the longitudes of Earth at departure and also arrival at Mars.

The 'shorter' and 'longer' transfers take just under and just over 0.5 revolutions.

These optimum transfers, short and long optima, or type 1 and type 2 optima, are also sometimes referred to as 'conjunction class' transfers. From the illustrations of the transfers shown previously, it is clear that no conjunctions occur between the planets at either the departure or arrival epochs. At departure Mars lies ahead of Earth in terms of solar longitude, and when the spacecraft arrives, Mars lies behind Earth in longitude. Therefore, at some point during the transfer, the Sun, Earth and Mars will be aligned in opposition (Mars and the Sun lying in opposite directions as seen from Earth). However, when the transfer trajectory is viewed from beginning to end and the locations of Earth at the start of the transfer and Mars at the end of the transfer are seen, the planets are aligned in a conjunction geometry. However, no actual conjunction occurs.

Table 1.1.3. Short and long local minimum conjunction-type transfers from Earth to Mars with launch in 2011.

Launch date	Vinf Esc (m/s)	Transfer time (days)	Vinf Cap (m/s)	Total Vinf (m/s)	Arrival date
19 Nov 2011	3,019	252	3,691	6,711	28 Jul 2012
10 Nov 2011	2,991	306	2,707	5,698	11 Sep 2012

1.1.5 Launch opportunities

The previous section described the generation of minimum speed change transfers, by comparing excess hyperbolic speed totals. These minima are generally close to a conjunction class transfer (a half-revolution Hohmann transfer). Therefore, when a given launch year is considered, the optimum launch epoch (the closest available launch after a given date) will correspond to dates that approximately satisfy the conjunction transfer condition.

A critical question is how frequently such transfer opportunities arise (when a given pair of planets are considered), and how long the opportunities last? The frequency is determined by the synodic period. This period is that between the repetition of a particular relative orbit geometry between the planets in question, such as a particular difference in solar longitude. Such repetitions occur at fixed intervals for two circular, co-planer planet orbits. If the orbits are assumed circular, then the synodic period is calculated as:

$$\tau_S = \frac{360}{\left(\frac{360}{\tau_{p1}} - \frac{360}{\tau_{p2}}\right)} = \frac{360}{(\omega_{p1} - \omega_{p2})} \tag{1.1.20}$$

where τ_{p1} is the orbital period of planet 1, τ_{p2} is the orbital period of planet 2, ω_{p1} is the angular velocity of planet 1 and ω_{p2} is the angular velocity of planet 2.

The absolute locations of the planets do not repeat at these intervals; only the relative locations repeat. The time between an exact repetition of an absolute transfer geometry is calculated by:

$$\tau_{\text{global}} = n\tau_S = m\tau_{p1} \tag{1.1.21}$$

The time is the number of synodic periods required to generate a whole number of orbits of the departure planet, the period of which is τ_{p1}. This may in practice be a very long period for a precise repeat, and therefore is often approximated, if the 'repeat' geometry departure longitude lies within a few degrees of the original departure longitude.

Table 1.1.4. Planet A/Planet B synodic periods (in years) assuming circular planetary orbits.

	Mercury	Venus	Earth	Mars	Jupiter	Saturn	Uranus	Neptune
Mercury								
Venus	0.3958							
Earth	0.3173	1.5987						
Mars	0.2762	0.9142	2.1354					
Jupiter	0.2458	0.6488	1.0920	2.2350				
Saturn	0.2428	0.6283	1.0351	2.0089	19.8618			
Uranus	0.2415	0.6198	1.0121	1.9241	13.8324	45.5665		
Neptune	0.2412	0.6175	1.0061	1.9026	12.7945	35.9576	170.5157	
Pluto	0.2411	0.6167	1.0041	1.8953	12.4719	33.5207	126.8006	494.6005

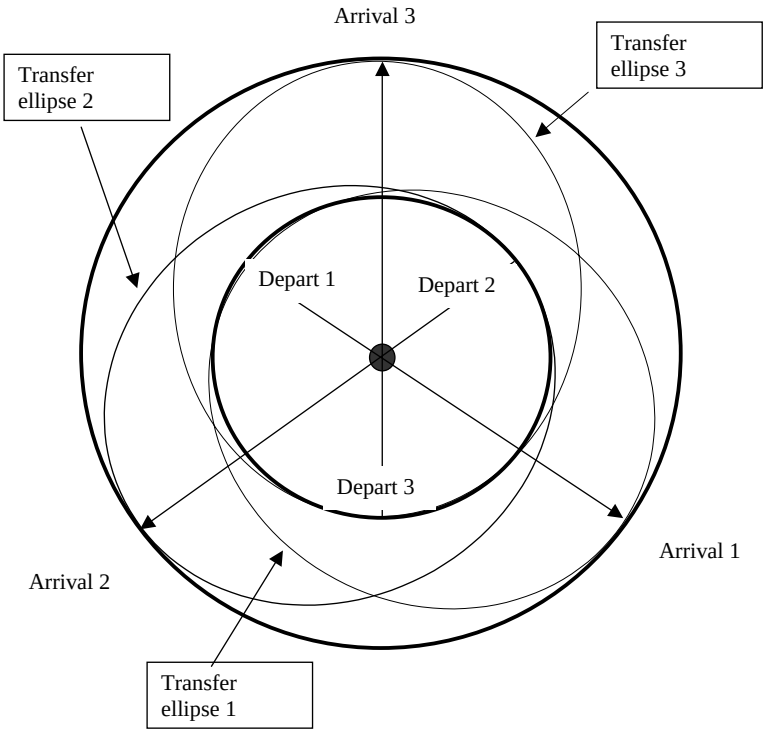

Figure 1.1.15. A set of transfers occurring with a given synodic period and making up a global repeat period after three synodic repeat periods.

Figure 1.1.15 shows the approximate locations of transfer opportunities arising at three synodic periods, globally repeating at the third case. This is the approximate situation for transfers between Jupiter and Saturn. The three arrows indicate the three arrival points at planet 2.

Having established the occurrence of regular launch opportunities, the next question is how long does such a launch opportunity last. This varies with planet to planet, but the information can be obtained from the Lambert problem generated charts previously obtained. In general, the mission will be designed with the fuel capability to execute the nominal transfer (at the optimal launch date) plus some relatively small margin for non-optimal transfers at later/earlier launch epochs. This allowed margin defines the range of possible launch dates, spreading on either side of the optimum launch epoch. Typically a period of 20 to 30 days is considered to be adequate for such a launch window.

1.1.6 Multi-revolution transfers

The transfers described so far involve performing approximately 0.5 revolutions around the Sun, such as in a classical Hohmann transfer. However, many locally

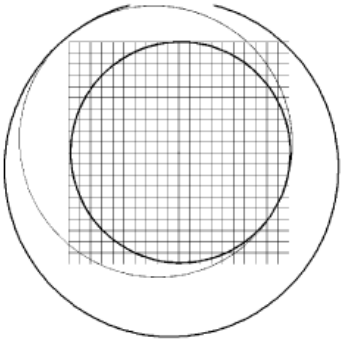

Figure 1.1.16. A 1.5-revolution transfer for a launch in 2011. Earth's and Mars' orbits are shown by the thicker line. The grid is 1 AU from centre to edge.

optimal transfers are possible when the range of possible transfer durations is extended. The key factor is the number of heliocentric revolutions. Instead of 0.5 revolutions, it is possible to use 1.5 or, in principle, n.5 revolutions.

If once again the case of co-planer, circular planetary orbits are considered, then it is immediately apparent that minimum speed change required of the spacecraft is independent of the number of revolutions. The optimal transfer duration is simply incremented by 'n' times the transfer orbit period.

When this technique is applied to real planetary orbits, a number of factors become significant:

- The optimal launch epochs will not be the same as the half-revolution class of transfers, due to the extended transfer period.
- The excess hyperbolic speeds required for departure and arrival will also differ from the half-revolution class transfers, because of the difference in planetary location at the departure and arrival epochs (i.e., when a given departure year is considered).

In practice, half-revolution class transfers are generally preferred to their longer alternatives, but occasionally mission constraints may arise that may make these longer transfers attractive. An example is the case of a mission to Mars, which may carry a lander. It is preferable that landing takes place outside of the martian dust-storm season. This season lasts for typically 6 months per Martian year. The use of a 1.5-revolution transfer opens the possibility for later arrival epochs at Mars, to avoid the dust-storms. Clearly, this depends on the probable launch epoch range.

The local minima for such long transfers occur with transfer durations of typically 700 days. Figure 1.1.17 was evaluated using the assumption that only two manoeuvres are used: departure and arrival. However, the insertion of an additional revolution opens the possibility of optimally inserting a third manoeuvre, in deep space. This may be beneficial, as it provides greater flexibility in transfer duration by changing the period of the first revolution. The option is most effective when a particular, non-optimal departure or arrival epoch is targeted.

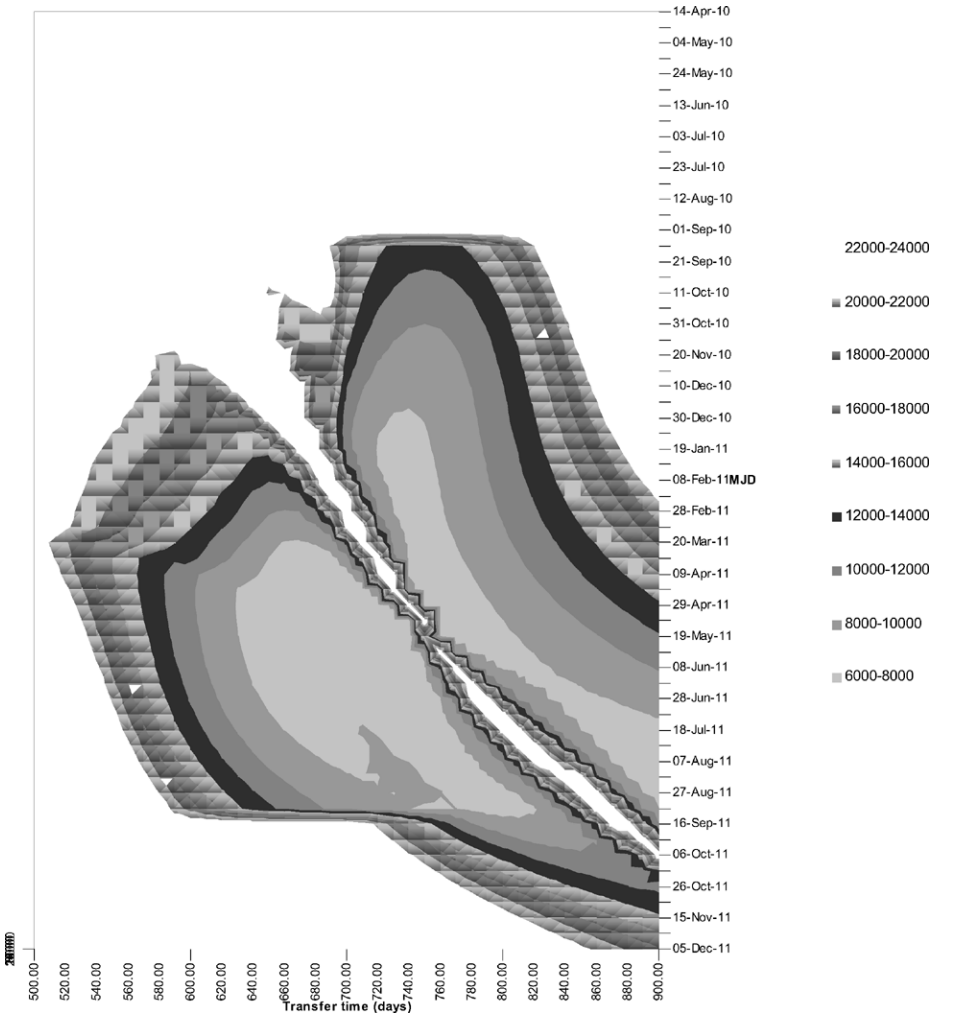

Figure 1.1.17. Extended-duration transfers in terms of Vinfinity contours, for Earth–Mars transfers starting 2011.

Table 1.1.5. One-and-a-half-revolution type transfers from Earth to Mars, with launch in 2011.

Launch date	Vinf Esc (m/s)	Transfer time (days)	Vinf Cap (m/s)	Total Vinf (m/s)	Arrival date
24 May 2011	2,855	710	2,782	5,637	3 May 2013

1.2 LEAVING A PLANET

The previous sections discussed the ΔV required to execute interplanetary transfers, in terms of the speed change relative to the planetary orbits. This has now to be related to the actual manoeuvre ΔVs needed to achieve these conditions. The problem of motion when leaving a planet is potentially complex, as the spacecraft starts its journey in a region where the planet's gravity field dominates the motion, transfers through a zone where there are two comparable gravity fields (Sun and planet), and then reaches a zone where only the Sun's gravity is of importance.

In the following discussion, some basic assumptions will be made by which this motion can be approximated. This motion will subsequently be examined in more detail.

1.2.1 Escape orbits

More than one strategy could be considered for an escape from a planet into an interplanetary transfer orbit. Two options are described here.

One means of calculating the manoeuvre ΔV would be to calculate the speed change needed to accelerate from the first bound orbit about the initial planet to a parabolic orbit with respect to that planet. As the spacecraft reaches a large distance from the first planet (typically several millions of kilometres) its speed with respect to that body tends towards zero (if the Sun's gravity is neglected), and so a planet co-orbiting state is achieved approximately. The position offset from the planet on reaching this state (millions of kilometres) is relatively small when compared with interplanetary distances (hundreds of millions of kilometres).

This would therefore imply a four-manoeuvre transfer:

- Burn 1 to reach parabolic orbit from planet 1.
- Burn 2 to accelerate into heliocentric transfer ellipse.
- Burn 3 to accelerate to planet 2 orbit speed.
- Burn 4 to decelerate from parabolic orbit with respect to planet 2.

The ΔV required to reach such a speed, from an initial bound orbit at the planet, is then given by:

$$\Delta V = \sqrt{\left(\frac{2\mu}{r_{pl1}}\right)} - \sqrt{\frac{\mu}{r_{pl1}}} \tag{1.2.1}$$

This applies for the example where the spacecraft is initially in a circular orbit of radius r_{pl1}. μ is the gravitational parameter for the planet.

However, such a scheme would be quite inefficient for a spacecraft with the capability to apply near-instantaneous speed changes (an impulsive ΔV). Such strategies as just described are only efficient where a spacecraft carries mixed propulsion types, including a high specific impulse (but typically low-thrust) system to achieve the deep-space accelerating manoeuvres.

A spacecraft with the capability to apply only high-thrust, moderate specific impulse manoeuvres must rely on utilising the gravity field of the initial planet to

the greatest extent. A hyperbolic orbit about a planet still has a non-zero speed even at infinite distance from the planet (if no other gravity field than the planet's were considered). Therefore, when at several millions of kilometres, its speed relative to the planet tends towards the 'excess hyperbolic velocity'. The excess velocity targeted is that needed to achieve the interplanetary transfer, as this now is approximately equal to the effective departure speed from the planet within the heliocentric domain. This quantity can be calculated from:

$$V_\infty = \sqrt{\frac{-\mu}{a}} \tag{1.2.2}$$

The direction of the excess hyperbolic departure vector can be chosen by correctly locating the orbit plane and the pericentre of the initial hyperbolic orbit. The asymptotic departure direction within the orbit plane is given by:

$$\theta = \cos^{-1}\left(-\frac{1}{e}\right) \tag{1.2.3}$$

where θ is the maximum true anomaly, and where the velocity vector is asymptotically aligned with the radius vector. Any component of the required interplanetary departure velocity vector that lies out of the planet's equatorial plane (the declination of the departure vector) must be achieved by using an initial planetary orbit with sufficient inclination to reach such a declination. This may depend on the launcher capability (but is discussed in a subsequent section, 'Interplanetary Departure Implications').

The ΔV required to reach such a speed, from an initial bound orbit at the planet, is then given by:

$$\Delta V = \sqrt{\left(\frac{2\mu}{r_{pl1}} + V_\infty^2\right)} - \sqrt{\frac{\mu}{r_{pl1}}} \tag{1.2.4}$$

for the example where the spacecraft is initially in a circular orbit of radius r_{pl1}, or

$$\Delta V = \sqrt{\left(\frac{2\mu}{r_{pl1}} + V_\infty^2\right)} - \sqrt{2\mu\left(\frac{1}{r_{pl1}} - \frac{1}{(r_{pl1} + r_{apl1})}\right)} \tag{1.2.5}$$

for a general elliptical orbit with apogee a_{p1}.

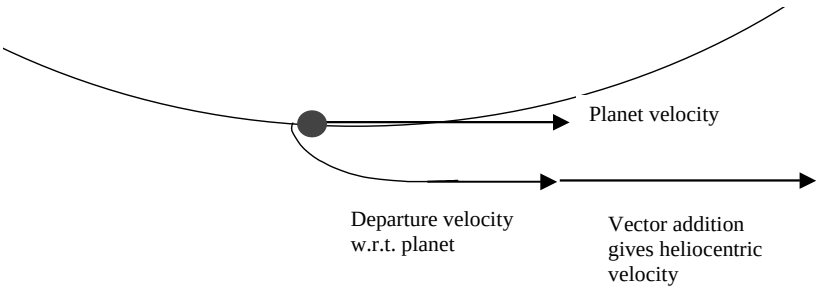

Figure 1.2.1. Departure orbit geometry.

The ΔV needed to reach a range of excess hyperbolic speeds from initially elliptical Earth orbits is shown in Figure 1.2.2.

This illustrates the point that escape planetary transfer manoeuvres are most efficiently performed when deep within the planet's gravity field, rather than when accelerating in deep space.

Figure 1.2.3 illustrates the point that injection to a high-pericentre initial orbit is not efficient in terms of reaching a subsequent escape trajectory.

Figure 1.2.4 shows the ΔV needed to reach the departure excess hyperbolic speeds for conjunction-type transfers through the Solar System. The initial Earth orbit is 500 km perigee altitude and 36,000 km apogee altitude. The ΔV to capture from the approach excess hyperbolic velocity at the target planet is also included. The orbit at the target planet has the same altitudes as the departure orbit. The actual radius of apocentre of the target, therefore varies considerably with the different radii of the planets.

1.2.2 Orbiting a planet

Due to significant differences in planetary mass throughout the Solar System, considerably different energies are required to reach a common orbit. In the following example, the orbit is chosen to have a semi-major axis of 100,000 km. This therefore implies different altitudes with respect to each planet (for the example of a circular orbit).This bound orbit energy deficit with respect to a zero energy orbit is shown in Figure 1.2.5.

The logarithmic plot shows that reaching this orbit about Jupiter requires a much greater insertion energy than, for example, such an orbit about Mars (over 1,000 times more). In fact, the energy deficit below escape, for a spacecraft orbiting Jupiter at such a radius, is comparable with that of the orbit of Venus when considered relative to the heliocentric zero-energy level.

This could imply that reaching an orbit about, for example, Jupiter is extremely difficult. However, advantage may be taken of special techniques in reaching such an orbit. Such methods are discussed in detail in Chapter 4.

1.2.3 Intermediate launch and apogee raising

The preceding discussion has shown that in order to reach the required interplanetary transfer, the spacecraft must reach a suitable speed at departure from the initial planet. This can be provided by a launch vehicle.

Most launch vehicles consist of multiple stages, to maximise the payload mass that they can inject into orbit. The required escape velocity is therefore achieved by the final or upper stage of the launcher.

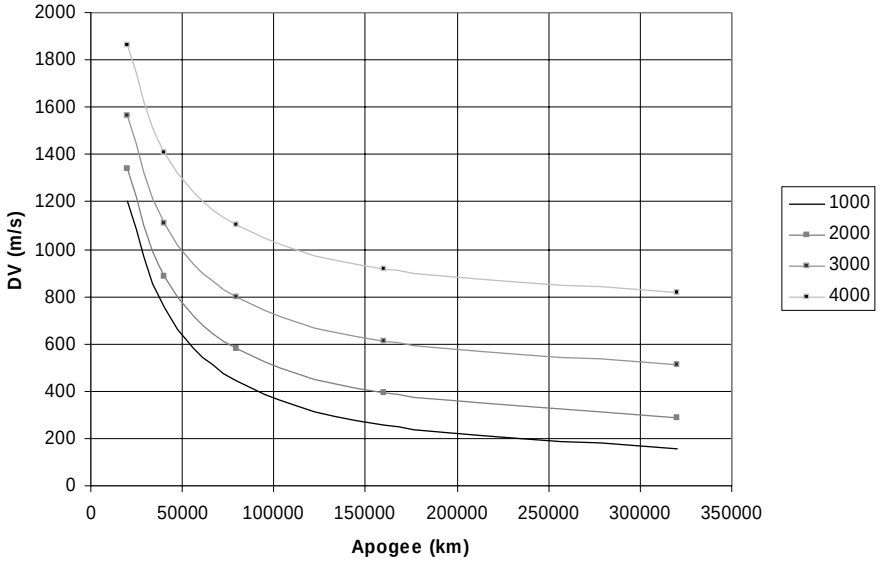

Figure 1.2.2. Apogee altitude vs pericentre ΔV to reach a given Vinfinity with perigee altitude at 200 km. In this first case the perigee altitude is at 200 km. Increase in the target excess hyperbolic speed requires a much smaller change in perigee velocity than the change in hyperbolic excess. Target V_∞ values are 1000 to 4000 m/s in this case.

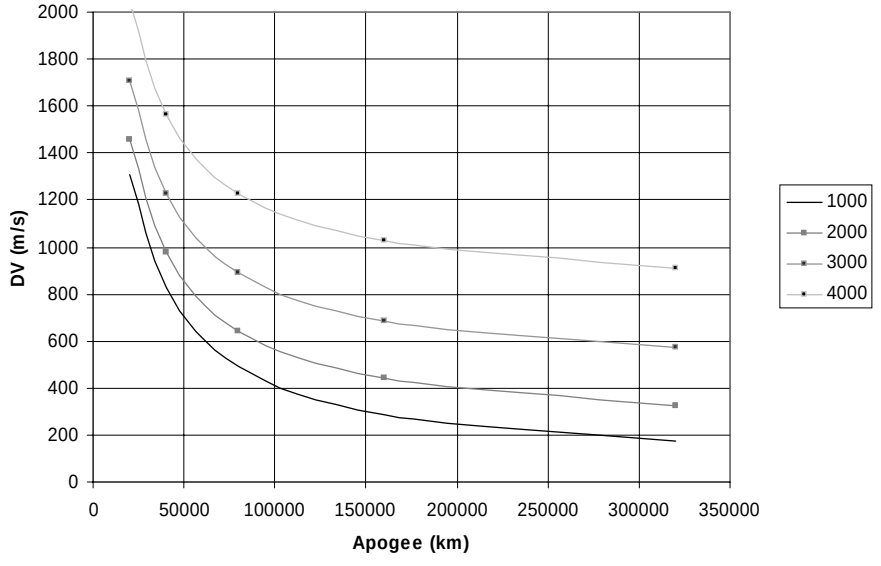

Figure 1.2.3. Apogee altitude vs pericentre ΔV to reach a given Vinfinity with perigee altitude at 2000 km. A second example is taken where a much higher perigee is considered at 2000 km. In this case, the ΔV needed to raise apogee to a given excess hyperbolic speed target is increased.

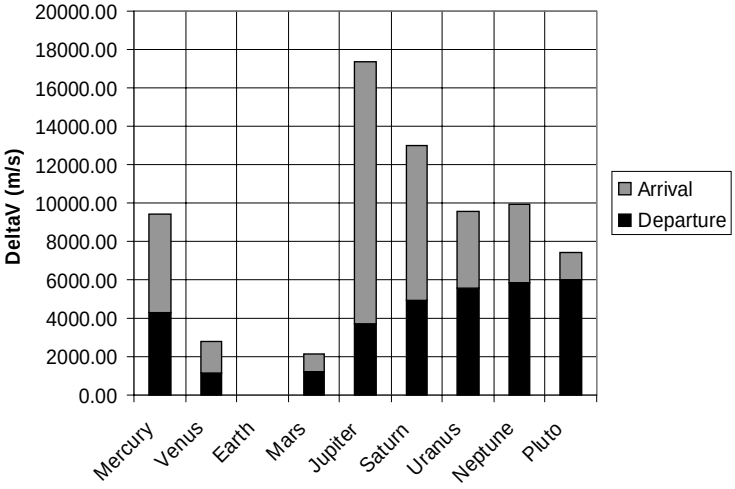

Figure 1.2.4. ΔV required to reach required excess hyperbolic speed for conjunction-class transfers from Earth.

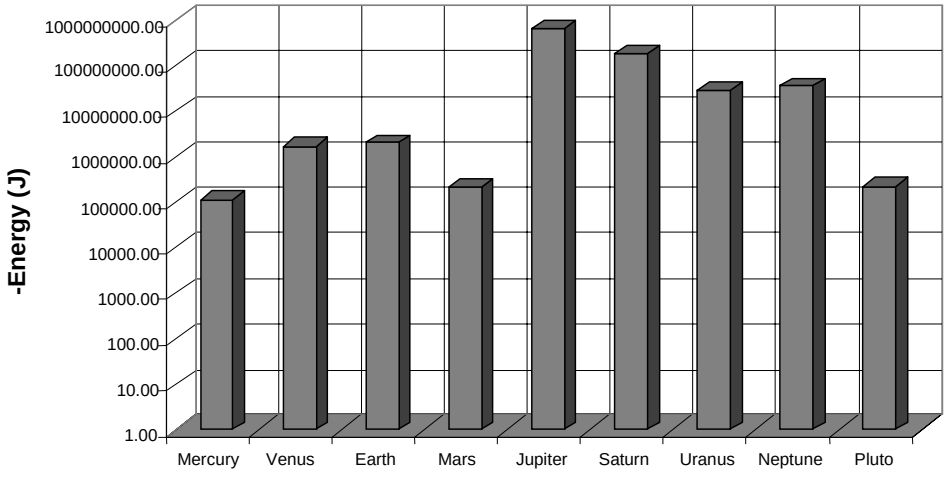

Figure 1.2.5. Orbital energy per unit mass of a 100,000-km semi-major-axis orbit with respect to the planet escape condition.

There will be an upper mass limit that can be injected into a given escape orbit. This can be predicted via application of the classical rocket equation:

$$m_f = m_0 \exp\left(\frac{-\Delta V}{Isp * g_0}\right)$$

where m_0 and m_f are the initial and final masses at the start and end, respectively, of the final stage burn. ΔV is the speed change implemented by the spacecraft

propulsion system. This is determined by the time integral of the spacecraft acceleration due to propulsive forces. *Isp* is the specific impulse of the rocket engine, determining the ratio of fuel usage to thrust:

$$Isp = -\frac{Thrust}{\dot{m} * g_0}$$

These relationships are discussed in Chapter 2.

The initial mass consists of the upper stage dry mass (m_{LDry}), the mass of fuel on-board the launcher upper stage (m_{Lfuel}), and the total mass of the spacecraft to be injected (m_{SC}).

$$m_0 = m_{LDry} + m_{Lfuel} + m_{SC}$$

The final mass (m_f) is achieved when all fuel is burnt, and is therefore:

$$m_f = m_{LDry} + m_{SC}$$

Direct injection performance

In the following discussion it is first necessary to derive the performance available by direct injection by the launcher. The speed change, or ΔV, is determined by the difference between the required escape velocity and the speed at the start of the final stage burn.

If this manoeuvre were effectively impulsive, then the speed change, or ΔV, could be determined by the difference in perigee speeds at the start and end of the burn. Such a burn is most efficiently applied at perigee, as the manoeuvre is effectively raising the apogee. The ΔV would then be given by Equation 1.2.5.

This direct injection performance may be derived as follows. In this simplified analysis it is assumed that no orbit plane changing is required. Assume that at start of its final stage burn the launcher lies in a parking orbit, such that the perigee speed is given by:

$$V_{parkp} = \sqrt{2\mu\left(\frac{1}{r_{parkp}} - \frac{1}{(r_{parkp} + r_{parka})}\right)}$$

where r_{parkp} is the pericentre radius of the parking orbit and r_{parka} is the apocentre radius of the parking orbit.

At the end of the burn needed to reach the target orbit, the new perigee speed is:

$$V_{\text{int}erp} = \sqrt{2\mu\left(\frac{1}{r_{\text{int}erp}} - \frac{1}{(r_{\text{int}erp} + r_{\text{int}era})}\right)}$$

where $r_{\text{int}erp}$ is the pericentre radius of the target orbit, $r_{\text{int}era}$ is the apocentre radius of the target orbit. If the manoeuvre were impulsive, the pericentre radius of the intermediate orbit would be the same as that of the parking orbit. Therefore, in such a case the ΔV required is $\Delta V = V_{\text{int}erp} - V_{parkp}$. If the manoeuvre is not impulsive, then a loss term must be added to find the total ΔV to be applied by the propulsion system.

Here, if the target orbit is bound then the target apocentre is positive, and if an escape orbit is targeted then the implied negative semi-major axis can be converted to an equivalent target apocentre, which will also be negative.

The speed change is accomplished by the main engine (or engines) of the upper stage. These engines are generally capable of delivering a high thrust-to-mass ratio, and so the 'losses' due to the spatial distribution of the burn (non-impulsive burn) are low. This issue will be considered in the following sections.

The mass directly injected by the launcher to this orbit is therefore:

$$m_f = (M_{LDry} + M_{SC}) = m_0 \exp\left(\frac{-(V_{\text{int}\,erp} - V_{parkp}}{Isp_L * g_0}\right) \tag{1.2.6}$$

where M_{LDry} is the dry mass of the launcher (mass after fuel is burnt to depletion), M_{SC} is the total mass of the spacecraft, m_0 is the initial total mass of the upper stage, and Isp_L is the specific impulse of the launcher propulsion system.

It is assumed that the total all-up mass of the upper stage (including the spacecraft mass) at the start of the upper stage burn cannot exceed an upper limit. The speed at the start of the upper stage burn is also assumed to be fixed. This would correspond to the situation where the same parking orbit is always used.

The mass in parking orbit is then made up of the stage dry mass, the fuel mass and the spacecraft mass. The ΔV required determines the ratio of spacecraft mass to fuel mass. The fuel mass is calculated by:

$$m_{fuel} = m_0\left(1 - \exp\left(\frac{-\Delta V}{Isp_L * g_0}\right)\right) \tag{1.2.7}$$

The maximum spacecraft mass that can be achieved is:

$$m_{SC} = m_0 - m_{fuel} - m_{LDry} = m_{0\,\max} \exp\left(\frac{-\Delta V}{Isp_L * g_0}\right) - m_{LDry} \tag{1.2.8}$$

where the initial mass, m_0, is always the maximum mass for the upper stage – $m_{0\,\max}$ if the mass of the spacecraft is to be maximised.

As the ΔV increases, then the fuel mass increases and so the spacecraft mass that may be injected decreases. A limiting ΔV is found when the spacecraft mass reaches zero, and therefore illustrates a fundamental limit in launcher injection orbit capability.

However, any such upper stage will in general have a fixed fuel tank size and therefore an upper limit in available fuel mass: $m_{fuel\,\max}$.

On reaching this limit, the required ΔV can be achieved only by reducing the mass injected into the parking orbit, with implications for the achievable spacecraft mass injected into the final orbit. If the spacecraft is fully fuelled, then the following expression shows the relationship between the initial mass of the upper stage and the ΔV that is available.

$$m_0 = \frac{m_{fuel\,\max}}{\left(1 - \exp\left(\frac{-\Delta V}{Isp_L * g_0}\right)\right)}$$

and therefore

$$m_{SC} = \frac{m_{fuel\,\max} \exp\left(\dfrac{-\Delta V}{Isp_L * g_0}\right)}{\left(1 - \exp\left(\dfrac{-\Delta V}{Isp_L * g_0}\right)\right)} - m_{LDry}$$

or:

$$m_{SC} = m_0 - m_{fuel\,\max} - m_{LDry}$$

The relationships between the total upper stage mass, the fuel mass and the spacecraft mass for a typical stage are shown in Figure 1.2.6. An example of an intermediate performance launcher is taken. The maximum upper stage mass that can be injected into a defined parking in this case is assumed to be ten tonnes. The parking orbit is a 200 km altitude circular orbit. The fuel tank limit of the upper stage is assumed to be 6.5 tonnes. The dry mass of the launcher upper stage is assumed to be 1.2 tonnes. The two parts of Figure 1.2.6 show the maximum upper stage mass of ten tonnes can be fully utilised for this range of target, high elliptical orbits, as the fuel mass required for the perigee speeds that must be reached does not meet the fuel tank limit. In the lower diagram, the specific impulse assumed for the launcher was 330 sec.

The analysis can be extended to Earth escape orbits, where the perigee target velocity is further increased. The full tank fuel mass can be used only to an injection orbit target of approximately 1 km/sec excess hyperbolic speed, or a perigee speed of just under 11,050 m/s. Below this target the fuel load required is less than the 6.5-tonne limit.

This is one example of a launcher performance, and many variants are possible, depending on:

- Maximum lift capability into the parking orbit, determining maximum upper-stage mass.
- Fuel tank limits of the upper stage.
- Dry mass fraction of the upper stage.
- Specific impulse of the upper-stage propulsion system.

However, qualitatively similar behaviour may be found for other launcher examples. Further examples of launcher variants are presented in the appendices. Launch vehicle performance data may be found in the references for this section.

Optimising injection performance

Using a strategy of a launch vehicle upper stage to directly inject the spacecraft to its target orbit may not maximise the mass that can be injected into that orbit. To derive the maximum possible injection mass, it is necessary to consider the possibility of the spacecraft performing its own manoeuvres, after injection into an intermediate orbit by the launcher. Such an intermediate orbit would in general be elliptical, with an apogee radius that must be optimised to achieve the maximum escape mass.

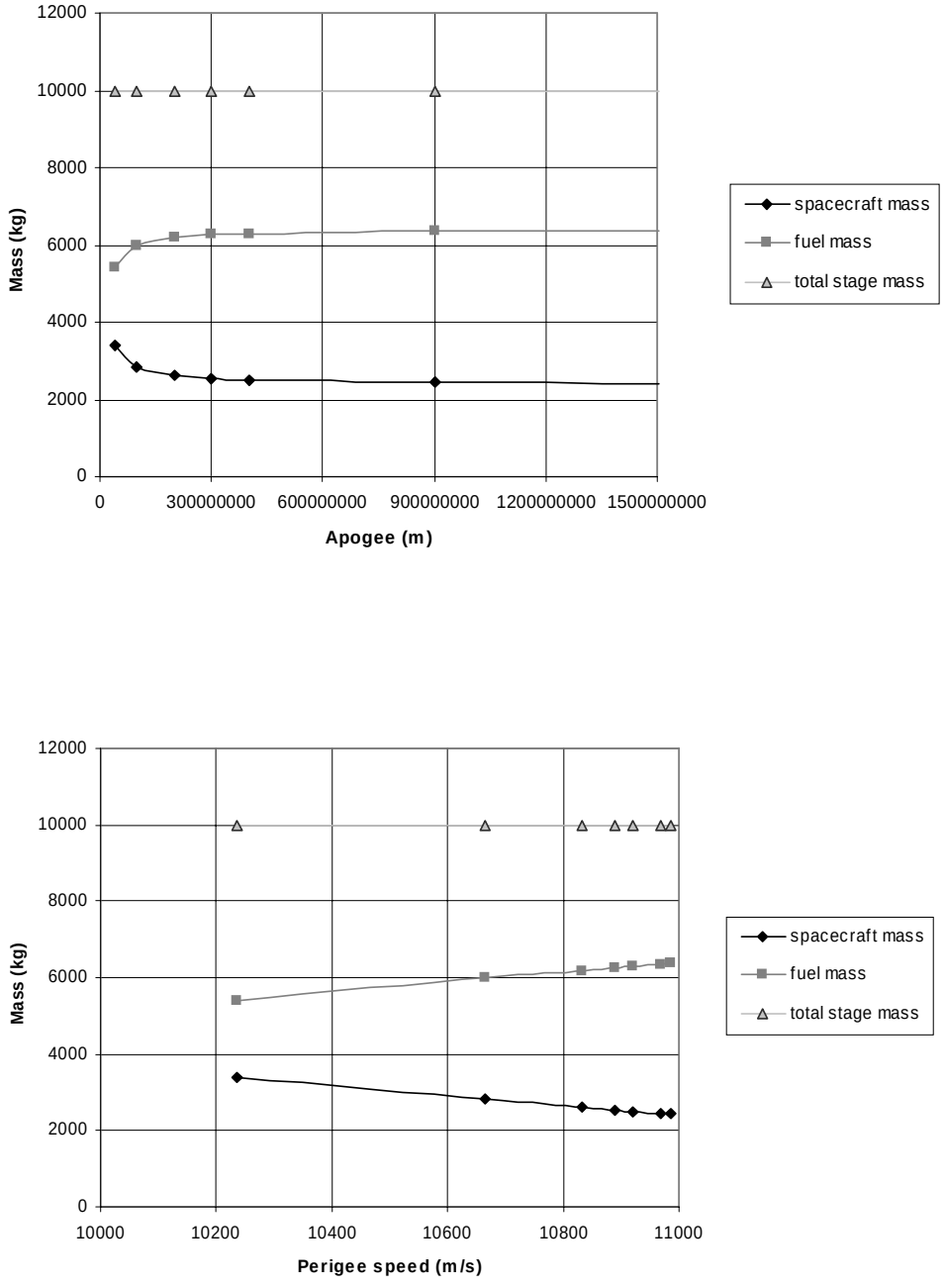

Figure 1.2.6. Fuel tank limited performance for spacecraft injection to high apogee and elliptical orbits. In the second figure, the mass components are plotted against the perigee speed that is required to reach the apogee shown in the first figure.

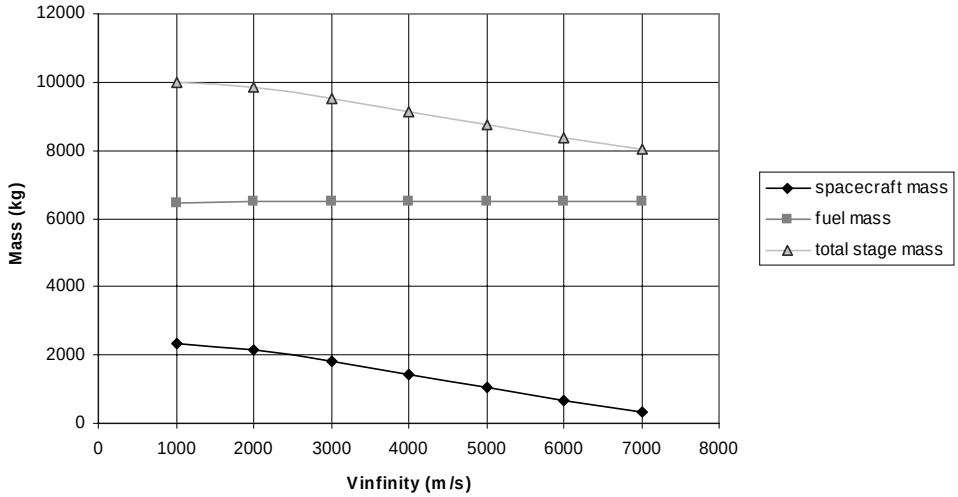

Figure 1.2.7. Fuel tank limited performance for spacecraft injection to high apogee and hyperbolic orbits.

The spacecraft mass may therefore be broken down into the following components:

$$m_{SC} = m_{SCpay} + m_{SCprop} + m_{SCfuel} = m_0 \exp\left(\frac{-\Delta V}{Isp_L * g_0}\right) - m_{LDry} \qquad (1.2.9)$$

m_{SCpay} is the 'useful mass' of the spacecraft, in this case, the basic spacecraft mass, including scientific payloads plus the spacecraft service modules (i.e., those equipments to maintain and support the science payloads), plus the fuel mass needed to execute any further transfer manoeuvres after the escape manoeuvre to the departing transfer orbit is performed (e.g., injection into a target planet orbit). m_{SCprop} is the mass associated with the spacecraft's own propulsion system needed to perform the manoeuvres from the intermediate injection orbit, to reach the target orbit. m_{SCfuel} is the fuel mass that the spacecraft needs to reach the departing target orbit, after launcher injection to the intermediate orbit.

The ΔV here is that needed to inject the upper stage and spacecraft to the intermediate apogee orbit, and therefore:

$$m_{SCpay} = \left(m_0 \exp\left(\frac{-\Delta V_a}{Isp_L * g_0}\right) - m_{LDry}\right) \exp\left(\frac{-\Delta V_b}{Isp_{SC} * g_0}\right) - m_{SCprop} \qquad (1.2.10)$$

where Isp_{SC} is the specific impulse of the spacecraft propulsion system, ΔV_a is the ΔV applied by the upper stage propulsion, and ΔV_b is the ΔV applied by the spacecraft. Each of these terms will consist of a speed change plus a loss term.

The constraint on total ΔV must apply:

$$\Delta V + \Delta V_{aLoss} + \Delta V_{bLoss} = \Delta V_a + \Delta V_b \qquad (1.2.11)$$

ΔV_{aLoss} is the 'loss' in the ΔV applied due to the spatial distribution of the burn, for the upper stage. This is given a nominal value of 2.5% in these examples.

ΔV_{bLoss} is the 'loss' in the ΔV applied due to the spatial distribution of the burn, for the spacecraft. The thrust available from the spacecraft's main engine generally tends to be more limited than that of an upper stage, but could itself be a mission optimisable parameter. This loss depends on the orbit raising strategy and will differ significantly with the target orbit.

This expression concerning spacecraft payload mass may be maximised with respect to the ΔV split. The result will be to determine if an intermediate injection orbit can be found into which the launcher upper stage should inject the spacecraft.

In the following examples, the specific impulse of the spacecraft propulsion system is assumed to be lower than that of the upper stage (at 320 sec compared with 330 sec). The mass of the spacecraft propulsion system may be treated parametrically. In this example, as an approximation, it is considered to be a fixed fraction of the fuel mass used by the spacecraft. The effects of different values for this fraction are now compared. The upper stage mass is assumed to be fixed at 10 tonnes, as in the previous examples.

The optimum intermediate injection orbit will be influenced by the choice of the final target orbit. Therefore, the first example is that of a transfer orbit to the Earth–Sun Lagrange points, where the target apogee is 1.5 million km.

The full mass capacity of the launcher – 10 tonnes in this example – can be used for the full range of intermediate apogee radii considered here. The spacecraft mass shown in Figure 1.2.8 includes the fuel and propulsion required to eventually reach the target apogee of 1.5 million km.

The results for this choice of target orbit indicate that the optimum apogee radius is 25,000–45,000 km, depending on the propulsion mass fraction (Figure 1.2.9).

Examples of higher-energy target orbits can now be considered. A range of Earth escape orbits, with excess hyperbolic speeds of 1–5 km/sec, are considered in Figure 1.2.10.

In Figure 1.2.10 the ΔV loss assumed is 10%. This is higher than the previous case because the speed change required to reach the target is significantly higher. This can be mitigated to some extent by performing multiple burns, but the final burn is a large single burn needed to accelerate the spacecraft to escape velocity.

The optimum intermediate injection orbit apogee is now higher, lying at between 50,000 and 100,000 km, the higher optimum occurring for the higher target excess hyperbolic speed.

The gain in useful mass available to the spacecraft depends upon the propulsion related mass fraction for the spacecraft. Gains of over 100 kg may be achieved, depending on the target orbit. However, this is also related to the launcher performance with increasing perigee speed. A key factor is the maximum launcher fuel fraction for the upper stage (which is related to the mass efficiency of the upper stage). In the case considered, the maximum fuel fraction is 65%. This allows good performance in reaching higher perigee speeds, when compared with an upper stage with a lower maximum fuel fraction.

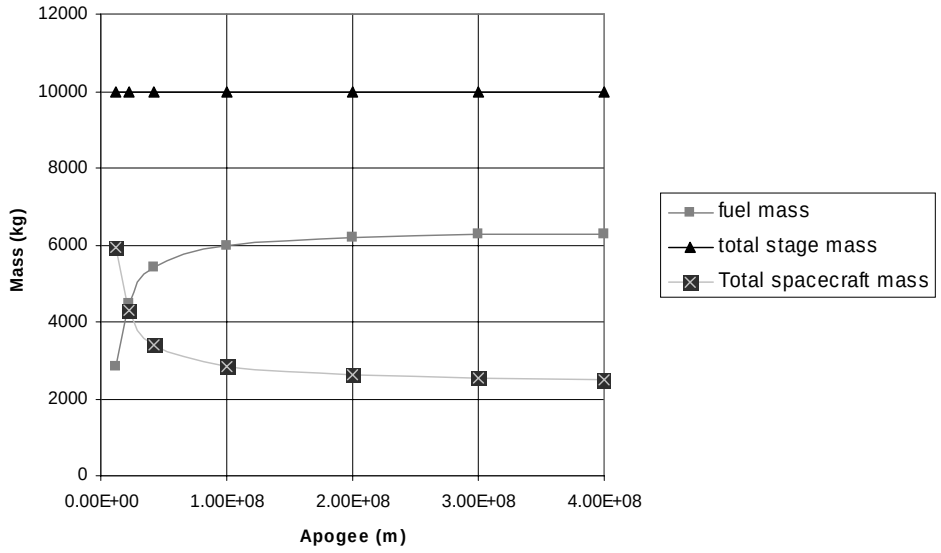

Figure 1.2.8. Mass components versus intermediate injection apogee radius. The above figure shows the total upper stage mass, upper stage fuel mass and the total spacecraft mass injected into the intermediate orbit, as a function of the apogee radius of that orbit.

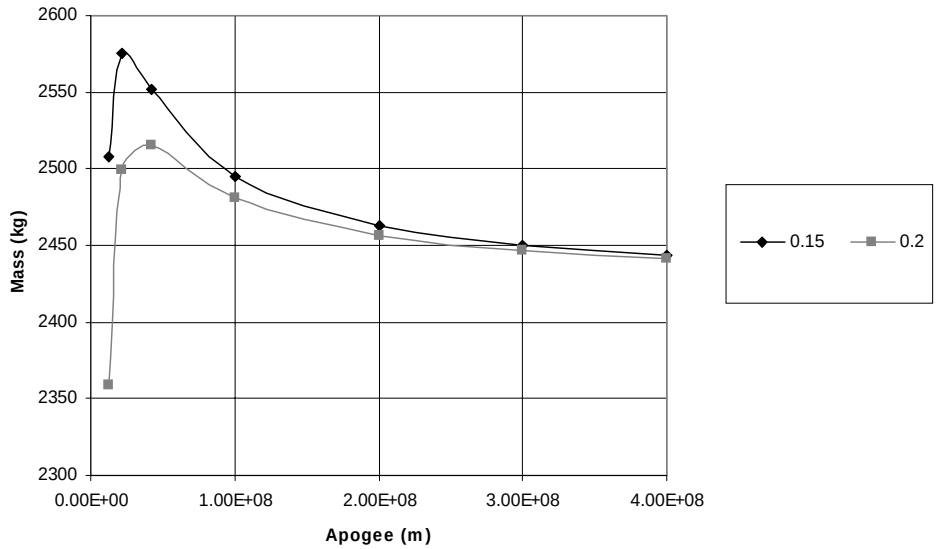

Figure 1.2.9. A case of fixed upper stage mass showing spacecraft mass versus intermediate injection apogee radius, for a target apogee of 1.5 million km for two spacecraft propulsion mass fractions. This figure shows the 'useful mass' of the spacecraft injected to the target orbit, depending on the choice of intermediate orbit apogee. Two values of spacecraft propulsion mass fraction are considered. The ΔV loss assumed here is 2.5% in the apogee raising by the spacecraft.

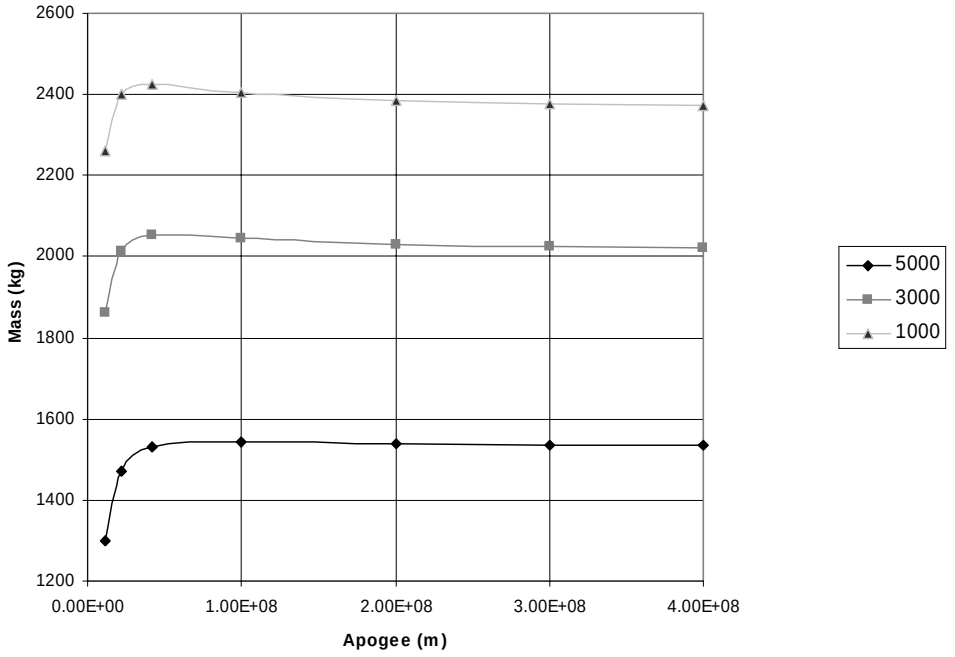

Figure 1.2.10. A case of fixed upper stage mass showing spacecraft useful mass versus intermediate injection apogee radius, for a range of target escape orbit Vinfinity, and for a spacecraft propulsion mass fraction of 0.15.

A second example may be considered (Figure 1.2.11), where this maximum fraction is lower at 60%. It is also assumed that in this case, the dry mass of the upper stage is reduced by 100 kg when compared with the previous example, due to the lesser fuel requirement. This means that direct launcher performance, to lower perigee speed cases, where less than maximum fuel is required, is improved when compared with the first example shown in Figure 1.2.6. However, the performance at higher perigee speeds will be compromised.

The effectiveness of this strategy of using intermediate apogee injection therefore depends on the characteristics of the launch vehicle and the mission target. A more detailed discussion on this subject may be found in Appendix 4.

Spacecraft apogee raising

In the previous section the subject of the spacecraft performing apogee raising was considered. The main performance-related issue is the ΔV loss associated with this manoeuvre.

The ΔV loss is related to the spatial distribution of the burn. The application of an accelerating manoeuvre at radii greater than perigee results in inefficiency, such that the ΔV required to complete the apogee raising exceeds that expected from impulsive predictions. If Figure 1.2.12 is examined, then the low injection apogees

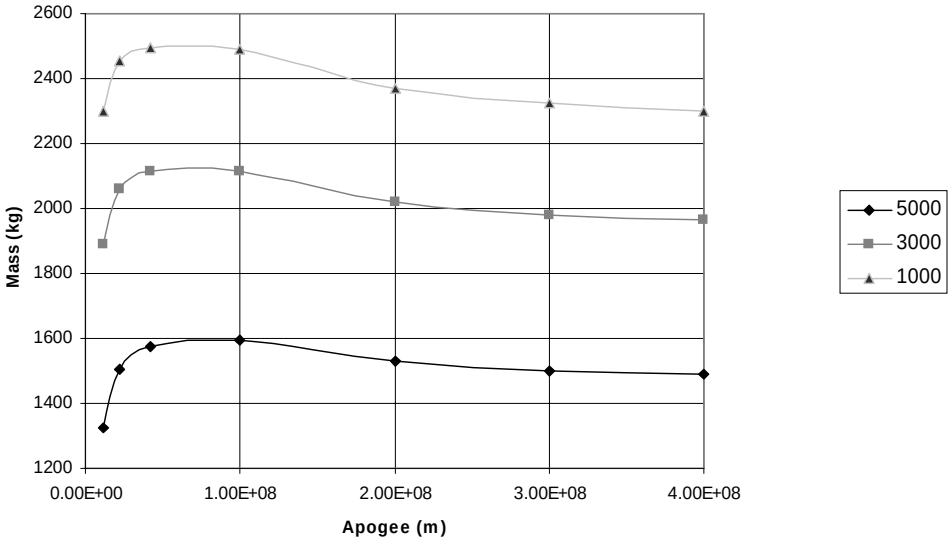

Figure 1.2.11. A second case of fixed upper stage mass showing spacecraft useful mass versus intermediate injection apogee radius, for a range of target escape orbit Vinfinity, for a spacecraft propulsion mass fraction of 0.15. The stage maximum fuel fraction is reduced to 60%. This lower upper stage fuel fraction case, with lower dry mass also, gives better performance at low apogee injection and worse at higher apogees, when compared with Figure 1.2.10.

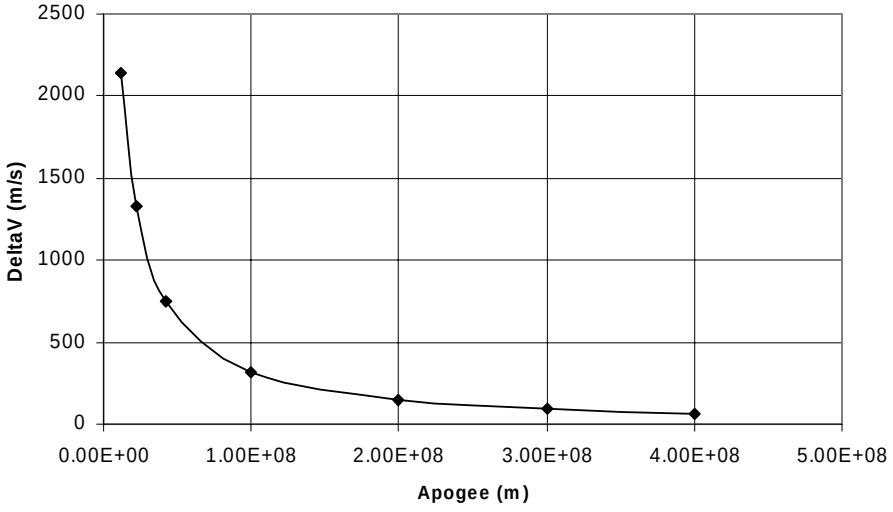

Figure 1.2.12. ΔV from injection orbit to 1.5-million km apogee target orbit. Perigee altitude of 200 km is assumed

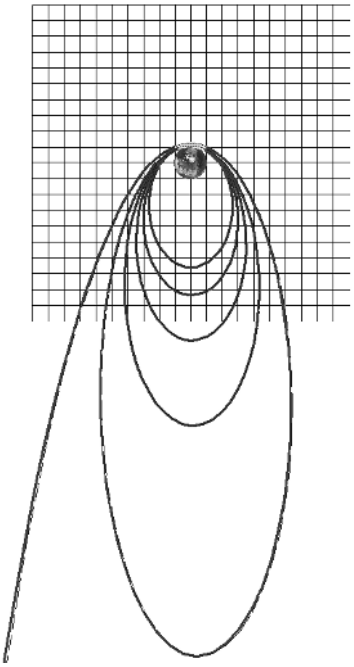

Figure 1.2.13. Example of apogee raising from a 42,000 km apogee injection orbit to reach a target orbit with apogee of 1.5 million km. A series of five apogee-raising burns are made to raise the apogee to its target. The extent of the burns can be seen by the lightly shaded regions of the trajectory around perigee. This corresponds to a thrust/mass ratio of approximately 0.1333 m/s at the start of the apogee raising. Such an initial acceleration is representative of typical spacecraft thrust/mass capabilities.

require a substantial ΔV to reach a target apogee of 1.5 million kilometres. Also, the injection mass is higher in these lower intermediate orbits. Therefore for similar propulsion system types (with comparable thrusts), the acceleration available to the spacecraft will be lower. This double penalising effect means that injecting to low-apogee intermediate orbits could potentially be an inefficient strategy, because of the ΔV loss that may be experienced.

However, this loss can be substantially reduced by adopting a multiple-burn apogee-raising strategy. In this way, a series of lower-apogee intermediate orbits are used, before finally injecting the spacecraft into the target orbit. If the loss when initially injecting to lower intermediate orbits is to be contained to low levels, then progressively more burns are required as the injection apogee reduces.

If, for example, an intermediate apogee orbit radius of 42,000 km is considered, with a target apogee at 1.5 million kilometres then splitting the apogee-raising to typically three to four burns can result in a reduction in the ΔV loss to only a few per cent. The actual value depends on the thrust used by the spacecraft. Figure 1.2.13 illustrates such an apogee-raising strategy.

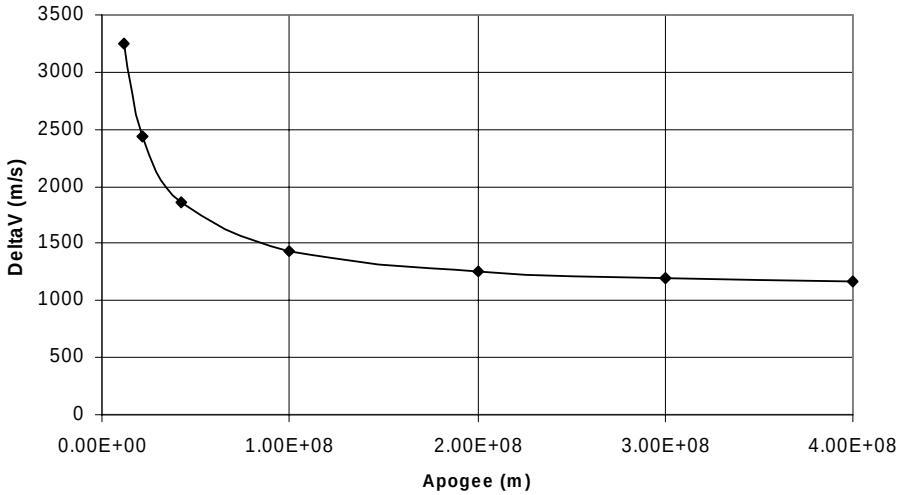

Figure 1.2.14. ΔV from injection orbit to 5 km/sec excess speed. If the example of a target excess hyperbolic speed of 5,000 m/s is considered then the impulsive speed change required is shown in the above figure. A perigee altitude of 200 km is assumed.

The case of a higher-energy target orbit can now be considered. An excess hyperbolic speed target of 5,000 m/s requires significantly higher ΔV change from the intermediate injection orbit than the case considered previously.

Figure 1.2.14 shows that even with an intermediate orbit apogee at 400,000 km, a ΔV of more than 1km/sec is needed to reach the escape orbit. In practice, apogee-raising to intermediate targets approaching 300,000 km, before finally injecting to the target orbit, can result in difficulties with perturbation of the intermediate orbits by solar gravity. Furthermore, little extra speed gain is found in using, for example, a 1 million-km apogee before injecting to escape, compared with 300,000 km.

Therefore, in such a scenario it is possible to perform a series of apogee raising manoeuvres until typically an altitude of between 100,000 and 300,000 km is reached. However, the next manoeuvre must be sufficient to reach the escape orbit directly, and will be over 1 km/sec in this example. This manoeuvre will then generally experience a greater ΔV loss. The actual loss depends on the details of the propulsion system, but a loss of 10–20% could be expected for such a manoeuvre.

1.2.4 Interplanetary departure implications

The previous sections described the requirement for velocities relative to Earth (or any planet) when leaving on an interplanetary trajectory. A hyperbolic orbit must be targeted. The magnitude of this departing relative velocity determines the excess hyperbolic speed needed when leaving Earth. The direction of the departing relative velocity vector is expressed in terms of right ascension and declination.

If a hyperbolic orbit is considered, then it is possible to calculate the asymptotic direction of the departure orbit. Firstly, the semi-major axis is given by:

$$a = \frac{-\mu_{planet}}{V_\infty^2} \tag{1.2.12}$$

The eccentricity, e, is then obtained from the perigee r_{pe}, of the departing orbit:

$$e = 1 - \frac{r_{pe}}{a} = 1 + \frac{r_{pe}\,\mu_{planet}}{V_\infty^2} \tag{1.2.13}$$

The eccentricity is therefore greater than 1. The true anomaly (θ) corresponding to the asymptotic direction is then calculated from the relationship $r = \dfrac{a(1-e^2)}{1+e\cos\theta}$, as r tends to an infinite value and is given by:

$$\theta = \cos^{-1}\left(-\frac{1}{e}\right) \tag{1.2.14}$$

The directions of the asymptotic escape vector with respect to a frame of reference in Earth's equatorial plane can now be calculated.

The angle from the ascending node to the departure vector direction (the angle in the orbit plane) is $\omega + \theta$, where ω is the argument of pericentre. For any given orbit plane containing the escape orbit, the two cases may be found that achieve the same direction of the asymptotic hyperbolic escape vector. These two solutions initially travel about the planet in an opposite sense. The geometry of the two solutions is illustrated in Figure 1.2.16.

The line of nodes is shown in this figure. The relationship between this direction, the argument of pericentre, the orbit inclination and the resulting asymptotic departure right ascension and declination will be derived. The location in Figure 1.2.16 could be that for the case of a 90-degree inclination orbit. In such a

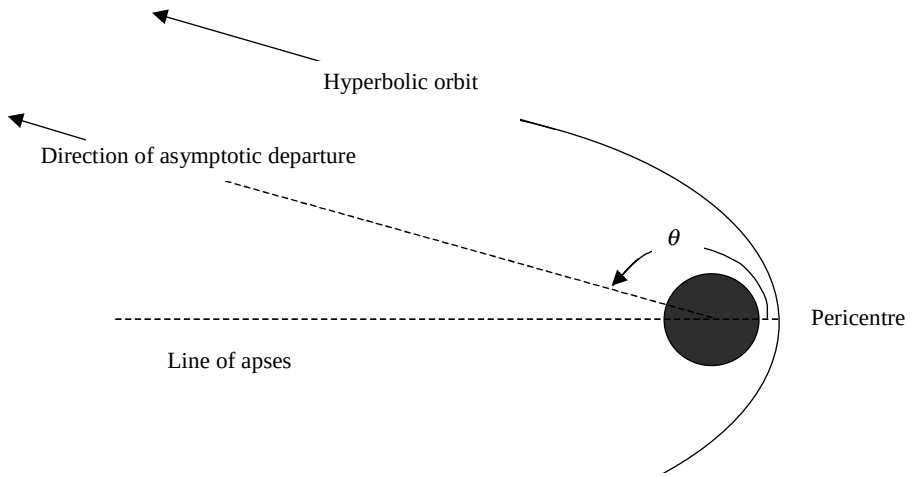

Figure 1.2.15. The departing hyperbolic orbit, showing the asymptotic true anomaly.

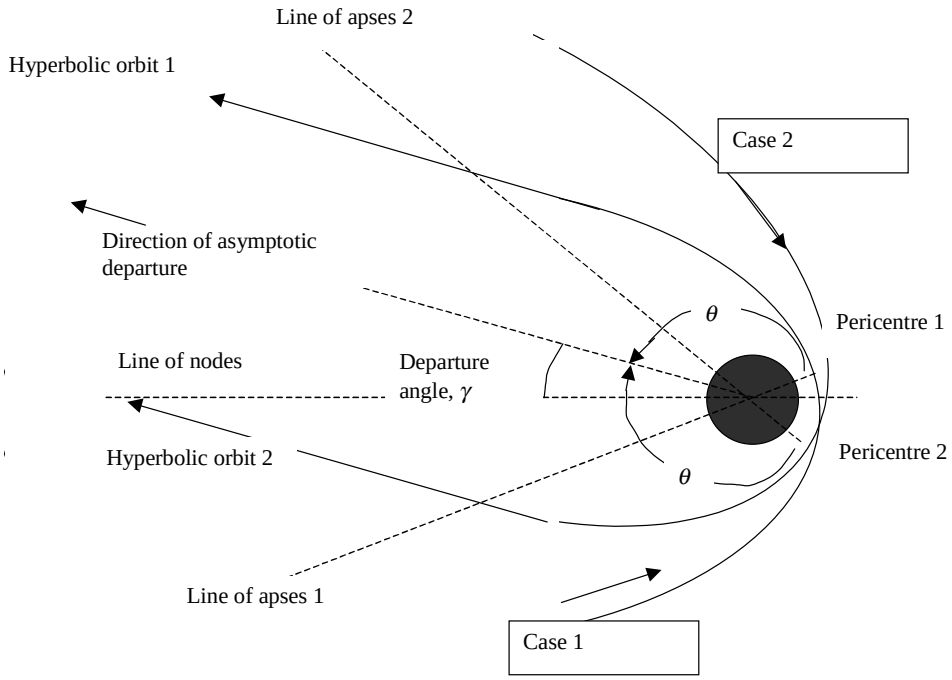

Figure 1.2.16. The departure vector seen within the orbit plane of the escape hyperbola, showing two alternative solutions attaining the same departure direction.

case, the direction of the escape hyperbola then lies in the vertical plane, and so the angle between the escape vector and the line of nodes determines the declination. In the above case, one escape orbit results after passing through the descending node, after pericentre, case 2) and the other case through the ascending node after pericentre.

Further relationships may be obtained between departure direction and the argument of pericentre. Firstly:

$$\omega_2 + \theta = \gamma + 2\pi$$
$$\omega_1 + \theta + \gamma = \pi \tag{1.2.15}$$

where γ is the angle between node direction and departure direction in the orbit plane. It is important to note that the argument of pericentre is always measured relative to the ascending node. The reference direction with respect to which the departure direction will be measured is taken as the line of nodes, and we can arbitrarily take the ascending node for case 2 as that reference.

Having evaluated the angle between the line of nodes and the departure vector, then the relationship between this and the two arguments of pericentre can be evaluated:

$$\omega_2 - \omega_1 = 2\gamma + \pi \tag{1.2.16}$$

Then, by spherical trigonometry, the declination of the asymptotic departure vector (the angle out of the equatorial plane) is given by the following identity.

$$\sin DEC = \sin i \sin(\omega + \theta) \tag{1.2.17}$$

This relationship applies for both of the cases discussed, because the argument of pericentre is always measured from the ascending node, from which the inclination of the hyperbolic orbit plane is also defined.

From this relationship it can be seen that for a given inclination, i, of the initial orbit there is a maximum achievable magnitude of declination, equal to the inclination of that initial orbit (for $i < 90^\circ$ or 180–i for $i > 90^\circ$). This initial orbit inclination is generally related to the launch vehicle performance and the latitude of its launch site. In the absence of range constraints that limit certain launcher departure azimuths, maximum launcher performance is achieved with an injection orbit inclination equal to the latitude of the launch site (i.e., an easterly launch).

This equation also illustrates the point that for a given argument of perigee, two different inclinations may be used to reach a given target declination. The sum of the two inclination solutions is 180 degrees.

An example of two departures achieving the same declination is shown in Figure 1.2.17, for the case of an Earth escape. These two departure solutions lie in the same plane. The sub-grid spacings are in Earth radii. The dashed lines indicate the projections of the two trajectories in the Earth equatorial plane. The asymptotic departure directions become parallel at greater distance from Earth. The magnitude of the excess hyperbolic speed is assumed to be 3,000 m/s. The inclinations of the two orbits are 60 and 120 degrees. The arguments of perigee are calculated from Equations 1.2.15 and 1.2.17 for the two solutions.

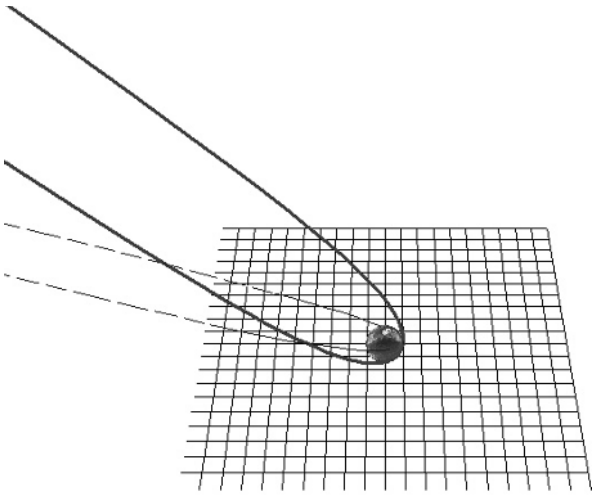

Figure 1.2.17. Simulation of two hyperbolic orbits with ascending nodes separated by 180 degrees (inclinations 60 and 120 degrees) achieving a 30 degree asymptotic departure declination.

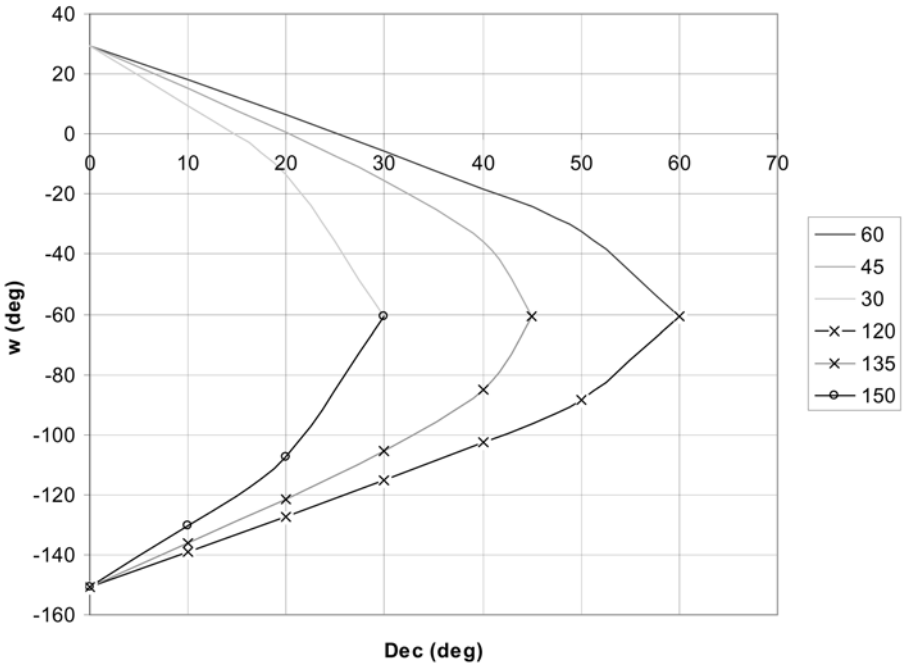

Figure 1.2.18. The effect of declination requirement on the hyperbolic orbit argument of perigee for a 3 km/sec excess hyperbolic speed orbit leaving Earth.

A further two solutions that achieve the same departure direction may now be added to the previous pair. The two new solutions lie in the same plane as each other but not the same plane as the first pair. In this case the argument of perigees are the same as the previous pair of solutions and the orbit inclinations are 180 degrees minus the inclinations of the previous case. The right ascension of the ascending must be adjusted for the second pair, in order to achieve the same departure azimuth for the second pair of hyperbolic orbits as the first pair.

The right ascension, α, of the departure vector, measured with respect to the same inertial longitude reference as the orbit ascending node, is given by:

$$\tan\alpha = \cos i \tan(\omega + \theta) \tag{1.2.18}$$

Then the right ascension of the departure with respect to the equatorial reference 'X' direction is given by: $RA = \alpha + \Omega$. Note that quadrant fixing must be considered, as the above equation does not uniquely determine the value, α.

Any required right ascension of departure may be achieved by selecting the appropriate right ascension of the injection orbit ascending node. This is itself determined by the time of day at which the spacecraft is launched.

It should be noted that the right ascension and declination targets discussed here are in Earth equatorial axes. In some analyses of interplanetary transfers, these are expressed with respect to the ecliptic and so the appropriate transformation must be made.

Therefore, given an inclination of the departure orbit, a target asymptotic departure right ascension and declination can be achieved by selecting the right ascension of ascending node and argument of perigee of that orbit, providing that the magnitude of the target declination does not exceed the magnitude of the orbit inclination.

In the following example, a specific Earth departure orbit is considered. The magnitude of the excess hyperbolic speed is assumed to be 3,000 m/s. The direction of the asymptote, θ, is then 159° (assuming a perigee radius for the departure orbit of 6,578 km). Figure 1.2.18 shows the argument of perigee that is required to achieve a given departure declination, for a set of three different initial orbit inclinations, ranging from 30° to 60°. The 60/120° inclination case is illustrated in Figure 1.2.17, targeting a declination of 30°.

Both solutions for the argument of perigee are shown, for a given declination. The sum of the inclinations for the two solutions is 180°. In this plot, the complementary inclination cases assume that the ascending node of the orbit is 180° from the other solution lying in the same plane.

1.3 PLANET ORBIT SELECTION AND INSERTION

1.3.1 Planetary approach and capture

The approach to a planet is characterised by three parameters: excess hyperbolic speed (the magnitude of the approach planet relative velocity vector) and the right ascension and declination of the approaching planet relative velocity vector.

These parameters determine the range of orbits that it is possible to reach with a single capture manoeuvre. The capture manoeuvre is a large retro-manoeuvre performed at planet pericentre. It is essentially the reverse of an escape manoeuvre discussed in the previous sections. This is the most efficient location for the capture manoeuvre, performing a capture manoeuvre removed from pericentre can be very inefficient in ΔV terms.

After capture, the spacecraft will generally lie in an elliptical orbit. As the capture manoeuvre can often have a relatively large ΔV (similar in magnitude to an escape manoeuvre) and the spacecraft is capable of only finite thrust, a ΔV loss will occur due to the spatial distribution of the retro-burn around pericentre.

1.3.2 Target orbit options

The spacecraft approach vector lies perpendicular to a plane passing through the centre of the planet. This is the 'B' plane. If the planet were to possess a negligible gravity field, then the spacecraft would be undeflected and pass normally through the B plane. This would be the closest approach to the planet. In the presence of the actual planet's gravity, the spacecraft approaches in a hyperbolic orbit and the pericentre does not appear in the B plane. However, the concept is of value, as it allows a categorisation of approach orbits.

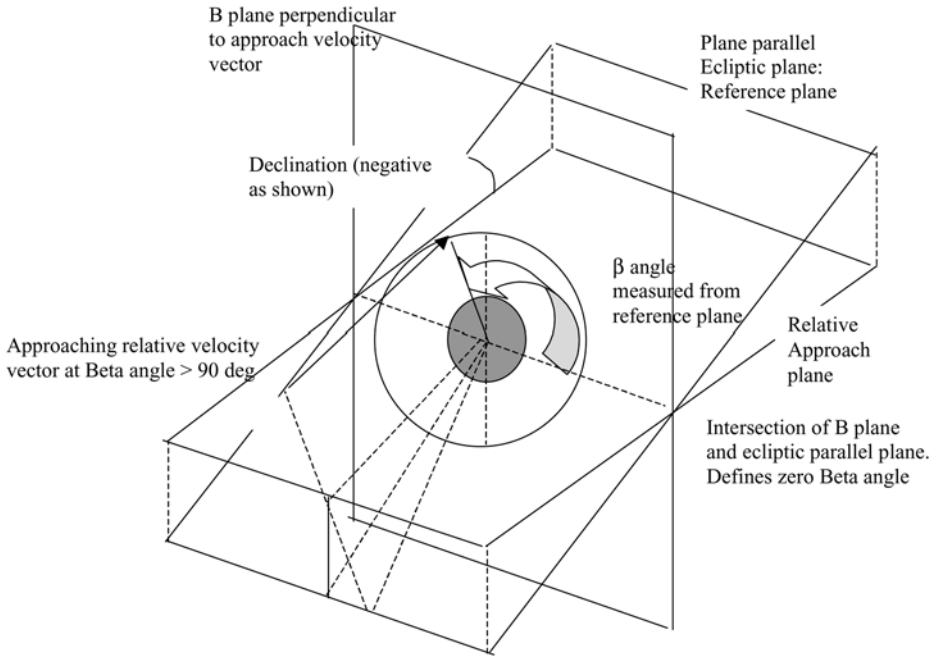

Figure 1.3.1. Definition of the B plane.

In Figure 1.3.1, the B plane is shown as the plane perpendicular to the hyperbolic approach vector. A second plane is shown. This is a reference plane, and could for example be either a plane parallel to the ecliptic or the planet's equatorial plane. A Beta angle of zero is then defined by an approach through the intersection of the B plane and the reference plane.

The approach orbit plane includes the arriving asymptotic excess hyperbolic velocity vector and the position offset in the B plane, defined by the Beta angle. Therefore, the angle between this approach orbit plane and the reference plane determines the inclination of the orbit plane with respect to that reference. To determine this inclination, a further intermediate reference plane may be considered, passing through the intersection of the B plane and the reference plane, but lying parallel to the approach vector. This will be referred to as the relative approach plane. In subsequent discussions in Chapter 4 on gravity assist this plane is a similar concept to the approach plane. The angle between this intermediate plane and the reference plane is given by the declination of the arrival vector – a rotation about the intersection of these planes. The angle between the approach orbit and the intermediate plane is given by the Beta angle – a rotation about a vector parallel to the approach direction. The inclination may therefore be determined by these two orthogonal rotations.

$$\cos i = \cos\beta \cos DEC \tag{1.3.1}$$

When at a distance of millions of km from the planet, a tiny transverse ΔV can

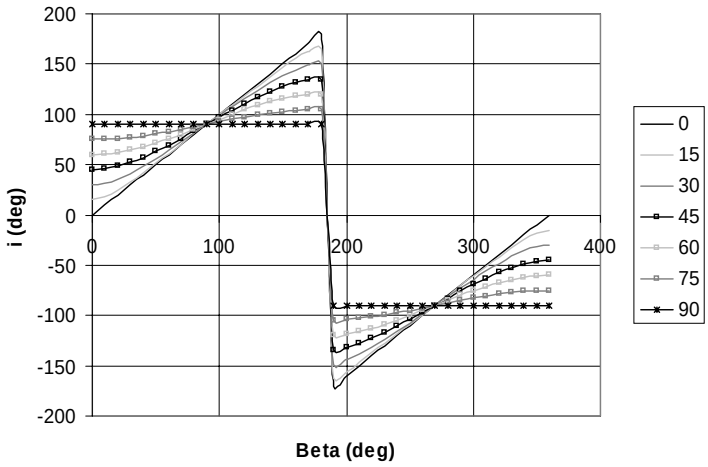

Figure 1.3.2. The relationship between Beta angle and inclination, for a range of different declinations. At Beta angles above 180 degrees, the negative inclination solution is applied.

allow the approach vector to intersect the B plane at any location. Such a manoeuvre can be implemented when the spacecraft is only days away from reaching the target planet.

When referring to the previous figure, a Beta angle between 0° and 360° can be selected without any significant manoeuvre being required. Having seleceted the Beta angle, the orbit plane with respect to the planet is now defined. The orbit plane then contains the pericentre, and its inclination is determined by the Beta angle. This situation is the reverse of the planetary departure condition described in section 1.2.4.

The angle between the asymptotic approach vector and pericentre is given by Equation 1.2.14. A similar set of relationships to those governing planet departure can now be used for the capture case. In the following equations, α and DEC define the orientation of the asymptotic velocity vector approaching the planet:

$$\sin DEC = \sin i \sin(\theta - \omega) \qquad \text{and} \qquad \tan\alpha = -\cos i \tan(\theta - \omega) \tag{1.3.2}$$

Then the right ascension of the departure with respect to the equatorial reference 'X' direction is given by: $RA = \alpha + \Omega$. Note that quadrant fixing must be considered, as the above equation does not uniquely determine the value, α.

The true anomaly of the asymptotic approach vector is given by the same relationship as the planet departure case. A wide range of inclinations about the target planet may be reached. However, a limitation exists that is imposed by the arrival declination.

$$|\sin i| \geq |\sin DEC| \tag{1.3.3}$$

A 360-degree range of Beta angles is possible. Therefore, for a given approach declination and right ascension, a wide range of arguments of pericentre can be

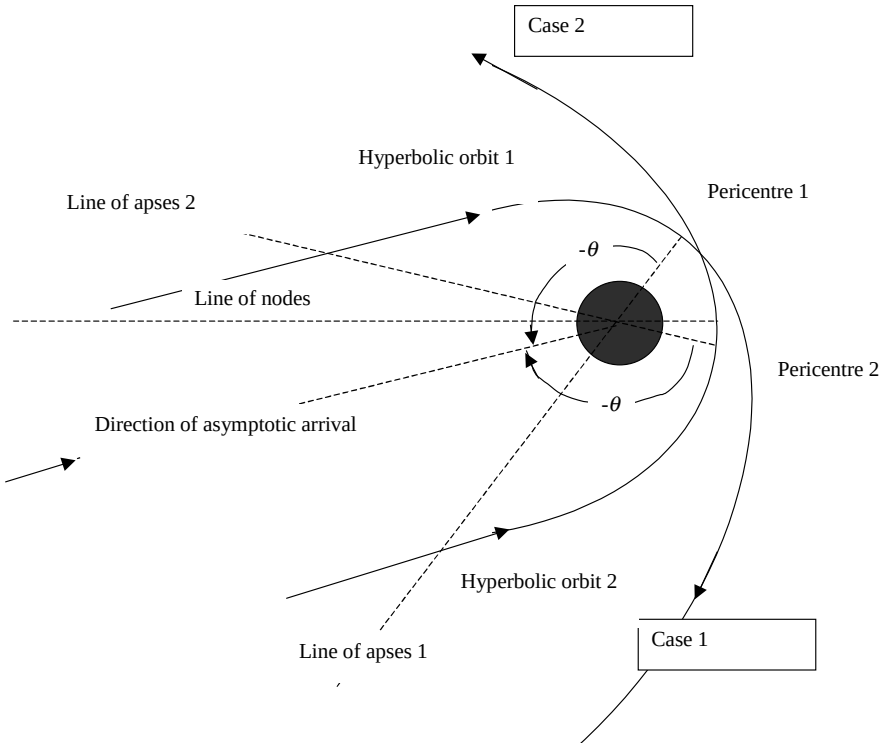

Figure 1.3.3. Arrival geometry seen in the orbit plane about the planet.

achieved. If cases at inclinations of $\pm 90^\circ$ are considered, then maximum and minimum latitude of the argument of pericentre can be found.

The argument of pericentre is an important parameter, as it determines key properties about the capture orbit about the planet. If the spacecraft is to be captured, then a retro-manoeuvre is performed at pericentre, and the pericentre of the approaching hyperbolic and capture orbits are therefore at the same location.

Some examples of the possible pericentres can be examined. The case of a spacecraft approaching Mars is considered. Firstly, a zero-declination approach is used. The locus of all possible pericentres can then be found via the previous equations relating argument of pericentre to inclination and Beta angle (attention must be paid to quadrant fixing in this calculation). The locus is expressed as a latitude and a longitude of the pericentre. The latitude is relative to the reference plane used to calculate inclination and argument of pericentre. The zero longitude point is defined to lie along the azimuthal approach direction to the planet. These relationships can be seen in Figure 1.3.4.

The effect of approach declination can now be examined. Once again, the case of an approach to Mars is considered. The excess hyperbolic speed is 3,000 m/s, and declinations from zero to 30° are examined. These relationships can be seen in Figure 1.3.5.

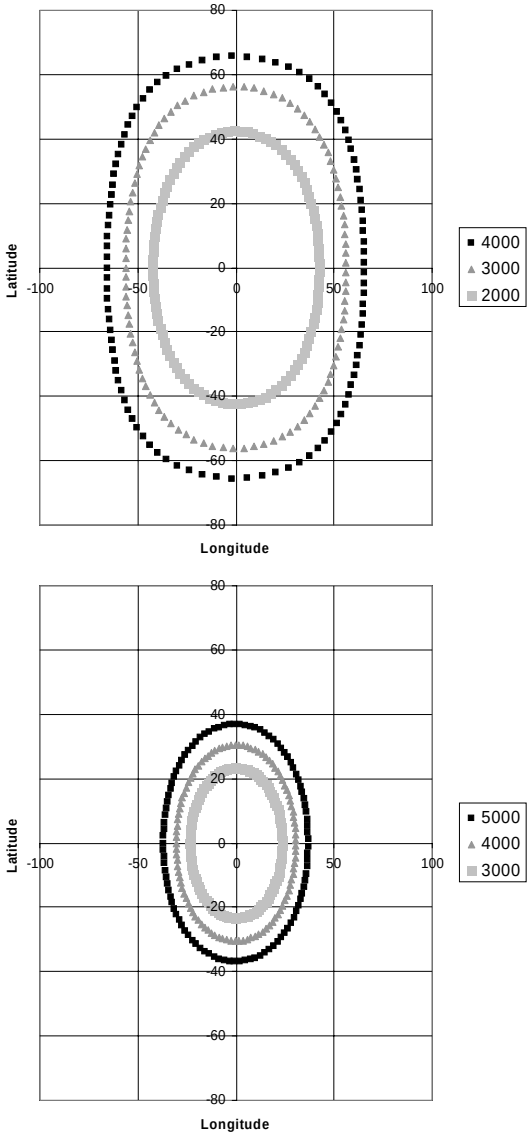

Figure 1.3.4. The effect of excess hyperbolic speed between 3,000 and 5,000 m/s on possible pericentre locations for approaches to Mars and Venus at zero declination. The locus of possible pericentres expands in size as the approach excess hyperbolic velocity increases. The first case is an approach to Mars, in which the pericentre radius considered was 3,800 km (approximately 400 km above the surface). In the case of a zero-declination approach, the plot is symmetric about zero latitude. In the second case, an approach to Venus is considered. Venus has a considerably greater gravitational constant than Mars (almost eight times as large). In this case, the pericentre radius considered was 6,450 km (again approximately 400 km above the surface). The stronger gravitational field at Venus means that pericentre experiences a greater deflection from the approach vector direction than in the case of an approach to Mars.

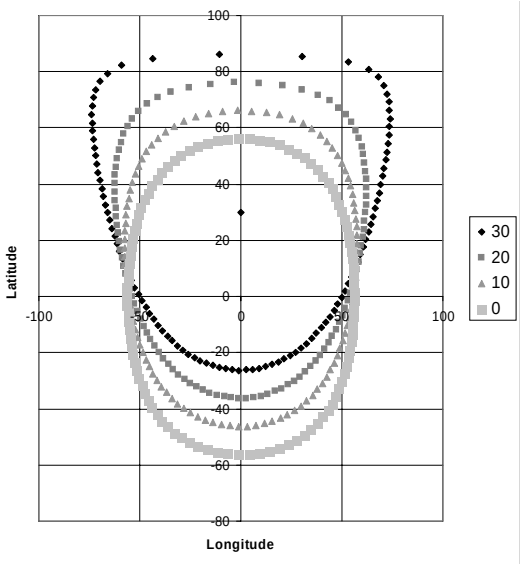

Figure 1.3.5. The effect of approach declination between 0° and 30° on possible pericentre locations for approaches to Mars with an excess hyperbolic speed of 3 km/sec. The locus of possible pericentres moves to the north as the approach declination increases in magnitude. In this case, the pericentre radius considered was again 3,800 km.

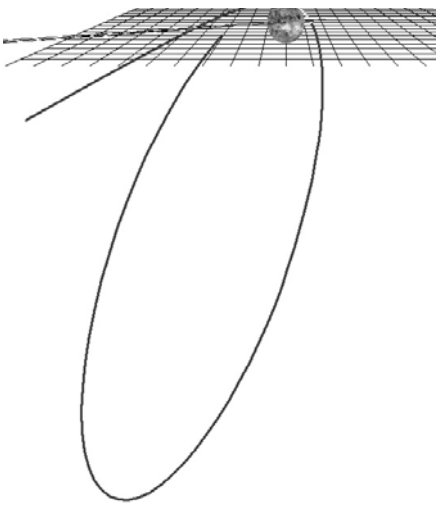

Figure 1.3.6. A hyperbolic approach to Venus with a pericentre retro-burn to reach a 5-day transfer orbit about Venus.

Figure 1.3.6 shows an example of a spacecraft approaching Venus and then performing a retro manoeuvre at pericentre. The approach orbit is polar. The pericentre latitude is approximately 70°, and the spacecraft is captured into a polar orbit. The approach conditions are those from a 2005 launch and transfer

to Venus. Therefore, the excess hyperbolic speed is approaching 5 km/sec and the declination is approximately 30°. The grid seen in the figure lies in a plane parallel to the ecliptic. The capture burn arc is shaded lightly and occurs around pericentre.

1.4 TRANSFERS THROUGH THE SOLAR SYSTEM

In this section, examples of transfers to every planet in the Solar System are considered. The techniques are two impulse transfers; that is, one leaving and one arriving at the target. The transfers are described principally in terms of the required excess hyperbolic speeds. In some cases, these are translated to ΔV implications for pericentre manoeuvres at planet departure and planet arrival.

1.4.1 Mercury

The synodic period of Mercury with respect to Earth is approximately 116 days. This defines the frequency of 'conjunction class' transfers from Earth.

The excess hyperbolic speed, V_∞, required for leaving Earth and arriving at Mercury varies with successive opportunities, as the solar longitudes of launch and arrival rotate with respect to Mercury's elliptical orbit. The whole cycle approximately repeats after three synodic periods, or 1 Earth year.

Figure 1.4.1 shows the sum of V_∞ (V_∞ leaving Earth and V_∞ approaching Mercury) for a range of launch epochs and transfer times. The V_∞ shows a period feature (with the synodic period) and also the repeat feature (at 1 year). Minimum V_∞ transfers can be seen between 80 and 100 days at each synodic period.

The V_∞ then define the ΔVs for these transfers. In Table 1.4.1 the initial orbit at Earth is assumed to be a GTO-like orbit with apogee at 36,000 km altitude. Capture at Mercury is into an elliptical orbit with apogee at 12,000 km altitude. Such an elliptical orbit at Mercury is typical of a science observation orbit at that planet.

The ΔVs are very high for such a transfer. High-thrust propulsion systems (generally chemical-based systems) would require a very large fuel fraction for such a mission, and such a scenario would effectively be unfeasible.

1.4.2 Venus

The orbital periods of Venus and Earth are more similar, with the result that the synodic period of Venus with respect to Earth is longer than that of Mercury. The period is approximately 1.6 years.

The V_∞ required for leaving Earth and arriving at Venus varies with successive opportunities, but to a much lesser extent than Mercury, as the orbit of Venus has a much lower eccentricity. Venus's inclination (and hence longitude of ascending node) influences the transfer V_∞ requirements. The whole cycle approximately repeats after five synodic periods, or 8 Earth years.

Table 1.4.2 shows long and short optimum transfers for adjacent launch epochs, separated by one synodic period. The first launch period considered is 2013. The ΔV

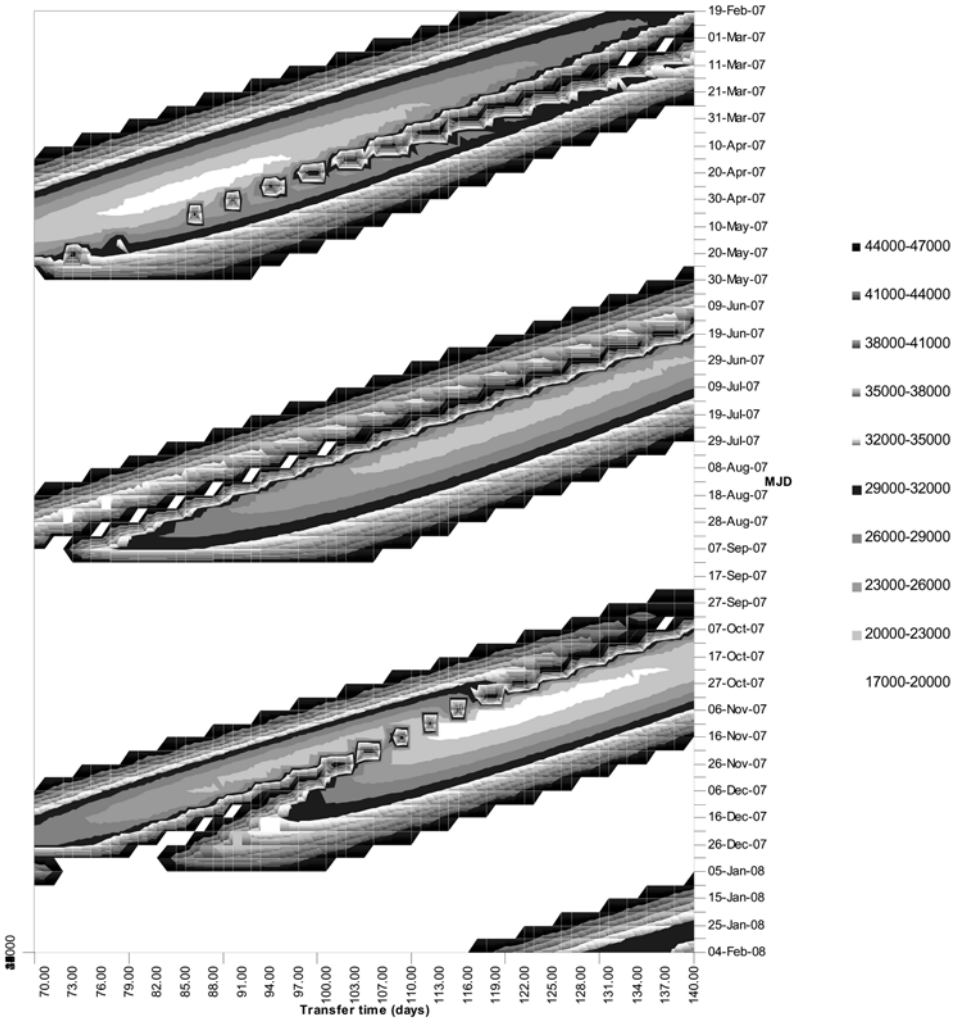

Figure 1.4.1. V_∞ sums for conjunction type two-impulse transfers to Mercury over the launch period 2007.

Table 1.4.1. Example of a direct transfer to Mercury.

Launch			Arrival			Total	
Date	Vinf (m/s)	DV (m/s)	Date	Vinf (m/s)	DV (m/s)	Transfer time	Vinf (m/s)
11 May 2012	9,378	4,296	18 Aug 2012	7,984	5,298	158	17,362

Table 1.4.2. Examples of optimal transfer from Earth to Venus.

Launch			Arrival			Total		
Date	Vinf (m/s)	DV (m/s)	Date	Vinf (m/s)	DV (m/s)	Transfer time	Vinf (m/s)	DV (m/s)
2 Nov 2013 Long opt	2,770	1,113	9 Apr 2014	4,601	1,786	158	7,371	2,899
15 Nov 2013 Short opt	4,190	1,540	5 Mar 2014	3,265	1,303	110	7,455	2,843
25 Apr 2015 Long opt	3,023	1,177	27 Oct 2015	4,078	1,580	185	7,101	2,757
8 Jun 2015 Short opt	3,230	1,234	19 Nov 2015	2,883	1,192	133	6,113	2,426

Table 1.4.3. Examples of optimal transfer from Earth to Venus for a one-day period target orbit.

Launch	Arrival			Total		
Date	Date	Vinf (m/s)	DV (m/s)	Transfer time	Vinf (m/s)	DV (m/s)
2 Nov 2013 Long opt	9 Apr 2014	4,601	1,413	158	7,371	2,526
15 Nov 2013 Short opt	5 Mar 2014	3,265	929	110	7,455	2,470
25 Apr 2015 Long opt	27 Oct 2015	4,078	1,207	185	7,101	2,384
8 Jun 2015 Short opt	19 Nov 2015	2,883	818	133	6,113	2,052

requirements at pericentre are calculated using two reference orbits. The elliptical reference at Earth has perigee at 200 km altitude and apogee at 35,787 km (GTO characteristics) and at Venus the pericentre is at 300 k altitude and apocentre at 29,950 km. This is typical of a science observation, elliptical orbit about Venus.

As shown in Table 1.4.3, a higher target orbit about Venus (with a period of 1 Earth day) reduces the ΔV requirements at orbit insertion. Therefore, target orbit compromise offers a means to significant ΔV reduction.

As the missions show a near repeat after eight years, then the 2013 launch parameters are similar to those used for ESA's Venus Express transfer opportunity, launched in 2005.

Figure 1.4.2 shows the sum of the V_∞ terms (V_∞ leaving Earth and V_∞ approaching Venus) for a range of launch epochs and transfer times. These transfer times cover the range of half-revolution-type transfers from Earth to Venus. In general, they divide into 'short' and 'long' transfers at each launch

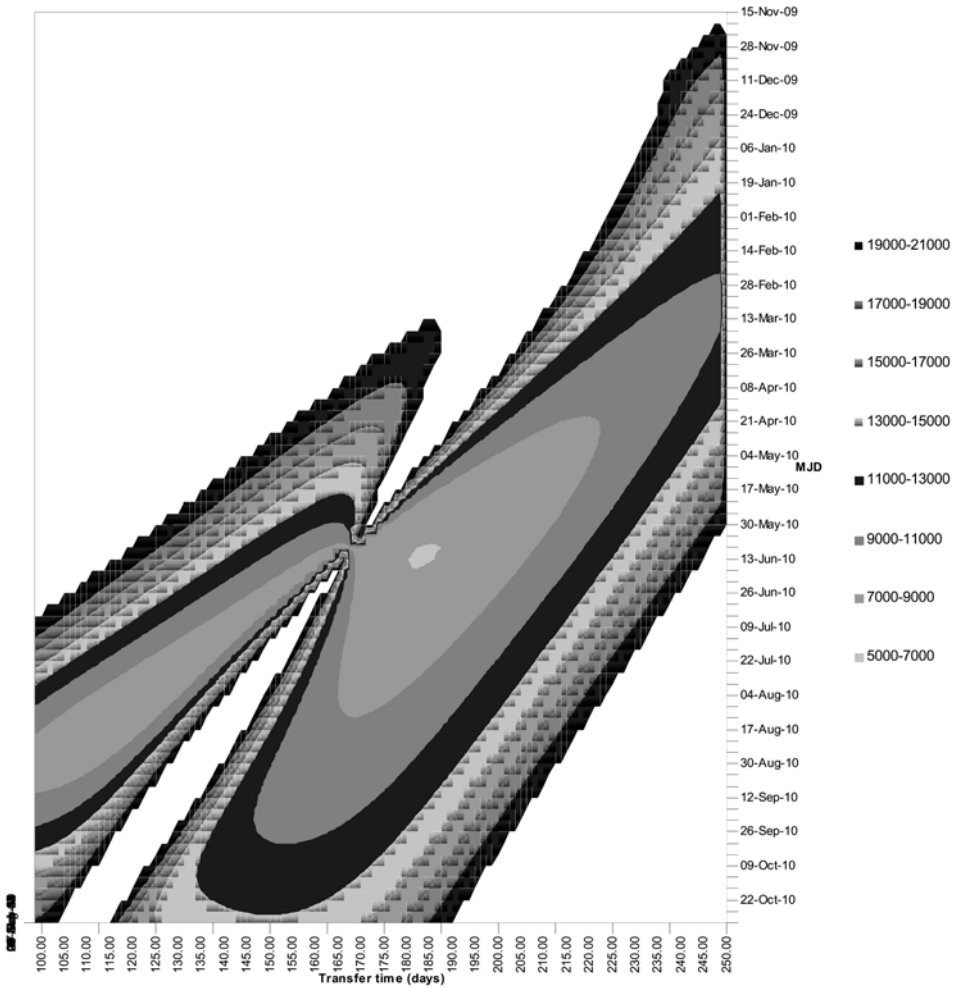

Figure 1.4.2. V_∞ sums for conjunction type 2 impulse transfers to Venus over the launch period 2010–2013.

opportunity, and the local minimum corresponding to each type is clearly seen in the figure. Minimum V_∞ transfers can be seen close to 120 days and 180 days for this particular launch opportunity in 2010.

The excess hyperbolic speed requirements for leaving Earth to reach Venus include the lowest for any interplanetary two impulse transfer in the Solar System.

1.4.3 Mars

The synodic period of Mars with respect to Earth is the largest of any of the planets in the Solar System. It is approximately 2.15 years.

As in the cases of Mercury and Venus, the V_∞ required in leaving Earth and

Table 1.4.4. Examples of optimal transfer from Earth to Mars.

Launch			Arrival			Total		
Date	Vinf (m/s)	DV (m/s)	Date	Vinf (m/s)	DV (m/s)	Transfer time	Vinf (m/s)	DV (m/s)
29 Nov 2011 Short opt	3,304	1,255	6 Aug 2012	3,491	1,375	251	6,710	2,630
10 Nov 2011 Long opt	2,990	1,169	11 Sep 2012	2,707	945	306	5,697	2,116
18 Jan 2014 Short opt	3,824	1,415	13 Aug 2014	3,915	1,636	224	7,644	3,051
5 Dec 2013 Long opt	3,083	1,193	25 Sep 2014	3,163	1,187	294	6,243	2,380
11 Mar 2016 Short opt	3,520	1,319	1 Oct 2016	3,739	1,525	204	7,225	2,844
10 Jan 2016 Long opt	3,471	1,304	12 Oct 2016	3,679	1,488	277	7,123	2,792

arriving at Mars varies with successive opportunities, due to the eccentricity and inclination of Mars' orbit. The whole cycle approximately repeats after seven synodic periods, or 15 Earth years.

The contours of excess hyperbolic speed variation for transfers to Mars have been closely examined for the example of solving Lambert's problem (see section 1.1.3).

In Table 1.4.4, some examples of locally optimal transfers to Mars are given, for both short and long transfer types. The variability over successive launch epochs is clearly seen. The elliptical reference orbit at Earth has perigee at 200 km altitude and apogee at 35,787 km (GTO characteristics), and at Mars the pericentre is at 400 k altitude and apocentre at 32,870 km. This elliptical target orbit has 1 Earth-day period (just less than one Mars day, which would imply a slightly higher apocentre).

The Earth departure speeds are slightly greater than the transfers to Venus, but remain low when compared with direct transfers to the other planets of the Solar System.

1.4.4 Jupiter

The orbital period of Jupiter is close to 12 years, and is therefore considerably larger than that of Earth. As a result, the synodic period becomes closer to 1 Earth-year. The synodic period of Jupiter with respect to Earth is approximately 1.1 years. The cycle approximately repeats after eleven synodic periods, or 12 Earth-years.

Figure 1.4.3 shows the sum of V_∞ (V_∞ leaving Earth and V_∞ approaching Jupiter) for a range of launch epochs and transfer times. These transfer times cover the range of half revolution type transfers, but are now considerably greater than considered for transfers to Venus and Mars. They again divide into 'short' and

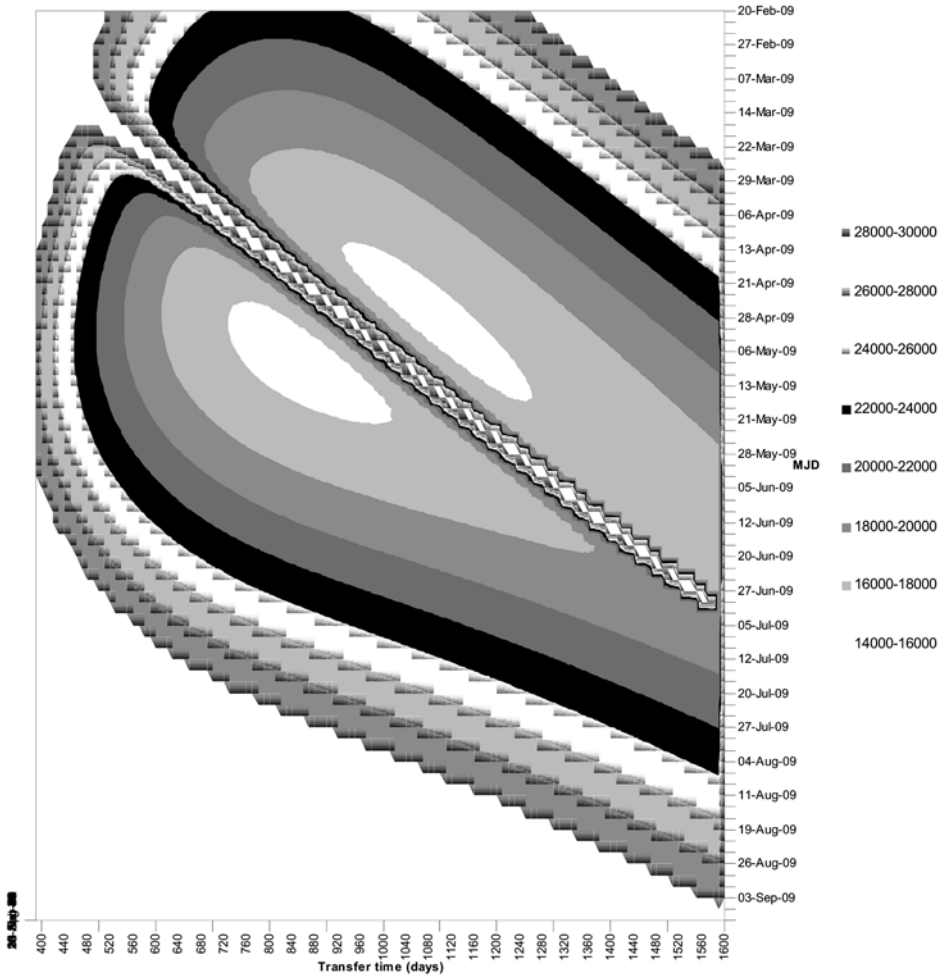

Figure 1.4.3. V_∞ sums for conjunction type, two-impulse transfers to Jupiter over launch period 2009.

'long' transfers at each launch opportunity. Minimum V_∞ transfers can be seen between 850 and 900 days transfer duration for the 'short' transfer type, and between 1,000 and 1,200 days for the 'long' transfer type. However, the extension of the local minima, in terms of transfer duration, is very wide, and therefore indicates considerable flexibility in terms of transfer duration to Jupiter.

Direct transfers are difficult to achieve, and in many cases special techniques are therefore required. An example of a direct transfer is given in Table 1.4.5. The elliptical reference orbit at Earth has perigee at 200 km altitude and apogee at 35,787 km (GTO characteristics). At Jupiter the pericentre is at 2,000 km altitude and apocentre at 430,000 km. This elliptical target orbit has a 1 Earth-day period. This orbit is not a realistic choice but is included for comparison with the Venus and

Table 1.4.5. Examples of optimal transfer from Earth to Jupiter with insertion to a one-day orbit at Jupiter.

Launch			Arrival			Total		
Date	Vinf (m/s)	DV (m/s)	Date	Vinf (m/s)	DV (m/s)	Transfer time	Vinf (m/s)	DV (m/s)
30 Apr 2009 Short opt	9,231	4,128	16 Jun 2011	6, 435	4,223	777	15,666	8,351
14 May 2009 Long opt	9,133	4,065	2 Nov 2012	6,843	4,269	1,268	15,976	8,334

Table 1.4.6. Examples of optimal transfer from Earth to Jupiter with insertion to a high orbit at Jupiter.

Launch			Arrival			Total		
Date	Vinf (m/s)	DV (m/s)	Date	Vinf (m/s)	DV (m/s)	Transfer time	Vinf (m/s)	DV (m/s)
4 May 2009 Short opt	9,321	4,186	11 Aug 2011	6,133	1,451	829	15,454	5,637
2 May 2009 Long opt	9,273	4,155	17 June 2012	6,427	1,554	1,142	15,700	5,709

Mars cases. A more likely choice of orbit about Jupiter has pericentre at 830,000 km altitude and apocentre at 20,000,000 km. This can then be the starting point of a gravity-assisted tour of the Jovian system (discussed in subsequent sections). The optimised transfers shown in the following two tables, each concerning a different target orbit at Jupiter, show a difference in the transfer dependent on that choice of target orbit. This is becaue the optimised parameter is the total ΔV. This is a non-linear function of the excess hyperbolic speed and the target orbit. Changing this target orbit changes the numerical relationship between ΔV and excess hyperbolic speed. However, the difference in solutions is not large. This effect of target orbit choice on the optimised transfer is particularly observable for the massive outer planets.

1.4.5 Saturn

The orbital period of Saturn is close to 29 years and therefore its synodic period lies even closer to 1 Earth-year; being approximately 1.04 years. This then defines the frequency of such 'conjunction class' transfers. The whole cycle approximately repeats after 28 synodic periods, or 29 Earth-years.

Minimum Vinfinity transfers take approximately 6 years with opportunities at each synodic period. As in the case of Jupiter, direct transfers are more difficult to achieve. An example of a direct transfer is given in Table 1.4.7. The elliptical

Table 1.4.7. Optimal transfer examples from Earth to Saturn with insertion to a one-day orbit at Saturn.

Launch			Arrival			Total		
Date	Vinf (m/s)	DV (m/s)	Date	Vinf (m/s)	DV (m/s)	Transfer time	Vinf (m/s)	DV (m/s)
6 Dec 2009	11,547	5,715	10 Dec 2014	5,739	3,410	1,830	17,286	9,125
22 Dec 2009	10,496	4,971	7 Mar 2019	5,927	3,441	3,362	16,423	8,413

Table 1.4.8. Optimal transfer examples from Earth to Saturn with insertion to a high orbit at Saturn.

Launch			Arrival			Total		
Date	Vinf (m/s)	DV (m/s)	Date	Vinf (m/s)	DV (m/s)	Transfer time	Vinf (m/s)	DV (m/s)
13 Dec 2009	11,702	5,827	3 Oct 2015	5,295	1,617	2,120	16,997	7,445
14 Dec 2009	10, 632	5,066	2 Aug 2018	5,735	1,844	3,153	16,367	6,910

reference at Earth has perigee at 200 km altitude and apogee at 35,787 km (GTO characteristics). At Saturn the pericentre is at 2000 km altitude and apocentre at 263,160 km. Once again, this elliptical target orbit has a 1 Earth-day period for comparison with the Venus and Mars cases. A more likely choice of orbit about Saturn has pericentre at 840,000 km altitude and apocentre at 20 million km. This can then be the starting point of a gravity-assisted tour of the Saturnian system.

Figure 1.4.4 shows the sum of Vinfinities (Vinfinity leaving Earth and Vinfinity approaching Saturn) for a range of launch epochs and transfer times. Minimum Vinfinity transfers can be seen between 1,500 and 3,500 days transfer duration for the 'short' transfer type and between 2,000 and 5,000 days for the 'Long' transfer type.

1.4.6 Uranus, Neptune and Pluto

The synodic period of these planets with respect to Earth is as follows:

Uranus 370 days
Neptune 368 days
Pluto 367 days

Therefore, frequent transfer opportunities arise.

Typical conjunction-type transfers are shown in Table 1.4.9. Some variation is seen between optimum launch epochs, due to the eccentricity of the orbits of these planets – particularly Pluto. The further complication with Pluto is its relatively high orbital inclination. Minimum Vinfinity transfers take approximately 16 and 31 years respectively for Uranus and Neptune.

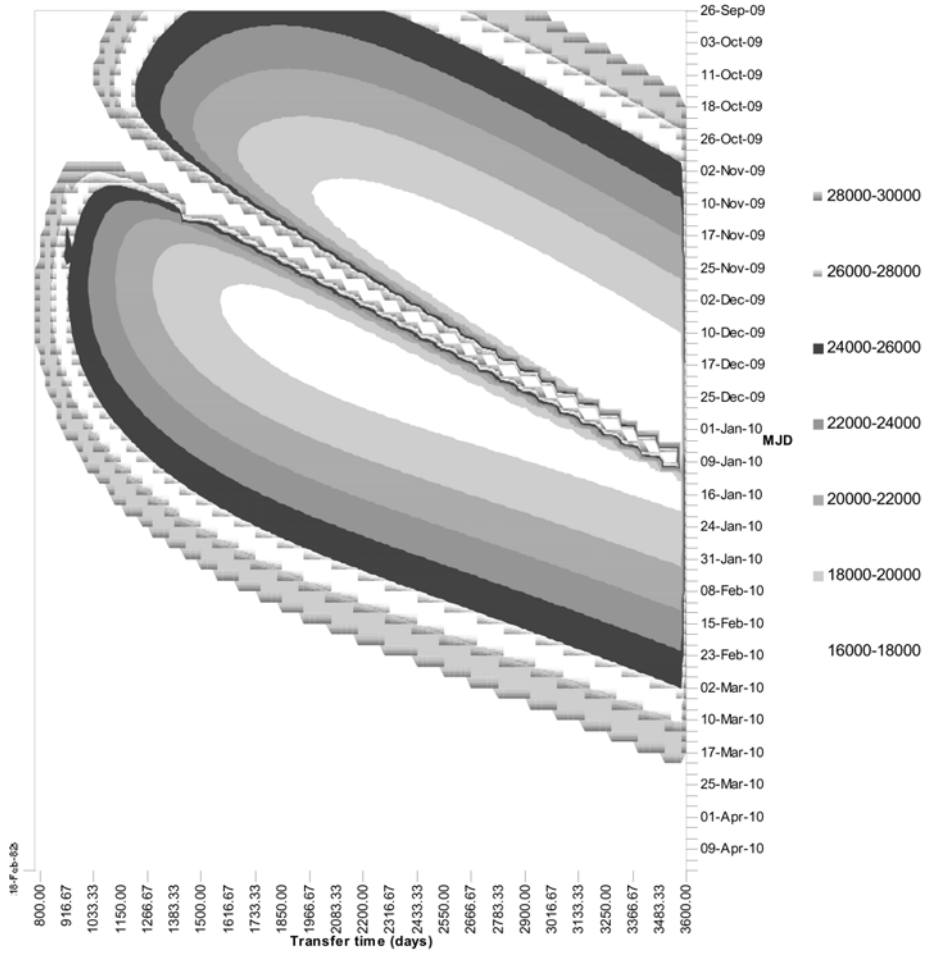

Figure 1.4.4. Vinfinity sums for conjunction-type two-impulse transfers to Saturn over launch period 2009–2010.

Table 1.4.9. Properties of conjunction type transfers to the outer planets.

Launch			Arrival		Total	
Date	Vinf (m/s)	DV (m/s)	Date	Vinf (m/s)	Transfer time (days)	Vinf (m/s)
Uranus						
24 May 2010	11,504	5,684	24 Mar 2027	4,607	6,148	16,111
Neptune						
10 Apr 2010	13,310	7,034	15 Sep 2040	4,122	11,116	17,432
Pluto						
11 Jan 2010	19,752	12,374	15 Mar 2037	4,141	9,925	23,893

The departure ΔV is measured from a reference elliptical orbit with perigee at 200 km altitude and apogee at 36,000 km altitude.

Missions to Pluto are strongly influenced by the departure epoch. The example in the previous table is constrained by the year of departure. The optimised transfer here is influenced by two factors: the mission ΔV reduction afforded by a 'conjuction' type transfer arriving typically 40–45 years after departure and that required to reach a rendez-vous with Pluto at a high latitude with respect to the ecliptic. Pluto crosses the ecliptic in 2018. Therefore, this solution is a 'compromise' transfer.

Such high launch energies or spacecraft ΔVs are not feasible for conventional mission designs. Special techniques must therefore be employed for transfers to the outer planets. (These will be described in Chapter 4.)

1.5 RETURN MISSIONS TO THE PLANETS

There is considerable scientific interest in the development of return missions to the planets. They enable the return to Earth of samples of the planets of our Solar System, or alternatively, allow the possibility of manned exploration of the planets. The design of such missions can be considered as an extension of the methods already studied for 'one way' missions.

Such a mission starts with a transfer from Earth to the target planet. The target most often considered in this context is Mars, and this will feature in the examples subsequently analysed. The spacecraft then stays for some specified time at the planet and then returns to Earth.

1.5.1 Optimal stay times

The most efficient return scenario in terms of minimisation of the total ΔV required for the mission is the following:

(1) Perform a 'conjunction'-type transfer from Earth to the target. This will minimise the outward ΔV.
(2) Wait at the planet until the optimal epoch to initiate a return conjunction-type transfer. This waiting period may in practice exceed the period needed to perform science operations at the planet.
(3) Perform the return conjunction-type transfer. This will minimise the return ΔV.

The key question is that of the required stay time at the target to enable such a strategy, as in general space mission designs drive towards minimising the required total mission duration.

A simplified analysis allows some basic properties of the mission to be predicted. It will be assumed that all trajectories are co-planar and that the planets move in circular orbits. The following definitions can be made:

λ_{D1}: heliocentric longitude of first departure (from planet 1).
λ_{RV1}: heliocentric longitude of first rendez-vous (with planet 2).

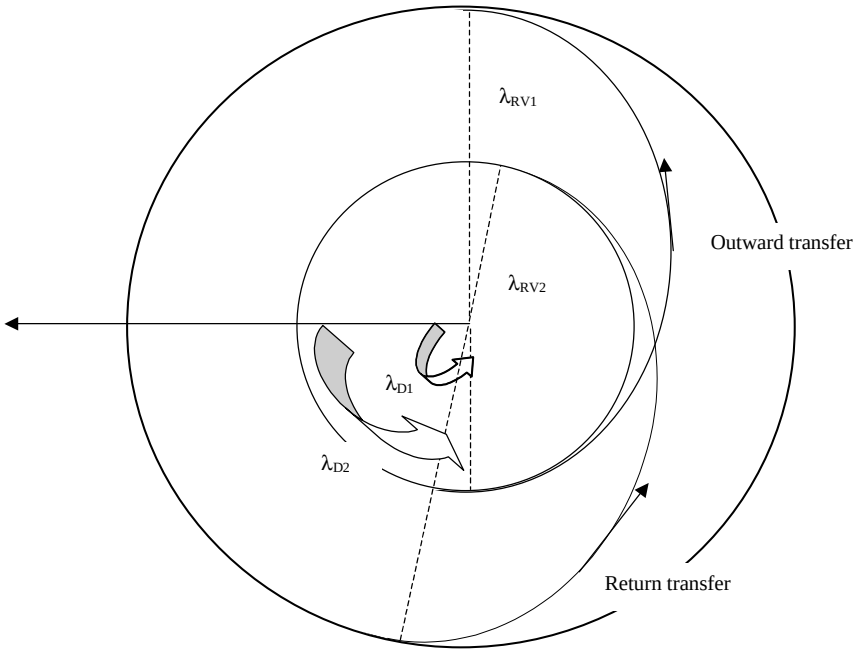

Figure 1.5.1. Return mission geometry.

λ_{D2}: heliocentric longitude of second departure (from planet 2).
λ_{RV2}: heliocentric longitude of second rendez-vous (with planet 1).
a_1: semi-major axis of planet 1.
a_2: semi-major axis of planet 2.

The period of planet 1's orbit is:

$$\tau_1 = 2\pi\sqrt{\frac{a_1^3}{\mu}}$$

The period of planet 2's orbit is:

$$\tau_2 = 2\pi\sqrt{\frac{a_2^3}{\mu}}$$

μ is the Sun's gravitational parameter. The time taken for the transfer from 1 to 2 is:

$$T_{12} = \pi\sqrt{\frac{(a_1 + a_2)^3}{8\mu}}$$

The fraction of the orbital period of planet 1 (τ_1) is:

$$\frac{T_{12}}{\tau_1} = \frac{1}{2}\sqrt{\left(\frac{(a_1 + a_2)}{2a_1}\right)^3}$$

The fraction of the orbital period of planet 2 (τ_2) is:

$$\frac{T_{12}}{\tau_2} = \frac{1}{2}\sqrt{\left(\frac{(a_1 + a_2)}{2a_2}\right)^3}$$

The change in longitude of the planets over the outward transfer is given by:

$$\Delta\lambda_{1-12} = \pi\sqrt{\left(\frac{(a_1 + a_2)}{2a_1}\right)^3} \quad \text{and} \quad \Delta\lambda_{2-12} = \pi\sqrt{\left(\frac{(a_1 + a_2)}{2a_2}\right)^3} \tag{1.5.1}$$

The change in longitude of the spacecraft over the transfer is π radians.

For the outward journey, the longitude of planet 2 at spacecraft rendezvous must lie π radians ahead of the longitude of planet 1 when the spacecraft leaves planet 1.

$$\lambda_{2-RV1} = \lambda_{1-D1} + \pi \tag{1.5.2}$$

where λ_{1-D1} is the longitude of planet 1 at the epoch of the spacecraft's departure from planet 1, and λ_{2-RV1} is the longitude of planet 2 at the epoch of the spacecraft's arrival at planet 2.

The relationship between the longitudes of the planets at the epoch of arrival at planet 2 can be derived:

$$\lambda_{1-RV1} = \lambda_{2-RV1} - \pi + \Delta\lambda_{1-12} \tag{1.5.3}$$

where λ_{1-RV1} is the longitude of planet 1 at the epoch of the spacecraft's arrival at planet 2.

For the return journey, which will take the same time as the outward journey, the longitude of planet 1 must lie π radians ahead of the longitude of planet 2 when the spacecraft leaves planet 2.

$$\lambda_{1-RV2} = \lambda_{2-D2} + \pi \pm n * 2\pi \tag{1.5.4}$$

where λ_{1-RV2} is the longitude of planet 1 at the epoch of the spacecraft's return to planet 1, and λ_{2-D2} is the longitude of planet 2 at the epoch of the spacecraft's departure from planet 2. $\pm n$ revolutions can be added. The minimum value of 'n' is sought, to give minimum stay time ('n' is an integer).

Also:

$$\lambda_{1-D2} = \lambda_{2-D2} + \pi - \Delta\lambda_{1-12} \tag{1.5.5}$$

where λ_{1-D2} is the longitude of planet 1 at the epoch of the spacecraft's departure from planet 2.

Given the angular velocity of the two planets, the following two equations apply regarding the change in planetary longitude over the period of time spent at planet 2:

$$\lambda_{1-D2} = \lambda_{1-RV1} + \omega_1\Delta t \tag{1.5.6}$$

$$\lambda_{2-D2} = \lambda_{2-RV1} + \omega_2\Delta t \tag{1.5.7}$$

where ω_1 is the angular velocity of planet 1, ω_2 is the angular velocity of planet 2, and Δt is the period of time between arriving at planet 2 and departing from planet 2.

Table 1.5.1. Hohmann transfer durations and optimum stay times for return missions from Earth to the outer planets.

Target	Mars	Jupiter	Saturn	Uranus	Neptune	Pluto
Duration (years)	0.71	2.73	6.06	15.97	30.53	45.21
Stay time (days)	454	214	335	21	346	214
Mission time (years)	2.66	6.05	13.03	32.00	62.01	91.00

The elapsed time, Δt, between the arrival and departure epochs at planet 2, can be found by subtracting Equation 1.5.7 from Equation 1.5.6 and using the relationships Equation 1.5.5 and Equation 1.5.3:

$$\Delta t = \frac{2\pi - 2\Delta\lambda_{1-12}}{\omega_1 - \omega_2} \tag{1.5.8}$$

In the case of an outward transfer, multiples of 2π can be added to the numerator to make it positive. Then, further additions of 2π give longer possible stay times, each incremented by the synodic period of planet 1–planet 2.

Some example stay time from return missions to Mars and the planets beyond can be calculated.

The idealised transfer durations (in Earth years), using circular orbit approximations and Hohmann transfers, from Earth to each outer planet are given in Table 1.5.1, together with the optimal stay times, calculated by the previously described approximations.

1.5.2 Case of an optimal stay time for a Mars return mission

Return missions to Mars have received much attention in proposals for exploration of that planet. These include both robotic missions and, ultimately, the possibility of a manned mission.

For robotic missions there is a greater degree of flexibility with regard to the stay time at Mars, when compared with a manned mission, which is likely to have more strict constraints on allowable stay time.

The previous section has shown that for the idealised case of circular planetary orbits, the minimum V_∞ solution requires a stay time at Mars of approximately 450 days. However, the more detailed discussion regarding the complete range of transfer scenarios has shown that multiple transfer possibilities exist. Firstly, when considering the outward transfer to Mars, the options include:

- A short conjunction-class transfer
- A long conjunction-class transfer
- A 1.5-revolution-type transfer.

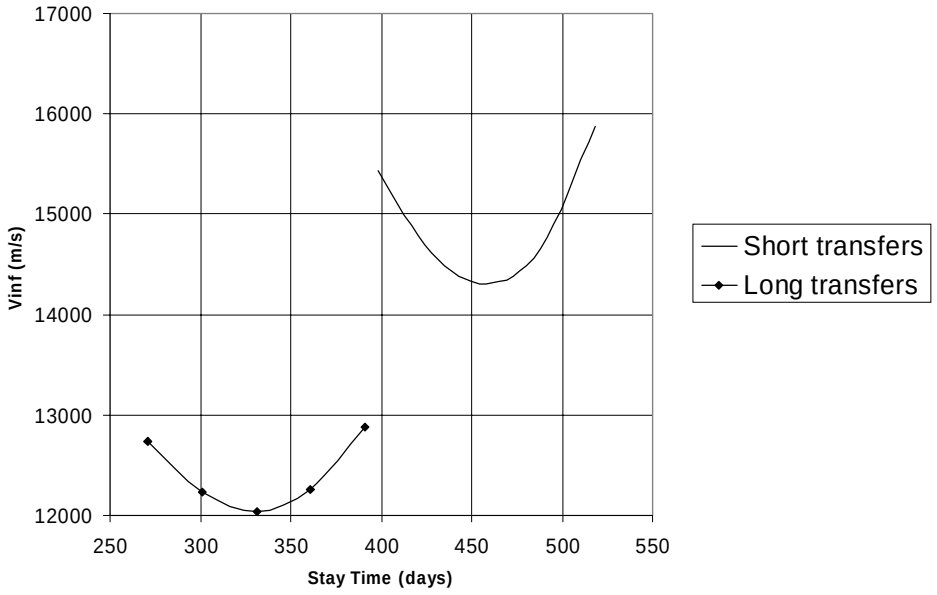

Figure 1.5.2. The effect of stay time on V_∞ total for different conjunction-type transfers for launch in 2011 to Mars.

This same set of options exists when considering the return scenario from Mars to Earth. For a given transfer opportunity occurring at the frequency of the Earth–Mars synodic period, each transfer type has its own optimal departure and arrival dates. These can be combined to achieve a range of corresponding stay times at Mars.

Firstly, it is possible to consider just the conjunction type transfers. Two examples are shown in Figure 1.5.2. The Earth launch opportunity considered here involves an Earth departure in 2011, but similar relationships can be found at each launch opportunity. The possibility of a 'short' conjunction-type transfer for the outward leg of the mission and a 'short' conjunction-type transfer for the return leg gives a minimum V_∞ solution with a stay time at Mars of approximately 460 days. Alternatively, a mission with a 'long' conjunction-type transfer for both outward and return legs gives an optimal stay time at Mars of approximately 330 days.

The V_∞ total considered is the sum of each of the excess hyperbolic speeds – leaving Earth, approaching Mars, leaving Mars and approaching Earth. In terms of an actual mission design, then a much more complex objective for minimisation would be chosen, as the staging of transfer vehicles would be considered and also the possibility of aero-assisted entry. However, the V_∞ choice is a good representation of the essential nature of the problem.

The variation in V_∞ shown in Figure 1.5.2, with stay time can be found by considering the variations in the arrival and departure dates from Mars, based around optimal conjunction-type transfers. At this launch opportunity, the long

transfers result in a lower V_∞ total than the short transfers. However, of the four conjunction-type transfer combinations for each launch opportunity, the best solution varies with the particular opportunity.

Further stay time options can be obtained by considering a combination of conjunction-type transfer and 1.5-revolution transfers. The case now considered is a launch in 2020. Both this 1.5-revolution and the conjunction-class transfers will be considered.

The 1.5-revolution transfer phase of the mission can be provided on either the outward or the return leg of the mission. These may also be combined with long or short conjunction-type transfers on the other leg. These possibilities lead to a considerable variety of optimal stay durations at Mars. The ΔV (or V_∞ requirements) for the 1.5-revolution transfers are generally similar to those for a conjunction-type transfer, and so the local minima in the V_∞ total are expected to have comparable magnitudes to the cases using conjunction-type transfers on both mission legs. A further complication of the 1.5-revolution trajectories is that for arrival or departure epochs removed from the optimal dates, a mid-course ΔV is required (as discussed in the section regarding multi-revolution transfers.)

However, an interesting factor with these missions is the total mission duration. For the 1.5-revolution cases, the durations are typically 1,100 days and 1,250 days for the 1.5-revolution returning case and 1.5-revolution outward cases respectively. This can be compared with the longer stay time but shorter transfer duration missions described previously. In these cases, the 'long–long' cases have a total mission duration of just under 1,000 days and the 'short–short' mission approximately 950 days. Therefore, finding a low V_∞, short stay-time mission does not necessarily shorten the total duration of the mission.

1.5.3 Short-stay time missions at Mars

The previous section has shown some possibilities for low ΔV missions with short stay-times. Although allowing a short stay-time at Mars, the total durations of these missions are often longer than the conjunction return mission.

An alternative approach to short stay-time can be considered that also shortens the total return mission duration. This uses a variation on conjunction type transfers for both legs of the mission. However, this strategy leads to a higher ΔV scenario. Stay-times of between typically 30 and 300 days can be considered in this category.

An optimal conjunction-type transfer may be used for the outward mission leg. Then, after a short stay time (typically 60 days at Mars) the spacecraft transfers back to Earth using a conjunction-type transfer (i.e., less than one revolution in this context). However, because of the non-optimal departure date from Mars, the return leg is now significantly different from a standard conjunction-type transfer mission.

The minimum ΔV case for the return leg, after a 60-day stay, implies a return trip duration of more than 500 days. Such a transfer results in the vehicle passing outside of Mars' heliocentric distance. The V_∞ leaving Mars is now increased beyond that for a standard conjunction-type return. The V_∞ at Earth arrival is

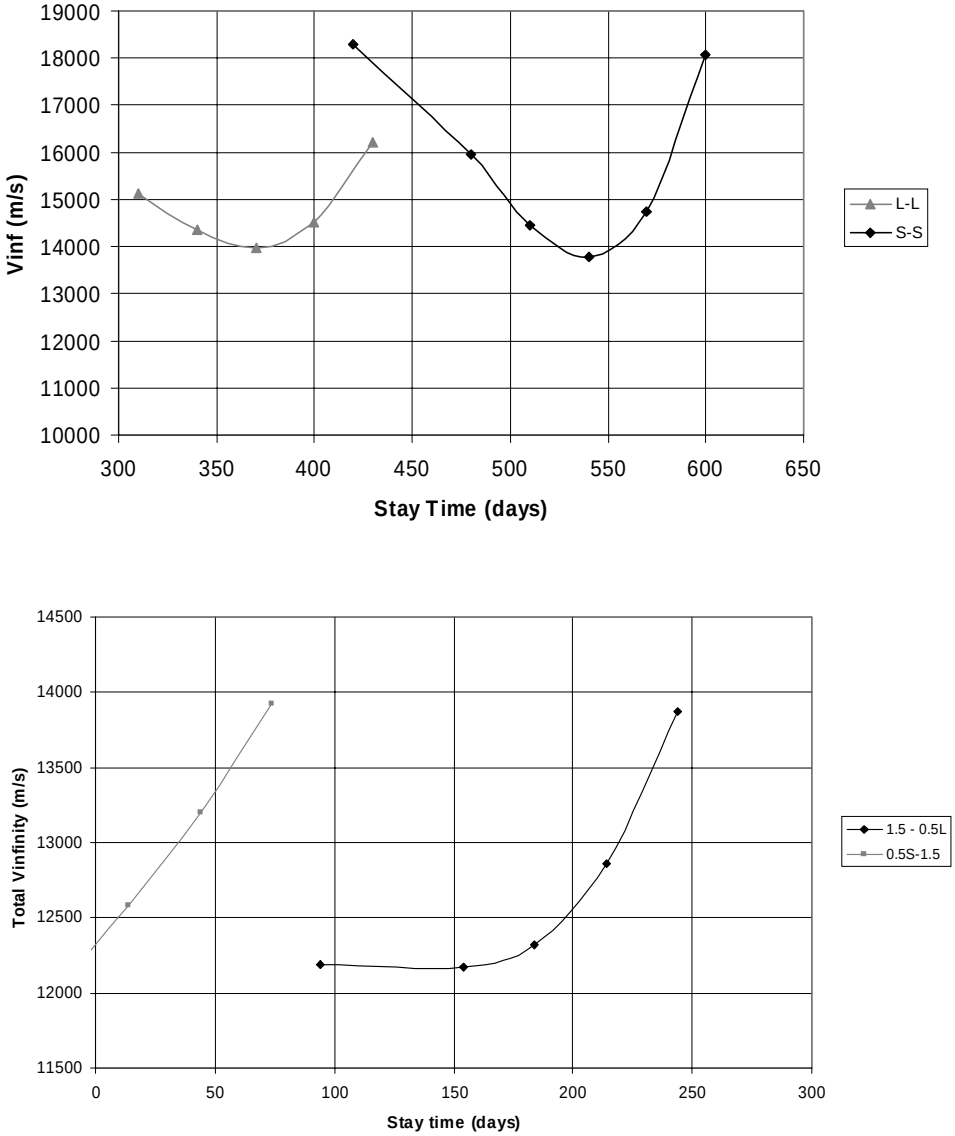

Figure 1.5.3. The effect of stay time on V_∞ total for different transfer types for launch in 2020. In the upper figure the conjunction-type outward and return missions for this launch epoch show a similar characteristic to the 2011 launch case. In this launch year, the V_∞ totals are higher than in 2011. Near-zero stay times can be accomplished in some scenarios (the example of a conjunction type outward leg and 1.5-revolution return leg). The second plot shows the solutions obtained with such a transfer 'leg' in terms of the V_∞ totals. In the case of the 1.5-revolutions return leg, then the minimum total V_∞ solution lies at a 'negative' stay duration. Clearly, such solutions are not possible so the minimum allowable V_∞ solution is for zero stay time.

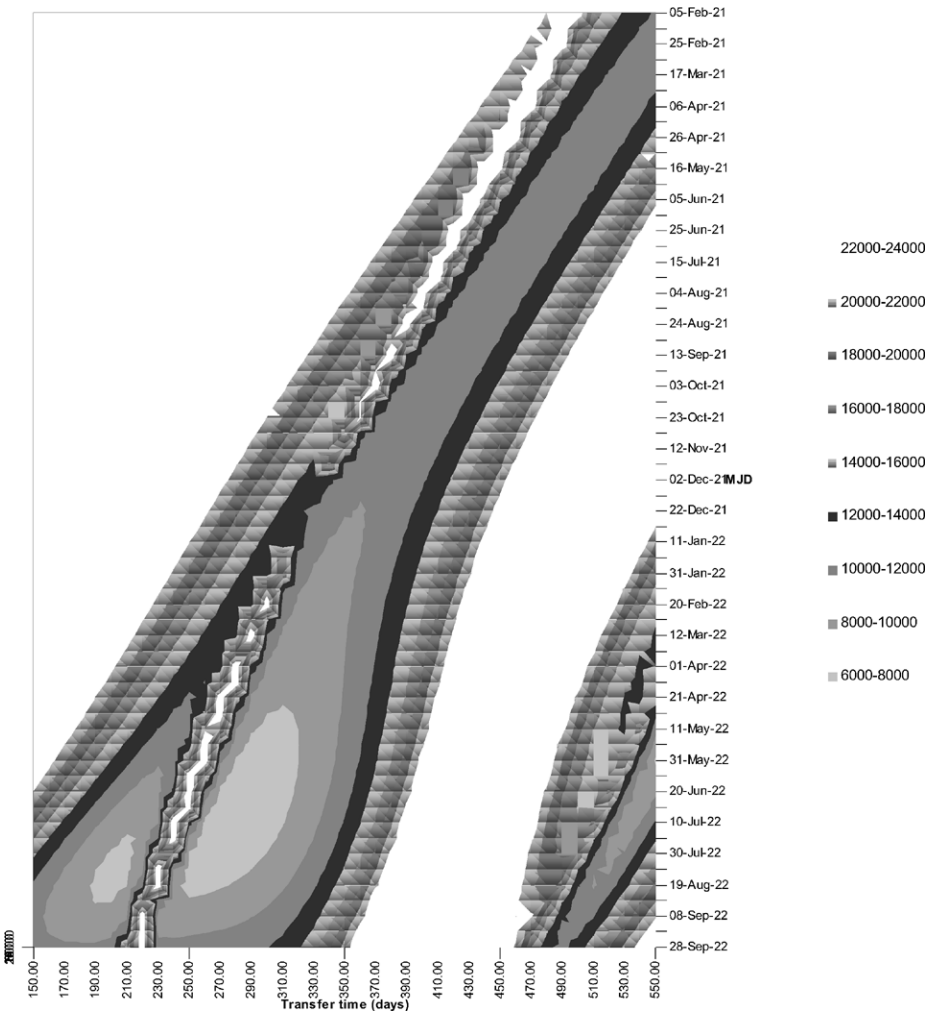

Figure 1.5.4. Transfer options from Mars to Earth leaving in 2021, with two local minima in V_∞ totals.

also increased. In fact, as in the case of non-optimal arrival and departure epoch 1.5-revolution transfers, a mid-course ΔV can be used advantageously in some of these modified conjunction type scenarios. That is, the total ΔV is reduced by using a mid-course manoeuvre.

An example of a transfer to Mars after launch in 2020 can be considered. If a locally optimal, short conjunction transfer is followed to Mars, the spacecraft will arrive in late February of 2021. A stay time of 60 days at Mars then implies a departure in late April 2021.

Figure 1.5.4, showing V_∞ total contours (Mars departure plus Earth arrival)

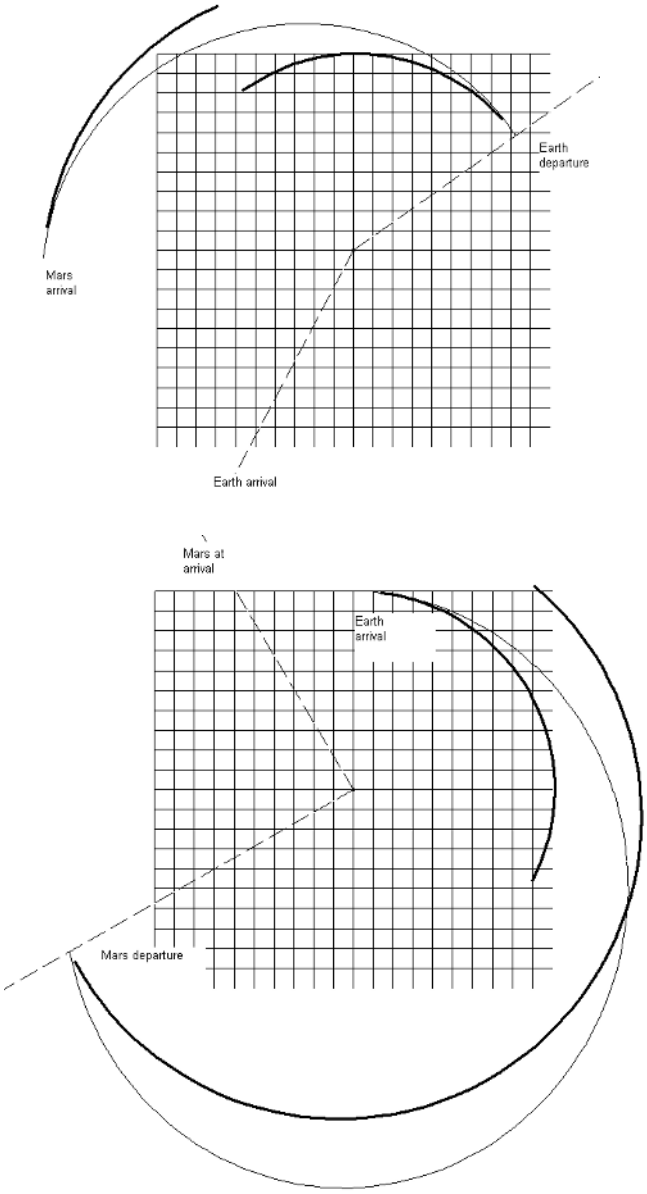

Figure 1.5.5. A return mission to Mars with optimal conjunction-type transfer (launch in 2020) on the outward leg, 60-day stay-time, and minimum ΔV trajectory on the return leg. The grid is 1 AU from centre to edge. Earth and Mars orbit sections are also shown. The sub-grid size is 0.1 AU. Departure from Mars takes place 60 days after arrival. The optimal return trip, with the constraint of this departure epoch, passes outside of the Mars' orbit and takes approximately 500 days for the return to Earth. The total mission duration is now typically 800 days.

versus departure dates from Mars and transfer durations, indicates that a minimum V_∞ transfer exists for a transfer duration of just over 500 days. A second minimum can be seen with a shorter transfer duration.

A range of stay-times at Mars can be considered with such a strategy, from short durations, such as 60 days, up to long-duration optimal stay-time cases where an optimal conjunction-type transfer can be used for the return leg of the mission. For the return leg, the departure date is fixed by the stay-time requirement, but the arrival date on return to Earth is optimised to minimise the ΔV for the return. As observed for the 60-day stay-time case, two local minima exist, analogous to the locally optimal short and long conjunction-type transfers.

The two locally minimum return solutions (for a given departure epoch from Mars and hence stay time) differ in the ΔV total. Both are evaluated in Figure 1.5.6.

However, a further impact of these return options must be considered: the total mission duration. Figure 1.5.7 shows the mission duration for the transfer using a mid-course manoeuvre, which is the minimum ΔV case. Therefore, although short stay-times can be achieved, the total mission duration is still approximately 800 days, compared with a value approaching 1,000 days for a 450-day stay-time.

If, alternatively, the long conjunction-class transfer were used for the outward leg from Earth to Mars, arrival at Mars would be approximately 100 days later. In the 2020 example, the long transfer type has a greater V_∞ requirement than the short case. The impact on stay-time and return ΔV can be seen by subtracting 100 days from the stay-times in the plots in Figure 1.5.6.

A further option is the use of a non-optimal outward transfer, modifying the arrival epoch at the expense of ΔV. The previous plots indicate that for short stay-time missions, a change of stay time of up to 300 days has little impact on ΔV. However, the effect of varying the arrival epoch on the outward leg has a much more adverse effect on ΔV. Therefore this approach, using an optimal outward leg, is the best strategy in this case.

With an even higher available ΔV, shorter returns are possible at approximately 300 days (or even less if required). These return options now use trajectories that in general pass inside Earth's heliocentric radius. Such mission types are sometimes referred to as 'opposition-type' missions, and offer the possibility of a return mission to Mars with a short total mission duration.

Once again, the 2020 mission example can be used. A 30-day stay is used (longer stay times actually increase the transfer duration in this case). This transfer requires a greater Vinfinity when leaving Mars and also a large deep-space manoeuvre. In this example, the return takes just over 300 days. An example is shown in Figure 1.5.8.

This type of fast return mission is sometimes described as an 'opposition-class' mission. It can sometimes be combined with a Venus gravity-assist manoeuvre in place of the deep-space ΔV that reduces aphelion in this case (see Chapter 4).

1.5.4 Short-duration Mars return missions

Alternative transfer options, specifically applicable to manned missions, are available to accelerate the transfer by using high-energy spacecraft propulsion

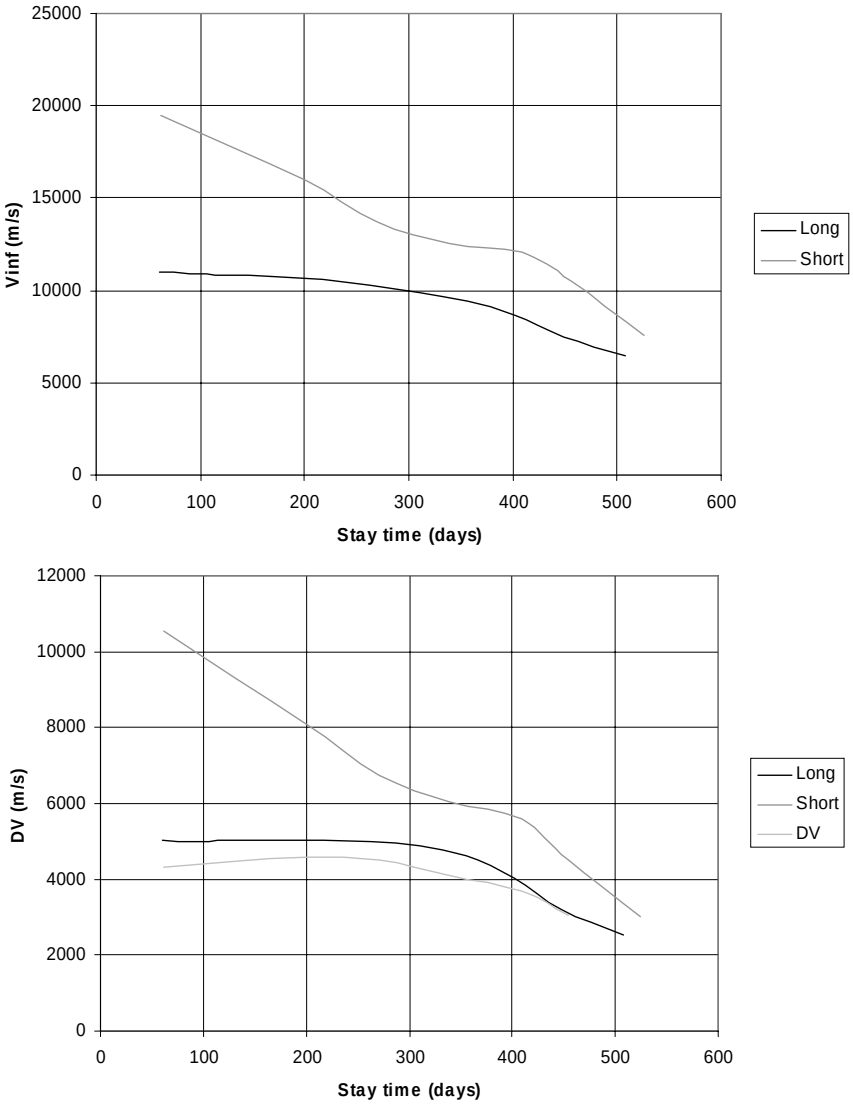

Figure 1.5.6. The effect of stay-time on return ΔV and V_∞ after a short conjunction-class transfer from Earth, departing in mid-2020. This shows the impact of the stay time at Mars, and hence the departure epoch, on the V_∞ total for the transfer back to Earth. Two impulse long and short transfer types are considered. Eventually, minimum V_∞ transfers are reached for both transfer types. A further option is to introduce an intermediate deep-space manoeuvre. Then the objective to be minimised is the sum of ΔVs for departure, deep space, and at arrival. ΔVs at departure and arrival assume initial reference orbits of 400 km by 36,000 km altitude at Mars, and 500 km by 36,000 km altitude at Earth. The impact of this additional manoeuvre is to reduce the total ΔV for the return transfer, for the shorter stay-time cases. Although the introduction of a deep space manoeuvre reduces ΔV total, it does not generally have a large impact on the return trajectory duration in such cases.

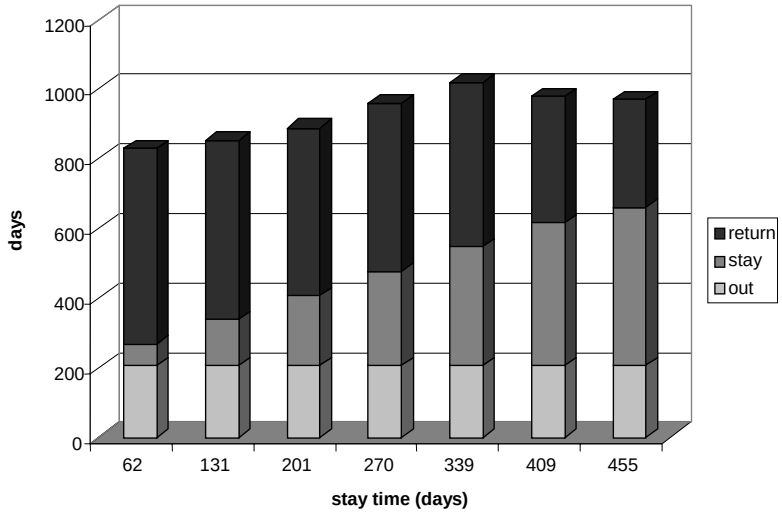

Figure 1.5.7. The effect of stay time on total mission duration after a short conjunction-class transfer from Earth, departing in mid-2020.

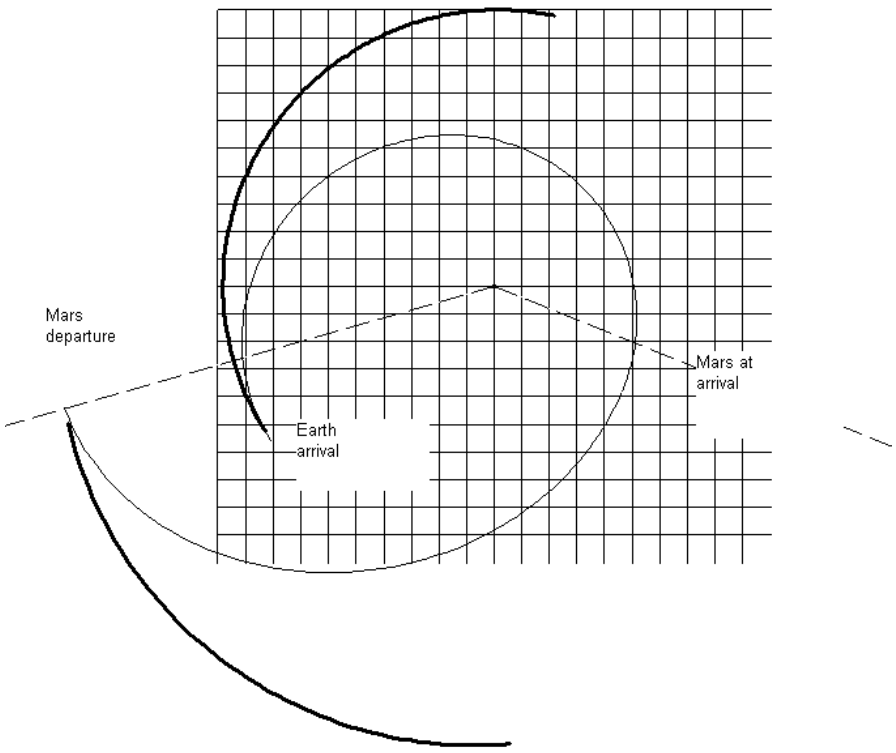

Figure 1.5.8. A fast return transfer from Mars to Earth with a short stay at Mars after a conjunction-class outward transfer.

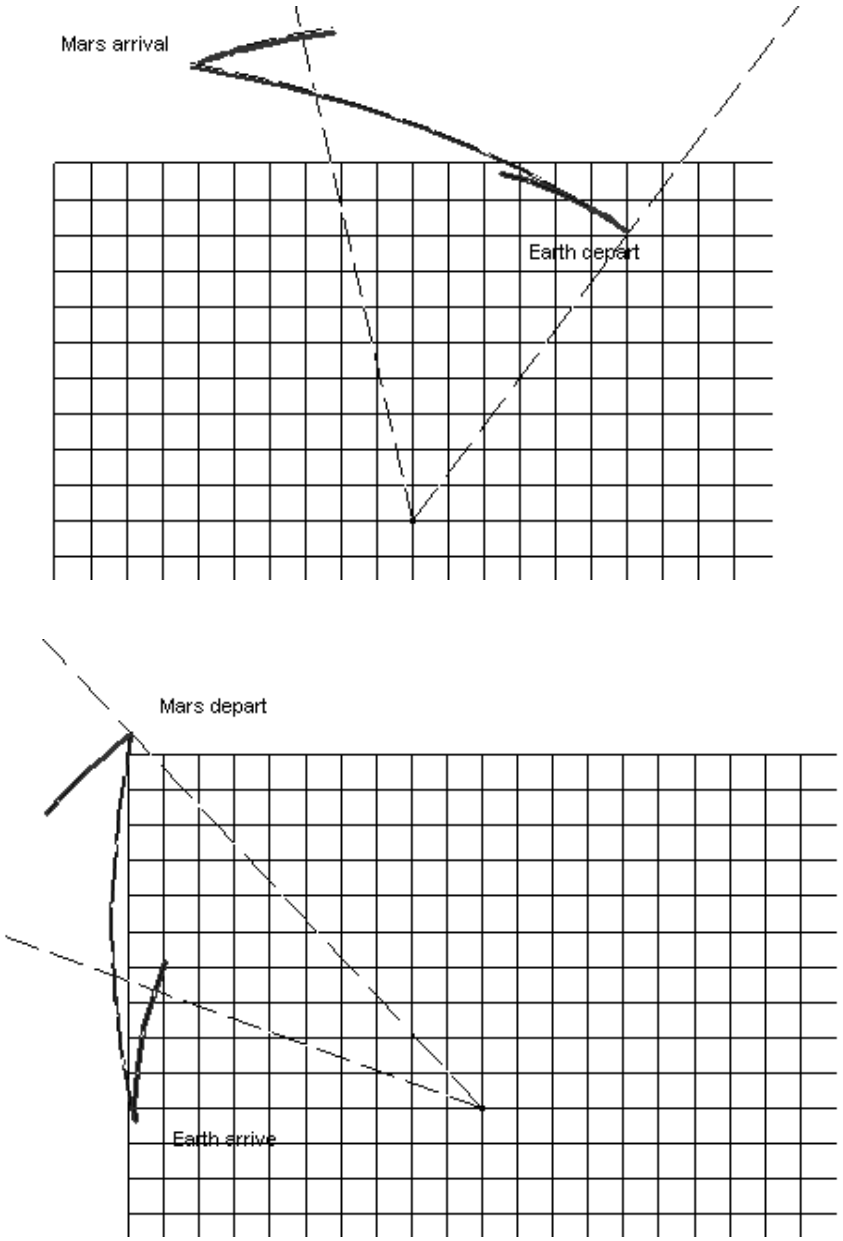

Figure 1.5.9. Examples of short transfers from Earth to Mars with short stay-time and return. This assumes a 50-day constraint on each of the outward and return trajectory legs. The stay-time at Mars is 30 days. The total mission duration in this case is now 130 days. The ΔVs that are required cannot be achieved by conventional propulsion systems. The sub-grid size is 0.1 AU. Earth's and Mars' orbital arcs are also shown.

systems. In this way, one-way transfers of as little as 50 days can be considered. There are high ΔV implications for the spacecraft/launcher. Excess hyperbolic speeds of 10–20 km/sec for each departure and arrival may be implied. Such a scenario can be applied with a short-stay manned mission and using a similar fast return trip to Earth. An example is shown in Figure 1.5.9.

2

Spacecraft propulsion

Nearly all interplanetary missions require the spacecraft to execute manoeuvres to change orbit, but many mission designs are constrained in their objective by the limitations in the capability of the spacecraft to execute such manoeuvres. This capability depends on the type of propulsion system used. Therefore, the design of a space mission cannot be carried without detailed consideration of the propulsion system type. Optimisation of a mission design, including the optimisation of an interplanetary trajectory, can involve the selection of the best parameters for the propulsion system. This chapter provides an overview of propulsion principles and also the performances available from different system types.

To carry out interplanetary transfers, spacecraft must achieve significant changes in their velocity, and some form of on-board propulsion is needed to accomplish this objective. A wide variety of propulsion types are available for spacecraft. Some are generally more suitable for certain manoeuvre types, whilst in other cases the choice is open. In such cases, the choice is often ultimately dictated by considerations of efficiency of the transfer and the cost.

The common theme for the application of most propulsion types is that the spacecraft will experience a change in linear momentum, or an impulse. This change in momentum is achieved by the expulsion of a propellant. The process of expulsion causes an equal and opposite reaction on the spacecraft, which consequently accelerates, ultimately achieving the required change in velocity.

In practice, propulsion system types are often divided into two categories: high thrust and low thrust. This parameter – thrust – can be a key consideration in the selection of a propulsion system type. High-thrust systems are well suited to manoeuvres that can only be accomplished efficiently at certain spatial locations, requiring the thrust arc to be short.

2.1 PROPULSION BASICS

Certain common considerations apply to almost all propulsion systems. These will be discussed in this section. The equations presented are without derivation here, as this is a specialist subject and details may be found in the reference texts listed.

A propulsion system utilising an expelled mass, or propellant, must obey certain fundamental rules. Firstly, it is possible to consider the system as a 'black box' without having knowledge of what happens inside. The key point is that the propellant is expelled through a reference surface. This could, for example, be a surface enclosing the exit of a rocket engine nozzle. The shape of the surface is to be determined. More detailed analyses of propulsion system dynamics and rocket engine principles are to be found in Cornelisse, Schoyer and Wakker (see references).

The rate at which mass is expelled can be described as follows:

$$-\dot{m} = \int_{A_{ref}} \rho \underline{V} \cdot \hat{n} dA \tag{2.1}$$

where $-\dot{m}$ is the rate at which propellant mass is expelled through the reference surface (the negative sign is used here because the term dm/dt is itself assumed to be negative; that is, fuel mass of the spacecraft is decreasing and so the rate of change of spacecraft mass with time is negative) and ρ is the density of the propellant. $\underline{V}$ is the velocity of the propellant relative to the spacecraft or 'black box' unit and n is the unit vector in the direction of the outward perpendicular to the reference surface, A_{ref}.

If the propellant is a gas under pressure then the force acting on the spacecraft is given by the following expression, the sum of a momentum flow term and a pressure thrust term:

$$\underline{T} = -\int_{A_{ref}} (\underline{V}(\rho \underline{V} \cdot \hat{n}) + (p - p_a)\hat{n}) dA \tag{2.2}$$

where $\underline{T}$ is the thrust vector acting on the spacecraft, p is the pressure of the propellant and p_a is the external ambient pressure (zero in the vacuum of space). The thrust is in a direction opposite to the expelled momentum flow. If the propellant is not a pressurised gas then the pressure thrust term may be neglected.

A detailed derivation of these expressions can be found in the references for this section. The discussion here derives from that in Cornelisse *et al.*. These generalised expressions can be reduced by assuming that the density, pressure and velocity are approximately constant over the reference surface. This assumption then defines the reference surface.

The mass flow can be reduced to the following (recalling that dm/dt is a negative qualtity):

$$-\dot{m} = \rho_{ex} V_{ex} A_{ref} \tag{2.3}$$

where A_{ref} is the area of the reference surface, ρ_{ex} is the density of the exhaust, and

V_{ex} is its velocity at the reference surface. Similarly the general thrust equation becomes:

$$\underline{T} = \left(\dot{m} \frac{V_{ex}}{A_{ref}} - (p_{ex} - p_a) \right) \int_{A_{ref}} \hat{n} dA \tag{2.4}$$

The first term in this expression is generally considerably greater than the second. The density and exhaust velocity of the propellant are therefore significant factors in the thrust achieved. The ratio between thrust and propellant mass flow is proportional to the exhaust velocity.

The integral in Equation 2.4 depends on the nature of the propulsion system, as the nature of the reference surfaces may differ. In the simplest case, where a propellant is accelerated along a single direction, the reference area is a surface normal to this axis. This expression can then be reduced to the following:

$$T = -\dot{m} V_{ex} \tag{2.5}$$

In this case the thrust-to-mass flow ratio is given identically by the exhaust velocity.

For a rocket system in which a pressurised, compressible gas is considered, then the system is more complex. Firstly, by assuming that the gas is approximately stationary but at a high pressure and temperature in the combustion or heating chamber, it is possible to obtain the following expression for the velocity of the propellant as a function of the pressure at some point away from the chamber:

$$V_{ex} = \sqrt{\frac{2\gamma}{\gamma - 1} \frac{RT_c}{M} \left(1 - \left(\frac{p_{ex}}{p_c} \right)^{\frac{\gamma - 1}{\gamma}} \right)} \tag{2.6}$$

where p_{ex} is the pressure on the exhaust reference surface and T_c and p_c are the pressure and temperature in the combustion or heat chamber, γ is the ration of specific heats, R is the universal gas constant and M is the mean molecular weight of the exhaust gas. Reducing the pressure at the exit from the propulsion system therefore increases the exhaust velocity. This expansion process can be achieved via a nozzle. An efficient nozzle will allow expansion of the gas to a pressure close to the ambient, external pressure. The thrust force is actually achieved by the action of the pressure on the surface of the nozzle:

It is possible to approximate the thrust produced through such a nozzle, based upon equation 2.4, in terms of the nozzle geometry – in particular the cone angle, θ, shown in Figure 2.1.1. The following equation describes the magnitude of the thrust. This acts along the horizontal axis in the figure.

$$T = \left(-\dot{m} V_{ex} \frac{(1 + \cos\theta)}{2} + (p_{ex} - p_a) A_{ex} \right) \tag{2.7}$$

where A_{ex} is now the area at the open end of the cone.

It is now possible to establish the relationship between the ideal change in speed, propellant mass expelled and the exhaust velocity. Firstly, a new term is introduced: the specific impulse. This is the impulse achieved per unit mass of propellant

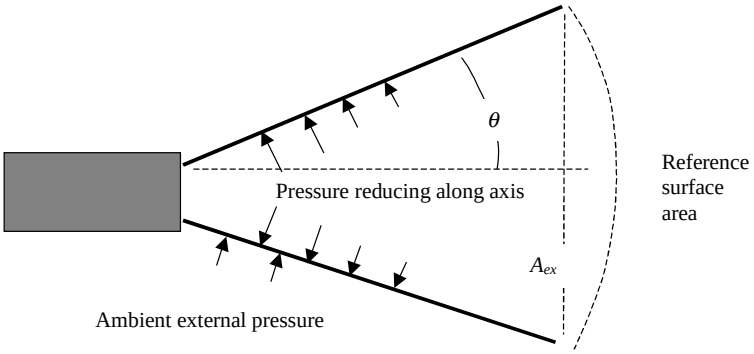

Figure 2.1.1. Illustration of a nozzle.

(denoted *Isp*). Therefore, the previous expression can be considered, over an infinitesimally short period of time, and so $Isp = V_{ex}\dfrac{(1+\cos\theta)}{2}$, giving an expression in m/s. The exit pressure term is now neglected. Specific impulse is often specified in seconds and uses a scaling term: Earth surface gravitational acceleration:

$$Isp = \frac{V_{ex}}{g_0}\frac{(1+\cos\theta)}{2} \tag{2.8}$$

where $g_0 = 9.80665\,\text{m/s}$ and specific impulse is measured in seconds, and so $T = -\dot{m}\,Isp\,g_0$.

The ideal speed change can now be introduced as:

$$\Delta V = \int_{t_0}^{t_f}\frac{dV}{dt} = \int_{t_0}^{t_f}\frac{T}{m}\,dt \tag{2.9}$$

This simple expression would represent the actual speed change when a force acts constantly along the velocity vector and no other forces act. It represents the maximum speed change that is achievable due the application of the force T over a period of time, $t_f - t_0$.

This speed change can now be related to fuel mass usage as follows:

$$\frac{dV}{dt} = \frac{T}{m} \qquad \text{and therefore} \qquad \dot{m} = -\frac{m}{Isp * g_0}\frac{dV}{dt}$$

Integrating over the manoeuvre yields:

$$Ln\left(\frac{m_f}{m_0}\right) = -Isp * g_0\Delta V \tag{2.10}$$

or alternatively

$$\left(\frac{m_f}{m_0}\right) = e^{-Isp*g_0\Delta V} \tag{2.11}$$

These last equations are forms of the classical 'rocket' equation.

2.2 HIGH-THRUST SYSTEMS

A number of high-thrust propulsion system types are possible. These include conventional chemical rockets and thermal rocket systems such as nuclear thermal and solar thermal. These will be considered in the following sections.

2.2.1 Chemical propulsion systems

Chemical systems are currently the most commonly used propulsion system type on spacecraft. Various types may be used, each with different characteristics.

Many such systems use a fuel and oxidant. A chemical reaction takes place, thus releasing energy, which expands the gaseous products of the chemical reaction. These products are then expelled at high pressure through a nozzle. Numerous fuels and oxidants are available.

Cryogenic systems

Cryogenic propellants may be used; often liquid oxygen (LOX) and liquid hydrogen (LH2) as the fuel. This reaction is efficient, and a relatively high specific impulse is achievable. Values exceeding 460 sec have been achieved with some rocket engine designs. A drawback of cryogenic systems is that the storage of the propellants is difficult. An extended-duration space mission would need special measures to ensure the long-term containment of these propellants until required for a manoeuvre. Cryogenic propellants currently have their greatest application in launchers, for which storage is less of an issue. Very high thrust is available in such cases, up to hundreds of kN.

Storable systems

To overcome the above difficulty with cryogenic systems, storable propellants are often used onboard spacecraft. A common oxidiser is nitrogen tetroxide (N_2O_4). A fuel often used with this oxidiser in hydrazine (NH_2NH_2). A variant of this fuel is unsymmetrical dimethyl hydrazine (UDMH). Although having the advantage of storability, these chemicals are both toxic and corrosive, requiring care when the spacecraft is loaded. This propellant combination has an intermediate specific impulse, typically less than 330 sec, and is therefore significantly less performant than a cryogenic system.

The oxidiser and fuel may either be pumped or forced under pressure into the combustion chamber. Spacecraft systems usually rely on pressure, either from a dedicated pressurant tank or simply the pressure of the storage tanks. This type of chemical propulsion system is the one most commonly used on spacecraft undergoing interplanetary transfers, and is also widely used on Earth-orbiting telecommunications satellites. The thrust available from such systems is typically in the range of tens to hundreds of Newtons for spacecraft applications. Higher thrust developments are also used for launch vehicle stages.

Monopropellant systems

Chemical propulsion systems may use a single propellant. These are known as monopropellant systems. A common fuel is hydrazine, which is burned by passing it over a catalyst. Such systems are simpler than bipropellant systems, but suffer from a reduced specific impulse (typically less than 220 sec). Thrust available from such systems is typically in the range of tens of Newtons.

The simplest chemical propulsion system type is perhaps the cold gas system, which involves the expulsion of a pressurised gas. Specific impulse is very low – typically less than 70 sec.

Solid propellant systems

Solid propellants may also be used. This usually involves the packaging of the propellant in a cylinder with an empty central core. Both fuel and oxidiser are packaged together. Fuel/oxidiser combinations such as synthetic polymers and ammonium perchlorate are used. The shape of this central 'hole' may be used to control the burn rate. Moderate specific impulses are available: typically 250 sec. A disadvantage of such systems is that they are nominally 'one-shot' devices; that is, once initiated the system burns until all propellants are consumed. However some developments are available that are hybrids that allow greater control of the engine. Potentially very high thrust can be generated with such systems.

2.2.2 Thermal rockets

The principle of a thermal rocket is to use a single propellant, heated and expelled to generate reactive thrust. Two systems are proposed for heat generation: nuclear power and solar power.

Nuclear thermal rockets

Nuclear thermal rockets have been studied for many years, and have been considered both in the context of launch vehicles and space vehicles. The underlying principle is to use a nuclear reactor as a heat source to heat a propellant. The propellant is then expanded through a nozzle, in the same way as a chemical rocket engine, producing thrust.

The key to such a system is the development of a suitable nuclear reactor for spaceflight. The reactor must be small enough to be contained in the spacecraft. A number of different reactor technologies are possible, the simplest being the solid core reactor. These are limited with regard to the temperatures that can be generated by the melting point of the construction materials. The specific impulse attainable is 800–900 sec. A preliminary development of such an engine was NASA's NERVA project that was tested between 1964 and 1972. The reactor developed more than 1,000 MW, and with a hydrogen propellant produced approximately 330 kN thrust. Such a system is targeted for use with stages of launch vehicles. Similar systems were also pursued in the former Soviet Union.

Considerably less thrust and hence power is needed for space vehicles. An example of a later development is the proposed MITEE system, based on a different reactor technology. Such a system would develop approximately 75 MW of thermal power, but achieve a specific impulse of typically 1,000 sec. A recent development is NASA's Project Prometheus, proposing the use a nuclear reactor to generate power in space. This could potentially be used either with a nuclear thermal rocket system or to generate power for an electric propulsion system.

A key issue with such propulsion systems is the mass of the system itself. The reactor mass is high, and although a significant increase in specific impulse is available when compared with a chemical rocket, the net mass gain is moderated by the system dry mass. A further issue is the risks associated with the use of nuclear materials in space.

Because of the relatively high mass of such units they are more generally applicable to large transport vehicles, such as may be considered for interplanetary manned missions or for large robotic explorers such as the recently proposed NASA Jupiter Icy Moons Orbiter (JIMO) mission. Potential performance improvements have been suggested by the use of liquid or gas core reactors, with which higher temperatures and ultimately higher specific impulses can be achieved.

Solar thermal rockets

The principle of a solar thermal rocket is similar to that of a nuclear thermal rocket. The Sun's energy is used to heat the propellant, which is then expanded through a nozzle. Hydrogen is most often considered for this application. To date, such systems remain as concept studies.

The first concept involves the solar heating of a heat exchanger through which the propellant passes, and a second alternative uses direct solar heating of the propellant. Specific impulses in the region of 900–1,200 sec are predicted.

Due to the relatively large mass of such a system they are more suitable for larger space transportation vehicles rather than small, lightweight satellites.

2.3 LOW-THRUST SYSTEMS

Propulsion system performance can be significantly improved if the specific impulse can be increased, therefore reducing the fuel mass needed. Several developments have been made to achieve this goal. However, such developments regarding specific impulse increase have also only been able to achieve a relatively low thrust. In fact, achieving a twin objective of high specific impulse and high thrust is a particularly demanding task in terms of the energy that must be imparted to the propellant.

If an impulse is calculated approximately by:

$$I = \Delta m V_{ex} \tag{2.12}$$

where Δm is the mass of propellant ejected, then the kinetic energy of the propellant that must be developed (as it is accelerated relative to the propulsion system) is given by $ke = \frac{\Delta m}{2} V_{ex}^2$, and so the ratio of kinetic energies needed to achieve a particular impulse, for systems with different specific impulses, is given by:

$$\frac{ke_1}{ke_2} = \frac{V_{ex1}}{V_{ex2}} \tag{2.13}$$

Therefore, if a system is developed that provides an order of magnitude gain in specific impulse, it also requires, for any given impulse, an energy to develop that is increased by the same ratio.

Similarly, the rate at which kinetic energy must be developed to produce a given thrust also scales by the same ratio, for systems with different specific impulses.

2.3.1 Electric propulsion

Electric propulsion has been developed over several decades. More recently it has been effectively applied in a series of space missions. A number of different types of electric propulsion are available. The two main categories are gridded ion thrusters (sometimes called Kaufman thrusters) and Hall-effect thrusters (sometimes called plasma thrusters). A further useful type of electric propulsion is the arcjet.

In the case of chemical propulsion, the energy used to provide the impulse to the propellant is derived from a chemical reaction. With electric propulsion, energy is required for field generation from which the propellant obtains its energy. Following the previous discussions regarding energy and specific impulse, a simple relationship can be obtained between power, thrust and specific impulse (or exhaust velocity):

$$P = \frac{Thrust * V_{ex}}{2} \tag{2.14}$$

This is the ideal case where the system operates with 100% efficiency. In practice, such efficiencies are not achievable, and so the power required for a given thrust and specific impulse is increased above this value.

Gridded ion thrusters

These thrusters work on the principle of the application of an electric field to accelerate ions between two grids. Xenon is often used as the propellant, which is ionised by bombardment by electrons produced by a central cathode. A magnetic field is used to confine the electrons that then collide with the propellant, causing ionisation.

The resulting positive ions are filtered from the electrons using an extraction grid that is slightly negatively biased. These ions are then accelerated between this and the second grid, as the second grid is set at a large negative potential. They are then ejected at high velocity, and the resulting reaction to the ejection process produces thrust on the spacecraft.

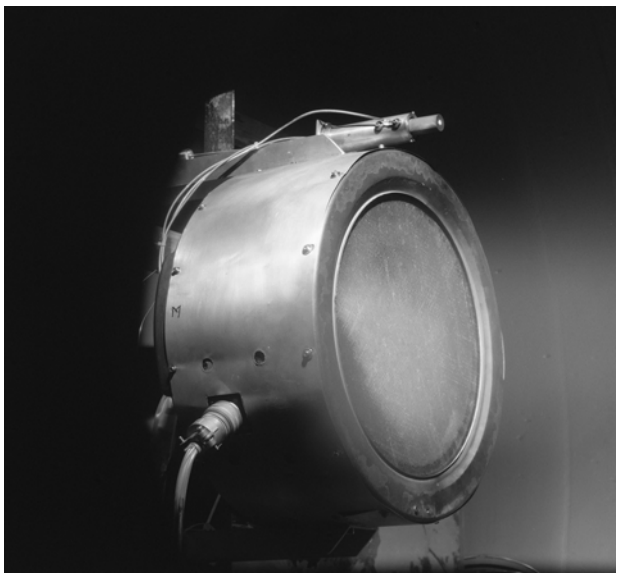

Figure 2.3.1. A gridded ion thruster in operation. Thruster diameter is typically 30 cm.
(Courtesy NASA)

Electrons are also ejected from a second cathode towards the ejected positive ions. This neutralises the ejected ions so that a build-up of charge on the spacecraft is avoided.

As an alternative to the use of a cathode-based system, ejecting electrons to cause the initial ionisation, a system using radio frequency ionisation is used in some thruster designs. This avoids erosion of the cathode.

The current thruster developments achieve target thrusts of typically 10–200 mN and specific impulses of 3,000–4,500 sec.

These thrusters have notably been used on NASA's Deep Space 1 mission. After departing Earth in 1998, this spacecraft essentially 'spiralled', with the assistance of a series of long-duration, low-thrust propulsion arcs, to achieve fly-bys of comets and asteroids. The first object encountered was an asteroid, 1992 KD, and it finally flew by comet Borrelly in 2001. The propulsion system used a gridded ion NSTAR-type thruster, approximately 30 cm in diameter and producing a thrust of 92 mN. The initial spacecraft mass was approximately 480 kg, with more than 80 kg of Xenon on board. Given a maximum operating specific impulse approaching 3,200 sec, this would theoretically allow a mission total ΔV of more than 5 km/sec. The ΔVs are applied over a series of long thrust arcs. With the maximum thrust available, approximately 60 days are needed to achieve a ΔV of 1 km/sec.

As well as the NSTAR unit used on Deep Space 1, a number of other gridded ion thrusters have been developed. The T5 and T6 thruster development in the UK provide thrust at typically 20 mN and 150 mN respectively. The T5 was flown on ESA's Artemis mission, together with the RIT thrusters developed in Germany. The

later thruster relies on radio frequency ionisation. The XIPS thrusters (developed in the USA) have been used on several geostationary satellites for north–south station-keeping.

Hall-effect thrusters

The principle of the Hall-effect thrusters (sometimes abbreviated as HET) is to use a rotating plasma of electrons to ionise a propellant injected through an anode. The configuration of the thruster is such that it generates a radial magnetic field, via inner and outer magnetic coils. An axial electric field is also generated, and the combined effect of these fields generates the Hall effect, which confines the electrons to move in a direction given by $E \wedge B$, therefore setting up the azimuthal rotation.

The ions are too heavy to be significantly effected by the magnetic fields. They accelerate axially under the influence of the electric field and exit the thruster at high velocity, producing thrust.

Currently available thrusters typically provide thrust in the region of 100 mN and a specific impulse of 1,500–1,700 sec.

This type of thruster was initially successfully developed by the Soviet Union, and has been used on a number of Soviet and more recently Russian spacecraft since the 1970s. It was named the Stationary Plasma Thruster (SPT). It also now used for north–south station-keeping on geostationary communications satellites.

It has also been used by ESA on the SMART-1 technology demonstration

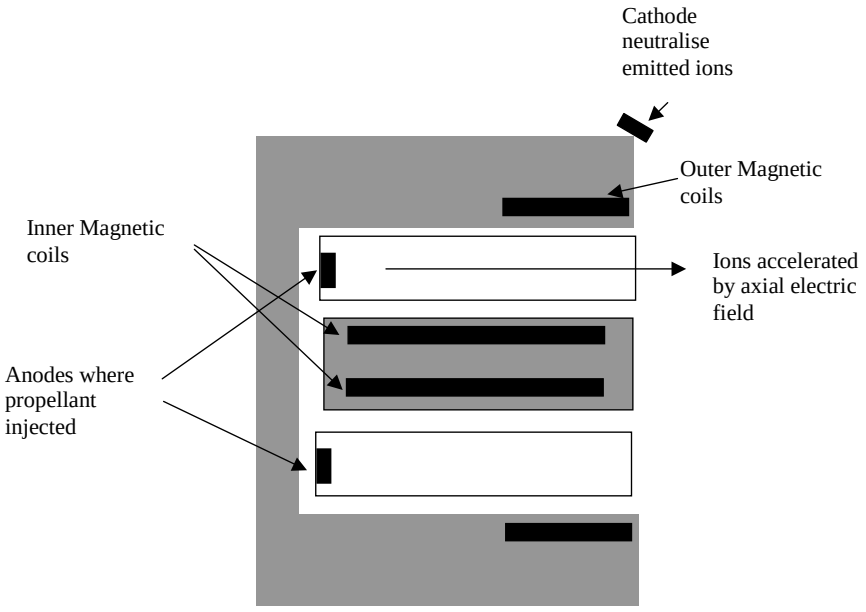

Figure 2.3.2. A conceptual illustration of a Hall-effect thruster. This is a cross-section and the electron Hall-effect current moves in the annular region between the magnets.

mission to the Moon. SMART-1 was initially launched into an elliptical GTO Earth orbit on an Ariane V in September 2003. The thrusters were used to provide a series of long thrust arcs to increase the semi-major axis of the orbit until the spacecraft could eventually approach the Moon. A thrust of approximately 70 mN was developed with a spacecraft initial mass of approximately 350 kg.

This 'spiralling' transfer took approximately 14 months, and the spacecraft was finally captured into lunar orbit in November 2004 after a gravitational capture sequence using the combined effects of the Earth's and Moon's gravity fields and a passage close to the lunar L1 Lagrange point. The initially high-apocentre elliptical orbit about the Moon was lowered with assistance from the thrusters. The target orbit was an elliptical, polar orbit.

Arcjets

Arcjet thrusters use an electric arc discharge to heat a propellant, which is then expanded through a nozzle to produce thrust. Hydrazine is commonly used as the propellant for such systems. Thrust is greater than most current electric propulsion systems, with values of up to typically 1N achievable. Specific impulse is also good when compared with chemical systems, being typically 500 sec.

Power generation

Several sources of power are considered for electric propulsion. These are solar and nuclear power generation systems, and also radioisotope thermal generators (RTGs).

Solar power is the most common source of energy, and is used in current-day applications. Solar arrays efficiently convert solar energy into electrical power. A measure of their efficiency is the specific power (power per unit array mass – W/kg). This efficiency is related to the solar cell technology used. Typical values are in the range 50–90 W/kg when operating at 1 AU from the Sun, depending on the type of technology used for the solar cells. The power required to drive the electric propulsion therefore generates an area requirement for the solar array.

The efficiency of a solar array also depends upon where it used, as the solar energy available varies with the inverse square of radial distance. Missions that require electric propulsion at large distances from the Sun are often not feasible if using solar power generation. Conversely, the use of solar electric propulsion in the inner Solar System can be an attractive proposition.

Nuclear reactors have been discussed in the context of nuclear thermal propulsion. Such reactors can also be used to generate large amounts of electrical power. They have an advantage over solar-powered systems in that they can operate at large distances from the Sun. However, the reactor masses proposed to date are relatively large (hundreds of kg when all the system elements including shielding and thermal control are added), so that they are often impractical for small spacecraft design, and more applicable to large spacecraft such as NASA's proposed JIMO.

A second position-independent power-generation system is the RTG, which uses radioactive decay to generate heat that is then converted to electrical energy. However, the specific power of these systems is relatively low (typically 5 W/kg,

with developments projected at reaching 10 W/kg), so that large amounts of radioactive fuel would be needed to provide sufficient power. As in the case of nuclear reactors, the environmental risks (both real and perceived) associated with these systems are a consideration in the design of such a mission.

The use of electric propulsion at large distances from the Sun therefore poses a number of challenges, yet to be fully resolved.

2.3.2 Solar sails

A solar sail utilises the Sun's radiation directly to provide thrust. Photons are reflected by the sail and the net momentum transfer executes a force on the sail. The direction of the force is controlled by changing the attitude of the sail, and as such has some analogies with a yacht sail. However, a solar sail spacecraft has no mechanism analogous to the keel of a yacht and so is less versatile than a sail boat!

The force due to solar radiation that can be experienced by a reflective surface placed normal to the Sun's direction, at 1 AU, is given by the relationship:

$$F = (1 + k)\frac{flux * area}{c} \tag{2.15}$$

where c is the speed of light ($3 * 10^8$ m/s), *flux* is the solar photon flux at 1 AU (typically 1,400 W/m^2), *area* is the area of the sail, and k is the reflectivity (1 for a totally reflective surface). The force that can be generated at 1 AU is therefore approximately $4.67 * 10^{-6}$ Nm^{-2}, for a non-reflective surface.

The principle of the sail is illustrated in Figure 2.3.3, which shows the possibility for varying the direction of the force by changing the attitude of the sail. However,

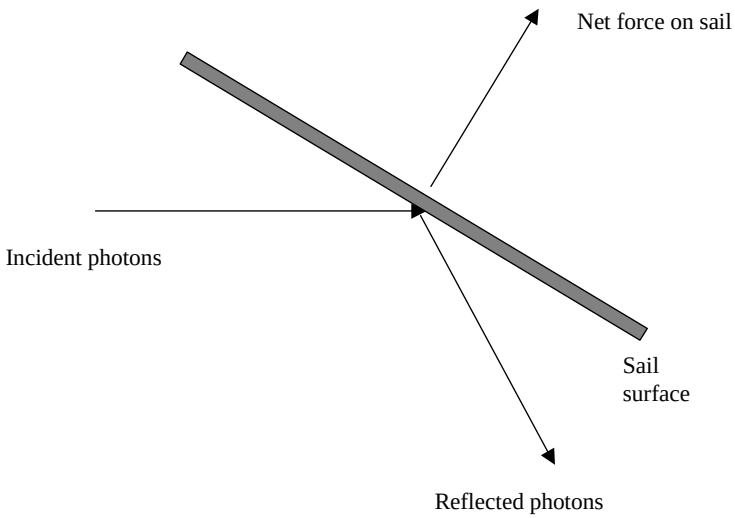

Figure 2.3.3. The principle of the solar sail.

the magnitude of the force also changes with attitude. Therefore, steering laws may be derived to calculate the optimum orientation that is needed to provide a maximum rate of change of certain orbital elements, such as semi-major axis or inclination. Alternatively, these steering angles (nominally 2 degrees of freedom) can be used as control parameters in a formal optimisation problem with a solution yielding an optimum transfer.

A solar sail provides a source of propulsion without a requirement for fuel, and therefore has an infinite specific impulse. However, there is a system mass associated with the sail, and the material mass and associated structure must be considered. Furthermore, during launch, the sail cannot be deployed due to its large area and fragile structure, and a deployment mechanism must therefore be considered. The desire to minimise the mass per unit area of sail has led to the use of very thin materials, of as little as 1 μm in thickness. Sail material densities that are considered are in the range 1–10 g/m^2. Sails sizes needed to develop sufficient acceleration to accomplish missions over acceptable timescales can have linear dimensions of hundreds of metres.

Solar sails have been successfully demonstrated in space. After being deployed from the Japanese ISAS mission in 2004, two sails were used, with thicknesses of 7.5 μm.

Applications of solar sails

'Solar sailing' has been used for attitude control for many years, where a system of additional 'flaps' or control surface are used. This allows the generation of a torque about the spacecraft's centre of gravity, from the effect of the solar pressure producing a force on the control surface. However, more recently it has been proposed as a propulsion system for interplanetary missions, both to the inner and outer planets.

The classical path of a solar sail in executing a planet-to-planet transfer is a spiral, as the sail generates either an accelerating or retarding force that affects the spacecraft's orbital semi-major axis. However, more ambitious missions have been proposed, venturing to the edge of the Solar System and beyond. In such cases, the optimal trajectory involves firstly lowering the perihelion towards the Sun and then modifying the attitude such that the sail accelerates the spacecraft at its new low perihelion. The resulting acceleration raises aphelion, and the spacecraft then follows a transfer to its target destination.

Other suggested applications of solar sails involve the creation of near-steady-state, non-Keplerian orbits. The force on the sail is used to partially counteract or assist gravity in order to create a modified but closed orbit. Examples are the creation of false Lagrangian points between the Earth and the Sun.

Some of the ultimate sail missions proposed – perhaps being more journeys of the imagination – have involved their use in conjunction with an Earth-bound laser system to accelerate them on an interstellar journey. The laser is focused on the sail at large heliocentric distances, where solar radiation is no longer effective. The laser requires rather high energy!

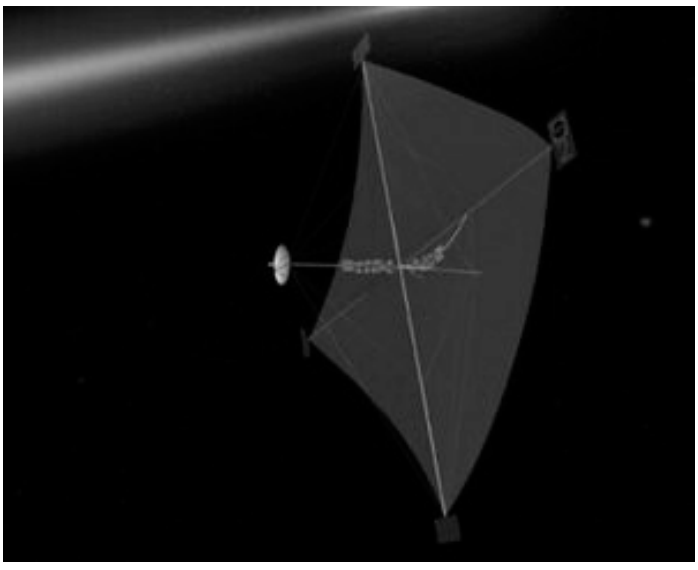

Figure 2.3.4. A solar sail concept proposed by NASA.
(Courtesy NASA)

Although posing many technological challenges, sails offer some fascinating and relatively simple mission options that may not be feasible with other propulsion technologies. As such, they are currently under serious consideration for future mission designs.

2.4 CHOICE OF PROPULSION SYSTEM

The previous discussions have shown the considerable variety of systems available for spacecraft propulsion. Some of them – such as chemical systems – are widely used, and offer cost-effective mission designs. They are, however, limited in their application due to the relatively low specific impulse, implying high fuel fractions.

Electric propulsion is now much more widely used in space, and has application on commercial telecommunications satellites. Its application to deep-space missions has also been demonstrated, and potentially offers some strong performance gains over chemical missions because of the very high specific impulse available. The application of electric propulsion at large distance from the Sun is adversely affected by the difficulties of power generation, implying nuclear or RTG systems. Nuclear systems attract considerable research and offer good performance, but tend to have a high system mass, and so the number of missions to which they may be applicable are limited.

Thermal rockets offer potential performance gains over chemical rocket systems, but because of their high basic system mass they are inefficient for small spacecraft.

The development of these systems is often considered in the context of large transport vehicles.

At the other end of the propulsion spectrum is the solar sail, offering only low acceleration but great mission flexibility and infinite specific impulse. At the present time the key issue is the space demonstration of sail technologies, including low-mass materials.

3

Optimisation

Optimisation is an important component of mission design. Interplanetary missions often have the choice of multiple routes and may use large numbers of manoeuvres. Efficient transfers are essential in order to maximise the useful mass that may be transported to the target.

Optimisation therefore falls into two categories: trajectory optimisation and system optimisation. Trajectory optimisation involves the determination of the most efficient launch and manoeuvre strategy, while system optimisation involves the selection of optimal system performance parameters. The objective is once again to maximise the useful mass. Such parameters are predominantly related to propulsion system performance.

3.1 THE TRAJECTORY OPTIMISATION PROBLEM

A trajectory optimisation problem aims to minimise or maximise a specified function by the time that the selected target is reached. Examples could typically be the fuel usage or ΔV required.

The general problem is to minimise the objective, J:

$$J = \Phi(\underline{X}(t_f), t_f) + \int_{t_0}^{t_f} L(\underline{X}, \underline{u}, t)\, dt \tag{3.1}$$

where $\underline{X}$ is the state vector, $\underline{u}$ is the control vector, t_0 and t_f are the initial and final times of the trajectory, Φ is a function of the final state and time, and L is a general function of the instantaneous state, control and time, integrated over time, along the trajectory. In this context, the state vector, $\underline{X}$ is a set of states whose evolution with time describes the trajectory and any associated parameters.

Minimisation is performed with respect to the control vector, $\underline{u}$, which consists of a set of mutually independent parameters. Each element of the control vector may be a function of time that may influence the vehicle trajectory:

$$\underline{u} = \begin{bmatrix} u_1(t) \\ \cdots \\ u_n(t) \end{bmatrix}$$

Also, there is a condition that the control vector must lie within an allowable control space.

Constraints

Two types of constraint may be applied to the trajectory:

- Terminal or 'fixed time': functions of the state and controls at the end of the trajectory (or at a fixed event).
- Path: functions of the state and control variables over regions of the trajectory.

Both constraint types may be divided into a further two classes:

- Equality: the function to be constrained must equal a specified value or function.
- Inequality: the function to be constrained must be less than or greater than a specified value or function.

General form for a terminal or 'event'-type constraint

Two types of these constraints may be considered, as follows:

Type 1: a function evaluated at a given time

$$C = f_1(\underline{X}(t_e), \underline{u}, t_e)$$

where t_e is the time at which the event takes place, f_1 is a specified function, and C has a specified value.

The above is an equality constraint. The inequality contraint of this type simply applies an upper or lower limit to the function and therefore replaces the equality sign with an inequality sign.

Type 2: a function evaluated over the trajectory

$$C(t_f) = f_1(\underline{X}(t_f), t_f) + \int_{t_0}^{t_f} f_2(\underline{X}, \underline{u}, t)\, dt$$

where f_1 and f_2 are general functions that may be specified. Once again the inequality constraint type applies an upper or lower limit to such a combination of functions.

Constraints of type 1 are more generally found than type 2.

General form for a path constraint

This is a function specified over the duration, or a sub-section of the trajectory:

$$C(\underline{X}, \underline{u}, t) \leq f_1(\underline{X}, \underline{u}, t)$$

where f_1 is a specified function, and C has a specified value at all times, t. The above is an inequality constraint – the most common form of path constraint.

3.2 TRAJECTORY OPTIMISATION METHODS

Trajectory optimisation methods broadly fall into two categories: direct and indirect.

Indirect methods are based on a variational calculus principle: the Pontryagin minimum principle (which also may be called a maximum principle, depending on the convention adopted). It is possible to formulate a two-point boundary problem involving a set of adjoint variables, the solution of which will yield a history of the time-dependent controls.

Direct methods differ from the indirect in that the time-dependent controls are described by a finite set of parameters. This necessarily limits the freedom of the control, but in many problems the effect of such a limitation on the optimal solution is negligible.

By using an optimal control formulation that is simpler than the indirect method the solutions obtained by the direct method are an approximation to the true optimum solution.

3.2.1 Indirect optimisation techniques

Optimal control of a vehicle trajectory may be derived from the application of the Pontryagin minimum principle. The following discussion outlines the principle of solution. A more detailed exposition can be found in the references for this section.

The vehicle trajectory state at any time is defined by the state vector $\underline{X}$.

Then a Hamiltonian function for this problem is defined to be:

$$H = \sum_i P_i \dot{X}_i + L \tag{3.2}$$

where $\underline{\dot{X}}$ is the state vector derivative with respect to time and the summation is over the number of states, $\underline{P}$ is an adjoint vector of the same number of dimensions as the state vector, L is a general function of the instantaneous state, control and time, as used in equation 3.1, and H is called the Hamiltonian.

The control vector, in the case of a trajectory optimisation problem, is generally comprised of elements such as thrust vector steering profiles or thrust throttle terms – the terms that determine the evolution of the trajectory.

Pontryagin's minimum principle derives the following conditions for the minimisation of the objective function:

$$\frac{\partial H}{\partial u_i} = 0 \tag{3.3}$$

$$\frac{\partial H}{\partial X_i} = -\dot{P}_i \tag{3.4}$$

The Hamiltonian, at any time, should be minimum with respect to each element of the control vector (Equation 3.3). This statement can be augmented by the more general statement that the Hamiltonian should be globally minimum with respect to the control vector at every point in time.

The adjoint derivatives are defined by the partial derivatives of the Hamiltonian with respect to the state elements.

The differential equations for the state and adjoint vectors must now be solved:

$$\underline{X} = \int_{t_0}^{t_f} \dot{\underline{X}}(\underline{X}, u, t)\, dt + \underline{X}(t_0)$$

$$\underline{P} = \int_{t_0}^{t_f} \dot{\underline{P}}(\underline{X}, \underline{u}, t)\, dt + \underline{P}(t_0)$$

where $\dot{\underline{P}}$ and $\underline{u}$ are derived from the partial derivatives of the Hamiltonian described previously. In principle, equation 3.3 gives $\underline{U}$.

The initial values of the state vector, $\underline{X}$, are generally known, from the definition of the trajectory starting point, but the initial values of the adjoint vector are not known. However, Pontryagin gives additional conditions on the final values of the adjoint vector and the Hamiltonian. In the case of unconstrained terminal states or functions of the terminal states then:

$$\frac{\partial \Phi(t_f)}{\partial X_i} = P_i(t_f)$$

where ϕ is that used in equation 3.1. Also:

$$\frac{\partial \Phi}{\partial t} = -H(t_f)$$

for a free terminal time problem.

When terminal states are constrained, then the above equation for P_i (where the state, i, is constrained) becomes:

$$P_i(t_f) = \lambda_i$$

where λ_i is an undefined constant to be determined via the terminal constraints during the solution of the problem.

A two-point boundary value problem is now defined, the solution of which will yield the optimal control and the optimal trajectory that minimises the objective function. The solution of this problem in general requires numerical methods. An

initial estimate of the adjoint variables may be made for the time, t_0. Then both state and adjoint vectors may be propagated to the termination of the trajectory.

An example could be considered where no constraints exist on the terminal states. Forwards propagation of this initial estimate will result in an error between the final adjoint vector and the required value. The initial values of the elements of the adjoint vector are then corrected until the final constraints are observed. This procedure may be implemented as follows.

A state transition matrix is evaluated relating the terminal adjoint variables to their initial values:

$$\left[\frac{\partial \underline{P}(t_f)}{\partial \underline{P}_0}\right] = \begin{bmatrix} \dfrac{\partial P_{1(t_f)}}{\partial P_{10}} & \cdots & \dfrac{\partial P_{N(t_f)}}{\partial P_{10}} \\ \dfrac{\partial P_{1(t_f)}}{\partial P_{20}} & \cdots & \dfrac{\partial P_{N(t_f)}}{\partial P_{20}} \\ \vdots & \cdots & \vdots \\ \dfrac{\partial P_{1(t_f)}}{\partial P_{N0}} & \cdots & \dfrac{\partial P_{N(t_f)}}{\partial P_{N0}} \end{bmatrix} \tag{3.5}$$

Evaluation of the state transition matrix for the adjoint vector requires the calculation of a set of partial derivatives. These are obtained most efficiently by the numerical integration of analytically derived expressions for the state transition rates:

$$\frac{\partial P_i(t_f)}{\partial P_{j0}} = \int_{t_0}^{t_f} \frac{\partial \dot{P}_i}{\partial P_{j0}}(\underline{X}, \underline{u})\, dt + \frac{\partial t_f}{\partial P_{j0}} \dot{P}_i(t_f) \tag{3.6}$$

where:

$\dfrac{\partial P_i(t_f)}{\partial P_{j0}}$ is the partial derivative of the terminal value of the adjoint element, i, wrt the initial value of the adjoint element, j,

$\dfrac{\partial \dot{P}_i(\underline{X}, \underline{u}, t)}{\partial P_{j0}}$ is the partial derivative of the instantaneous value of the adjoint element, i, time derivative, wrt the initial value of the adjoint element, j, and

$\dfrac{\partial t_f}{\partial P_{j0}}$ is the partial derivative of the terminal time wrt the initial value of the adjoint element, j.

The rate derivatives typically decompose in the following manner:

$$\frac{\partial \dot{P}_i}{\partial P_{j0}} = \sum_k^{ns} \frac{\partial \dot{P}_i}{\partial X_k}(\underline{X}, \underline{u}, t) * \frac{\partial X_{ki}}{\partial P_{j0}} + \sum_k^{nc} \frac{\partial \dot{P}_i}{\partial u_k}(\underline{X}, \underline{u}, t) * \frac{\partial u_{ki}}{\partial P_{j0}} \tag{3.7}$$

where ns is the number of states, nc is the number of control variables and:

$\dfrac{\partial X_k}{\partial P_{j0}}$ is the partial derivative of the state element, k, wrt the initial value of the adjoint element, j,

$\dfrac{\partial u_k}{\partial P_{j0}}$ is the partial derivative of the instantaneous value of the control element, k, wrt the initial value of the adjoint element, j,

$\dfrac{\partial \dot{P}_i(\underline{X}, \underline{u}, t)}{\partial X_k}$ is the partial derivative of the instantaneous value of the adjoint element, i, time derivative, wrt the state element, k, and

$\dfrac{\partial \dot{P}_i(\underline{X}, \underline{u}, t)}{\partial u_k}$ is the partial derivative of the instantaneous value of the adjoint element, i, time derivative, wrt the control element, k.

The state element partial derivatives are obtained in the same manner as the adjoint element partials:

$$\frac{\partial X_i(t)}{\partial P_{j0}} = \int_{t0}^{t} \frac{\partial \dot{X}_i}{\partial P_{j0}}(\underline{X}, \underline{u}, t)\, dt \tag{3.8}$$

The state vector rate derivatives decompose in a manner similar to those of the adjoint variables:.

$$\frac{\partial \dot{X}_i}{\partial P_{j0}} = \sum_{k}^{ns} \frac{\partial \dot{X}_i}{\partial X_k}(\underline{X}, \underline{u}, t) * \frac{\partial X_{ki}}{\partial P_{j0}} + \sum_{k}^{nc} \frac{\partial \dot{X}_i}{\partial u_k}(\underline{X}, \underline{u}, t) * \frac{\partial u_{ki}}{\partial P_{j0}} \tag{3.9}$$

where

$\dfrac{\partial \dot{X}_k}{\partial P_{j0}}$ is the partial derivative of the instantaneous value of the state element, i, time derivative, wrt the initial value of the adjoint element, j.

The instantaneous partial derivatives of the control elements with respect to the adjoint element initial values are obtained in the following manner.

The condition that the Hamiltonian is always minimum along the trajectory; that is, the control variables are derived from the condition that $\dfrac{\partial H}{\partial u_i} = 0$ means that $\dfrac{\partial^2 H}{\partial P_{k0} \partial u_i} = 0$, and therefore:

$$\frac{\partial u_i}{\partial P_{j0}} = \frac{\left(-\sum_k \dfrac{\partial^2 H}{\partial X_k \partial u_i} * \dfrac{\partial X_k}{\partial P_{j0}} - \sum_k \dfrac{\partial^2 H}{\partial P_k \partial u_i} * \dfrac{\partial P_k}{\partial P_{j0}} \right)}{\sum_k \dfrac{\partial^2 H}{\partial u_k \partial u_i}} \tag{3.10}$$

unless the control element is on a limiting boundary, in which case: $\dfrac{\partial u_i}{\partial P_{j0}} = 0$.

Therefore, the adjoint state transition matrix given in Equation 3.5 is obtained by numerical integration of the expressions derived here, The increments in the initial values of the adjoint variables, needed to reach the required terminal values may then be calculated by inversion of the state transition matrix.

The method described here presents an outline of the mathematical problem to be solved. Any specific trajectory optimisation problem of this type must be formulated to include the effects of the specific constraints and objective function for that problem. A definitive description of the methods to formulate and solve such problems may be found notably in Bryson and Ho (see references for this section).

3.2.2 Direct optimisation techniques

An interplanetary transfer may, in general, be controlled by a series of manoeuvres, which may be near-impulsive manoeuvres, or long-duration, typically low-thrust manoeuvres. In the impulsive case, a fixed steering direction may be used to characterise the manoeuvre. Such directions may be used directly as optimisable parameters. However, in the case of the long-duration manoeuvre, the steering profiles that determine the thrust directions are continuously variable. This steering profile will nominally have two independent components: azimuth or right ascension angle, and elevation angle. Both of these may vary independently with elapsed time along the trajectory. Further continuously variable control parameters may include the thrust magnitude. In many traditional transfer trajectory cases, thrust magnitude tends to the maximum that is allowed, but the application of specific constraints or propulsion models can change this situation.

Unlike the indirect method, from which the optimal, continuous steering profile is obtained, the direct method requires a parameterisation of each of the independent control elements. This is a finite set of parameters, and a number of different methods could be used:

- A grid of values at set time intervals with interpolation at intermediate time values.
- More general mathematical functions with time as the independent variable (Fourier series).

The number of degrees of freedom available to each element of the control vector is now limited by the number of parameters set for that element. In the indirect case, there is effectively an infinite number of parameters, as the optimal control history is continuously variable.

The objective may take the same form as that of the indirect problem, and a set of constraints may be specified, both equality and inequality. The problem is then to determine the values of the parameters that result in observation of the constraints and maximise the objective function.

3.2.3 An example of control parameterisation

A simple example of a control parameterisation is given in Figure 3.2.1. The control variable is a steering angle with a value specified at a series of set time points. The values at these times are then the optimisable parameters that define the control variable. At intermediate times, the value of the control angle is obtained by linear interpolation.

This example shows a steering profile defined at seven points in time. The quality of the optimisation is improved by using a finer grid of points. Studies are needed for particular cases to establish satisfactory time spacing. The grid can be irregular, with higher concentrations of points in critical areas. Such a dense control grid may, for example, be used for manoeuvres close to pericentre of a planet fly-by. For manoeuvres in deep space, where the time periods of the motion are much larger, a much

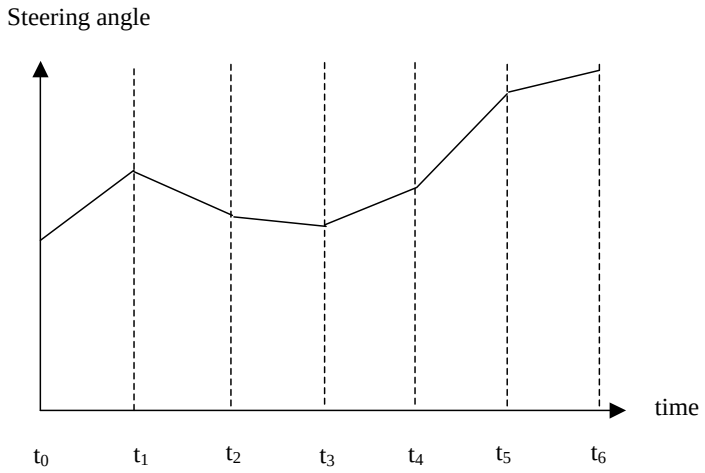

Figure 3.2.1. An example of a parameterisation of a continuously variable steering angle.

larger time interval may be used (hours or even day intervals could be considered). The key point is that the grid spacing should be sufficient to allow an accurate representation of the probable frequency content of the parameterised variable.

Solution of the direct optimisation problem

The following is an example of such a problem:

- Maximise the objective function, J, subject to the equality constraint set, n_{eq} equality constraints and n_{ineq} inequality constraints:

$$C_i = 0 \qquad \text{for } i = 1 \text{ to } n_{\text{eq}}$$

$$C_i \leq 0 \qquad \text{for } i = n_{\text{eq}} + 1 \text{ to } n_{\text{eq}} + n_{\text{ineq}}$$

with respect to the following set of control parameters (using the example of thrust vector steering angles):

- $u(1, 1)$ to $u(1, n_{\text{azimuth}})$, control vector element 1, the azimuth angle, with n_{azimuth} parameters.
- $u(2, 1)$ to $u(2, n_{\text{elevation}})$, control vector element 2, the elevation angle, with $n_{\text{elevation}}$ parameters.

$u(1, i)$ is the ith control parameter of the azimuth control angle.
$u(2, i)$ is the ith control parameter of the elevation control angle.

In practice, the trajectory will incorporate a series of such manoeuvres and so the above parameterisation is needed for each manoeuvre. The duration and start time of each manoeuvre are also optimisable parameters. The number of optimisable control parameters therefore becomes $(n_{\text{elevation}}, n_{\text{azimuth}} + 2) * n_{\text{burns}}$.

Given an initial estimate of the control parameters, the solution may be found by numerical, iterative methods using non-linear programming.

Non-linear programming

Non-linear programming is a method of calculating increments in the vector of control parameters that allows the maximum (or minimum) of the objective function to be reached, whilst observing all constraints. These methods require at least first-order gradient information about the objective function and the constraints, with respect to the control parameters, $\frac{\partial J}{\partial u(i,j)}$. Ideally, second-order gradient information would also be available, $\frac{\partial^2 J}{\partial u(i,j)\,\partial u(i,k)}$.

As an example, with only first-order gradients available, the steepest ascent direction can be found (subject to constraints) and a 'hill-climbing' method used to find the maximum by a sequence of iterations. Numerous algorithms are available for such a task.

With additional second-order information, local quadratic models can be formulated to approximate the objective function and ultimately allow determination of the location of the maximum after a sequence of iterations.

Non-linear programming is discussed in greater detail in Section 3.3.3.

3.2.4 Techniques for solving direct optimisation problems

A number of methods can be used to assist in the solution of direct optimisation problems. The common feature is that each uses some method to parameterise the control variables and non-linear programming to achieve a solution. Three techniques are commonly considered, but a number of variations of these also exist.

Single shooting algorithms

This is conceptually the simplest method. The initial state vector values are specified and the trajectory propagated forwards in time, using the control variable values obtained from the parameterised representation. An initial guess is made at the control parameter values. At the end of the propagation, some of the required final states may be met and others not. Non-linear programming is used to solve the constrained maximisation or minimisation problem.

The number of control parameters used by the non-linear programming method is equal to the number of parameters used to represent the continuously variable controls plus any further free parameters, such as manoeuvre start and stop times.

Multiple shooting algorithms

Multiple shooting algorithms may be adopted for the solution of this class of problem. They offer the possibility of an efficient solution, together with a robust approach to the adoption of initial trajectory estimates.

The trajectory must be segmented (in time) into a set of phases or segments. The exact choice of segmenting is arbitrary, but it is more efficient to make use of natural

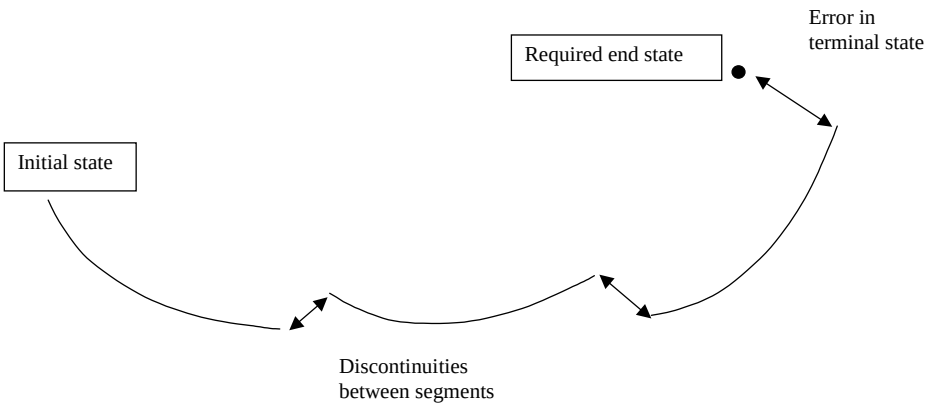

Figure 3.2.2. Trajectory segmentation used by multiple shooting algorithms.

discontinuities in the trajectory, such as coast and engine-burn phases. Further segmentation within particularly long coast phases is also possible. After the initial values for a segment are estimated, the trajectory is propagated forwards (or even backwards) in time for an estimated duration.

The initial conditions for each segment (the initial values of the state vector for that segment) are determined by the optimisation process; that is, they are treated as optimisable controls. Clearly, the state vector at the end of the preceding phase must eventually match this initial value. This matching requirement appears as an equality constraint.

This treatment means that in any one evaluation of the trajectory there are effectively 'n' independent trajectory evaluations: one per segment. Each segment-starts with state vector values given by the optimisation process at the current iteration.

The idea of multiple shooting was notably explored by Well, particularly in the context of launch trajectory optimisation (see references for this section)

The nature of the starting points for each of the segments can be chosen in a variety of ways. It could simply be that a very long manoeuvre can be best represented by a series of shorter segments that together make up the manoeuvre, and the same could be true for a long coast arc (perhaps subject to a variety of perturbations; different mathematical models may be used in different segments to best represent the differing nature of the trajectory during a transfer). Alternatively, a starting point could correspond to some significant event, such as when entering the sphere of influence of a planet before the spacecraft performs a gravity-assist manoeuvre.

Figure 3.2.3 illustrates a trajectory segmented into a series of disjointed sections, each of which contains either a thrust arc or a coast arc. Such a trajectory may be typical of the initial guess to an optimal solution. In this case, a 'guess' is made regarding the nature of the trajectory at each gravity-assist manoeuvre and the epochs of the gravity-assist manoeuvres, together with the initial Earth departure epoch and the Jupiter arrival epoch. A number of adjacent, multiple shooting trajectory segments are then propagated forwards and backwards in time from

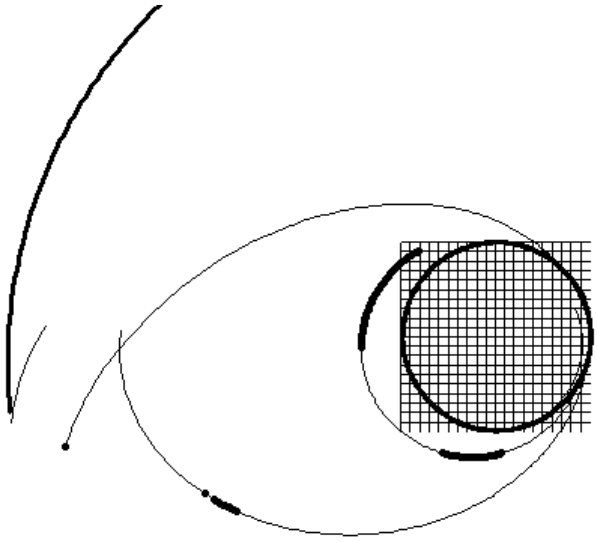

Figure 3.2.3. Initial trajectory segmentation for multiple shooting, for the case of a transfer from Earth escape orbit to Jupiter approach using two Earth GAs. Thrust arcs in the trajectory are thick lines, and coast arcs are lighter. The width of the grid cells is 0.1 AU. The orbit arcs of Earth and Jupiter are also shown.

each gravity-assist event. These propagated sequences do not meet initially. In total, nineteen segments are used in this trajectory example. Non linear programming is then used to link the blocks of segments associated with each gravity-assist in an optimal manner, to minimise total fuel usage.

Method of solution

It is assumed that any time-dependent spacecraft control function history, such as azimuth angle history during a burn, can be specified by a finite set of optimisable parameters. Some defined function of the parameters involving time then defines the control history.

If it were required to achieve the absolute value of the optimum (that can be obtained with the indirect method), then in principle an infinite number of parameters would be needed. In practice, maxima or minima lying very close to the absolute values can generally be obtained with only a limited number of parameters. The driving force behind keeping to a low number of parameters is to avoid the computational overhead imposed by the use of a large numbers of parameters.

Once the parameterisation of the spacecraft control functions has been decided upon, the optimisation problem reduces to a non-linear programming problem, to maximise the objective function with respect to the specified finite parameter set.

The full optimisation problem is to maximise the objective function with respect to the parameter set, subject to the constraints, which may either be equality or inequality constraints.

An initial guess is made at the values of the optimisable parameters. The trajectory segments are each integrated forwards in time from a specified initial optimisable time, over an optimisable duration. The vehicle control functions for each segment are derived from the applicable set of optimisable parameters. The values of the objective function and all constraints are then evaluated.

An increment in the parameters is calculated by means of a non-linear programming algorithm. This increment is calculated to increase the value of the objective function and to ensure that the constraints are observed.

This procedure is repeated until the objective function can no longer be increased.

When the optimum solution is obtained and all constraints are observed, the end and beginning of adjacent phases will match, giving a continuous trajectory from the initial to the final states.

An example of the application of a multiple shooting algorithm is given in the references for this section.

Advantages of multiple shooting

The efficiency of a multiple shooting algorithm, compared with a single shooting algorithm, can be understood through the following effects, which result in reduced computing time to obtain a solution:

- Gradient evaluation. Because controls only have a 'localised' effect (restricted to that segment), gradients only need be generated for that segment, rather than for the whole trajectory.
- Linearity. Because each trajectory segment is shorter than in the single shooting case, the effect of changing a particular control element is more predictable (the gradients show greater local linearity). However, the algorithm may require large changes in the initial state vector values for the segments as it progresses towards a solution. At this point, control step size limits on these initial states can directly prevent excessive initial state changes which would otherwise give rise to highly non-linear behaviour of the final states. The net result is a much improved convergence behaviour.
- The method is more robust with respect to poor initial guesses of the nominal trajectory control parameters, as some estimation of the probable form of the final trajectory can be included in the initial guess of the initial state values for each segment.

There is, however, one drawback: the number of constraints is significantly increased. This tends to lead to larger matrix inversion problems in the NLP algorithm. If a large number of segments were to be used, the above benefits would be outweighed by the increased computing effort in solving the associated matrix problems. Therefore, it is important to carefully choose the number of segments to be used.

Time segmentation

In some applications of multiple shooting problems, time is treated as continuous between adjacent segments. This is the best approach when the trajectory has no dependence on absolute time. However, when the equations of motion contain terms that *are* dependent upon absolute time, it can be advantageous to use a time segmentation; that is, to use the initial time of each segment as an optimisable control.

An example of this is the planetary fly-by case. Fly-by dynamics are critically effected by the phasing of the approach and therefore the absolute time. In planning a mission, it is possible to generate segments that experience close planetary encounters by specifying the correct combination of initial position/velocity and absolute time.

A constraint is applied such that the end and start times of adjacent segments is continuous. The convergence to a fly-by solution is much improved if the initial estimate contains an approximation of such a manoeuvre.

The use of time segmentation is therefore employed for such problems.

Multiple shooting problem formulation

The formal problem using a multiple shooting approach can be stated as follows: Assuming that the trajectory is divided into n segments,

- Maximise the specified objective function (e.g., mass at termination of nth phase).

subject to the equality constraints:

- Specified functions of the state vector at the termination of the nth phase, ne_{term} in total: final orbit apogee height, orbit perigee height, orbit inclination, orbit right ascension, and orbit argument of perigee.
- Specified functions of the state vector at the start of the first segment, ne_{initial} in total (e.g., initial orbit apogee height, orbit perigee height).
- Specified functions of the state vector at the start of the intermediate segments, ne_{inter} in total: e.g., optional osculating planet relative ephemeris elements at start of fly-by segments.
- The error between the state vector at the termination of each segment, i, and the initial value of the state vector at the start of the next segment, for $i = 1$ to $n - 1$, ms (the number of state vector elements) + 1(time continuity) continuity constraints, i.e.,:
  $\underline{X}_i(t_{fi}) = \underline{X}_{i+1}(t_{0i+1})$; $t_{fi} = t_{0i+1}$, for $i = 1$ to $n - 1$; where $\underline{X}_i$ is the state vector evaluated for segment i, t_{fi} is the time at which segment i terminates, and t_{0i} is the time at which the ith segment starts.

The optimisable controls are now:

- Thrust vector azimuth and elevation angles (for each segment i).

- The initial values of the state vector for each segment, $\underline{X}_i(t_{0i})$ for $i = 1$ to n (this assumes that the initial conditions of the trajectory are optimisable, although certain constraints are applied at this point).
- The duration and start time of each phase, t_{di}, t_{0i} for $1 = 1$, n (or termination time instead of start time for those phases to be numerically integrated backwards).

For each phase, the vehicle attitude control function histories are parameterised; for example, ma_i optimisable parameters define the azimuth profile for each phase, i, and mb_i parameters define the elevation angle profile. The control function parameterisation can be critical in achieving good convergence to an optimal solution.

The final problem then involves (in the above control function example):

$$\text{NP} = \sum_{i=1}^{i=n}(ma_i + mb_i + ms + 2) \quad \text{optimisable controls}$$

where ms is the number of states in the state vector, n is the number of segments, and

$$\text{NE} = \sum_{i=1}^{i=n-1}(ms + 1) + ne_{\text{term}} + ne_{\text{initial}} + ne_{\text{inter}}$$

equality constraints.

It is assumed here that all inequality constraints are transformed to equality constraints by the use of 'slack variables', discussed later in this chapter.

For each constraint (C_j, for $j = 1$ to (NE)) and the objective function (J), the gradient with respect to each control (optimisable parameter, p_i, $i = 1$, NP) is evaluated:

$$\frac{\partial C_j}{\partial p_i} \quad \text{and} \quad \frac{\partial J}{\partial p_i}$$

Then non-linear programming is used to solve for the NP parameters.

Collocation

The principle of collocation, when applied to trajectory optimal control problems, involves the representation of the trajectory by a set of states and their time derivatives over a grid of defined points in time. The technique removes the need for reintegration of the trajectory over repeated iterations.

The values of the states and their derivatives at intermediate points can be derived by interpolation using piecewise polynomials (nominally third order). Additionally, the values of the derivatives are explicitly evaluated at these intermediate points by their dependence on the interpolated states.

The difference between the calculated and interpolated derivatives at coincident times define a constraint set, the values of which must be iteratively reduced to zero. The problem is initialised by selecting a set of state values over the grid, that are

judged to approximate the final solution. This selection causes errors in the initial constraint set.

The optimisation problem becomes the following:

- Maximise the chosen objective function (which must also be represented in terms of the discrete grid), subject to the constraints:
  - Nominal set (path and terminal constraints).
  - Collocation constraints of derivatives on the grid.
- The optimisable control parameters are:
  - Nominal control parameters (such as parameters defining control angle and thrust histories).
  - State vector values at the grid points.

This approach was notably developed for trajectory optimisation by Hargraves and Paris (see references for this section). The advantages associated with this approach are the following:

- Gradient evaluation is simplified, as the effects of a control need only be evaluated at the local grid points.
- Numerical integration is replaced by piecewise interpolation. The interval determines the accuracy of the interpolated representation. Therefore, initial estimates may be based on a sparse grid and accuracy refined as the solution proceeds.
- The linearity of the problem is improved – the response of constraints and objective function to control parameter changes – allowing larger increments in the control parameters in the iteration.
- The method is robust with regard to poor initial guesses at the solution.

The major disadvantage is that for problems requiring a denser grid to maintain an accurate representation of the trajectory, large numbers of controls and constraints are required which in turn lead to large matrix inversion problems in the non-linear programming process. However, much research has been performed on the methods for processing the sparse matrices that are used by the NLP methods, and a number of effective algorithms have been produced (see references for this section)

In the application to deep space missions, collocation offers the possibility of starting the solution process, using a sparse grid. Progressive refinement of the grid, either locally or globally, leads to an increasingly accurate solution. Multiple shooting segments may progressively replace regions containing grid point representations. In this way, an intermediate hybrid problem can be solved, containing both collocation and multiple shooting.

Application of collocation

The collocation-based optimisation problem has the features of any general, direct optimisation problem (as described in Section 3.2.2). The key details specifically relating to collocation are now considered.

Firstly, a set of nodes must be defined, spanning the duration of the trajectory. The state vector element, j, at node i, that applies at time t_i, is denoted as X_{ij}.

A control vector, $\underline{u}$, influences the state vector derivatives. This vector has K elements, with unique values at each node.

The state vector derivatives are dependent on the state vector and the control parameters:

$$\dot{X}_{ij} = \dot{X}_{ij}(X_{ij}, u_{i,k=1,K})$$

In practice only a subset of the k control parameters influence $\dot{X}_{ij}$. The state vector at an intermediate time, between nodes i and $i+1$, can be obtained by interpolation. The time is calculated as:

$$t_{i+1/2} = \frac{t_i + t_{i+1}}{2}$$

Several methods of interpolation are possible. One of the simplest is a piecewise Hermite interpolation method. This uses the state vector elements and their derivatives at adjacent nodes to obtain the state vector at the intermediate times between nodes. Therefore:

$$X'_{i+1/2,j} = f_1^n(X_{ij}, X_{i+1,j}, \dot{X}_{ij}, \dot{X}_{i+1,j}, \Delta_i)$$

Where $\Delta_i = t_{i+1} - t_i$ and $'$ denotes an interpolated quantity. Similarly, the state vector derivative can be obtained by interpolation:

$$\dot{X}'_{i+1/2,j} = f_2^n(X_{ij}, X_{i+1,j}, \dot{X}_{ij}, \dot{X}_{i+1,j}, \Delta_i)$$

The state vector derivative can then be explicitly evaluated from its dependence on the state vector:

$$\dot{X}_{i+1/2,j} = \dot{X}_{i+1/2,j}(X'_{i+1/2,j}, u_{i+1/2,k=1,K})$$

The error between interpolated and evaluated derivatives can then be calculated.

Therefore, if N nodes exist, there are $N-1$ intermediate points.

Note that a solution can often be found, irrespective of the spacing in the nodes. However, an error in the solution will exist if the node spacings are too large, such that the state vector values obtained at these nodes will not accurately represent the trajectory. The effect arises from the limitations of the accuracy of the interpolation.

A short discussion of the interpolation problem is warranted to examine possible ways of maximising the efficiency of the method.

Interpolation

The principle of the interpolation techniques described is based on a truncated Taylor series, such as the following example.

$$X(t_0+\delta t) = X(t_0) + \dot{X}(t_0)\,\delta t + \ddot{X}(t_0)\frac{\delta t^2}{2} + \dddot{X}(t_0)\frac{\delta t^3}{3!} + \ddot{\dot{X}}(t_0)\frac{\delta t^4}{4!} + \ddot{\ddot{X}}(t_0)\frac{\delta t^5}{5!} + \dddot{\dddot{X}}(t_0)\frac{\delta t^6}{6!}$$

This example truncates at order 6. Such a series includes an error in the predicted term that depends on the $(n+1)$th derivative and a function of the time step to the $(n+1)$st power plus higher derivatives when the series is truncted at order n.

It is generally possible to assume that terms (derivatives) beyond a given order become negligible. It is also possible to derive similar expressions for the extrapolated state vector derivative. From these expansions it is possible to obtain a series of coefficients.

These higher derivatives are generally not known, but can be obtained by use of lower derivatives obtained at two or more time points. An example of such an interpolation method, well suited to this problem, is now described.

Position interpolation with respect to time can be accomplished by piecewise, 5th order Hermite interpolation. This algorithm makes better use of the available information (than for example a 3rd order interpolator) when interpolating for the state, X, by employing knowledge of the second derivative of the state, $\ddot{X}$. By comparison the 3rd order interpolator uses only the state and its first derivative when interpolating for the state. The state vector rates are denoted by $\dot{X}$.

In qualitative terms the truncation error of a 5th order interpolator is of order 6 (when interpolating the state). The truncation error of the 3rd order interpolator is of order 4 (when interpolating the state).

The exact equation for interpolating the state using a 5th order method is:

$$X(t_0 + \delta t) = AX(t_0) + BX(t_0 + \Delta) + C\dot{X}(t_0) + D\dot{X}(t_0 + \Delta) + E\ddot{X}(t_0) + F\ddot{X}(t_0 + \Delta) \tag{3.11}$$

where δt is the time elapsed from t_0 at which the information is required, and Δ is the full time step size.

A to F are coefficients, being dependent on δt and Δ.

Solving for the coefficients A to F from a set of truncated Taylor series yields:

$$F = \frac{\delta t^3}{2\Delta^3}(\delta t - \Delta)^2$$

$$D = \frac{\delta t^3(\delta t - \Delta) - 6\Delta^2 F}{\Delta^3}$$

$$B = \frac{\delta t^3 - 3\Delta^2 D - 6\Delta F}{\Delta^3}$$

$$A = 1 - B$$

$$C = \delta t - B\Delta - D$$

$$E = \frac{\delta t^2}{2} - \frac{\Delta^2 B}{2} - \Delta D - F$$

A 3th-order algorithm can be used to interpolate velocity:

$$X(t_0 + \delta t) = AX(t_0) + BX(t_0 + \Delta) + C\dot{X}(t_0) + D\dot{X}(t_0 + \Delta) \tag{3.12}$$

$$A = 1 + \frac{\delta t^2}{\Delta^2}\left(\frac{2\delta t}{\Delta} - 3\right)$$

$$B = -\frac{\delta t^2}{\Delta^2}\left(\frac{2\delta t}{\Delta} - 3\right)$$

$$C = \delta t\left(1 - \frac{\delta t}{\Delta}\right)^2$$

$$D = \frac{\delta t^2}{\Delta}\left(\frac{\delta t}{\Delta} - 1\right)$$

where X now represents velocity and $\dot{X}$ acceleration.

Higher-order interpolation methods are possible. The objective is to maximise the node time spacing, consistent with a given level of accuracy of trajectory representation.

3.2.5 Selection of appropriate techniques

The nature of the problem to be solved influences the selection of the technique. The first choice lies between direct and indirect optimisation methods. Some of the features can be summarised:

Indirect:

Evaluation of state and adjoint rates.
Evaluation of optimum control variable expressions along the trajectory.
Numerical integration to obtain states and adjoints.
Evaluation of state and adjoint vector partial derivative rates.
Numerical integration of state and adjoint vector partial derivative rates.
Solution by matrix inversion and iteration.

Direct:

Evaluation of state rates.
Optimum control variable expressions along the trajectory from parameterisation.
Numerical integration to obtain states from their derivatives for shooting methods or use of collocation methods to solve time-dependent differential equations.
Evaluation of state vector partial derivative rates.
Numerical integration of state vector partial derivative rates for shooting methods.
Solution by matrix inversion and non linear programming.

The comparison shows that both methods attract a considerable computational overhead, and that the overhead per iteration can depend on the details of the

particular problem under consideration. A further factor to be considered is the flexibility of the algorithms. In general, indirect methods require the derivation of a greater number of analytical expressions (unless automatic differentiation methods are used). Therefore, if the mathematical models representing the problem are modified, or the constraints or objective are modified, a greater effort is required to obtain the new set of derivatives for the indirect case when compared with the direct case. This flexibility of direct methods is a significant factor in an environment where models and requirements change frequently.

A further selection, regarding direct methods, lies in the choice of shooting methods or collocation. Both methods have strengths, as outlined in the previous discussions. The choice between these methods could be made on the basis of computational efficiency, but this could vary from problem to problem. The result is therefore not a clear decision. The techniques require a number of common elements, such as state vector rate evaluation and the evaluation of the partial derivatives of these rates with respect to control parameters. These terms are defined by the mathematical model employed, and there is scope for switching between methods.

3.3 APPLICATION OF DIRECT TRAJECTORY OPTIMISATION METHODS

The application of the methods discussed will now be described to enable the solution of a general trajectory optimisation problem. Firstly, the problem must be formulated, in mathematical terms. Then, the information needed for the solution of the problem – including gradient information – must be assembled.

3.3.1 Formulating the mathematical problem

The mathematical problem has several components. Firstly, the fundamental objective, constraints and optimisable controls must be identified, and then the mathematical models that define the motion of the spacecraft must be defined.

Basic problem formulation

The trajectory optimisation problem has the following format, as described previously:

Minimise the objective function, J, subject to the equality constraints, $C_i = 0$, $i = 1$ to n, and the inequality constraints, $C_i <= 0$, $i = n + 1$ to $n + q$, with respect to a control vector, $\underline{u}$.

The objective function can take the general form, as given previously:

$$J = f^n(\underline{X(t_f)}, \underline{u(t_f)}, t_f) + \int f^n(\underline{X}, \underline{u}, t)\, dt$$

where X_i, $i = 1$ to m, are the elements of the state vector, $\underline{X}$; u_j, $j = 1$ to p, are the elements of the optimisable control vector, $\underline{u}$; and t_f is the time at which the trajectory terminates. t_0 is the time at which the trajectory starts, and X_i are obtained by integrating the state vector rates, recalling that:

$$\underline{X} = \underline{X}(t_0) + \int_{t_0}^{t_f} \dot{\underline{X}}(\underline{X}, \underline{u}, t)\, dt$$

An objective that often occurs in the context of interplanetary missions is the minimisation of fuel mass, therefore:

$$J = m(t_f)$$

where m is the fuel mass used, which may be a component of the state vector, together with position and velocity vectors. This can be expressed equivalently as:

$$J = -\int_{t_0}^{t_f} \dot{m}(\underline{X}, \underline{u}, t)\, dt$$

where the integrand is the fuel mass flow rate which is a negative quantity. This will generally depend upon thrust and specific impulse. Thrust may have a positional dependence, and is controlled in magnitude by the throttle that is applied.

In the context of a multiple shooting algorithm, sections of the trajectory where thrusting occurs may often form separate segments. Therefore, the objective effectively becomes:

$$J = -\sum_{i=1}^{i=NT} \int_{t0i}^{tfi} \dot{m}(\underline{X}, \underline{u}, t)\, dt$$

where i represents the thrusting segments, of which there are NT. However, because the multiple shooting formulation links the adjacent segments through equality constraints, the objective can be specified simply as:

$$J = m(t_{fN})$$

where t_{fN} is the terminal time of the last multiple shooting segment.

In some trajectory optimisation problems, the total duration of the transfer may be the objective to be minimised. Such an example could apply to a spacecraft using solar sails, where no fuel is used, but the minimum transfer time is sought for a given sail size.

Yet another form of objective is the minimisation of ΔV for a transfer, where the spacecraft manoeuvres may be represented as impulsive velocity changes. These velocity changes then form components of the control vector, and so the objective is of the form

$$J = f^n(\underline{u}(t_f))$$

where the elements of $\underline{u}$ are now the individual ΔV vectors per manoeuvre, and so

$$J = \sum_{i=1}^{i=Nm} \sqrt{\Delta V_{xi}^2 + \Delta V_{yi}^2 + \Delta V_{zi}^2}$$

and ΔV_{xi}, ΔV_{yi}, ΔV_{zi} are the Cartesian components of the ΔV for manoeuvre number i, Nm manoeuvres in total.

Equality constraints

The equality constraints for this type of optimisation problem are generally functions that can be associated with particular events during the evaluation of the trajectory, $Ci = f^n(\underline{X}(t_e), \underline{u}, t_e)$, where t_e can be a fixed intermediate time or the trajectory termination time. It may be convenient to arrange the function such that each constraint becomes $C_i = 0$.

Examples of such constraints are final orbit injection constraints at a target planet. Alternatively, a planet rendezvous constraint implies that the locations of the spacecraft and planet must coincide at termination of the trajectory.

In the case of multiple shooting, further equality constraints arise from the matching of the state vector at the end and beginning of adjacent segments.

Alternatively, some function or element of the state vector reaching a required value may determine the event, which then imposes a further equality constraint on other elements or functions of the state vector. The optimisation process determines the time at which the event ultimately occurs. An example could be that the trajectory is terminated when the spacecraft reaches a particular distance from the Sun.

Inequality constraints and slack variables

These constraints are of the form $Ci \leq 0$. They may be conveniently handled by employing slack variables to convert the inequality to an equality constraint. The constraints therefore become:

$$Ci + Si = 0$$

A constraint is applied on the control parameter, Si, such that:

$$Si \leq 0$$

This approach uses additional controls, but is often a more convenient formulation for such constraints, because the inequality can be handled more simply for a control parameter that is handled directly in the iterative solution of the problem.

Examples of such constraints may be the distance that a fly-by takes place at a planet, as some minimum altitude may apply. Alternatively, in the context of multiple shooting, the duration of each trajectory segment should not be less than zero.

There are also inequality path constraints. Examples of this type of constraint are restrictions in the aspect angle of a spacecraft (for example, where direct solar illumination may cause difficulty). In these cases, a grid of inequality constraints

could be specified. Alternatively, an integral of the excursions of the constraint above its allowed limiting value can be made equal to zero.

Control parameters

The optimisable control parameters now include a range of different parameter types. In this context, control variables are distinguished from control parameters. Control variables are typically the actual control methods that make up the vector $\underline{u}$, while control parameters are used to define the time histories of the control variables where appropriate. Therefore, a control vector exists:

$$\underline{u} = \begin{bmatrix} u_1 \\ u_2 \\ u_3 \end{bmatrix}$$

where the components, $u_1 \ldots$ are free variables that have a physical significance for the control of the trajectory, such as thrust vector steering angles or throttle parameters.

Direct methods then express the control variables, u_i, in terms a set of optimisable control parameters, so that $u_i = u_i(p_{i1}, p_{i2}, \ldots, p_{in}, t)$ where n parameters are used to represent the control variable, i and the independent variable in this case is the time, t (although other options such as range angle could be employed). A control parameter vector, $\underline{p}_i$, is therefore used to generate the value of the control variable, u_i at any time.

Further control parameters include the start and end times of thrust segments, and in the case of multiple shooting algorithms, the initial states of each segment that is propagated, $\underline{X}(t_{0i})$.

These control parameters form the optimisable control parameter vector. A vector can be assembled for each segment, in the case of a multiple shooting algorithm, as the control parameter vector elements for one segment do not in general directly influence the trajectory in another segment.

A typical control parameter vector for a single segment would appear as follows:

$$\underline{p} = \begin{bmatrix} \underline{p_1} \\ \underline{p_2} \\ \underline{X_0} \\ \underline{t} \end{bmatrix} \tag{3.13}$$

where $\underline{t}$ is a vector containing the segment start and end times. These vectors are then collected together to form the total control parameter vector.

Mathematical models for optimisation

A mathematical model is required to represent the detailed evolution of the thrust or coast arcs. In addition to the full mathematical models, requiring numerical integration for the propagation of the trajectory, approximation models can be used to

represent particular regions of trajectory, such as Keplerian arcs and fly-by patched conics.

The forces acting on the spacecraft can be divided into two categories: environmental terms and propulsion terms. These will both now be described.

Environmental terms

For general interplanetary transfer modelling, the Sun is taken as the origin of this reference system. The orientation of the system is inertially fixed.

The primary effects are gravity, and so the gravity fields of the Sun and a specified planet (or a number of planets) are taken into consideration in this model. The locations of the planets must therefore be evaluated. A number of such models of planet position exist, each with different degrees of accuracy. Probably the most accurate model is the JPL ephemeris model (see references for this section).

The model used depends on the type of analysis to be performed. If the manoeuvres for a particular spacecraft during flight operations are to be evaluated, the most accurate models are used. Conversely, if in the earlier stages of a mission design, where computing speed is a greater issue (because many alternative trajectories are evaluated), mean ephemeris models can be used. These assume that the ephemeris of a particular planet remains fixed between a specified reference epoch and the mission period of interest. In such a model the Sun may be assumed to be at the origin. The subsequent motions of the individual planets can then each be specified by six mean orbital elements given at a reference epoch.

The planet's state (position and velocity vectors) at any subsequent time is then by determined by calculating the new mean anomaly as a function of the elapsed time from the reference epoch. These elements are converted to Cartesian coordinates to determine the velocity and position with respect to the Sun.

Now that the motion of the major bodies has been established, it is possible to calculate the motion of the spacecraft, which is assumed to be of negligible mass in comparison to the mass of the planets.

The equations of motion for the spacecraft under the influence of gravity are the following:

$$\frac{d^2\underline{r}}{dt^2} = \frac{\underline{Force}}{mass} - \frac{\mu}{r^3}\,\underline{r} - \sum_{i=1}^{i=N}\left[\frac{\mu_{pi}}{r_{pi}^3}\underline{r_{pi}} + \frac{\mu_{pi}}{r_{relpi}^3}\underline{r_{relpi}}\right] \tag{3.14}$$

$$\frac{d\underline{r}}{dt} = \underline{V} \tag{3.15}$$

where r is the spacecraft position with respect to the Sun, V is the velocity of the spacecraft relative to the Sun, r_{pi} is the planet, i position with respect to the Sun, r_{relpi} is the spacecraft position with respect to the planet, i, μ is the Sun's gravitational constant, and μ_{pi} is the i planet's gravitational constant. N is the number of planets represented. Force is a non-gravitational force arising from perturbations or manoeuvres.

The above terms in $\underline{r}_{pi}$ are present so as to include the acceleration of the Sun caused by the planet's gravity field. It should be noted that the term is generally very small in magnitude in comparison with the other gravity terms.

Further environmental terms can be considered:

- The effects of forces in close proximity to the planets; namely atmospheric drag, and harmonic terms in the planet's gravity field.
- Solar radiation pressure.

The inclusion of these terms depends on the nature of the mission under consideration. For interplanetary transfers these are often neglected (unless solar sailing, where solar radiation pressure is required).

Propulsion terms

The key aspects of a propulsion model are the generation of the thrust vector and any fuel usage. For general models, a nominal thrust and specific impulse are specified. It is often assumed that this thrust and specific impulse remain constant for the transfer – which would often be true for a chemical system. Solar electric systems are discussed later. Nuclear electric propulsion systems may also be assumed to provide constant thrust (although in practice some form of degradation often occurs).

The rate of fuel mass usage is calculated (from Chapter 2) as:

$$\dot{m} = \frac{-Thrust}{Isp * g_0} \tag{3.16}$$

with thrust specified in Newtons and Isp is the specific impulse in seconds. g_0 is constant, normally $9.80665\,\mathrm{m/s^2}$.

Solar electric propulsion

An ideal solar array can be assumed for power generation in this example, so that maximum available power varies with the inverse square of the distance to the Sun. A reference thrust and specific impulse are then specified, applying at some reference distance from the Sun.

The actual power available is used to scale the nominally specified thrust or specific impulse, dependent on the selection of the power utilisation. For example, the thrust can be scaled with available power:

$$Thrust = \frac{r_{nom}^2}{r^2} * Thrust_{nom} \tag{3.17}$$

where r_{nom} is a specified radius at which scaling is unity.

Alternatively, thrust may be constant and specific impulse scaled with available power:

$$Isp = \frac{r_{nom}^2}{r^2} * Isp_{nom} \tag{3.18}$$

Optimal control formulation for low thrust

The physical controls in these problems, in addition to the locations and durations of the thrusting segments, are the thrust vector steering angles and also, in some scenarios, the magnitude of the thrust.

A number of parameterisations of such profiles are possible. The simplest is to represent, for example, the steering angles by polynomials in time. The steering angles are then measured with respect to the velocity vector of the spacecraft, or alternatively a vector perpendicular to the radial position vector. These are expressed as an azimuth in the orbit plane and an elevation perpendicular to the plane. A sufficiently large number of parameters allows the generation of complex control profiles.

In the case of the radial referenced set, the directions of the unit vectors are obtained by:

$$\hat{x}_T = \frac{\underline{r}}{|\underline{r}|}$$

$$\hat{y}_T = \frac{\underline{V} - (\hat{x}_T \cdot \underline{V})\,\hat{x}_T}{|\underline{V} - (\hat{x}_T \cdot \underline{V})\,\hat{x}_T|}$$

$$\hat{z}_T = \hat{x}_T \wedge \hat{y}_T$$

The propulsion force components in the above defined x_T, y_T and z_T directions are then calculated from the optimisable steering angles by:

$$Fx_T = Thrust \times \cos(elevation) \times \cos(azimuth)$$

$$Fy_T = Thrust \times \cos(elevation) \times \sin(azimuth)$$

$$Fz_T = Thrust \times sin(elevation)$$

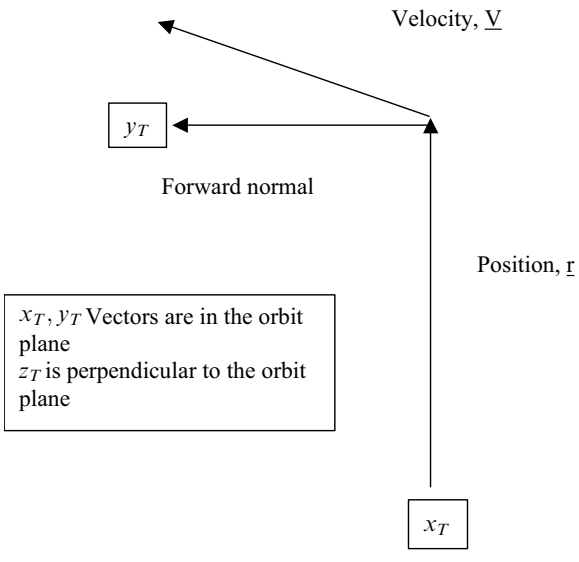

where thrust is the spacecraft thrust, *azimuth* is the spacecraft thrust vector azimuth angle measured in the radius vector frame (azimuth is in the orbit plane, measured from the normal to the radius vector), and *elevation* is the spacecraft thrust vector elevation angle measured out of the orbit plane.

The thrust force in an inertially oriented reference frame is then obtained by $\underline{Force} = [A]_I^T \underline{Force_T}$ where $[A]_I^T$ is the transformation matrix between the orbit frame set and the inertial set. The elements of this matrix are obtained from the unit vector direction cosines of Equation 3.19.

Some examples of parameterisations are now considered.

(1) The azimuth and elevation steering angles are measured with respect to the velocity vector or transverse radial vector, and are obtained from polynomials of the form:

$$Angle = p_0 + p_1 t + p_2 t^2 + p_3 t^3$$

where the p terms are four optimisable parameters, in this third order example.

(2) In situations where the spacecraft undergoes many revolutions, such as spiralling lunar transfers from initial low Earth orbit, two approaches are possible. The first is to split the trajectory into many, relatively short-duration segments and provide a simple parameterisation similar to that of the previous example. The second is to schedule the control history against range angle or another orbital parameter, so that the periodic nature of the control can be readily implemented. This later approach allows the use of fewer segments but with longer duration.

(3) A number of expressions in azimuth and elevation steering angles, α, β, can be obtained to instantaneously maximise terms such as semi-major axis rate of change, apogee altitude rate, argument of perigee rate, and inclination and node rates.

The problem is then to represent the optimal control history in terms of these solutions:

$$u_1 = \alpha = \frac{\sum_{i=1}^{i=N} C_{1i} u\max_{1i}}{\sum_{i=1}^{i=N} C_{1i}}, \quad u_2 = \beta = \frac{\sum_{i=1}^{i=N} C_{2i} u\max_{2i}}{\sum_{i=1}^{i=N} C_{2i}}$$

where $u\max_{1i}$, $u\max_{2i}$ are the individual optimal control profiles relating to specific manoeuvre types labelled i. In these cases, the steering laws, $u\max$, depend upon the instantaneous ephemeris of the spacecraft. Such steering laws are described in Chapter 4 regarding low thrust.

C_{1i}, C_{2i} ... are coefficients that may themselves be made up of functions of the optimisable control parameters, p_j, and, for example, trigonometric functions of the

true anomaly:

$$C_{1i} = \sum_{j=1}^{j=N/2} p_j \sin j\theta + \sum_{j=N/2+1}^{j=N} p_j \cos j\theta$$

In this way the weighting of a given control law may be varied with true anomaly in the spacecraft's orbit.

3.3.2 Evaluation of gradients

The non-linear programming algorithm requires gradients of the objective function and the constraints. These gradients are those with respect to the optimisable control parameters.

Gradient evaluation can potentially be one of the most computationally intensive tasks performed by an optimisation procedure. Particular attention should therefore be paid to the ways in which this may be achieved.

First-order gradients can be calculated in a number of ways:

- Numerical differencing by re-evaluating the trajectory with perturbations in each of the control parameters and using the difference to calculate the gradient.
- Numerical integration along the trajectory of analytically derived gradient rate terms. This is a variational calculus method.

The second method can be shown to be considerably more efficient in terms of computing time, and is therefore examined in some detail here. Such methods also necessitate the evaluation of the partial derivatives of the state vector components with respect to the control parameters. When using a general mathematical model to define state vector derivatives, all states are often obtained via numerical integration. To obtain gradients of the states with respect to control parameters, partial derivatives of the state vector time derivatives with respect to the control parameters are required.

The gradients are therefore to be derived from the application of variational calculus methods. Further details of such methods can be found in the references for this section. The functional forms of the objective function and constraints, whose gradients are required, are similar: a function of terminal state and control values and the integral of a further function of the state and control elements, or a function of the state and control vector elements at a given time.

Variational methods require the numerical integration of expressions that define the gradient's time derivatives. These expressions may either be obtained by analytical methods or alternatively by numerical techniques such as automatic differentiation. For a typical objective function (as in equation 3.1) the gradients with respect to a control parameter, p_i, as defined by equation 3.13, are expressed as:

$$\frac{\partial J(t_f)}{\partial p_i} = \int_{t_0}^{t_f} \frac{\partial L}{\partial p_i}(\underline{X}, \underline{u}, t)\, dt + \frac{\partial t_f}{\partial p_i} L(t_f) + \frac{\partial \Phi(t_f)}{\partial p_i} - \frac{\partial t_0}{\partial p_i} L(t_0) \qquad (3.20)$$

where

$\frac{\partial J(t_f)}{\partial p_i}$ is the partial derivative of the terminal value of the objective function, wrt the control vector element, i,

$\frac{\partial L(\underline{X}, \underline{u}, t)}{\partial p_i}$ is the partial derivative of the instantaneous value of the objective function derivative, wrt the control parameter, i,

$\frac{\partial t_f}{\partial p_i}$ is the partial derivative of the terminal time wrt the control parameter, i, and

$\frac{\partial \Phi(t_f)}{\partial p_i}$ is the partial derivative of the terminal component of the objective function, J, wrt the control parameter, i.

The rate derivatives typically decompose in the following manner.

$$\frac{\partial L}{\partial p_i} = \sum_{k}^{ns} \frac{\partial L}{\partial X_k}(\underline{X}, \underline{u}, t) * \frac{\partial X_k}{\partial p_i} + \sum_{k}^{nc} \frac{\partial L}{\partial u_k}(\underline{X}, \underline{u}, t) * \frac{\partial u_k}{\partial p_i} \tag{3.21}$$

where ns is the number of states and nc is the number of control variables and:

$\frac{\partial X_k}{\partial p_i}$ is the partial derivative of the state element, k, wrt the control parameter, i,

$\frac{\partial u_k}{\partial p_i}$ is the partial derivative of the instantaneous value of the control variable, k, wrt the control parameter, i,

$\frac{\partial L(\underline{X}, \underline{u}, t)}{\partial X_k}$ is the partial derivative of the instantaneous value of the objective function time derivative, wrt the state element, k, and

$\frac{\partial L(\underline{X}, \underline{u}, t)}{\partial u_k}$ is the partial derivative of the instantaneous value of the objective function time derivative, wrt the control variable, k.

In general, the gradient of some function evaluated at termination of the trajectory (such as the objective function, J) with respect to a control parameter, p_i, is required. The function J may be the result of integration of a function of state ($\underline{X}$) and control variables ($\underline{u}$).

The gradients of the propagated state vector are therefore required to obtain the gradients of the constraints and objective function.

The final state for any element of the state vector is obtained by integration as follows:

$$X_i(t_f) = X_i(t_0) + \int_{t_0}^{t_f} \left(\frac{dX_i(\underline{X}, \underline{u}, t)}{dt} \right) dt$$

The state element partial derivatives are obtained in the same manner as described in the indirect optimisation methods case:

$$\frac{\partial X_i(t)}{\partial p_j} = \int_{t_0}^{t} \frac{\partial \dot{X}_i}{\partial p_j}(\underline{X}, \underline{u}, t)\, dt + \frac{\partial t_f}{\partial p_i}\dot{X}_i(t_f) - \frac{\partial t_0}{\partial p_i}\dot{X}_i(t_0) \tag{3.22}$$

where

$\frac{\partial X_i}{\partial p_j}$ is the partial derivative of the instantaneous value of the state element, i, wrt the control parameter, j, and

$\frac{\partial \dot{X}_i}{\partial p_j}$ is the partial derivative of the instantaneous value of the state element, i, time derivative, wrt the control parameter, j.

The state vector rate derivatives then decompose as follows:

$$\frac{\partial \dot{X}_i}{\partial p_j} = \sum_k^{ns} \frac{\partial \dot{X}_i}{\partial X_k}(\underline{X}, \underline{u}, t) * \frac{\partial X_{ki}}{\partial p_j} + \sum_k^{nc} \frac{\partial \dot{X}_i}{\partial u_k}(\underline{X}, \underline{u}, t) * \frac{\partial u_{ki}}{\partial p_j} \tag{3.23}$$

where

$\frac{\partial \dot{X}_i(\underline{X}, \underline{u}, t)}{\partial X_k}$ is the partial derivative of the instantaneous value of the state vector element, i, time derivative, wrt the state element, k, and

$\frac{\partial \dot{X}_i(\underline{X}, \underline{u}, t)}{\partial u_k}$ is the partial derivative of the instantaneous value of the state vector element, i, time derivative, wrt the control variable, k.

The various partial derivatives of this state vector with respect to different types of control parameter will now be considered.

Initial state dependence

Firstly, the state transition matrix of the final Cartesian states with respect to the initial states is evaluated.

$$\frac{\partial X_i(t_f)}{\partial X_j(t_0)} = \frac{\partial X_i(t_0)}{\partial X_j(t_0)} + \int_{t_0}^{t_f} \frac{\partial(\dot{X}_i(\underline{X}, \underline{u}, t))}{\partial X_j(t_0)}\, dt + \frac{\partial t_f}{\partial X_j(t_0)}(\dot{X}_i(\underline{X(t_f)}, \underline{u(t_f)}, t_f)) - \frac{\partial t_0}{\partial X_j(t_0)}(\dot{X}_i(\underline{X(t_0)}, \underline{u(t_0)}, t_0)) \tag{3.24}$$

where

$\frac{\partial X_i(t_f)}{\partial X_j(t_0)}$ is the partial derivative of the value of the state element, i, at time t_f, wrt the state vector element j at time t_0, and

$\frac{\partial(\dot{X}_i(\underline{X}, \underline{u}, t))}{\partial X_j}$ is the partial derivative of the instantaneous value of the state element, i, time derivative, wrt the state vector element j at time t_0. This term is obtained from the previously defined mathematical model of the state vector derivatives by the following expansion:

$$\frac{\partial(\dot{X}_i(\underline{X}, \underline{u}, \underline{t}))}{\partial Xj(t_0)} = \sum_k^{ns} \left[\frac{\partial(\dot{X}_i(\underline{X}, \underline{u}, t))}{\partial X_k} \frac{\partial X_k(\underline{X}, \underline{u}, t)}{\partial X_j(t_0)} \right] \tag{3.25}$$

The partial derivatives of the initial and final epochs wrt the initial states are

assumed to be zero for a multiple shooting application, and can therefore be eliminated.

A matrix of partial derivatives of the state vector rates with respect to the state vector components is required to evaluate the preceding expressions:

$$\left[\frac{\partial \dot{\underline{X}}(\underline{X},\underline{u},t)}{\partial \underline{X}}\right] = \begin{bmatrix} \frac{\partial \dot{X}_1}{\partial X_1}(\underline{X},\underline{u},t) & \cdots & \frac{\partial \dot{X}_{ns}}{\partial X_1}(\underline{X},\underline{u},t) \\ \frac{\partial \dot{X}_1}{\partial X_2}(\underline{X},\underline{u},t) & \cdots & \frac{\partial \dot{X}_{ns}}{\partial X_2}(\underline{X},\underline{u},t) \\ \cdots & \cdots & \cdots \\ \frac{\partial \dot{X}_1}{\partial X_{ns}}(\underline{X},\underline{u},t) & \cdots & \frac{\partial \dot{X}_{ns}}{\partial X_{ns}}(\underline{X},\underline{u},\underline{t}) \end{bmatrix} \tag{3.26}$$

These expressions will be discussed later in this section.

The above state transition is with respect to the initial Cartesian states. In a multiple shooting problem, the initial states of a segment may themselves be optimisable control parameters, or alternatively be derived from optimisable control parameters that determine the initial state vector. These could be an ephemeris set used to specify the initial state. The initial control parameters will in general either be:

- Heliocentric referenced osculating ephemeris for motion in deep space.
- Planet-relative osculating ephemeris for those segments that occur close to a planet, such as, for example, where a gravity-assist manoeuvre is to be performed.

The state transition with respect to these optimisable control parameters is then required, and is achieved by the following:

$$\frac{\partial X_i(t_f)}{\partial E_{j0}} = \sum_k^{ns} \left[\frac{\partial X_i}{\partial X_k(t_0)} \frac{\partial X_k(t_0)}{\partial E_{j0}}\right] \tag{3.27}$$

where E_{j0} are now the initial ephemeris set ($j = 1$ to 6), for a particular segment. These parameters form a part of the optimisable parameter set.

The Jacobian, $\dfrac{\partial \underline{X}(t_0)}{\partial \underline{E_0}}$, must therefore be evaluated, and can be obtained analytically.

In practice, an intermediate stage may be necessary, as in the case of planet relative ephemeris, it may be referenced to a local equatorial plane. This must then be transformed to ecliptic co-ordinates:

$$\frac{\partial X_i}{\partial E_{j0}} = \sum_k^{ns} \left[\frac{\partial X_i(t_0)}{\partial X_k^{Eq}(t_0)} \frac{\partial X_k^{Eq}(t_0)}{\partial E_{j0}}\right] \tag{3.28}$$

Initial time dependence

The partial derivatives of the final states wrt the initial epoch is also required. The total dependence of the final state on t_0 is given generally by:

$$\frac{\partial \underline{X}(t_f)}{\partial t_0} = \frac{\partial \underline{X}(t_f)}{\partial \underline{X}(t_0)}_{t_0,t_f} * \frac{\partial \underline{X}(t_0)}{\partial t_0} + \frac{\partial \underline{X}(t_f)}{\partial t_f}_{X_0,t_0} * \frac{\partial t_f}{\partial t_0} + \frac{\partial \underline{X}(t_f)}{\partial t_0}_{t_f,X_O} \tag{3.29}$$

In this expression the subscripts after a partial derivative specifically indicate the terms that are fixed in the partial derivative to which they are assigned.

The final term is a state transition term given by:

$$\frac{\partial X_i(t_f)}{\partial t_0}_{t_f,X_0} = \int_{t_0}^{t_f} \frac{\partial (\dot{X}_i(\underline{X},\underline{u},t))_i}{\partial t_0}\, dt - (\dot{X}_i(\underline{X(t_0)},\underline{u(t_0)},t_0)) \tag{3.30}$$

for each element i, where

$$\frac{\partial (\dot{X}_i(\underline{X},\underline{u},t))}{\partial t_0} = \sum_k^{ns} \left[\frac{\partial (\dot{X}_i(\underline{X},\underline{u},t))}{\partial X_k} \frac{\partial X_k}{\partial t_0} \right] \tag{3.31}$$

The first term of equation 3.29 includes any explicit dependence of the initial state vector on the initial time, t_0.

$\frac{\partial \underline{X}(t_0)}{\partial t_0}$ does not include the time rate of change of the initial state vector. However, planetary positions, for example, are modelled with explicit time dependence, and so these terms contribute.

The dependence of the initial state on the initial epoch is dependent on the initial state specification. The partial derivative with respect to time means with constant values for all other control parameters (including control initial states). If, however, the initial control states are relative to the major body at which the fly-by occurs, the absolute time dependence arises from the dependence of the major body state on absolute time:

$$\underline{X}(t_0) = \underline{X}_{\text{planet}}(t_0) + \underline{X}_{\text{REL}}(t_0)$$

Final time dependence

The partial derivatives of the final states wrt the final epochs is also required. The final state dependence on final time, t_f is given by the final derivative rate:

$$\frac{\partial X_i(t_f)}{\partial t_f} = (\dot{X}_i(\underline{X(t_f)},\underline{u(t_f)},t_f)) \tag{3.32}$$

Thrust control parameter dependence

The state transition matrix of the propagated Cartesian states with respect to the thrust vector steering control parameters is now described. The gradient can be

found as follows:

$$\frac{\partial X_i(t_f)}{\partial p_j} = \int_{t_0}^{t_f} \frac{\partial(\dot{X}_i(\underline{X}, \underline{u}))}{\partial p_j}\, dt \tag{3.33}$$

where

$$\frac{\partial(\dot{X}_i(\underline{X}, \underline{u}))}{\partial p_j} = \sum_{k}^{nc} \left[\frac{\partial(\dot{X}_i(\underline{X}, \underline{u}))}{\partial u_k} \frac{\partial u_k}{\partial p_j} \right] \tag{3.34}$$

where k represents the steering parameters, azimuth and elevation, in this case, and noting that each control, u_k, is a function of an optimisable parameter set and time. The initial and final times do not depend on the thrust control parameters, and are omitted here.

A matrix of partial derivatives of the state vector rates with respect to the control variables is required to evaluate the preceding expressions:

$$\left[\frac{\partial \dot{\underline{X}}(\underline{X}, \underline{u}, t)}{\partial \underline{u}} \right] = \begin{bmatrix} \frac{\partial \dot{X}_1}{\partial u_1}(\underline{X}, \underline{u}, t) & \cdots & \frac{\partial \dot{X}_{ns}}{\partial u_1}(\underline{X}, \underline{u}, t) \\ \frac{\partial \dot{X}_1}{\partial u_2}(\underline{X}, \underline{u}, t) & \cdots & \frac{\partial \dot{X}_{ns}}{\partial u_2}(\underline{X}, \underline{u}, t) \\ \cdots & \cdots & \cdots \\ \frac{\partial \dot{X}_1}{\partial u_{nc}}(\underline{X}, \underline{u}, t) & \cdots & \frac{\partial \dot{X}_{ns}}{\partial u_{nc}}(\underline{X}, \underline{u}, t) \end{bmatrix} \tag{3.35}$$

The control variables are terms such as thrust steering angles and throttle controls.

State vector derivative partials

The previous sections have shown the need for a series of derivatives of the state vector time derivatives. These time derivatives are defined by the mathematical model employed. Therefore:

$$\frac{\partial(\dot{X}_i(\underline{X}, \underline{u}, t))}{\partial X_k}, \quad \frac{\partial(\dot{X}_i(\underline{X}, \underline{u}, t))}{\partial u_k}$$

are required.

This series of partial derivatives of the components of the state vector rates and any constraints will be evaluated by analytical methods. These partial derivatives are with respect to the state vector elements themselves and also with respect to the control variables, such as thrust steering angles.

This method, requiring the analytical derivation of many partial derivatives, leads to an initial overhead in the development time of the algorithms, when compared with a numerical differencing method. However, once established, the gains due to improvements in computing time to reach a solution are large. A typical overhead in obtaining the partial derivatives with respect to the state variables is a factor of 3 to 4 on numerical integration of the standard state vector rates and constraint evaluations. The evaluation of partial derivatives with respect to

a steering control parameter then requires only a fractional increase in the total overhead.

As an illustration of this principle, a series of partial derivatives for a typical mathematical model are now obtained. Firstly, the partial derivatives with respect to position are given by the following expressions. When the applied propulsive force is zero, only gravitational forces are assumed to act, and therefore the partial derivatives of acceleration, or the velocity time derivative, are given by:

$$\frac{\partial \dot{\underline{V}}}{\partial X_k} = 3\frac{\mu}{r^4}\underline{r}\frac{\partial r}{\partial X_k} - \frac{\mu}{r^3}\frac{\partial \underline{r}}{\partial X_k} - \sum_{i=1}^{i=N}\left[-3\frac{\mu_{pi}}{r_{relpi}^4}\frac{\partial r_{relpi}}{\partial X_k}\underline{r_{relpi}} + \frac{\mu_{pi}}{r_{relpi}^3}\frac{\partial \underline{r_{relpi}}}{\partial X_k}\right] \tag{3.36}$$

where the position vector is given by:

$$\underline{r} = r_x\hat{x} + r_y\hat{y} + r_z\hat{z}$$

and the state vector is constructed as follows: $X_1 = r_x$, $X_2 = r_y$, $X_3 = r_z$, $X_4 = V_x$, $X_5 = V_y$, $X_6 = V_z$

The following results are then obtained:

$$\frac{\partial r}{\partial X_1} = \frac{r_x}{r}, \frac{\partial r}{\partial X_2} = \frac{r_y}{r}, \frac{\partial r}{\partial X_3} = \frac{r_z}{r}, \frac{\partial r}{\partial X_4} = \frac{\partial r}{\partial X_5} = \frac{\partial r}{\partial X_6} = 0 \tag{3.37}$$

and

$$\frac{\partial \underline{r}}{\partial X_1} = \hat{x}, \frac{\partial \underline{r}}{\partial X_2} = \hat{y}, \frac{\partial \underline{r}}{\partial X_3} = \hat{z}, \frac{\partial \underline{r}}{\partial X_4} = 0, \frac{\partial \underline{r}}{\partial X_5} = 0, \frac{\partial \underline{r}}{\partial X_6} = 0 \tag{3.38}$$

The relative position vector is given by (dropping subscript i for this evaluation):

$$\underline{r_{relpx}} = (r_x - r_{px})\,\hat{x} + (r_y - r_{py})\,\hat{y} + (r_z - r_{pz})\,\hat{z}$$

where $\hat{x}$, $\hat{y}$, $\hat{z}$ are a set of unit vectors defining an inertial axis set.

Therefore:

$$\frac{\partial r_{relp}}{\partial X_1} = \frac{r_{relpx}}{r_{relp}}, \frac{\partial r_{relp}}{\partial X_2} = \frac{r_{relpy}}{r_{relp}}, \frac{\partial r_{relp}}{\partial X_3} = \frac{r_{relpz}}{r_{relp}}, \frac{\partial r_{relp}}{\partial X_4} = \frac{\partial r_{relp}}{\partial X_5} = \frac{\partial r_{relp}}{\partial X_6} = 0 \tag{3.39}$$

$$\frac{\partial r_{relp}}{\partial X_1} = \hat{x}, \frac{\partial \underline{r_{relp}}}{\partial X_2} = \hat{y}, \frac{\partial \underline{r_{relp}}}{\partial X_3} = \hat{z}, \frac{\partial \underline{r_{relp}}}{\partial X_4} = 0, \frac{\partial \underline{r_{relp}}}{\partial X_5} = 0, \frac{\partial \underline{r_{relp}}}{\partial X_6} = 0 \tag{3.40}$$

When a propulsive force is considered – such as a low-thrust force with steering angles – the following state vector derivatives are obtained. Firstly, the prolusion force is defined by:

$$\underline{F} = F_{xT}\hat{x}_T + F_{yT}\hat{y}_T + F_{zT}\hat{z}_T$$

where the propulsion force components are expressed in terms of its own axis set (defined by 3.19). In case of a radial-based set, as described previously, for the specification of the thrust vector directions, the directions of the unit vectors are obtained by:

$$\hat{x}_T = \frac{\underline{r}}{|\underline{r}|}, \hat{y}_T = \frac{\underline{V} - (\hat{x}_T \cdot \underline{V})\,\hat{x}_T}{|\underline{V} - (\hat{x}_T \cdot \underline{V})\,\hat{x}_T|}, \hat{z}_T = \hat{x}_T \wedge \hat{y}_T$$

The partial derivatives of this force with respect to a state vector element, X_i, are:

$$\frac{\partial \underline{F}}{\partial X_i} = \frac{\partial F_{xT}}{\partial X_i}\,\hat{x}_T + \frac{\partial F_{yT}}{\partial X_i}\,\hat{y}_T + \frac{\partial F_{zT}}{\partial X_i}\,\hat{z}_T + F_{xT}\frac{\partial \hat{x}_T}{\partial X_i} + F_{yT}\frac{\partial \hat{y}_T}{\partial X_i} + F_{zT}\frac{\partial \hat{z}_T}{\partial X_i} \tag{3.41}$$

and the partial derivatives of this force with respect to a control vector element, u_i, are:

$$\frac{\partial \underline{F}}{\partial u_i} = \frac{\partial F_{xT}}{\partial u_i}\,\hat{x}_T + \frac{\partial F_{yT}}{\partial u_i}\,\hat{y}_T + \frac{\partial F_{zT}}{\partial u_i}\,\hat{z}_T + F_{xT}\frac{\partial \hat{x}_T}{\partial u_i} + F_{yT}\frac{\partial \hat{y}_T}{\partial u_i} + F_{zT}\frac{\partial \hat{z}_T}{\partial u_i} \tag{3.42}$$

The partial derivatives of the unit vector set with respect to the state vector elements, X_k, must therefore be evaluated as follows:

$$\frac{\partial \hat{x}_T}{\partial X_k} = -\frac{\underline{r}}{r^2}\frac{\partial r}{\partial X_k} + \frac{\partial \underline{r}}{\partial X_k}\frac{1}{r} = \frac{\partial \hat{r}}{\partial X_k} \tag{3.43}$$

and then using 3.37 and 3.38 to complete the expression.

Using the identities:

$$|\underline{x}| = \sqrt{\underline{x}\cdot\underline{x}} \qquad \text{and} \qquad \frac{\partial |\underline{x}|}{\partial y} = \frac{\underline{x}\cdot\dfrac{\partial \underline{x}}{\partial y}}{\sqrt{\underline{x}\cdot\underline{x}}}$$

then:

$$\frac{\partial \hat{y}_T}{\partial X_k} = \frac{\dfrac{\partial \underline{V}}{\partial Xk} - \left(\dfrac{\partial \hat{r}}{\partial X_k}\cdot\underline{V} + \hat{r}\cdot\dfrac{\partial \underline{V}}{\partial X_k}\right)\hat{r} - (\hat{r}\cdot\underline{V})\dfrac{\partial \hat{r}}{\partial X_k}}{|\underline{V_T} - (\hat{x}\cdot\underline{V_T})\,\hat{x}|}$$

$$-\frac{\underline{V_T} - (\hat{r}\cdot\underline{V_T})\,\hat{r}}{|\underline{V_T} - (\hat{x}\cdot\underline{V_T})\,\hat{x}|^3}\left(\frac{\partial \underline{V}}{\partial X_k} - \left(\frac{\partial \hat{r}}{\partial X_k}\cdot\underline{V} + \hat{r}\cdot\frac{\partial \underline{V}}{\partial X_k}\right)\hat{r} - (\hat{r}\cdot\underline{V})\frac{\partial \hat{r}}{\partial X_k}\right)\cdot(\underline{V_T} - (\hat{r}\cdot\underline{V_T})\,\hat{r}) \tag{3.44}$$

and finally:

$$\frac{\partial \hat{z}_T}{\partial X_k} = \frac{\partial \hat{x}_T}{\partial X_k}\wedge\hat{y}_T + \hat{x}_T\wedge\frac{\partial \hat{y}_T}{\partial X_k} \tag{3.45}$$

The partial derivatives of the unit vector set with respect to the control variables are zero.

The partial derivative of the force components may also be obtained as follows from the following force component definitions:

$$F_{xT} = \mathit{Thrust} * \cos\varphi\cos\phi$$

$$F_{yT} = \mathit{Thrust} * \cos\varphi\sin\phi$$

$$F_{zT} = \mathit{Thrust} * \sin\varphi$$

where φ is elevation and ϕ is azimuth of the thrust vector in the local reference frame. These angles are control variables, and can be denoted as u_1 and u_2, respectively, in this example.

The partial derivatives of these force components with respect to the general control variables, u_k, are given by:

$$\frac{\partial F_{xT}}{\partial u_k} = -Thrust * \sin\varphi \frac{\partial \varphi}{\partial u_k}\cos\phi - Thrust * \sin\phi \frac{\partial \phi}{\partial u_k}\cos\varphi$$
$$\frac{\partial F_{yT}}{\partial u_k} = -Thrust * \sin\varphi \frac{\partial \varphi}{\partial u_k}\sin\phi + Thrust * \cos\phi \frac{\partial \phi}{\partial u_k}\cos\varphi$$
$$\frac{\partial F_{zT}}{\partial u_k} = Thrust * \cos\varphi \frac{\partial \varphi}{\partial u_k} \tag{3.46}$$

The expressions $\frac{\partial \phi}{\partial u_k}$ and $\frac{\partial \varphi}{\partial u_k}$ are then 1 or 0, depending on k.

The partial derivatives of the control variables with respect to the control parameters $\frac{\partial u_k}{\partial p_i}$ are obtained from the parametric expression that relates the thrust vector steering angle to the optimisable parameters, p_k.

An example would be where:

$$\phi = p_0 + p_1 t + p_2 t^2 + p_3 t^3$$

and then

$$\frac{\partial \phi}{\partial p_0} = 1, \frac{\partial \phi}{\partial p_1} = t, \frac{\partial \phi}{\partial p_2} = t^2, \frac{\partial \phi}{\partial p_3} = t^3 \tag{3.47}$$

It can be seen from the example of equation 3.47 that for a large set of parameters defining a given control variable, the additional evaluations per optimisable parameter are very small.

The partial derivative of the force components with respect to the state vector elements depends on the specification of the propulsion system. In the example of a radially dependent thrust, such as a solar electric propulsion system, the thrust depends upon the state vector. The following expressions may be derived:

$$\frac{\partial F_{xT}}{\partial X_k} = -Thrust * \sin\varphi \frac{\partial \varphi}{\partial X_k}\cos\phi - Thrust * \sin\phi \frac{\partial \phi}{\partial X_k}\cos\varphi + \frac{\partial Thrust}{\partial X_k} * \cos\varphi\cos\phi$$
$$\frac{\partial F_{yT}}{\partial X_k} = -Thrust * \sin\varphi \frac{\partial \varphi}{\partial X_k}\sin\phi + Thrust * \cos\phi \frac{\partial \phi}{\partial X_k}\cos\varphi + \frac{\partial Thrust}{\partial X_k} * \cos\varphi\sin\phi$$
$$\frac{\partial F_{zT}}{\partial X_k} = Thrust * \cos\varphi \frac{\partial \varphi}{\partial X_k} + \frac{\partial Thrust}{\partial X_k} * \sin\varphi \tag{3.48}$$

In the case of the steering angle definitions given previously, there is no dependence on the state vector and so these partial derivative terms are zero.

However, using the model described previously (3.17), the thrust dependence on radial distance results in:

$$\frac{\partial Thrust}{\partial r} = -2\frac{r_{nom}^2}{r^3} * Thrust_{nom} = -2\frac{Thrust}{r} \tag{3.49}$$

and

$$\frac{\partial Thrust}{\partial X_k} = \frac{\partial Thrust}{\partial r} * \frac{\partial r}{\partial X_k} \tag{3.50}$$

where $\frac{\partial r}{\partial X_k}$ is given by equation 3.37.

The spacecraft mass is an element of the state vector when fuel-using propulsion systems are considered. Mass flow then varies with thrust and specific impulse, and its derivative with respect to state vector elements is therefore:

$$\frac{\partial \dot{m}}{\partial X_k} = \frac{-1}{Isp * g_0} \frac{\partial Thrust}{\partial X_k} \tag{3.51}$$

3.3.3 Non-linear programming

When the gradients of all states, constraints and the objective function are available, an increment in the control parameters can be calculated, by using a non-linear programming (NLP) algorithm to approach the optimum solution.

The form of algorithm that is most applicable is dependent on the information available. In complex trajectory optimisation problems it may be the case that only first-order gradient information is available about the objective and constraints. This is due to the computational overhead in obtaining higher derivatives, but depends on the detail of the optimisation method employed. However, good performance is available using only first-order gradient information.

Many NLP methods have been developed, and this is a specialised subject with application to many fields of optimisation. Further information is available in the references for this section. An illustration of a relatively simple method is outlined here to illustrate some of the principles and considerations when using such algorithms.

Lagrangian method

The method chosen here is a first-order method based on a constrained steepest descent idea. It can be applied to a wide range of problems.

The problem is once again stated as the following:

Find the optimisable control parameters, $\underline{p}$, required to meet the final state constraint vector condition, $\underline{C} = 0$, and minimise the objective, J.

Given an initial estimate for $\underline{p}$, $\underline{C}$ will not equal zero, but will be equal to an error, $\underline{E}$. It is possible to define an augmented objective by adjoining the constraint vector to the objective as follows:

$$J^* = J + \underline{\lambda}^T \cdot \underline{C} \tag{3.52}$$

where $\underline{\lambda}$ is a vector of undetermined Lagrange multipliers.

A change in J^* is such that:

$$\Delta J^* = \Delta J + \underline{\lambda}^T \cdot \underline{\Delta C} \tag{3.53}$$

For a control increment, $\underline{\Delta p}$, then, $\Delta J = \underline{g}^T \cdot \underline{\Delta p}$ to first order, where $\underline{g}$ is the gradient vector of J w.r.t. $\underline{p}$:

$$\underline{g} = \begin{bmatrix} \dfrac{\partial J}{\partial p_1} \\ \cdots \\ \dfrac{\partial J}{\partial p_m} \end{bmatrix}$$

for m parameters.

Also to first order:

$$\underline{\Delta C} = A^T \underline{\Delta p} \tag{3.54}$$

where A is the gradient matrix of C:

$$A = \begin{bmatrix} \dfrac{\partial C_1}{\partial p_1} & \dfrac{\partial C_n}{\partial p_1} \\ \cdots & \cdots \\ \dfrac{\partial C_1}{\partial p_m} & \dfrac{\partial C_n}{\partial p_m} \end{bmatrix}$$

The problem specified is such that the number of optimisable control parameters, m, is greater than the number of constraints, n.

A steepest descent step in J^* can therefore be made by making $\underline{\Delta U}$ be parallel to the gradient vector:

$$\underline{\Delta p} = k(\underline{g} + [\underline{\lambda}^T A^T]^T) \tag{3.55}$$

where k is a positive constant, and $\Delta J^* = k[(\underline{g} + A\underline{\lambda})]^2$ to first order in $\underline{\Delta U}$.

If an error exists in the constraint vector ($\underline{C} = \underline{E}$), then we can require that the step in $\underline{p}$ is such that $\underline{\Delta C} = -\underline{E}$.

Therefore $-\underline{E} = kA^T(\underline{g} + [\underline{A}\lambda])$, and so the Lagrange multipliers are now found from the following expression:

$$\underline{\lambda} = [A^T A]^{-1}\left(-\frac{\underline{E}}{k} - A^T \underline{g} \right) \tag{3.56}$$

Consequently, $\underline{\lambda}$ is found that both reduces J^* and removes the error $\underline{E}$. However, reduction in J^* in the presence of an error E does not imply reduction in J.

The choice of the constant, k, has so far been arbitrary. Expansion of Δp gives:

$$\underline{\Delta p} = k\left(\underline{g} + A[A^T A]^{-1}\left(-\frac{\underline{E}}{k} - A^T \underline{g} \right) \right) \tag{3.57}$$

and hence to first order:

$$\Delta J = \underline{g}^T \cdot k\left(\underline{g} + A[A^T A]^{-1}\left(-\frac{\underline{E}}{k} - A^T \underline{g} \right) \right) \tag{3.58}$$

However, the system is not linear. Therefore, the size of the step in $\underline{p}$ may be deliberately limited in size and then the gradient re-evaluated before a subsequent

step is taken. In this way a series of steps in $\underline{p}$ can be made until the gradient in J^* reduces to zero. Alternatively, a line search method can be used to find the minimum along a direction indicated by the calculated gradient. The gradient calculation is then updated at that point and the process repeated until the gradient of J^* reaches zero. It could then be assumed that a constrained minimum is located. However, this is not guaranteed.

When the situation is reached within the iteration process that $\underline{\Delta p}$ is zero, then no improvement in the constrained objective is possible. However, equation 3.57 also indicates that it is in principle possible to obtain values $\underline{\Delta p}$ of zero when $\underline{E}$ is non-zero, depending on the choice of k.

A more robust approach can be taken that first guarantees that $\underline{E}$ is reduced to zero and is then maintained at its zero value as iteration towards the constrained minimum is made.

If k is very small then equation 3.57 gives:

$$\underline{\Delta p} = -(A[A^T A]^{-1} E)$$

In a linear system such a step would reduce the error in $\underline{C}$ to zero. However, in this non-linear system a series of limited steps may be taken until $\underline{E}$ reduces to zero. The variation in J is determined by the step made to satisfy the constraints, but J does not necessarily improve with such a step.

Now that the error $\underline{E}$ has been reduced to zero, the step $\underline{\Delta p}$ is found by the following method.

Inspection of equation 3.57 shows that when E is zero:

$$\underline{\Delta p} = k(\underline{g} - A[A^T A]^{-1} A^T \underline{g}) \tag{3.59}$$

Also, equation 3.58 gives:

$$\Delta J = k(\underline{g}^T \cdot \underline{g} - \underline{g}^T \cdot A[A^T A]^{-1} A^T \underline{g})$$

This is a steepest descent in J subject to maintaining the constraint $C = 0$ (note that ΔJ also reduces to zero in the case where A is square: $n = m$).

The condition that the calculated value of $\underline{\Delta p}$ is zero now indicates that the constrained minimum has been found. A rigorous treatment of non-linear programming methods can be found in the references for this section.

Other methods

This discussion has indicated how an iterative, gradient-based strategy can be used to find the solution of a constrained optimisation problem. However, a range of non-linear programming strategies are possible, the selection of which may be influenced by the formulation of the problem. For example, a solution using collocation methods leads to the need for large numbers of optimisable parameters and also a large number of constraints. Certain methods that make use of sparse matrix-based systems can be used efficiently for this type of problem. These may be found in the references for this section.

3.4 COMBINING SYSTEM AND TRAJECTORY OPTIMISATIONS: THE OPTIMAL TRANSPORT PROBLEM

The previous sections have considered trajectory optimisation problems and methods of their solution. However, when a spacecraft undergoes an orbital transfer it is possible to go beyond just trajectory optimisation. In principle it is possible to maximise the net useful mass transported to the target orbit. This leaves the maximum possible amount of mass available for scientific payloads and the spacecraft bus to support those payloads.

The extent to which the transfer optimisation may be extended beyond just the trajectory depends strongly on the nature of the spacecraft design, and in particular the nature of the propulsion system.

It should be noted here that in some literature an optimal transport problem may be related to the rate at which useful mass is transported to the target, and so the objective can be defined as useful mass divided by time taken. In the examples discussed here, only useful mass is considered in the transportation problem.

3.4.1 Propulsion system optimisation parameters

Some of the various types of propulsion that are available have been discussed in Chapter 2. They generally break down into two categories: high-thrust, near impulsive systems based on chemical propulsion, and low-thrust systems, of which there are a number of types. It is this latter category that has the greater number of system optimisation parameters, due to the greater complexity of their design.

The propulsion system may be optimised in two ways. The first is a design optimisation problem, regarding the combined optimisation of the system configuration with the transfer trajectory. The second is the optimal utilisation of a given system during the different phases of a transfer. The utilisation is therefore optimised for a given system design. Some examples of the potential for such optimisation will now be discussed.

Design optimisation: solar electric propulsion system optimisation

This concept is best illustrated through the example of a solar electric propulsion system, for which power generation is a key factor. Furthermore, this power must be converted to a useful form for the thrusters. The following fundamental relationship describes the power requirement P:

$$P = \frac{Thrust * Isp_A}{2\eta} \tag{3.60}$$

where η is an efficiency-related factor and Isp_A is the specific impulse measured in m/s. The power available from a solar array varies with solar flux and so with distance from the Sun. The previous equation can therefore be used to define the power requirement when at a nominal distance from the Sun (e.g., P_1 at 1 AU). It can then be assumed that variations in this power when not at 1 AU are translated to

variations in either thrust or specific impulse, or both. For example, assuming a fixed specific impulse:

$$P = P_1\left(\frac{r_1}{r}\right)^2 = \frac{Thrust * Isp_1}{2\eta} \tag{3.61}$$

and

$$Thrust = Thrust_1\left(\frac{r_1}{r}\right)^2$$

Here it assumed that power varies with the inverse square of distance from the Sun. $Thrust_1$ is therefore the nominal thrust, or thrust at 1 AU and Isp_1 a constant specific impulse. Alternatively, thrust may be constant and a varying specific impulse used, characterised by a nominal specific impulse. A general relationship can be assumed:

$$P = P_1\left(\frac{r_1}{r}\right)^2 = \frac{Thrust * Isp_A}{2\eta} \tag{3.62}$$

and

$$Thrust = Thrust_1\left(\frac{r_1}{r}\right)^{k_T} Isp_A = Isp_1\left(\frac{r_1}{r}\right)^{2-k_T}$$

where $k_T(\leq 2)$ is a constant with a value which may be determined to optimise the total transfer performance.

Increasing nominal thrust and nominal specific impulse for the low thrust propulsion therefore increases the power required. The development of a parametric mass model describing the relationship between power required and the system mass is a complex task, and is closely related to the particular design under consideration. However, certain simplifying approximations can be made, and a generic relation of the following type could be assumed as the simplest model:

$$m_{prop} = k_{p0} + k_{p1} * P_1 \tag{3.63}$$

where k_{p0} and k_{p1} are system-dependent constants, and P_1 is the power required at the nominated reference radius.

A further mass related term arises from the mass of the fuel tanks needed to store the propellant. This can be approximated as:

$$m_{\tan k} = k_{T1} * m_{fuel} \tag{3.64}$$

where k_{T1} is a constant, m_{fuel} is the fuel mass. In the case of a constant specific impulse over the trajectory, the fuel mass is obtained by the standard rocket equation:

$$\frac{m_f}{m_0} = e^{-\frac{\Delta V}{Isp * g_0}} \tag{3.65}$$

where m_f and m_0 are the final and initial spacecraft masses, and ΔV is the total ΔV for the transfer. Note that $Isp * g_0 = Isp_A$.

The fuel mass is therefore given by:

$$m_{fuel} = m_0 \left(1 - e^{-\frac{\Delta V}{Isp * g_0}}\right) \tag{3.66}$$

For the case of a variable specific impulse, then the fuel mass must be obtained by numerical integration of the rate of fuel usage, which depends upon the instantaneous specific impulse. The total mass of the propulsion system is:

$$m_{sys} = m_{prop} + m_{\tan k} \tag{3.67}$$

and using the previous relationships yields

$$m_{sys} = k_{p0} + k_{p1} * \frac{Thrust_1 * Isp_1}{2\eta} + k_{T1} m_0 \left(1 - e^{-\frac{\Delta V}{Isp * g_0}}\right) \tag{3.68}$$

The total propulsion-related mass is the sum of the masses of the propulsion system and the fuel for the transfer, and so:

$$m_{transprop} = k_{p0} + k_{p1} * \frac{Thrust_1 * Isp_1}{2\eta} + (1 + k_{T1}) m_0 \left(1 - e^{-\frac{\Delta V}{Isp * g_0}}\right) \tag{3.69}$$

Two key parameters dominate the total propulsion related mass in this system type: specific impulse and the thrust.

However, the ΔV for the transfer must be considered further (and is described in greater detail in subsequent sections). At this point it is sufficient to state that the ΔV is generally made up of a term needed to accomplish the 'impulsive' transfer, assuming a series of point impulses (implying infinite thrust) and a loss term related to the fact the thrust is applied over a region of space and so is not all applied at the optimal location. Therefore:

$$\Delta V = \Delta V_{ideal} + \Delta V_{loss} \tag{3.70}$$

This second term is principally related to the thrust that is available. Lower thrust generally implies a greater loss. The exact relationship depends on the nature of the transfer. It is minimised by the application of trajectory optimisation. The loss term is generally weakly dependent on specific impulse, because fuel mass usage determines the remaining mass and thus the instantaneous acceleration that is achieved for a given thrust. This type of dependence is greatest when the fuel mass fraction is high. A further factor effecting the loss is the power distribution term, k_T, described previously, as this determines the ratios of thrust and specific impulse change with distance from the Sun. The previous equation 3.69, describing the transfer propulsion mass, is multiply dependent on both specific impulse and thrust, and also on k_T.

It is therefore possible to define an objective of the form of equation 3.69 and extend the optimisable control parameter set to include thrust and specific impulse. If the following form is used it is possible to demonstrate how such an objective can be linked with the optimisation methods described previously:

$$m_{transprop} = k_{p0} + k_{p1} * \frac{Thrust_1 * Isp_1}{2\eta} + (1 + k_{T1}) m_{fuel} \tag{3.71}$$

The key issue is to calculate the gradient of the objective with respect to the new control set. The gradients of all constraints must also be evaluated. The objective has an explicit dependence on thrust and specific impulse, and also a dependence arising from the fuel fraction:

$$\frac{\partial m_{transprop}}{\partial Thrust_1} = k_{p0} + k_{p1} * \frac{Isp_1}{2\eta} + (1 + k_{T1}) \frac{\partial m_{fuel}}{\partial Thrust_1} \tag{3.72}$$

with a similar expression regarding the specific impulse parameter and radial power term. Therefore the terms $\frac{\partial X_i}{\partial Thrust_1}, \frac{\partial X_i}{\partial Isp_1}, \frac{\partial X_i}{\partial k_T}$ must be evaluated to determine the components of the objective $\frac{\partial m_{fuel}}{\partial Thrust_1}, \frac{\partial m_{fuel}}{\partial Isp_1}, \frac{\partial m_{fuel}}{\partial k_T}$. The fuel mass is simply (initial mass – final mass) – the final mass being a component of the state vector. The calculation of this term is achieved by the methods described in the previous sections.

Design optimisation: nuclear electric propulsion system optimisation

The optimisation problem previously discussed considered the power being generated by a solar-power generator such as the solar array of a spacecraft. This introduced an optimisable radial distribution term in equation 3.60. However, in the case of power generation by a nuclear-based system, the power remains constant. (In practice, some variations may result from reactor or RTG performance variations, but the power variation is generally less pronounced than with a solar power generator.)

The previous methodology for using system optimisation parameters may be equally applied to this constant power case, with the exception that k_T is no longer a relevant parameter.

Performance optimisation

It has been seen that for a given system design, power is limited by the performance of the power-generating system (that is, solar arrays for solar electric propulsion). Furthermore, there is a relationship between power, thrust and specific impulse that may be exploited to optimise the local performance of the system. For a given available power it is in principle possible to locally vary the thrust and specific impulse to satisfy equation 3.62. Such variability is not always possible in a 'real world' system, but some variation is possible and so will be explored here.

The principle of local thrust optimisation will now be considered. If a transfer is implemented by a series of manoeuvres, then each manoeuvre could be optimised with respect to the thrust used for that manoeuvre. The objective would be to minimise the fuel mass used for the manoeuvre. It is therefore a local optimisation, not considering the full transfer. It will be assumed in the following discussion that the power available over the manoeuvre remains constant.

A local manoeuvre – such as providing a given change in apocentre, for example – is characterised by an ideal ΔV. There is also a loss that is associated

with a non-ideal manoeuvre (i.e., finite thrust). The fuel fraction for such a manoeuvre is given by equation 3.66.

This may be rewritten, using equations 3.60 and 3.70, as:

$$m_{fuel} = m_0 \left(1 - e^{-\frac{(\Delta V_{ideal} + \Delta V_{loss})\, Thrust}{2\eta P}} \right) \tag{3.73}$$

where m_{fuel} here is the fuel mass for the local manoeuvre (part of the total transfer). The gradient of this local fuel usage, with respect to thrust, can be evaluated as follows:

$$\frac{\partial m_{fuel}}{\partial Thrust} = \left(\frac{\Delta V_{ideal} + \Delta V_{loss})}{2\eta P} + \frac{\partial \Delta V_{loss}}{\partial Thrust} \frac{Thrust}{2\eta P} \right) m_0 e^{-\frac{(\Delta V_{ideal} + \Delta V_{loss})\, Thrust}{2nP}} \tag{3.74}$$

It is, in principle, possible to minimise this local fuel fraction by requiring this expression to be equal to zero and solving for the *Thrust* value. Having determined the thrust in this way, the specific impulse to be used for the manoeuvre is obtained from equation 3.60.

Alternatively, if this is one element of a series of fuel fractions (manoeuvres) making up a whole transfer, the local fraction need not be minimised, but the gradient is required to solve the full optimisation problem, which may be to minimise the total fuel usage.

The ΔV loss will vary with the type of manoeuvre being performed, and will be strongly influenced by the thrust. An example can be considered to demonstrate the point. The following is an evaluation of the raising of the apogee of an elliptical orbit which may perform a part of an escape orbit targeting sequence. This case has a perigee at 200 km altitude and apogee at 36,000 km. The objective is to raise the apogee by 100 km, using a low-thrust manoeuvre. The actual ΔV – which includes the ideal and loss terms – is evaluated.

Figure 3.4.1 shows the significance of the length of the thrust arc as thrust drops from 300 mN to 200 mN. The manoeuvre now takes place much closer to apocentre, where it is far less efficient at achieving its purpose.

Figure 3.4.2 shows the percentage loss with varying thrust/mass.

It is then possible to evaluate the optimum thrust for this manoeuvre.

For this apogee-raising example, the fuel-fraction dependence on thrust, for a fixed available power, is shown in Figure 3.4.3.

Where the range of thrust and/or specific impulse variation does not allow the minimum case to be achieved, the constrained minimum can be taken; that is, the lowest allowable fuel fraction case.

Although this example relates to an example in Earth-bound orbit, the same principle applies to manoeuvres applied to interplanetary orbits. In these cases, the power availability may vary over the manoeuvre, due to the change in distance from the Sun.

It is now possible to consider the full potential of this method. This is an extension of the principle described in the previous discussion. Having illustrated the principle of finding locally optimal thrust with a fixed power availability (or more

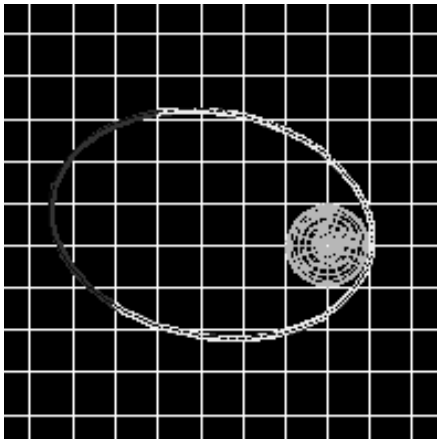

200 mN/tonne

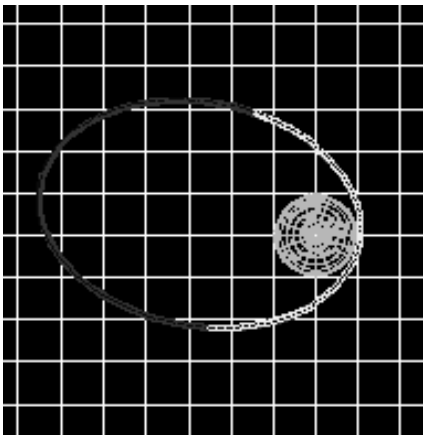

300 mN/tonne

Figure 3.4.1. Thrust arc dependence on thrust/mass for an apogee raising manoeuvre of 100 km.

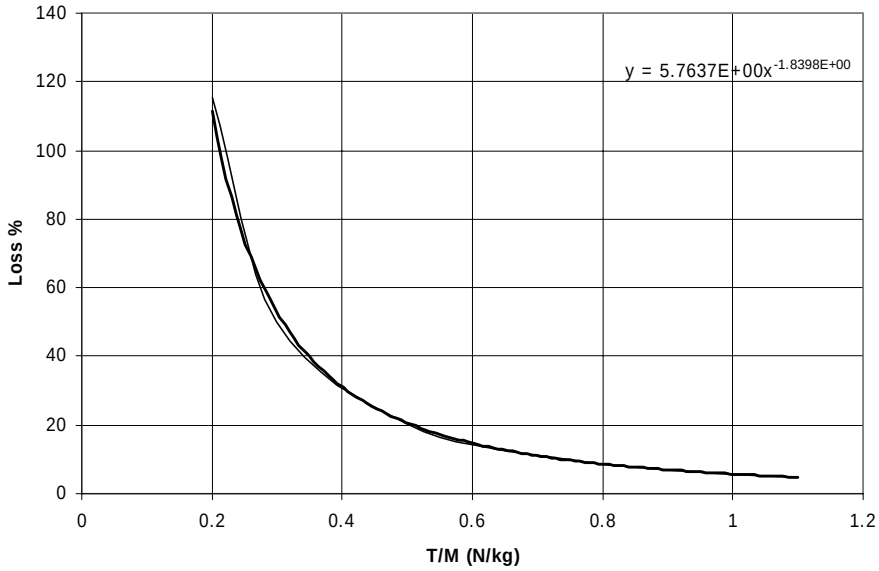

Figure 3.4.2. The relationship between ΔV loss and thrust for a low-thrust apocentre raise manoeuvre of 100 km.

literally, a given solar array size for a solar electric propulsion system), it is possible to consider how to achieve an optimal end-to-end transfer. This is achieved, in the context of the direct parameterisation methods previously discussed, by describing the thrust as a time-dependent function with optimisable parameters, in a similar manner to the optimisable steering angle parameterisation. Having obtained the

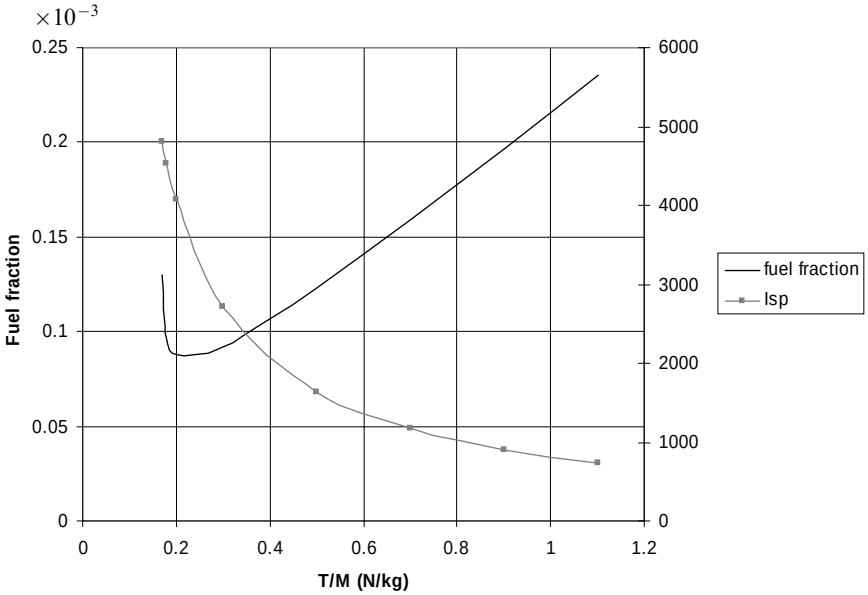

Figure 3.4.3. The relationship between fuel mass, specific impulse and thrust for a low-thrust apocentre raise manoeuvre of 100 km with an initial mass of 1,000 kg. In this example it is assumed that 5 kW of power per tonne of spacecraft is available and an efficiency of 80% is achieved. The variation in specific impulse with thrust is also shown. In practice, such a wide range of thrust and specific impulse variation would not be possible with a single thruster.

thrust from the parametric expression (which may be limited between specified bounds), the specific impulse to be used for the manoeuvre is obtained from equation 3.60. In this case, the system design is not considered within the optimisation problem, and so the objective would typically be the minimisation of the final total fuel mass. This can be achieved by non-linear programming with the methods described previously; and with an additional set of optimisable parameters (and constraints limiting thrust).

Combining system and performance optimisation

In the previous discussion, system and propulsion performance optimisation are considered separately; but it is possible to combine these into a single problem. This is achieved by using the thrust parameterisation method described in the previous case, in conjunction with a new system optimisation parameter: the power available (nominally defined at a reference radius of 1 AU for SEP or a fixed constant for NEP).

The objective is again given by:

$$m_{transprop} = k_{p0} + k_{p1} * P_1 + (1 + k_{T1})\, m_{fuel}$$

The optimisable extended parameter set now contains, in addition to the thrust parameterisation, the nominal power term, P_1.

The instantaneous specific impulse is then derived from the instantaneous thrust, which in turn is derived from the thrust profile and the optimised nominal power.

4

Special techniques

The design of an interplanetary mission can utilise a number of special techniques that are aimed at improving the efficiency of the transfer. These methods include the exploitation of multiple gravity fields, and the application of low-thrust propulsion. Such high specific impulse systems can be particularly effective in interplanetary missions.

This chapter describes a variety of these techniques, giving details both of the nature of the method and also descriptions of certain mission types that may benefit from such techniques.

4.1 MOTION IN MULTI-BODY GRAVITY FIELDS

One of the key differences between interplanetary missions and Earth-orbiting missions is the significant influence of multi-body gravity fields. Analytical results for this problem are limited, but a number of important derivations and conclusions may be drawn. These concern establishing the dominant gravity field and methods of approximating the motion as the spacecraft passes through regions where the dominant field changes. A further very significant aspect is the consideration of motion in regions where two gravity fields are in near equilibrium.

4.1.1 The multi-body problem

The multi-body problem discussed here is the description of motion of a number of objects where each exerts a gravitational force on all of the others. A number of conserved properties may be derived for such a system. Detailed descriptions of this problem may be found through the references for this chapter.

Firstly, defining $\underline{R_{relij}} = \underline{R_i} - \underline{R_j}$ as the relative position vector between two such bodies, the acceleration of any body, labelled i, is given, from Newtonian gravity, by:

$$m_i \underline{\ddot{R}_i} = -\sum_j G m_j m_i \frac{\underline{R_{relij}}}{R_{relij}^3} \qquad i \neq j \tag{4.1.1}$$

considering that $\underline{R_{relij}} = \underline{R_i} - \underline{R_j} = -\underline{R_{relji}}$.

Then sum of all rates of change of momentum is zero:

$$\sum_i m_i \underline{\ddot{R}_i} = 0 \tag{4.1.2}$$

This equation may be integrated twice with respect to time, to obtain two vector constants:

$$\sum_i m_i \underline{\dot{R}_i} = \underline{C_1} \tag{4.1.3}$$

and

$$\sum_i m_i \underline{R_i} = \underline{C_1} t + \underline{C_2} \tag{4.1.4}$$

These six constants of motion express the conservation of linear momentum of the total system, and that the centre of gravity of the system moves at a constant velocity, because:

$$\sum_i m_i \underline{R_i} = M \underline{R} \tag{4.1.5}$$

where $\sum_i m_i = M$ is the total mass of the system and $\underline{R}$ is the position of the centre of gravity.

Further constants of the motion may be identified as follows. If the vector products of position and acceleration are summed (after substituting the relationship equation 4.1.1), they are found to equal zero:

$$\sum_i m_i \underline{R_i} \wedge \underline{\ddot{R}_i} = 0 \tag{4.1.6}$$

This may be integrated again with respect to time to obtain a further vector constant of motion:

$$\sum_i m_i \underline{R_i} \wedge \underline{\dot{R}_i} = \underline{C_3} \tag{4.1.7}$$

This relationship expresses the conservation of angular momentum for the system. The vector, C_3, defines a plane, known as the Laplace invariable plane of the system. For the Solar System, this plane lies close to the ecliptic. Its slight inclination is strongly dependent on Jupiter's orbital inclination about the Sun.

One further constant of motion may be derived for this system: the total energy, obtained as follows. The scalar products of velocity and acceleration are now summed. Using equation 4.1.1, the following relationship is obtained:

$$\sum_i m_i \underline{\dot{R}_i} \cdot \underline{\ddot{R}_i} - \sum_i \sum_j G m_j m_i \underline{\dot{R}_i} \cdot \frac{\underline{R_j} - \underline{R_i}}{R_{relij}^3} = 0 \qquad i \neq j \tag{4.1.8}$$

The equation may be integrated with respect to time to yield a constant. This is found to be the total energy of the system; namely, the total kinetic energy and the total potential energy.

$$\frac{1}{2}\sum_i m_i V_i^2 - \frac{1}{2}\sum_i \sum_j \frac{G m_j m_i}{R_{relij}} = Energy \qquad i \neq j \tag{4.1.9}$$

where $V_i = |\dot{\underline{R}}_i|$.

Ten constants of motion are therefore available to define the macro-system behaviour. However, no more quantities are conserved in this general case. In order to find any more conserved values, special cases must be examined with particular assumptions regarding the nature of the motion. Some of these cases will be examined in subsequent sections.

4.1.2 Identifying the dominant gravity field

The masses of the planets in the Solar System are significantly lower than the mass of the Sun. However, when relatively close to a planet, its gravity field may far exceed that of the Sun in magnitude. It is beneficial to be able to categorise motion in such a way that the dominant gravity effect is identified. This ultimately allows approximations to the motion to be developed.

This zone could be identified in different ways. Each of these will be discussed.

Gravitational equality

The simplest way would be to identify a region around a planet where its gravity field is greater than that of the Sun. It is the 'sphere' of gravitational equality.

The zone is defined as the locus of points where the gravity fields of the central body and the orbiting major body are of equal magnitude. Such a zone is not a sphere centred on the major body, but is slightly distorted due to the fall-off in the gravity field of the central body with increasing radius. The principle is shown in Figure 4.1.1.

The maximum and minimum radii of the 'sphere' of influence are therefore calculated by:

$$\frac{\mu_{central}}{(r_{major} - r_{\min})^2} = \frac{\mu_{major}}{r_{\min}^2} \qquad \text{and} \qquad \frac{\mu_{central}}{(r_{major} + r_{\max})^2} = \frac{\mu_{major}}{r_{\max}^2}$$

where $r_{\min}$ and $r_{\max}$ are the radii with respect to the major body of the 'sphere' of influence. r_{major} is the orbital radius of the major body.

However, such an idea does not describe the true effect on the motion, in terms of the perturbation by the second gravity field.

The sphere of influence

A better idea arises from consideration of the perturbing acceleration due to the second gravity field, when motion about the first body is considered. This is the formulation originally developed by Laplace and is the conventionally adopted

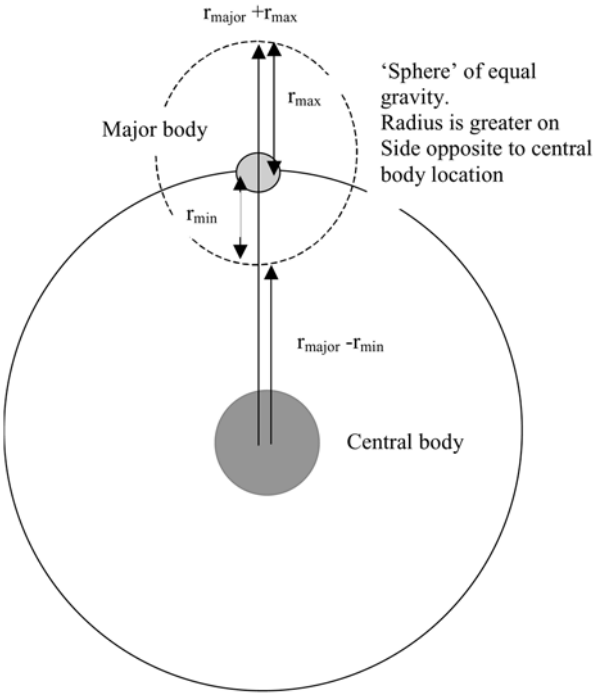

Figure 4.1.1. Illustration of gravitational equality 'sphere'.

definition. The objective is to express the ratio of the perturbing acceleration (from the second body) to the main acceleration (from the first body). This may be obtained for both the Sun's perturbation on motion about the planet and the planet's perturbation on motion about the Sun. A surface may then be found where these ratios are equal. An elaboration of this subject may be found in Cornelisse, Schoyer and Wakker (see references), and is summarised here.

Firstly, the perturbing effect of the Sun's gravity on motion about a planet must be calculated. In the following analysis, r_{ps} is the vector from planet to spacecraft, r_{cs} is the vector from central body to spacecraft, r_{pc} is the vector from planet to central body, μ_c is the gravitational constant of the central body, and μ_p is the gravitational constant of the planet (see Figure 4.1.2).

The acceleration of the spacecraft relative to the planet is given by the gravitational acceleration minus the acceleration of the planet, i.e.,:

$$\underline{\ddot{r}_{ps}} = \underline{g} - \underline{\ddot{r}_p} \qquad \text{and} \qquad \underline{\ddot{r}_p} = \frac{\mu_c \underline{r_{pc}}}{r_{pc}^3}$$

Similarly, the acceleration of the spacecraft relative to the central body is given by the gravitational acceleration minus the acceleration of the central body, i.e.,:

$$\underline{\ddot{r}_{cs}} = \underline{g} - \underline{\ddot{r}_C} \qquad \text{and} \qquad \underline{\ddot{r}_C} = -\frac{\mu_P \underline{r_{pc}}}{r_{pc}^3}$$

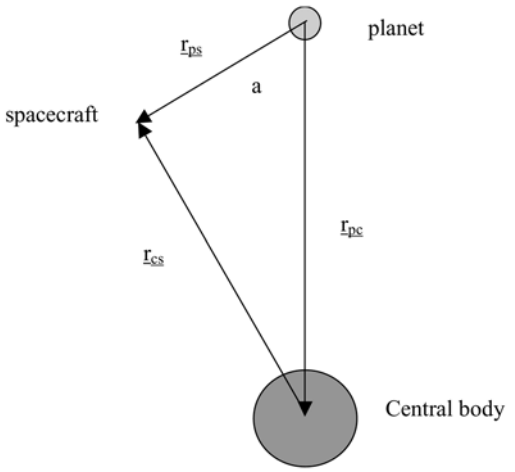

Figure 4.1.2. Motion in the presence of two gravity fields.

The gravitational acceleration of the spacecraft with respect to the planet, p, is given by $\ddot{\underline{r}}_{ps} = -\dfrac{\mu_p \underline{r}_{ps}}{r_{ps}^3} - \dfrac{\mu_c \underline{r}_{cs}}{r_{cs}^3} - \dfrac{\mu_c \underline{r}_{pc}}{r_{pc}^3}$ in the presence of a second gravity field from the central body, c. The gravitational acceleration of the spacecraft with respect to the central body, c, is given by $\ddot{\underline{r}}_{cs} = -\dfrac{\mu_c \underline{r}_{cs}}{r_{cs}^3} - \dfrac{\mu_p \underline{r}_{ps}}{r_{ps}^3} + \dfrac{\mu_p \underline{r}_{pc}}{r_{pc}^3}$ in the presence of a second gravity field from the planet, p.

The magnitude of the disturbing acceleration for motion with respect to the planet is given by:

$$\ddot{r}_{psD} = \sqrt{\left(\frac{\mu_c \underline{r}_{cs}}{r_{cs}^3} + \frac{\mu_c \underline{r}_{pc}}{r_{pc}^3}\right) \cdot \left(\frac{\mu_c \underline{r}_{cs}}{r_{cs}^3} + \frac{\mu_c \underline{r}_{pc}}{r_{pc}^3}\right)} \tag{4.1.10}$$

where $\ddot{r}_{psD}$ is the disturbing acceleration of motion with respect to the planet caused by the central body gravity.

Series expansions may be obtained, and neglecting terms of order greater than $\left(\dfrac{r_{ps}}{r_{pc}}\right)^2$, the following result may be found:

$$\ddot{r}_{psD} = \mu_c \frac{r_{ps}}{r_{pc}^3} (1 + 3\cos^2 a)^{0.5} \tag{4.1.11}$$

The angle 'a' is defined in Figure 4.1.2.

This may be compared with the magnitude of the nominal acceleration with respect to the planet:

$$\ddot{r}_{psN} = \frac{\mu_p}{r_{ps}^2} \tag{4.1.12}$$

where $\ddot{r}_{psN}$ is the nominal gravitational acceleration of motion about the planet. The

ratio of disturbing to nominal accelerations is then:

$$\frac{\ddot{r}_{psD}}{\ddot{r}_{psN}} = \frac{\mu_c}{\mu_p}\frac{r_{ps}^3}{r_{pc}^3}(1 + 3\cos^2 a)^{0.5} \tag{4.1.13}$$

The magnitude of the disturbing acceleration for motion with respect to the Sun is given by:

$$\ddot{r}_{csD} = \sqrt{\left(-\frac{\mu_p \underline{r_{ps}}}{r_{ps}^3} + \frac{\mu_p \underline{r_{pc}}}{r_{pc}^3}\right) \cdot \left(-\frac{\mu_p \underline{r_{ps}}}{r_{ps}^3} + \frac{\mu_p \underline{r_{pc}}}{r_{pc}^3}\right)}$$

This becomes:

$$\ddot{r}_{csD} = \mu_p\left(\frac{1}{r_{ps}^2}\right) \tag{4.1.14}$$

This may now be compared with the magnitude of the nominal acceleration with respect to the Sun (neglecting again small terms):

$$\ddot{r}_{csN} = \frac{\mu_c}{r_{cs}^2} \tag{4.1.15}$$

Assuming that the difference between r_{cs} and r_{pc} is much less than either distance, then the ratio of disturbing to nominal accelerations is:

$$\frac{\ddot{r}_{csD}}{\ddot{r}_{csN}} = \frac{\mu_p}{\mu_c}\frac{r_{cs}^2}{r_{ps}^2} \tag{4.1.16}$$

On equating these ratios (equations 4.1.16 and 4.1.13) to establish a surface where the perturbation proportions are of equal magnitude, the relationship defining this distance from the planet is obtained:

$$r_{ps} = r_{pc}\left(\frac{\mu_p^2}{\mu_c^2}\frac{1}{(1 + 3\cos^2 a)^{0.5}}\right)^{1/5} \tag{4.1.17}$$

There is a small angular dependence, given by the angle a. Even when a is zero, this term (raised to the power of 1/10) lies close to 1. Therefore, the surface of 'equal disturbance ratios' is close to a sphere.

Hill's sphere

Hill obtains a further definition of a sphere of influence equivalent to the Roche limit. This value may be derived as follows.

Firstly, consider the acceleration of the satellite with respect to the planet. There are two components: the Sun's differential acceleration with respect to the planet, and the gravitational force of the planet itself (neglecting the effect of the planet's gravity on the Sun). This net acceleration was calculated in the previous section by:

$$\ddot{\underline{r}}_{ps} = -\frac{\mu_p \underline{r_{ps}}}{r_{ps}^3} - \frac{\mu_c \underline{r_{cs}}}{r_{cs}^3} - \frac{\mu_c \underline{r_{pc}}}{r_{pc}^3}$$

A point may be found between the Sun and planet where this acceleration is zero;

differential acceleration is in equilibrium with the gravitational force from the planet. The above equation can be solved to find r_{ps} that meets this criterion, along the Sun–planet axis.

Roche devised a criterion for the break-up of a fluid natural body orbiting the Sun (or more particularly, a moon orbiting a planet) whereby the perturbing acceleration from the Sun exceeds the attractive force from the rest of the planet. This limit is reached (in terms of distance from the centre of the planet) when this net acceleration towards the planet, at its surface, reaches zero. It presupposes that there is no internal rigidity to the orbiting body.

The net acceleration along the planet–Sun axis, at the hypothetical surface of the planet, may be approximated by use of the Sun's gravity gradient at the planet, so that:

$$\ddot{r}_{ps} = -\frac{\mu_p}{r_{ps}^2} + \frac{2\mu_c r_{ps}}{r_{pc}^3} \tag{4.1.18}$$

Setting this to zero gives the condition that:

$$\frac{2r_{ps}^3}{r_{pc}^3} = \frac{\mu_p}{\mu_c} \tag{4.1.19}$$

This criterion can be refined by assuming that the planet rotates at a rate that is locked with the rate of rotation of the planet about the Sun (it always presents the same face to the Sun). This effect is common in orbiting natural moons.

The criterion for stability is now extended to take into account the required centripetal force on the surface of the planet.

$$\frac{\mu_p}{r_{ps}^2} - \frac{2\mu_c r_{ps}}{r_{pc}^3} \geq r_{ps}\omega^2 \qquad \text{where} \qquad \omega^2 = \frac{\mu_c}{r_{pc}^3} \tag{4.1.20}$$

for the planet maintaining a circular orbit about the Sun. Therefore:

$$\frac{\mu_p}{r_{ps}^2} - \frac{3\mu_c r_{ps}}{r_{pc}^3} = 0 \tag{4.1.21}$$

This criterion is comparable to that for the condition that a spacecraft maintains a circular orbit about the Sun under the combined gravity fields of the Sun and planet. This effectively defines two points along the Sun–planet axis, that are the first two colinear libration points. The idea of libration points is discussed more fully in subsequent sections.

This distance is used to define the radius of Hill's sphere, which is an alternative type of the sphere of influence of a planet.

4.1.3 Motion in the three-body problem

The three-body problem is often the name given to the problem where a spacecraft passes through a combined gravity field. The first body is the central body, the second is the orbiting, major body, and the third is the spacecraft itself, the mass of which is considered to be negligible in comparison to the other two.

Table 4.1.1. The radius of various spheres of influence, including Hill's sphere, calculated by gravity gradient approximation.

	Gravitational equilibrium	Conventional sphere of influence	Hill's sphere radius
Mercury	23697	112837	221387
Venus	169035	616277	1011199
Earth	258814	924648	1496629
Mars	129387	577131	1083965
Jupiter	23333186	48216966	53150917
Saturn	23749258	54615354	65244392
Uranus	18849552	51747112	70038854
Neptune	32058928	86634373	115989405
Pluto	3391752	15079253	28259593

No known analytical solutions exist to describe the subsequent motion (unlike the case of the two body problem), although generalisations that describe the overall properties of the motion in certain circumstances have been obtained. Also, approximation methods exist that enable certain classes of motion to be described by analytical expressions. The precise motion can be obtained only by numerical integration of the spacecraft state vector derivatives, including both gravity vectors. More detailed descriptions of this problem may be found in the references for this chapter – notably Roy and Cornelisse, Schoyer and Wakker (this later derivation is outlined below).

The circular restricted three-body problem

Firstly, a reference frame is considered, the origin of which lies at the centre of mass of the set of two major bodies. Position relative to this origin is denoted $\underline{r}$. The acceleration of the spacecraft is given by:

$$\frac{d^2\underline{r}}{dt^2} = -\frac{\mu_1 \underline{r}_1}{r_1^3} - \frac{\mu_2 \underline{r}_2}{r_2^3} \tag{4.1.22}$$

where $\underline{r}_1$ and $\underline{r}_2$ are the radial distances from bodies 1 and 2 respectively, and μ_1 and μ_2 are the gravitational parameters of those bodies.

The general three-body problem describes the motion of a spacecraft under the influence of two major gravitational sources. In an attempt to characterise the motion, certain simplifying assumptions can be made. If the two gravity sources are assumed to move in circular orbits about a common barycentre, then the possible motions of a satellite can be analysed. This is known as the circular, restricted three-body problem. In such a situation, the two bodies move about a common barycentre.

A rotating reference frame may be used where x lies in the direction of the barycentre to body 2, y is perpendicular in the orbit plane of the two major bodies, and z completes the right-handed axis set and is therefore perpendicular to the motion plane.

The acceleration of the spacecraft with respect to such a rotating frame is obtained from the classical relationship:

$$\left(\frac{d^2\underline{r}}{dt^2}\right)_R = -\frac{\mu_1 \underline{r}_1}{r_1^3} - \frac{\mu_2 \underline{r}_2}{r_2^3} - \underline{\omega} \wedge (\underline{\omega} \wedge \underline{r}) - 2\underline{\omega} \wedge \left(\frac{d\underline{r}}{dt}\right)_R \tag{4.1.23}$$

where subscript R denotes a time derivative with respect to the rotating frame.

A potential may be defined as:

$$U = \left(-\frac{\mu_1}{r_1} - \frac{\mu_2}{r_2}\right) - \frac{\omega^2}{2}(r_x^2 + r_y^2) \tag{4.1.24}$$

where r_x, r_y and r_z are the components of position with respect to the barycentre, or centre of mass of the two major bodies. The angular velocity is given by $\underline{\omega} = \omega \hat{r}_Z$.

Then, equation 4.1.23 can be expressed in terms of the grad function of this potential:

$$\left(\frac{d^2\underline{r}}{dt^2}\right)_R = -\nabla U - 2\underline{\omega} \wedge \left(\frac{d\underline{r}}{dt}\right)_R \tag{4.1.25}$$

If this equation is multiplied by the rotating frame velocity (as a scalar product), then:

$$\left(\frac{d\underline{r}}{dt}\right)_R \cdot \left(\frac{d^2\underline{r}}{dt^2}\right)_R = -\left(\frac{d\underline{r}}{dt}\right)_R \cdot \nabla U - \left(\frac{d\underline{r}}{dt}\right)_R \cdot \left(2\underline{\omega} \wedge \left(\frac{d\underline{r}}{dt}\right)_R\right) \tag{4.1.26}$$

The last term on the right-hand side of the equality is identically zero, and the first term is the time derivative of the potential, U:

$$\frac{dU}{dt} = \left(\frac{d\underline{r}}{dt}\right)_R \cdot \nabla U$$

and therefore integration of equation 4.1.26 yields the following expression:

$$V^2 + 2U = -C \tag{4.1.27}$$

where C is a constant of the motion known as the Jacobi constant, and V is the speed with respect to the rotating frame, in this case defined by the motion of the planet about the central body.

In this context:

$$V^2 = \left(\frac{d\underline{r}}{dt}\right)_R \cdot \left(\frac{d\underline{r}}{dt}\right)_R$$

This expression may be used to derive boundaries of the possible motion for a given value of the constant, C, but is not effective in predicting the detailed motion of the spacecraft in such an environment.

Expansion of the expression for Jacobi's constant

The speed in the rotating frame may be converted to speed in an inertial frame.

Expanding the Jacobi integral and introducing a new notation as follows gives:

$$V^2 + 2U = -C = V^2 - 2\left(\frac{\mu_p}{r_p} + \frac{\mu_c}{r_c}\right) - (\underline{\omega} \wedge \underline{r}) \cdot (\underline{\omega} \wedge \underline{r}) \tag{4.1.28}$$

where, r_p is the distance of the spacecraft from the planet (or body), p, orbiting the central body c, r_c is the distance of the spacecraft from the central body, and r is the distance from the system barycentre of bodies p and c.

The various expressions for the velocity of the spacecraft are:

$$\underline{V_{IC}} = \underline{V_R} + \underline{\omega} \wedge \underline{r_c} \tag{4.1.29}$$

$$\underline{V_{IP}} = \underline{V_R} + \underline{\omega} \wedge \underline{r_P} \tag{4.1.30}$$

$$\underline{V_{IC}} = \underline{V_{IP}} + \underline{V_{Planet}} \tag{4.1.31}$$

$$\underline{r_P} = \underline{r_C} - \underline{r_{Planet}} \tag{4.1.32}$$

The following formal notations are used:

Subscript p denotes a quantity measured with respect to the planet.
Subscript c denotes a quantity measured with respect to the central bodies state.
Subscript I denotes a quantity expressed with respect to an inertial frame of reference.
Subscript R denotes a quantity expressed with respect to a rotating state of reference (with the planets angular velocity about the central body).

Also, r_{planet} and V_{planet} are the planet's position and velocity with respect to the central body. This notation is abbreviated, as fully it would be $V_{I,C,planet}$.

Also, velocities with respect to the inertial frame may also be abbreviated in some cases: from V_{IP} to V_P and also r_{IP} to r_P, and from V_{IC} to V_C and also r_{IC} to r_C.

Because the planet is in circular motion, then:

$$\underline{V_{planet}} = \underline{\omega} \wedge \underline{r_{planet}} \tag{4.1.33}$$

The Jacobi integral may now be expressed in terms of velocity with respect to the central body, and so becomes:

$$-C = (\underline{V_{IC}} - \underline{\omega} \wedge \underline{r_c}) \cdot (\underline{V_{IC}} - \underline{\omega} \wedge \underline{r_c}) - 2\left(\frac{\mu_p}{r_p} + \frac{\mu_c}{r_c}\right) - (\underline{\omega} \wedge \underline{r}) \cdot (\underline{\omega} \wedge \underline{r}) \tag{4.1.34}$$

If the central body is much more massive than the planet, the barycentre can be assumed to lie very close to the centre of the central body, and so r becomes r_C.

$$-C = V_{IC}^2 - 2(\underline{V_{IC}} \cdot \underline{\omega} \wedge \underline{r_c}) - 2\left(\frac{\mu_p}{r_p} + \frac{\mu_c}{r_c}\right) \tag{4.1.35}$$

The Jacobi integral may also be expressed in terms of velocity with respect to the planet body, and so becomes:

$$-C = (\underline{V_{IP}} - \underline{\omega} \wedge \underline{r_p}) \cdot (\underline{V_{IP}} - \underline{\omega} \wedge \underline{r_p}) - 2\left(\frac{\mu_p}{r_p} + \frac{\mu_c}{r_c}\right) - (\underline{\omega} \wedge \underline{r}) \cdot (\underline{\omega} \wedge \underline{r}) \tag{4.1.36}$$

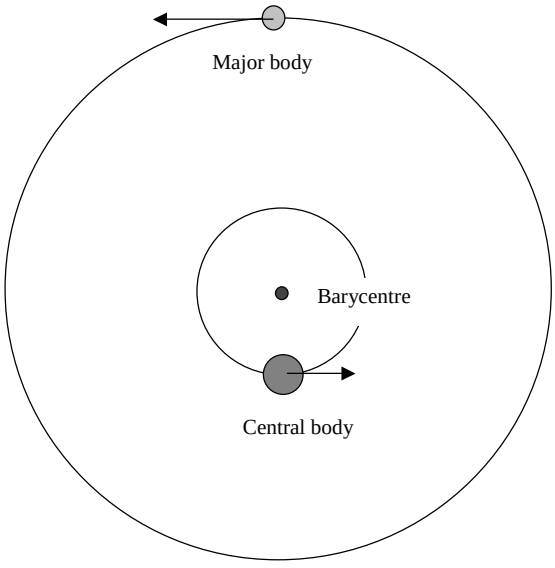

Figure 4.1.3. Orbital geometry in the circular, restricted three-body problem.

And so, again assuming that r equates to r_c:

$$-C = V_{IP}^2 - 2(\underline{V_{IP}} \cdot \underline{\omega} \wedge \underline{r_p}) + (\underline{\omega} \wedge \underline{r_p}) \cdot (\underline{\omega} \wedge \underline{r_p}) - 2\left(\frac{\mu_p}{r_p} + \frac{\mu_c}{r_c}\right) - (\underline{\omega} \wedge \underline{r_c}) \cdot (\underline{\omega} \wedge \underline{r_c}) \tag{4.1.37}$$

If the motion is close to the ecliptic, then this expression becomes:

$$-C = V_{IP}^2 - 2(\underline{V_{IP}} \cdot \underline{\omega} \wedge \underline{r_p}) + \omega^2 r_p^2 - 2\left(\frac{\mu_p}{r_p} + \frac{\mu_c}{r_c}\right) - \omega^2 r_C^2 \tag{4.1.38}$$

4.2 ESCAPE FROM A PLANET

The previous sections described the principles of the many-body problem and motion in the presence of multiple gravity fields. Particular attention was paid to results that may be obtained with a set of approximations known as the circular, restricted three-body problem. Also, when departing from a planet, approximations to the motion in the presence of multi-body gravity fields have also been discussed in the context of interplanetary transfers with an escape orbit from a planet into a heliocentric trajectory (Chapter 1).

In this section, a series of more detailed analyses are performed that allow comparison of the approximated motion with the true motion. This allows an assessment of the effectiveness of the approximation techniques and any implications arising from them. It also provides an insight into the nature of the motion when a spacecraft leaves or approaches a planet from the heliocentric domain.

4.2.1 Analysis of escape

In Chapter 1, the principle of escape orbits was discussed. In order to reach a given heliocentric orbit, the required speed relative to the planet must first be achieved. This translates into the departing excess hyperbolic velocity vector required for a planetary escape orbit. In this section the details of the motion of the spacecraft leaving the planet with such an escape orbit will be evaluated. This will be compared with the motion resulting from the simple assumption of a velocity vector addition occurring at the planet's location. In this latter case, the gravitational effect of the planet is not included in the details of the motion. Firstly, the problem is analysed using the three-body formulation described in the previous section.

Analysis using the three-body problem basis

First, a more detailed analysis of the predicted properties of the motion can be made. In section 4.1 the Jacobi constant is identified as a constant of motion, for the case of the circular, restricted three-body problem.

Jacobi's integral is given by

$$V^2 + 2U = -C$$

where C is a constant of the motion known as the Jacobi constant, and V is the speed with respect to the rotating frame, which is defined by the motion of the planet about the central body. U is a potential combining gravitational potential and a rotational term, and $\underline{\omega}$ is the angular velocity of the rotating frame.

In section 4.3 Tisserand's criterion is derived by considering the conservation of this integral to compare heliocentric orbits before and after a gravity-assist manoeuvre. The integral may also be used to compare motion close to a planet and at large distance.

If the expression for motion with respect to the planet is examined, obtained from section 4.1.3, then it may be expressed in terms of the osculating excess hyperbolic speed:

$$-C = V_\infty^2 - 2(\underline{V_{IP}} \cdot \underline{\omega} \wedge \underline{r_p}) + (\underline{\omega} \wedge \underline{r_p}) \cdot (\underline{\omega} \wedge \underline{r_p}) - 2\left(\frac{\mu_c}{r_c}\right) - (\underline{\omega} \wedge \underline{r_c}) \cdot (\underline{\omega} \wedge \underline{r_c}) \tag{4.2.1}$$

where $V_\infty^2 = V_p^2 - 2\frac{\mu_p}{r_p}$

The first objective is to obtain a simplified expression that applies when the spacecraft is close to the planet, in terms that apply at the pericentre. This expression contains components of very different magnitudes, and so some further expansion is required.

The term $(\underline{\omega} \wedge \underline{r_c}) \cdot (\underline{\omega} \wedge \underline{r_c})$ can be expanded to yield $\omega^2 r_c^2 - (\underline{\omega} \cdot \underline{r_c})^2$. Then, because the angular velocity is assumed to be perpendicular to the planet's orbit, this becomes $\omega^2 r_c^2 - (\underline{\omega} \cdot \underline{r_p})^2$. Also, $(\underline{\omega} \wedge \underline{r_p}) \cdot (\underline{\omega} \wedge \underline{r_p})$ becomes $\omega^2 r_p^2 - (\underline{\omega} \cdot \underline{r_p})^2$.

A series expansion for $1/r_c$ may be obtained as follows:

$$\frac{1}{r_c} = \frac{1}{\sqrt{(\underline{r_{planet}} + \underline{r_p}) \cdot (\underline{r_{planet}} + \underline{r_p})}}$$

$$\frac{1}{r_c} = \frac{1}{r_{planet}} \left(1 + \frac{r_p^2}{r_{planet}^2} + \frac{2\underline{r_{planet}} \cdot \underline{r_p}}{r_{planet}^2} \right)^{-1/2} \tag{4.2.2}$$

becomes

$$\frac{1}{r_c} = \frac{1}{r_{planet}} \left(1 - \frac{\underline{r_{planet}} \cdot \underline{r_p}}{r_{planet}^2} - \frac{1}{2} \frac{r_p^2}{r_{planet}^2} + \frac{3}{2} \left(\frac{\underline{r_{planet}} \cdot \underline{r_p}}{r_{planet}^2} \right)^2 + 0 \left(\frac{r_p}{r_{planet}} \right)^3 \right) \tag{4.2.3}$$

Furthermore, geometry gives $\omega^2(r_c^2 - r_p^2) = \omega^2(r_{planet}^2 + 2\underline{r_{planet}} \cdot \underline{r_p})$.

Using these expressions in equation 4.2.1 gives:

$$-C = V_\infty^2 - 2(\underline{V_{IP}} \cdot \underline{\omega} \wedge \underline{r_P}) - 2\left(\frac{\mu_c}{r_{planet}} \right) - \omega^2 r_{planet}^2 + \omega^2 r_p^2 - 3\omega^2 \left(\frac{\underline{r_{planet}} \cdot \underline{r_p}}{r_{planet}} \right)^2 \tag{4.2.4}$$

When the spacecraft is very close to the planet, for example, at the pericentre of the departure orbit, r_p is relatively small, and using the angular momentum per unit mass, $\underline{h_p} = (\underline{r_p} \wedge \underline{V_{IP}})$, the following is obtained:

$$-C = V_{\infty 0}^2 - 2\underline{\omega} \cdot (\underline{h_{p0}}) - 2\left(\frac{\mu_c}{r_{planet}} \right) - V_{planet}^2 + 0(\omega^2 r_p^2) \tag{4.2.5}$$

where $V_{\infty 0}^2$ is the osculating excess hyperbolic speed (or $\sqrt{(2 * \text{energy})}$) evaluated at a position close to the major body or planet, and h_{p0} is the angular momentum per unit mass at that point. The angular momentum $*$ angular velocity term is in general much smaller for an escape orbit than the excess hyperbolic speed (or initial energy) term.

If the expression for the Jacobi constant in terms of central body relative terms is considered, at a distance r_p that may be distant, then the following expression is obtained from section 4.1.3:

$$-C = V_{IC}^2 - 2(\underline{V_{IC}} \cdot \underline{\omega} \wedge \underline{r_c}) - 2\left(\frac{\mu_c}{r_c} \right) - 2\left(\frac{\mu_p}{r_p} \right) \tag{4.2.6}$$

Equating and rearranging these two expressions (4.2.5 and 4.2.6) yields:

$$V_{IC}^2 - 2(\underline{V_{IC}} \cdot \underline{\omega} \wedge \underline{r_c}) + V_{planet}^2 = 2\left(\frac{\mu_c}{r_c} - \frac{\mu_c}{r_{planet}} \right) + 2\left(\frac{\mu_p}{r_p} \right) + V_{\infty 0}^2 - 2\underline{\omega} \cdot (\underline{h_{p0}}) \tag{4.2.7}$$

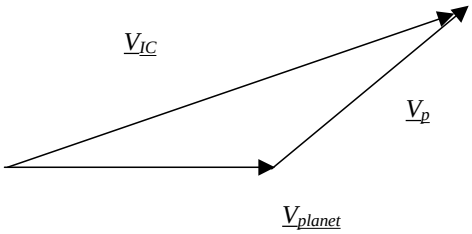

Figure 4.2.1. Relative velocity geometry.

The previous expression may be rewritten as:

$$V_{IC}^2 - 2(\underline{V_{IC}} \cdot \underline{V_{planet}}) + V_{planet}^2 = V_{\infty 0}^2 - 2\underline{\omega} \cdot (\underline{h_{p0}}) + 2\left(\frac{\mu_c}{r_c} - \frac{\mu_c}{r_{planet}}\right) + 2(\underline{V_{IC}} \cdot \underline{\omega} \wedge \underline{r_p}) + 2\left(\frac{\mu_p}{r_p}\right) \tag{4.2.8}$$

Although r_p here is still considerably smaller than r_{planet}, it is not a negligible quantity, because it may be typically at a value beyond the radius of the sphere of influence of the body. Therefore, this expression reveals the nature of the evolution of the velocity relative to the planet. It can be seen in a more obvious form by returning to completely planet-relative terms, as shown through the following discussion.

It is possible to evaluate an expression for the evolution of the velocity relative to the planet, and to compare this with the initial departure, osculating excess hyperbolic speed.

In vector terms: $\underline{V_p} = \underline{V_{IC}} - \underline{V_{planet}}$ (Figure 4.2.1).

The geometric relationship from Figure 4.2.1 is therefore:

$$V_{IC}^2 - 2(\underline{V_{IC}} \cdot \underline{V_{planet}}) + V_{planet}^2 = V_p^2 \tag{4.2.9}$$

Equation 4.2.8 then becomes:

$$V_p^2 = V_{\infty 0}^2 - 2\underline{\omega} \cdot (\underline{h_{p0}}) + 2\frac{\mu_c}{r_{planet}}\left(\frac{r_{planet} - r_c}{r_c}\right) + 2([\underline{V_{planet}} + \underline{V_p}] \cdot \underline{\omega} \wedge \underline{r_p}) + 2\left(\frac{\mu_p}{r_p}\right) \tag{4.2.10}$$

The planet velocity term may be expanded as follows:

$$2([\underline{V_{planet}}] \cdot \underline{\omega} \wedge \underline{r_p}) = 2V_{planet}^2\left(\frac{r_p \cdot \hat{r}_{planet}}{r_{planet}}\right)$$

Also

$$2V_{planet}^2\left(\frac{r_{planet} - r_c}{r_c}\right) = 2V_{planet}^2\left(\frac{r_{planet}}{r_c} - 1\right) = 2V_{planet}^2\left(-\frac{\underline{r_{planet}} \cdot \underline{r_p}}{r_{planet}^2} - \frac{1}{2}\frac{r_p^2}{r_{planet}^2} + \frac{3}{2}\left(\frac{\underline{r_{planet}} \cdot \underline{r_p}}{r_{planet}^2}\right)^2 + 0\left(\frac{r_p^3}{r_{planet}^3}\right)\right) \tag{4.2.11}$$

Then using the relationships $V_{planet} = \omega r_{planet}$ and $V^2_{planet} = \dfrac{\mu_c}{r_{planet}}$ for a circular planet orbit, and also recalling that $\underline{h}_p = (\underline{r}_p \wedge \underline{V}_{IP})$, equation 4.2.10 becomes:

$$V_p^2 = V_{\infty 0}^2 - 2\underline{\omega}\cdot(\underline{h_{p0}}) + 2\omega^2\left(-\frac{1}{2}r_p^2 + \frac{3}{2}\left(\frac{\underline{r_{planet}}\cdot\underline{r_p}}{r_{planet}}\right)^2 + 0\left(\frac{r_p}{r_{planet}}\right)^3\right) + 2\underline{\omega}\cdot(\underline{h_p}) + 2\left(\frac{\mu_p}{r_p}\right) \tag{4.2.12}$$

or alternatively:

$$V_\infty^2 - 2\underline{\omega}\cdot(\underline{h_p}) = V_{\infty 0}^2 - 2\underline{\omega}\cdot(\underline{h_{p0}}) + 2\omega^2\left(-\frac{1}{2}r_p^2 + \frac{3}{2}\left(\frac{\underline{r_{planet}}\cdot\underline{r_p}}{r_{planet}}\right)^2 + 0\left(\frac{r_p}{r_{planet}}\right)^3\right) \tag{4.2.13}$$

This equation represents a relationship between the osculating V_∞ and angular momentum and the position relative to the planet.

Analysis using the two-body problem basis

The preceding expression may be compared with that which is implied by the approximation of the escape orbit excess hyperbolic velocity vector addition to the velocity of the body, p. This is analysed on the basis of Keplerian motion predictions from the two-body problem. The central body is the Sun. Figure 4.2.2 shows an idealised planet relative velocity vector added to the planet's velocity to achieve the heliocentric velocity.

However, an additional notation must be introduced, as these terms are those existing at the instant of the relative velocity vector addition, which takes pace at the planet position defined by that epoch. Therefore, $\underline{V_{IC0}}$ and $\underline{V_{planet0}}$ are the velocity vectors at the epoch of the escape, and $\underline{V_{rel0}}$ is the relative velocity with respect to the planet at the escape epoch.

The vector addition gives the following expression:

$$V_{IC0}^2 - 2(\underline{V_{IC0}}\cdot\underline{V_{planet0}}) - V_{rel0}^2 + V_{planet0}^2 = 0 \tag{4.2.14}$$

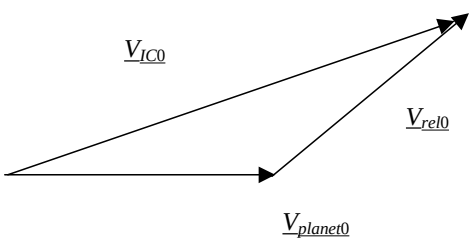

Figure 4.2.2. Idealised planetary escape geometry by vector addition of an instantaneous excess hyperbolic departure vector.

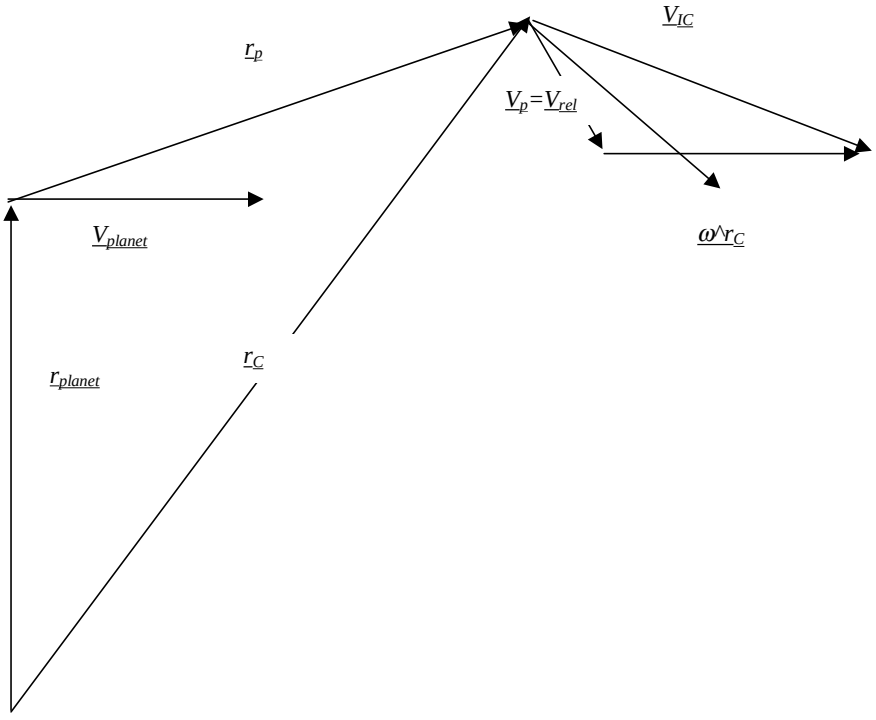

Figure 4.2.3. Motion relative to the planet after departure.

Given that this vector addition occurs at the planet at the escape epoch, then at a subsequent time the relative velocity will be modified. This can be found by the process shown in Figure 4.2.3.

At this instant, some time after the initial epoch, the velocity relative to the planet is given by the same geometrical relationship as equation 4.2.9:

$$V_{IC}^2 - 2(\underline{V_{IC}} \cdot \underline{V_{planet}}) + V_{planet}^2 = V_{rel}^2 = V_p^2 \tag{4.2.15}$$

Note that V_p and V_{rel} are equivalent expressions for the velocity relative to the planet. As purely Keplerian motion of the two body problem is under consideration, the heliocentric velocity is given by:

$$V_{IC}^2 = 2\mu_c\left(\frac{1}{r_c} - \frac{1}{2a}\right) \tag{4.2.16}$$

and so

$$V_{IC}^2 - V_{IC0}^2 = 2\mu_c\left(\frac{1}{r_c} - \frac{1}{r_{planet}}\right) \tag{4.2.17}$$

Recalling that $\underline{V_{IC}} = \underline{V_{IP}} + \underline{V_{Planet}}$ and $\underline{r_P} = \underline{r_C} - \underline{r_{Planet}}$, and because the planet is in circular motion, $\underline{V_{planet}} = \underline{\omega} \wedge \underline{r_{planet}}$. Then:

$$(\underline{V_{IC}} \cdot \underline{V_{planet}}) = \underline{V_{IC}} \cdot (\underline{\omega} \wedge (\underline{r_c} - \underline{r_p})) = \underline{\omega} \cdot \underline{h_c} - (\underline{V_{planet}} + \underline{V_p}) \cdot (\underline{\omega} \wedge \underline{r_p}) \tag{4.2.18}$$

where $\underline{h}_c$ is the angular momentum vector (per unit spacecraft mass) relative to the central body. This is a constant of motion in the two-body problem, and as the angular velocity of the planet or major body is also constant for this problem, then the quantity $\underline{\omega}\cdot\underline{h}_c$ is a constant of motion. Equation 4.2.14 then becomes:

$$V_{IC0}^2 - 2\underline{\omega}\cdot\underline{h_c} - V_{rel0}^2 + V_{planet0}^2 = 0 \tag{4.2.19}$$

The velocity relative to the planet can now be expressed as:

$$V_p^2 = V_{rel0}^2 + 2\mu_c\left(\frac{1}{r_c} - \frac{1}{r_{planet}}\right) + 2(\underline{V_{planet}} + \underline{V_p})\cdot(\underline{\omega}\wedge\underline{r_p}) \tag{4.2.20}$$

Comparison of two-body and three-body solutions

Comparing Equation 4.2.20 – which is obtained from equation 4.2.15 by consideration of the evolution of the motion in the central body system (from the two-body problem) – with equation 4.2.8, leading to equation 4.2.10, obtained from the Jacobi constant conservation (from the three-body problem), it is clear that they both possess the same dependence on position relative to the planet. However, these two expressions may not be equated, as they describe motion in two different situations: the two-body problem and the three-body problem. In the three-body problem, the details of the V_p, r_p evolution is not the same as those for the two-body problem.

Examination of the evolution of the motion may lead to series of simplifications. These depend on the details of the initial orbit and the resulting planet departure.

In the two-body problem, equation 4.2.20 describes the motion relative to the planet. This may be expanded to yield the following expression for the case where $r_p \ll r_c$ (as in the derivation of equation 4.2.12):

$$V_p^2 = V_{rel0}^2 + 2\omega^2\left(-\frac{1}{2}r_p^2 + \frac{3}{2}\left(\frac{\underline{r_{planet}}\cdot\underline{r_p}}{r_{planet}}\right)^2 + 0\left(\frac{r_p}{r_{planet}}\right)^3\right) + 2\underline{\omega}\cdot\underline{h_p} \tag{4.2.21}$$

The last term is initially zero, as the spacecraft moves away from the point mass representing the planet in the initial phases two-body representation. Eventually, at large r_p this statement becomes untrue as the heliocentric gravitational term dominates the evolution of the motion.

However, in the three-body problem, the motion is described by equation 4.2.12:

$$V_p^2 = V_{\infty 0}^2 + 2\underline{\omega}\cdot(\underline{h_p}) - 2\underline{\omega}\cdot(\underline{h_{p0}}) + 2\omega^2\left(-\frac{1}{2}r_p^2 + \frac{3}{2}\left(\frac{\underline{r_{planet}}\cdot\underline{r_p}}{r_{planet}}\right)^2 + 0\left(\frac{r_p}{r_{planet}}\right)^3\right) + 2\left(\frac{\mu_p}{r_p}\right)$$

These equations are both evaluated over a region where $r_p \ll r_{planet}$. One of the differences between the two cases is the term $2\underline{\omega}\cdot(\underline{h_p})$ – the scalar product of the planets angular velocity vector with the angular momentum vector relative to the planet. In the three-body case this is a constant of motion in the regions dominated

by the planet's gravity field, and so the term $2\underline{\omega}\cdot(\underline{h_p}) - 2\underline{\omega}\cdot(\underline{h_{p0}})$ should remain relatively small in this region and will achieve a more significant magnitude as the spacecraft passes beyond the sphere of influence. As the spacecraft passes beyond the sphere of planetary gravitational influence, this term will become progressively perturbed. In the two-body case the term $2\underline{\omega}\cdot(\underline{h_p})$ is initially zero. However, as the spacecraft moves further away from the planet, this term will also eventually achieve a significant magnitude.

The other difference in the two equations is the presence of the Earth's gravitational potential term. However, at large distances, when the spacecraft has effectively left the gravitational influence of the planet, this term will become negligible.

The term $2\underline{\omega}\cdot(\underline{h_p})$ may be examined more closely. Using the definition of planet relative angular momentum: $\underline{h_p} = \underline{r_p} \wedge \underline{V_p}$, its time derivative is:

$$\frac{d\underline{h_p}}{dt} = \frac{d\underline{r_p}}{dt} \wedge \underline{V_p} + r_p \wedge \frac{d\underline{V_p}}{dt} \tag{4.2.22}$$

The first term is identically zero, and so any change in planet relative angular momentum is caused by the second term.

Then, using the planet velocity term, $\underline{V_p} = \underline{V_{IC}} - \underline{V_{planet}}$,

$$\frac{d\underline{V_p}}{dt} = \frac{d\underline{V_{IC}}}{dt} - \frac{d\underline{V_{planet}}}{dt} \tag{4.2.23}$$

It is assumed that the central body is much more massive than the major body, and so the acceleration of the spacecraft with respect to the central body equates to the inertial acceleration arising from the gravitational forces. The value depends on whether the two-body or three-body problem is being considered:

$$\frac{d\underline{V_{IC}}}{dt} = -\frac{\mu_c \underline{r_c}}{r_c^3} - \frac{\mu_p \underline{r_p}}{r_p^3} \qquad \text{three-body problem} \tag{4.2.24}$$

$$\frac{d\underline{V_{IC}}}{dt} = -\frac{\mu_c \underline{r_c}}{r_c^3} \qquad \text{two-body problem} \tag{4.2.25}$$

Similarly, the acceleration of the planet or major body is given by:

$$\frac{d\underline{V_{planet}}}{dt} = -\frac{\mu_c \underline{r_{planet}}}{r_{planet}^3} \tag{4.2.26}$$

If the two-body problem is first considered, then

$$\frac{d\underline{V_p}}{dt} = -\mu_c \left(\frac{\underline{r_c}}{r_c^3} - \frac{\underline{r_{planet}}}{r_{planet}^3} \right) \tag{4.2.27}$$

Then, recalling equation 4.2.2, the following is derived:

$$\frac{1}{r_c^3} = \frac{1}{r_{planet}^3} \left(1 - 3\frac{\underline{r_{planet}}\cdot\underline{r_p}}{r_{planet}^2} - \frac{3}{2}\frac{r_p^2}{r_{planet}^2} + \frac{15}{2}\left(\frac{\underline{r_{planet}}\cdot\underline{r_p}}{r_{planet}^2} \right)^2 + 0\left(\frac{r_p}{r_{planet}} \right)^3 \right) \tag{4.2.28}$$

Then

$$\frac{d\underline{V_p}}{dt} = \frac{-\mu_c}{r_{planet}^3}\left(\left(1 - 3\frac{\underline{r_{planet}}\cdot\underline{r_p}}{r_{planet}^2} - \frac{3}{2}\frac{r_p^2}{r_{planet}^2} + \frac{15}{2}\left(\frac{\underline{r_{planet}}\cdot\underline{r_p}}{r_{planet}^2}\right)^2 + 0\left(\frac{r_p}{r_{planet}}\right)^3\right)\underline{r_c} - \underline{r_{planet}}\right)$$

Using the definition of ω, the rate of change of angular momentum is given by:

$$\underline{r_p} \wedge \frac{d\underline{V_p}}{dt} = -\omega^2\left(\left(-3\frac{\underline{r_{planet}}\cdot\underline{r_p}}{r_{planet}^2} - \frac{3}{2}\frac{r_p^2}{r_{planet}^2} + \frac{15}{2}\left(\frac{\underline{r_{planet}}\cdot\underline{r_p}}{r_{planet}^2}\right)^2 + 0\left(\frac{r_p}{r_{planet}}\right)^3\right)\underline{r_p} \wedge \underline{r_{planet}}\right) \tag{4.2.29}$$

When considering the three-body case, then the planet or major body gravity term does not contribute to the rate of change of angular momentum with respect to that body. Therefore, when considering the terms $2\underline{\omega}\cdot(\underline{h_p})$ and $2\underline{\omega}\cdot(\underline{h_p}) - 2\underline{\omega}\cdot(\underline{h_{p0}})$ appearing in the velocity expressions in the two-body and three-body cases (equations 4.2.21 and 4.2.12) then the zero difference at the epoch of departure would be expected to be maintained if both models lead to the same position evolution of the spacecraft with respect to the planet. This is because in both cases the rate of change is the same, both being given by equation 4.2.29. The time derivative depends on r_p. However, in practice the history of r_p varies between the two-body and three-body cases because the initial relative velocities are different (due to the presence of the planet's gravity field), and so the integral of equation 4.2.29 will accrue a difference.

The mathematical description of the departure in the two-body and three-body cases is therefore very similar. A difference between two-body and three-body predictions of relative velocity when leaving the planet may arise from the difference in the evolution of this angular momentum related term. When compared with the square of a typical excess hyperbolic speed, for a direct, high-energy escape orbit, the effect on the actual relative velocity is generally very small. However, this consideration will be revisited when techniques utilising gravitational escape methods are considered in Section 4.8.5.

Analysis in central-body terms

The departure may also be considered from the central body perspective.

If a two-body case is considered then the fundamental relationships can be calculated. The heliocentric angular momentum, discussed previously, is given by the initial velocity:

$$\underline{V_{IC0}} = \underline{V_{rel0}} + \underline{V_{planet0}} \qquad \text{and then} \qquad \underline{h_{c0}} = \underline{r_{planet0}} \wedge \underline{V_{IC0}}$$

where $\underline{V_{planet0}}$ and $\underline{r_{planet0}}$ are the position and velocity vectors at the epoch of the application of the planet relative velocity increment, $\underline{V_{rel0}}$.

The previous expression (equation 4.2.19), gives a relationship between the velocity and angular momentum terms:

$$V_{IC0}^2 = V_{rel0}^2 + 2\underline{\omega}\cdot\underline{h_{c0}} - V_{planet0}^2 \tag{4.2.30}$$

The velocity with respect to the central body is therefore dependent on the initial angular momentum with respect to the central body, because of the importance of the direction of the velocity when leaving a planet.

The energy with respect to the central body E_{c0} is then obtained as:

$$2E_{c0} = V_{IC0}^2 - 2\left(\frac{\mu_c}{r_{planet}}\right) \qquad \text{or} \qquad 2E_{c0} - 2\underline{\omega}\cdot\underline{h}_{c0} = \frac{-3\mu_c}{r_{planet}} + V_{rel0}^2 \tag{4.2.31}$$

In the two-body analysis case then these heliocentric terms remain constant, However, this is not the case in the three-body model. The evolution of heliocentric energy and angular momentum can be considered in detail.

In the case of the three-body problem, the conservation of the Jacobi constant may be expressed in heliocentric terms as:

$$-C = V_{IC}^2 - 2(\underline{V_{IC}}\cdot\underline{\omega}\wedge\underline{r_c}) - 2\left(\frac{\mu_p}{r_p} + \frac{\mu_c}{r_c}\right) = 2E_C - 2\underline{\omega}\cdot\underline{h_c} - 2\frac{\mu_p}{r_p} \tag{4.2.32}$$

The variation in the term $2E_C - 2\underline{\omega}\cdot\underline{h_c}$ depends on the planet potential energy and is only a function of distance from the planet. It tends to zero as the spacecraft leaves the planet. When far removed from the planet's gravitational perturbation the heliocentric energy and angular momentum terms will each reach a constant value. This effect can be examined by closer inspection of the heliocentric angular momentum term.

Using the definition of heliocentric, or central body, relative angular momentum, $\underline{h_c} = \underline{r_c}\wedge\underline{V_{IC}}$, then its time derivative is:

$$\frac{d\underline{h_c}}{dt} = \underline{r_c}\wedge\frac{d\underline{V_{IC}}}{dt} + \frac{d\underline{r_c}}{dt}\wedge V_{IC} \tag{4.2.33}$$

As in the analysis with respect to the major body, the second term is identically zero, and so any change in angular momentum is caused by the first term. This acceleration in the three-body problem is restricted to gravitational terms, as so (neglecting acceleration of the central body):

$$\frac{d\underline{V_{IC}}}{dt} = -\frac{\mu_c\underline{r_c}}{r_c^3} - \frac{\mu_p\underline{r_p}}{r_p^3} \tag{4.2.34}$$

Therefore, using this expression in the previous one the rate of change of angular momentum is given by:

$$\frac{d\underline{h_C}}{dt} = -\underline{r_c}\wedge\frac{\mu_p\underline{r_p}}{r_p^3} = -(\underline{r_{planet}} + \underline{r_p})\wedge\frac{\mu_p\underline{r_p}}{r_p^3} = -(\underline{r_{planet}})\wedge\frac{\mu_p\underline{r_p}}{r_p^3}$$

Therefore, the rate of change of angular momentum depends on the direction of escape. A resultant escape in a radial direction will quickly see the angular momentum reach its asymptotic value. In a tangential direction the perturbation reduces with $1/r_p^2$.

4.2.2 Examples of escape

Illustration of a low-energy departure from Earth

The actual motion of a spacecraft leaving a planet in a moderate-energy escape orbit can be simulated by numerical integration in the multi-gravity field and compared with the approximated cases discussed in the previous section. The first example to be considered is that of a spacecraft leaving Earth. An idealised case is initially considered, where the Earth's orbit is approximated as a circular orbit. Departures both tangential and perpendicular to the Earth's velocity are analysed. The tangential case is then considered further with a departure from the true Earth's orbit.

Tangential escape using circular-Earth initial orbit

In this case the orbit of Earth is modified to be circular, so that the details may be closely examined, with the knowledge that the Jacobi constant must be constant throughout the simulation.

A tangential departure is generated by targeting a high circular heliocentric orbit. The transfer is optimised in terms of obtaining a minimum ΔV. This means that the impulsive ΔV needed to transfer from an initially Earth-bound orbit, to reach the required excess hyperbolic velocity needed to achieve the transfer, is minimised. The resulting transfer after leaving Earth will be a Hohmann transfer between the Earth's represented circular orbit and the target circular orbit.

The following example is taken.

- Planet of departure is Earth. Earth's orbital radius at departure is 1.0 AU.
- Target a heliocentric orbit (not a planetary rendezvous). This orbit is circular at approximately 207 million km (1.383 AU) and in the ecliptic.
- The transfer is optimised to minimise the departure ΔV. This means that the departure excess hyperbolic velocity lies very close to tangential to the Earth's orbit.

The optimised transfer orbit has the following parameters:

- Semi-major axis: 1.1917 AU.
- Eccentricity: 0.16049.
- Aphelion: 1.383 AU.
- Perihelion: 1.00 AU.

The following shows a comparison between theoretical and actual (numerical simulation) heliocentric terms after departing from Earth. The 'theoretical' values are calculated by performing a tangential velocity vector addition of the osculating excess hyperbolic speed (calculated at perigee) to the planet's velocity.

	Theoretical	*Actual*
Heliocentric sma	1.779E + 11 m	1.783E + 11 m
Eccentricity	1.591E−01	1.605E−01

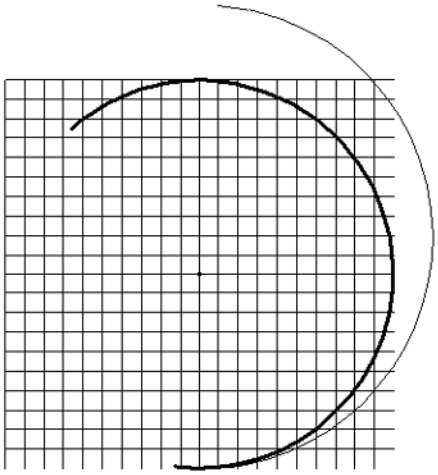

Figure 4.2.4. Transfer from Earth to raised aphelion orbit with Earth Vinfinity at 2.3 km/sec. The transfer is a half ellipse in the ecliptic, moving from perihelion at Earth to the target aphelion radius. Departure from Earth is tangential. The grid is 1 AU from centre to edge, with a sub-grid size of 0.1 AU. Earth's circular orbit is shown in addition to the transfer trajectory.

Alternatively this allows the excess hyperbolic velocity required to achieve the actual transfer to be calculated, by the previous approximations on Hohmann transfers, as 2.3 km/sec (if the initial and final orbits are considered circular). The actual optimised value is found to be 2.28 km/sec. This is the osculating value at Earth-orbit pericentre of the departure orbit. Therefore, agreement between the prediction using the two-body case and the actual departure using a three body case are very close. Figure 4.2.4 shows the transfer trajectory and Earth's orbit about the Sun.

The evolution of the osculating orbital parameters may be monitored during the escape and transfer phase. The Earth relative semi-major axis and energy are shown in Figure 4.2.5.

The variation in energy with respect to the Sun follows a different trend as the spacecraft leaves Earth. This is shown in Figure 4.2.7. The heliocentric term initially undergoes a significant variation when within the Earth's sphere of influence (within a radius of 1 million km).

Figure 4.2.8 shows the evolution of the heliocentric angular momentum of the spacecraft. The total value plotted is the value less the component due to the Earth's velocity component. It clearly tends to an asymptote as the spacecraft leaves the Earth's sphere of influence beyond 1 million km.

The heliocentric angular momentum may be broken down into its constituent components.

$$\underline{h_c} = (\underline{r_{planet}} + \underline{r_p}) \wedge (\underline{V_{planet}} + \underline{V_p}) = \underline{r_c} \wedge \underline{V_{IC}} \tag{4.2.35}$$

The dominant term is $(\underline{r_{planet}}) \wedge (\underline{V_{planet}})$, which remains constant. As a 'bias' term it

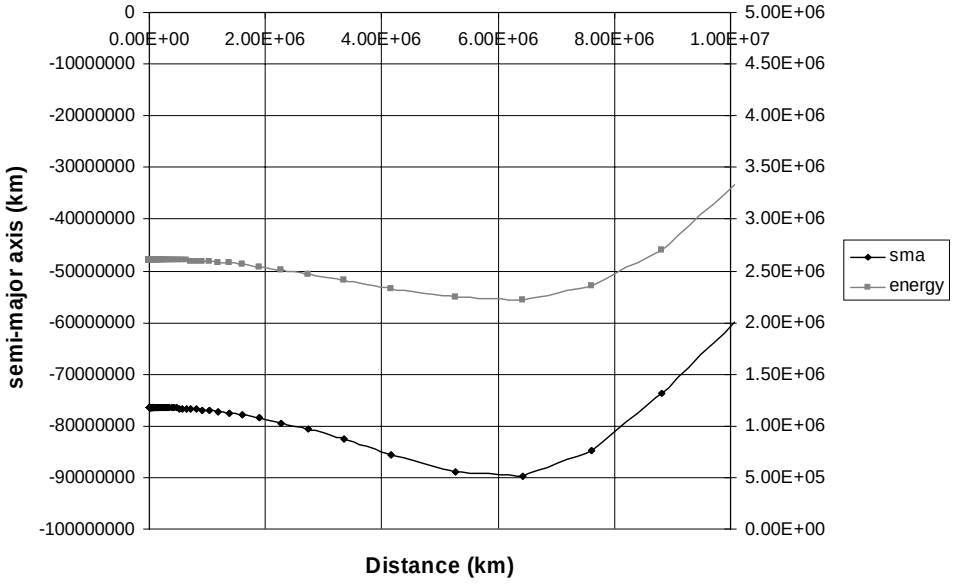

Figure 4.2.5. Semi-major axis and energy with respect to Earth, evolution over distance from circular orbiting Earth. The semi-major axis and energy stay approximately constant whilst leaving the Earth's sphere of influence (within a radius of approximately 1 million km). As the spacecraft enters the heliocentric sphere the variation becomes more pronounced. Energy is plotted against the right axis.

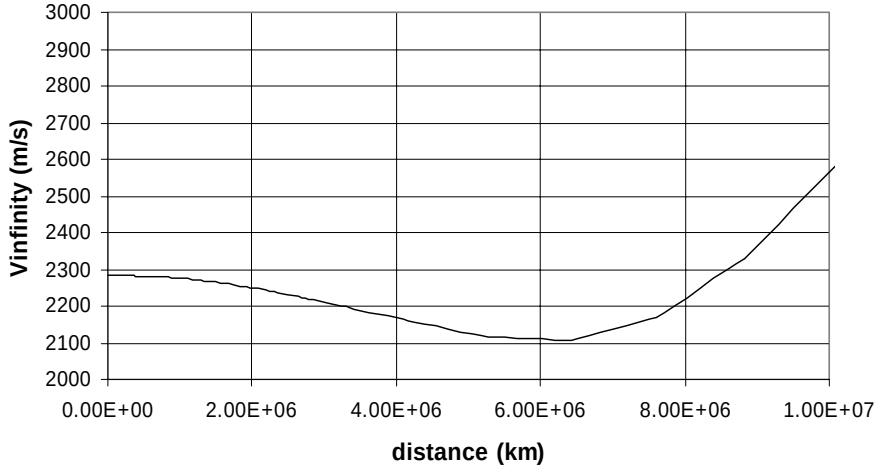

Figure 4.2.6. Osculating excess hyperbolic speed evolution with respect to Earth, evolution over distance from circular orbiting Earth. The excess hyperbolic speed profile follows the energy trend as the spacecraft leaves Earth, and stays approximately constant when within Earth's sphere of influence.

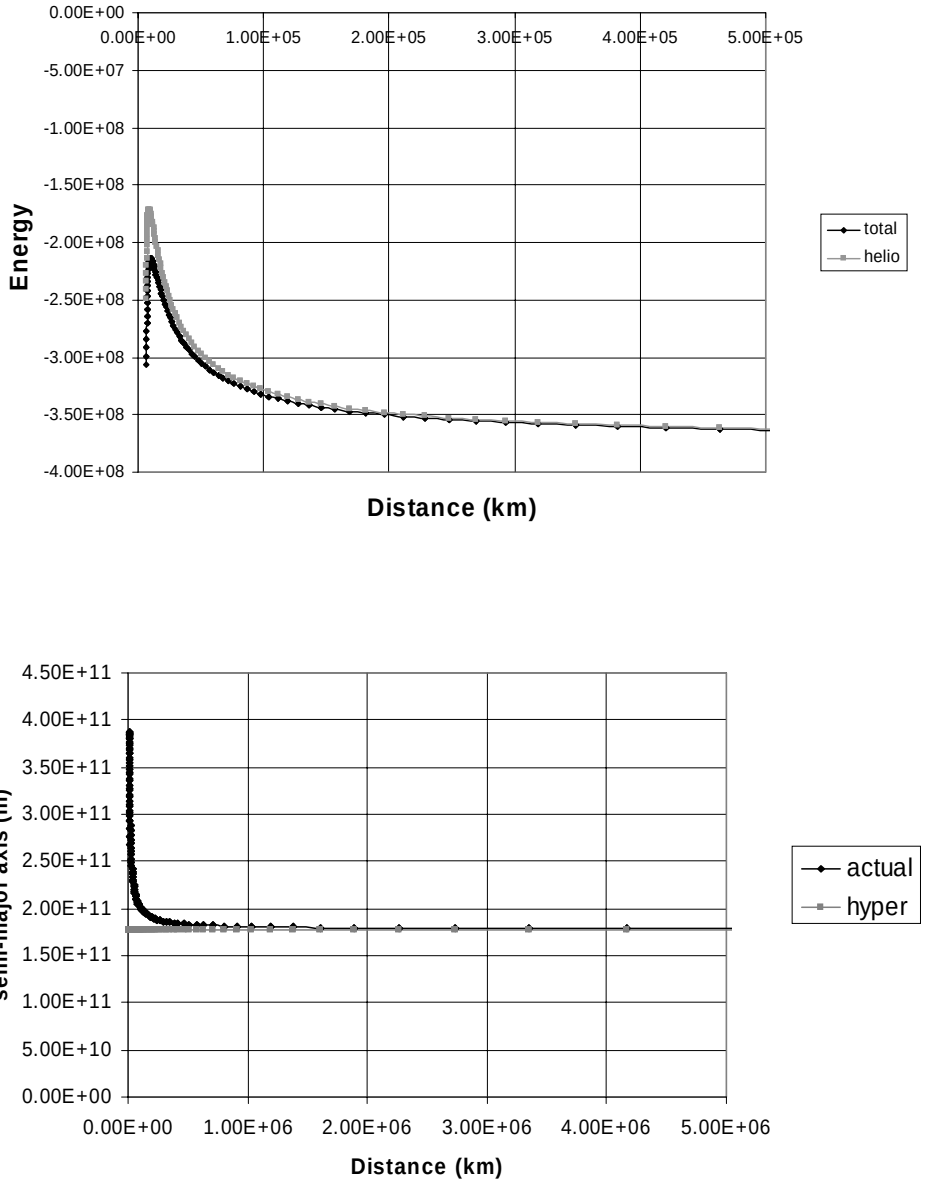

Figure 4.2.7. Energy with respect to Sun, evolution over distance from a circular orbiting Earth. In the upper figure, the total energy (the sum of kinetic and both body potential energy terms) and Sun-relative energy differ initially due to the Earth's gravity potential but converge at greater distance from Earth. The energy asymptotically tends to its final value that corresponds to a semi-major axis of value 1.192 AU. Similarly (in the lower figure) the heliocentric semi-major axis asymptotically tends to its predicted value as the spacecraft leaves the Earth's sphere of influence. 'Hyper' indicates the two-body predicted value from vector addition of the initial osculating excess hyperbolic velocity.

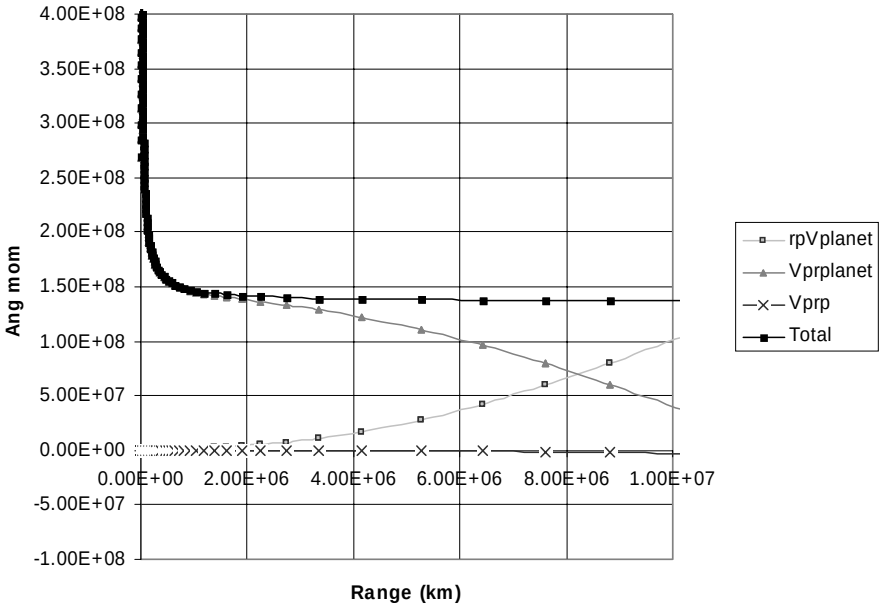

Figure 4.2.8. Angular momentum with respect to Sun, evolution over distance from circular orbiting Earth.

is removed from the total angular momentum shown in Figure 4.2.8. The remaining terms shown are:

$$(\underline{r_p}) \wedge (\underline{V_{planet}}), (\underline{r_{planet}}) \wedge (\underline{V_p}), (\underline{r_p}) \wedge (\underline{V_p})$$

However, neither of these quantities – the spacecraft's heliocentric energy and the angular momentum – is expected to be conserved during the course of such a planetary departure. The quantity that is conserved is the Jacobi constant. This conservation depends upon the assumption of a circular orbital motion for the planet, which is the case here in the representation of the Earth's orbit.

Using equivalent Earth circular initial orbit and radial escape direction

The orbit of Earth is again modified to be circular in this case, so that the Jacobi constant will remain constant throughout the simulation. The direction of the initial orbital line of apses is rotated by 90° when compared with the previous example. This will result in a near radial 'escape' direction when seen in an Earth centred frame. An outward radial direction is chosen.

The resulting heliocentric orbit is shown in Figure 4.2.10. The evolution of energy is shown in Figure 4.2.9.

Case of tangential departure from the true Earth orbit

The tangential departure case is now examined for a departure from a more accurate representation of Earth's orbit. That is, the eccentricity is set to its nominal value at

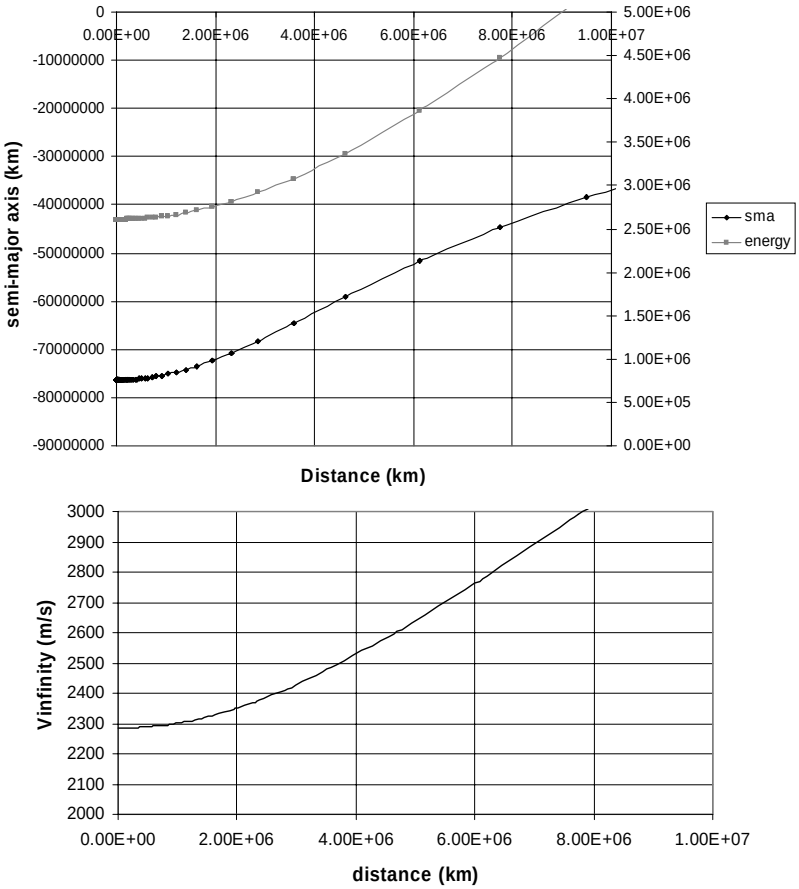

Figure 4.2.9. Semi-major axis and energy with respect to Earth, evolution over distance from circular orbiting Earth, for a radial Earth relative departure case. In the upper figure the semi-major axis and energy (with respect to the planet) now show a different radial dependence to that seen in the tangential departure case. This is predicted by the effect of the transition to the central body dominated motion described in the previous section. Energy is plotted against the right axis. In the lower figure the excess hyperbolic speed (based on planet relative energy) once again follows the same trend as the energy, increasing significantly with radial distance when beyond the Earth's sphere of influence.

0.0167, and the motion, then modelled as a Keplerian arc about the Sun. The same circular heliocentric orbit is targeted. The transfer is optimised by minimising the ΔV from a reference Earth-bound orbit.

The resulting optimised transfer orbit has the following parameters:

- Semi-major axis: 1.196 AU.
- Eccentricity: 0.1685.
- Aphelion: 1.397 AU.
- Perihelion: 0.9943 AU.

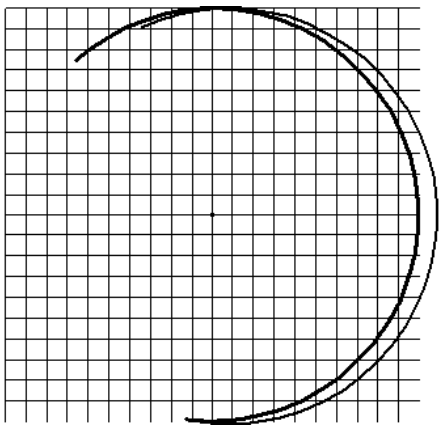

Figure 4.2.10. Transfer from Earth to increased eccentricity orbit with Earth relative radial Vinfinity at 2.3 km/sec. The principal effect of a radial vector addition is to increase the eccentricity with respect to the central body but leave the semi-major axis almost unchanged. Earth's orbit is shown. The grid is 1 AU from centre to edge.

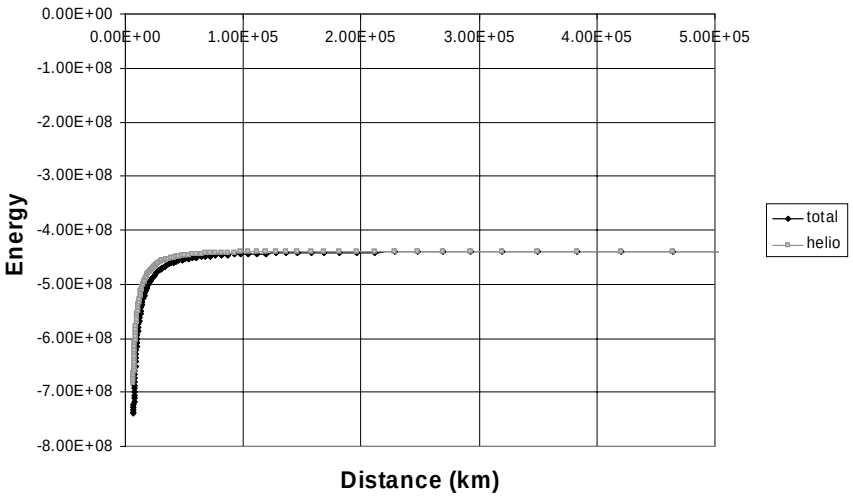

Figure 4.2.11. Energy with respect to Sun, evolution over distance from circular orbiting Earth, for a radial Earth departing case. The heliocentric energy quickly approaches an asymptote as the perturbing effect of the planetary gravity field becomes negligible. This is reached at a lesser distance in this radial case than in the tangential case. This was predicted previously from considerations of motion relative to the central body.

This allows the excess hyperbolic velocity required to be calculated, by the previous approximations on Hohmann transfers, as 2.33 km/sec (if the initial and final orbits are considered circular). The actual optimised value is found to be 2.32 km/sec, which is the value at Earth perigee for the departure orbit. This transfer includes

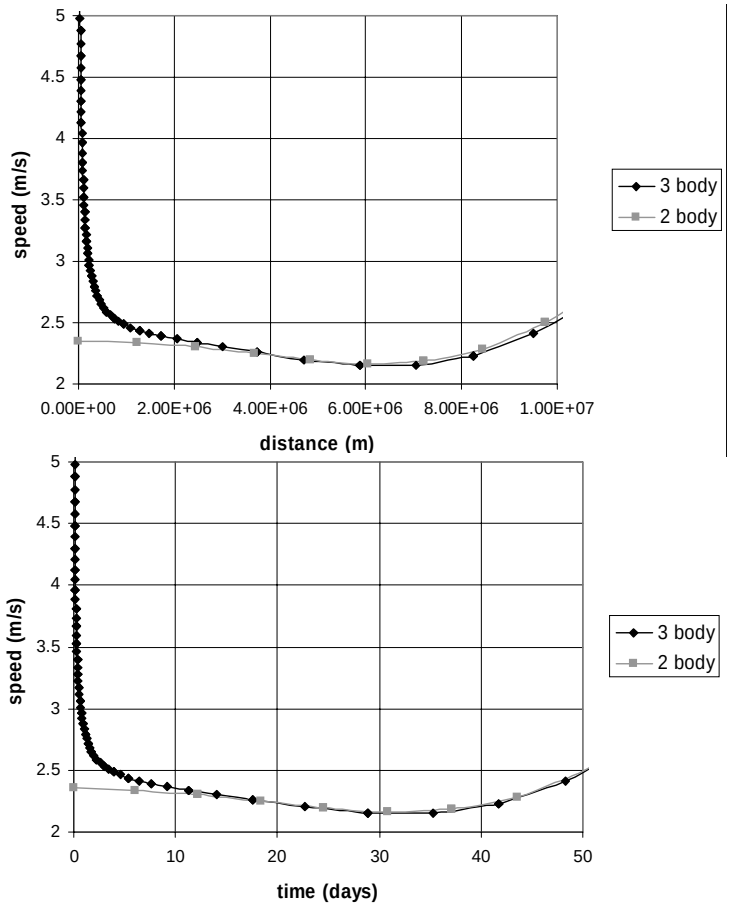

Figure 4.2.12. Comparison of Earth relative semi-major axis evolution for two-body and three-body departure cases. The upper plots show the evolution of the speed relative to Earth versus distance. The lower plot shows the evolutuion relative to elapsed time. Both two-body and three-body cases are shown. The long-range evolution shows the convergence at large distances. When closer to Earth, a greater difference is observed due to the effects of Earth gravitation in the three-body case. However, once a range of typically 3 million km is reached, the profiles are very similar.

the small effect of the Earth's initial orbital eccentricity. Therefore, a similar degree of agreement is seen as in the circular Earth orbit case.

Comparison of the two-body and three-body problems of tangential departure from the true Earth orbit

A comparison can be made between two optimised transfers, one using the combined Earth–Sun gravity fields, and one using only solar gravity. Both target the same orbit from Earth and leave at the same epoch. Therefore, the two-body transfer also

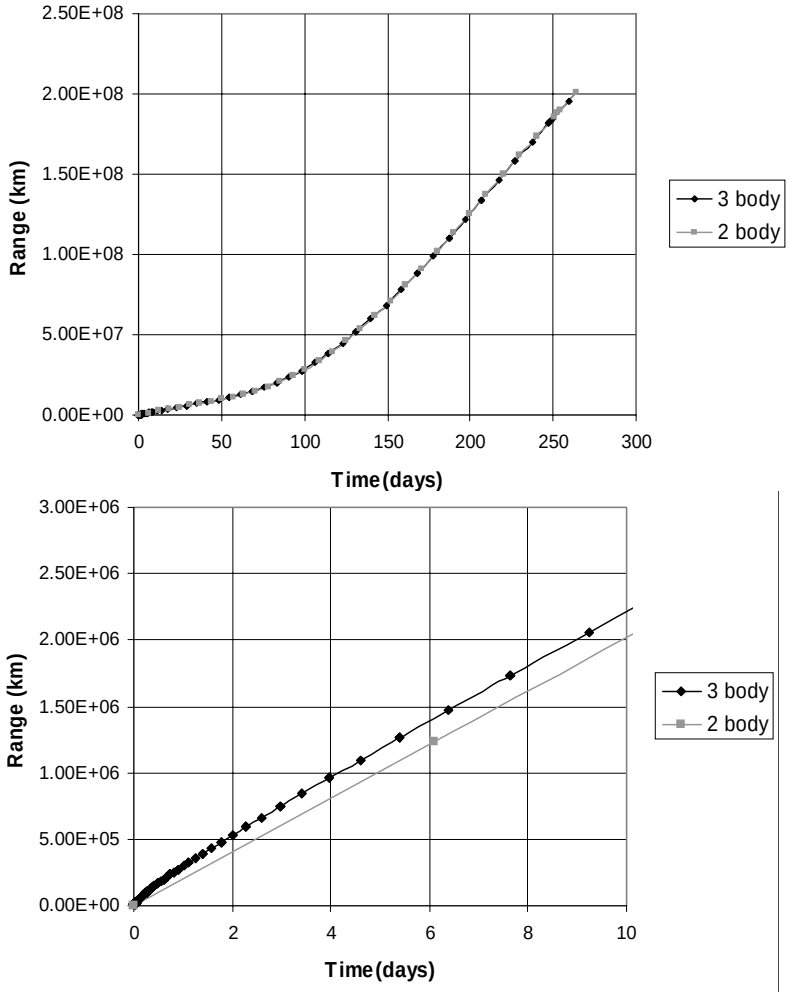

Figure 4.2.13. Comparison of Earth relative range evolution for two-body and three-body departure cases. The plots of range to Earth, with time from departure, show considerable similarity between the two-body and three-body solutions, when viewed over the whole transfer timeline. When examined more closely (in the lower figure), in the vicinity of Earth, a difference is seen, as in this early phase motion is strongly influenced by the Earth's gravity.

reaches a heliocentric orbit with the same semi-major axis and aphelion as that described for the three-body solution.

A departure from Jupiter

Jupiters's gravity field is significantly greater than that of Earth, and an examination of a departure from such a massive body is of interest. Jupiter's true orbit is taken.

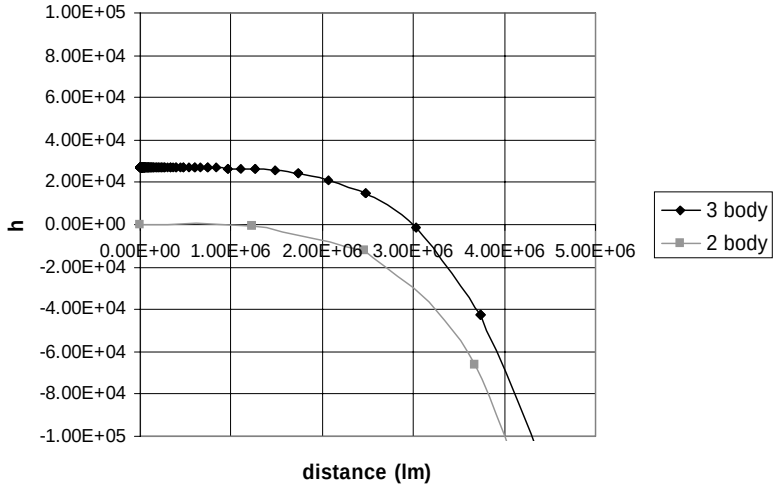

Figure 4.2.14. Comparison of Earth relative angular momentum evolution for two-body and three-body departure cases. The plots of Earth relative angular momentum (per unit mass) versus distance from Earth, also show the anticipated behaviour. The initial difference is the spacecraft's Earth relative angular momentum of the three-body problem. This term is identically zero at start of the two-body problem departure.

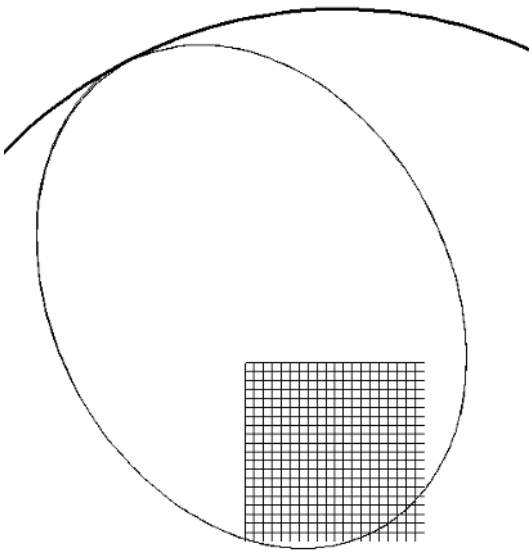

Figure 4.2.15. Transfer from Jupiter to reduced perihelion orbit with Jupiter osculating Vinfinity at 5.86 km/sec. This figure shows the transfer trajectory and Jupiter's orbit about the Sun. The initial departure from Jupiter and the resulting heliocentric orbit over a full orbit period can be seen. Close inspection shows that the aphelion lies slightly below Jupiter at the departure point, and the linking transfer through the gravitationally perturbed region can be seen. Jupiter's orbit is also shown. The grid is 1 AU from centre to edge.

Its orbital eccentricity is approximately 0.048, approximately three times greater than that of the Earth, but still relatively small.

The following example is taken.

- Planet of departure is Jupiter. Jupiter's orbital radius at departure is 4.965 AU. This lies very close to Jupiter's perihelion. Jupiter's orbital eccentricity results in a perihelion passage at 4.95 AU and aphelion at 5.45 AU.
- Target a heliocentric orbit (not a planetary rendezvous). This orbit is circular at approximately 149.6 million km (1 AU) and in the ecliptic.
- The transfer is optimised to minimise the departure ΔV. The departure excess hyperbolic velocity must therefore lie very close to being tangential to Jupiter's orbit.

The optimised transfer orbit has the following parameters:

- Semi-major axis: 2.965 AU.
- Eccentricity: 0.666.
- Aphelion: 4.937 AU.
- Perihelion: 0.992 AU.

These transfer orbit parameters are evaluated when far away from Jupiter (outside its gravitational influence).

This transfer may be compared with an idealised impulsive transfer (the two-body problem), from a departure at the above radius to reach a perihelion of 1 AU from Jupiter. The velocity relative to Jupiter (the excess hyperbolic speed) is approximately 5,930 m/s.

The actual optimised value of excess hyperbolic speed is also found to be 5,860 m/s. This is the osculating value at Jupiter orbit pericentre of the departure orbit, and so determines the manoeuvre required to implement the transfer. This lower value than the impulsive case results from the effect of the combined gravitational perturbations of the Sun and Jupiter when leaving the planet. The eventual aphelion of the transfer orbit (at 4.937 AU) is also less than the radius at which the spacecraft left Jupiter (4.965 AU). This effect is also a result of the combined gravity fields. Therefore, the three-body-problem effects on the departure orbit, when compared to merely the vector sum of the excess hyperbolic velocity with Jupiter's orbital velocity, shows a larger difference in Jupiter's case than in that of Earth. Figure 4.2.15 shows the transfer trajectory and Jupiter's orbit.

The evolution of the osculating orbital parameters may once again be monitored during the escape and transfer phase. The Jupiter relative semi-major axis and energy is shown in Figure 4.2.16. The radius of Jupiter's sphere of influence is just under 50 million km, and the planet relative ephemeris terms are therefore not expected to show strong deviations within such a radius. Energy is plotted on the right axis.

Figure 4.2.17 shows that this initial semi-major axis is equivalent to a hyperbolic orbit with the Vinfinity of 5.86 km/sec. As the spacecraft passes through and out of Jupiter's sphere of influence, this energy is eventually increased as the spacecraft moves into the heliocentric domain. This energy only shows a large deviation

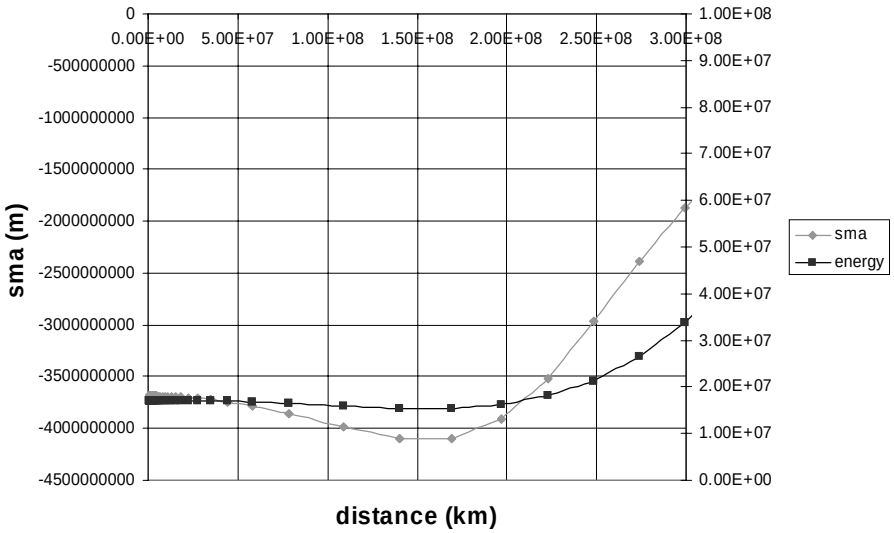

Figure 4.2.16. Semi-major axis with respect to Jupiter, evolution over distance from Jupiter.

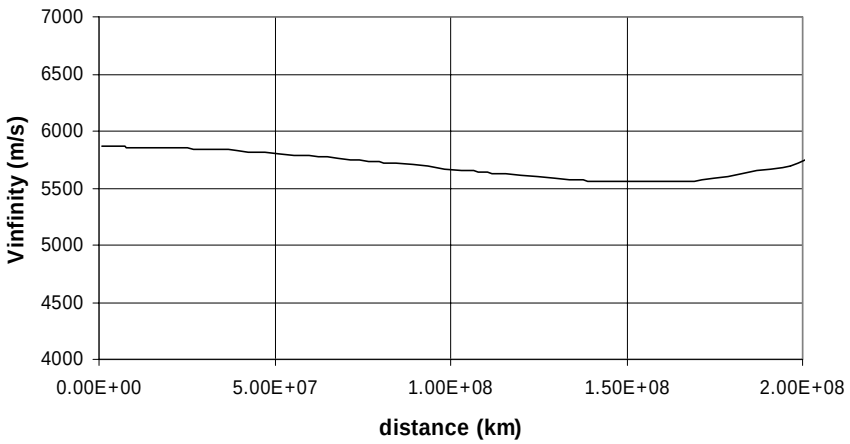

Figure 4.2.17. Excess hyperbolic speed with respect to Jupiter, evolution over distance from Jupiter.

from the pericentre values when distances of approximately 1 AU from Jupiter are reached.

The quantity that is again most conserved is the Jacobi constant. Jupiter's actual orbit has an eccentricity of more than 0.048. The variation in the angular velocity, a key component in the Jacobi constant therefore shows greater variation over an orbital period than in the Earth departure case. Because the orbit is slightly elliptical the angular velocity of Jupiter about the Sun changes with its orbital location and the elapsed time. The conditions of the circular, restricted three-body problem are

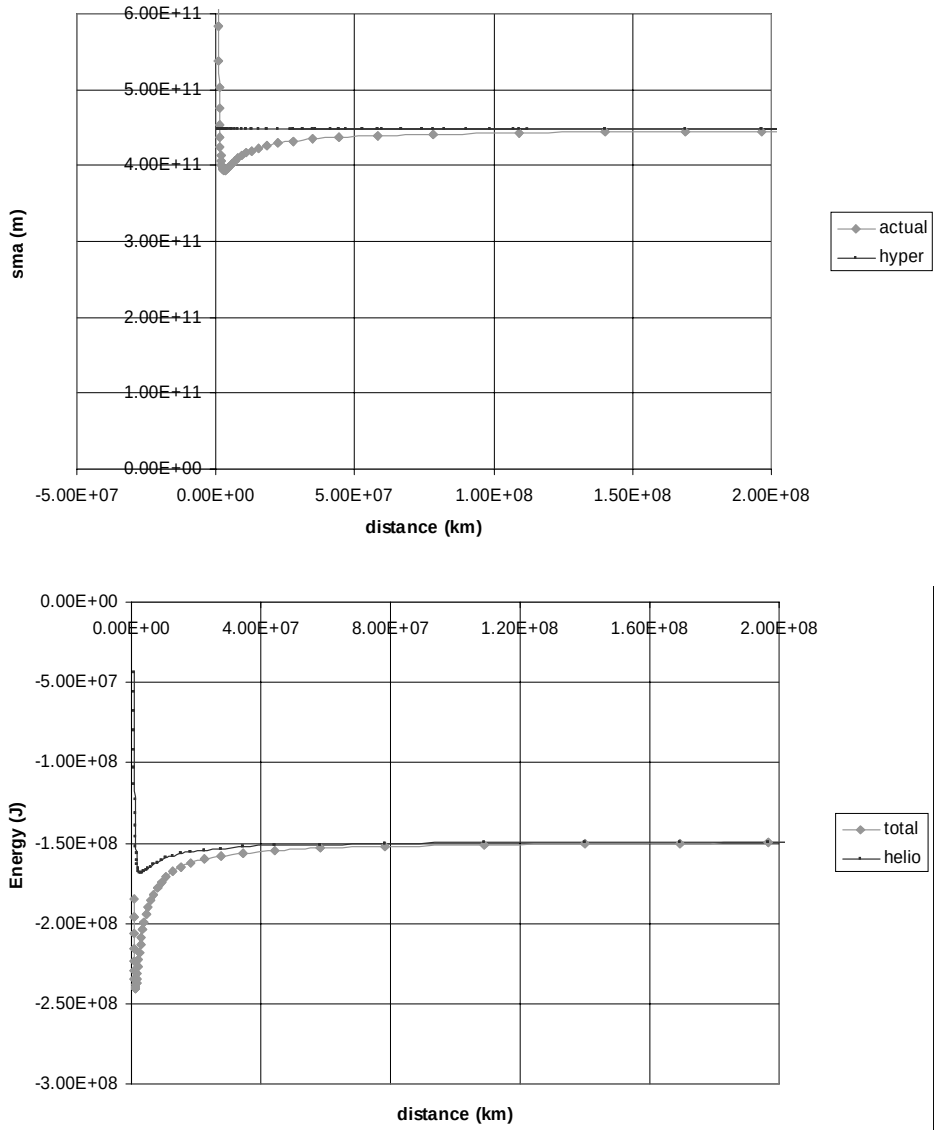

Figure 4.2.18. Semi-major axis and energy with respect to Sun, evolution over distance from Jupiter. In the upper figure, evolution of the semi-major axis asymptotically tends towards the expected value – the value calculated by the tangential vector addition of the initial excess hyperbolic speed. However, as previously seen, the effective escape velocity is higher than might be expected from the pericentre prediction and so the perihelion of the transfer is slightly lower. The semi-major axis therefore reaches an asymptote slightly below the predicted value. In the lower figure total and Sun relative energy values converge towards an asymptote. This convergence is slower than the Earth departure case. Examination of this evolution close to Jupiter again shows that considerable variation in Sun relative energy occurs when inside Jupiter's sphere of influence.

therefore no longer observed and the quantity C (the Jacobi constant, as defined previously) will no longer be a constant of the motion. However, the eccentricity is low and so a large deviation from the circular case is not observed.

4.3 PRINCIPLES OF GRAVITY-ASSIST MANOEUVRES

One of the most effective and elegant methods that may be employed in interplanetary mission transfer design is the gravity-assist manoeuvre. The technique can be used both in transfers from planet to planet and also for transfers between bound planetary orbits by using orbiting moons. Certain terms used previously will be retained: central body is the body about which the secondary body orbits. This secondary could be a planet or moon and is referred to as the major body.

4.3.1 Analysis of patched conics

The effect on a spacecraft of a fly-by of a major body within a dominant central gravity field can only be predicted precisely by numerical integration, when flying within the domain of the combined gravity fields. However, approximation is possible by considering the motion as a sequence of phases with dominant influences.

The first phase is the approach to the major body. This is an arc of an orbit about the central body. Far from the major body its gravity field can be neglected. The second phase starts when the spacecraft reaches the sphere of influence of the major body. Now the gravity field of that body dominates the gravitational forces. Eventually the spacecraft will pass outside of this sphere of influence and return to a region where its motion is dominated by the central body. These three phases – approach, fly-by and departure – can be analysed independently to predict the total effect on the motion of the spacecraft. The major interest lies in the change in orbit (with respect to the central body) from before to after the fly-by.

This technique is known as the patched conic method, because three conic sections are generated to describe the orbital phases. The first is that of the approach orbit, expressed in terms with respect to the central body. This may be any kind of orbit (elliptical or hyperbolic). The second is the fly-by orbit, expressed in terms relative to the major body. This will be a hyperbolic orbit (otherwise a fly-by could not occur). The third is again expressed in terms relative to the central body and may once again be any kind of orbit.

The different phases of this event can be evaluated to obtain a method for prediction of the effect of a gravity assist at a major body. A discussion on patched conics can be found in the references for this section.

The approach phase

A number of terms may be derived regarding the spacecraft orbit approaching the rendezvous with the planet, by considering only Keplerian motion with respect to the

central body. This approximation is good when the gravity field of the central body is significantly greater than that of the major body under consideration.

The speed of the spacecraft with respect to the central body, when at the major body's location, is given by $V = \sqrt{2 * \mu_C{}^* \left(\frac{1}{r_{planet}} - \frac{1}{2a} \right)}$

Here, r_{planet} is the radius of the planet at the fly-by and μ_c is the gravity constant of the central body. This need not imply a circular orbit for the major body, but the analysis is simplified if circular orbits may approximate the major body's orbit. If the major body's orbit is elliptical, then r_{planet} will be determined by the intersection of its orbit with the approach orbit.

The true anomaly at the rendezvous (in the example of an initially elliptical orbit with respect to the central body) is $\cos\theta = \frac{1}{e}\left(\frac{a(1-e^2)}{r_{planet}} - 1 \right)$.

The flight path angle (Γ) at rendezvous with the major body is given by $\tan\Gamma = \frac{e\sin\theta}{1 + e\cos\theta}$

The major body's speed at rendez-vous is given by:

$$V_{planet} = \sqrt{2 * \mu_c{}^* \left(\frac{1}{r_{planet}} - \frac{1}{2a_{Planet}} \right)}$$

where a_{planet} is the semi-major axis of the planet or major body. The relative velocity between spacecraft and major body is given by:

$$V_{rel}^2 = V_{planet}^2 + V^2 - 2\underline{V_{planet}} \cdot \underline{V} \tag{4.3.1}$$

In the case of a simplified, 2D analysis, where it is assumed that the major body and spacecraft orbits are coplanar, the speed relative to major body at rendezvous is given by geometry as:

$$V_{rel} = \sqrt{V_{planet}^2 + V^2 - 2V_{planet}V\cos(\Gamma - \Gamma_{planet})} = V_\infty \tag{4.3.2}$$

where the flight path angle of the planet (Γ_{planet}) at the rendezvous is found by:

$$\tan\Gamma_{planet} = \frac{e_{planet}\sin\theta_{planet}}{1 + e_{planet}\cos\theta_{planet}}$$

where e_{planet} is the eccentricity of the planet's orbit, and θ_{planet} is the true anomaly of the planet at the rendezvous.

This relative velocity is also the excess hyperbolic speed (as discussed in earlier sections regarding planetary escape orbits and the approximation therein).

The ephemeris relative to the major body or planet can now be found from the following expressions. The semi-major axis relative to the major body or planet is $a_{rel} = -\frac{\mu_{planet}}{V_{rel}^2}$, where μ_{planet} is the gravitational parameter of the planet.

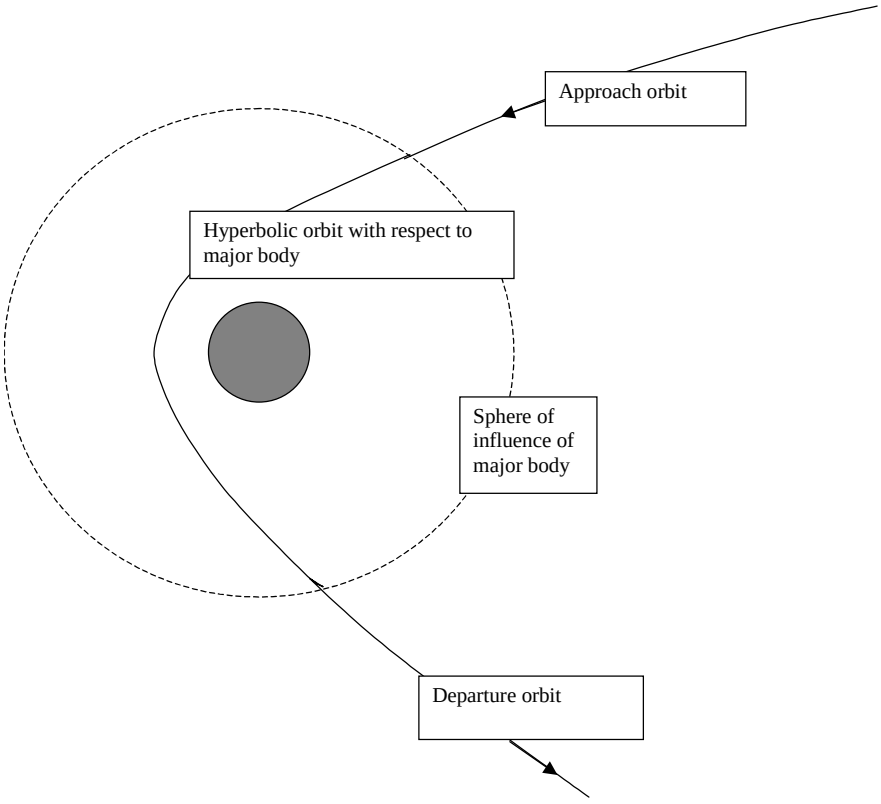

Figure 4.3.1. The principle of patched conics.

The planet relative eccentricity is $e_{rel} = 1 - r_{perirel}/a_{rel}$, where $r_{perirel}$ is the required pericentre radius of the major body's relative orbit. This is a parameter that can be specified in the design of the gravity assist.

Velocity with respect to the major body or planet at pericentre can also be found (although is not needed to model the gravity assist by patched conics):

$$V_{perirel} = \sqrt{2 * \mu_{planet} * \left(\frac{1}{r_{perirel}} - \frac{1}{2a_{rel}}\right)} = \sqrt{\frac{2 * \mu_{planet}}{r_{perirel}} + V_{\infty}^2} \tag{4.3.3}$$

The fly-by phase for a 2D case

A '2D' fly-by is a case where all orbits are assumed to be coplanar: spacecraft, major body and the spacecraft orbit relative to the major body. The B plane is defined as the plane that is perpendicular to the asymptotic approach velocity vector, which is also the excess hyperbolic velocity vector. If the spacecraft were undeflected by the

major body's gravity (e.g., if the gravity field is negligible) then the minimum approach distance (the fly-by pericentre) is the closest approach in the B plane.

Once the gravity field of the body becomes significant, the approach velocity vector is deflected, by following its hyperbolic path about the planet. Now from conservation of angular momentrum a different relationship can be obtained between fly-by pericentre and B plane distance (B_{dist}):

$$B_{dist} = \sqrt{\left(r_{perirel} + \frac{\mu_{planet}}{V_\infty^2}\right)^2 - \left(\frac{\mu_{planet}}{V_\infty^2}\right)^2} \tag{4.3.4}$$

where $r_{perirel}$ is the specified pericentre radius with respect to the major body, and μ_{planet} is the gravitational constant for the major body. The eccentricity is given by:

$$e = 1 - \frac{r_{perirel}}{a} = 1 + \frac{r_{perirel} * V_\infty^2}{\mu_{planet}} \tag{4.3.5}$$

The deflection angle of the relative velocity vector with respect to the major body is obtained from the true anomaly of the asymptotic departure vector. That is, if position is given by $r = \dfrac{a(1-e^2)}{(1+e\cos(\theta))}$, then as r tends to an infinite value the true anomaly is given by $\cos\theta = -\dfrac{1}{e}$. If the relationship between the approaching and departing asymptotic vectors is considered, the deflection of this velocity over the fly-by can be found. This is shown in Figure 4.3.2.

It can be seen that $2\pi - 2\theta = \pi - \alpha$, where α is the deflection angle of the aproaching hyperbolic vector. Using the previous expression for the true anomaly of the hyperbolic departure vector, an expression for the deflection angle is obtained:

$$\alpha = 2 * \sin^{-1}\left(\frac{1}{e}\right) \tag{4.3.6}$$

The deflection is clearly dependent on the excess hyperbolic speed with respect to the major body and its gravitational constant.

In Figure 4.3.3, Γ_{relp} is the angle between the planet velocity vector and the approaching relative velocity vector. For the sace of a 2D fly-by, deflection can take place in one of two possible directions, depending on which side of the the planet the spacecraft approaches. This is seen in Figure 4.3.4.

The flight path angle of the relative velocity vector wrt the major body's velocity vector is:

$$\Gamma_{relp} = \tan^{-1}\left(\frac{V * \sin(\Gamma - \Gamma_{planet})}{V * \cos(\Gamma - \Gamma_{planet}) - V_{planet}}\right) \tag{4.3.7}$$

The flight path angle of the departure velocity vector is obtained by velocity vector addition, as illustrated in Figure 4.3.5. This is given by:

$$\Gamma_{departure} = \tan^{-1}\left(\frac{V_\infty * \sin(\alpha + \Gamma_{relp})}{V_{planet} + V_\infty * \cos(\alpha + \Gamma_{relp})}\right) \tag{4.3.8}$$

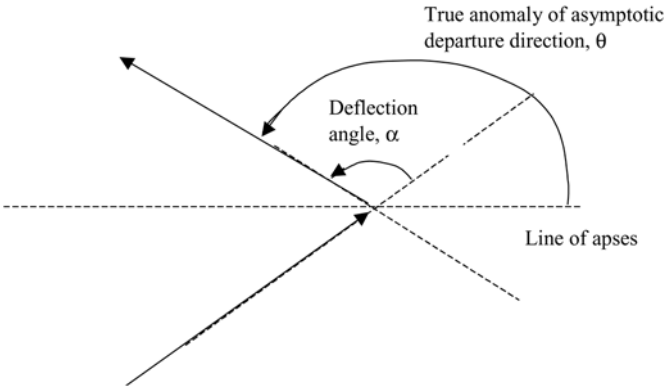

Figure 4.3.2. Deflection of the asymptote velocity vector.

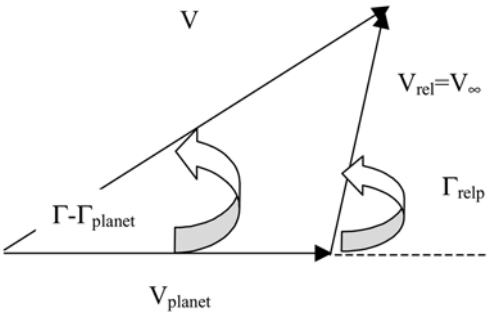

Figure 4.3.3. Geometry of the 2D fly-by with coplanar planet and spacecraft orbits.

The departure velocity is given by:

$$V_{departure} = sqrt((V_\infty * \sin(\alpha + \Gamma_{relp}))^2 + (V_{planet} + V_\infty * \cos(\alpha + \Gamma_{relp}))^2) \quad (4.3.9)$$

The departure energy per unit mass is given by:

$$E_{departure} = \left(\frac{V_{departure}^2}{2} - \frac{\mu_c}{r_{planet}} \right) \quad (4.3.10)$$

The departure semi-major axis is given by:

$$a_{departure} = -\left(\frac{\mu}{E_{departure} * 2} \right) \quad (4.3.11)$$

The departure angular velocity is given by:

$$h_{departure} = ((V_{departure} * \cos(\Gamma_{departure}) * r_{planet})) \quad (4.3.12)$$

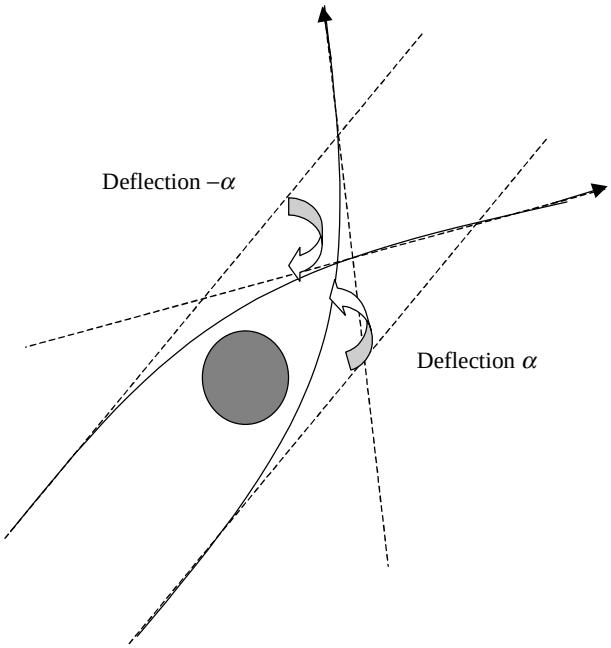

Figure 4.3.4. Alternative deflection possibilities for 2D fly-by.

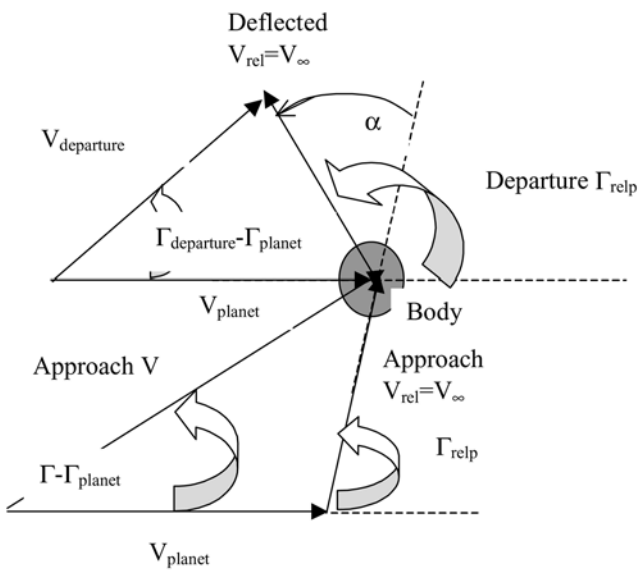

Figure 4.3.5. Velocity vector addition at the fly-by for a 2D case.

The departure eccentricity is given by:

$$e_{departure} = \sqrt{\left(1 + 2E_{departure}\left(\frac{h_{departure}}{\mu_c}\right)^2\right)} \tag{4.3.13}$$

If the departure energy is less than zero (a bound orbit), the aphelion radius is given by:

$$r_{ap\,departure} = a_{departure}(1 + e_{departure}) \tag{4.3.14}$$

If the energy is greater than zero, then escape from the central body is indicated. The corresponding excess hyperbolic speed is given by:

$$V_{\infty\,departure} = \sqrt{2 * E_{departure}} \tag{4.3.15}$$

The osculating perigee in both cases is given by:

$$r_{pe\,departure} = a_{departure}(1 - e_{departure}) \tag{4.3.16}$$

The departure state has been calculated as if the velocity undertook an instantaneous change in direction during the flight through the centre of the planet. Yet, the asymptotic arrival and departure excess hyperbolic velocity vectors only take their specified values at large distances from the planet. However, the previous discussions on escape from a planet (Section 4.2), have shown that the excess hyperbolic velocity when leaving a planet in a hyperbolic orbit may be treated as a velocity vector addition at the position of the planet. The same situation applies for an approach to a planet. The previous assumptions are therefore very effective in modelling the effects of a gravity assist manoeuvre.

If a more precise model is required, still using the ideas of patched conics, a time delay may be introduced to the departure, corresponding to the time taken for the spacecraft to traverse the sphere of influence of the planet. This is a relatively short time when compared with interplanetary mission durations, and often need not be included in the early stages of a mission design. In later stages, when planning actual manoeuvres at a planet, the motion of the spacecraft is obtained by numerical integration of the trajectory under the influence of the combined gravity fields.

When the geometry of the two orbits relative to the central body are considered, there are two opportunities for fly-by corresponding to the two orbit intersections seen in Figure 4.3.6. A special case arises when the orbit of the major body or planet is a circle.

If the orbit of the major body is circular, then at both intersections the relative velocity between spacecraft and planet (the asymptotic approach velocity vector) is the same in magnitude. The flight path angles of the spacecraft change sign at the two intersections. If both cases are subjected to identical fly-bys (in terms of the pericentre radius and on which side of the planet the fly-by takes place, relative to the forwards planet velocity direction), the deflection angle is the same in magnitude but opposite in direction. However, two fly-by solutions are possible using different sides of the planet (and the 2D gravity assist assumption) Equations 4.3.7 and 4.3.8 show that the departing flight path angles change in sign at the two cases, when the

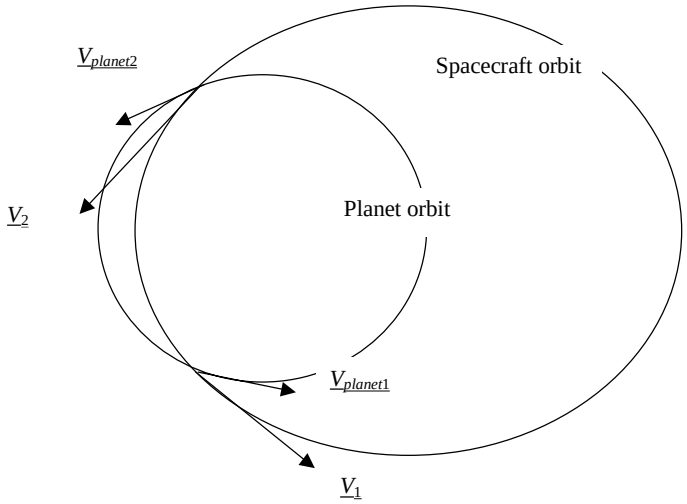

Figure 4.3.6. Two possible locations for a fly-by.

appropriate sign for the deflection angle is chosen. Also, in this situation, the magnitude of the departing velocity is the same in both cases. Hence both fly-bys produce the same change in semi-major axis. The departing angular momentum relative to the central body is the same in both cases, and both produce the same eccentricity. The difference is that the two fly-bys result in a different location for the longitude of the pericentre relative to the central body.

The example in Figure 4.3.7 shows a fly-by at location 1 close to the pericentre. The resulting gravity assist results in an increase in semi-major axis. Both apocentre and pericentre with respect to the central body are raised. The fly-by takes place after the new pericentre (which must lie at a radius relative to the central body less than that of the fly-by). The true anomaly of the post fly-by orbit is reduced in this example, and so the apse line of the new orbit is rotated, as shown in the diagram. The true anomaly after the fly-by, when still very close to the planet is given by:

$$\cos\theta = \frac{1}{e}\left(\frac{a(1-e^2)}{r_{planet}} - 1\right) \tag{4.3.17}$$

The longitude (λ) in the orbit plane of the spacecraft is almost unchanged over the fly-by (in this 2D case), and so as $\lambda = \omega + \theta$ then the argument of pericentre must be increased as depicted in Figure 4.3.7.

The same analysis can now be performed for a fly-by at location 2, as identified in Figure 4.3.6. In this case, the fly-by takes place before pericentre of the initial orbit. The same apocentre and pericentre raising of the post-fly-by orbit occur. The pericentre is now rotated towards the fly-by location again, but in an opposite sense to the previous example.

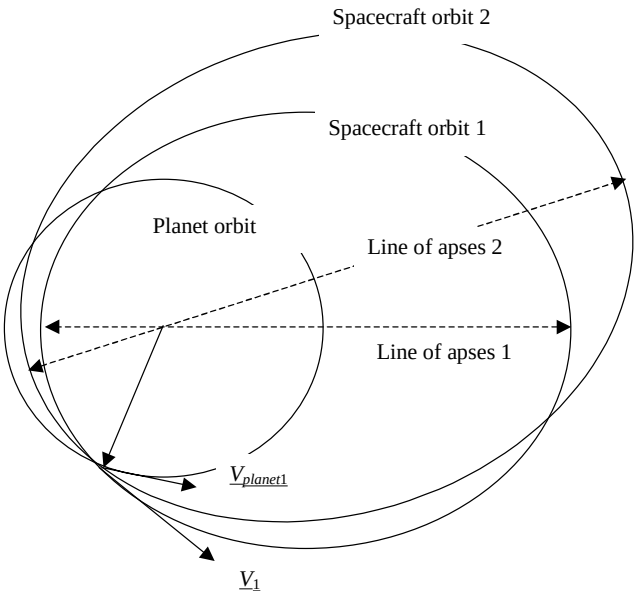

Figure 4.3.7. The rotation of the line of apses after a gravity assist at location 1.

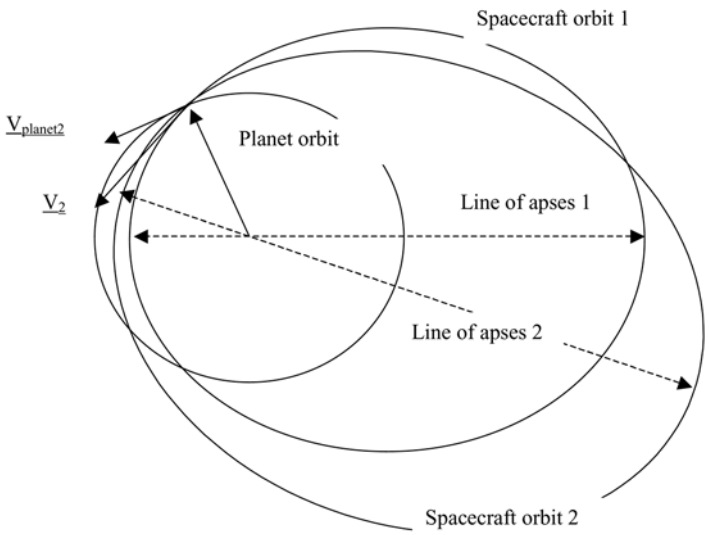

Figure 4.3.8. The rotation of the line of apses after a gravity assist at location 2.

The fly-by altitude and the gravitational constant of the major body have a significant effect. Close fly-bys result in much greater orbit deviation. This is illustrated in Figure 4.3.9.

The effectiveness of the gravity assist can be assessed by the change in the orbit ephemeris relative to the central body that is achieved after the fly-by. In the case of a

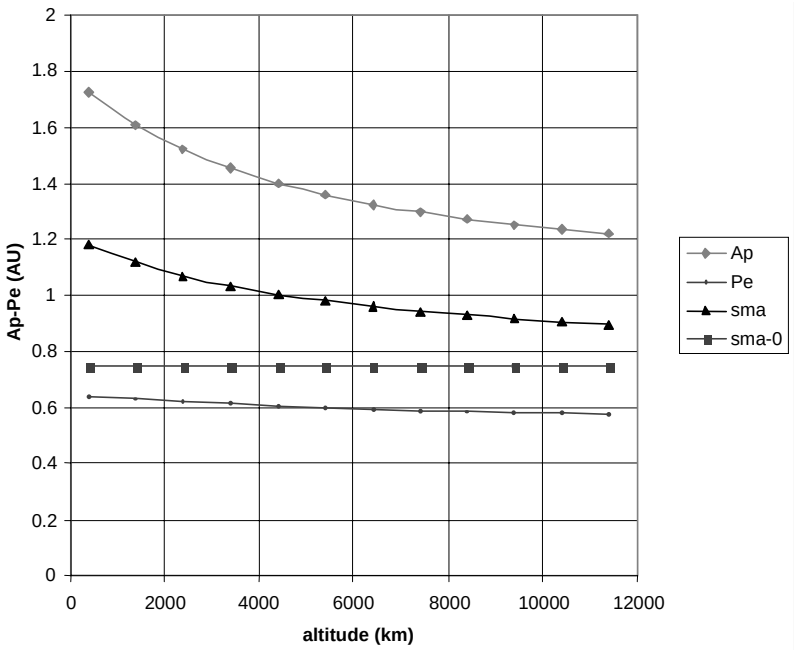

Figure 4.3.9. The effect of fly-by altitude on the final orbit. The plot shows the effect of the fly-by altitude for a gravity assist at Venus. In this plot, sma-0 is the initial semi-major axis, sma that after the fly-by and Ap and Pe the post fly-by aphelion and perihelion. It is assumed here that the initial aphelion lies at 1 AU and perihelion at 0.5 AU. The closest fly-by altitude considered is 400 km.

planar fly-by, the objective is generally to increase or decrease the energy of the spacecraft with respect to the central body. Figure 4.3.10 shows the effect of varying the approach orbit parameters and hence the excess hyperbolic speed relative to the major body.

The orbit in these cases is initially elliptical, with perihelion below the major body and aphelion higher than the major body's orbital radius. Different initial orbits are studied with different perihelions. The initial aphelion is the same in each case, and the objective of this gravity assist is to raise it.

In the first example, a gravity assist at Venus is considered. The aphelion is 1.0 AU, and perihelion is varied from just below Venus's orbital radius – 0.7 AU to 0.4 AU. This is typical of a spacecraft departing Earth and crossing Venus's orbit. In this case the fly-by altitude above the surface of Venus is 400 km.

The value of excess hyperbolic speed at which the maximum energy change occurs is dependent on the details of the initial orbit under consideration. The effect of repeating the above analysis for a case where the initial aphelion is at 1.2 AU is shown in Figure 4.3.11.

A similar analysis can be performed for Earth (Figure 4.3.12). The initial aphelion is assumed to be 1.1 AU, and this is then compared with a case at

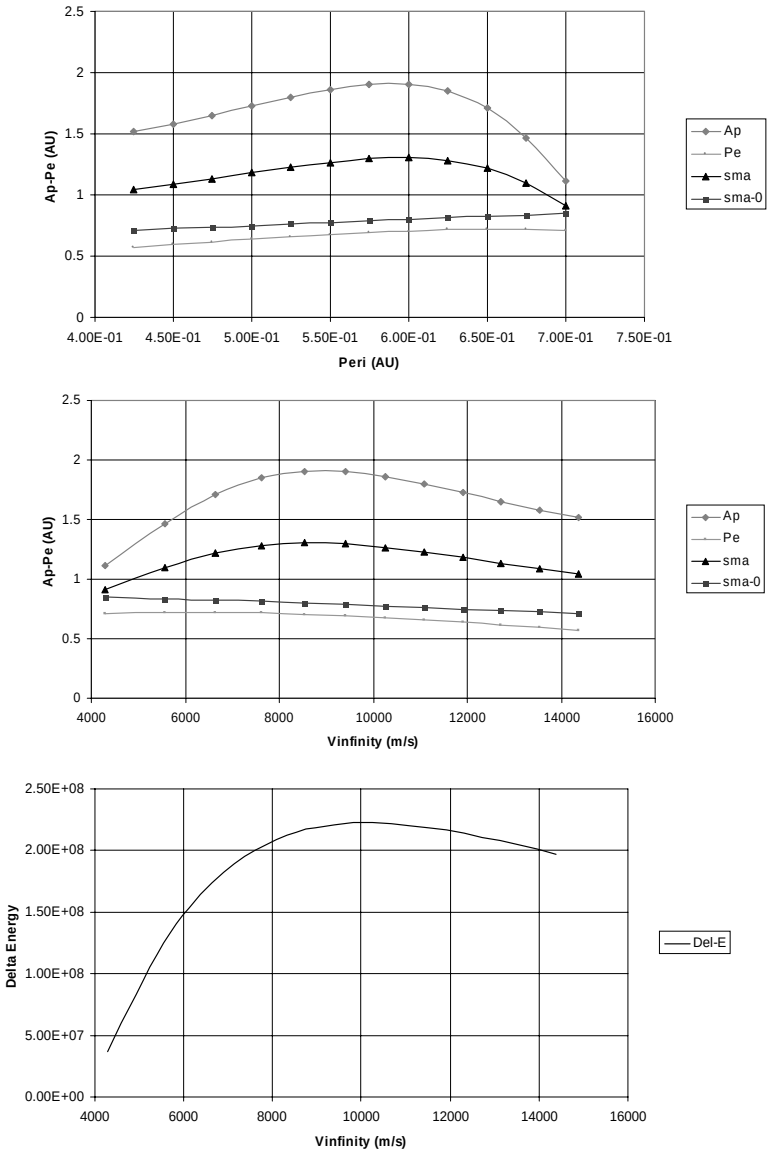

Figure 4.3.10. The effect of initial orbit perihelion and eccentricity on gravity assist effectiveness at Venus. In the upper figure, as the perihelion of the initial orbit is lowered a maximum in the achievable post-gravity assist semi-major axis is found. In the centre figure the presence of the maximum is related to the excess hyperbolic speed of the Venus approach orbit, and so in this example the maximum semi-major axis after the gravity assist is reached at 9 km/sec V_∞. The lower V_∞ corresponds to the higher initial perihelions shown in the upper figure. In the lower figure the variation in excess hyperbolic speed at the fly-by reveals an optimum value, in terms of maximising the energy change from before to after the gravity assist. The maximum is at approximately 10 km/sec V_∞.

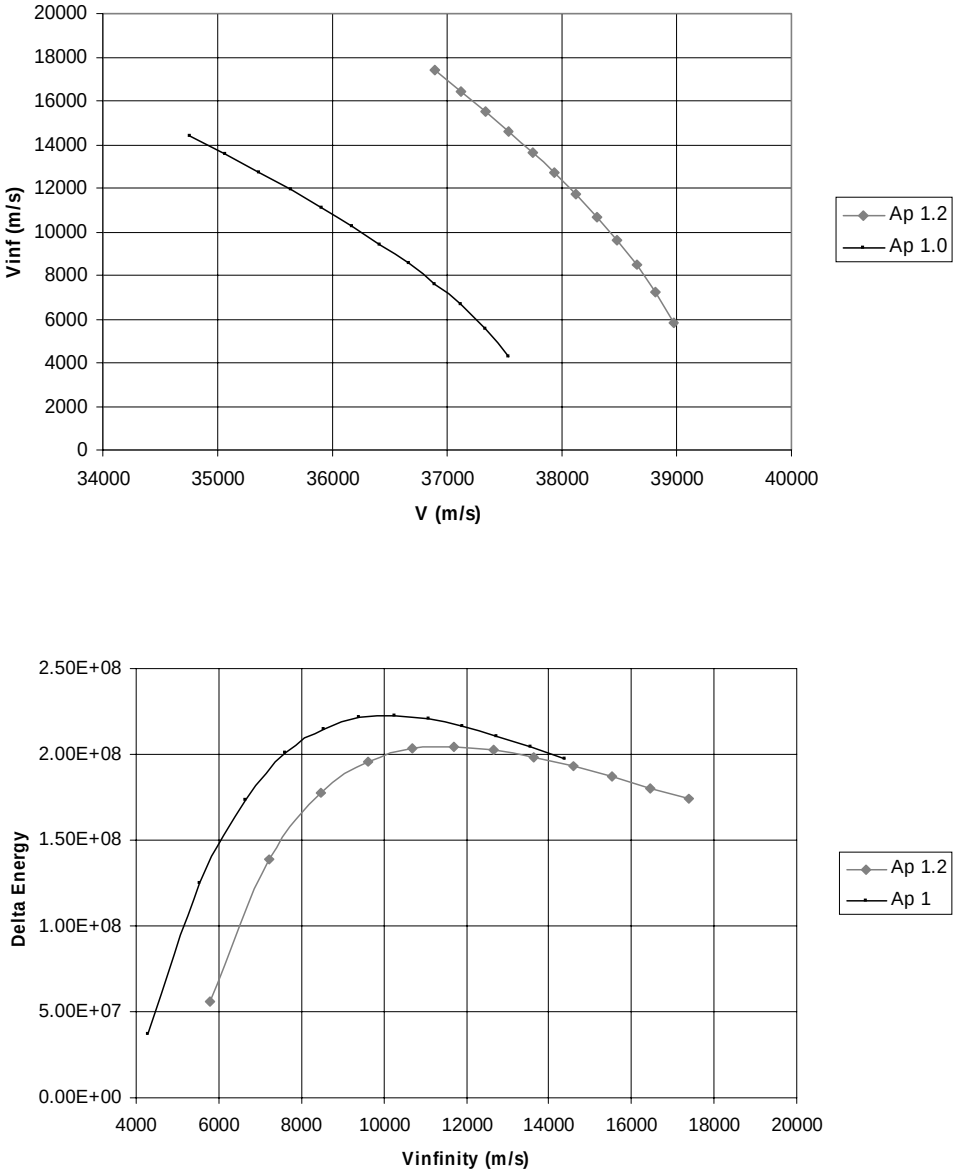

Figure 4.3.11. The effect of initial orbit excess hyperbolic speed on gravity assist effectiveness at Venus for different initial aphelions. In the upper figure, different initial orbit aphelion–perihelion relationships result in variations in the relationship between speed with respect to the central body (at major body orbital radius) and excess hyperbolic speed at the major body. In the lower figure, the optimum excess hyperbolic speed that maximises energy change is dependent on the details of the initial orbit (aphelion and perihelion). The lower initial aphelion is more effective at energy change at lower V_∞ when compared with the higher aphelion case.

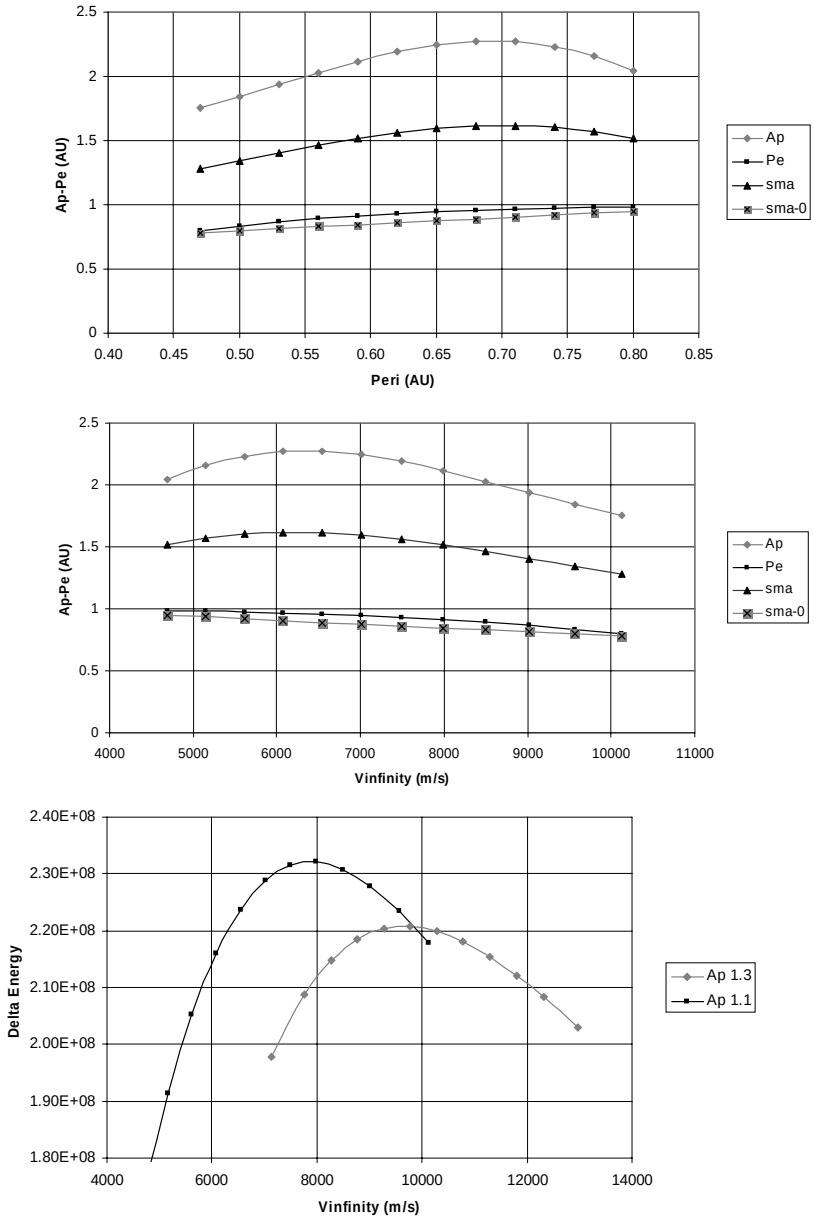

Figure 4.3.12. The effect of initial orbit perihelion and eccentricity on gravity assist effectiveness at Earth. The upper figure shows that, as in the example of Venus, lowering the perihelion of the initial orbit results in a maximum in the achievable post-gravity assist semi-major axis. The centre figure shows that when related to the excess hyperbolic speed of the Earth approach orbit the maximum semi-major axis occurs at between 6 and 7 km/sec. In the lower figure, in the case of Earth gravity assist, the optimum excess hyperbolic speed that maximises energy varies between 8 and 10 km/sec for aphelions between 1.1 and 1.3 AU.

1.3 AU, for a range of perihelions and thus excess hyperbolic speeds. In this case the fly-by altitude above the surface of the Earth is 400 km.

The effect of fly-by gravity assists at a range of bodies will now be considered and compared. A higher speed for the major body is advantageous in achieving a greater change in the spacecraft orbit. This implies that major bodies at lower orbital radius may be used beneficially when compared with those at greater radii. However, the total scenario must be taken into account, as for a given orbit the excess hyperbolic speed and flight path angle will vary with the orbital radius of the major body at which the gravity assist is executed.

The efficiency of various major bodies in effecting orbital change can be illustrated within the Jovian moon system. The comparisons can be made in two ways. The first is to consider the four major Jovian moons in terms of their different orbits. However, to explore the effects of the fly-by geometry and orbital location, each moon is notionally assigned the same gravitational constant and radius (that of Ganymede for the results presented in Figure 4.3.13). A comparison can then be made using the true gravitational constants and radii. The properties of these moons are shown in Table 4.3.1.

The following comparisons (Figures 4.3.13 and 4.3.14) were made using an initial orbit with apocentre at 5 million km and pericentre varied from just below the moon's orbital radius down to approximately 200,000 km. The fly-by altitude in all cases is 400 km.

If the equal mass case is examined, then for a given pericentre the inner moons provide greater orbit-raising than the outer moons. As the pericentre is raised, the outer moons eventually provide the greatest orbit-raising, as the pericentre is raised above that of the inner moons. However, this is a compound effect and not just a function of the orbital velocity of a given moon, because the comparison is made with the same initial orbit and so the excess hyperbolic speed is different at each moon considered.

When the true gravity fields and fly-by radii are considered, the relative effectiveness of Europa is reduced in comparison with Io, as Io is considerably more massive than Europa. However, the relative effectiveness of Ganymede is improved, as it has the greatest mass of the set. Figure 4.3.14 shows the change in orbital energy when the true gravity fields are considered.

Case of a 2D gravity assist with ΔV applied at pericentre

The velocity at pericentre of the fly-by can be incremented with an impulsive ΔV:

$$V_{DVperirel} = V_{perirel} + \Delta V \tag{4.3.18}$$

The modified excess hyperbolic speed is given by:

$$V^2_{DV\infty} = V^2_{DVperirel} - 2\frac{\mu_{planet}}{r_{perirel}}$$

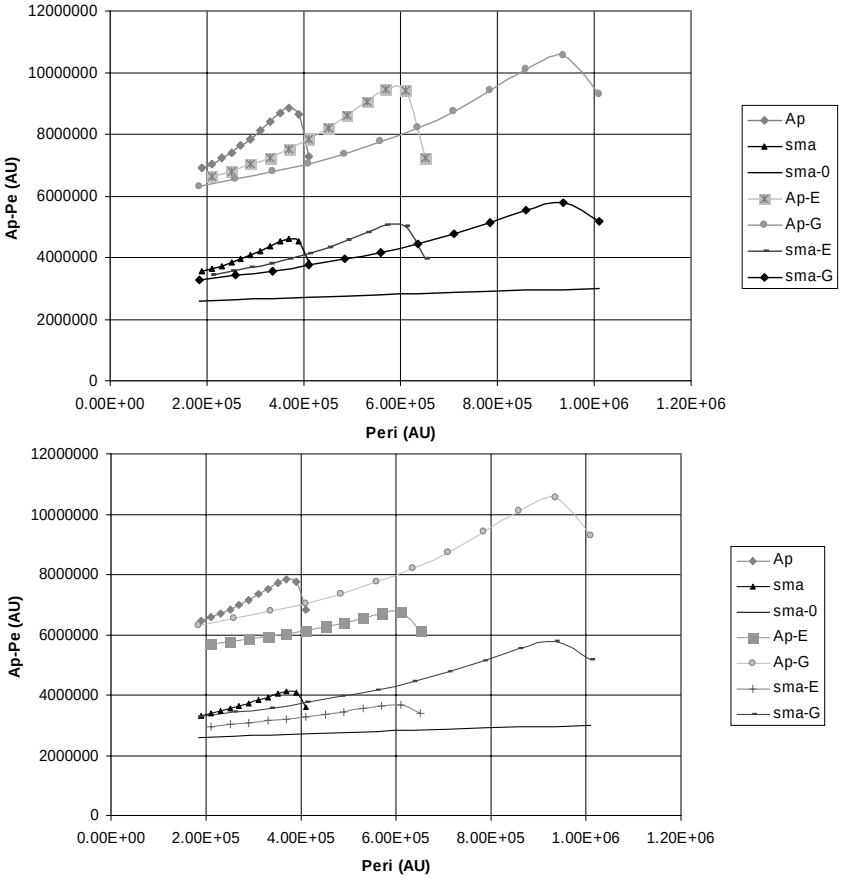

Figure 4.3.13. The effect of gravity assists at different Jovian moons for the same spacecraft orbits. The upper figure compares the effectiveness of orbit-raising at three notionally identical Jovian moons, in terms of their mass. Each is given the mass of Ganymede. The initial semi-major axis (sma-0) is shown for comparison with the post-gravity assist values at Ganymede (sma-G), Europa (sma-E) and Io, (sma). The corresponding post fly-by apocentres are also shown (Ap-). The lower figure compares the effectiveness of orbit-raising for the three real Jovian moons, including the different local gravity and fly-by radius effects. The initial semi-major axis is shown for comparison.

Table 4.3.1. Properties of the Jovian moons.

Moon	Semi-major axis (km)	Eccentricity	Inclination (deg)	Radius (km)	Gravitational parameter (m^3s^{-2})	Period (days)
Io	421,600	0.0041	0.04	1,821	$5.960 * 10^{12}$	1.77
Europa	670,900	0.0101	0.47	1,560	$3.203 * 10^{12}$	3.55
Ganymede	1,070,000	0.0015	0.195	2,634	$9.887 * 10^{12}$	7.15
Callisto	1,883,000	0.007	0.281	2,400	$7.180 * 10^{12}$	16.69

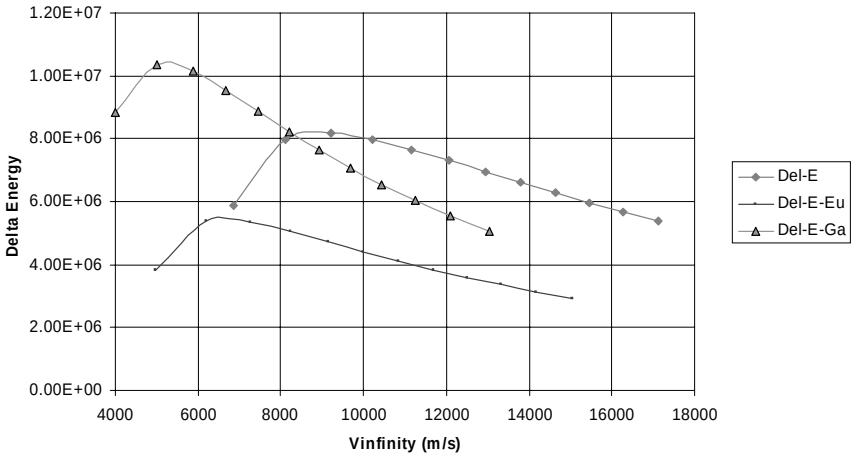

Figure 4.3.14. The effect of gravity assists on orbital energy at different Jovian moons for the same spacecraft orbits. Del-E-Eu, Del-E-Ga and Del-E are the energy changes after gravity assist at Europa, Ganymede and Io respectively. Different pericentres generate the V_∞ plotted on the horizontal axis.

The implied B plane distance for such a departure speed is:

$$B_{dist} = \sqrt{\left(r_{perirel} + \frac{\mu_{planet}}{V_{DV\infty}^2}\right)^2 - \left(\frac{\mu_{planet}}{V_{DV\infty}^2}\right)^2}$$

where $r_{perirel}$ is the specified pericentre radius for the flyby, and μ_{planet} is the gravitational constant for the major body.

The eccentricity of the departing orbit is $e_{DV} = 1 + \dfrac{r_{perirel} * V_{DV\infty}^2}{\mu_{planet}}$.

The total deflection angle of the modified excess hyperbolic velocity vector, if the spacecraft had possessed the corresponding approach velocity to yield the modfied velocity at pericentre, is given by:

$$\alpha_2 = 2 * \sin^{-1}\left(\frac{1}{e_{DV}}\right) \tag{4.3.19}$$

Here $\alpha_2/2$ is the deflection of the asymptotic departure vector from the pericentre velocity vector direction. The flight path angle of the approach relative velocity vector with respect to the major body velocity vector is that of the non-ΔV assisted case:

$$\Gamma_{relp} = \tan^{-1}\left(\frac{V * \sin(\Gamma - \Gamma_{planet})}{V * \cos(\Gamma - \Gamma_{planet}) - V_{planet}}\right)$$

However, the flight path angle of the departure velocity vector now uses a modified deflection:

$$\Gamma_{departure} = \tan^{-1}\left(\frac{V_{DV\infty} * \sin((\alpha + \alpha_2)/2 + \Gamma_{relp})}{V_{planet} + V_{DV\infty} * \cos((\alpha + \alpha_2)/2 + \Gamma_{relp})}\right) \tag{4.3.20}$$

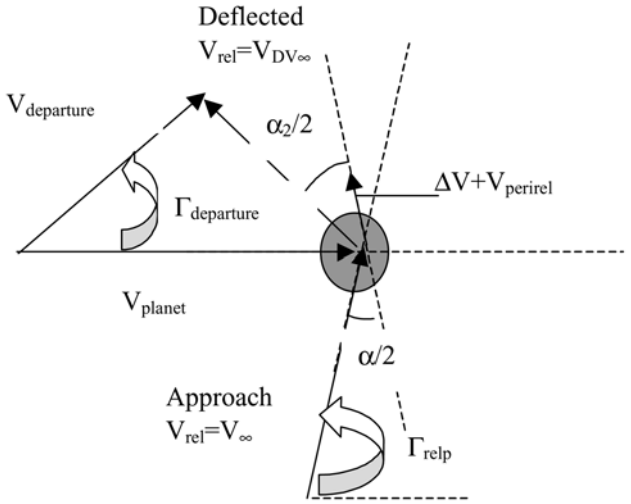

Figure 4.3.15. Velocity vector addition at the ΔV assisted fly-by.

This is illustrated in Figure 4.3.15. The departure velocity is given by:

$$V_{departure} = sqrt((V_{DV\infty} * \sin((\alpha + \alpha_2)/2 + \Gamma_{relp}))^2 + (V_{planet} + V_{DV\infty} * \cos((\alpha + \alpha_2)/2 + \Gamma_{relp}))^2) \quad (4.3.21)$$

Examples of the effectiveness can be seen by considering the example of a Jupiter gravity assist. This is illustrated in Figure 4.3.16. The method would be expected to be most beneficial when it is possible to apply the manoeuvre at pericentre in a strong gravity field. Jupiter gravity assist is well suited to such a manoeuvre.

An example is taken of a Jupiter-crossing orbit, typical of that obtained after a gravity assist from a two-year Earth-resonant orbit with aphelion ΔV applied (see Chapter 5 for details of such a mission). The nominal parameters at Jupiter are: aphelion, 5.012 AU; perihelion, 0.997 AU; Vinfinity at Jupiter, 6,176 m/s. Jupiter rendezvous is at 4.95 AU in this example.

4.3.2 Plane-changing by gravity assist

The preceding analysis is confined to the case where the fly-by takes place in the same plane as the body's orbit about the central body. However, this is not the only possibility. For a given, targetted fly-by pericentre radius, the intersection of the forward projection of the approach hyperbola with the B plane can take place at any point on a circle around the planet. A plane can be defined – the approach plane – as that plane containing the velocity vectors of the planet or major body targetted for the fly-by, and the asymptotic approach velocity vector of the spacecraft. This plane definition assumes an approach towards the centre of the target planet. The approaching velocity vector relative to the target major body (calculated

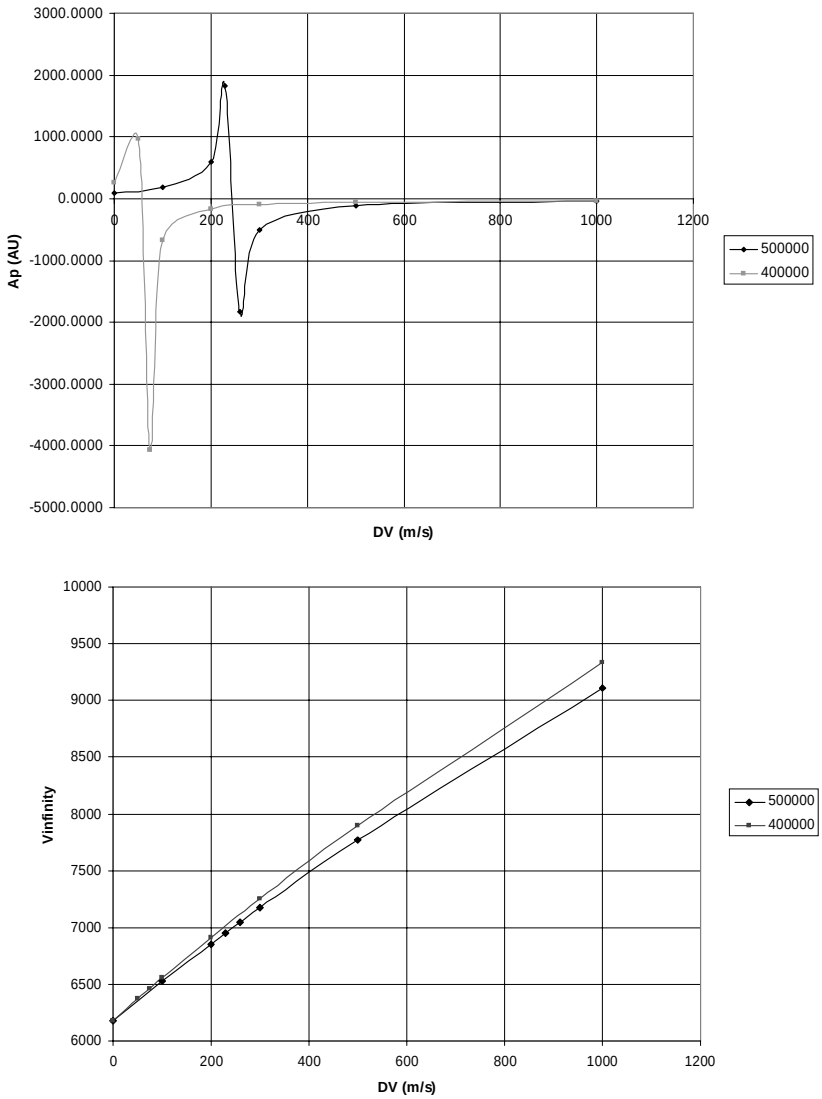

Figure 4.3.16. The effectiveness of ΔV at pericentre of Jupiter fly-by. The upper plot show the post-gravity assist orbit aphelion for two example fly-by altitudes at Jupiter (400,000 and 500,000 km). As the applied Jupiter fly-by ΔV is increased, the post-gravity assist aphelion increases such that it passes through plus and then minus infinity as a heliocentric escape condition is reached. A significant increase in the departure V_∞ relative to Jupiter is also seen as the ΔV is increased. This is seen in the lower plot, for two fly-by altitudes. The last plot (seen on next page) shows the effect of the fly-by altitude with respect to Jupiter on the departure V_∞. In this example, a ΔV of 100 m/s at Jupiter pericentre is assumed. Reducing this altitude significantly increases the effectiveness of the manoeuvre. The ratio of increase in departure V_∞ to ΔV varies between approximately 3.5 and 6.8 as fly-by pericentre altitude reduces from 500,000 km to 60,000 km.

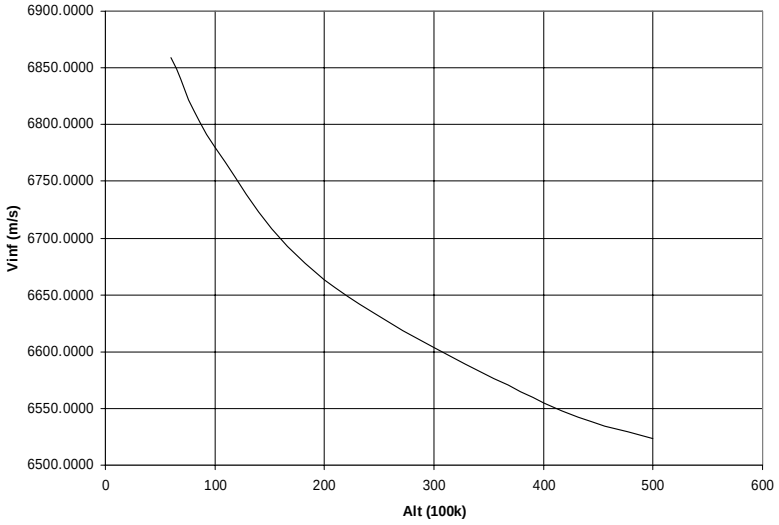

Figure 4.3.16. (*cont.*)

from the centre of the major body target) is therefore also contained within this approach plane. The approach plane and B plane are therefore perpendicular.

In Figure 4.3.17 an axis set, X_B, Y_B, Z_B is shown. The X axis lies along the intersection of the approach and B planes and the Y axis parallel to the direction of the approaching relative velocity vector. The Z axis is perpendicular to the approach plane. The Z axis is aligned with that subsequently defined in Figure 4.3.19. The Beta angle, β, is the angle between the X axis and the location of the intersection of the approach relative velocity vector with the B plane. Cases 1 and 2 in the figure are therefore at β of 0 and 90°.

In order to achieve an offset in the B plane, such as shown in approach case 2 in Figure 4.3.17 a small manoeuvre is performed by the spacecraft when at a very large distance from the major body. The resulting angular deviation in the approaching relative vector direction may be effectively neglected for this initial planning purpose. The key point is the ability to achieve a 360-degree range of Beta angles.

In certain situations it may be that the spacecraft's initial orbit is co-planar with that of the planet or major body, in which case the approach plane and the orbit plane of the major body are the same. The plane of the fly-by, with respect to the approach plane, is given here by β. Angles of 0° and 180° correspond to the 2D case described previously. Angles of 90° and 270° achieve a maximum out of approach plane deflection after the fly-by (a deflection relative to the approach plane).

The deflection angle of the fly-by relative velocity vector remains unchanged from that in the 2D fly-by case:

$$\alpha = 2 * \sin^{-1}\left(\frac{1}{e}\right)$$

where the eccentricity of the approach orbit relative to the major body, e, depends on the pericentre and approach excess hyperbolic speed.

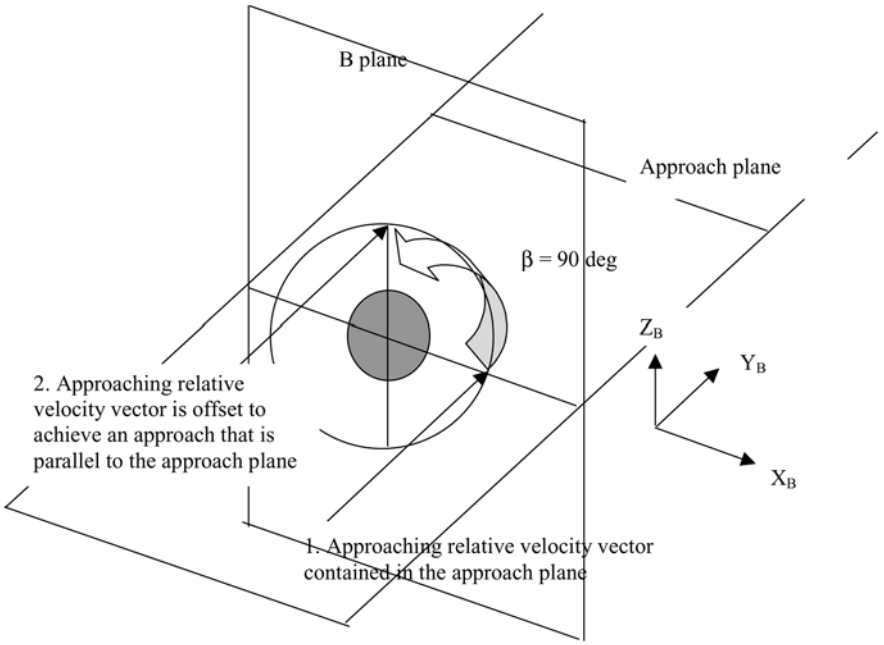

Figure 4.3.17. Definition of the B plane and approach plane.

Changes in this angle vary the effect of the fly-by-induced gravity assist on the departure orbit. The key parameter in this generalised 3D case is, as well as the post fly-by semi-major axis and eccentricity, the inclination of the departure orbit with respect to the central body.

It is now necessary to define a further plane, the *fly-by plane*, as the plane containing the approaching asymptotic velocity vector relative to the major body and also the departing asymptotic relative velocity vector. This plane is defined by the Beta angle, described previously.

It may be assumed that this deflection angle can be expressed in terms of two orthogonal rotations, firstly an angle α_θ in the approach plane, and then an angle α_ϕ perpendicular to this plane. The relationship between the Beta angle, β, and these rotations can be seen in Figure 4.3.18.

The relationship between the deflection angle components and the angle in the B plane, β, is now obtained by spherical trigonometry. It should be noted that α_θ is negative as shown in Figure 4.3.18. A Beta angle between 90° and 270° would be needed to achieve a positive angle.

Spherical trigonometry gives the following relationships:

$$\tan \alpha_\theta = \tan \alpha \cos(\pi - \beta) = -\tan \alpha \cos \beta \tag{4.3.22}$$

and

$$\sin \alpha_\phi = \sin \alpha \sin(\pi - \beta) = \sin \alpha \sin \beta \tag{4.3.23}$$

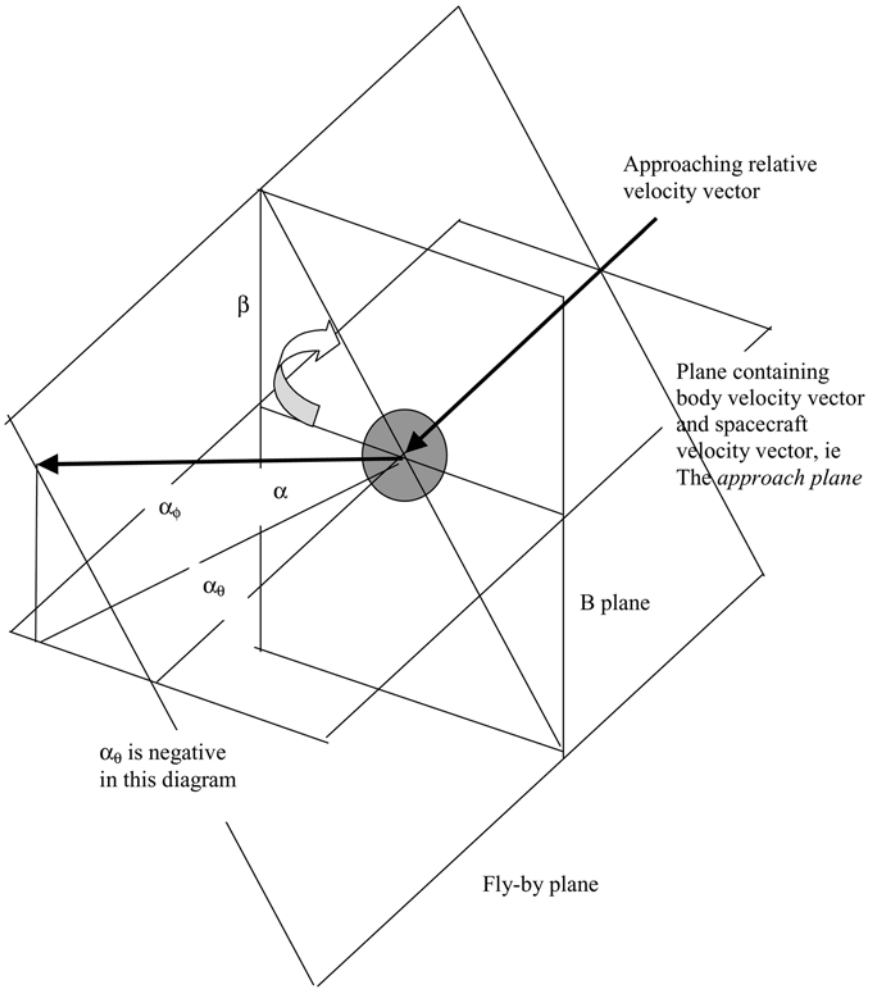

Figure 4.3.18. The fly-by plane and the relationship between Beta angle, deflection angle, deflection angle components and the approach plane.

These equations give the two angles defining the deflected direction of the departing body relative velocity relative to the approach plane.

Once the fly-by plane is known, by specification of the Beta angle, the deflection is effectively assumed to take place at the centre of the planet (as assumed in the previous 2D case calculations).

In Figure 4.3.19, the planet velocity, V_{planet}, and the initial relative velocity vector lie in the approach plane. The initial angle between these two vectors, in the co-planar, 2D case was given by Γ_{rel}. In the 3D case where the approach plane is not necessarily the orbit plane of the planet a more general notation is adopted, and this angle is defined as θ. V is the departing velocity in Figure 4.3.19.

The previous expressions are now modified as follows. Firstly, a frame of

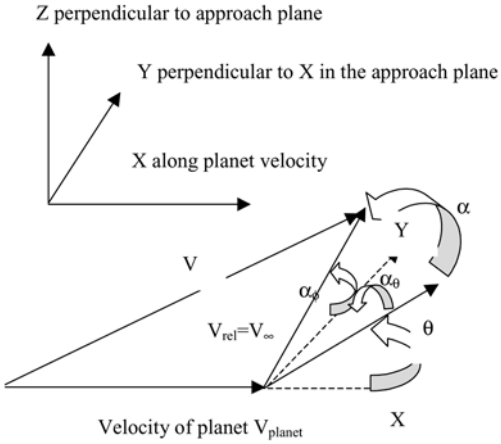

Figure 4.3.19. Definition of deflection angles and axis set.

reference is defined where X lies along the major body's velocity vector. Y is perpendicular to this and lies in the approach plane, and Z is orthogonal to the approach plane and completes the right-handed axis set. For near circular planet orbits Z is almost aligned with the negative spacecraft orbital angular momentum vector.

The fly-by Beta angle is allowed to take any value, by allowing the spacecraft's approach velocity vector to be displaced slightly from, but parallel to, the approach plane. The fly-by plane is defined in this way, but the effect of the fly-by will be evaluated by calculating the change in relative velocity vectors with respect to the major body. In this regard, the actual displacement of the approaching relative velocity vector does not play a role in the vector geometry that determines the subsequent departure calculations.

A vector algebra approach is now used to evaluate the effects of the fly-by. The approach velocity vector is expressed in the above frame as follows:

$$\underline{V_{ap}} = V_{apx}\hat{x} + V_{apy}\hat{y} + V_{apz}\hat{z}$$

$$V_{apx} = V_{planet} + V_\infty \cos\theta \tag{4.3.24}$$

$$V_{apy} = V_\infty \sin\theta \qquad \text{and} \qquad V_{apz} = 0 \tag{4.3.25}$$

where V_{planet} is the speed of the major body and V_∞ is the excess hyperbolic speed of the spacecraft with respect to that body. θ is the angle between the approaching relative velocity asymptote and the major body velocity vector. It is therefore an angle contained in the approach plane. In the previous co-planar, 2D case notation this is the angle Γ_{rel}.

The departing velocity vector can now be expressed in the previously defined frame as follows:

$$\underline{V} = V_x\hat{x} + V_y\hat{y} + V_z\hat{z}$$

$$V_X = V_{planet} + V_\infty \cos\alpha_\phi \cos(\theta + \alpha_\theta) \tag{4.3.26}$$

$$V_Y = V_\infty \cos\alpha_\phi \sin(\theta + \alpha_\theta) \tag{4.3.27}$$

$$V_Z = V_\infty \sin\alpha_\phi \tag{4.3.28}$$

The departure velocity is given by:

$$V_{departure} = \sqrt{(V_X^2 + V_Y^2 + V_Z^2)} \tag{4.3.29}$$

Therefore:

$$V_{departure} = \sqrt{(V_{planet}^2 + V_\infty^2 + 2V_{planet}V_\infty \cos\alpha_\phi \cos(\theta + \alpha_\theta)} \tag{4.3.30}$$

The angle of the departing relative velocity vector with respect to the major body velocity vector is:

$$\theta' = \cos^{-1}(\cos\alpha_\phi \cos(\theta + \alpha_\theta)) \tag{4.3.31}$$

The rotation of the plane containing the spacecraft and major body velocity vectors, about an axis along the major body's velocity vector, is given by:

$$\varphi = \tan^{-1}\left(\frac{V_Z}{V_Y}\right) \tag{4.3.32}$$

If the analysis is first performed by assuming that the spacecraft's initial orbit is co-planar with that of the fly-by body, the velocity vector of the spacecraft initially lies in the body's orbit plane. The approach plane and major body orbit plane then coincide. The resulting post fly-by inclination relative to the major body's orbit plane can then be calcuated by:

$$i_{departure} = \sin^{-1}\left(\frac{-V_Z}{V_{departure}}\right) \tag{4.3.33}$$

This assumes that the node of the new orbit lies at the planet's location at the fly-by.

The evaluation of inclination however, can be performed for any orientation of the approach plane with respect to the major body's orbit plane.

Calculation of initial relative conditions

In the previous discussion the evaluation of the actual initial relative velocity vector that defines the initial excess hyperbolic velocity was not considered. The co-planar, 2D case may rely on the use of flight path angles. However, in a general 3D case, the orbits of the spacecraft and planet will not be co-planar.

Firstly, the notation will be slightly modified such that the initial approach plane axis set, x, y, z, is now re-named x_0, y_0, z_0. This will become useful when multiple gravity assits are considered in a subsequent section. A new frame of reference is defined where X_M lies along the major body's velocity vector. Y_M is perpendicular to this and lies in the plane containing the major body velocity and position (its orbit plane), and Z_M is orthogonal to this plane and completes the right-handed axis set.

In Figure 4.3.20, θ_M is angle between the projection of the initial relative velocity vector into the body's orbit plane and the body velocity vector, and ϕ_M is the angle

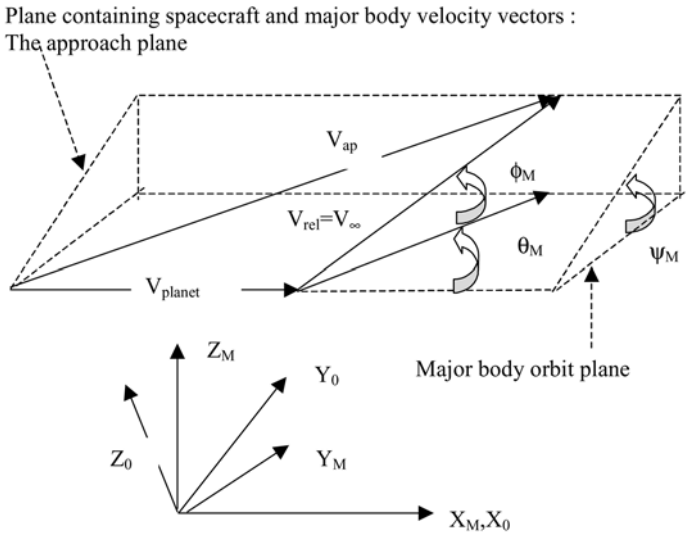

Figure 4.3.20. Definition of relationships between the initial approach plane and major body orbit plane.

between this projection and the actual initial relative velocity vector. The angle between the major body orbit plane and the initial aproach plane is given by ψ_M.

For such a fly-by, it is assumed that the initial velocity vectors of the spacecraft and major body will be defined. The orbital ephemeris will define these values at the epoch of the fly-by. Clearly, the orbits must intersect at that epoch. The direction cosines of the initial approach velocity vector to the planet, V_{ap}, relative to the planet orbit frame, then allow the calculation of the angles depicted in the figure.

$$\underline{V_{ap}} = (\underline{V_{ap}} \cdot \hat{X}_M)\,\hat{X}_M + (\underline{V_{ap}} \cdot \hat{Y}_M)\,\hat{Y}_M + (\underline{V_{ap}} \cdot \hat{Z}_M)\,\hat{Z}_M \tag{4.3.34}$$

The relative velocity (the excess hyperbolic speed) is expressed in this frame as:

$$\underline{V_{rel}} = (\underline{V_{ap}} \cdot \hat{X}_M)\,\hat{X}_M + (\underline{V_{ap}} \cdot \hat{Y}_M)\,\hat{Y}_M + (\underline{V_{ap}} \cdot \hat{Z}_M)\,\hat{Z}_M - V_{planet}\hat{X}_M \tag{4.3.35}$$

Then:

$$\begin{aligned}
\tan\theta_M &= \frac{(\underline{V_{ap}} \cdot \hat{Y}_M)}{(\underline{V_{ap}} \cdot \hat{X}_M - V_{planet})} \\
\tan\psi_M &= \frac{(\underline{V_{ap}} \cdot \hat{Z}_M)}{(\underline{V_{ap}} \cdot \hat{Y}_M)} \\
\sin\phi_M &= \frac{(\underline{V_{ap}} \cdot \hat{Z}_M)}{\sqrt{(\underline{V_{ap}} \cdot \hat{X}_M - V_{planet})^2 + (\underline{V_{ap}} \cdot \hat{Y}_M)^2}}
\end{aligned} \tag{4.3.36}$$

The angle between the initial relative velocity vector and the planet or major body velocity vector is given by:

$$\theta = \cos^{-1}(\cos\phi_M \cos\theta_M) \tag{4.3.37}$$

Calculation of the post-fly-by orbit

The previous expression for inclination, given in equation 4.3.33, is the inclination of the post-fly-by orbit relative to the approach plane. This can be converted to an inclination relative to the major body's orbit plane using the angle ψ_M derived previously and the values of the departure velocity, V_X, V_Y and V_Z calculated previously in a frame defined by the initial approach plane. Recalling that previously x, y, z notation is now x_0, y_0, z_0, $V_y = V_{y0}$ and $V_z = V_{z0}$ (i.e., equations 4.3.27 and 4.3.28).

$$V_{YM} = V_{Y0}\cos(\psi_M) - V_{Z0}\sin(\psi_M) \tag{4.3.38}$$

$$V_{ZM} = V_{Z0}\cos(\psi_M) + V_{Y0}\sin(\psi_M) \tag{4.3.39}$$

$$i_{departure} = \sin^{-1}\left(\frac{-V_{ZM}}{V_{departure}}\right) \tag{4.3.40}$$

The node of this inclined orbit (relative to the major body orbit plane) is defined by the position of the fly-by. The inclination may also be calculated with respect to the ecliptic, from consideration of the major body's orbit plane and the location of the fly-by with respect to the ascending node of the major body orbit.

The departure velocity has already been found from equation 4.3.29. This allows the energy and semi-major axis of the post fly-by orbit to be calculated.

Having now obtained the departure velocity with components relative to the major body's orbit plane it is possible to calculate the eccentricity of the departure orbit. The angular momentum of the departure orbit, per unit mass, is given by:

$$\underline{h} = \underline{r_{planet}} \wedge \underline{V} \tag{4.3.41}$$

where r_{planet} is the position vector of the major body. This can be expressed in the X_M, Y_M, Z_M axis set as:

$$\underline{r_{planet}} = r_{planet}\sin\Gamma_{planet}\,\hat{X}_M - r_{planet}\cos\Gamma_{planet}\,\hat{Y}_M$$

where Γ_{planet} is the flight path angle of the major body. For a circular orbit this will be zero.

The magnitude of the angular momentum is given by:

$$h = r_{planet}\sqrt{V_{ZM}^2 + (V_{XM}\cos\Gamma_{planet} + V_{YM}\sin\Gamma_{planet})^2} \tag{4.3.42}$$

which reduces to

$$h = r_{planet}\sqrt{(V_{ZM}^2 + V_{XM}^2)} \tag{4.3.43}$$

for the case of a circular planetary orbit.

The eccentricity of the spacecraft departure orbit may now be calculated from the expression:

$$h = \sqrt{\mu a(1-e^2)}$$

Examples of 3D gravity assist at the Jovian moons

Having seen the analytical predictions regarding orbit change for a 3D gravity assist, the effects of plane-changing gravity assists can best be assessed be examining specific cases. An example is a gravity assist at the Jovian moon Ganymede, which lies in a near circular orbit about Jupiter, with semi-major axis at 1.07 million km.

A range of initial orbits can be considered, each crossing Ganymede's orbit. In the following examples, the apocentre is 5 million km, and a range of pericentres from 500,000 km to 900,000 km are considered. The object is to generate a range of excess hyperbolic speeds with respect to Ganymede.

It is instructive to examine the change in orbital ephemeris for each pericentre. The initial orbits are then as shown in Table 4.3.2. The flight path angles and speeds are those of the initial Jupiter-centred orbit, when crossing Ganymede's orbit.

Figure 4.3.21 shows the effect of Beta angle on post-fly-by speed relative to Jupiter. This is done for a range of initial orbits about Jupiter given in Table 4.3.2, each defined by a different pericentre and therefore different hyperbolic speed relative to Ganymede. In each case it is assumed that the initial spacecraft orbit is co-planar with the orbit of Ganymede.

Figure 4.3.22 shows the affect of Beta angle on apocentre, pericentre and inclination after the fly-by.

An alternative visualisation (Figure 4.3.23) of the effect shows the achievable apocentre and inclination in a polar plot against Beta angle. Apocentre is along the radial axis and Beta the polar angle. Loci of semi-major axis/inclination for different pre-fly-by pericentres are shown in Figure 4.3.24.

It is possible to find a Beta angle that maintains the Jupiter relative speed, after the fly-by (that is, the semi-major axis is unchanged). This idea is useful if the spacecraft is to stay in a resonant orbit (the same orbital period about Jupiter). This strategy is described in detail in the next sections regarding multiple gravity assists. A 90-degree β angle (that maximises inclination change) results in some small change in the departure speed relative to the central body. Constant departure speeds (relative to the major body) that are needed to maintain the same resonance can generally be maintained by high β angles (approaching 90°). The exact value of β required depends on the approach orbit.

Table 4.3.2. Approach orbit parameters for plane-changing gravity assist at Ganymede.

Pericentre (km) (km)	Speed at Ganymede (m/s)	Vinfinity (m/s)	Flight path angle (deg)
500,000	13,803.64	9,853.09	43.445
600,000	13,833.40	8,900.53	38.140
700,000	13,862.06	7,954.81	32.829
800,000	13,889.67	6,990.59	27.282
900,000	13,916.30	5,975.76	21.114

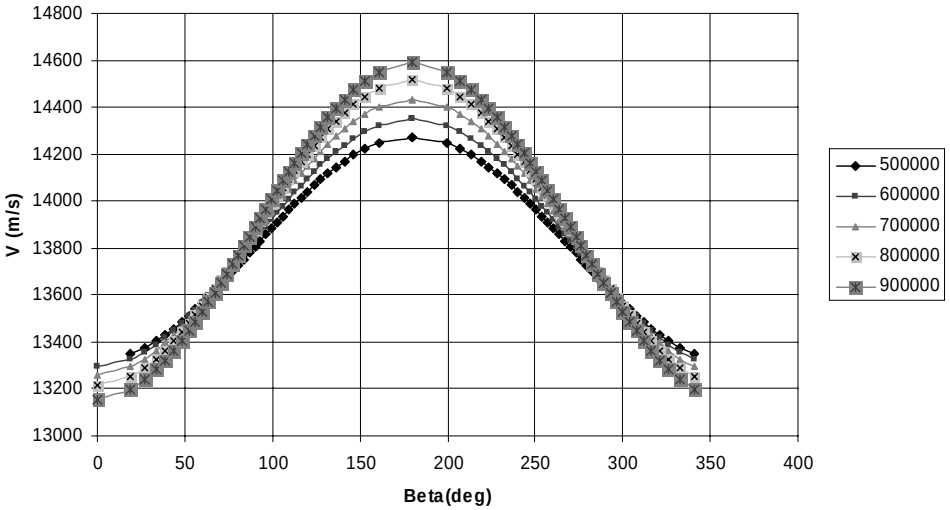

Figure 4.3.21. Post-Ganymede gravity-assist Jupiter-centred speed versus fly-by Beta angle, evaluated for a range of approach orbit pericentres from 500,000 to 900,000 km. Values of β at zero and 180° result in minimum and maximum velocity after the gravity assist.

4.3.3 Multiple gravity assists and resonance

The previous sections have shown the limitations on orbit change that may be achieved with gravity assist manoeuvres. However, gravity assists can be used in sequence to perform large modifications to the spacecraft orbit.

A particularly interesting phenomenon may be utilised involving repeated gravity assists at the same planetary body or moon.

This is the resonant gravity assist sequence. If a spacecraft executes a gravity assist its orbit on departure from that body will be modified. Generally the semi-major axis and thus the orbital period will be modified. It is possible to plan that the spacecraft revisits this same body at some subsequent epoch. Clearly, the phasing of the two orbits must be considered. A simple solution is for the spacecraft to reach, after its previous gravity assist, an orbit that is resonant with the body in question, so that after an integer number of revolutions the spacecraft will re-encounter the body. Resonance ratios of $n : 1$ (n revolutions by the spacecraft, 1 revolution by the body), $n : m$ (m revolutions by the body) or $1 : m$ can be used for this purpose. An interesting application is discussed in the references for this section.

In such a scenario, at the re-encounter the spacecraft will approach the body with the same relative velocity vector (or excess hyperbolic velocity vector) as it left after the previous gravity assist. A coplanar, 2D case is considered in the following analysis. The scenario is illustrated in Figure 4.3.25.

If the spacecraft now passes by the body with the same pericentre radius as the last, the hyperbolic deflection will also be the same as the last fly-by. However, the departing flight path angle will once again be modified with respect to the approaching flight path. Therefore, the absolute velocity, and consequently the semi-major

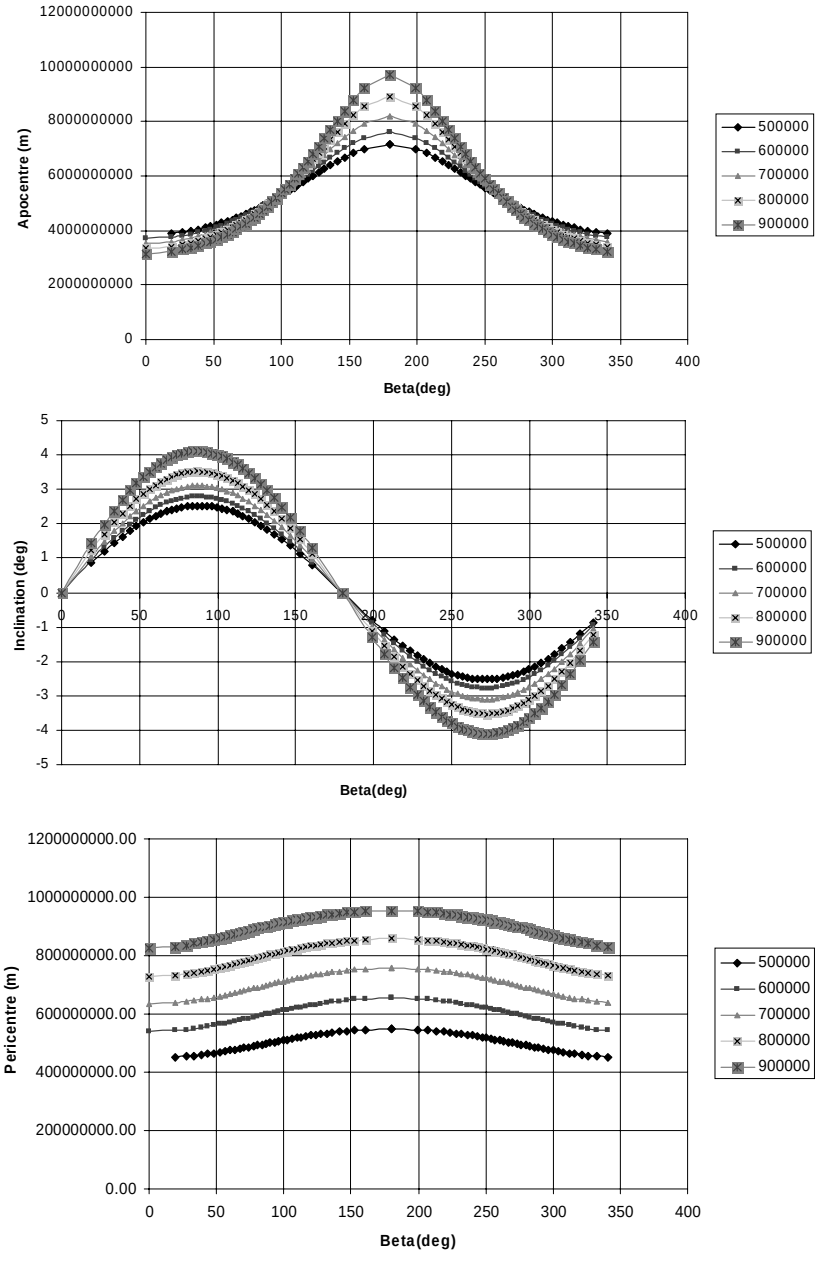

Figure 4.3.22. Post-Ganymede gravity-assist Jupiter-centred inclination, apocentre and pericentre change, versus fly-by Beta angle, evaluated for a range of approach orbit pericentres from 500,000 to 900,000 km. A β angle of 90° maximises the inclination change, but yields a small change in the subsequent apocentre and pericentre (and speed or semi-major axis). Inclination change here is measured with respect to the initial approach plane, which coinsides with Ganymede's orbital plane.

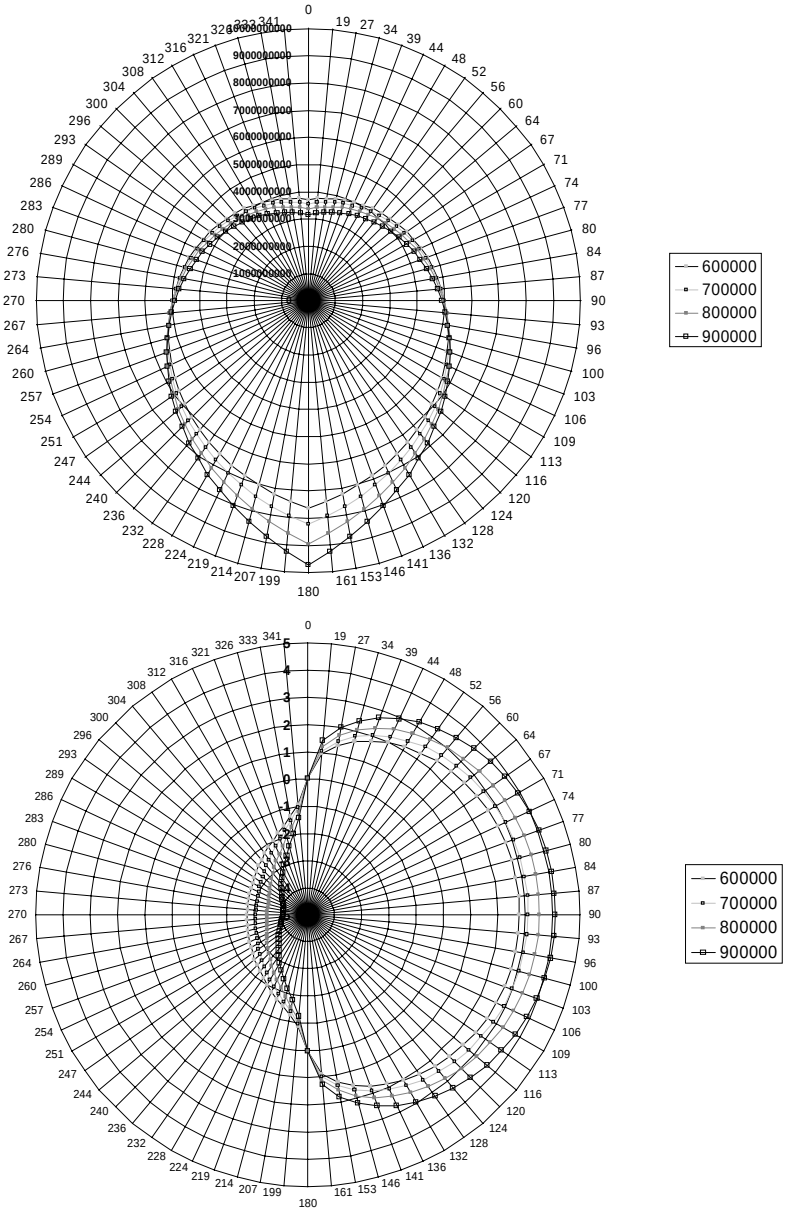

Figure 4.3.23. Post-Ganymede gravity-assist Jupiter-centred inclination and apocentre change, polar plot versus fly-by Beta angle, evaluated for a range of approach orbit pericentres from 600,000 to 900,000 km. In the upper illustration the Beta angle in this plot ranges through 360°. Apocentre radius is plotted for a range of initial orbit pericentres and therefore excess hyperbolic speeds at the target moon. In the lower figure, inclination is plotted (radial axis) for a range of initial orbit pericentres. Beta is the polar angle. Inclination change varies between approximately ±5° over the range of Beta angles.

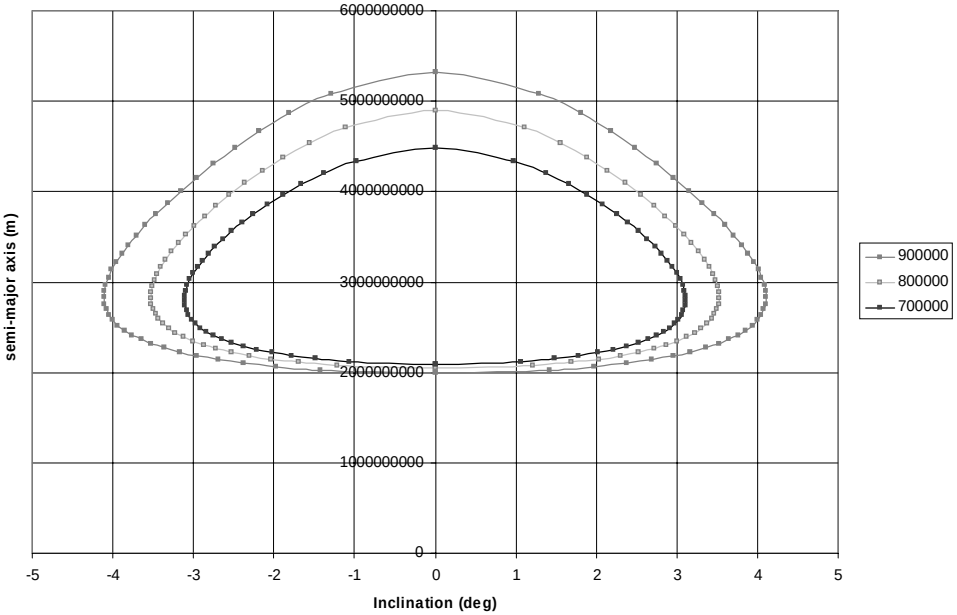

Figure 4.3.24. Post-Ganymede gravity-assist Jupiter-centred inclination and apocentre change loci, evaluated for a range of approach orbit pericentres, between 700,000 and 900,000 km.

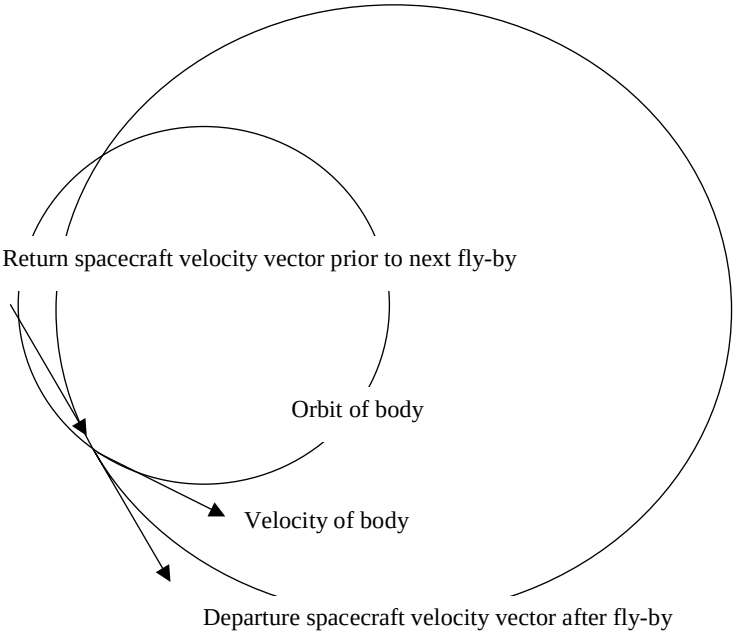

Figure 4.3.25. Relative velocity in a resonant orbit.

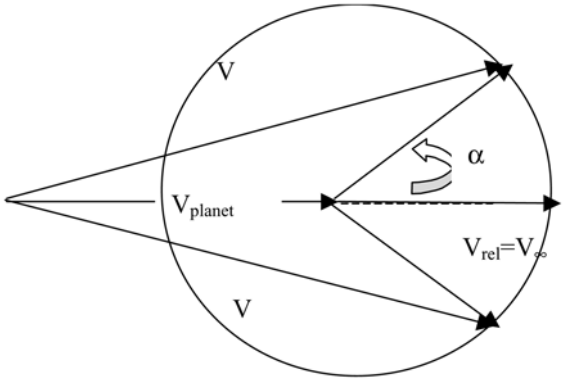

Figure 4.3.26. Limiting fly-by geometry. In this case the approach flight path is zero but after deflection the velocity is reduced. Therefore, speed after fly-by cannot be increased.

axis is further modified. Close inspection of the following equations for post fly-by speed shows that when the approaching flight path is zero or 180° it is no longer possible to progress in the previously accomplished increase or decrease of the speed after the fly-by. This phenomenon is illustrated in Figure 4.3.26. The flight path angle of the departure velocity vector in the case of a zero flight path angle is given by:

$$\Gamma_{departure} = \tan^{-1}\left(\frac{V_\infty * \sin(\alpha + \Gamma_{relp})}{V_{planet} + V_\infty * \cos(\alpha + \Gamma_{relp})}\right) = \tan^{-1}\left(\frac{V_\infty * \sin(\alpha)}{V_{planet} + V_\infty * \cos(\alpha)}\right) \tag{4.3.44}$$

The departure velocity is given by:

$$\begin{aligned} V_{departure} &= sqrt((V_\infty * \sin(\alpha + \Gamma_{relp}))^2 + (V_{planet} + V_\infty * \cos(\alpha + \Gamma_{relp}))^2) \\ &= sqrt((V_\infty * \sin(\alpha))^2 + (V_{planet} + V_\infty * \cos(\alpha))^2) \end{aligned} \tag{4.3.45}$$

Where the flight path angle is zero and so the approach speed is greater than the major body speed, the result after fly-by is always to reduce the post-fly-by speed. Such a scenario arises when the initial orbit has pericentre below the fly-by body and apocentre above. Progressive fly-bys are used to increase the semi-major axis until this limiting case is met. This occurs when the pericentre radius reaches the orbital radius of the major body (in a circular orbit case for the major body).

The location of the fly-by is fixed (with respect to the central body) by the resonance requirement. The maximum semi-major axis that may be obtained is:

$$V_{\max} = ((V_\infty + V_{planet})) \tag{4.3.46}$$

and therefore:

$$a_{\max} = \frac{1}{2\left(\frac{1}{r} - \frac{V_{\max}^2}{\mu}\right)} \tag{4.3.47}$$

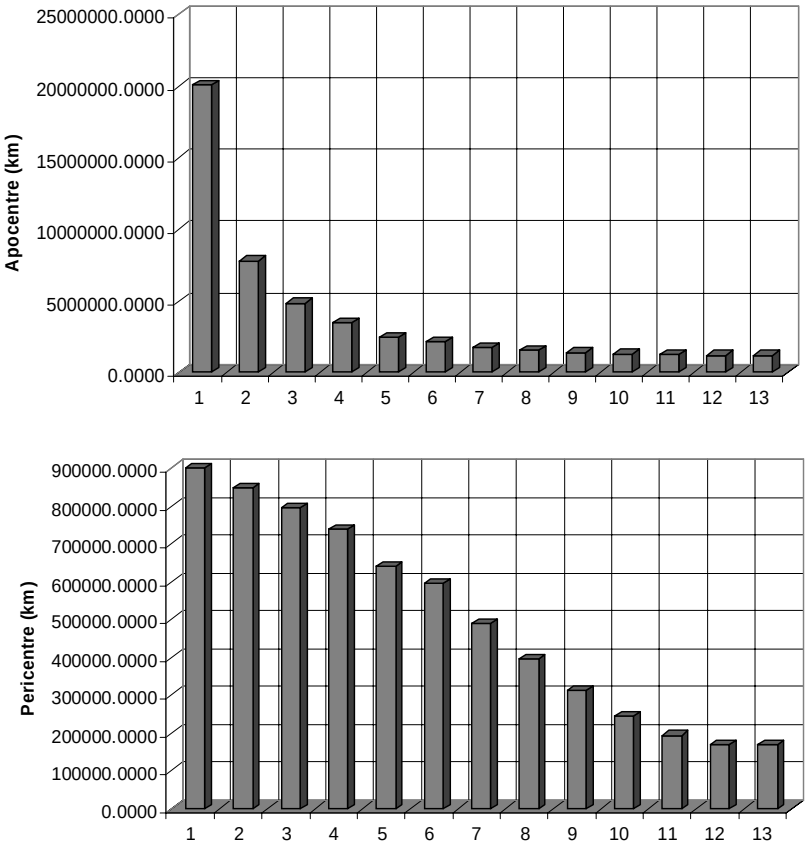

Figure 4.3.27. Apocentre and pericentre evolution for a Ganymede gravity assist sequence in the Jovian system. The initial orbit is apocentre = 20 million km, pericentre = 900,000 km. This orbit is typical of a capture orbit after the initial insertion manoeuvre. Ganymede's orbit = 1.07 million km.

Conversely, if a semi-major axis reduction sequence is being employed, the minimum apocentre speed is given by:

$$V_{\min} = ((V_{planet} - V_{\infty})) \tag{4.3.48}$$

defining the minimum semi-major axis. In this case the flight path angle is 180°.

An example of a resonant series is shown in Figure 4.3.27. The initial pericentre lies just below Ganymede's orbit, and the excess hyperbolic speed with respect to Ganymede is 6.65 km/sec. In order to maintain resonance, the post-gravity assist semi-major axis is tuned by adjusting the altitude of the fly-by pericentre. A minimum altitude of 200 km above Ganymede's surface is allowed. The resonant sequence adopted is shown in Table 4.3.3.

The evolution of the Jupiter relative orbit for such a sequence of resonant gravity assists is shown in Figure 4.3.28. Only the first four gravity assists and the

Table 4.3.3. Example of a resonant gravity assist sequence at Ganymede.

Target revs	Orbit Revs	Time between fly-bys (days)
31	1	221.70
8	1	58.41
4	1	30.74
3	1	20.04
2	1	12.53
3	2	21.23
11	10	77.85
9	10	61.68
3	4	20.33
2	3	13.00
3	5	19.05
4	7	25.05
1	2	6.93
3	7	22.35

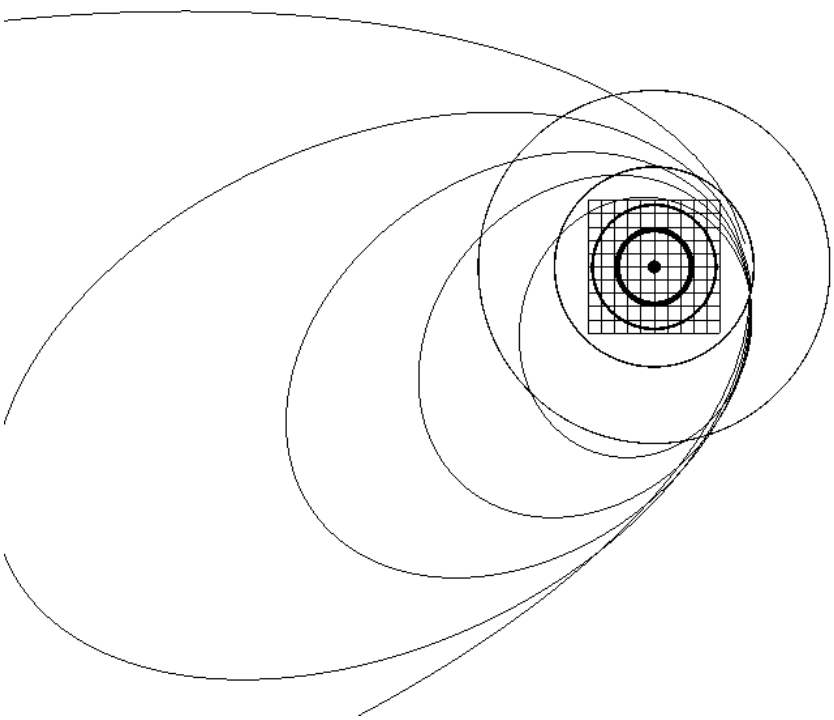

Figure 4.3.28. Examples for four resonant gravity assists at Ganymede.

resulting orbits are shown. The near circular orbits of the four major jovian moons – Io, Europa, Ganymede and Callisto – are shown. As the pericentre radius with respect to Jupiter is progressively reduced after each fly-by, the argument of pericentre is also changed, causing a progressive rotation of the line of apses.

4.3.4 Tisserand's criterion

Comets in the outer Solar System often pass close to Jupiter. In this situation a gravity assist fly-by takes place. Such encounters are not always precisely predicted or even observed. Therefore, if a comet is observed before and after a suspected gravity assist, some verification is helpful to determine if indeed this is the same comet under observation.

Tisserand derived a criterion from which it is possible to compare such perturbed orbits and deduce whether the relationship between them may be due to a gravity assist at a planet. The basis of the method is the circular, restricted three-body problem, details of which are described in previous section of this chapter. A discussion of Tisserand's criterion may be found in the references given for this section.

Recalling Jacobi's integral, $V^2 + 2U = -C$ – where C is a constant of the motion known as the Jacobi constant, V is the speed with respect to the rotating frame, defined by the motion of the planet about the central body in this case, and $\underline{\omega}$ is the angular velocity of that frame – Tisserand's criterion may be derived.

When motion is considered at a sufficiently large distance from the fly-by planet, its gravity field may be neglected. Also, the speed in the rotating frame may be converted to speed in an inertial frame, V_{IC}. Here r_c is the distance from the central body. μ is the gravitational parameter of the central body.

$$V_{IC}^2 - 2\omega(\underline{r_C} \wedge \underline{V_{IC}}) \cdot \hat{z} - \frac{2\mu}{r_C} = -C \tag{4.3.49}$$

This relationship is obtained from equation 4.1.35 but now the gravity potential of the major body is neglected.

Then, using the basic relationships, $V_{IC}^2 = \dfrac{2\mu}{r_C} - \dfrac{\mu}{a}$ from orbital energy (where 'a' is the semi-major axis) and the angular momentum per unit spacecraft mass, $h = \sqrt{\mu a(1 - e^2)}$, (where 'e' is the eccentricity) the above equation becomes $-\dfrac{\mu}{a} - 2\omega h \cos i = -C$ (where 'i' is the inclinaion), and so a relationship between semi-major axis, eccentricity and orbital inclination can be found that is preserved when comparing orbits before and after the gravity assist. If the motion is assumed to be planar (and the inclination is zero), the relationship simplifies further:

$$-\frac{\mu}{a_1} - 2\omega\sqrt{\mu a_1(1 - e_1^2)} = -\frac{\mu}{a_2} - 2\omega\sqrt{\mu a_2(1 - e_2^2)} \tag{4.3.50}$$

where 1 and 2 denote the states before and after gravity assist. This relationship can be used to examine the relationship between orbital period and pericentre before and

after a gravity assist. As such, it may be used as a design aid in planning a sequence of gravity assist manoeuvres. This may be particularly useful when all the permutations of gravity assist routes are considered, either in the case of an interplanetary transfer, or sequences of gravity assists at the Jovian moons. This technique has been used in the application to the design of gravity assist sequences at Jupiter, notably developed at JPL (Bonfiglio *et al.*) and Purdue University (Longuski *et al.*) (see references for this section).

If a particular planet is targeted for a gravity assist, and an initial, intersecting orbit defined, then the relative speed, or excess hyperbolic speed, may be calculated. This is a useful way to categorise the orbit. This may be obtained as follows. The planet or major body orbit is assumed circular, and the calculation simplifies to $V_{sc}^2 = \dfrac{2\mu}{r_{sc}} - \dfrac{\mu}{a_{sc}}$ for the spacecraft and $V_{planet}^2 = \dfrac{\mu}{r_{planet}}$ for the planet, where subscript 'sc' denotes the spacecraft orbit.

Then $V_{rel}^2 = V_{sc}^2 + V_{planet}^2 - 2V_{sc}V_{planet}\cos\Gamma$, where the flight path angle of the spacecraft orbit at the planet radius is given by:

$$\cos\Gamma = \sqrt{\frac{a_{sc}(1-e_{sc}^2)}{r_{planet}\left(2 - \dfrac{r_{planet}}{a_{sc}}\right)}}$$

The velocity relative to the planet may therefore be calculated. This is equivalent to the excess hyperbolic speed (in the patch conic approximations).

For a given initial spacecraft orbit and therefore for a given excess hyperbolic speed corresponding to the initial semi-major axis and eccentricity, the evolution of the possible orbits under repeated gravity assists at the target major body may be evaluated. The locus of the evolution of the orbital elements is given by the previous relationship, Tisserand's criterion, equation 4.3.50. This result defines a relationship between semi-major axis and eccentricity, or may be expressed as an apocentre–pericentre or orbit period–pericentre relationship. The use of the orbit period–pericentre relationship has been proposed as a useful relationship for transfer design (see references for this section).

This relationship can be evaluated at the Earth, for a range of excess hyperbolic speeds. Figure 4.3.29 shows the evolution of orbital period against pericentre radius.

Clearly, the sequence terminates when the perihelion rises to the orbital radius of the Earth at 1 AU.The equivalent relationship may be in terms of apocentre relationship to pericentre, shown in Figure 4.3.30.

The second, apocentre, plot shows the effect of the apocentre limit (it must exceed Earth radius), and as such limits the minimum pericentre radius for a given excess hyperbolic speed.

The maximum 'step' along such a curve, achieved at a gravity assist at the major body in question, is limited by the closest allowable fly-by distance. Close fly-bys result in greater progress along the curve. Also, because the same body is used for the fly-bys, resonance must be considered. Therefore, arbitrary steps are not possible but must be targeted to the closest resonant orbit. In fact when a general n : m resonance

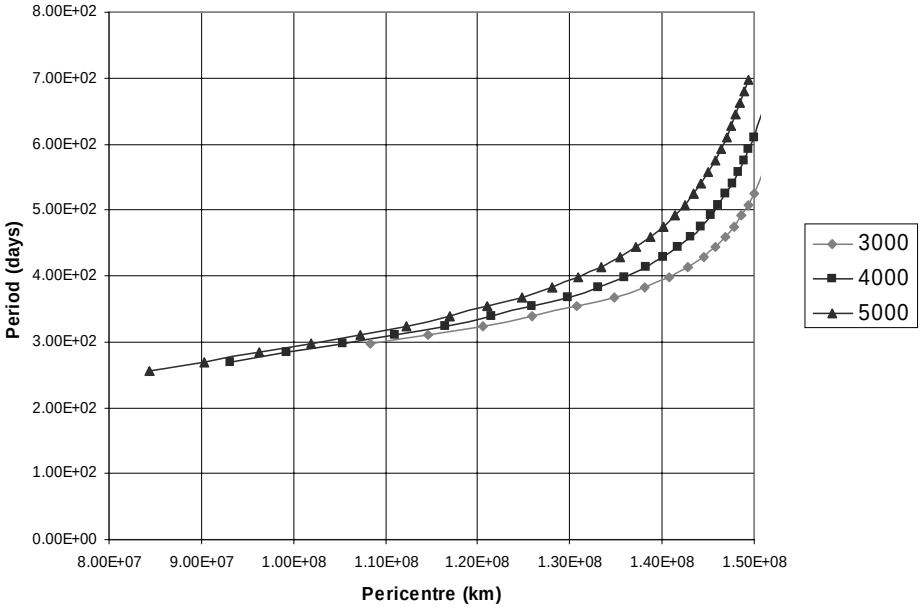

Figure 4.3.29. Orbital period–pericentre relationship for gravity assist at Earth for a range of excess hyperbolic speeds between 3,000 and 5,000 m/s.

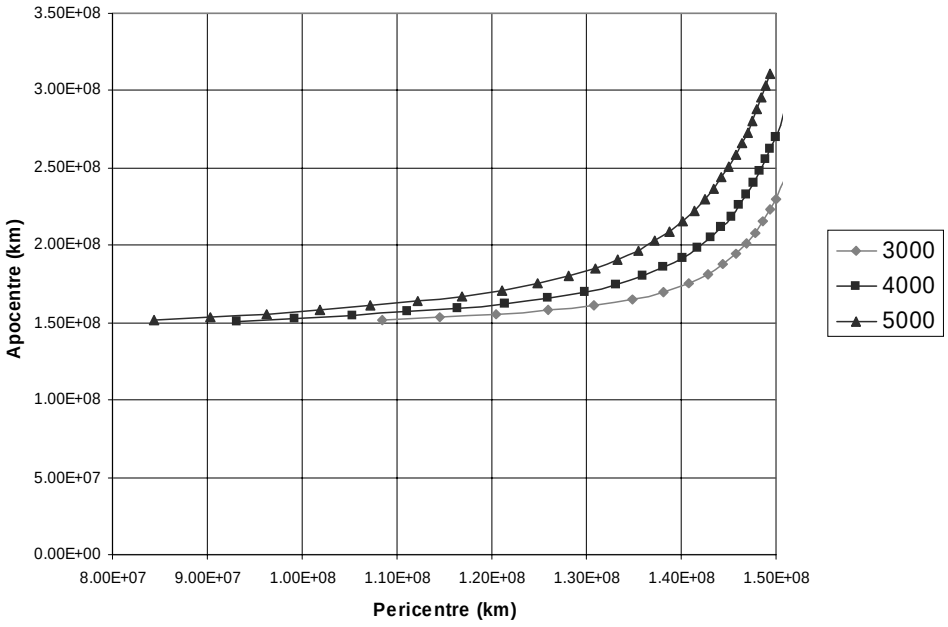

Figure 4.3.30. Apocentre–pericentre relationship for gravity assist at Earth for a range of excess hyperbolic speeds between 3,000 and 5,000 m/s.

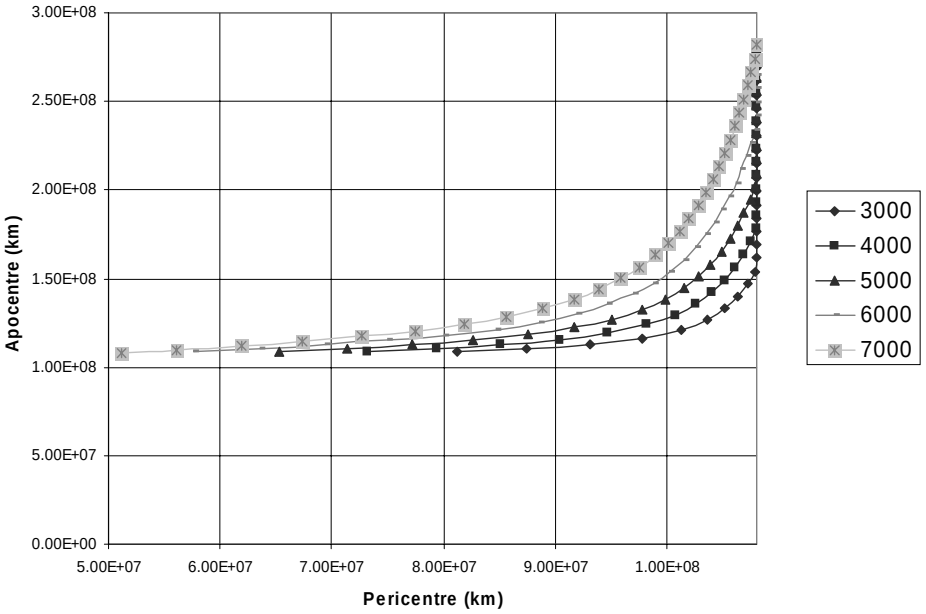

Figure 4.3.31. Apocentre–pericentre relationship for gravity assist at Venus for a range of excess hyperbolic speeds from 3,000 to 7,000 m/s.

is considered, it is possible to achieve a return at a second intersection of the two orbits and this therefore increases the flexibility of the sequence.

The same type of relationship for gravity assist may be found at Venus, as shown in Figure 4.3.31, for a range of excess hyperbolic speeds in which the limiting apocentre radius is that of Venus orbital radius. A sequence of gravity assists, starting from Earth and progressing to Venus, can be considered. Figure 4.3.32 shows the overlap of the orbits with the associated excess hyperbolic speeds at Earth and Venus.

For a given excess hyperbolic speed at Earth, an apocentre–pericentre relationship may be found crossing the excess hyperbolic speed curves at Venus. An example would be to consider the 4 km/sec excess speed at Earth. With aphelion at 1.5e8 km (1 AU) a perihelion of approximately 9.2e7 km can be achieved. This orbit crosses Venus, where an excess hyperbolic speed of 7 km/sec can be achieved (in fact, greater excess speeds at Venus are possible in this case). This curve may be followed (implying a sequence of gravity assists at Venus), until perihelion is lowered to just over 5e7 km. This is sufficient to achieve a rendezvous with Mercury. This analysis relies on the assumption that all orbit are co-planar.

This technique allows the achievable transfers to be quickly assessed, and as such is a valuable aid to planning gravity assist sequences.

A further interesting example can be considered at Jupiter's moons. Gravity assist loci at Callisto, Ganymede and Europa may be evaluated, and in this case the overlapping loci indicate the multitude of options for gravity assist combinations. If the target is to inject to an orbit at Europa (from an orbit with initially high

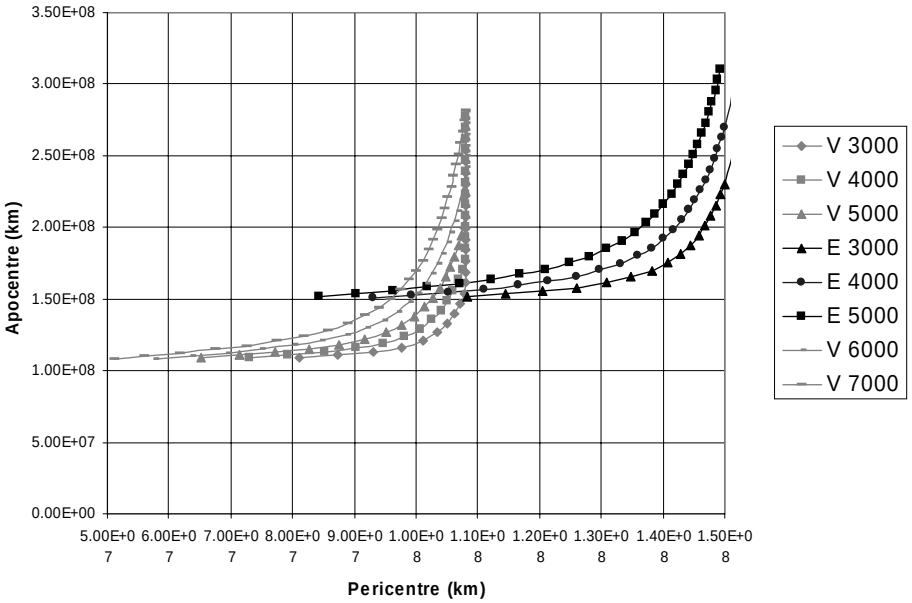

Figure 4.3.32. Apocentre–pericentre relationship for gravity assists at Earth and Venus for a range of excess hyperbolic speeds. Speeds of 3,000 to 5,000 m/s at Earth are considered, and 3,000 to 7,000 m/s at Venus.

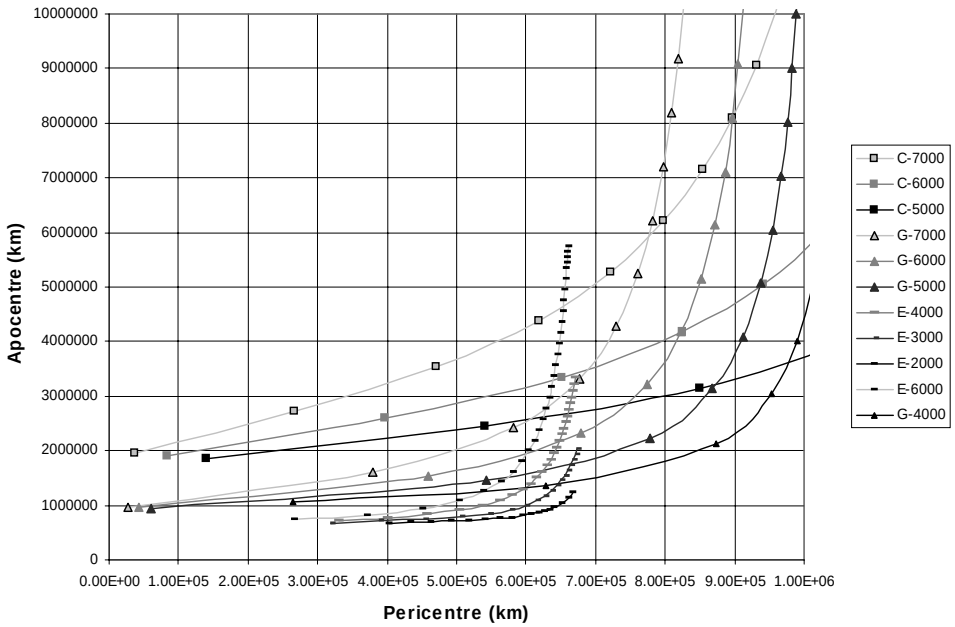

Figure 4.3.33. Apocentre–pericentre relationship for gravity assist at Europa, Ganymede and Callisto for a range of excess hyperbolic speeds. Speeds of 2,000 to 6,000 m/s at Europa are considered, 4,000 to 7,000 m/s at Ganymede and 5,000 to 7,000 m/s at Callisto.

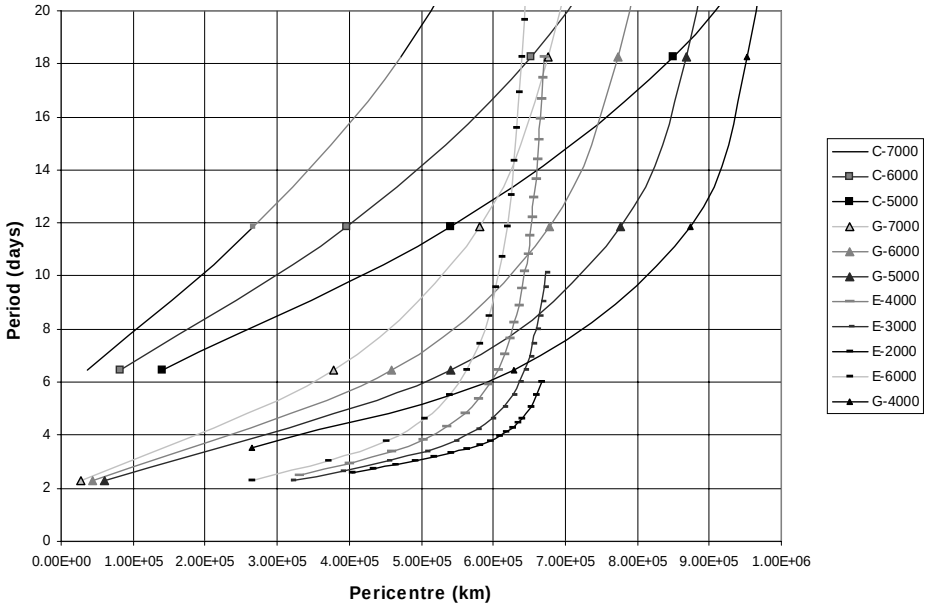

Figure 4.3.34. Period–pericentre relationship for gravity assist at Europa, Ganymede and Callisto for a range of excess hyperbolic speeds. The same range as Figure 4.3.33 is considered.

apocentre), gravity assist sequences at Ganymede are clearly effective in reducing pericentre and achieving reduced apocentre. As pericentre drops below Europa's orbital radius, gravity assist there can be considered, as for a subsequent pericentre a lower apocentre is achieved than when following the locus at Ganymede.

This case is discussed further in the context of a detailed mission design example in a later chapter.

4.3.5 Multiple gravity assists for plane-changing

The previous sections discussed multiple gravity assists in the context of targeting large changes in semi-major axis and eccentricity. However, this phenomenon can also be utilised to achieve an accumulated inclination change for the spacecraft.

A particularly useful effect may be achieved from repeated gravity assists at the same planetary body or moon. A fly-by may be designed such that the effect of the gravity assist is to increase inclination and also to achieve a velocity relative to the central body that yields a resonant orbit with respect to the major body used. In this situation, the spacecraft will return to the major body, after some integer number of revolutions about the central body, with the same relative velocity with which it previously departed, providing that no intermediate manoeuvres are applied or perturbations from other sources occur. A second fly-by then occurs, which may be used to further increase inclination. The post-fly-by velocity relative to the central body can be maintained by choosing an appropriate Beta angle (as discussed in Section 4.3.2).

It is assumed that in the case of the first gravity assist of the sequence, the approach plane is defined by the spacecraft's velocity and that of the target major body. It is possible for the approach velocity to lie in the orbit plane of the major body, in which case the approach plane is co-planar with that of the orbit of the major body. However, in general these planes will by separated by a rotation about the major body velocity vector, the angle ψ, discussed in Section 4.3.2.

After a gravity assist, the plane containing the spacecraft and major body velocity vectors is rotated by and angle, φ, out of the approach plane, as previously given by equation 4.3.32 in Section 4.3.2. The details of such a fly-by are described in that section. The fly-by Beta angle is allowed to take any value, by allowing the spacecraft approach vector to the major body to be displaced slightly in a direction perpendicuar to the approach plane. If the plane change is to be maximised then the Beta angle will be 90°. In the case of resonance, a solution is sought that will also preserve the velocity of the spacecraft. This constraint will define the Beta angle, and it will no longer be 90°, but in practice it is still likely to lie close to 90°. If the examples in Section 4.3.2 are examined, a Beta angle of 90° results in a small change in velocity relative to the central body.

The geometry of the new approach plane and second fly-by after such a resonant orbit are illustrated in Figure 4.3.35. The initial axis set used in conjuction with the first approach plane prior to the first fly-by was denoted X_0, Y_0, Z_0. After the gravity assist a new set, X', Y' and Z', may defined, simply rotated by the angle, φ, about the major body velocity vector. This is the departure plane – the plane containing the velocity vector of the spacecraft after the fly-by and the velocity vector of the major body. For a resonant case where the spacecraft returns to the same major body, with no intermediate manoeuvres, then this is also the new approach plane for the second fly-by at that planet. The approach geometry of the second fly-by is now defined by the departure geometry from the first fly-by.

Recalling that V_{planet} is the speed of the major body, V_∞ is the excess hyperbolic speed of the spacecraft with respect to that body, and θ' is the angle between the approaching relative velocity and the major body velocity vector. In

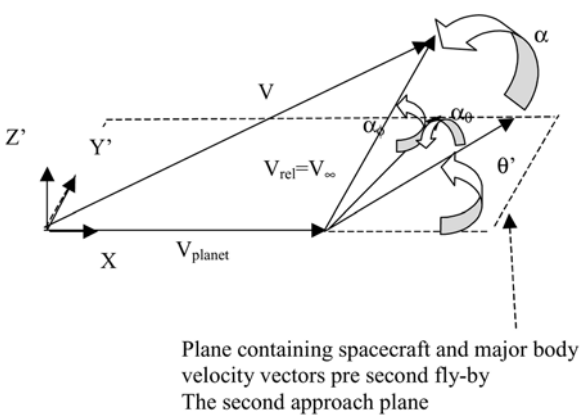

Figure 4.3.35. The definition of deflection angles in a multi-gravity assist case.

Section 4.3.2 the value of this angle was found to be $\theta' = \cos^{-1}(\cos\alpha_\phi \cos(\theta + \alpha_\theta))$, where α_θ and α_ϕ are the deflections from the first fly-by.

In a similar manner to the single fly-by case, the departing velocity vector can be expressed in the approach plane defined frame as follows:

$$V_{X'} = V_{planet} + V_\infty \cos\alpha_{\phi 2} \cos(\theta' + \alpha_{\theta 2}) \tag{4.3.51}$$

$$V_{Y'} = V_\infty \cos\alpha_{\phi 2} \sin(\theta' + \alpha_{\theta 2}) \tag{4.3.52}$$

$$V_{Z'} = V_\infty \sin\alpha_{\phi 2} \tag{4.3.53}$$

where $\alpha_{\theta 2}$ and $\alpha_{\phi 2}$ are the deflection angles from the second fly-by. X', Y', Z' are directions defined by the previous departure plane, such that X' and Y' lie in that plane. The deflection angles are not necessarily the same as in the first fly-by, as the Beta angle may be different, or the total deflection angle, α, could also be modified (for example, by change in pericentre altitude of the fly-by).

The flight path angle of the departing relative velocity vector with respect to the major body velocity vector is:

$$\theta'' = \cos^{-1}(\cos\alpha_{\phi 2} \cos(\theta' + \alpha_{\theta 2})) \tag{4.3.54}$$

If resonance is to be maintained then the departure velocity relative to the central body must equal the arrival velocity. Also, the relative velocity is maintained. Considering the velocity vector triangle describing the relationship between relative velocity, departure velocity and major body velocity, it may be seen that the angle between the relative velocity vector and the major body velocity vector must remain a constant. Therefore, in the previous expression, $\theta' = \theta''$.

This implies the following relationship between the two deflection angles:

$$\cos\alpha_{\phi 2} = \frac{\cos\theta'}{(\cos(\theta' + \alpha_{\theta 2}))} \tag{4.3.55}$$

These two angles are also related via the Beta angle (Equations 4.3.22 and 4.3.23), and in this way a Beta angle may be obtained that ensures that resonance is maintained.

The velocity of the departing spacecraft is transformed into the initial approach plane axis system (denoted by subscript 0) by a single axis transformation, defined by the angle φ (calculated for the first gravity assist). The initial approach plane geometry is described in Section 4.3.2.

$$V_{Y0} = V_{Y'} \cos\varphi - V_{Z'} \sin\varphi \tag{4.3.56}$$

$$V_{Z0} = V_{Z'} \cos\varphi + V_{Y'} \sin\varphi \tag{4.3.57}$$

In Figure 4.3.36, V_{rel} is shown as constant, which is the case when the spacecraft returns to the same major body in a resonant orbit. The departing velocity vector relative to the central body is also shown as constant. This will be the case if the spacecraft stays in the same resonant orbit after the two fly-bys. However, in principle it could switch from one resonance to another, in which case, although V_{rel} remains constant, the velocity relative to the cental body changes.

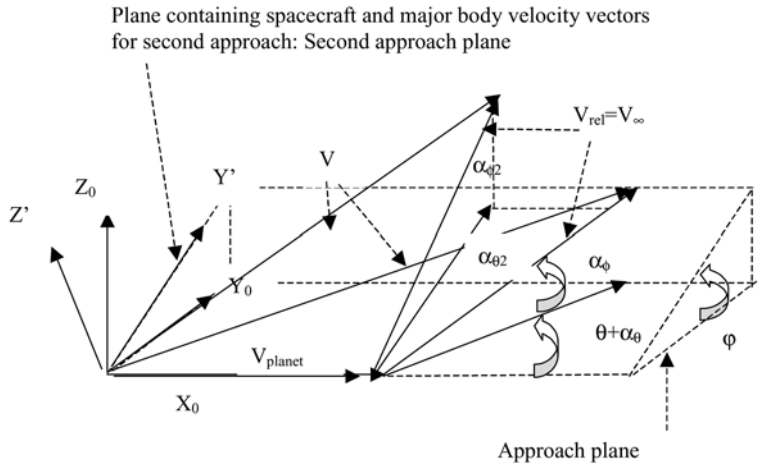

Figure 4.3.36. Two gravity assists maintaining resonance, showing both approach planes.

The departure velocity is given by:

$$V_{departure} = \sqrt{(V_X^2 + V_{Y'}^2 + V_{Z'}^2)} = \sqrt{(V_{X0}^2 + V_{Y0}^2 + V_{Z0}^2)} \tag{4.3.58}$$

The rotation of the new velocity vector departure plane (defined by the major body velocity and the departure velocity vector) about an axis along the major body's velocity vector, relative to the initial aproach plane, is given by an updated value of the angle φ:

$$\varphi' = \tan^{-1}\left(\frac{V_{Z0}}{V_{Y0}}\right) \tag{4.3.59}$$

This angle will define the relationship between the next approach plane and the initial approach plane if this gravity assist also results in a resonant orbit and subsequent return to the same major body.

Finally, the inclination of the spacecraft's new orbit, with respect to the initial approach plane, is given by the prevously established relationships (Section 4.3.2):

$$i_{departure} = \sin^{-1}\left(\frac{-V_{Z0}}{V_{departure}}\right)$$

The inclination relative to the orbit plane of the major body can also be calculated using the previously established relationship between the initial approach plane and the orbit plane.

$$V_{YM} = V_{Y0}\cos(\psi_M) - V_{Z0}\sin(\psi_M)$$
$$V_{ZM} = V_{Z0}\cos(\psi_M) + V_{Y0}\sin(\psi_M)$$

Then:

$$i_{departure} = \sin^{-1}\left(\frac{-V_{ZM}}{V_{departure}}\right)$$

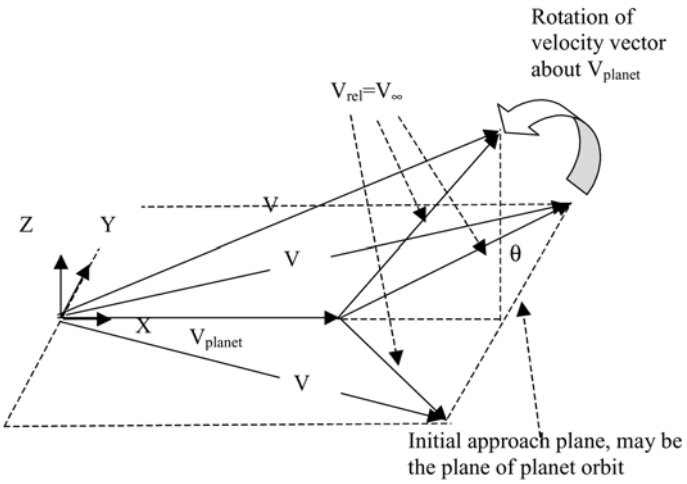

Figure 4.3.37. Effect of progressive deflection of the fly-by plane for resonant orbits targeted at inclination increase.

In this case, the angle ψ_M is obtained from equation 4.3.36. The eccentricity may also be calculated as described in Section 4.3.2.

Such a sequence of gravity assists may be repeated at the same major body if the spacecraft maintains a resonant orbit with the major body and therefore the same orbital period. The effect of such repeated gravity assists is to progressively rotate the approach plane of the spacecraft about the velocity vector of the planet or major body. This is shown in Figure 4.3.37. In this example the initial velocity of the spacecraft is greater than that of the planet, and so its orbital period is greater than that of the planet. If this velocity is such that resonance is achieved, then the selection of the appropriate Beta angle at each fly-by will eventually result in a large rotation of the relative velocity vector out of the initial plane containing the planet and spacecraft velocity vectors.

The definition of the Beta angle used here is such that the fly-by targeting is defined with respect to the plane containing planet and spacecraft velocity vectors (the current approach plane).

Figure 4.3.38 shows the plane containing planet and spacecraft velocities reaching 90° relative to the initial approach plane, and the initial approach plane which in this case is chosen to be co-planar with the planet or major body orbit plane. If resonant fly-bys are maintained then this plane will continue to rotate past 90°. The case of a rotation through 180° is shown in Figure 4.3.7. However, this 90-degree case is a limiting case with respect to achieving maximum inclination of the spacecraft orbit relative to the initial approach plane. If the spacecraft is to remain in the resonant orbit, then the maximum inclination achieved is shown in Figure 4.3.38.

The maximum inclination with respect to the fly-by body orbit plane is given by:

$$i_{\max} = \tan^{-1}\left(\frac{V_\infty \sin\theta}{V_{planet} + V_\infty \cos\theta}\right) \tag{4.3.60}$$

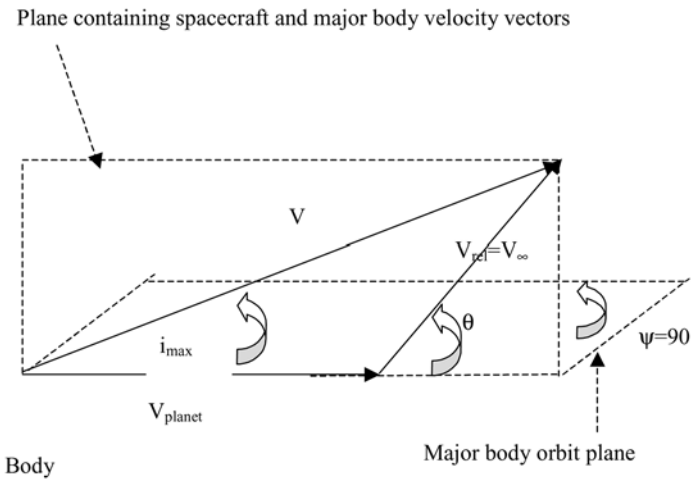

Figure 4.3.38. Limiting case defining maximum inclination relative to the major body orbit plane when in a resonant orbit.

If resonance need not be maintained then a further fly-by may be performed (with Beta close to 0° or 180° in the approach plane). With this value of Beta angle, no deflection perpendicular to the approach plane occurs, and the velocity vector is instead rotated in the approach plane. The subsequent velocity vector deflection, in the approach plane, means that initial velocity magnitude is no longer maintained, but the rotation is such that inclination may increase. One possibility is to target a further resonant orbit with the planet, such that a subsequent gravity assist may be targeted, if inclination can still be increased further.

There is ultimately a geometrical limitation if the spacecraft always returns to the planet with the same excess hyperbolic velocity. This is illustrated in Figure 4.3.39. The maximum inclination is reached when the central body relative velocity is modified from its value, V_1 from the resonant sequence, to a value V_{limit}.

The maximum inclination is given by:

$$i_{\max} = \sin^{-1}\left(\frac{V_\infty}{V_{plant}}\right) \tag{4.3.61}$$

These observations are still based on the assumptions of patch conics and a spacecraft orbit with a node that lies at the fly-by with the planet or major body.

In Figure 4.3.40, a maximum inclination is reached whilst maintaining the same resonant orbit with Ganymede. The orbits of Io, Europa, Ganymede and Calisto are shown on the plot.

Multiple plane-changing gravity assists at Venus

A heliocentric example of plane changing with multiple gravity assists is now considered. This can be an important consideration for missions that are required to perform out-of-ecliptic observations. A single gravity assist at Jupiter can achieve a

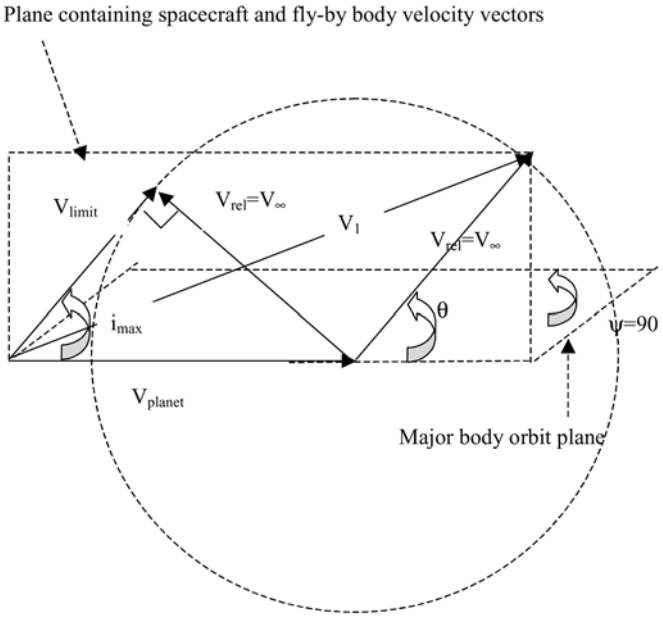

Figure 4.3.39. A maximum inclination case when central body relative velocity may be varied at subsequent fly-bys from V_1 to V_{limit}.

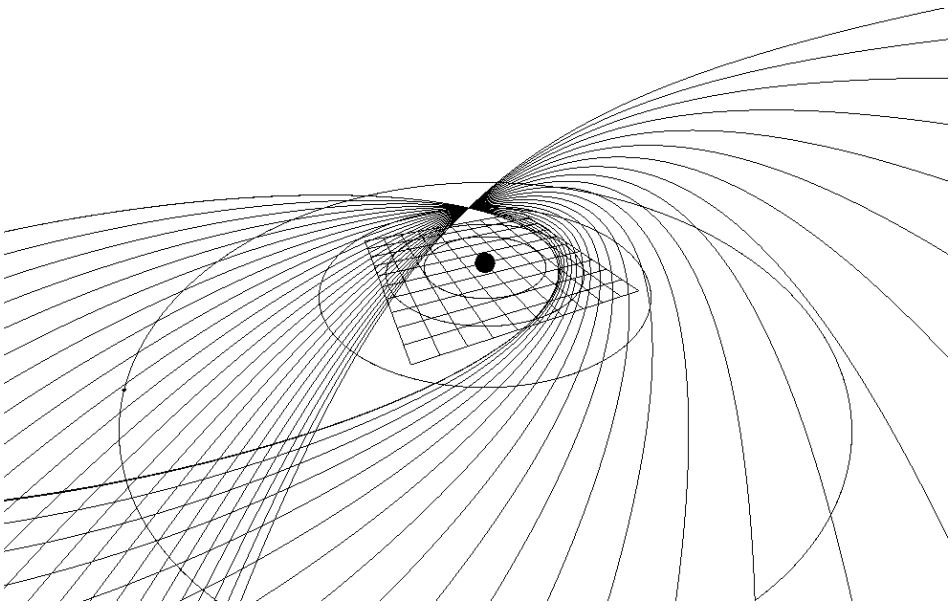

Figure 4.3.40. Example of multiple resonant gravity assists at Ganymede, with excess hyperbolic speed at Ganymede of 9.5 km/sec. The orbits of Jupiter's four inner moons are also shown.

90-degree inclination with respect to the ecliptic, but such a transfer may not be practical. Considerable time and/or fuel is needed to reach Jupiter. Then, after the gravity assist, the spacecraft aphelion is still close to 5.2 AU. An alternative strategy to reach high inclinations could therefore be considered at planets within the inner Solar System. Venus is a good choice, as it is relatively massive and easily reached.

The maximum total inclination change that is achievable is dependent on the excess hyperbolic speed with respect to Venus. Repeated gravity assists will be required to achieve high inclinations.

An example of a sequence is evaluated in Figure 4.3.41. The theoretical maximum inclination that may be reached in the case presented in Figure 4.3.41, if remaining in the 2 : 1 resonance orbit example chosen, would be 39 degrees. The velocity vectors are close to orthogonal at this point and so this resonant solution at this excess hyperbolic speed is close to optimal. If this excess hyperbolic speed is maintained, then there is little scope for increasing the inclination by changing the resonance. This sequence requires a low perihelion and results in an extreme environment for spacecraft.

A resonant plane changing sequence is currently considered as an option for the European Space Agency's SOLO mission (more details can be obtained through the references given). The objective of this mission is to observe the Sun from high latitudes when relatively close to the Sun. Therefore, such a sequence is well suited to this type of Solar observing mission.

Figure 4.3.42 illustrates a second sequence of gravity assists at Venus, generated after a transfer from an initial Earth departure and intermediate gravity assists to build up the required excess hyperbolic speed at Venus. In this case a 3 : 2 resonant orbit is used with lower excess hyperbolic speeds at Venus. The perihelion is higher which benefits the spacecraft. The inclination is progressively raised until a value of over 30 degrees is reached with respect to the ecliptic plane. The orbital inclination of Venus itself is also a factor in the final inclination here. Such strategies have been proposed by Janin *et al.* for the future SOLO mission (see references for this section).

4.3.6 Gravity assist at planetary moons for escape and capture

A gravity-assisted fly-by at a major moon of a planet may be used to help a spacecraft either escape from or be captured by the planet. The gravity assist either increases or reduces the orbital energy of the spacecraft with respect to the planet, such that a transition from a bound to unbound orbit (or vice versa) occurs.

Gravity-assisted escape

Lunar gravity assist can be used to increase the Earth relative speed of the spacecraft. However, there are limitations to the final escape velocity that can be obtained by such a method, when starting from an initially bound orbit. These arise from consideration of the spacecraft's closest approach distance and the approach velocity at the moon. An initially elliptical Earth-centred orbit can be utilised to engineer the lunar encounter.

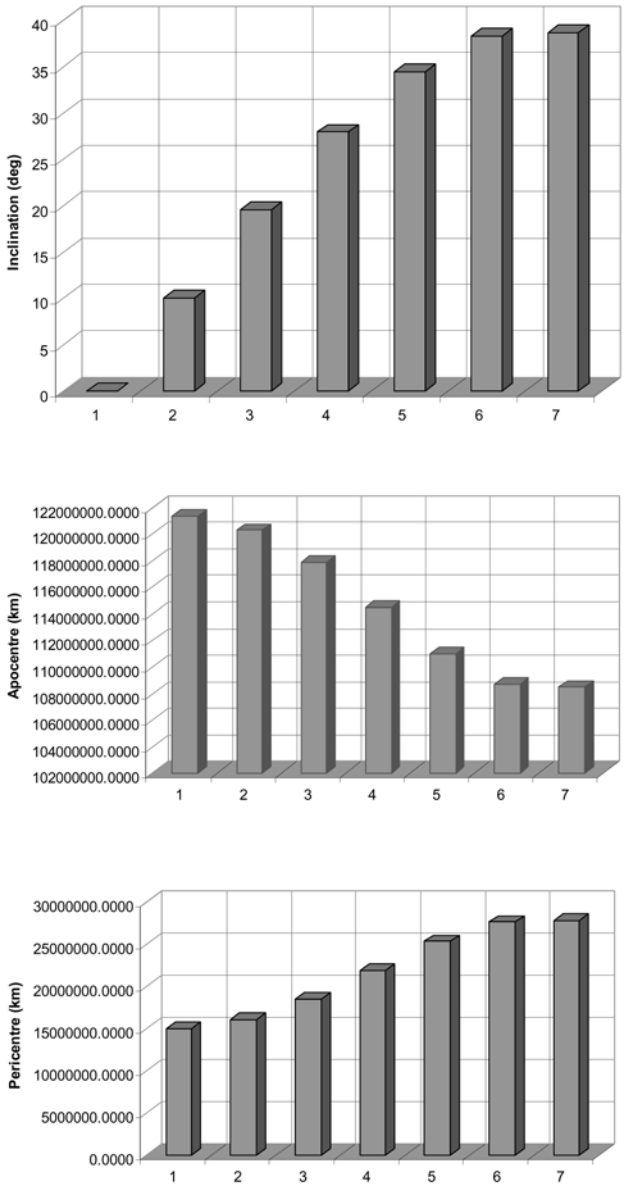

Figure 4.3.41. Inclination, aphelion and perihelion evolution for a sequence of gravity assist at Venus with Vinfinity at 22.4 km/sec. The initial orbit is: apocentre = 121 million km, pericentre = 15 million km. The orbital period is 112.5 days. Therefore, a 2 : 1 resonance may be reached with Venus. This means that fly-bys occur approximately every 225 days. This orbit results in an excess hyperbolic speed with respect to Venus of 22.4 km/sec. Six gravity assists are used in reaching a maximum inclination of approximately 39°. This procedure will therefore take approximately 1,350 days from reaching an initially zero inclination orbit, or approaching 3.7 years.

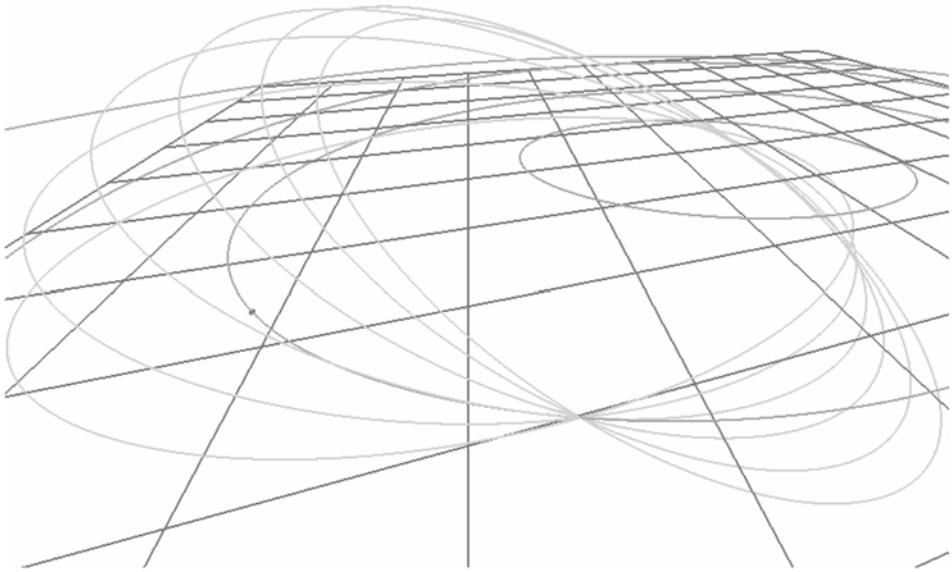

Figure 4.3.42. Orbit evolution for a sequence of gravity assist at Venus. In this figure the orbits of Venus and Mercury can be seen. The repeated gravity assists at Venus can be seen in the same location.

If the orbit perigee altitude is fixed and apogee altitude increased beyond lunar altitude, the effect of lunar gravity assist can be to generate an escape velocity. However, as higher apogee altitudes are considered, an asymptote is reached. The analysis in Figures 4.3.43 and 4.3.44 assumes co-planar spacecraft and moon orbits and a patch conic analysis.

This technique has been discussed in the context of ESA's Bepi-Colombo mission. Also, lunar gravity assists were used for the Hiten mission (More information can be found in the references for this chapter.)

Gravity-assisted capture

A gravity assist manoeuvre may be utilised to achieve planetary capture by executing a close fly-by at the moon, after starting from an initially hyperbolic approach orbit with respect to the planet (and a hyperbolic approach with respect to the moon). The subsequent deflection of the moon-relative asymptotic departure velocity vector causes a change in the energy of the spacecraft with respect to the planetary system. This is the reverse of the method described previously for escape from a planet. The example considered here is a capture using one of Jupiter's moons.

After such a gravity assist the energy of the spacecraft in Jupiter's system may be reduced or increased, depending on which side of the moon the spacecraft passes. The possibilities for energy reduction are dependent on certain parameters at approach:

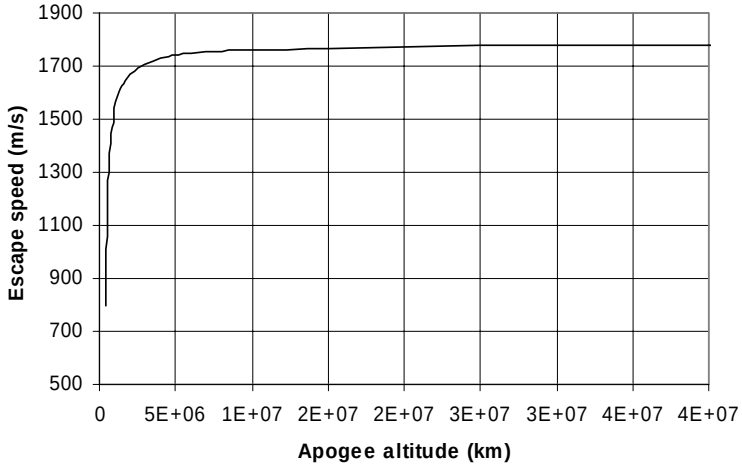

Figure 4.3.43. The effect of apogee altitude on Earth excess hyperbolic speed after lunar fly-by for a fly-by altitude of 260 km. Increasing apogee altitude of the lunar rendezvous orbit tends to increase Earth escape velocity after lunar fly-by, but also tends to an asymptote with respect to apogee altitude as the initial orbit becomes parabolic.

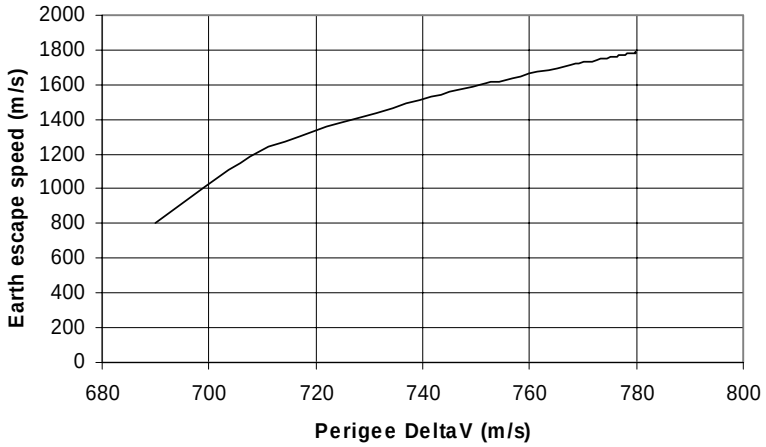

Figure 4.3.44. The effect of ΔV for apogee raising on Earth excess hyperbolic speed. The same effect of increasing V_∞ can be observed with increase in perigee speed (i.e., with respect to an initial GTO-like orbit with 42,165 km radius apogee). The initial perigee velocity can be increased beyond that required for Earth escape and advantage sill be obtained by using a gravity assist at the Moon.

(1) The initial approach velocity direction and hence excess hyperbolic speed.
(2) The targeted pericentre with respect to the moon and the orientation with respect to the local equator (the Beta angle discussed in Section 4.3.2).

The possibilities for transfer from an initially hyperbolic orbit with respect to Jupiter to a highly elliptical, captured orbit are shown in Figures 4.3.46. Co-planar motion is

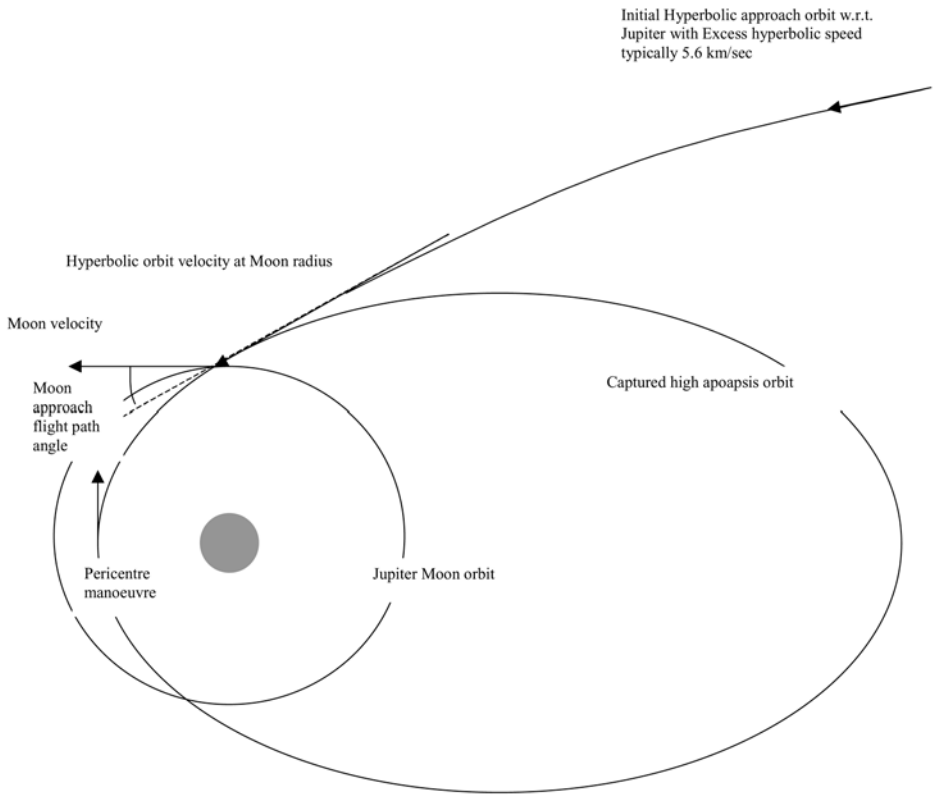

Figure 4.3.45. The principle of planetary capture using gravity assist at a moon.

assumed at all times. Capture apocentres assessed here range from 25 million km to 50 million km. The assumed pericentre altitude at Ganymede is 300 km.

The effectiveness of the gravity assist at the moon is related to the pre-fly-by pericentre (and hence excess hyperbolic speed at the moon). This in turn determines the post fly-by pericentre. Therefore, the following figure illustrates the effect of this post fly-by pericentre on the excess hyperbolic speed (approaching Jupiter) from which the spacecraft may be captured into the specified apocentre orbit at Jupiter.

A similar result can be obtained for Callisto. The excess hyperbolic speeds for capture to a bound orbit are less than 3 km/sec. The different apocentre curves denoted are in millions of km.

In the case of a standard, bi-impulsive transfer to Jupiter using a semi-elliptical orbit, the excess hyperbolic speed with respect to Jupiter is typically 5.6 km/sec. This clearly exceeds the possibilities for capture at Jupiter's largest moons in a single gravity assist manoeuvre. Figure 4.3.46 indicates that no more than 4 km/sec is possible.

When approaching at 5.6 km/sec then after the gravity assist, the spacecraft may still posses an osculating excess hyperbolic speed of typically 2 km/sec. Additional manoeuvres must therefore be considered to achieve capture at Jupiter.

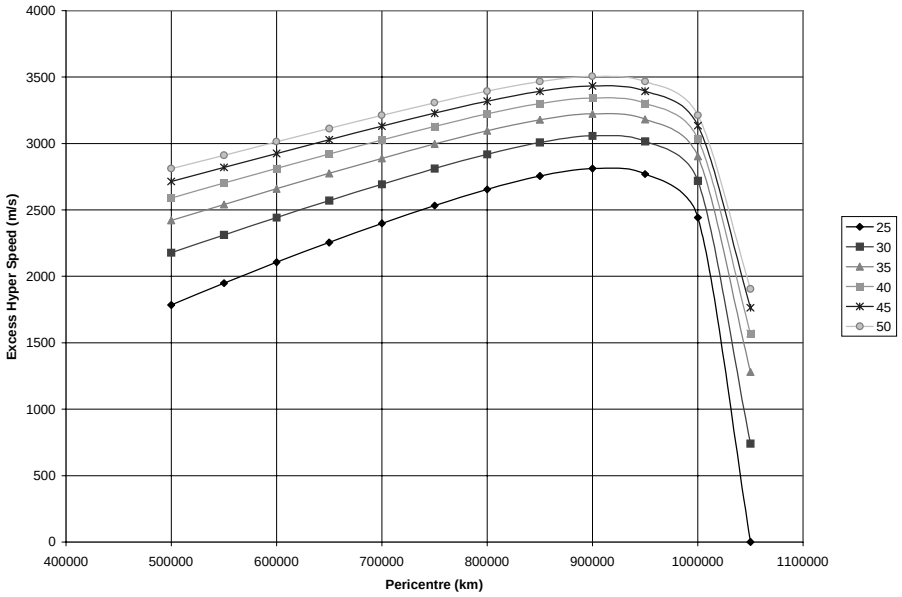

Figure 4.3.46. Approach excess hyperbolic speed versus target Jupiter pericentre altitude after Ganymede fly-by for a range of post-gravity assisted captured apocentre altitudes. These altitudes range from 25 million to 50 million km.

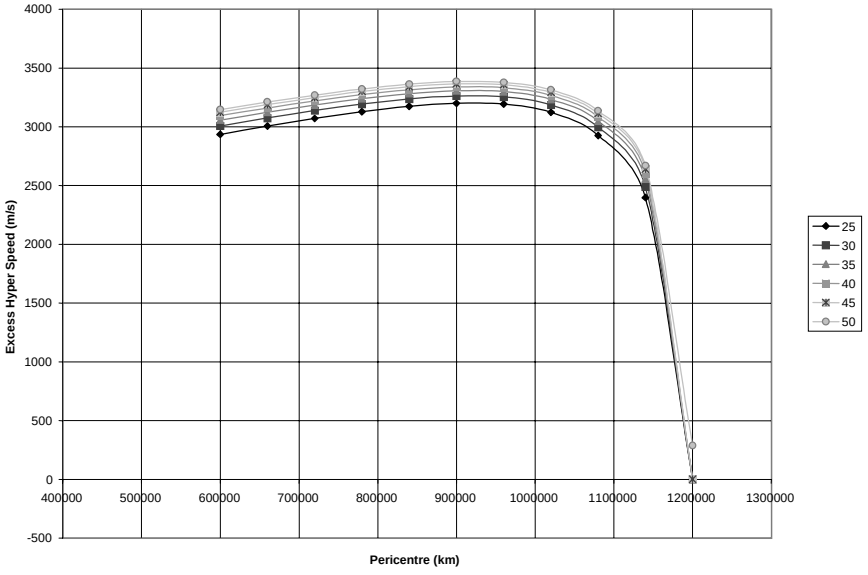

Figure 4.3.47. Approach excess hyperbolic speed versus target Saturn pericentre altitude after Tital fly-by for a range of post-gravity assist captured apocentre altitudes. These altitudes range from 25 million to 50 million km. The assumed pericentre altitude of the fly-by at Titan is 300 km.

(1) Apply a near impulsive ΔV at pericentre of the gravity assist at the moon to further reduce the excess hyperbolic speed
(2) Apply an additional retarding ΔV at Jupiter pericentre passage to reduce the velocity and achieve capture. Pericentre passage is assumed to take place after the fly-by. This speed reduction then results in capture. In this case, an optimal post-gravity assist pericentre altitude may be obtained, that minimises ΔV to reach a given apocentre target.
(3) Apply a retarding ΔV to reduce the excess hyperbolic velocity on approaching Jupiter, such that the moon gravity assist can be effective in achieving capture.

A second gravity assist manoeuvre can also be arranged with a second moon before the spacecraft recedes from the planet. This can further reduce the excess hyperbolic speed.

This analysis may be repeated for the case of capture using Titan at Saturn. This is shown in Figure 4.3.47.

In the case of a standard bi-impulsive transfer to Saturn using a semi-elliptical orbit, the excess hyperbolic speed with respect to Saturn on approach is typically 5.4 km/sec. This again exceeds the possibilities for capture at Titan in a single gravity assist manoeuvre. The osculating excess hyperbolic speed after the gravity assist will be typically 3 km/sec.

A second capture gravity assist is not feasible in the case of Saturn, as the other moons are much smaller, with only small asymptotic deflection available. However, the other strategies described for the Jupiter case can be considered.

Further moon-assisted capture possibilities exist with Neptune's moon, Triton.

4.3.7 Modelling gravity assist manoeuvres

Fly-by gravity-assist manoeuvres are modelled either by numerical integration of the dynamics of the three body problem or by a patched conic approach.

Numerical integration

This approach is the most accurate model, as any errors arising in the simulation are a function of drift in the numerical integrator or the accuracy of the gravity model.

The dynamics of a gravity assist in a heliocentric system are basically described by:

$$\frac{d^2\underline{r}}{dt^2} = -\frac{\mu}{r^3}\underline{r} - \frac{\mu_M}{r_M^3}\underline{r_M} - \frac{\mu_M}{r_{relM}^3}\underline{r_{relM}}$$

where r is spacecraft position wrt the Sun, r_M is the major body position wrt the Sun, and r_{relM} is spacecraft position wrt the major body.

The start of the fly-by manoeuvre may generally be defined by a specified osculating ephemeris with respect to the major body. This ephemeris is referred to a specified start epoch of the fly-by, and would start at or outside the sphere of influence of the planet.

This initial ephemeris must be converted to a heliocentric state, for subsequent propagation using the above equations of motion expressed in a heliocentric form. Alternatively, the simulation may be performed in a planet-centred system.

The initial Cartesian state relative to the central body is evaluated by $\underline{X}(t_0) = \underline{X}_{planet}(t_0) + \underline{X}_p(t_0)$, where t_0 is the initial epoch, $\underline{X}_{planet}$ is the planet state, and $\underline{X}_p$ is the state relative to the planet.

After numerical integration of the trajectory, the final Cartesian state relative to the major body is found. This can be found from the state relative to the central body.

The initial distance from the major body, for start of the simulation, and also the final distance, are chosen such that the gravitational influence of the major body is negligible. This is the most accurate method to model a fly-by.

Patched conic over specified sphere of influence

In this option, a sphere of influence over which the fly-by patched conic is applied is specified. This could be the classical 'sphere of influence' discussed at the beginning of this chapter.

To evaluate the initial fly-by body relative Cartesian states, a similar procedure to that described in the previous method is used to convert the osculating ephemeris. However, due to the specification of the initial radial distance, the initial anomaly is calculated rather than specified. The process is as follows.

Calculate the initial true anomaly:

$$\cos\theta = \frac{a\dfrac{(1-e^2)}{r_{sphere}} - 1}{e}$$

where r_{sphere} is the radius of the sphere of influence, and a and e are the semi-major axis and eccentricity of the hyperbolic orbit. Mean anomaly can be calculated to determine the time spent within the sphere of influence.

The value of the true anomaly is assumed to lie between 0° and -180°.

Then, evaluate the hyperbolic anomaly:

$$\tanh\frac{F}{2} = \sqrt{\frac{e-1}{e+1}}\tan\frac{\theta}{2}$$

and the initial mean anomaly:

$$M_0 = e\sinh F - F$$

where M_0 is the initial mean anomaly at the defined sphere of influence, and F is the hyperbolic anomaly.

To evaluate the Cartesian states at a subsequent time, the mean anomaly must be updated to take into account the elapsed time, as follows:

$$M = M_0 + \sqrt{-\frac{\mu_{planet}}{a^3}} * (t - t_0)$$

where μ_{planet} is the gravitational constant of the major body or planet.

The period of the fly-by manoeuvre (the time spent within the sphere of influence) is calculated as follows:

$$T = -2 * M_0 * \sqrt{\frac{-a^3}{\mu}}$$

Using the mean or true anomaly on exiting the sphere of influence allows the calculation of the Cartesian states relative to the major body.

The final Cartesian state relative to the central body is evaluated as before:

$$\underline{X}(t_f) = \underline{X}_{planet}(t_f) + \underline{X}_p(t_f)$$

The state of the major body must be evaluated at the terminal epoch, t_f. An error in the modelling of a gravity assist in this way arises from the approximation that the evolution of the spacecraft motion after leaving the sphere of influence is no longer effected by the major body's gravity. This results in an error in the velocity change predicted by the gravity assist. However, the error is relatively small and the method offers a good approximation.

Link conic method

The link conic method is a variation on the patch conic method. The patch conic method identifies a boundary where the single central field can be switched, and 'patches' the Keplerian orbital arcs together. With the link conic method, the fly-by or gravity assist is specified in a similar way, generally by ephemeris with respect to the major body. From this ephemeris it is possible to evaluate the asymptotic approach and departure velocity vectors; that is, the relative velocity at infinite distance from the planet.

The asymptotic directions are determined by $\theta = \pm\cos^{-1}\left(-\frac{1}{e}\right)$, where e is the eccentricity of the hyperbolic orbit (>1)

The velocity is given by:

$$V = \sqrt{\frac{-\mu_{planet}}{a}}$$

The flight path angle is $\pm 90^\circ$, and so the following expressions yield the asymptotic approach or departure velocity vector, depending on the sign of θ.

The velocity vector components calculated in an intermediate reference frame are:

$$V'_x = -V\cos\left(\omega + \theta - \frac{\pi}{2} - \Gamma\right)$$

$$V'_y = -V\sin\left(\omega + \theta - \frac{\pi}{2} - \Gamma\right)\sin i$$

$$V'_z = -V\sin\left(\omega + \theta - \frac{\pi}{2} - \Gamma\right)\cos i$$

where Γ is 90° and θ is given by the expression above and is positive (i.e., departing) Arrival implies negative θ and negative Γ. These components are now calculated with respect to an axis set relative to the reference planet system, with X pointing to Aries,

Y perpendicular to X in the ecliptic plane, and Z perpendicular to the ecliptic:

$$V_x = V'_x \cos(\Omega) - V'_y \sin(\Omega)$$
$$V_y = V'_x \sin(\Omega) + V'_y \cos(\Omega)$$
$$V_z = V'_z$$

The initial and final central body relative states are updated with the above velocity values and a planet-relative position vector of zero. It is assumed that the effect of the gravity assist is an instantaneous change in direction. This method is therefore equivalent to the method of modelling planet escape with an instantaneous hyperbolic velocity vector.

4.3.8 Anatomy of a gravity assist

The motion of a spacecraft performing a gravity assist about a planet may be simulated by numerical integration in the multi-gravity field and compared with the patched conic approximation. The following example uses the same type of Earth escape trajectory as in Section 4.2, but is preceded by an Earth approach phase and gravity assist. A higher excess hyperbolic speed at Earth is compared with the analysis in the previous section.The sequence is summarised as follows:

- Planet of gravity assist is Earth. Earth's orbital radius at gravity assist is 0.9944 AU.
- Target heliocentric orbit (not a planetary rendezvous) after EGA is circular at approximately 390 million km (2.6 AU), and in the ecliptic.
- The gravity assist is such that this fly-by reaches the maximum possible aphelion with the given excess hyperbolic approach speed. The departure excess hyperbolic velocity lies very close to tangential to the Earth's orbit.

The approach and departure orbits, obtained from a full simulation by numerical integration, have the parameters shown in Table 4.3.4.

The expected excess hyperbolic velocity is calculated by the intersection of the approach orbit with Earth's orbit as 5.97 km/sec. This value includes the effect of Earth's orbital eccentricity, and so implies a particular true anomaly for the rendezvous. This velocity is close to the osculating value when at Earth orbit pericentre of the fly-by hyperbolic orbit, the value here being 5.96 km/sec. The pre and post fly-by orbits are shown in Figure 4.3.48 with the energy evolution in Figure 4.3.49.

Table 4.3.4. Orbits obtained by numerical integration before and after gravity assist.

	Approach orbit	Departure orbit
Semi-major axis	1.21 AU	1.80 AU
Eccentricity	0.258	0.447
Aphelion	1.52 AU	2.60 AU
Perihelion	0.897 AU	0.9946 AU

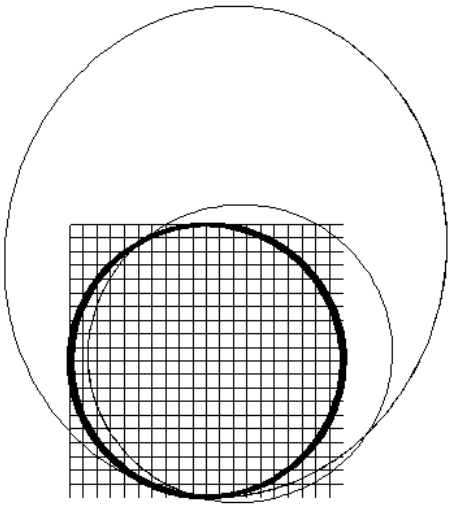

Figure 4.3.48. Gravity assisted transfer at Earth to reach raised aphelion with Earth V_∞ at 6 km/sec. The illustration shows the gravity-assisted heliocentric trajectory and Earth's orbit about the Sun (bold). The grid is 1 AU from centre to edge. The initial orbit is the lower one, and the post-gravity assist orbit the higher aphelion.

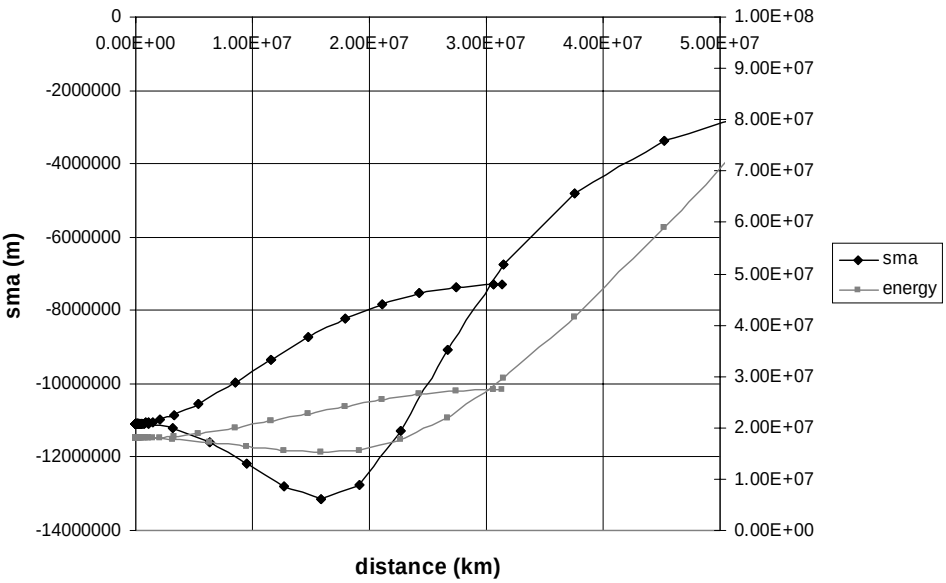

Figure 4.3.49. Semi-major axis and energy with respect to Earth during an Earth gravity assist, evolution over distance from Earth. The evolution of the osculating orbital parameters may be monitored during the approach, fly-by and departure phases. Energy is plotted against the right axis.

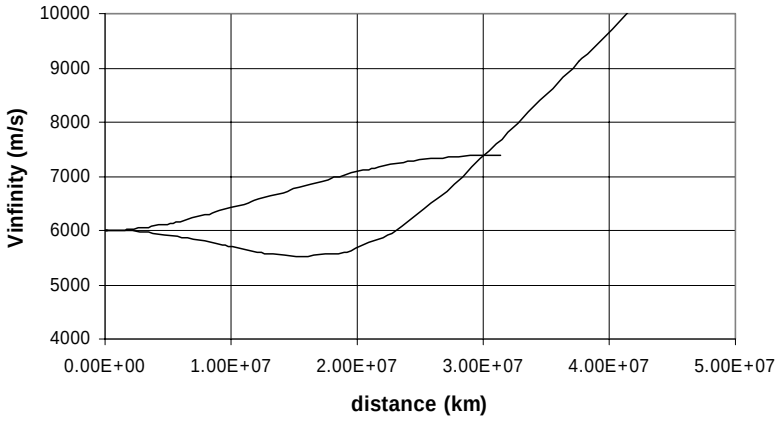

Figure 4.3.50. Excess hyperbolic speed with respect to Earth during an Earth gravity assist, evolution over distance from Earth. The Earth relative energy may be equivalently expressed as the osculating excess hyperbolic speed. The evolution of the parameter is shown.

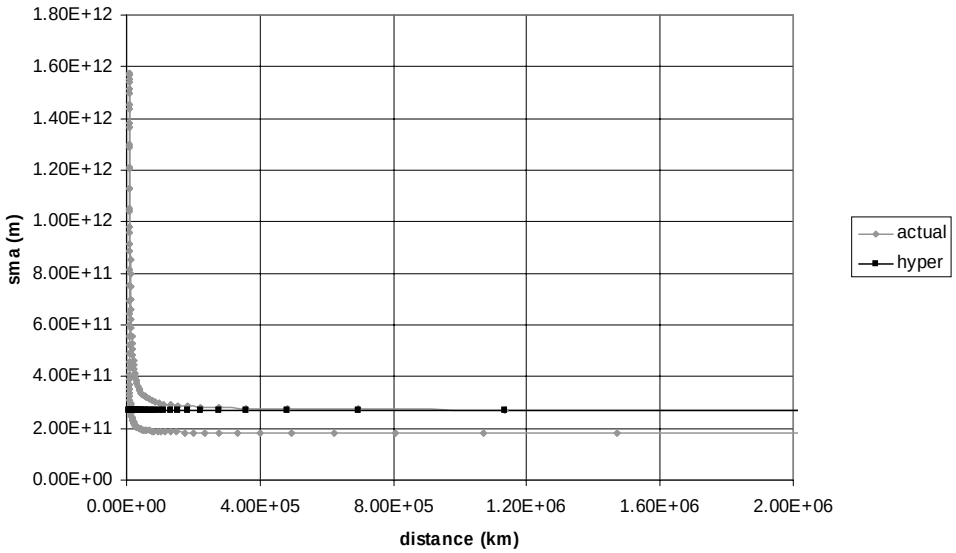

Figure 4.3.51. Semi-major axis with respect to Sun during an Earth gravity assist, evolution over distance from Earth. The 'hyper' value is the semi-major axis of the eventual departure orbit. It this case it corresponds to the semi-major axis calculated from the aphelion as calculated by adding the excess hyperbolic speed at Earth perigee to Earth's orbital velocity.

Figure 4.3.50 shows that the osculating V_∞ at Earth perigee is 5.96 km/sec. As the spacecraft passes into, through and out of the Earth's sphere of influence, the Earth relative energy and hence excess hyperbolic speed first decreases as perigee is approached and then eventually increases after fly-by as the spacecraft again moves into the heliocentric domain.

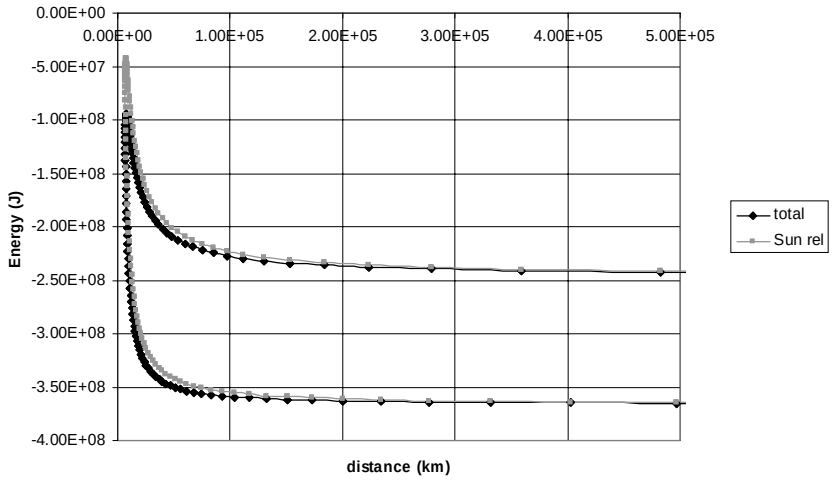

Figure 4.3.52. Energy with respect to Sun, evolution over distance from Earth. The maximum energy occurs just after Earth perigee, because of the orientation of the Earth relative velocity vector at perigee. Perigee location is determined by the required asymptotic departure direction.

This gravity assist is such that no further subsequent aphelion raising would be possible if further fly-bys were to occur at Earth (assuming that no intermediate manoeuvres occur) as the departure direction is tangential to Earth's orbit.

When the energy with respect to the Sun is examined (Figure 4.3.51 shows semi-major axis), it evolves firstly from a state corresponding to the initial heliocentric orbit, experiences a strong perturbation during the fly-by, and then during departure asymptotically reaches the value required for the eventual heliocentric orbit. The evolution of the spacecraft energy close to the Earth is shown in Figure 4.3.52, and is an extension of the behaviour seen in the Earth escape example described in the previous section.

As in the analysis of planetary departure, neither of these energies is expected to be conserved during such a planetary fly-by. The total energy is again conserved, but this includes the Earth's energy with respect to the Sun, which experiences a slight modification during the fly-by.

This observed dynamic behaviour may be compared with the predictions of a patched conic analysis. Table 4.3.5 shows the results from a patched conic analysis.

Table 4.3.5. Orbits obtained by patch conic analysis before and after gravity assist.

	Before	After
Aphelion	1.522	2.603
Perihelion	0.897	0.994
Semi-major axis	1.209	1.799

The altitude of the fly-by is assumed to be 600 km (the value used in the preceding simulation).

Earth rendezvous occurs at 0.994 AU (true anomaly of 71°) for this analysis. The relative velocity at rendezvous is calculated as 5.97 km/sec. The results in the table clearly show very close agreement with the actual change in orbit parameters after the fly-by, shown in Table 4.3.4.

4.4 THE VARIATIONAL EQUATIONS OF LAGRANGE AND GAUSS

4.4.1 Orbital perturbations

If unperturbed by any external forces or internally generated reaction forces, a spacecraft orbiting a single, uniform-density central body will remain indefinitely in that orbit. In reality, this situation does not exist, as some form of perturbation will always be present, whether generated externally or internally.

Examples of external perturbations include the effects of multi-body gravity fields, non-uniformity in the density of the central body, radiation pressure (nominally from the Sun) on the spacecraft, and, depending on the local environment, the effects of atmospheric drag.

The effects of such perturbations generally result in a gradual evolution of the spacecraft orbit parameters or ephemeris. The perturbations have short-term, periodic effects and long-term secular effects. In this context, the term 'secular' describes a perturbation whose effect accumulates over successive orbits, and the term 'periodic' a perturbation that sees the orbit return to its nominal state after a complete orbit.

The perturbations of most interest to spacecraft designers are generally the secular terms – the exception being where very precise orbital position control is required. Very well known secular terms are, for example, the effect of Earth's J2 gravity potential harmonic on the right ascension of the ascending node. (A detailed description of the effects may be found in many of the references for this section.)

A second source of perturbations is those deliberately generated by the spacecraft itself. Clearly, a high-thrust main engine cannot be regarded as a perturbation, but a low-thrust propulsion systems can. Examples of such low-thrust systems are electric propulsion and solar sails. Typical orders of magnitudes of the accelerations generated by electric propulsion are 0.0001 m/s^2, and the accelerations from a solar sail spacecraft could be even smaller.

Such propulsive terms can be classed as perturbations, being much less than the gravitational acceleration from the central body (0.0059 m/s^2 from the Sun at 1 AU).

4.4.2 Lagrange's planetary equations

A mathematical formulation was developed by Lagrange to describe the effects of such perturbations on an orbit. These are known as Lagrange's planetary equations.

The following is a summary of the derivation (treated more fully in the references, notably Battin and Roy).

Firstly, the differential equation for the orbital position vector $\underline{r}$ is given by:

$$\frac{d\underline{r}}{dt} = \underline{v} \qquad \text{and} \qquad \frac{d\underline{v}}{dt} = \frac{d^2\underline{r}}{dt^2} = \frac{-\mu}{r^3}\,\underline{r} + \left[\frac{\partial R}{\partial \underline{r}}\right]^T \tag{4.4.1}$$

where R is a position-only dependent potential term generating the perturbation, $\underline{r}$ and $\underline{v}$ are position and velocity vectors.

In the unperturbed case, the solution of equation 4.4.1 yields a set of six constant parameters of integration, denoted by the vector α:

$$\underline{r} = r(\underline{\alpha}, t) \qquad \text{and} \qquad \underline{v} = v(\underline{\alpha}, t)$$

The elements of $\underline{\alpha}$ could therefore be the orbital ephemeris. The solution of the perturbed equations will assume that the parameters, $\underline{\alpha}$, in fact vary with time.

Time differentiation of the perturbed vectors, r and v, gives:

$$\frac{d\underline{r}}{dt} = \frac{\partial \underline{r}}{\partial t} + \frac{\partial \underline{r}}{\partial \alpha}\frac{d\alpha}{dt} \qquad \text{and} \qquad \frac{d\underline{v}}{dt} = \frac{\partial \underline{v}}{\partial t} + \frac{\partial \underline{v}}{\partial \alpha}\frac{d\alpha}{dt} \tag{4.4.2}$$

The time derivatives of the parameter set, $\underline{\alpha}$, arise from a perturbation to the acceleration, which is the rate of change of velocity. The velocity of the spacecraft is obtained directly from the current parameter set:

$$\frac{d\underline{r}}{dt} = \frac{\partial \underline{r}}{\partial t}$$

that is, velocity is obtained from the explicit time dependence of the parameter set. Therefore:

$$\frac{\partial \underline{r}}{\partial \alpha}\frac{d\alpha}{dt} = 0 \tag{4.4.3}$$

Similarly, the unperturbed acceleration is:

$$\frac{\partial^2 \underline{r}}{\partial t^2} = \frac{\partial \underline{v}}{\partial t} = -\frac{\mu}{r^3}\,\underline{r}$$

The partial derivative here signifies that the parameters, $\underline{\alpha}$, are constant. Therefore:

$$\frac{\partial \underline{v}}{\partial \alpha}\frac{d\alpha}{dt} = \left[\frac{\partial R}{\partial \underline{r}}\right]^T \tag{4.4.4}$$

A set of six variational equations therefore define the time derivatives of the parameters, $\underline{\alpha}$.

The solution of this set of equations was first performed by Lagrange. Details of the derivation may be found in the references for this section. The result is Lagrange's planetary equations, given by the following equations:

$$\begin{aligned}
\frac{da}{dt} &= \frac{2}{na}\frac{\partial R}{\partial \lambda} \\
\frac{de}{dt} &= \frac{1}{na^2}\frac{1}{e}\left(-\sqrt{1-e^2}\frac{\partial R}{\partial \omega} + (1-e^2)\frac{\partial R}{\partial \lambda}\right) \\
\frac{di}{dt} &= \frac{1}{h}\left(-\frac{1}{\sin i}\frac{\partial R}{\partial \Omega} + \cot i \frac{\partial R}{\partial \omega}\right) \\
\frac{d\Omega}{dt} &= \frac{1}{h\sin i}\frac{\partial R}{\partial i} \\
\frac{d\omega}{dt} &= \frac{1}{h}\left(-\cot i \frac{\partial R}{\partial i} + \frac{(1-e^2)}{e}\frac{\partial R}{\partial e}\right) \\
\frac{d\lambda}{dt} &= -\frac{2}{na}\frac{\partial R}{\partial a} - \frac{(1-e^2)}{na^2 e}\frac{\partial R}{\partial e}
\end{aligned} \tag{4.4.5}$$

The orbital elements are here defined as: a, semi-major axis; e, eccentricity; i, inclination; Ω, right ascension of ascending node; ω, argument of perigee; λ: $\lambda = -n\tau$, where τ is the time of pericentre passage and n is the mean motion; that is, $n = \sqrt{\dfrac{\mu}{a^3}}$, and therefore the mean anomaly is referenced to this event by $M = nt + \lambda = n(t - \tau)$. h is the angular momentum per unit mass.

A number of different expressions may be used to describe the location in the orbit plane at a given time. If, alternatively, the initial mean anomaly is used as a variational parameter, a slightly modified set of equations is obtained:

$$\begin{aligned}
M &= n(t - t_0) + M_0 \\
\frac{da}{dt} &= \frac{2}{na}\frac{\partial R}{\partial M_0} \\
\frac{de}{dt} &= \sqrt{\frac{1}{\mu a}}\frac{1}{e}\left(-\sqrt{1-e^2}\frac{\partial R}{\partial \omega} + (1-e^2)\frac{\partial R}{\partial M_0}\right) \\
\frac{di}{dt} &= \frac{1}{\sqrt{\mu a(1-e^2)}}\left(\frac{-1}{\sin i}\frac{\partial R}{\partial \Omega} + \cot i \frac{\partial R}{\partial \omega}\right) \\
\frac{d\Omega}{dt} &= \frac{1}{\sqrt{\mu a(1-e^2)}\sin i}\frac{\partial R}{\partial i} \\
\frac{d\omega}{dt} &= -\frac{\cos i}{\sqrt{\mu a(1-e^2)}\sin i}\frac{\partial R}{\partial i} + \sqrt{\frac{1-e^2}{\mu a}}\frac{1}{e}\frac{\partial R}{\partial e} \\
\frac{dM_0}{dt} &= -2\sqrt{\frac{a}{\mu}}\frac{\partial R}{\partial a} - \sqrt{\frac{1}{\mu a}}\frac{1}{e}(1-e^2)\frac{\partial R}{\partial e}
\end{aligned} \tag{4.4.6}$$

These sets of equations were derived for the case in which the disturbing acceleration is given by the gradient of a potential function. However, this need not be the case, and the equation can be derived for any perturbing acceleration:

$$\frac{d\underline{r}}{dt} = \underline{v} \qquad \text{and} \qquad \frac{d\underline{v}}{dt} = \frac{d^2\underline{r}}{dt^2} = \frac{-\mu}{r^3}\,\underline{r} + \underline{a}$$

The equations obtained previously to describe the time derivatives of the parameter set, α, are simply modified to:

$$\frac{\partial \underline{r}}{\partial \alpha}\frac{d\alpha}{dt} = 0 \qquad \text{and} \qquad \frac{\partial \underline{v}}{\partial \alpha}\frac{d\alpha}{dt} = \underline{a}$$

Details of the solution of this system of equations can be found in the references for this section, notably Battin. The original derivation is attributed to Gauss, and hence the solution is therefore known as Gauss's solution.

The perturbing acceleration is best expressed in the local orbit frame coordinates, the axes of which correspond to the directions, $\underline{r}$, normal to $\underline{r}$, and in the orbit plane (in the forward velocity direction), and completing the right-handed set, perpendicular to the orbit plane. Thus for example, in this frame the position vector $\underline{r}$ is $(r, 0, 0)$.

The perturbing acceleration will be expressed in this frame as $a = (a_r, a_\theta, a_\phi)$. The result is the following equations:

$$\begin{aligned}
\frac{da}{dt} &= \frac{2a^2}{h}\left(e\sin\theta * a_r + \frac{p}{r} * a_\theta\right)\\
\frac{de}{dt} &= \frac{1}{h}\left(p\sin\theta * a_r + ((p+r)\cos\theta + re) * a_\theta\right)\\
\frac{di}{dt} &= \frac{r\cos(\omega+\theta)}{h} * a_\phi\\
\frac{d\Omega}{dt} &= \frac{r\sin(\omega+\theta)}{h\sin i} * a_\phi\\
\frac{d\omega}{dt} &= \frac{1}{he}\left(-p\cos\theta * a_r + ((p+r)\sin\theta) * a_\theta\right) - \frac{r\sin(\omega+\theta)\cos i}{h\sin i} * a_\phi\\
\frac{dM}{dt} &= n + \frac{1}{na^2e}\left((p\cos\theta - 2re) * a_r - ((p+r)\sin\theta) * a_\theta\right)
\end{aligned} \tag{4.4.7}$$

where M is the mean anomaly, θ is the true anomaly, p is the semi-latus rectum, $a(1-e^2)$, and h is the angular momentum, per unit mass. $h = \sqrt{a\mu(1-e^2)}$.

These equations suffer the drawback of singularities when eccentricity or inclination is zero. However, alternative non-singular forms can be derived to eliminate this problem.

The variation in eccentric or true anomalies (E and θ) can also be derived to give the following:

$$\frac{dE}{dt} = \frac{na}{r} + \frac{1}{nae}\left((\cos\theta - e) * a_r - \left(\left(1 + \frac{r}{a}\right)\sin\theta\right) * a_\theta\right) \tag{4.48}$$

$$\frac{d\theta}{dt} = \frac{h}{r^2} + \frac{1}{he}(p\cos\theta * a_r - (p + r)\sin\theta * a_\theta) \tag{4.4.9}$$

These expressions may be rearranged into a more convenient format and using the assumption of a steerable thrust vector, with magnitude T, angle α from the normal to the radius vector in the orbit plane, and angle β out of the orbit plane (azimuth and elevation angles as descirbed in Section 3.3.1). The quantity T is the thrust per unit mass, or perturbing acceleration due to the propulsion.

In this case, then:

$$\frac{da}{dt} = \frac{2a^2}{\sqrt{\mu p}} T\cos\beta(e\sin\theta\sin\alpha + \cos\alpha(1 + e\cos\theta))$$

$$\frac{de}{dt} = \sqrt{\frac{p}{\mu}} T\cos\beta(\cos(\alpha - \theta) + \cos\alpha\cos E)$$

$$\frac{di}{dt} = \frac{r\cos(\omega + \theta)}{h} * T\sin\beta$$

$$\frac{d\Omega}{dt} = \frac{r\sin(\omega + \theta)}{h\sin i} * T\sin\beta$$

$$\frac{d\omega}{dt} = T\left(\frac{1}{he}\cos\beta(-p\cos\theta * \sin\alpha + ((p + r)\sin\theta) * \cos\alpha) - \sin\beta\frac{r\sin(\omega + \theta)\cos i}{h\sin i}\right)$$

$$\frac{dM}{dt} = n + \frac{1}{na^2e} T\cos\beta((p\cos\theta - 2re) * \sin\alpha - ((p + r)\sin\theta) * \cos\alpha) \tag{4.4.10}$$

and

$$\frac{d\theta}{dt} = \frac{h}{r^2} + T\cos\beta\frac{1}{he}(p\cos\theta * \sin\alpha - (p + r)\sin\theta * \cos\alpha) \tag{4.4.11}$$

$$\frac{dE}{dt} = \frac{na}{r} + \frac{1}{nae} T\cos\beta\left((\cos\theta - e) * \sin\alpha - \left(\left(1 + \frac{r}{a}\right)\sin\theta\right) * \cos\alpha\right) \tag{4.4.12}$$

where

$$r = \frac{a(1 - e^2)}{1 + e\cos\theta} = a(1 - e\cos E)$$

4.4.3 Secular effects

The previous equations express the instantaneous rate of change of the ephemeris of a spacecraft. The effect of a perturbation can often be expressed as the sum of two components: a periodic effect (with the frequency of the orbital period of the space-

craft) and a secular effect. In this context, 'secular' implies a slowly varying or even constant rate of change.

Secular effects are of particular importance to the long-term evolution of an orbit. They tend to occur in the presence of constant perturbing terms, when expressed in the local orbital frame. Therefore, in the context of the previous expressions, this would imply a constant or slowly changing steering angle in the applied thrust vector.

This secular effect can be derived by integrating over the changing anomaly of a spacecraft over an orbital period. A suitable choice is eccentric anomaly.

Using the relationships:

$$\cos\theta = \frac{\cos E - e}{1 - e\cos E} \qquad \text{and} \qquad \sin\theta = \frac{\sin E\sqrt{1-e^2}}{1 - e\cos E}$$

the secular rates may be derived for each orbit element. Some examples follow.

This area was notably researched by King-Hele and Burt at the Royal Aircraft Establishment in the 1960s, with the objective of application to electric propulsion systems. The following derivations regarding secular rates are based upon those methods.

Semi-major axis

The expression for the rate of change of the semi-major axis can be modified to be in terms of eccentric anomaly. This may ultimately allow some rationalisation of the derived expressions.

$$\frac{da}{dt} = \frac{2a^2}{\sqrt{p\mu}} T\cos\beta\left(\frac{1}{1 - e\cos E}(e\sin E\sqrt{1-e^2}\sin\alpha + \cos\alpha(1-e^2))\right) \qquad (4.4.13)$$

The relationship $\frac{da}{dE}\frac{dE}{dt} = \frac{da}{dt}$, may then be used.

The following is the approximation for rate of change of eccentric anomaly: $\frac{dE}{dt} = \frac{na}{r} = \frac{n}{(1 - e\cos E)}$; that is, only the rate due to Keplerian motion is included, and the perturbation effect on this rate is small, therefore implying that eccentricity is not too small.

The relative effect of the 1/eccentricity dependent term on the rate of change of eccentric anomaly can be approximated as follows by comparing the relative magnitudes of the first and second terms in equation 4.4.12:

$$\frac{Term1}{Term2} = \frac{na}{r} \Big/ \frac{T}{nae} = \frac{1}{T}\frac{n^2a^2e}{r} \approx \frac{1}{T}n^2ae = \frac{1}{T}\frac{\mu}{a^2}\,e$$

For the first to significantly exceed the second there is the condition that:

$$e \gg \frac{T}{\left(\frac{\mu}{a^2}\right)} \qquad (4.4.14)$$

The ratio of the thrust per unit mass to gravitational acceleration should be a small fraction for such analyses to apply, and the above condition will therefore be satisfied for a wide range of scenarios. Alternatively, non-sigular formulations may be used for cases with very low eccentricity.

Then, recalling that $n = \sqrt{\frac{\mu}{a^3}}$, the rate of change of semi-major axis with respect to eccentric anomaly reduces to:

$$\frac{da}{dE} = \frac{2a^3}{\mu} T \cos\beta (e \sin E \sin\alpha + \cos\alpha \sqrt{1 - e^2}) \tag{4.4.15}$$

The change in semi-major axis over an orbit period (0 to 2π in eccentric anomaly) is (assuming that the thrust magnitude and direction with respect to the orbit frame remain constant) given by:

$$\Delta a = \frac{4\pi a^3}{\mu} \sqrt{(1 - e^2)}\, T \cos\beta \cos\alpha \tag{4.4.16}$$

The orbit period is given by $\tau = 2\pi\sqrt{\frac{a^3}{\mu}}$, and the mean rate of change of semi-major axis over that period is therefore:

$$\frac{\Delta a}{\tau} = 2\sqrt{\frac{a^3}{\mu}} \sqrt{(1 - e^2)}\, T \cos\beta \cos\alpha \tag{4.4.17}$$

This is the secular rate of change of the semi-major axis.

As implied previously, this analysis could alternatively be performed in terms of the true anomaly, leading ultimately to the same result regarding secular rates.

Eccentricity

Considering the change in eccentricity, $\frac{de}{dt} = \sqrt{\frac{p}{\mu}} T \cos\beta (\cos(\alpha - \theta) + \cos\alpha \cos E)$ may be expanded as $\frac{de}{dE} = \sqrt{\frac{p}{\mu}} \frac{1}{\frac{dE}{dt}} T \cos\beta (\cos\alpha \cos\theta + \sin\alpha \sin\theta + \cos\alpha \cos E)$

This results in the following:

$$\frac{de}{dE} = \frac{a^2 \sqrt{1 - e^2}}{\mu} T \cos\beta (\sqrt{1 - e^2} \sin E \sin\alpha + \cos\alpha (2\cos E - e - e\cos^2 E)) \tag{4.4.18}$$

The change in eccentricity over an orbit period (0 to 2π in eccentric anomaly) is (again assuming that the thrust magnitude and direction with respect to the orbit frame remain constant) given by:

$$\Delta e = -3\pi * e \frac{a^2 \sqrt{1 - e^2}}{\mu} T \cos\beta \cos\alpha \tag{4.4.19}$$

In a similar manner to that for the semi-major axis, the secular rate of change of eccentricity can be expressed as:

$$\frac{\Delta e}{\tau} = -\frac{3}{2} e \sqrt{\frac{a(1-e^2)}{\mu}}\, T \cos\beta \cos\alpha \tag{4.4.20}$$

A constant radial thrust component ($\alpha = 90^\circ$) would therefore mean that the eccentricity secular rate is zero. Conversely, a thrust direction in the orbit plane and perpendicular to the radius vector ($\alpha = 0^\circ$) maximises the secular rate.

A change in the plane thrust direction when passing through the minor axis leads to an increased secular rate in eccentricity; that is, using $\alpha = 0^\circ$ switched to $\alpha = 180^\circ$. The switching therefore occurs at eccentric anomaly of $\pm 90^\circ$. If it is further assumed that $\beta = 0$ and so the change per revolution is given by:

$$\Delta e = \frac{8a^2\sqrt{1-e^2}}{\mu}\, T$$

or the secular rate is given by:

$$\frac{\Delta e}{\tau} = \frac{4}{\pi} \sqrt{\frac{a(1-e^2)}{\mu}}\, T \tag{4.4.21}$$

The corresponding secular rate in semi-major axis is zero. It may be seen that equation 4.4.21 will in general yield a substantially greater rate of change in eccentricity than equation 4.4.20, and is therefore an effective strategy for producing such a change.

4.5 LOW-THRUST TRANSFERS

The techniques discussed in the previous section can now be applied to evaluate the possible orbit changes that may be effected.

4.5.1 Low-thrust transfer fundamentals

Analytical methods can be applied to the prediction of some of the properties of transfers using low thrust. The previous section evaluated the secular rates in the ephemeris elements that depend on the strategy for application of the low thrust vector. In this section some locally optimal steering laws will be derived that may be used with full solution (i.e., including periodic terms).

A particularly interesting case is that of a spiral transfer between circular orbits of different radii. Recall that the osculating rate is given by:

$$\frac{da}{dt} = \frac{2a^2}{\sqrt{\mu p}}\, T \cos\beta (e \sin\theta \sin\alpha + \cos\alpha (1 + e\cos\theta)$$

where a is the semi-major axis, e is the eccentricity, μ is the gravitational constant, T is the magnitude of the applied thrust (assumed applied in the orbital plane in this case), and α is the offset of the thrust vector from the normal to the radius vector.

Then, if the initial condition is taken that thrust is only applied normal to the radius vector, then the osculating rate of change of semi-major axis and eccentricity will reduce to:

$$\frac{da}{dt} = \frac{2a^2}{\sqrt{\mu p}} T(1 + e\cos\theta) \qquad \frac{de}{dt} = \sqrt{\frac{p}{\mu}} T(\cos\theta + \cos E) \tag{4.5.1}$$

The osculating eccentricity will therefore experience periodic fluctuations, as will the semi-major axis, even with zero initial eccentricity.

However, it has been demonstrated that the secular rate of change of the semi-major axis is, for the steering angle case here, given by:

$$\frac{\Delta a}{\tau} = 2\sqrt{\frac{a^3}{\mu}}\sqrt{(1-e^2)}\, T\cos\beta\cos\alpha = 2\sqrt{\frac{a^3}{\mu}}\sqrt{(1-e^2)}\, T$$

This may be treated as a continuously evolving time derivative of semi-major axis for small perturbing acceleration and times significantly greater than a single period.

The secular rate of change of eccentricity is given by:

$$\frac{\Delta e}{\tau} = -\frac{3}{2} e\sqrt{\frac{a(1-e^2)}{\mu}}\, T\cos\beta\cos\alpha = -\frac{3}{2} e\sqrt{\frac{a(1-e^2)}{\mu}}\, T$$

In the case where the initial eccentricity is zero, and only 'secular' derivatives are considered, a simple integral may be obtained. For the case of constant thrust and mass (recalling that in this expression T is thrust/mass):

$$\sqrt{\frac{\mu}{a_0}} - \sqrt{\frac{\mu}{a_f}} = T\Delta t \tag{4.5.2}$$

This is equivalent to the following statement:

$$\Delta V = T\Delta t = \sqrt{\frac{\mu}{a_0}} - \sqrt{\frac{\mu}{a_f}} = Vcirc_0 - Vcirc_f \tag{4.5.3}$$

where ΔV is the equivalent ΔV given by acceleration $*$ time, and $Vcirc$ is the speed in a circular orbit. This assumes that fuel mass is very small.

Therefore, a secular analysis will predict, by approximation, the evolution of the semi-major axis with time. The following numerical evaluation describes the effect with full perturbations included. Figure 4.5.1 illustrates the case of an initially near circular orbit with radius at 24,371 km. A constant perturbing acceleration of 0.0004 m/s/s is applied in a direction perpendicular to the radius vector.

Continuing the secular analysis, if mass is varying with fuel usage then:

$$\sqrt{\frac{\mu}{a_0}} - \sqrt{\frac{\mu}{a_f}} = \int_{t_0}^{t_f} \frac{T}{M} dt = -Isp * g_0 * Ln\left(\frac{m_f}{m_0}\right) \tag{4.5.4}$$

where Isp is specific impulse (expressed in seconds), and g_0 is the reference gravitational acceleration at 9.80665 m/s/s.

It is possible to obtain further interesting results, and these are now described.

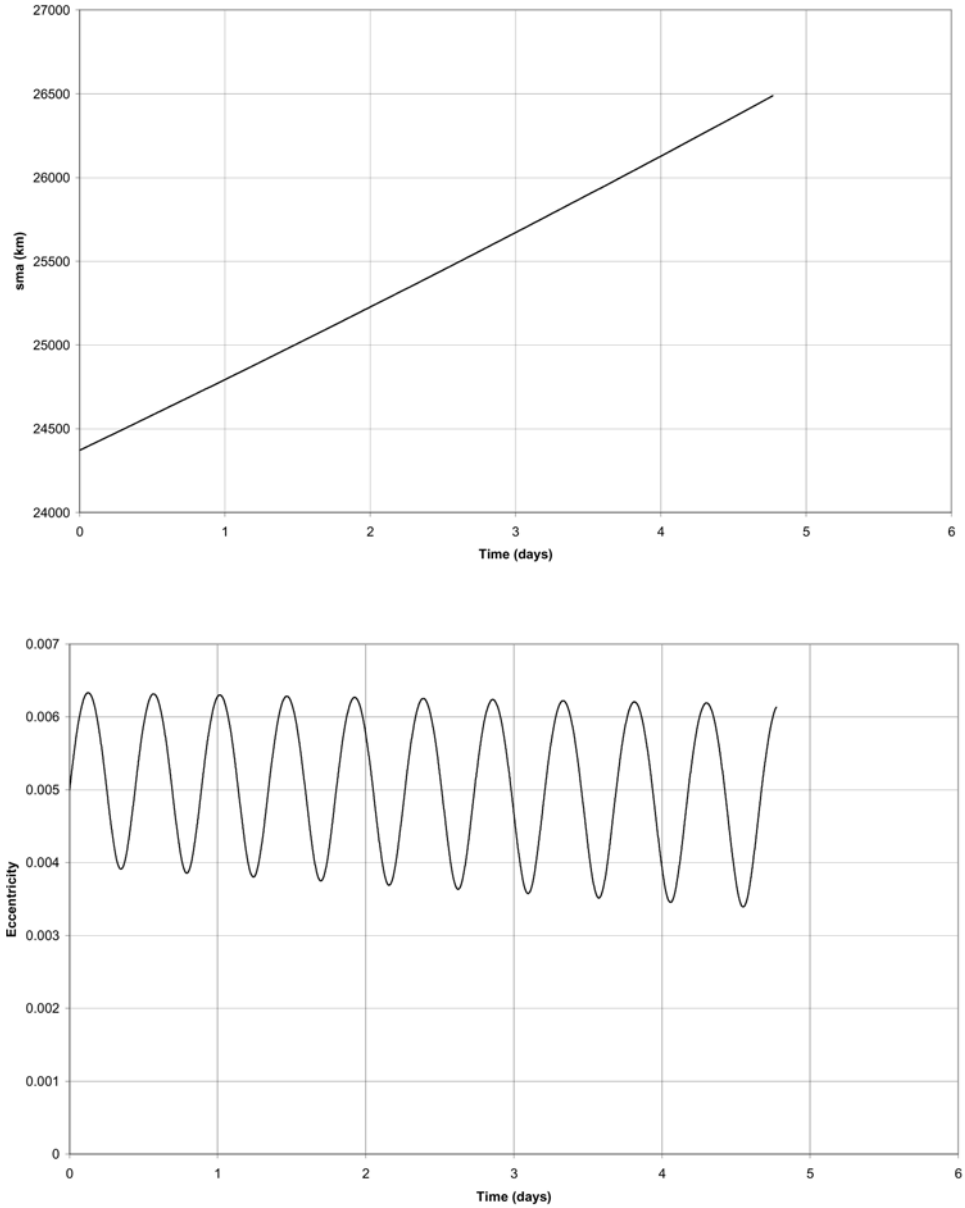

Figure 4.5.1. Evolution of a near circular orbit with constant perturbing acceleration perpendicular to the radius vector. In the upper figure the semi-major axis shows a steady increase with time, as predicted by the secular equations. In the lower figure the eccentricity maintains an average close to its initial value, as predicted by the secular rates. A small secular draft is also present. The periodic nature of the full solution results in the small-amplitude oscillation seen here.

The strategy is to devise steering laws that can instantaneously maximise the rate of change of a given orbital element. Such a steering law can then be applied in a particular phase of a transfer. This analysis will consider the full perturbation equations.

Maximum rate of change of orbital energy

In this case, the objective is to provide a steering law that will maximise the rate at which the spacecraft's orbital energy changes.

The orbital energy is given by:

$$Energy = -\frac{\mu}{2a}$$

Therefore:

$$\frac{dEnergy}{dt} = \frac{\mu}{2a^2}\frac{da}{dt}$$

Consequently, the rate of change of energy is maximised for maximum rate of change of the semi-major axis. Applying the condition that $\frac{\partial \frac{da}{dt}}{\partial \alpha} = 0$ at a max/min, the following expression for optimum α is obtained:

$$\tan\alpha = \frac{e\sin\theta}{1 + e\cos\theta} \tag{4.5.5}$$

Comparison with the expression for flight path angle (Γ, the angle by which the velocity is offset from the normal to the radius vector) reveals that $\alpha = \Gamma$; that is, the thrust must take place along the velocity vector. This is an alternative derivation of the classical result for maximising the energy increase of a system; that is, applying an acceleration along the direction of the instantaneous velocity vector.

This optimum rate of change can be compared with the case of a constant steering angle, perpendicular to the radius vector ($\alpha = 0$). In Figure 4.5.2, the orbit considered is GTO (i.e., low perigee and apogee at geostationary radius), the thrust/mass is assumed constant at 0.0001 m/s/s, and the ephemeris is assumed to remain constant throughout the revolution. The plots simply illustrate the effect of using the optimum thrust direction and shows the instantaneous apogee rate in the given orbit.

An example of the application of this optimum steering law is now considered. The example evaluated here is the case of a spacecraft again in a standard geostationary transfer orbit. The thrust/mass in the following trajectory is 0.0004 m/s/s.

The low-thrust ΔV applied in this case is approximately 300 m/s. The semi-major increases to approximately 28,000 km. Comparison of the effects of optimum and zero in plane steering angles is shown in Figure 4.5.4.

As the orbit under consideration becomes less eccentric, the effect of using the optimum steering angle diminishes, as expected.

In this second example (Figure 4.5.5), the perigee is the same as in the first case, but the apogee is reduced. Not only is the effect of optimal steering reduced, but the rate of change of the semi-major axis is reduced at all points in the orbit.

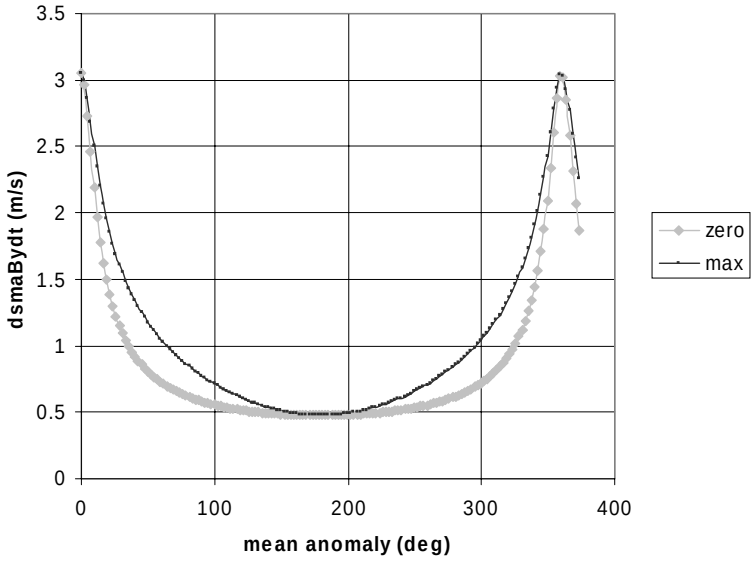

Figure 4.5.2. A comparison of optimum and zero steering-angle options for increasing the semi-major axis for an initial elliptical orbit with an eccentricity of 0.73 (GTO). The two steering-law solutions provide the same rate of change of semi-major axis at zero and 180-degree mean anomalies. Between these, significant variations in rate are observed. Thrust/mass $= 0.0001\,\mathrm{m/s^2}$.

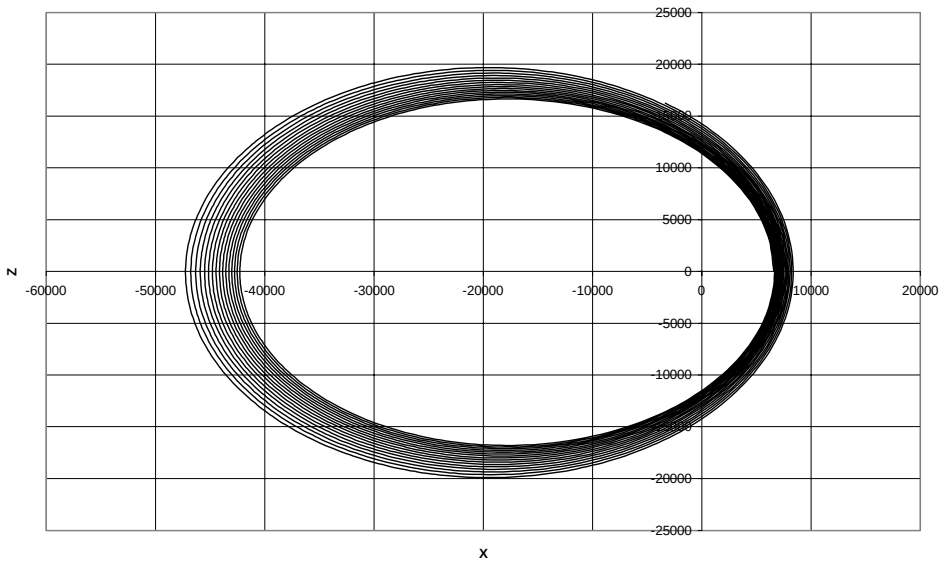

Figure 4.5.3. A low-thrust trajectory with maximum rate of change of semi-major axis steering over a period of nearly 9 days. The application of an optimum semi-major axis steering profile results in a secular increase in both apogee and perigee. Thrust/mass $= 0.0004\,\mathrm{m/s^2}$.

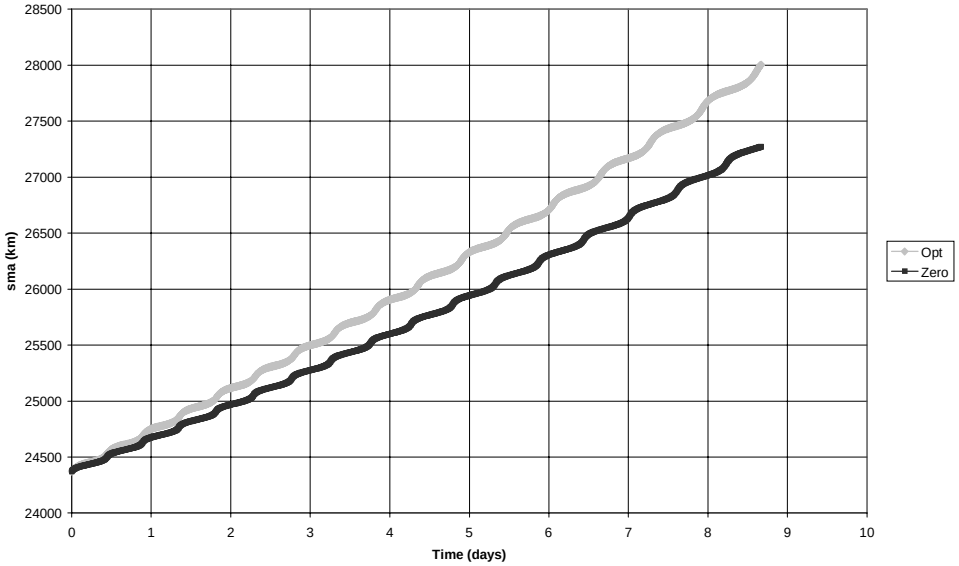

Figure 4.5.4. Low-thrust semi-major axis evolution with maximum rate of change of semi-major axis and zero α steering over a period of nearly 9 days. The steering law for maximum rate of change of semi-major axis demonstrates a significant gain over the zero α case. Thrust/mass $= 0.0004\,\mathrm{m/s^2}$.

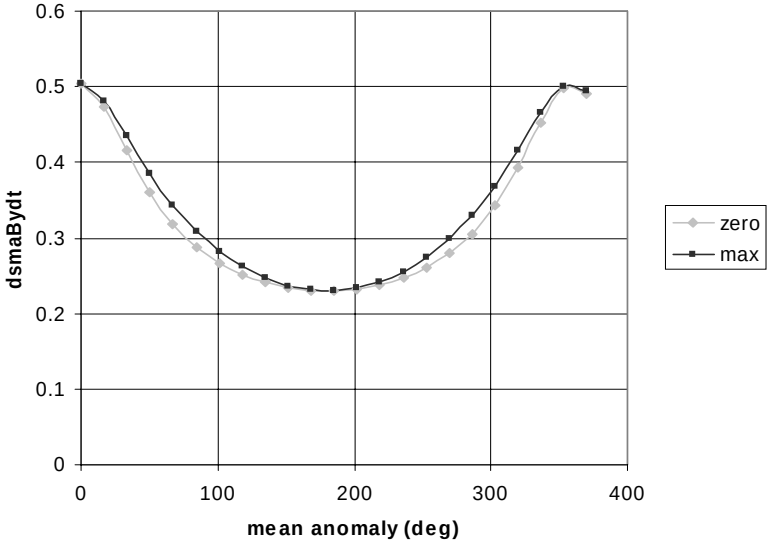

Figure 4.5.5. A comparison of optimum and zero steering-angle options for increasing the semi-major axis for an initial elliptical orbit with an eccentricity of 0.37. Thrust/mass $= 0.0001\,\mathrm{m/s^2}$.

Maximum rate of change of apogee altitude

In this second case of an optimal steering law, the objective is to maximise the rate at which the spacecraft's apogee altitude changes.

The osculating apogee is given by $rapogee = a(1+e)$
The time derivative is therefore:

$$\frac{drapogee}{dt} = \frac{da}{dt}(1+e) + a\frac{de}{dt} \tag{4.5.6}$$

This results in the following expression:

$$\frac{drapogee}{dt} = T\cos\beta\frac{a^2}{\sqrt{\mu p}}(1+e)(\cos\alpha(2+(1-e)\cos E)+(1+e)\cos(\alpha-\theta)) \tag{4.5.7}$$

In the same way that, in the previous discussion, the rate of change of semi-major axis, or energy, was maximised, the rate of change of apogee radius can now be maximised. Taking the partial derivative and finding the stationary point, to obtain the expression for α that gives the max/min rate of change of apogee yields the following expression for the optimal steering angle:

$$\tan\alpha = \frac{\sin\theta(1+e)(1+e\cos\theta)}{(1+\cos\theta)(2+e(1+\cos\theta)+e^2(\cos\theta-1))} \tag{4.5.8}$$

The effect of this steering law is shown in Figure 4.5.6, and compared with a maximum semi-major axis rate steering law. It can be seen from this figure that

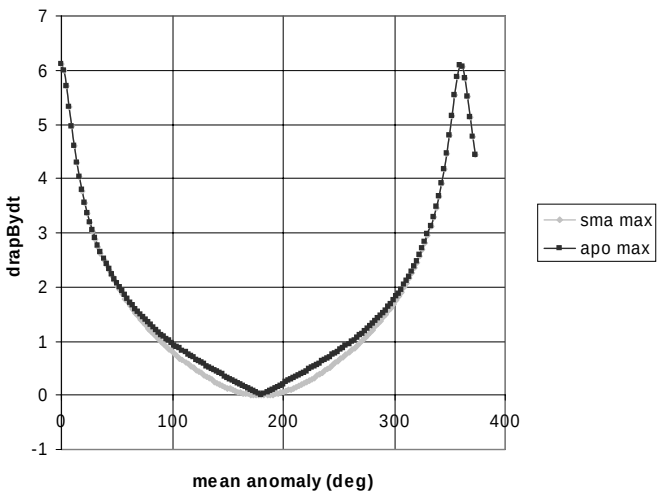

Figure 4.5.6. A comparison of optimum apogee raising and optimum semi-major axis raising steering-angle options for increasing apogee for an initial elliptical orbit with an eccentricity of 0.73 (GTO). The application of Equation 4.5.8 may be used to examine the maximised rate of change of apogee altitude. The maximised rate of change of apogee is here shown as a function of mean anomaly, and is compared with the rate of change that results from the maximum semi-major axis rate law. Thrust/mass = 0.0001 m/s^2.

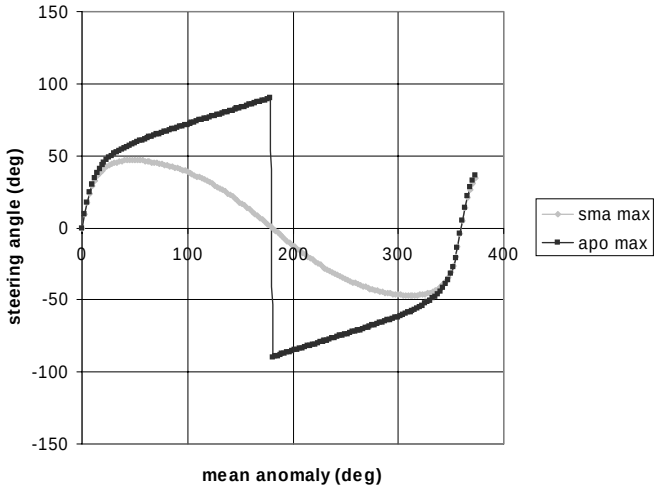

Figure 4.5.7. A comparison of steering angles for optimum apogee raising and optimum semi-major axis raising steering-angle options for increasing apogee for an initial elliptical orbit with an eccentricity of 0.73 (GTO).

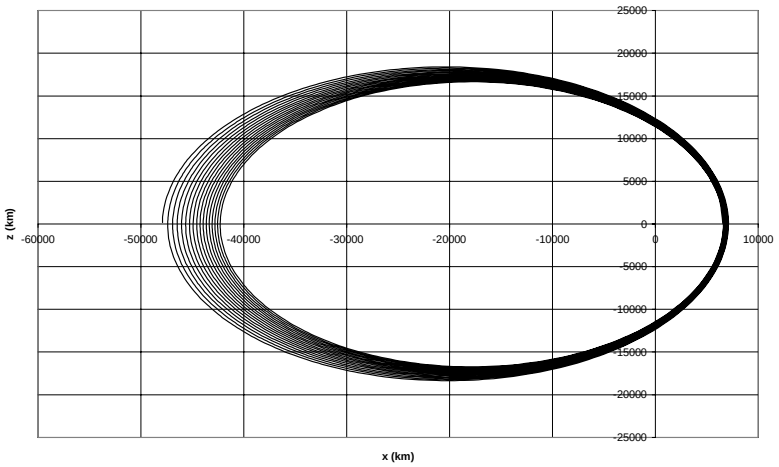

Figure 4.5.8. A low-thrust trajectory with maximum rate of change apogee altitude steering over a period of nearly 9 days. The application of an optimum apogee raising steering profile results in a secular increase in apogee but only a very small change in perigee. This behaviour can be contrasted with the semi-major axis maximisation case. Thrust/mass $= 0.0004\,\mathrm{m/s^2}$.

using thrust aligned along the velocity vector results in an apogee rate only slightly reduced from the optimum case.

The steering profiles used in Figure 4.5.6 are shown in Figure 4.5.7. The evolution of the orbit using the maximum apogee rate steering law is shown in Figure 4.5.8.

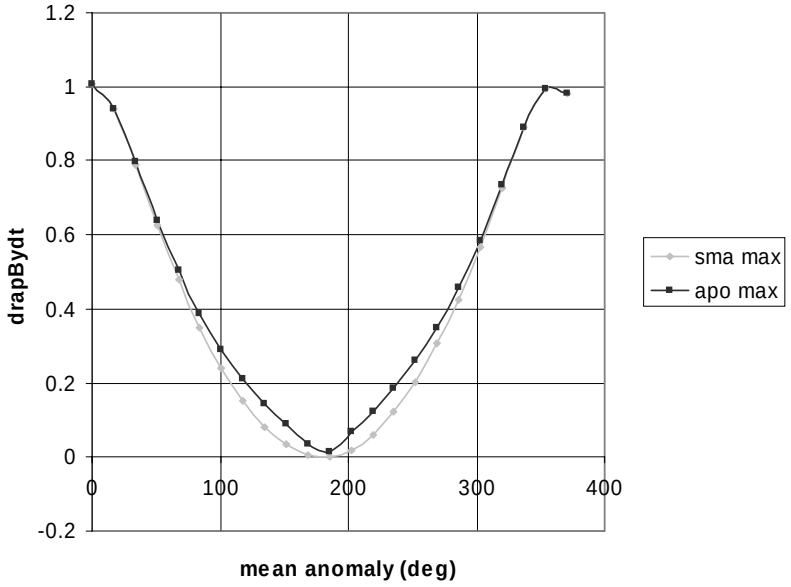

Figure 4.5.9. A comparison of optimum apogee raising and optimum semi-major axis raising steering angle options for increasing apogee for an initial elliptical orbit with an eccentricity of 0.37.

Reducing the eccentricity to 0.37 results in the apogee change rate being significantly reduced when compared to the higher-eccentricity case. This is seen in Figure 4.5.9.

Maximum rate of change of inclination

In this third case the objective is to provide a steering law that will maximise the rate at which the spacecraft's orbital inclination changes.

The rate of change of inclination can be maximised by using an out-of-plane steering angle set at $\pm 90^\circ$, with a direction that switches at crossings of the orbit antinode ($\omega + \theta$ reaching $\pm 90^\circ$):

$$\frac{di}{dt} = \frac{r\cos(\omega+\theta)}{h} * T * sign(\cos(\omega+\theta)) \tag{4.5.9}$$

In this situation (out-of-plane steering at 90°), the semi-major axis and eccentricity remain approximately constant. The right ascension of the ascending node and the argument of pericentre will be influenced by the thrust with such a steering law:

$$\frac{d\Omega}{dt} = \frac{r\sin(\omega+\theta)}{h\sin i} * T * sign(\cos(\omega+\theta)) \tag{4.5.10}$$

$$\frac{d\omega}{dt} = -\frac{r\sin(\omega+\theta)\cos i}{h\sin i} * T * sign(\cos(\omega+\theta)) \tag{4.5.11}$$

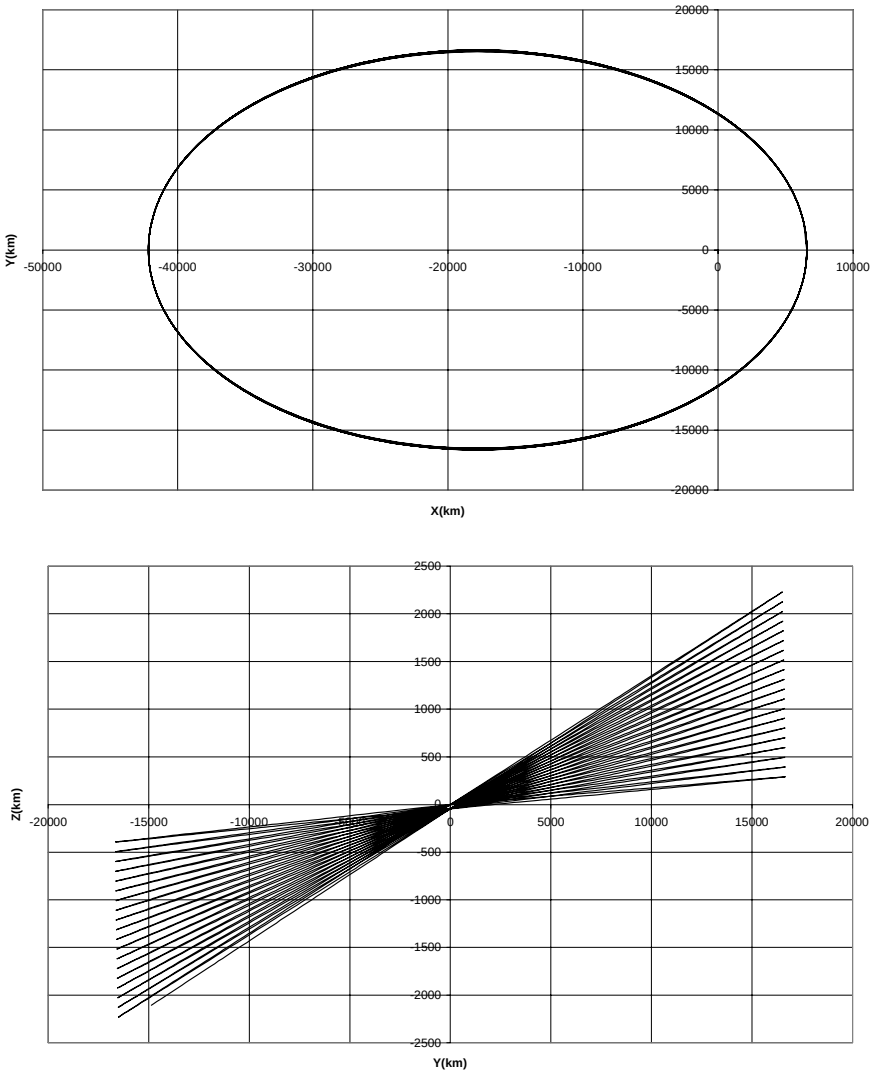

Figure 4.5.10. Low-thrust GTO trajectory evolution with thrust/mass at 0.0004 and initial inclination at 1°. An out of phase steering law is applied to increase inclination.

For low inclinations, the node and pericentre rotate in opposite directions at almost the same rate.

Such an example can be illustrated for the following, initially GTO. The thrust/mass is set to a constant value of 0.0004 m/s/s. The orbit is propagated for approximately 9 days, with out-of-plane thrust vectoring to maximise the rate of change of inclination. The evolution of the trajectory is shown in Figure 4.5.10. The semi-major axis and eccentricity remain constant, but the orbital inclination shows a secular rate of change.

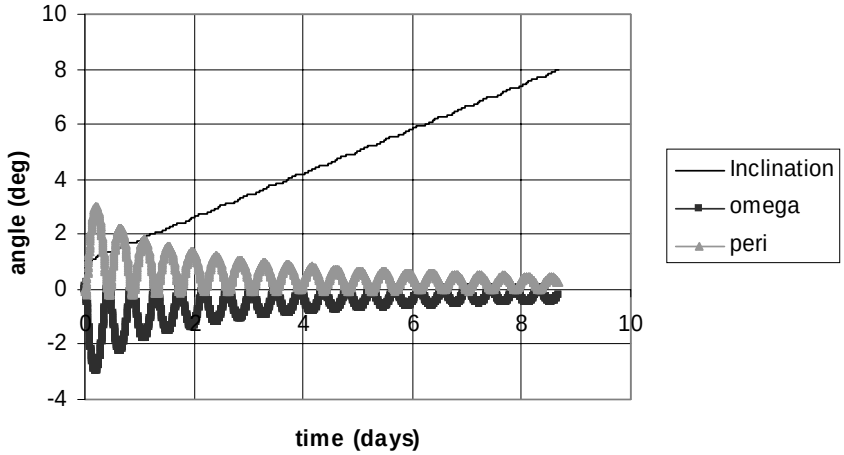

Figure 4.5.11. Low-thrust GTO trajectory evolution with thrust/mass at 0.0004 and initial inclination at 1°. The periodic rates of right ascension of the ascending node and argument of pericentre are almost opposite, As the inclination increases, the periodic excursions reduce in amplitude as predicted by Equations 4.5.10 and 4.5.11.

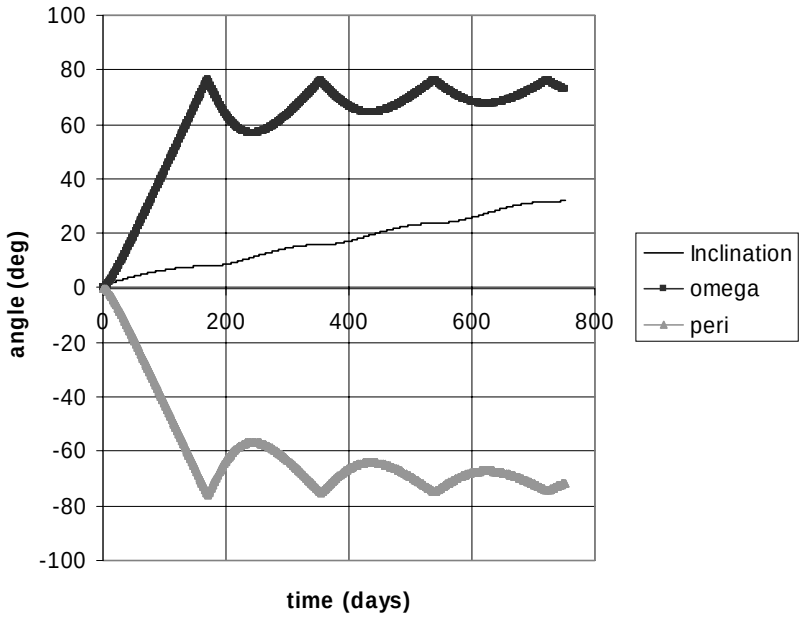

Figure 4.5.12. Low-thrust heliocentric 1-AU orbit ephemeris evolution with thrust/mass at 0.0004 m/s/s and initial inclination at 1°. The inclination increases more quickly than in the previous example (per orbit period). The periodic excursions reduce in amplitude more significantly as the inclination increases.

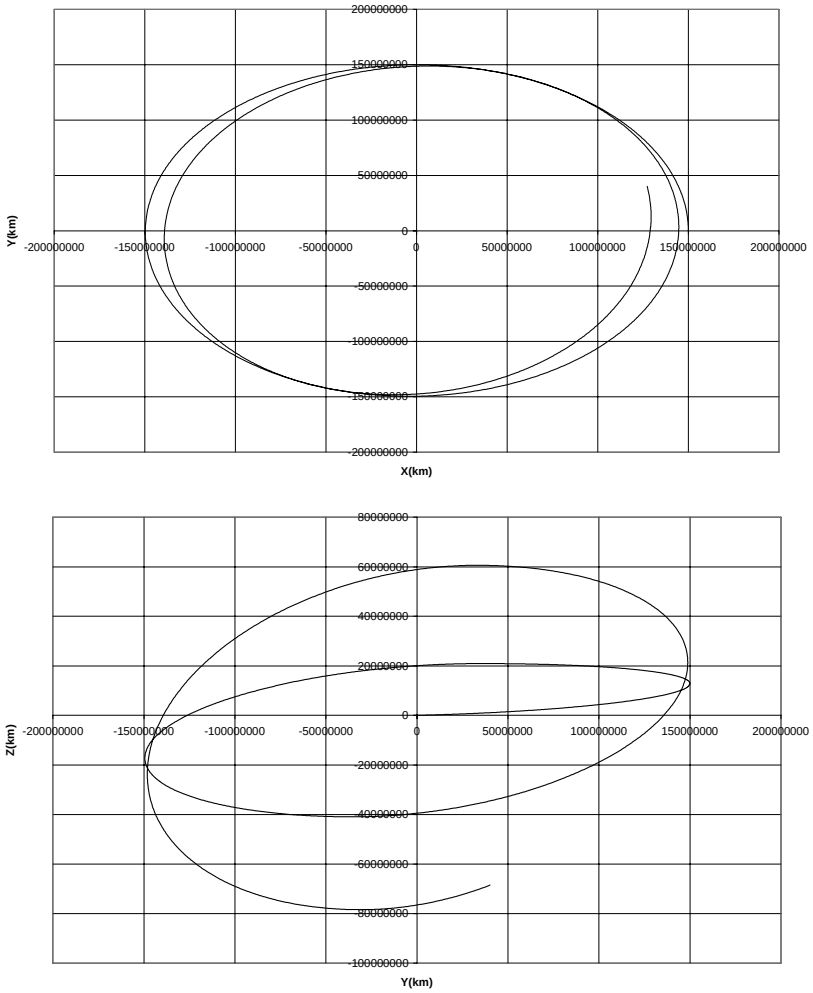

Figure 4.5.13. Low-thrust heliocentric 1-AU trajectory evolution with thrust/mass at 0.0004 m/s/s and initial inclination at 1°, over a period of two years. Motion both in (upper figure) and perpendicular to (lower figure) the eliptic is shown.

In Figure 4.5.11, the relationship between the right ascension of ascending node and the argument of perigee is explored. The ΔV applied by the low thrust system to achieve this transfer is 300 m/s.

A similar example can be demonstrated for an interplanetary spacecraft in a circular orbit at 1 AU with an initial inclination of 1°. A constant thrust/mass of 0.0004 m/s/s is again applied, for a period of two years. The results are shown in Figure 4.5.12 and 4.5.13. The thrust is applied over a long period of time and so the inclination change per revolution is relatively high. The ΔV applied by the low-thrust system to accomplish this transfer is 26 km/sec.

4.6 LOW-THRUST FOR PLANETARY ESCAPE AND CAPTURE

Low thrust may be used to transfer from an initially Earth-bound orbit to reach escape. Many strategies are available to execute such a manoeuvre, and it is therefore important to first analyse their efficiency.

4.6.1 Using thrust-coast arcs for energy gain

In the previous section, analysis of semi-major axis steering laws shows that the most effective area of application is at perigee. The term $\frac{da}{d\Delta V}$ may be evaluated as follows:

$$\frac{da}{d\Delta V} = \frac{\overline{\frac{da}{dt}}}{\overline{\frac{d\Delta V}{dt}}} \qquad \text{where} \qquad \frac{d\Delta V}{dt} = \frac{Thrust}{Mass}$$

for an extremely high specific impulse system (in which the mass remains approximately constant).

This expression may now be evaluated. It is similar to that shown in Figure 4.5.2, but now it is illustrated with respect to true anomaly rather than mean anomaly. The following example uses a GTO. The thrust/mass is assumed constant at 0.0001 m/s/s. The result may be seen in Figure 4.6.1.

The time average over a range of true anomalies over which the burn is applied may be calculated:

$$\frac{\overline{da}}{d\Delta V} = \frac{\int_0^t \frac{da}{d\Delta V} dt}{\int_0^t dt}$$

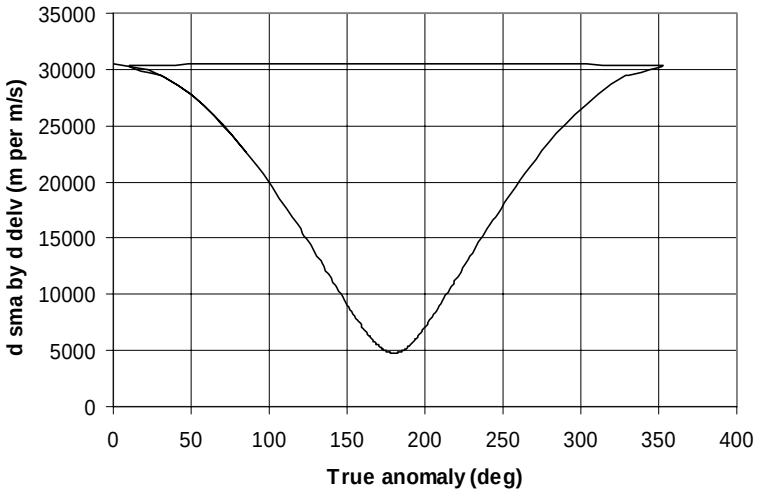

Figure 4.6.1. The change in semi-major axis per unit applied ΔV versus true anomaly.

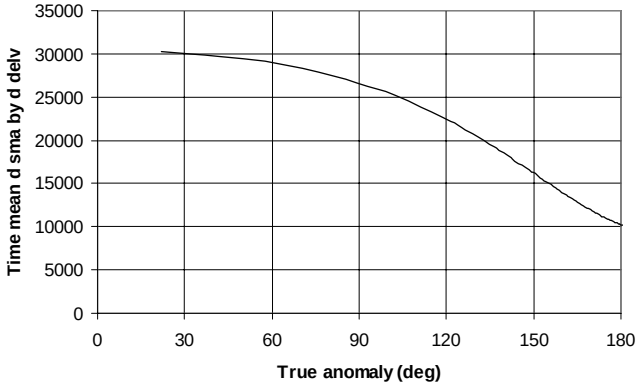

Figure 4.6.2. The change in semi-major axis per unit applied ΔV (time averaged over an applied true anomaly range) versus true anomaly range from perigee. Here the true anomaly is half of the thrust arc, as it is assumed to be applied symmetrically about perigee. The use of a short thrust arc over a small range of true anomaly is far more effective than thrusting over 180° of true anomaly (half thrust arc angle). The orbit is GTO in this example.

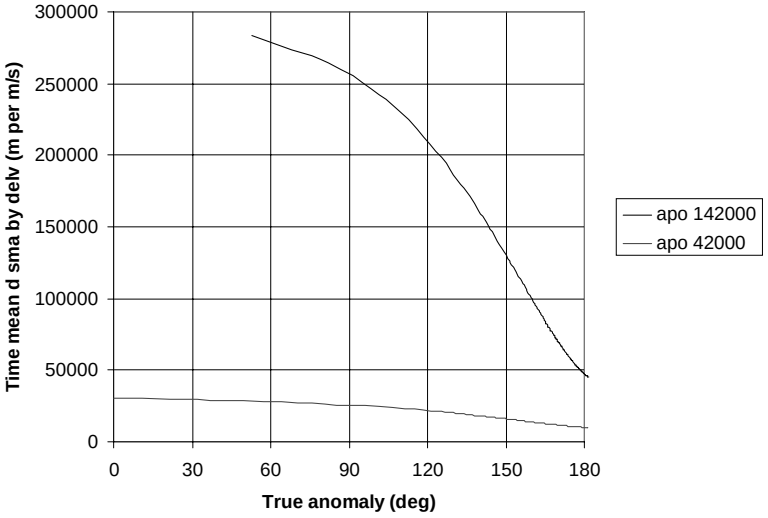

Figure 4.6.3. The change in semi-major axis per unit applied ΔV (time averaged over an applied true anomaly range) versus true anomaly range from perigee. Different orbit apogees are considered (at 42,000 and 142,000 km). Perigee is an altitude of 200 km.

This average quantity is now evaluated over a range of thrust arc lengths, assuming a constant orbit ephemeris (except anomaly). This means that the effect of the perturbing acceleration is neglected over the application of the thrust arc. The effect is shown in Figure 4.6.2.

As the orbit becomes more eccentric, the sensitivity to true anomaly is even further exaggerated. This can be seen in Figure 4.6.3.

4.6.2 Application of a low-thrust strategy for escaping Earth

Having considered the theoretical basis for efficiently raising the apocentre, consideration can be given to a number of practical examples of escaping Earth's influence.

Use of continuous thrust

Firstly, continuous thrust is considered. It has been shown previously that when using a very-low-thrust system, certain analytical predictions are available for circular orbit transfers. Transfers from both initially circular and elliptical orbits may be considered.

In the case of initially circular orbits, a series of analytical predictions may be made. These are analysed in Figure 4.6.4.

Transfers from the initial elliptical injection orbit to Earth escape points can be simulated using continuous thrust directed along the velocity vector. This is the optimal direction to obtain the greatest instantaneous rate of increase of energy of the orbit, and as such is a good approximation to any globally optimal apogee raising strategy.

For the following simulations the initial elliptical orbit considered corresponds to an orbit with an apogee altitude equivalent to GTO: semi-major axis: 24,000 km; eccentricity, 0.72.

Other ephemeris components (inclination, node and perigee) are generally optimised on an individual mission basis depending on the requirement on the departure vector.

Semi-major axis raising is then performed until escape is reached. Two possible escape conditions are considered. The escape points are defined as follows:

(1) The spacecraft reaching a lunar crossing and performing a gravity assist. Assuming that a lunar encounter is possible, then the post-fly-by orbit may be calculated by patched conics. In general, this post-fly-by orbit will be an escape orbit relative to Earth. However, due to the low speed in approaching the Moon (due to the perigee raising effect in spiralling), only low V_∞ escapes from the Earth system are possible (i.e., the energy marginally exceeds zero).
(2) The spacecraft reaching a point where eccentricity first exceeds 1.0 (assuming that lunar gravity assist is not available). This point is often reached after crossing the lunar radius (except in higher-thrust cases).

Simulation shows that typically a ΔV of 4,000 m/s is required to reach escape directly and 3,200 m/s to reach the lunar crossing orbit from which escape may be achieved after gravity assist. These results clearly show the penalty incurred by low thrust. These numbers can be compared with the impulsive ΔV required for such a marginal escape, being typically 750 m/s. The ΔV loss lies between the two loss factors implied by the two apogee cases shown in Figure 4.6.3. Such a loss factor is obtained by the ratio of values at 180 degrees true anomaly thrust application about perigee (i.e., constant thrust) and zero true anomaly thrust arc (i.e., impulsive thrust application).

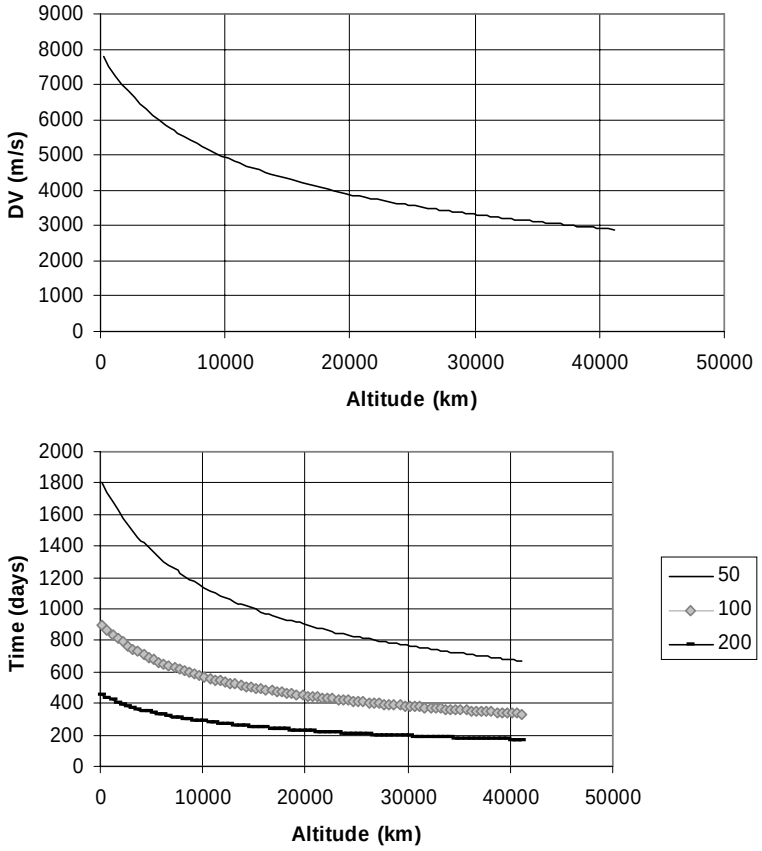

Figure 4.6.4. Transfer duration and ΔV dependence on initial circular orbit altitude in reaching Earth escape. In the upper figure, if transfer is started in low Earth orbit (for example, a 200 km altitude parking orbit) then a large ΔV (over 7 km/sec) is required to reach escape (where the orbit speed is effectively zero at a very high radius). Increasing this initial orbit altitude to GEO (36,000 km) the ΔV requirement drops to approximately 3 km/sec. The other aspect of such a transfer is the time taken. If it is assumed that the specific impulse is so high that the fuel mass is negligible, the results in the lower figure are obtained. Three different acceleration levels are considered, in terms of mN per tonne. With a typical low thrust available at 100 mN/tonne, it takes three years to reach escape from LEO.

The actual loss of course depends on the average of the loss factor over the complete range of intermediate apogee altitudes in the sequence.

In the case of direct thrust to achieve escape, the actual ΔV s and times to escape are greater than for the lunar crossing case, indicating that considerable advantage can be taken of an escape generated by employing a lunar gravity assist manoeuvre.

A typical ΔV saving of 800 m/s is obtained by use of lunar gravity assist. In practice, it is possible to engineer a lunar gravity assist for almost any launch date, because of the extended transfer time required to reach the Moon (many revolutions

of the Moon about the Earth occur during the transfer). The encounter is achieved by the introduction of a series of coast arcs to achieve the required phase with respect to the Moon.

However, the post-gravity assist state must be considered. In general it is not sufficient to simply engineer an encounter with the Moon. In order to achieve the required post-fly-by conditions (escape in the required direction with respect to the Earth–Moon system) it is necessary to control the location of the lunar encounter. Without this constraint, marginal escape conditions can result in subsequent recapture under the influence of solar perturbations. To ensure the desired escape conditions requires additional phasing manoeuvres and, in some circumstances, restrictions on the launch window.

It is possible to utilise lunar gravity to assist in the orbit raising prior to lunar encounter. This takes the form of a 'gravitational pumping' effect if the correct phase with respect to the Moon can be established. However, launch window restrictions are again implied.

Utilisation of this type of orbit raising is particularly attractive when very-low-thrust (and thus long transfer times) are considered. An example of such a mission is ESA's SMART-1.

Figure 4.6.5 shows a continuous thrust spiral, starting from GTO until Earth escape is reached.

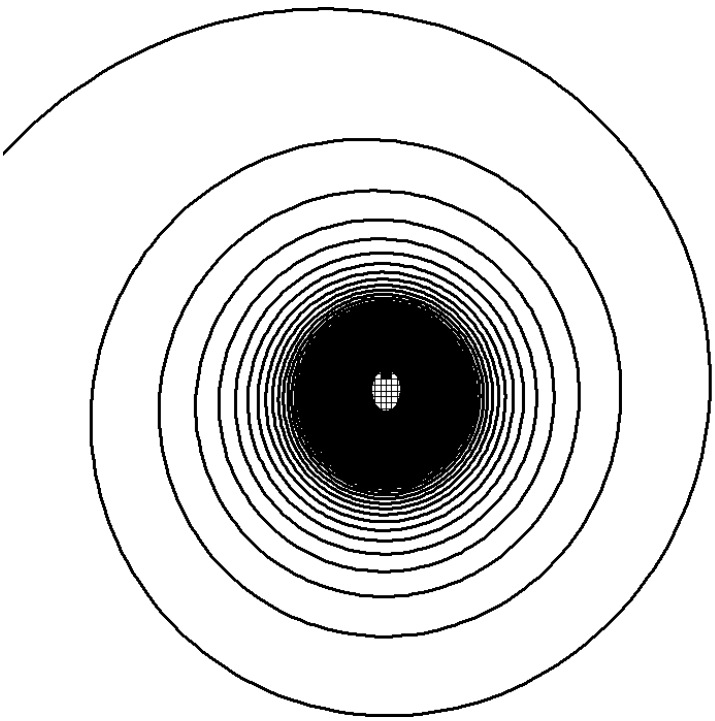

Figure 4.6.5. Transfer from GTO to earth escape. Initial acceleration = 100 mN/tonne.

The effect of coast arcs on the transfer from GTO to Earth escape

Insertion of coast arcs allows the apogee raising input to be concentrated closer to perigee and hence increase efficiency of the transfer (in terms of ΔV required). However, there is inevitably a penalty in terms of the time taken to reach escape.

The coast arcs considered are centred about apogee. Such a thrust-coast arc trajectory is illustrated in Figure 4.6.6. Figure 4.6.7 shows the effect of these arcs on ΔV for both the case of thrust until Lunar encounter and thrust to direct Earth escape.

The results obtained here can be compared qualitatively with the previous prediction for the efficiency of different thrust arc lengths for a given orbit eccentricity. In the case in Figure 4.6.7, the results are obtained from simulation, and the eccentricity of the orbit changes through the course of the transfer. If it is possible to increase the transfer time to escape by approximately 120 days (from the continuous case), then these results show that a ΔV saving of 1 km/sec is possible (in the Lunar gravity assist case). The analysis can be expressed as ΔV/thrust relationships, seen in Figure 4.6.8.

It should once again be noted that when considering lunar gravity assist, restrictions on the launch window may be implied. There is, in fact, a greater potential restriction when coast arc transfers are considered, in that the initial direction of the apse line requires greater control. This is because the eventual lunar encounter will

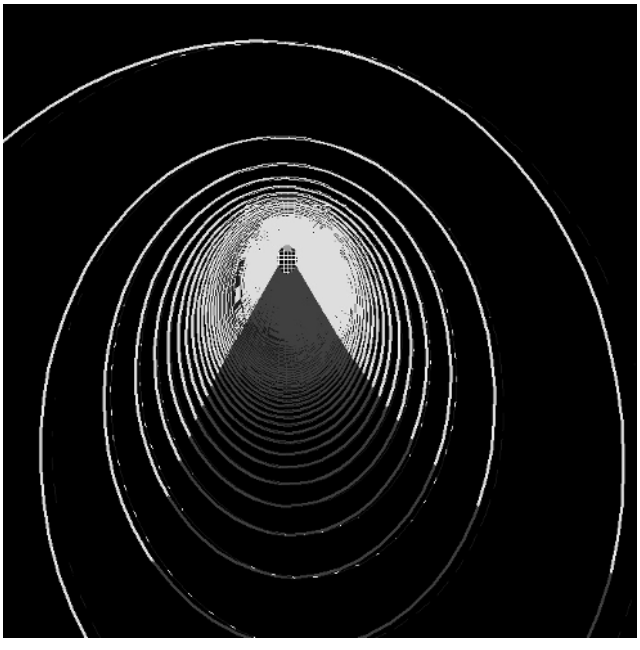

Figure 4.6.6. Transfer from GTO to Earth escape with 60-degree coast phase at apogee. In the figure the thrust arcs are the light shaded segments of the trajectory.

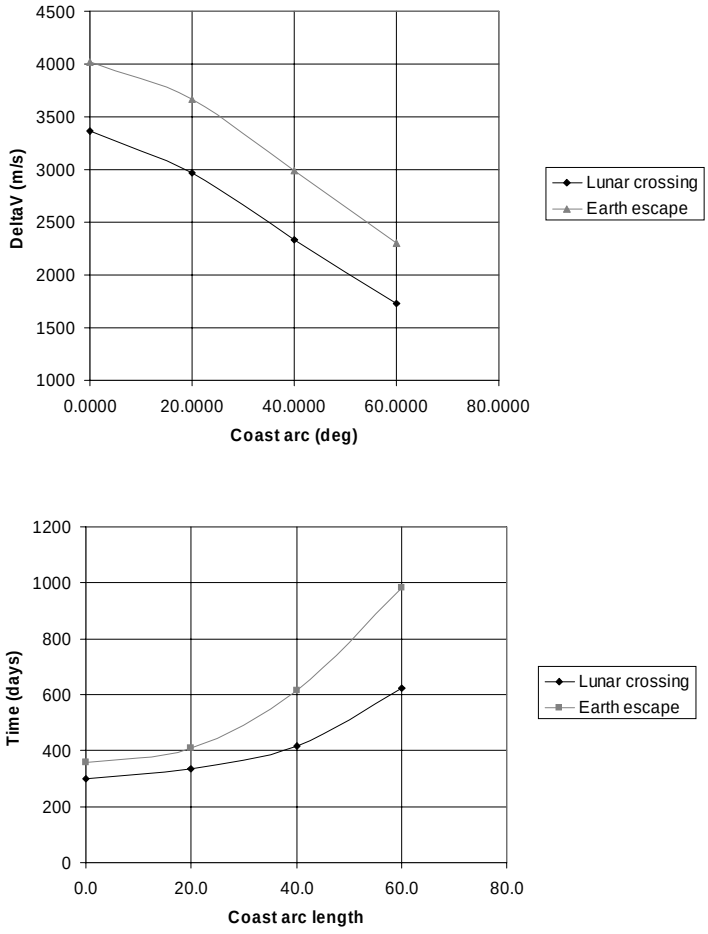

Figure 4.6.7. The effects of coast arcs on ΔV and the time to escape for the transfer to Earth escape using lunar gravity assist and direct thrust to Earth escape. The initial orbit is again a GTO case. There is a strong relationship due to the relatively high initial eccentricity of the initial orbit. The comparison with the continuous thrust case (denoted by the arc = 0 case) shows that considerable ΔV savings are possible in the transfer to lunar radius. The penalty is the effect on transfer time, which increases as the coast arc length increases. The results here assume a thrust per tonne of approximately 165 mN.

tend to occur close to the apse line, the direction of which remains relatively unaffected by the progressive apogee raising.

Launch window restrictions also apply in the non-gravity assist case, as the direction of the initial elliptical injection orbit apogee direction is closely related to the final escape direction.

The evolution of the trajectory shows that initially the apogee is raised, and the perigee is also progressively raised. This factor contributes to the ΔV loss in reaching the target escape orbit.

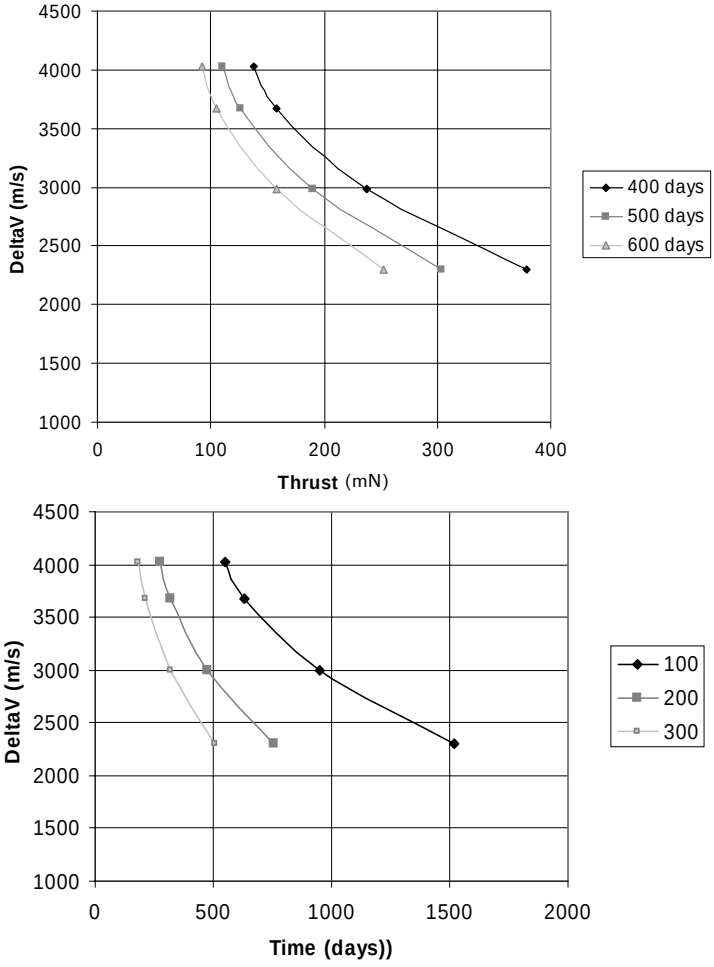

Figure 4.6.8. ΔV versus thrust and transfer duration for low-thrust Earth escape from GTO. The upper figure shows the relationships between ΔV, thrust and transfer duration, determined by the length of the coast arc employed. A distinct trade-off exists between ΔV and thrust, for a given target transfer duration. Alternatively, if a given thrust level is considered, the trade-off is between transfer duration and ΔV. The lower figure shows the relationship between ΔV to reach escape and transfer time (for given thrust per tonne levels). Each ΔV/time curve is obtained from use of different coast arc lengths around apogee. These results apply to a direct escape case.

The analysis here illustrates the wide variation in transfer strategies with regard to selecting coast arcs in an apogee raising strategy. Once a given area of interest has been established it is possible to proceed from these initial solutions to a formally optimised solution in which a precise escape target orbit is specified and the location and duration of each coast arc is optimised, together with details of the steering profile during the thrust arcs. In fact, such optimal solutions often possess a second,

shorter thrust arc at each apocentre, to maintain a low pericentre. This would otherwise rise and reduce the efficiency of the apocentre raising.

4.6.3 Planetary capture and orbit insertion with low thrust

The reverse of this escape procedure may be performed to insert the spacecraft into orbit about a target planet. The previous analyses have considered the manoeuvre required to reach escape (zero energy). Therefore, in the capture and orbit insertion strategies the starting point is a parabolic approach condition.

The initial pericentre target is much higher than in a chemical, high-thrust case, because the low-thrust spiral will result in considerable pericentre reduction before the final target orbit about the planet is reached.

4.6.4 Optimal utilisation of low-thrust for interplanetary transfers

Low-thrust systems may be used effectively for an interplanetary transfer. A number of questions exist regarding the most effective utilisation of such a system. There are three phases to consider for a basic interplanetary mission: escape from the original planet, the transfer between planets, and the capture at the target planet.

The previous section considered the options for escaping and capturing at planets. Having reached an escape condition (an osculating parabolic orbit), the spacecraft must be further accelerated to gain sufficient velocity change in the heliocentric system to reach the target planet. Then, when approaching the planet, a reverse of this procedure is employed to remove the planet relative approach velocity and so allow capture into a bound orbit.

Use of low thrust for planetary escape and/or capture has a significant implication for the duration of the transfer. Such manoeuvres generally imply a large speed change to be imparted by the low-thrust system. Therefore, an attractive alternative is to consider using low thrust only for the interplanetary phase and conventional high-thrust chemical propulsion to achieve the escape and capture manoeuvres. In such a scenario the key question is which orbit the spacecraft should be injected into by the high-thrust system, and at the end of the transfer, from which approach orbit it should be captured. This problem was analysed by Hechler (see references for this chapter).

Therefore, a well-defined optimisation problem may be posed:

- Minimise the fuel usage for an interplanetary transfer given upper limits on the transfer duration.

The fuel usage then has three components:

(1) Chemical fuel used for escaping the planet, after initial injection to a low bound orbit about the planet.
(2) Solar electric propulsion fuel used for the deep-space transfer manoeuvres.
(3) Chemical fuel to capture at the destination planet into a specified, bound target orbit.

A first estimation may imply that the chemical system should inject into the lowest

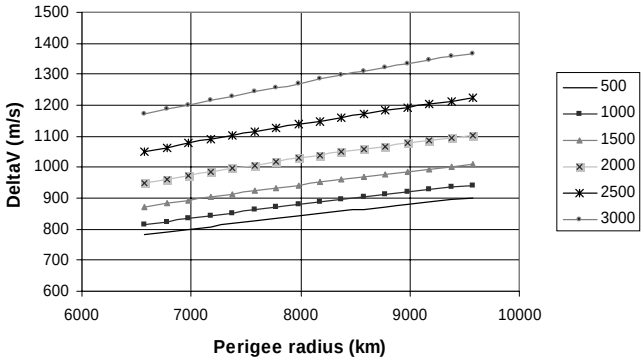

Figure 4.6.9. ΔV needed to reach a given Vinfinity from an initial GTO orbit about Earth. The ΔV increases as the perigee of the initial orbit is raised. The initial orbit considered in this case is an Earth bound GTO-like orbit with apogee at 42,165 km. Target V_∞ values from 500 to 3,000 km are considered.

possible energy escape orbit (parabolic). However, this is not necessarily the optimal solution. The use of a high-thrust manoeuvre at pericentre of a low planet orbit is very effective in achieving low-energy escape orbits. The ΔV to reach a given V_∞ from a perigee, r_{p1}, is given by the following:

$$\Delta V = \sqrt{\left(\frac{2\mu_1}{r_{p1}} + V_{\infty E1}^2\right)} - \sqrt{2\mu_1\left(\frac{1}{r_{p1}} - \frac{1}{(r_{p1} + r_{ap1})}\right)} \tag{4.6.1}$$

where $V_{\infty E1}$ is the excess hyperbolic speed with which the planet, 1, is left. r_{p1} is the pericentre radius of the initial orbit and r_{ap1} the apocentre radius. Also μ_1 is the gravitational parameter of the initral planet. Figure 4.6.9. shows the effect of the choice or pericentre on ΔV needed to reach a target orbit.

When approaching the planet, the capture ΔV is given by:

$$\Delta V = \sqrt{\left(\frac{2\mu_2}{r_{p2}} + V_{\infty C2}^2\right)} - \sqrt{2\mu_2\left(\frac{1}{r_{p2}} - \frac{1}{(r_{p2} + r_{ap2})}\right)} \tag{4.6.2}$$

where $V_{\infty C2}$ is the excess hyperbolic speed with which the planet, 2, is approached after relative speed reduction by the low-thrust system. Also r_{p2} is the pericentre radius of the final orbit about the target planet, r_{ap2} is the apocentre radius and μ_2 the gravitational parameter of the target planet.

The interplanetary phase is now considered. It was previously shown that the relationship between the excess hyperbolic speeds at the planets, assuming idealised circular planet orbits, is given by the following:

$$V_{\infty 1} = \sqrt{2\mu\left(\frac{1}{r_{pL1}} - \frac{1}{2a}\right)} - \sqrt{\frac{\mu}{r_{pL1}}} \tag{4.6.3}$$

$$V_{\infty 2} = \sqrt{\frac{\mu}{r_{pL2}}} - \sqrt{2\mu\left(\frac{1}{r_{pL2}} - \frac{1}{2a}\right)} \tag{4.6.4}$$

where r_{pL1} and r_{pL2} are the planet orbital radial, 'a' is the transfer semi-major axis and μ the gravitational parameter of the central body.

As a first approximation it could be assumed that the initial ΔV required of the low-thrust system is that needed to increase the initial excess hyperbolic speed to the value required in Equation 4.6.3. At the other end of the transfer the low thrust system ΔV is that needed to reduce the above approach excess velocity in Equation 4.6.4 to the value from which capture ultimately occurs at the planet. A ΔV loss term can also be added to this sum.

The total fuel use is then derived via the following three mass fractions:

$$mf_1 = \exp^{-\frac{\Delta V_1}{IspC}}$$
$$mf_2 = \exp^{-\frac{\Delta V_T}{IspL}}$$
$$mf_3 = \exp^{-\frac{\Delta V_2}{IspC}}$$

where *IspC* is the specific impulse of the chemical system, and *IspL* is that of the low-thrust system. ΔV_1 and ΔV_2 are given by the previous equations for impulsive escape and capture manoeuvres. Also the transfer ΔV_T is given by $\Delta V_T = (V_{\infty 1} - V_{\infty E1}) + (V_{\infty 2} - V_{\infty C2})$.

The total mass fraction is then given by:

$$mf = \exp^{-\frac{\Delta V_1}{ISpC}} \exp^{-\frac{\Delta V_T}{IspL}} \exp^{-\frac{\Delta V_2}{IspC}} \tag{4.6.5}$$

A maximum final mass (i.e., minimum fuel mass) can be sought with respect to the injection and capture excess hyperbolic speeds. The maximum with respect to the departure V_∞ must satisfy the following:

$$\begin{aligned}\frac{\partial mf}{\partial V_{\infty E1}} = &-\frac{1}{IspC} \exp^{-\frac{\Delta V_1}{IspC}} \frac{\partial V_1}{\partial V_{\infty E1}} \exp^{-\frac{\Delta V_T}{IspL}} \exp^{-\frac{\Delta V_2}{IspC}} \\ &-\frac{1}{IspL} \exp^{-\frac{\Delta V_T}{IspL}} \frac{\partial \Delta V_T}{\partial V_{\infty E1}} \exp^{-\frac{\Delta V_1}{IspC}} \exp^{-\frac{\Delta V_2}{IspC}} \\ &-\frac{1}{IspC} \exp^{-\frac{\Delta V_2}{IspC}} \frac{\partial \Delta V_2}{\partial V_{\infty E1}} \exp^{-\frac{\Delta V_1}{IspC}} \exp^{-\frac{\Delta V_T}{IspL}} = 0\end{aligned} \tag{4.6.6}$$

where

$$\frac{\partial \Delta V_1}{\partial V_{\infty E1}} = \frac{V_{\infty E1}}{\sqrt{\left(\frac{2\mu}{r_{p1}} + V^2_{\infty E1}\right)}}, \frac{\partial \Delta V_T}{\partial V_{\infty E1}} = -1, \frac{\partial \Delta V_1}{\partial V_{\infty E1}} = 0$$

The solution of this optimal problem can be examined over a range of examples. A transfer from Earth to Mars will be considered. In this case it is approximated that the excess hyperbolic speeds leaving Earth and approaching Mars are both 3,000 m/s. The behaviour of the minimum fuel use with respect to Earth departure excess hyperbolic is first considered. The effect of the specific impulse of the low-thrust system (compared with the high-thrust chemical system) is a significant aspect of this problem. In the following example in Figures 4.6.10 and 4.6.11, the initial

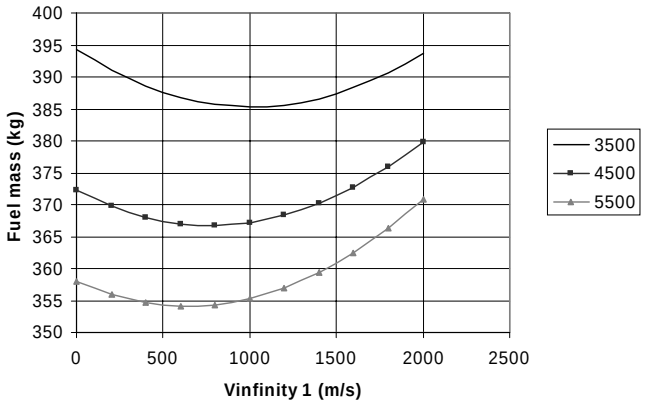

Figure 4.6.10. The effect of Earth departure V_∞ on total transfer fuel usage for a Mars approach V_∞ of 500 m/s. Low-thrust specific impulses of 3,500 to 5,500 seconds are considered. The location of the optimum (minimum total fuel mass) with respect to Earth departure V_∞ can be seen to lie between 500 and 1,000 m/s, depending on the specific impulse of the low-thrust system. High specific impulse for the low-thrust system results in the optimum V_∞ moving closer to a parabolic departure case.

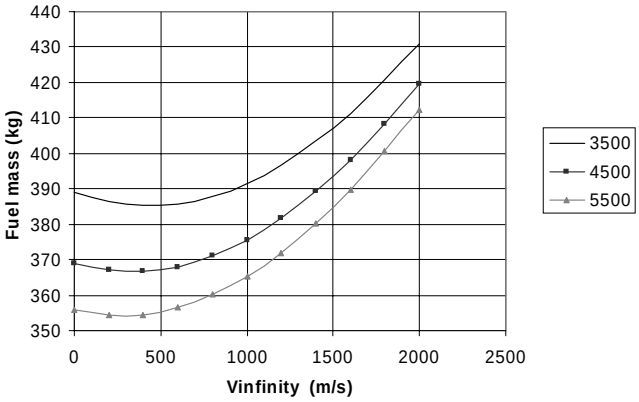

Figure 4.6.11. The effect of Mars approach V_∞ on total transfer fuel usage for an Earth departure V_∞ of 1,000 m/s. Low-thrust specific impulses of 3,500 to 5,500 seconds are considered. The location of the optimum (minimum total fuel mass) with respect to Mars departure V_∞ can be seen to lie between 0 and 500 m/s, depending on the specific impulse of the low-thrust system. This is lower than the Earth departure case, as Mars has a weaker gravity field than that of Earth.

mass is taken as 1,000 kg. The specific impulse of the low-thrust system is that of a typical bi-propellant system at 320 seconds. The initial orbit at Earth is assumed to be a 200 km perigee altitude, GTO like orbit (such that only apogee raising is rquired to reach escape, i.e., no plane changes). The target orbit at Mars has a pericentre altitude of 400 km and an apocentre radius of 30,000 km.

4.7 COMBINING LOW THRUST WITH GRAVITY ASSIST

4.7.1 Use of manoeuvres between gravity assists

In previous sections the use of gravity assist manoeuvres has been discussed with regard to improving transfer efficiency, and the use of low-thrust propulsion to effect orbit change. These tools of mission design may be combined to provide a much more flexible and potentially more efficient transfer strategy. Large deep-space manoeuvres are made possible with high specific impulse propulsion. These manoeuvres may be used in conjunction with gravity assist manoeuvres in several ways.

The simplest use is to apply a high specific impulse system to carry out the deep-space manoeuvres already identified for more conventional gravity assisted transfers, that generally use modest ΔVs. However, only limited fuel savings are available, as the ΔVs are low.

An alternative use is to increase the magnitude of the deep-space manoeuvres to provide greater approach velocity changes when the next gravity assist takes place. This can result in, for example, transfers using fewer gravity assists, because each one is more effective. The traditional dependence on resonant orbits is removed, as significant orbit period change is caused by these larger deep-space manoeuvres.

Another option is to use the deep-space manoeuvres to reduce the approach speed at the target planet after a series of gravity assists. In this way, the insertion manoeuvre – often carried out with a high-thrust (but low specific impulse) system – can be significantly reduced.

A number of such mission options are discussed in the following sections.

4.7.2 The Earth gravity assist escape loop

An alternative strategy to that of a direct Earth escape to initiate an interplanetary transfer can be sought. Launcher mass injection performance is generally significantly penalised when high-energy escape orbits are targeted. The possible injection to a low-energy escape orbit followed by deep-space manoeuvres using a high specific impulse, low-thrust system has been previously discussed. It was established that an optimum escape velocity could be derived in such situations. However, even further improvement may be sought with the use of high specific impulse, low-thrust propulsion systems. A strategy may be devised that enables injection to a much less energetic Earth-bound orbit, and therefore has the potential for a significant mission performance gain.

One option that may be considered is the use of a lunar gravity assist. Previous sections have indicated that it is possible to achieve Earth-departing excess hyperbolic speeds of 1,000–1,700 m/s from a lunar gravity assist following an approach from an initial high-apogee, trans-lunar orbit. However, unassisted lunar fly-bys from initial Earth bound orbits do not produce sufficient speed to reach either Mars or Venus. Typical excess hyperbolic speeds required for these targets are 3 and 2.8 km/sec respectively (dependent on launch date). The extra ΔV can be provided by assisted fly-bys (burns at periselenium with a high thrust system), or in deep space after Earth departure.

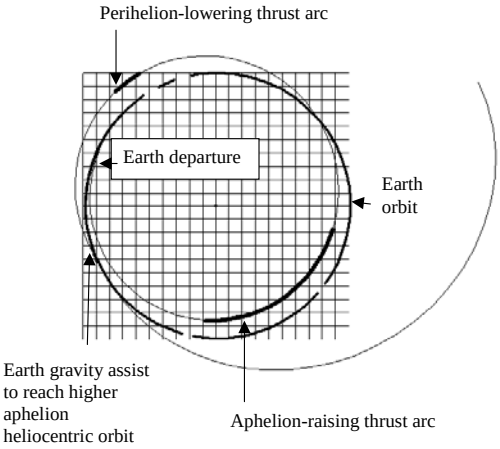

Figure 4.7.1. Example of a scheme for utilisation of Earth gravity assist.

A further option is to use Earth gravity assist manoeuvres, which can be efficiently used after a lunar fly-by yielding a low-energy Earth escape. An intermediate deep-space burn is applied to increase the eccentricity of the heliocentric orbit after first leaving the Earth–Moon system. This increases the fly-by speed when returning to Earth, and so increases the potential gain from the gravity assist manoeuvre. (This strategy is discussed in the references for this section)

The strategy is as follows:

(1) Inject to a high elliptical Earth orbit.
(2) Perform a lunar gravity assist.
(3) Alternatively inject directly to a low-energy Earth escape orbit.
(4) Use the escape velocity achieved after the lunar gravity assist to place the spacecraft in an eccentric heliocentric orbit, with semi-major axis close to 1 AU.
(5) A deep-space burn is then implemented to increase the excess hyperbolic speed on returning to Earth. A combination of two manoeuvres can be used.
(6) Subsequent Earth rendezvous is achieved by planning correct ratios of semi-major axes after initial Earth escape and the intermediate deep-space manoeuvre(s).
(7) The significantly increased excess hyperbolic speed may now be sufficient to execute an interplanetary transfer.

A number of free parameters are available to optimise such a strategy. The basic problem is given an initial Earth departing V_∞ and a target Earth departing V_∞, to minimise the deep space ΔV that is required. It can be assumed that the direction of the initial departing V_∞ is optimisable, by choosing the appropriate point in the lunar orbit to perform the fly-by. The complete range of possible departure right ascensions are therefore attainable over a 28-day period, and repeat at that interval. This means that the initial aphelion and perihelion are optimisable, within the constraint of a given initial V_∞ leaving the Earth/Moon system. One potential

compromise is that in achieving a given departure direction and waiting for the associated epoch for implementation of the lunar gravity assist can have a detrimental effect on the remainder of the mission, as the resulting final Earth gravity assist and subsequent interplanetary transfer do not in general occur at an optimal epoch. However, the effect of such a waiting period for Lunar position is generally acceptable in terms of ΔV penalty.

Other free variables that may be optimised are the magnitudes of the deep-space burns. Two burns may be considered – one at aphelion and one at perihelion – to modify both the intermediate perihelion and aphelion, respectively. A measure of the efficiency of the transfer is the ratio of deep space ΔV to the V_∞ gain achieved at Earth. This is because if the gain were not obtained by this method, a direct deep-space manoeuvre would be needed with the low-thrust system. This would be at least equal to the V_∞ difference (i.e., that required minus injection V_∞), and in practice greater because of ΔV loss.

In a particular example considered, the initial V_∞ is assumed to be 1,500 m/s on initially leaving the Earth–Moon system, and a range of target V_∞'s between 5,000 and 8,000 m/s on returning to Earth are chosen. In these examples the deep-space ΔVs are assumed to be impulsive. An analysis is then performed to optimise the deep-space ΔV required to meet these return targets for a range of initial departure geometries. These may be categorised by the aphelion of the departure orbit for an initially inwards departure, or perihelion for outwards departure. This, combined with the magnitude of the initial V_∞, defines the opposite apse. There is then an implication for the azimuth of the initial departing excess hyperbolic vector. The optimisation finds the optimal burn, split between manoeuvres, that is required to achieve the change in orbit. The analysis here makes no allowance for phasing restrictions on return to Earth. This will be considered later. Figure 4.7.2 shows the effect of initial aphelion on the ΔV requirement. For an initially inwards departure optimum aphelion is at 1 AU when leaving Earth. The ΔV distribution changes as the injection aphelion is varied. At the optimum case, with minimum departure aphelion, the ΔV used for lowering perihelion is zero. Figures 4.7.3 and 4.7.4 show the same analysis for an initially outwards departing transfer.

An important aspect of a total mission optimisation lies in the selection of a number of key parameters in this phase of the mission. Clearly, minimum initial aphelion or maximum perihelion are targeted. However, further factors are the choice of initial V_∞. This may be the result of a lunar gravity assist, and so depends on the pre-fly-by apogee. The penalty in reaching higher apogee leading to greater initial V_∞ must be considered in the context of increased deep-space ΔV.

The trade-off is further complicated by the fact that the apogee-raising ΔV is generally performed by chemical propulsion or a launcher, and the deep space ΔV is performed by electric propulsion.

4.7.3 Examples of raising aphelion with single Earth gravity assist

The previous discussion has shown that an optimum strategy can be used to magnify the achievable V_∞ when returning to Earth. This analysis made certain idealised

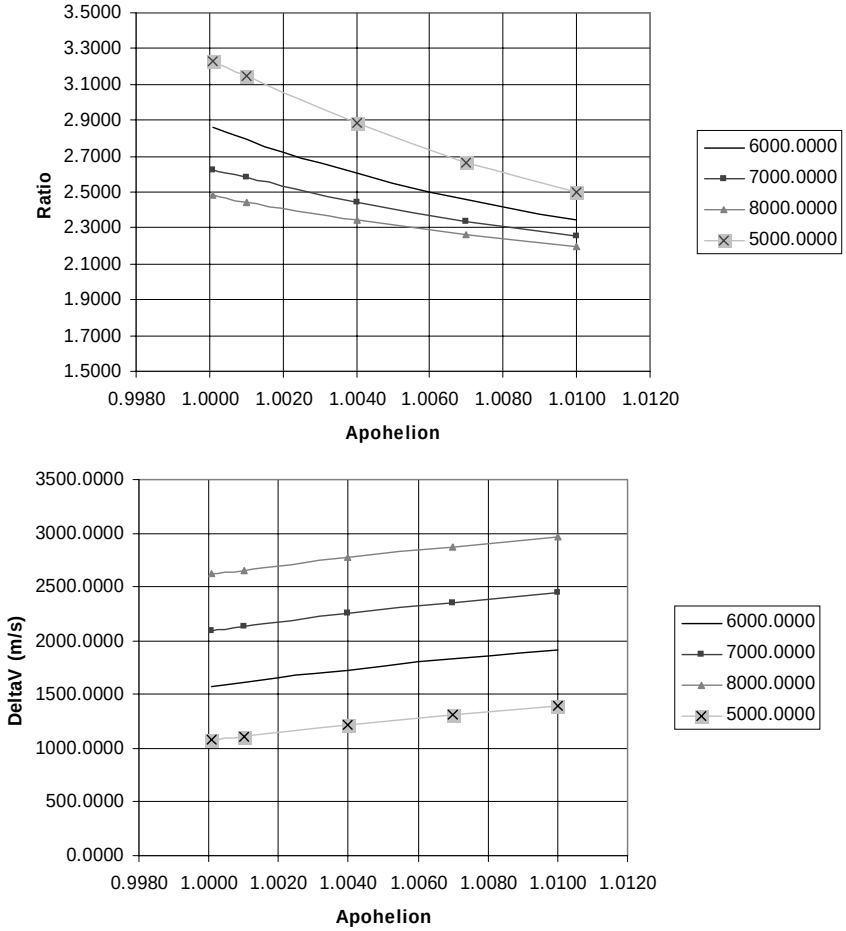

Figure 4.7.2. ΔV implications to reach alternative targets by varying initial orbit aphelion, the initial V_∞ is 1,500 m/s and inwards departure is used. The upper figure shows the ratio of the V_∞ change to the ΔV that is required to reach the target return V_∞. A set of target values from 5 to 8 km/sec are considered. The lower figure shows the actual optimised ΔV needed to achieve the return V_∞. It is clear that the optimum ΔV solution occurs with the aphelion at that of the Earth. The initial departure V_∞ is therefore applied entirely to reduce the initial perihelion.

assumptions, including the impulsive nature of the manoeuvres and also that a perfect phasing can be achieved when returning to Earth. In practice, neither of these assumptions are completely true.

Therefore, the 'real world' case of such a transfer can be studied to assess the true effectiveness of this strategy. The previous section indicated that in the case of an initial inwards departure, the minimum ΔV strategy involves injection to a low perihelion orbit with initial aphelion at 1 AU. A perihelion manoeuvre then raises aphelion to increase the V_∞ on return to Earth. However, the analysis also shows

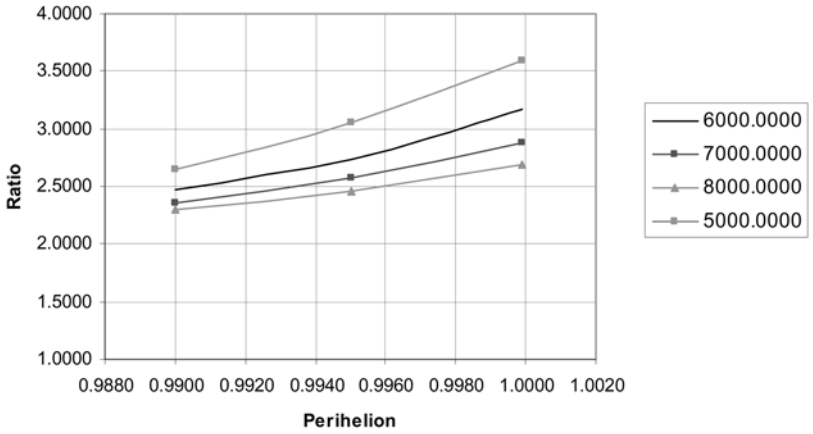

Figure 4.7.3. $\Delta V/V_\infty$ change ratio implications to reach alternative targets by varying the initial orbit aphelion. Initial V_∞ is 1,500 m/s and outwards departure is used. The figure shows the ratio of the V_∞ change to the ΔV that is required to reach the target return V_∞. A set of target values from 5 to 8 km/s are considered.

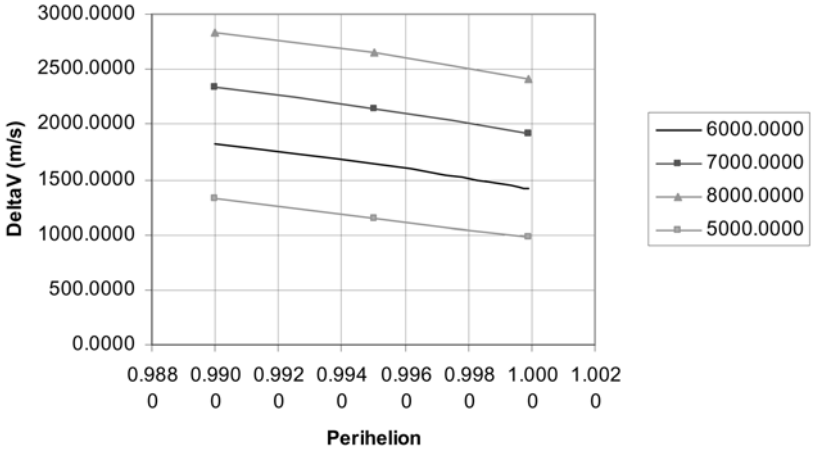

Figure 4.7.4. ΔV implications to reach alternative targets by varying initial orbit aphelion. Initial V_∞ is 1,500 m/s and outwards departure is used. The figure shows the optimised ΔV needed to achieve the return V_∞. The illustration shows clearly that the optimum ΔV solution occurs with the perihelion at that of the Earth. The initial departure V_∞ is therefore applied to increase the initial aphelion.

that the optimum is rather 'flat', such that initial aphelion at greater that 1 AU and a combination of aphelion raising and perihelion lowering manoeuvres can be used. This is important, as it may be used to advantage in obtaining the correct phasing on return to Earth. Initial outwards departure offers a second strategy that may be optimised

A series of transfers can be studied that start from a typical state after a lunar gravity assist and optimise the deep-space ΔVs in reaching a subsequent Earth fly-by

and eventually a particular heliocentric target orbit that is assumed to be effectively circular. The problem is to minimise the deep-space ΔV in raising aphelion to rendezvous with this target. This simplification means that problems of phasing with a target planet can be avoided in this analysis.

A series of strategies can be identified, and will be compared in their effectiveness. They all use the previously described idea of amplification of the V_∞ at Earth, but differ in their approach to the problem of achieving the correct phasing with Earth.

The strategies are as follows:

Case A: nominal

Inject to low perihelion orbit.
Perform aphelion-raising manoeuvre after approximately half a revolution.
Perform perihelion-lowering manoeuvre after approximately a further half a revolution.
Rendezvous with Earth for gravity assist after approximately a further quarter revolution.
Time taken from lunar gravity assist to Earth rendezvous is approximately 1.25 years.

Case B: initial perihelion-reducing manoeuvre

Inject to high-aphelion orbit.
Perform perihelion-lowering after approximately a half revolution.
Perform aphelion-raising manoeuvre after approximately half a revolution.
Rendezvous with Earth for gravity assist after approximately a further three quarter revolution.
Time taken from lunar gravity assist to Earth rendezvous is approximately 1.25 years.

Case C: extended transfer

Inject to low-perihelion orbit.
Perform aphelion-raising manoeuvre after approximately one-and-a-half revolutions.
Perform perihelion lowering manoeuvre after approximately half a revolution.
Rendezvous with Earth for gravity assist after approximately a further quarter revolution.
Time taken from lunar gravity assist to Earth rendezvous is approximately 2.25 years.
It also possible to consider an additional manoeuvre approximately 0.5 years after leaving Earth. This would also be aphelion-raising.

Each of these three strategies can be modified by adding a third manoeuvre after the Earth gravity assist to further boost the aphelion.

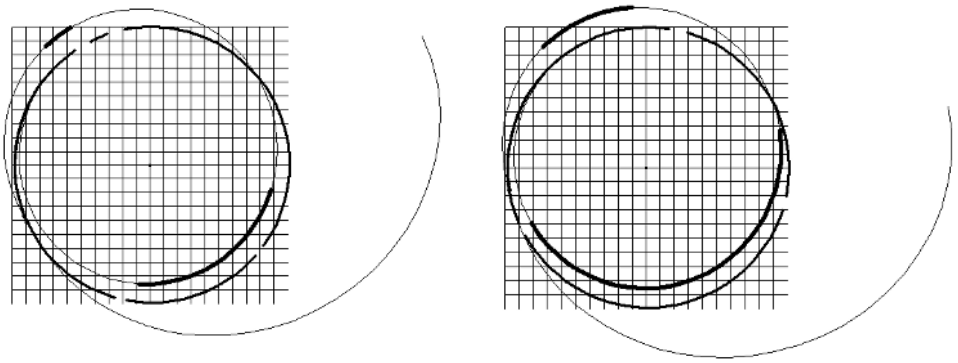

Figure 4.7.5. Thrust-mass of 0.2 and 0.1 N/t for transfer to a 2.2-AU orbit. Earth's orbit is shown as a thick line and the trajectory thrust and coast arcs as thick and thin arcs. The grid is 1AU from centre to edge, and the sub-grid size is 0.1 AU.

A study of case A

The first case can be examined in greater detail. The effect of a range of target orbits and the effect of different thrust/mass ratios can both be considered. The initial Earth departing V_∞ after lunar gravity assist is assumed to be 1,200 m/s.

Firstly, a target at 2.2 AU is considered. This requires a relatively high V_∞ at Earth of approximately 5 km/sec. The transfer begins with injection such that aphelion lies at approximately 1 AU and perihelion at 0.86AU. Aphelion is then raised to 1.15 AU and, eventually, perihelion lowered to 0.83 AU. The first manoeuvre (aphelion raising) is the largest at approximately 1,120 m/s, and the second perihelion lowering manoeuvre is 230 m/s. Rendezvous with Earth occurs approximately 15 months after lunar gravity assist. The total ΔV is therefore 1,380 m/s, and the V_∞ gain is 3,800 m/s – a ratio of 1 : 2.75. Thrust/mass is assumed to me near impulsive.

The effects of different thrust/mass ratios can also be considered. Figure 4.7.5 shows the transfers for thrust/initial mass ratios of 100 mN per tonne and 200 mN per tonne. In the case of 100 mN a significant proportion of the Earth-to-Earth transfer is taken up with thrust application. The effect of changing the thrust/mass ratio, in terms of ΔV, is shown in Figure 4.7.6.

The effect of different energy target orbits can now be considered. A relatively high thrust/mass is considered so that very low-thrust effects do not obscure the nature of the problem. The initial Earth departing V_∞ is 1,200 m/s.

For cases of target aphelions up to approximately 2.33 AU (Figures 4.7.7 and 4.7.8) the required ΔV follows the expected trend observed in the previous analysis that was based upon the approximation of neglecting phasing. However, as the target aphelion increases significantly beyond this, more ΔV is required than predicted. This effect occurs because of the increasing difficulty in achieving a rendezvous with the Earth after the two manoeuvres. Their efficiency is compromised in establishing the required phasing.

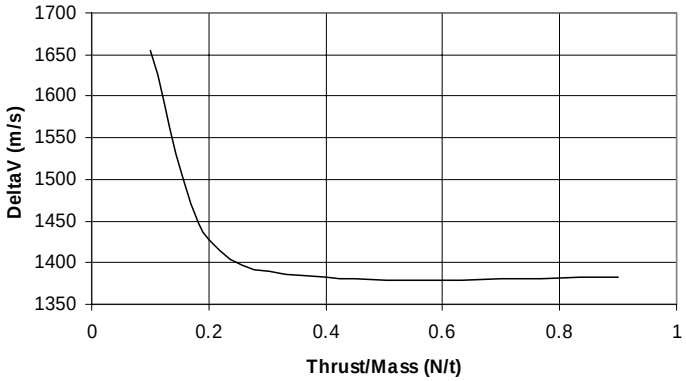

Figure 4.7.6. The ΔV penalty for reducing thrust/mass for transfer to a 2.2-AU target.

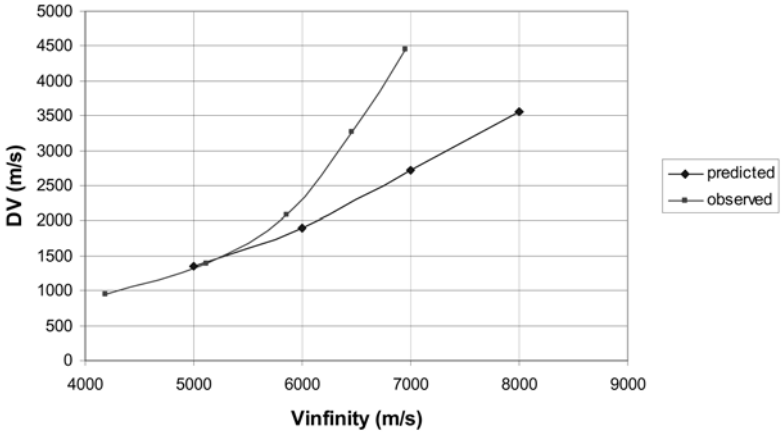

Figure 4.7.7. Comparison of observed and predicted ΔVs for reaching target aphelion or equivalently targetting Earth relative V_∞. 'Predicted' is the ΔV required when leaving Earth to reach the target V_∞ when phasing is neglected. 'Observed' is the ΔV when time orbits are considered, making phasing a significant factor. A significant divergence occurs between the initial prediction and the actual ΔV at approximately 5,500 m/s in V_∞ at Earth return, which is approximately equivalent to a target aphelion of 2.33 AU after leaving Earth. Initial V_∞ is 1,200 m/s.

The same effect is shown in Figure 4.7.9, but in terms of a target aphelion radius rather than a Vinfinity when returning to Earth.

The effect of the additional manoeuvre offers significant ΔV saving as higher orbits are targeted.

A study of case B

The second case can also be examined in more detail. The effect of a range of target orbits can be considered. The initial Earth-departure V_∞ after lunar gravity assist is

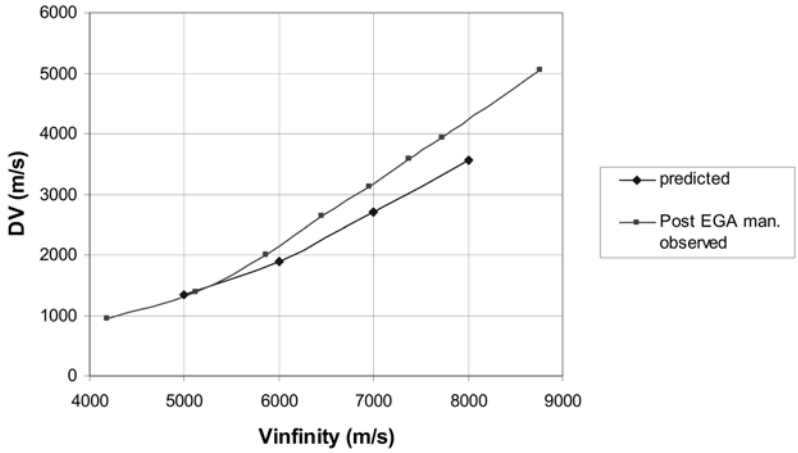

Figure 4.7.8. Comparison of observed ΔV using final manoeuvre after EGA and predicted ΔVs for reaching target aphelion or equivalently targetting Earth-relative V_∞. This performance degradation (seen in Figure 4.7.7) can be mitigated to some extent by introducing a further aphelion-raising burn after the Earth gravity assist. This enables a lower V_∞ at Earth to be targeted and the final target aphelion reached by the final manoeuvre immediately after Earth gravity assist.

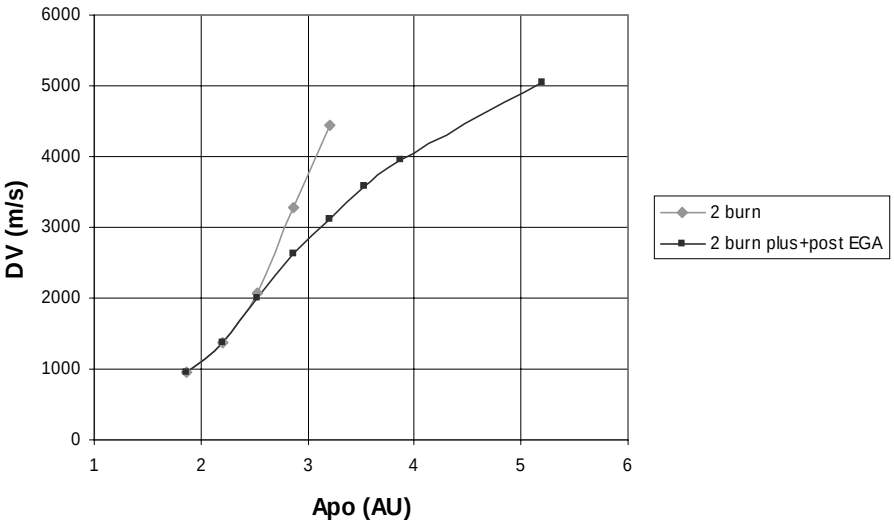

Figure 4.7.9. Comparison of ΔVs for reaching target aphelion for a two-burn strategy (pre EGA) and the effect of introducing a third burn after Earth gravity assist.

again assumed to be 1,200 m/s. In practice, when lower Vinfinities are targeted at Earth, little difference in time or ΔV is seen between this method and that of case A; but as the V_∞ increases, some differences appear.

A target aphelion at 2.87 AU is considered in detail. This requires a higher V_∞ at

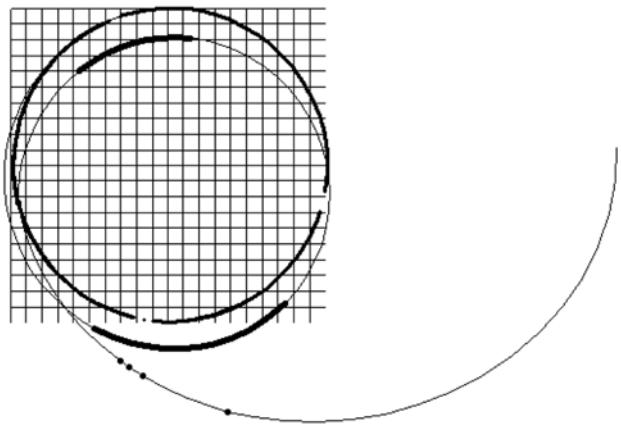

Figure 4.7.10. Transfer to a 2.87-AU orbit using strategy B. The plot shows the two burn arcs. The first thrust arc starts close to aphelion after leaving Earth. The second then occurs at perihelion. The grid is 1 AU from centre to edge, with a sub-grid of 0.1 AU.

Earth of approximately 6.7 km/sec. The transfer begins with injection such that perihilion lies at approximately 1 AU and aphelion at 1.18 AU. Perihelion is then lowered by the first burn to 0.81 AU, and aphelion is raised by the second burn to 1.29 AU. The first manoeuvre (perihelion-lowering) is now the larger at approximately 1,560 m/s, and the second, aphelion-raising manoeuvre is 660 m/s. Rendezvous with Earth occurs approximately 15 months after lunar gravity assist. The transfer is shown in Figure 4.7.10.

The total ΔV is therefore 2,220 m/s and the V_∞ gain is 5,500 m/s – a ratio of 1 : 2.47. A third burn after EGA can be considered, as in case A, but at this target aphelion it is non-optimal. As aphelion is raised further, then a third burn is advantageous, as found in case A. The effect of this post EGA manoeuvre is shown in Figure 4.7.11.

This can be compared with the two-burn case A for the same target. The ΔV here is 3,270 m/s. In this case a burn after EGA is optimal, reducing the ΔV to 2,630 m/s. This strategy (type B) allows some ΔV reduction when compared with type A, depending on the target orbit after EGA.

A study of case C

The third case is now examined, and the effect of a range of target orbits is again considered. The initial Earth departing V_∞ after lunar gravity assist is assumed to be 1,200 m/s. This method is advantageous when compared with cases A and B at higher aphelion targets.

A target aphelion at 2.87 AU is considered in detail. This requires with this strategy a V_∞ at Earth of approximately 6.5 km/sec. The transfer begins with injection such that aphelion lies at approximately 1 AU and perihelion at 0.85 AU. Perihelion is then lowered slightly by the first burn to 0.83 AU, and aphelion is raised

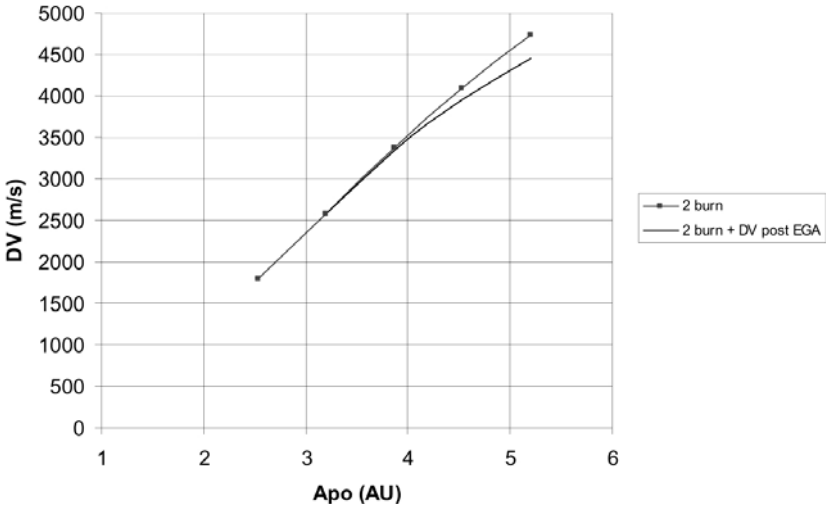

Figure 4.7.11. The effect of a final post-EGA burn for case B. The effect of the additional manoeuvre after EGA offers significant ΔV saving as higher orbits are targeted.

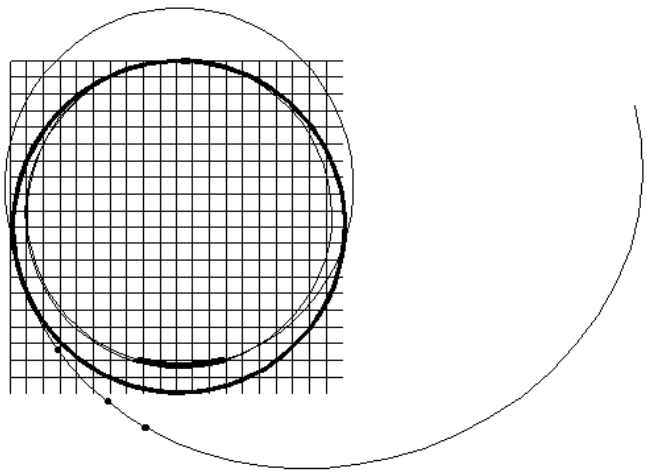

Figure 4.7.12. Transfer to a 2.87-AU orbit using strategy C. Earth's orbit is shown, and the grid is 1 AU from centre to edge with a sub-grid of 0.1 AU. The second revolution with raised aphelion, and the corresponding perihelion thrust arc, are also shown.

by the second burn to 1.3 AU. The first manoeuvre (perihelion-lowering) is now the smaller at approximately 150 m/s, and the second, aphelion-raising manoeuvre is 2,040 m/s. Rendezvous with Earth occurs approximately 27 months after lunar gravity assist. The transfer is shown in Figure 4.7.12.

The total ΔV is therefore 2,220 m/s and the V_∞ gain is 5,300 m/s – a ratio of 1 : 2.39. A third burn, after EGA, can be considered, as in case A. At this target aphelion, it is non-optimal, but as aphelion is raised further it is again advantageous,

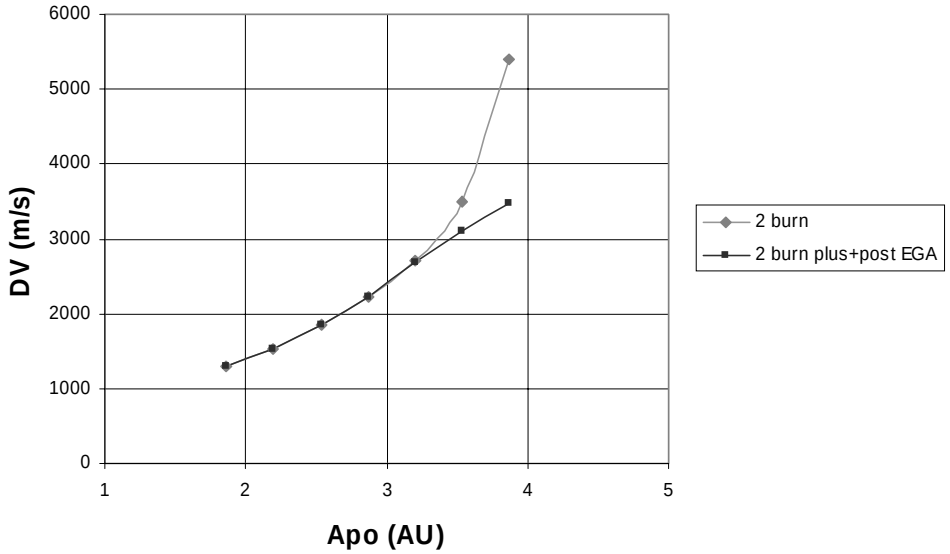

Figure 4.7.13. The effect of a final, post-EGA burn for case C.

as found in cases A and B. The effect of the post EGA manoeuvre is shown in Figure 4.7.13.

This can be compared with the two-burn cases A and B for the same target aphelion. The ΔV here is 3,270 m/s for case A and 2,220 m/s for case B. A burn after EGA is optimal in case A, reducing the ΔV to 2,630 m/s. Therefore, strategy C allows some reduction in ΔV when compared with A.

Comparisons between all three cases are shown in Figure 4.7.14. The comparison is made allowing the three burn strategies (two before EGA and one after EGA).

4.7.4 Examples of raising aphelion with double Earth gravity assist

The previous section described the use of a low excess hyperbolic velocity escape, followed by a deep-space manoeuvre and Earth gravity assist. The strategy provides an efficient technique for achieving greater effective escape energy than applying deep-space manoeuvres directly. Therefore, when considered in conjunction with low-thrust, high specific impulse propulsion systems a fuel-efficient method of reaching distant planets is achieved.

The strategy does, however, become naturally less efficient as the required excess velocity on finally leaving Earth increases. A further factor reducing efficiency is that as the deep-space ΔVs increase, so do the demands on the propulsion system. Low-thrust systems that provide large ΔVs eventually suffer a loss due to the extended spatial distribution of the thrust. Therefore, a modified strategy may be sought to achieve high escape energies, which also retains a high efficiency.

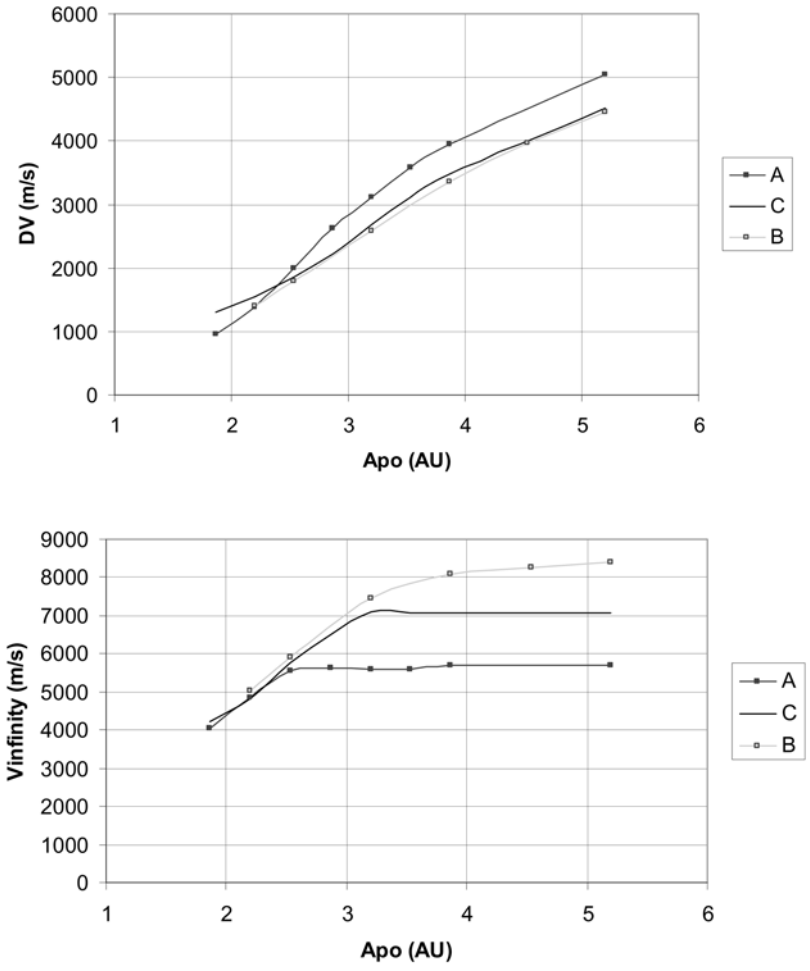

Figure 4.7.14. Comparison of ΔVs and EGA Vinfinities for the three alternative cases over a range of target aphelions. Manoeuvre is allowed after EGA. Strategy B is the optimal. At lower aphelion targets there is much less difference between strategies. The effect of the optimal V_∞ at EGA for the three strategies is compared in the lower figure. Strategy B is able to utilise a higher V_∞ for the higher target aphelion orbits.

This strategy is the introduction of a second Earth gravity assist manoeuvre, after a two year Earth resonant orbit. An intermediate manoeuvre is applied at aphelion to increase the excess hyperbolic speed on returning to Earth for the second time. An idealised analysis regarding the effectiveness of such a manoeuvre may be performed, in a similar manner to the previous single EGA case. The approximation is once again that the phasing of the return trajectory with Earth is not considered, and the V_∞ is just calculated when the return orbit crosses Earth's orbit. The effectiveness of the ΔV at raising aphelion is demonstrated in Figure 4.7.15.

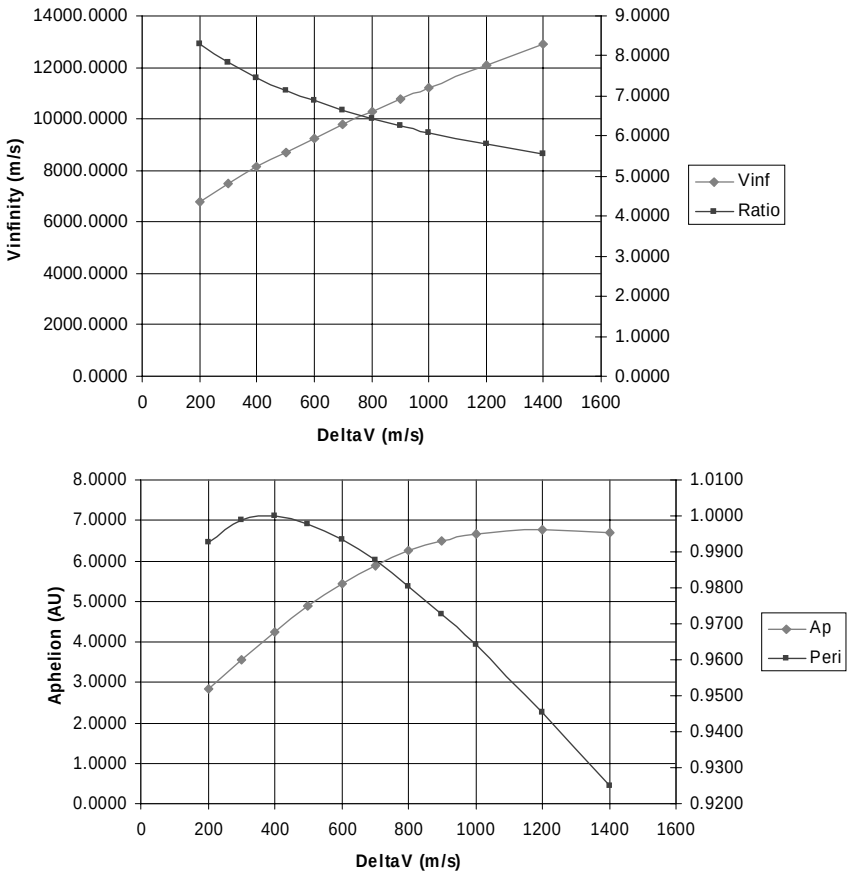

Figure 4.7.15. Effect of manoeuvre on achievable excess hyperbolic speed at Earth and post-GA aphelion in a 2-year Earth resonant orbit. In the upper figure, increasing the ΔV applied at aphelion of the two-year orbit progressively increases the excess hyperbolic speed on return to Earth. The ratio of excess hyperbolic speed gain to ΔV is higher than the previously considered EGA loop with a lower period. This is plotted against the right axis. In the lower figure, increasing the ΔV applied at aphelion of the two-year orbit also initially increases the aphelion that is achieved after the second EGA, but perihelion also reduces. The result is that eventually the final aphelion no longer rises with applied ΔV. Perihelion is plotted against the right axis in the lower figure.

The fact that the aphelion stops increasing with increasing applied ΔV implies a limitation to the strategy. If this second EGA were used to enter a higher-period, Earth-resonant orbit, then a subsequent EGA would result in a large increase in aphelion after that gravity assist. However, this would add significant extra time to the transfer.

An alternative strategy can therefore be used, similar to that of the single EGA case. A manoeuvre is allowed after the second EGA to assist in raising aphelion. Such a transfer is shown in Figure 4.7.16

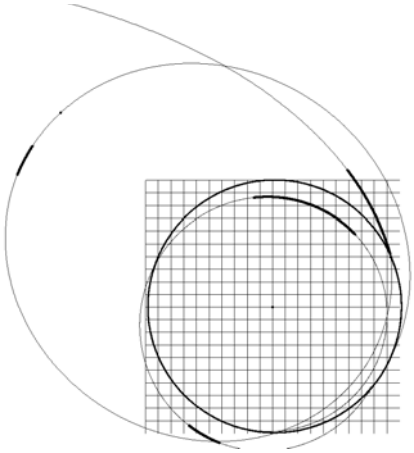

Figure 4.7.16. The use of a double EGA to raise aphelion to a target at 10 AU, using manoeuvres in the two-year resonant loop and also after the final EGA. Earth's orbit is shown with an intermediate-thickness line, the coast phases of the trajectory with the lighter line, and thrust phases with a thick line. The grid is 1 AU from centre to edge.

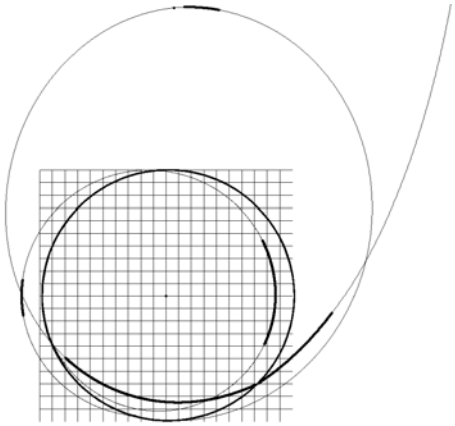

Figure 4.7.17. The use of a double EGA to raise aphelion to a target at 80 AU, using manoeuvres in the two-year resonant loop and also after the final EGA.

Earth's orbit is shown with an intermediate-thickness line, the coast phases of the trajectory with the lighter line, and thrust phases with a thick line. The grid is 1 AU from centre to edge. The motion of the spacecraft may be observed first in the one-year resonant orbit with two deep-space manoeuvres to increase the hyperbolic excess speed on returning to Earth to typically 5.2 km/sec (the precise value depends on where the Earth's orbit is crossed, as the planet's eccentricity has a small effect). After the first EGA the spacecraft enters a two-year resonant loop. A deep-space manoeuvre is applied near aphelion. The excess hyperbolic speed on returning to Earth is now approximately 10.7 km/sec. A deep-space manoeuvre is then applied after the second EGA to assist in aphelion-raising to the target value of 10 AU.

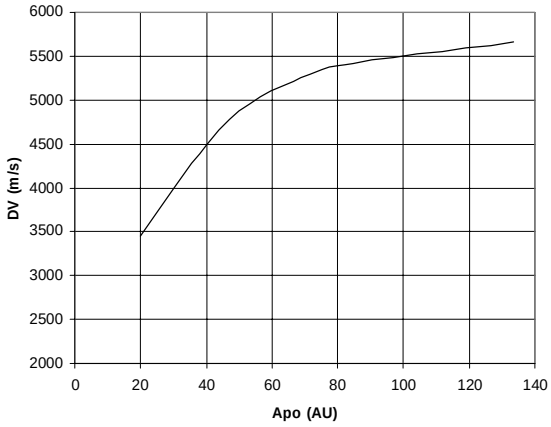

Figure 4.7.18. The deep-space ΔV required to reach a target aphelion after a low-energy escape after lunar gravity assist and 2 EGAs.

The aphelion target may be progressively raised and achieved by the application of additional deep-space manoeuvres. Figure 4.7.17 illustrates an example of a target at 80 AU. The strategy is identical to the 10-AU target case, with the difference that the manoeuvre ΔV after the second EGA is increased. Also, a namoeuvre just prior to the second EGA is applied.

The relationship between target aphelion and deep space ΔV is shown in Figure 4.7.18. The thrust/mass used in this analysis is given a constant value at 300 mN/tonne The initial ΔV is 1,200 m/s. Lower thrust/mass values will require greater ΔVs, as discussed in Section 4.7.3.

4.8 USING MULTI-BODY GRAVITY PERTURBATIONS

4.8.1 The three-body problem

Motion in multiple gravity fields is best described in terms of the framework of the three-body problem. Analysis of the three-body problem shows that the motion can be characterised in terms of the Jacobi constant. An understanding of the characteristics of this motion suggests methods for prediction of the requirements for planetary approach and escape under which multiple gravity field perturbations may be effectively used for mission design.

The constant of motion is:

$$V^2 + 2U = -C$$

where C is the Jacobi constant and V is the speed with respect to the rotating frame.

The generalised potential is:

$$U = \left(-\frac{\mu_1}{r_1} - \frac{\mu_2}{r_2} \right) - \frac{\omega^2}{2}(r_x^2 + r_Y^2)$$

where $\underline{\omega} = \omega \hat{r}_Z$; r_1 and r_2 are the radial distances from body 1 and body 2 respectively; r_x, r_y, r_z are the components of position w.r.t. the system barycentre; $\mu_1 = \mathrm{Gm}_1$, the gravitational parameter for mass m_1; $\mu_2 = \mathrm{Gm}_2$, the gravitational parameter for mass m_2; and G is the universal gravitational constant.

The limiting regions of the motion can be obtained by considering the case where speed is zero:

$$2\left(-\frac{\mu_1}{r_1} - \frac{\mu_2}{r_2}\right) - \omega^2(r_x^2 + r_Y^2) + C = 0$$

Such surfaces clearly show limitations of the possible motion. Figure 4.8.1 shows contours of zero velocity for different values of the constant, C. Only motion in the ecliptic is considered ($r_z = 0$). This is now a case of a planar, circular, restricted three-body problem. In the figure, motion is excluded within a particular shaded area that corresponds to a given value of C. Here X lies along the Sun-to-planet vector, and Y (vertical axis, in km) lies perpendicular to X in the ecliptic.

In the first example, Earth lies on the X axis at 1.496e8 km. A series of constant velocity surfaces may be evaluated over a range of values of the Jacobi constant, C, starting with Cmaximum = 2,641,000,000 $(\mathrm{m/s})^2$.

This value (Cmaximum) results in a case where escape from Earth is not possible. However, a series of further surfaces may be generated with reducing C ($-C$ increasing). With such a reduction there is no longer a barrier to an initially Earth-bound state moving away from Earth and into the heliocentric domain. These surfaces of constant velocity are plotted in the figure. The contours represents the absolute value of the reduction in the Jacobi constant below the maximum (Cmaximum). Therefore, a large value for the contour shows that C now lies significantly below Cmaximum.

The plot shows clearly that as C is reduced, the inaccessible regions shrink, until eventually motion becomes possible through the locations of the first two co-linear Lagrange points, L1 and L2, at approximately ± 1.5 million km along the X axis from Earth.

This analysis is repeated for Jupiter, as its gravity field is far more expansive than that of Earth. Qualitatively, the same behaviour as in the Earth case will result. Figure 4.8.2 shows these surfaces plotted over a wide area. Only motion in the ecliptic is considered. Here, X again lies along the Sun-to-Jupiter vector, and Y (vertical axis, in km) lies perpendicular to X in the ecliptic.

These surfaces are evaluated a range of values of the Jacobi constant, C, with Cmaximum = 516,000,000 $(\mathrm{m/s})^2$.

As in the Earth example, the plot shows a case just below the limiting case for escape from Jupiter ($C = C$maximum), and progresses to a range of cases allowing escape from Jupiter.

In this analysis the 'idealised' circular orbit of Jupiter lies at approximately 7.8e8 km from the Sun, on the X axis of the figure. The locations of Jupiter's first two co-linear Lagrangian points can be seen on the X axis.

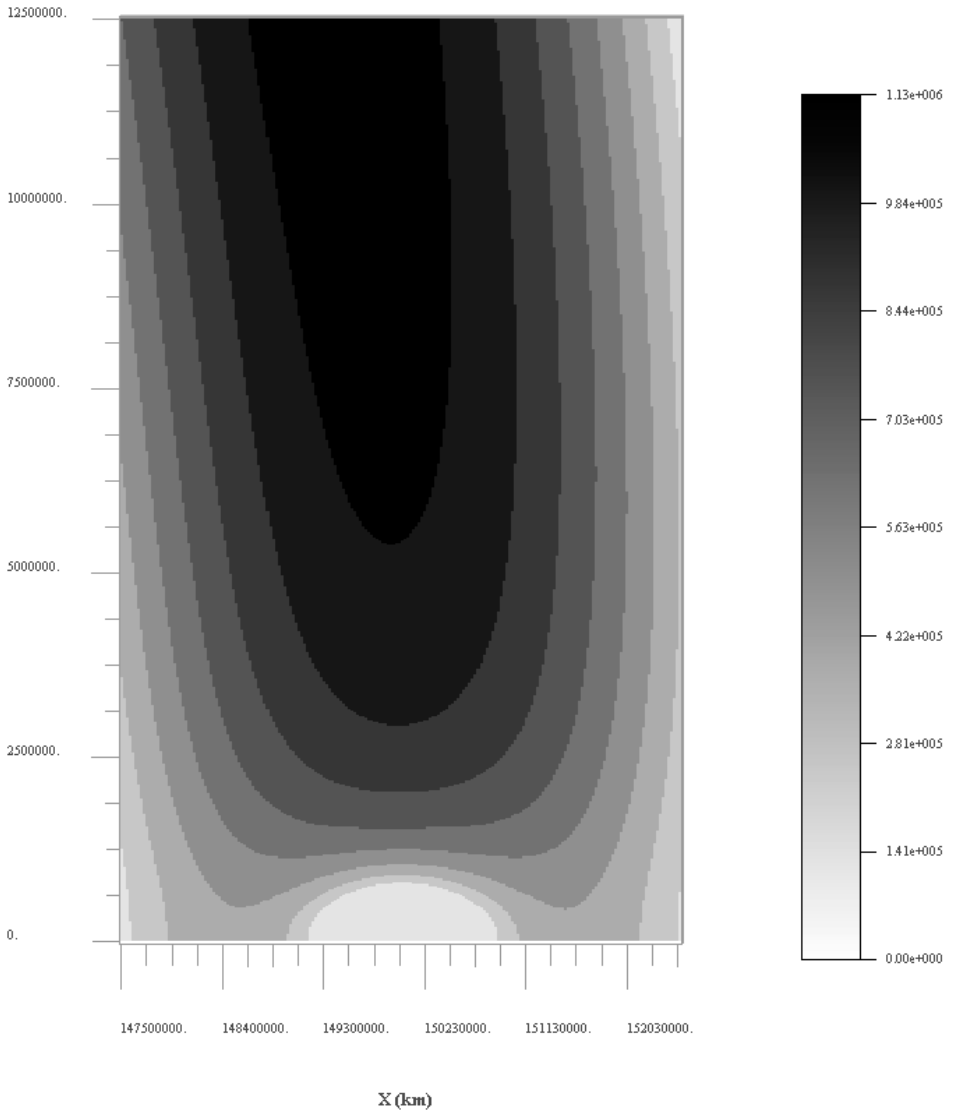

Figure 4.8.1. Zero-velocity boundaries for the Earth–Sun system, showing the zone centred on Earth on the rotating system X axis. The vertical axis is the rotating system Y direction.

4.8.2 The Lagrange libration points

The Jacobi constant of motion for the restricted circular three-body problem has been found to be $V^2 + 2U = -C$, where C is a constant and V is the speed with respect to the rotating frame (the rotating frame being defined by the motion of the planet about the central body).

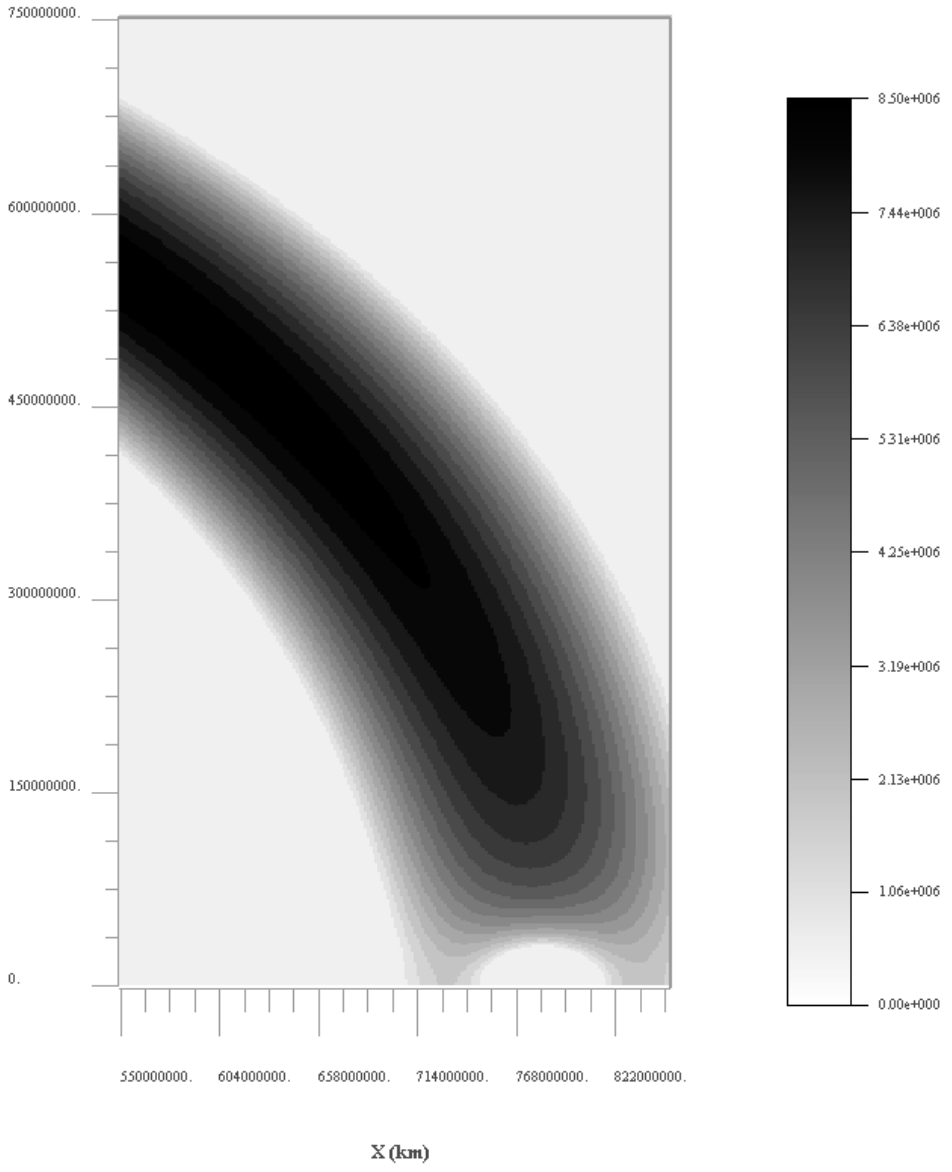

Figure 4.8.2. Zero-velocity boundaries for the Jupiter–Sun system, showing a wide area zone centred on the Jupiter and Sun co-linear Lagrange points. X is Sun–Jupiter direction, vertical axis is the rotating system Y direction.

The expression for acceleration in this frame was obtained previously as:

$$\left(\frac{d^2\underline{r}}{dt^2}\right)_R = -\nabla U - 2\underline{\omega} \wedge \left(\frac{d\underline{r}}{dt}\right)_R$$

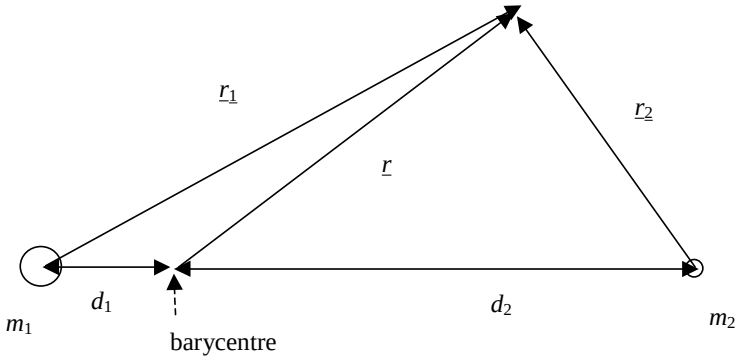

Figure 4.8.3. The positions relative to the two bodies in the rotating reference frame. d_1 and d_2 are the scalar distances of body 1 and body 2 from the barycentre, $\underline{r}_1$ is the position of the spacecraft relative to body 1, and $\underline{r}_2$ is the position of the spacecraft relative to body 2.

The positions relative to the two bodies are shown in Figure 4.8.3. It can be noted that:

$$r_{1x} = r_x + d_1 \qquad \text{and} \qquad r_{2x} = r_x - d_2$$

Positive x is measured from the barycentre towards m_2, y lies perpendicular to x in the ecliptic and is positive in the direction of rotation; and z is perpendicular to the ecliptic.

It is possible to identify the presence of points where a particle, if placed there, with no velocity in the rotating frame, will experience no resultant acceleration with respect to this rotating frame. The condition is therefore:

$$\nabla U = 0 \tag{4.8.1}$$

where

$$U = \left(-\frac{\mu_1}{r_1} - \frac{\mu_2}{r_2} \right) - \frac{\omega^2}{2}(r_x^2 + r_Y^2)$$

Therefore:

$$\frac{\partial U}{\partial r_x} = \left(\frac{\mu_1}{r_1^3}(r_x + d_1) - \frac{\mu_2}{r_2^3}(d_2 - r_x) \right) - \omega^2 r_x = 0 \tag{4.8.2}$$

$$\frac{\partial U}{\partial r_y} = \left(\frac{\mu_1}{r_1^3} r_y + \frac{\mu_2}{r_2^3} r_y \right) - \omega^2 r_Y = 0 \tag{4.8.3}$$

$$\frac{\partial U}{\partial r_z} = \left(\frac{\mu_1}{r_1^3} r_z + \frac{\mu_2}{r_2^3} r_z \right) = 0 \tag{4.8.4}$$

The last equation indicates that r_z must be zero. Equation 4.8.3 gives the condition that either r_y must be zero, or $\left(\frac{\mu_1}{r_1^3} + \frac{\mu_2}{r_2^3} \right) - \omega^2 = 0$.

Recalling that the combined mass of the central and major body and their

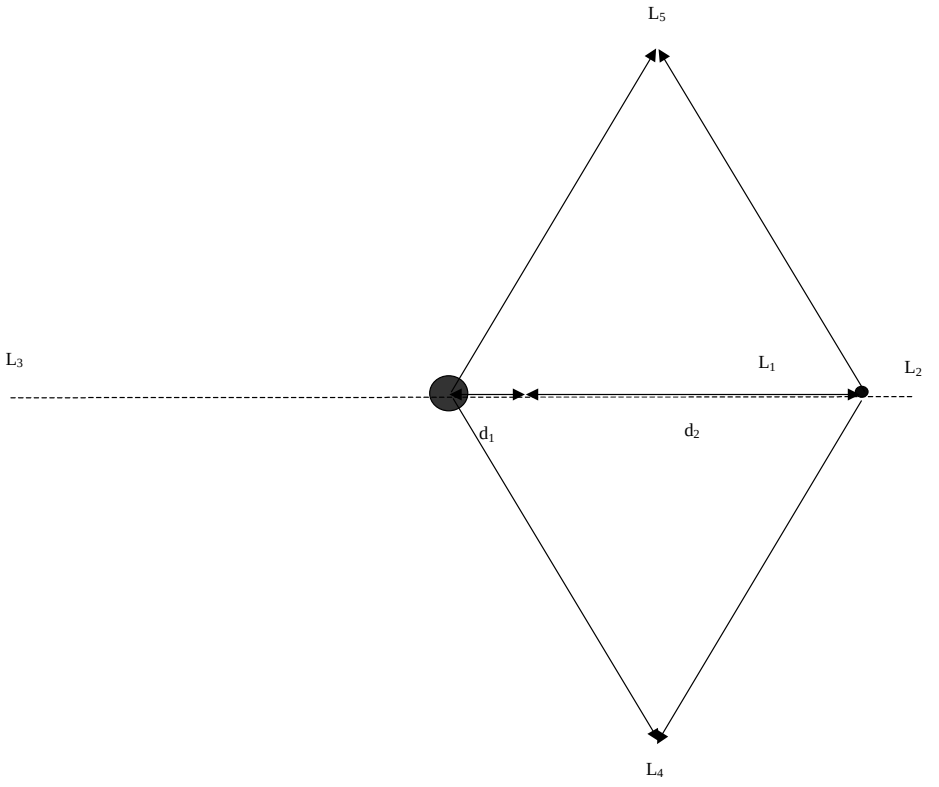

Figure 4.8.4. Locations of the Lagrange libration points.

separation define the angular velocity, $\omega^2(d_1 + d_2) = \dfrac{\mu_1 + \mu_2}{(d_1 + d_2)^2}$ a further solution to equation 4.8.3 is that:

$$r_1 = r_2 = d_1 + d_2 \tag{4.8.5}$$

The first solution is therefore a location at the vertex of an equilateral triangle with the central and major body forming one side. Two such solutions exist, and are denoted L4 and L5.

Using the solution, $r_y = r_z = 0$ with equation 4.8.2, the following equation is obtained:

$$\left(\frac{\mu_1}{|r_x + d_1|^3}(r_x + d_1) - \frac{\mu_2}{|(d_2 - r_x)|^3}(d_2 - r_x) \right) - \omega^2 r_x = 0 \tag{4.8.6}$$

The solution of this equation for r_x yields the locations of three collinear points, denoted L1, L2 and L3. Therefore, in total, five solutions are obtained for the Lagrange libration points.

Table 4.8.1 shows the locations of the first two co-linear points for the planets of the Solar System with the Sun. Two values are calculated for Earth: the first for

Table 4.8.1. The location of the L1 and L2 planetary Lagrange libration points.

	$m_2/(m_1m_2)$	L1 (km)	L2 (km)
Mercury	1.660E-07	2.204E + 05	2.210E + 05
Venus	2.448E-06	1.008E + 06	1.014E + 06
Earth	3.003E-06	1.492E + 06	1.501E + 06
Earth–Moon	3.040E-06	1.498E + 06	1.508E + 06
Mars	3.227E-07	1.082E + 06	1.086E + 06
Jupiter	9.537E-04	5.209E + 07	5.418E + 07
Saturn	2.857E-04	6.425E + 07	6.606E + 07
Uranus	4.366E-05	6.954E + 07	7.061E + 07
Neptune	5.150E-05	1.150E + 08	1.169E + 08
Pluto	6.607E-09	7.594E + 06	7.537E + 06

Earth alone with the Sun, the second with the combined mass of the Earth–Moon system with the Sun. Distance is towards the Sun (L1) and away from the Sun (L2).

This analysis assumes that each planet lies in a circular orbit about the Sun at a value corresponding to its semi-major axis. The semi-major axis used is that from JPL mean ephemeris (J2000) (see appendix). It is possible to perform an analysis where the major body lies in an elliptical orbit with respect to the central body. This is then the elliptical three-body problem, In this case, there is no corresponding integral of the motion to the Jacobi constant. Techniques have been devised to explore this phenomenon in detail, and references to such analyses are given in the references for this chapter.

Stability of the Lagrange libration points

The stability of the Lagrange points may be examined. Such an analysis also provides a first indication of the nature of some of the possible motions about a Lagrange point. Recalling that the acceleration is given by:

$$\left(\frac{d^2\underline{r}}{dt^2}\right)_R = -\nabla U - 2\underline{\omega} \wedge \left(\frac{d\underline{r}}{dt}\right)_R$$

A notation may be introduced to represent a perturbation about the location of a given Lagrange point.

$$\underline{\delta r} = \underline{r} - \underline{r_{Ln}} \tag{4.8.7}$$

where $\underline{r_{Ln}}$ is the location of the nth Lagrange point. Then:

$$\left(\frac{d^2\underline{\delta r}}{dt^2}\right)_R = -\nabla U - 2\underline{\omega} \wedge \left(\frac{d\underline{\delta r}}{dt}\right)_R$$

The potential gradient term, ∇U, can be expanded by a Taylor series about its zero value at the Lagrange point.

$$\frac{\partial U}{\partial r_x} = \delta r_x \frac{\partial^2 U}{\partial r_{x_{rLn}}^2} + \delta r_y \frac{\partial^2 U}{\partial r_y \partial r_{x_{rLn}}} + \delta r_z \frac{\partial^2 U}{\partial r_z \partial r_{x_{rLn}}}$$

$$\frac{\partial U}{\partial r_y} = \delta r_x \frac{\partial^2 U}{\partial r_x \partial r_{y_{rLn}}} + \delta r_y \frac{\partial^2 U}{\partial^2 r_{y_{rLn}}} + \delta r_z \frac{\partial^2 U}{\partial r_z \partial r_{y_{rLn}}}$$

$$\frac{\partial U}{\partial r_z} = \delta r_x \frac{\partial^2 U}{\partial r_x \partial r_{z_{rLn}}} + \delta r_y \frac{\partial^2 U}{\partial r_y \partial r_{z_{rLn}}} + \delta r_z \frac{\partial^2 U}{\partial^2 r_{z_{rLn}}} \tag{4.8.8}$$

Higher order terms are neglected. It is implicit in the notation assumed here and subsequently that the second derivatives of the potential term, U, are evaluated at the Lagrange point in question, at the point $\underline{r}_{Ln}$.

Substituting this into the previous acceleration expression gives:

$$\frac{d^2\delta r_x}{dt^2} - 2\omega\frac{d\delta r_y}{dt} + \delta r_x \frac{\partial^2 U}{\partial r_{x_{rLn}}^2} + \delta r_y \frac{\partial^2 U}{\partial r_y \partial r_{x_{rLn}}} + \delta r_z \frac{\partial^2 U}{\partial r_z \partial r_{x_{rLn}}} = 0$$

$$\frac{d^2\delta r_y}{dt^2} + 2\omega\frac{d\delta r_x}{dt} + \delta r_x \frac{\partial^2 U}{\partial r_x \partial r_{y_{rLn}}} + \delta r_y \frac{\partial^2 U}{\partial^2 r_{y_{rLn}}} + \delta r_z \frac{\partial^2 U}{\partial r_z \partial r_{y_{rLn}}} = 0$$

$$\frac{d^2\delta r_z}{dt^2} + \delta r_x \frac{\partial^2 U}{\partial r_x \partial r_{z_{rLn}}} + \delta r_y \frac{\partial^2 U}{\partial r_y \partial r_{z_{rLn}}} + \delta r_z \frac{\partial^2 U}{\partial^2 r_{z_{rLn}}} = 0 \tag{4.8.9}$$

Then, using the previously obtained expressions for the potential gradients (Equations 4.8.2, 4.8.3 and 4.8.4) and also the fact that all of the Lagrange point solutions lie in the x–y plane, it may be seen that:

$$\frac{\partial^2 U}{\partial r_x \partial r_{z_{rLn}}} = \frac{\partial^2 U}{\partial r_y \partial r_{z_{rLn}}} = 0 \qquad \text{and also} \qquad \frac{\partial^2 U}{\partial^2 r_{z_{rLn}}} > 0$$

The motion perpendicular to the ecliptic reduces to:

$$\frac{d^2\delta r_z}{dt^2} + \delta r_z \frac{\partial^2 U}{\partial^2 r_{z_{rLn}}} = 0 \tag{4.8.10}$$

This is a simple harmonic motion, and therefore motion in the z direction is stable. The remaining expressions in x and y become:

$$\frac{d^2\delta r_x}{dt^2} - 2\omega\frac{d\delta r_y}{dt} + \delta r_x \frac{\partial^2 U}{\partial r_{x_{rLn}}^2} + \delta r_y \frac{\partial^2 U}{\partial r_y \partial r_{x_{rLn}}} = 0$$

$$\frac{d^2\delta r_y}{dt^2} + 2\omega\frac{d\delta r_x}{dt} + \delta r_x \frac{\partial^2 U}{\partial r_x \partial r_{y_{rLn}}} + \delta r_y \frac{\partial^2 U}{\partial^2 r_{y_{rLn}}} = 0 \tag{4.8.11}$$

At this stage it is convenient to consider a dimensionless form of these equations that facilitate solution.

Let $\mu = \dfrac{m_2}{m_1 + m_2}$ and $1 - \mu = \dfrac{m_1}{m_1 + m_2}$; define a new time-related parameter, $t' = \omega t$, and let all of the positions be scaled by separation between m_1 and m_2 (ie $d_1 + d_2$), such that $\underline{r} = \underline{r}'(d_1 + d_2)$. The more massive central body is nominated to be m_1, and therefore $\mu < \dfrac{1}{2}$.

Therefore, $r'_{1x} = \mu + r'_x$, $r'_{1y} = r'_y$, $r'_{1z} = r'_z$ and $r'_{2x} = 1 - \mu - r'_x$, $r'_{2y} = r'_y$, $r'_{2z} = r'_z$.

Then:

$$\left(\frac{d^2\delta r'}{dt'^2}\right)_R = -\nabla U' - 2\underline{\hat{\omega}} \wedge \left(\frac{d\underline{\delta r'}}{dt'}\right)_R \tag{4.8.12}$$

where the potential is now modified to:

$$U' = -\left(\frac{(1-\mu)}{r'_1} + \frac{\mu}{r'_2}\right) - \frac{1}{2}(r'^2_x + r'^2_Y) \tag{4.8.13}$$

Therefore:

$$\frac{\partial U}{\partial r'_x} = -\left(-\frac{(1-\mu)}{r'^3_1}(r'_x + \mu) - \frac{\mu}{r'^3_2}(r'_x - (1-\mu))\right) - r'_x \tag{4.8.14}$$

$$\frac{\partial U}{\partial r'_y} = -\left(-\frac{(1-\mu)}{r'^3_1}\, r'_y - \frac{\mu}{r'^3_2}\, r'_y\right) - r'_Y \tag{4.8.15}$$

$$\frac{\partial U}{\partial r'_z} = -\left(-\frac{(1-\mu)}{r'^3_1}\, r'_z - \frac{\mu}{r'^3_2}\, r'_z\right) \tag{4.8.16}$$

The minus sign is used in front of the previous expressions to facilitate comparison with some references that express U as the negative of the function used here.

Then, using equations 4.8.14, 4.8.15 and 4.8.16, the second derivatives may be evaluated:

$$\frac{\partial^2 U'}{\partial r'^2_x} = -\left(-\frac{(1-\mu)}{r'^3_1} - \frac{\mu}{r'^3_2} + 3\frac{(1-\mu)}{r'^5_1}(r'_x + \mu)^2 + 3\frac{\mu}{r'^5_2}(r'_x - (1-\mu))^2\right) - 1 \tag{4.8.17}$$

$$\frac{\partial^2 U'}{\partial r'^2_y} = -\left(-\frac{(1-\mu)}{r'^3_1} - \frac{\mu}{r'^3_2} + 3\frac{(1-\mu)}{r'^5_1}\, r'^2_y + 3\frac{\mu}{r'^5_2}\, r'^2_y\right) - 1 \tag{4.8.18}$$

$$\frac{\partial^2 U'}{\partial r'^2_z} = -\left(-\frac{(1-\mu)}{r'^3_1} - \frac{\mu}{r'^3_2} + 3\frac{(1-\mu)}{r'^5_1}\, r'^2_z + 3\frac{\mu}{r'^5_2}\, r'^2_z\right) \tag{4.8.19}$$

$$\frac{\partial^2 U'}{\partial r_y \partial r_x} = -\left(3\frac{(1-\mu)}{r'^5_1}(r'_x + \mu)\, r'_y + 3\frac{\mu}{r'^5_2}(r'_x - (1-\mu))\, r'_y\right) \tag{4.8.20}$$

Also, the modified expression equation 4.8.11 is:

$$\frac{d^2\delta r'_x}{dt'^2} - 2\frac{d\delta r'_y}{dt'} + \delta r'_x \frac{\partial^2 U'}{\partial r'^2_{x_{rLn}}} + \delta r'_y \frac{\partial^2 U'}{\partial r'_y \partial r'_{x_{rLn}}} = 0$$
$$\frac{d^2\delta r'_y}{dt'^2} + 2\frac{d\delta r'_x}{dt'} + \delta r'_x \frac{\partial^2 U'}{\partial r'_x \partial r'_{y_{rLn}}} + \delta r'_y \frac{\partial^2 U'}{\partial^2 r'_{y_{rLn}}} = 0 \tag{4.8.21}$$

Using equations 4.8.17, 4.8.18, 4.8.19, 4.8.20, in equation 4.8.21 evaluated at each of the five Lagrange point solutions allows the corresponding expressions to be obtained for the coupled differential equations at each Lagrange point.

The values of the second partial derivatives must therefore be obtained at each of the Lagrange points of interest.

Firstly, a rationalisation of these equations is to substitute auxiliary constants as follows:

$$c_{11} = \left(\frac{(1-\mu)}{r'^3_1} + \frac{\mu}{r'^3_2}\right) \tag{4.8.22}$$
$$c_{12} = 3\left(\frac{(1-\mu)}{r'^5_1} + \frac{\mu}{r'^5_2}\right) \tag{4.8.23}$$
$$c_{13} = 3\left(\frac{(1-\mu)}{r'^5_1}(r'_x + \mu) + \frac{\mu}{r'^5_2}(r'_x - (1-\mu))\right) \tag{4.8.24}$$

This results in the following:

$$\frac{\partial^2 U'}{\partial r'^2_x} = -\left(-c_{11} + 3\frac{(1-\mu)}{r'^5_1}(r'_x + \mu)^2 + 3\frac{\mu}{r'^5_2}(r'_x + \mu - 1)^2\right) - 1 \tag{4.8.25}$$
$$\frac{\partial^2 U'}{\partial r'^2_y} = -(-c_{11} + c_{12}r'^2_y) - 1 \tag{4.8.26}$$
$$\frac{\partial^2 U'}{\partial r'^2_z} = -(-c_{11} + c_{12}r'^2_z) \tag{4.8.27}$$
$$\frac{\partial^2 U'}{\partial r_y \partial r_x} = -(c_{13}r'_y) \tag{4.8.28}$$

These partial derivatives must now be evaluated at the Lagrange point of interest. Therefore, r'_x, r'_y and r'_z must now be the rotating frame x co-ordinate of the Lagrangian point that is the subject of the local expansion.

The co-linear points may be considered, $r'_y = r'_z = 0$, and C_{11} is evaluated for the particular Lagrange point under consideration.

$$\frac{\partial^2 U'}{\partial r'^2_{x_{rLn}}} = -(1 + 2c_{11}) \tag{4.8.29}$$
$$\frac{\partial^2 U'}{\partial r'^2_{y_{rLn}}} = -(1 - c_{11}) \tag{4.8.30}$$
$$\frac{\partial^2 U'}{\partial r'_y \partial r'_{x_{rLn}}} = 0 \tag{4.8.31}$$
$$\frac{\partial^2 U'}{\partial r'^2_{z_{rLn}}} = c_{11} \tag{4.8.32}$$

where $n - 1$, 2 or 3 for the above partial derivatives (i.e., for L_1, L_2 and L_3).

These linear, second-order differential equations (Equation 4.8.21) may be solved using a standard exponential function substitution. The general solutions then become:

$$\delta r'_x = \sum_{i=1}^{4} A_i e^{\lambda_i t'} \qquad \delta r'_y = \sum_{i=1}^{4} B_i e^{\lambda_i t'} \tag{4.8.33}$$

The terms A_i and B_i and λ_i are constants. Then:

$$\lambda^4 + \left(4 + \frac{\partial^2 U'}{\partial r'^2_{x_{rLn}}} + \frac{\partial^2 U'}{\partial r'^2_{y_{rLn}}}\right)\lambda^2 + \frac{\partial^2 U'}{\partial r'^2_{x_{rLn}}}\frac{\partial^2 U'}{\partial r'^2_{y_{rLn}}} - \frac{\partial^2 U'}{\partial r'_y \partial r'_{x_{rLn}}} = 0 \tag{4.8.34}$$

and so substituting the previous expressions for the second partial derivatives at the Lagrange points gives:

$$\lambda^4 + (2 - c_{11})\lambda^2 + (1 + 2c_{11})(1 - c_{11}) = 0 \tag{4.8.35}$$

This yields solutions for λ^2 as follows:

$$\lambda^2 = \tfrac{1}{2}\left(c_{11} - 2 \pm \sqrt{9c_{11}^2 - 8c_{11}}\right) \tag{4.8.36}$$

Evaluating c_{11} at the co-linear Lagrange points results in the value $(1 - c_{11}) < 0$. Therefore, the resulting two solutions for λ^2 may have both positive and negative values, yielding exponential and oscillatory solutions for equation 4.8.33.

The presence of exponential terms in the solution means that the solution has an unstable motion component about the three, co-linear Lagrange points.

The analysis may be performed at the L4 and L5 points. In these cases, it may be shown that the solutions are stable provided that $\mu < 0.0385$. This can be compared with a value of approximately 0.001 for the Sun–Jupiter system, and so all of the planetary L4 and L5 Lagrange points satisfy this criterion for stability.

4.8.3 Orbits at the Lagrange libration points

The previous analysis considered the nature of the motion at the Lagrange points. It is possible to consider this further by examining the solutions to the locally linearised equations obtained in the previous section. At the collinear Lagrange points, these become:

$$\begin{aligned} \frac{d^2\delta r'_x}{dt'^2} - 2\frac{d\delta r'_y}{dt'} &= \delta r'_x(1 + 2c_{11}) \\ \frac{d^2\delta r'_y}{dt'^2} + 2\frac{d\delta r'_x}{dt'} &= \delta r'_y(1 - c_{11}) \\ \frac{d^2\delta r'_z}{dt'^2} &= -\delta r'_z c_{11} \end{aligned} \tag{4.8.37}$$

The general solutions may be obtained (as described by Cobos, Masdemont and Hechler, see references for this section), and are as follows:

$$\begin{aligned}\delta r'_x &= A_1 e^{st'} + A_2 e^{-st'} + A_3 \cos \omega_{xy} t' + A_4 \sin \omega_{xy} t' \\ \delta r'_y &= a A_1 e^{st'} - a A_2 e^{-st'} - b A_4 \cos \omega_{xy} t' + b A_3 \sin \omega_{xy} t' \\ \delta r'_z &= C_1 \cos \omega_z t' + C_2 \sin \omega_z t'\end{aligned} \tag{4.8.38}$$

The two frequencies for the harmonic motion in the xy plane and in the z plane can be calculated. For the motion in the ecliptic, equation 4.8.36 gives:

$$\omega_{xy} = \sqrt{\tfrac{1}{2}\left(2 - c_{11} + \sqrt{9c_{11}^2 - 8c_{11}}\right)} \tag{4.8.39}$$

For the motion out of the ecliptic, equations 4.8.10 and 4.8.32 give:

$$\omega_z = \sqrt{c_{11}} \tag{4.8.40}$$

The exponential term, s, may also be found:

$$s = \sqrt{\tfrac{1}{2}\left(c_{11} - 2 + \sqrt{9c_{11}^2 - 8c_{11}}\right)} \tag{4.8.41}$$

It also possible to calculate the constants a and b in equation 4.8.38:

$$b = -\frac{1 + 2c_{11} + \omega_{xy}^2}{2\omega_{xy}} \tag{4.8.42}$$

and

$$a = \frac{s^2 - 1 - 2c_{11}}{2s} \tag{4.8.43}$$

The values of the coefficients A_1, A_2, A_3 and A_4 are determined by the initial states of the x and y displacements and their time derivatives. Therefore, it is possible to obtain solutions where A_1 and A_2 are both zero, leaving only oscillatory motion.

The relative amplitudes of the oscillating motion in the rotating x and y directions is determined by the previously established constant, b. This means that an orbit about a given planetary Lagrange point always has the same 'shape' when seen in the rotating xy plane, irrespective of its amplitude in the x direction.

This constant, together with the periods of the in-plane motion on which it depends, can be calculated for the planets of the Solar System, neglecting the masses of the planetary moons, as shown in Table 4.8.2.

The table gives both the values for angular velocity xy and z components, in the normalised units described previously. These are also given in terms of time periods (T_{xy} and T_z), converted into standard units. In this calculation, the planets are assumed to move in circular orbits about the Sun. Similar values are found for the L2 Lagrange points.

Halo orbits

The previous analysis is based upon a linearisation of the motion about the co-linear Lagrange points. This result is a prediction that closed orbits are not in general

Table 4.8.2. Periods of in-ecliptic and out-of-ecliptic motion for orbits about the planetary co-linear L1 Lagrange libration points derived from second order expansion of potential gradient.

	μ	ωxy	ωz	Txy (days)	Tz (days)	b
Mercury	1.660E-07	2.077	2.006	42	44	3.216
Venus	2.448E-06	2.085	2.014	108	112	3.228
Earth	3.003E-06	2.086	2.015	175	181	3.229
Mars	3.227E-07	2.079	2.007	330	342	3.218
Jupiter	9.537E-04	2.170	2.100	1,998	2,064	3.349
Saturn	2.857E-04	2.138	2.068	5,031	5,201	3.304
Uranus	4.366E-05	2.108	2.037	14,570	15,076	3.260
Neptune	5.150E-05	2.110	2.039	28,542	29,531	3.263
Pluto	6.607E-09	2.099	2.028	43,173	44,683	3.247

possible, because of the difference in the periods of motion in two orthogonal directions. The motion appears closed in the xy plane, but when viewed in the yz plane the orbit will follow a Lissajous orbit.

However, when motions further removed from the Lagrange points are considered, the approximations for the linearisation introduce significant errors. Techniques have been developed to include higher-order terms in the motion, noteably by Richardson (see references for this section). An example is the following:

$$\begin{aligned}
\frac{d^2\delta r'_x}{dt'^2} - 2\frac{d\delta r'_y}{dt'} - \delta r'_x(1+2c_{11}) &= \frac{\partial}{\partial \delta r'_x}\sum_{n\geq 3} c_n \delta r^n P_n\left(\frac{\delta r'_x}{\delta r}\right) \\
\frac{d^2\delta r'_y}{dt'^2} + 2\frac{d\delta r'_x}{dt'} - \delta r_y(1-c_{11}) &= \frac{\partial}{\partial \delta r'_y}\sum_{n\geq 3} c_n \delta r^n P_n\left(\frac{\delta r'_x}{\delta r}\right) \\
\frac{d^2\delta r'_z}{dt'^2} + \delta r'_z c_{11} &= \frac{\partial}{\partial \delta r'_z}\sum_{n\geq 3} c_n \delta r^n P_n\left(\frac{\delta r'_x}{\delta r}\right)
\end{aligned} \tag{4.8.44}$$

where $\delta r^2 = \delta r'^2_x + \delta r'^2_y + \delta r'^2_z$, P_n is a Legendre polynomial and c_n is a constant.

The series on the right-hand side of the equation results in a non-linear differential equation. Solutions have been obtained, for a third-order case, using the Lindstedt–Poincaré method, notably by Richardson. Many contributions on this subject have also been made by Farquhar.

One practical consequence of this solution is that it is found that the period of the two components of motion vary with the amplitude of that component. The result is that for in-plane motion amplitude exceeding approximately 640,000 km, it is possible to find an amplitude of an out-of-plane motion that gives the same period. Therefore, closed orbits can be found in the rotating reference frame. These are called 'halo' orbits, because with the selection of the appropriate phasing between the motions, the motion, when viewed in the yz plane, forms a 'halo' about the Lagrange point and remains in this orbit (providing that other perturbations are neglected).

An example of such a halo orbit was adopted for ISEE3, with in-plane amplitude of 665,000 km and out of plane amplitude of 110,000 km.

Stable and unstable motions

The solutions given in equation 4.8.38 indicate that in addition to the oscillatory solutions already discussed, there are exponential time-dependent terms. These components may be suppressed by suitable selection of the initial states such that the constants A_1 and A_2 are zero. However, in situations where this is not the case, the nature of the motion may be considered.

If the constant A_1 takes a non-zero value, an exponentially increasing time-dependent term is present in the solution. The result is that a small perturbation to an oscillatory solution will eventually lead to a complete departure from that orbit. Such motions are unstable. This process of applying a perturbation to an oscillatory solution yielding non-zero values for the constant A_1 is one of 'stepping' onto the 'unstable manifold' of the orbit at the Lagrange point.

If the constant A_2 takes a non-zero value, an exponentially decreasing time-dependent term is present in the solution. In this case a small perturbation to an oscillatory solution will eventually lead to the perturbation reducing to zero and returning to the oscillatory solution. This process of applying a perturbation to an oscillatory solution yielding non-zero values for the constant A_2 is one of 'stepping' onto the 'stable manifold' of the orbit at the Lagrange point. An interesting feature of a stable manifold is that when propagated backwards in time, the solution diverges from the oscillatory solution.

This stable manifold may be used to execute transfers to reach the oscillatory solution, by starting at a point on the stable manifold that is far removed from the target orbit. The forward propagation of the trajectory with time then results in the spacecraft approaching the orbit described by the oscillatory solution, as the exponential term tends to zero.

The conditions for the constant A_1 remaining at zero in the presence of a velocity perturbation to an oscillatory solution can be found in terms of a direction in which this velocity perturbation may be applied. This direction lies in the ecliptic plane. A perturbation that has a component that is perpendicular to this direction, and in the ecliptic, will lead to an unstable solution where A_1 is non-zero. This fact may be used as a feature of orbit generation and maintenance strategies, and has been used notably by Hechler, Cobos and Masdemont *et al.* (see references).

4.8.4 Transfers to the Lagrange libration points

The previous section discussed the existence and use of periodic orbits at the co-linear Lagrange points. Such orbits are being increasingly proposed and utilised for deep-space observatory missions. In the context of mission design, a particularly attractive feature of such orbits is that they may be reached efficiently from initially bound Earth orbits. Analysis of transfers here will be restricted to the L1 and L2 points of the Earth–Sun system.

Invariant manifolds

The key aspect of this problem is the understanding of the nature of the invariant manifolds of such orbits. This may still be addressed in the context of the circular, restricted three-body problem. The constant integral of motion is then the Jacobi constant. An invariant manifold of such a system describes all possible locations of a spacecraft in a six-parameter phase space; that is, three position and three velocity co-ordinates: $f^n(\underline{X_p}, \underline{\dot{X}_p}, C) = 0$, where $\underline{X_p}, \underline{\dot{X}_p}$ are the position and velocity relative to the planet.

The nature of these manifolds is complex, and they require numerical simulation for any detailed exploration. An important aspect is, however, the spatial connection of the manifolds of halo or Lissajous orbits with low-perigee orbits about the Earth. This principle opens the possibility of a direct transfer from a low Earth orbit via a single manoeuvre.

Such a manifold will now be examined. For simplification it will be assumed that the Earth moves in a circular orbit about the Sun, and so the Jacobi integral will remain constant. The initial orbit starts at a perigee altitude of 500 km, with an osculating semi-major axis (at Earth perigee) of 700,000 km. This results in an osculating apogee (again evaluated at perigee) of nearly 1.4 million km. As the spacecraft leaves perigee and moves towards apogee, solar gravity perturbs the motion. The effect is such that the perigee is raised and the energy and angular momentum with respect to Earth are modified. The extent of this perturbation is strongly dependent on the location of the apogee with respect to the Earth–Sun direction. The manifold here examined is such that the solar gravity perturbation results in the spacecraft entering a Lissajous orbit about the L1 Lagrange point.

This transition can be accomplished by finding a suitable direction for the line of apses of the initial orbit, implying a particular longitude of the initial oscilating apocentre. Methods for locating such a direction are discussed subsequently. An example of such a manifold is shown in Figure 4.8.5. The 'free injection' behaviour can be explained in terms of a trajectory that at perigee lies on a stable manifold of a Lissajous orbit.

Examination of the osculating orbital ephemeris terms shows the effect of the solar gravity perturbations. The key terms, semi-major axis (and hence energy) and angular momentum (and hence eccentricity) undergo significant variations over the manifold. These are shown in Figure 4.8.6.

Properties of Lissajous orbit manifolds

The previous discussion showed the general characteristics of an invariant manifold that links a close Earth approach with a Lissajous orbit at the Lagrange point. An infinite number of such manifolds exist, each differing in the exact detail of the Earth perigee motion and the motion close to the Lagrange point. However, there are restrictions on the possible motions. The motion in the ecliptic (XY rotating reference frame) will be considered.

The previous example illustrated a manifold where the Lissajous orbit amplitude is approximately 1.2 million km. This amplitude (the extension measured along the

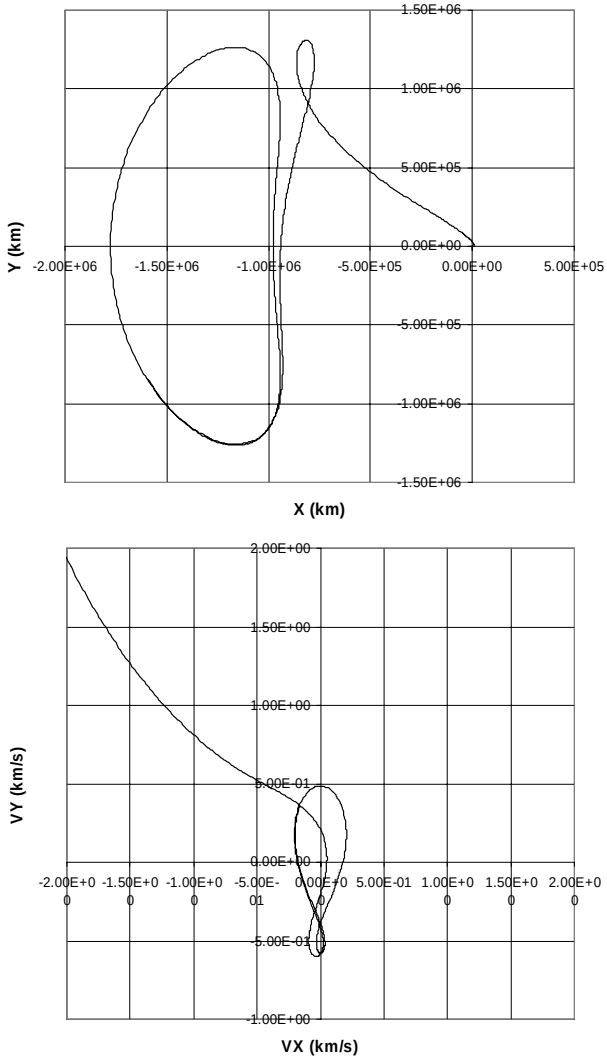

Figure 4.8.5. A manifold at the Earth–Sun L1 Lagrange point exhibiting Lissajous and high Earth elliptical orbit behaviour. In the upper figure, the trajectory, seen in the Earth–Sun rotating reference frame (X in the Sun–Earth direction) shows the spacecraft entering a periodic Lissajous orbit from an initial perigee at 500 km above the Earth. The amplitude of the Lissajous orbit (the maximum extent of the motion in the Y direction of this plot) is approximately 1.2 million km. The period of this simulation is one year. In the lower figure, the velocity profile, transformed to the Earth–Sun rotating reference frame and measured relative to the rotating frame (X in the Sun–Earth direction) shows the spacecraft exibiting periodic behaviour after entering the Lissajous orbit, from a much higher velocity at initial perigee. The maximum speed in the rotating frame, when in this Lissajous orbit, is approximately 500 m/s, and occurs in the Y direction. The inertial/rotating velocity relationship is given by $\left(\frac{d\underline{r}}{dt}\right)_I = \left(\frac{d\underline{r}}{dt}\right)_R + \underline{\omega} \wedge \underline{r}$, where R denotes rotating frame and I inertial.

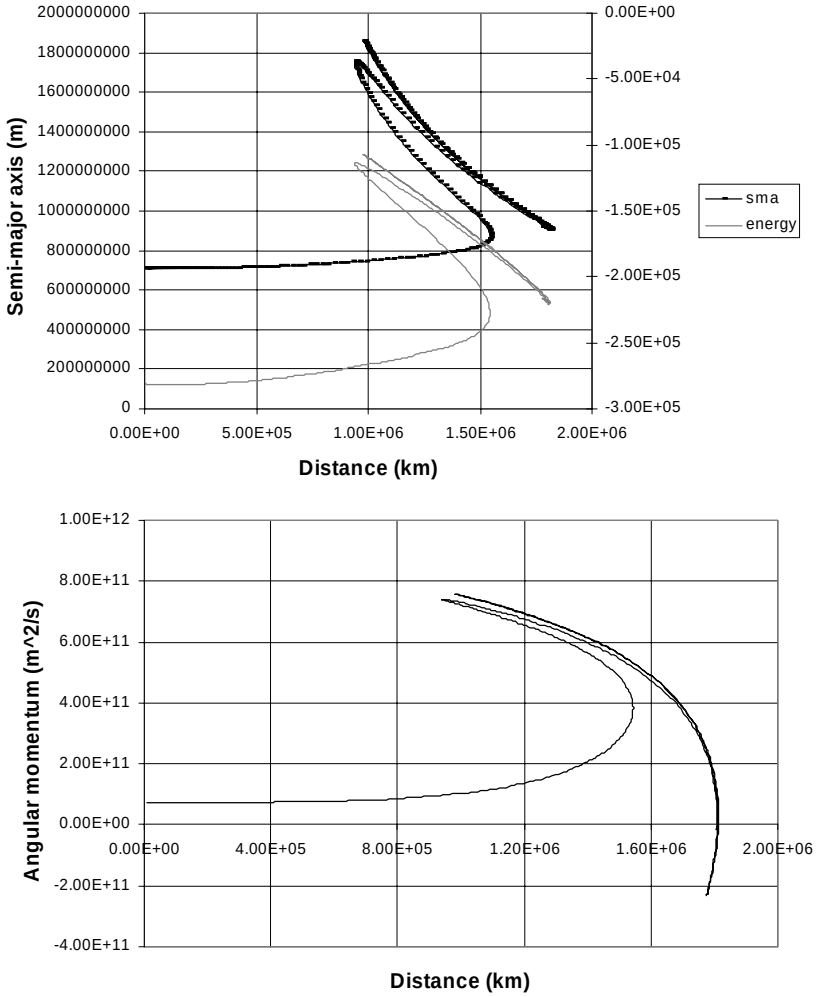

Figure 4.8.6. Energy and angular momentum variation over a manifold at the Earth–Sun L1 Lagrange point exhibiting Lissajous and initial high Earth elliptical orbit behaviours. In the upper figure, the semi-major axis (relative to Earth, plotted against the left axis) and the corresponding energy (plotted against the right axis) are significantly increased as the spacecraft enters the Lissajous orbit, where they exhibit a periodic behaviour. In the lower figure the Earth relative angular momentum also experiences a significant increase on entering the Lissajous orbit. Its evolution then demonstrates periodic behaviour.

Y axis measured in the rotating reference frame) is a design parameter for certain classes of science mission, where restrictions on the size of the Lissajous orbit are often desirable. Therefore, the range of such manifolds can be examined to assess the consequences of the size of the Lissajous orbit. Figure 4.8.7 shows comparisons between members of a family of manifolds, each with a different size of Lissajous orbit.

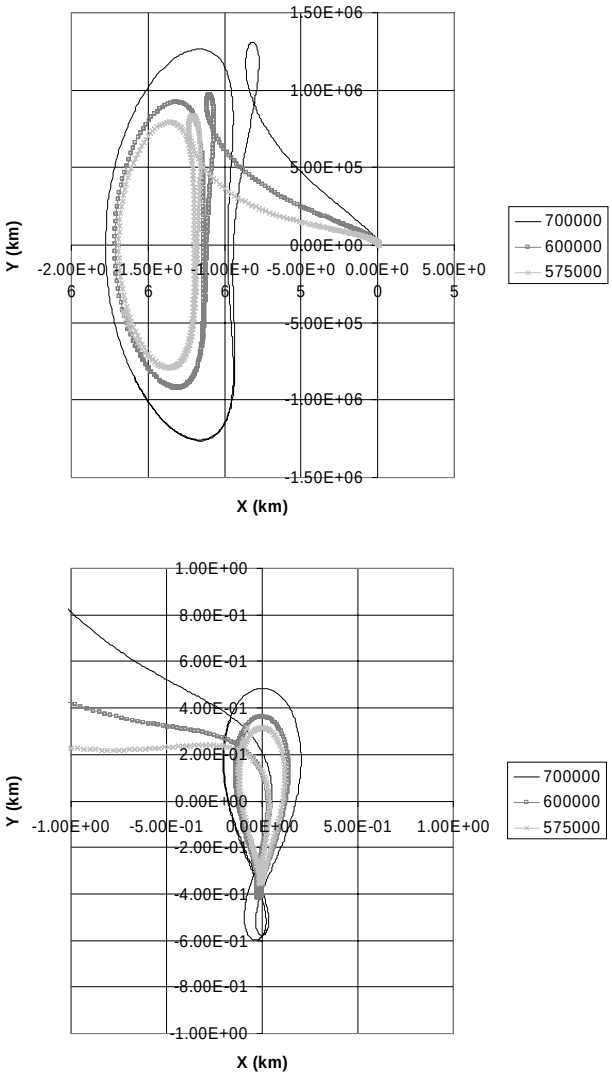

Figure 4.8.7. Manifolds at the Earth–Sun L1 Lagrange point exhibiting Lissajous and initial high Earth elliptical orbit behaviours, for a range of initial orbit osculating semi-major axes from 575,000 to 700,000 km. In the upper figure the trajectories are seen in the Earth–Sun rotating reference frame (X in the Sun–Earth direction). Examination of the three different manifolds shows the spacecraft entering different-amplitude periodic Lissajous orbits, each starting from an initial perigee at 500 km above the Earth. The amplitude of the Lissajous orbit varies between approximately 1.2 million km and 790,000 km. The period of this simulation is one year. The lower figure shows the velocity profile, transformed to the Earth–Sun rotating reference frame (VX is the velocity component in the Sun–Earth direction).The different manifolds display different velocities when in the periodic Lissajous orbit. The maximum speed in the rotating frame, when in the Lissajous orbit, lies between approximately 500 m/s and 300 m/s for the different orbits under consideration.

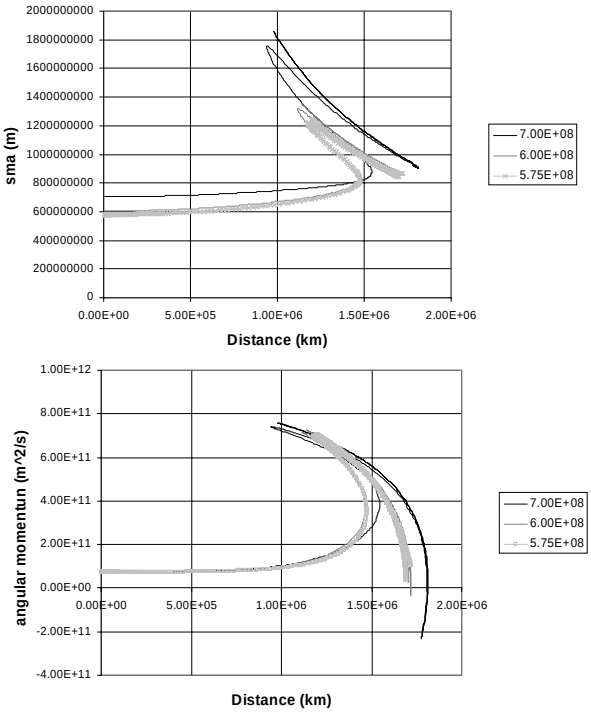

Figure 4.8.8. Energy and angular momentum variation over manifolds at the Earth–Sun L1 Lagrange point exhibiting Lissajous and initial high Earth elliptical orbit behaviours, for a range of initial orbit osculating semi-major axes between 575,000 and 700,000 km. In the upper figure the semi-major axis (relative to Earth), as the spacecraft enters the Lissajous orbit, is significantly different for the three manifolds examined here. The initial difference becomes amplified. In the lower figure, the Earth relative angular momentum in the Lissajous orbit phase of the motion also shows significantly different values over the three manifolds illustrated, but with almost identical values at Earth perigee.

In these cases, the initial orbit inclination at Earth perigee is set to a near-zero value, relative to the plane of the ecliptic, so that the motion out of the ecliptic is limited. This is not a requirement, and out-of-ecliptic effects will be examined subsequently. For each manifold, the initial Earth perigee altitude is fixed at 500 km. The manifolds are generated by assigning different values of the osculating initial apogee. As well as the initial semi-major axis of 700,000 km in the previous example, lower values at 600,000 km and 575,000 km are used. These correspond to apogees of approximately 1.2 million km and 1.1 million km respectively (that is, their osculating values measured at perigee). The evolution of the ephemeris is shown in Figure 4.8.8.

The lowest initial Earth relative energy manifold shown here results in the smallest Lissajous orbit amplitude (or semi-major axis). However, any significant further reduction in the initial energy (at perigee) of the manifold is not possible if a Lissajous orbit target is to be reached. Below a range of critical values (this value

depending on the precise detail of the other orbital elements at perigee that determine, for example out-of-ecliptic motion as well as in-ecliptic motion under discussion here), the apogee is insufficiently high to allow the solar gravity perturbation to enable a free transition to a Lissajous orbit. The consequence of this is that there is a minimum initial apocentre that realises free injection. Associated with this is a minimum amplitude of Lissajous orbit that may be achieved by free transfer from an orbit with a given initial perigee altitude. The value of this minimum amplitude will be seen to depend on the details of the Earth perigee state and the type of transfer route taken to the orbit at the Lagrange point.

The relationship between the Earth perigee state and the minimum achievable amplitude of the Lissajous orbit, with initial Earth perigee values at 500 km, 18,000 km and 36,000 km, will now be considered. Each has the same initial semi-major axis (osculating value at perigee) of 575,000 km. Figure 4.8.9 shows a comparison of the three manifolds. The evolution of the ephemeris for the three cases is shown in Figure 4.8.10.

In the previous illustrations, the semi-major axis value is close to the minimum value from which it is possible to achieve free injection to an orbit about the Lagrange point. In fact, the minimum value of semi-major axis varies with the initial perigee altitude, as this influences the osculating apogee altitude. Furthermore, the minimum amplitude of Lissajous orbit for a given initial semi-major axis is also found to depend on the transfer route. For example, a transfer consisting of multiple revolutions (i.e., apogee perigee passages) may be capable of reaching smaller amplitude orbits at the Lagrange point.

Finding Lissajous orbit manifolds

The previous discussion regarding invariant manifolds containing Lissajous orbits described certain features of the manifolds. A crucial element of mission design lies in obtaining these manifolds and deciding upon which ones are best suited to the current mission. This decision will generally be influenced by two main factors:

- The ease of a transfer to such a manifold.
- The operational properties of the Lissajous orbit (amplitude in and out of ecliptic, plus phasing of the two motions).

Two general approaches to finding the best transfer orbit can be considered. It is nominally assumed that the initial orbit has a low perigee. This enables the transfer orbit to be reached efficiently from a typical injection orbit from a launch vehicle.

(1) Generate the target Lissajous orbit about the Lagrange point and explore the evolution of the orbit by backwards propagation to perigee.
(2) Start from a given perigee and search over a state space consisting of a subset of the full initial orbit ephemeris. Forwards propagation from the initial state is continued for a period within which a Lissajous orbit can be reached.

These approaches will now be considered in greater detail. They can be summarised as a backwards or forwards propagation method.

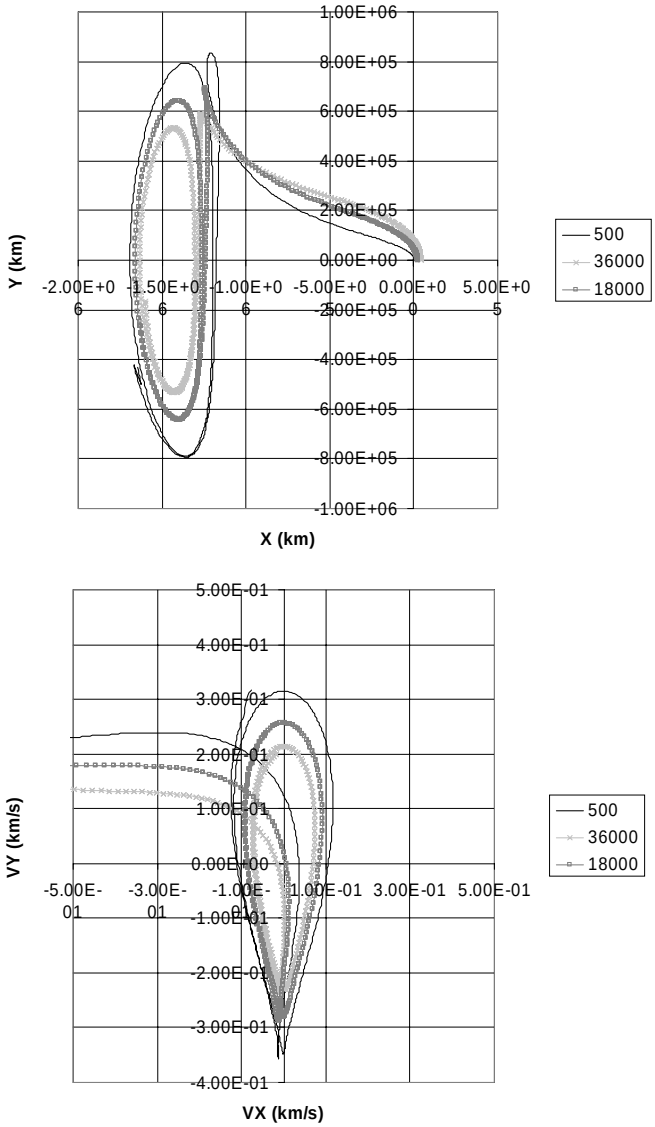

Figure 4.8.9. Manifolds at the Earth–Sun L1 Lagrange point exhibiting Lissajous and initial high Earth elliptical orbit behaviours, for a range of initial orbit osculating perigee altitudes from 500 to 36,000 km. The upper figure shows the transfer trajectories and orbits, in the Earth–Sun rotating reference frame (X in the Sun–Earth direction). As progressively higher perigees are considered, the lower is the resulting Lissajous orbit amplitude. The period of this simulation is one year. The lower figure shows the velocity profile, transformed to the Earth–Sun rotating reference frame (VX is the velocity component in the Sun–Earth direction). Higher initial perigees result in lower, rotating frame relative velocities when in the Lissajous orbit state. This corresponds to the reduced size of these orbits, which all have approximately the same period.

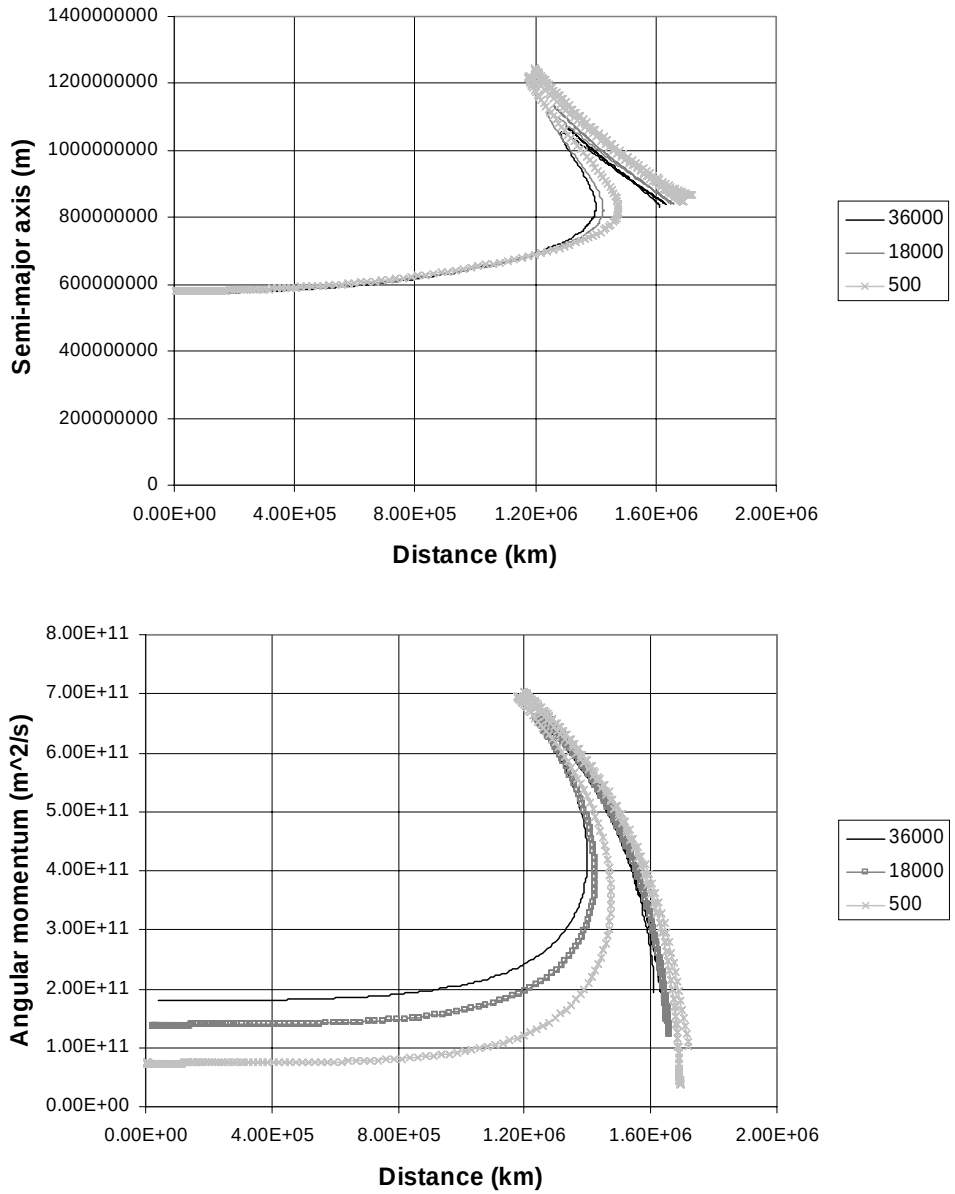

Figure 4.8.10. Energy and angular momentum variation over manifolds at the Earth–Sun L1 Lagrange point exhibiting Lissajous and initial high Earth elliptical orbit behaviours, for a range of initial orbit osculating perigee altitudes from 500 to 36,000 km. The upper figure shows the semi-major axis (relative to Earth). As the spacecraft enters the Lissajous orbit the energies of the three orbits diverge, having had near-identical values at the initial perigee. The lower figure shows the Earth relative angular momentum. The different initial perigee altitudes result in significantly different angular momenta, but these tend to converge as the Lissajous orbit state is approached.

Forwards propagation method This method relies on the partial specification of the initial orbit properties, and allows exploration over the range of the free parameters. Several 'search' methods can be considered. These range from global optimisation techniques to simple nested parameter loops or even a single parameter search. The initial state vector is defined by the following:

Parameter	*Influence*
Apogee	Classifies the possible solution types. It must exceed a minimum value to achieve a Lissajous orbit, and its value strongly influences the amplitude or in-plane semi-major axis of the Lissajous orbit.
Perigee	This will often be fixed to enable linking to an initial low Earth orbit or launch injection orbit. This may be determined by the launch vehicle capability.
Inclination	Influences the achievable, maximum out of ecliptic motion. In practice it may again be fixed by considerations regarding the initial injection orbit.
Argument of perigee	In conjunction with the inclination, this strongly influences the actual out-of-ecliptic motion.
Right ascension of ascending node	In conjunction with the argument of perigee, this determines the longitude of the line of apses. It is therefore a key parameter, as it determines whether a Lissajous orbit may be achieved for a given apogee altitude.
Mean anomaly	Nominally set to zero to achieve a start at perigee.

The six potentially free parameters are therefore generally reduced to typically two or three. This would assume that perigee altitude and inclination are fixed. Higher out of ecliptic motions than those that can be reached efficiently by the launch vehicle are often only considered when there is a specific mission design requirement.

The period of propagation for each initial condition of the search should be between 180 and 360 days to establish that a Lissajous orbit is achieved. The final state sensitivity to the initial parameters described is high.

The sensitivity can be analysed in terms of the state transition matrix, defined as:

$$\left[\frac{\partial \underline{X}_f}{\partial \underline{X}_0}\right] = \begin{bmatrix} \dfrac{\partial X_{1f}}{\partial X_{10}} & \cdots & \dfrac{\partial X_{Nf}}{\partial X_{10}} \\ \dfrac{\partial X_{1f}}{\partial X_{20}} & \cdots & \dfrac{\partial X_{Nf}}{\partial X_{20}} \\ \cdots & \cdots & \cdots \\ \dfrac{\partial X_{1f}}{\partial X_{N0}} & \cdots & \dfrac{\partial X_{Nf}}{\partial X_{N0}} \end{bmatrix}$$

That is, the state transition matrix of final Cartesian states with respect to initial Cartesian states. This matrix may be obtained by numerical integration, as described in the section 3.

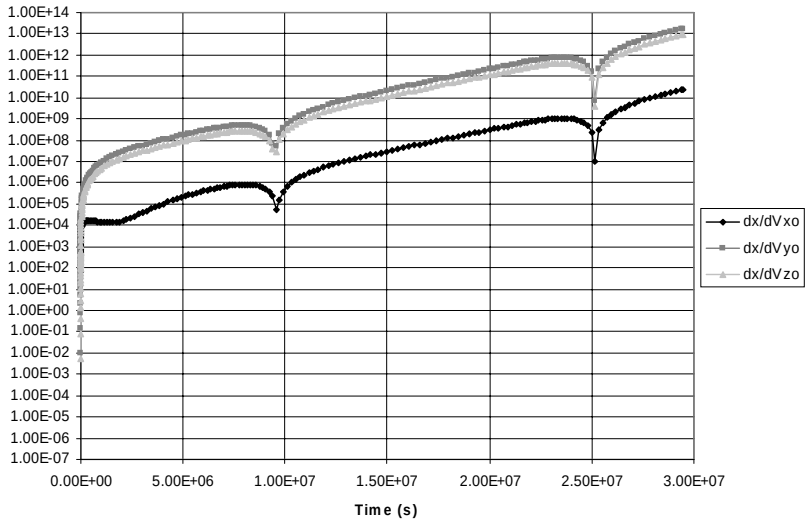

Figure 4.8.11. State transition elements showing final position sensitivity to initial velocity, for a manifold linking low Earth perigee to a Lissajous orbit at L1. The sensitivity of the final Cartesian X component with respect to initial velocity perturbations increases exponentially with time. After one year (3.1e7 secs) the sensitivity approaches 10e + 14 m/s.

An example of such a state transition matrix is shown in Figure 4.8.11, in which the modulus of the final 'x' component of the matrix is plotted. The initial state is at Earth perigee.

This high sensitivity immediately indicates the difficulty in obtaining a solution in this way. If a parametric search method is used, tiny steps must be used in order to capture the range of possible evolutions of the motion. If an optimisation or iteration method is used then the sensitivity to the control parameters is extremely high.

However, robust search techniques are able to locate solutions, and particularly effective methods that have been used are rule-based systems. An example of such a procedure has been developed by Bello-Mora (see references for further details).

The effects of a search in initial argument of perigee can be seen in Figure 4.8.12, starting from a high elliptical orbit (the osculating value defined at Earth perigee). The possible motions in this example, after leaving perigee, include reaching Lissajous orbits, completing a revolution of the Lagrange point, and then returning to perigee and also escaping beyond a Lissajous orbit into the heliocentric domain after a partial revolution of the Lagrange point. This later class of trajectories can be seen in Figure 4.8.12 and are discussed in the section regarding gravitational escape.

This figure clearly demonstrates the high sensitivity to the initial direction of the line of apses. Radically different orbit types result from a variation of 0.05°. This corresponds to a perpendicular velocity increment, at initial perigee, of less than 0.5 m/s.

Figure 4.8.12 has demonstrated a spectrum of possible orbits that may be reached with small variations in initial orbit ephemeris. In fact, allowing a greater

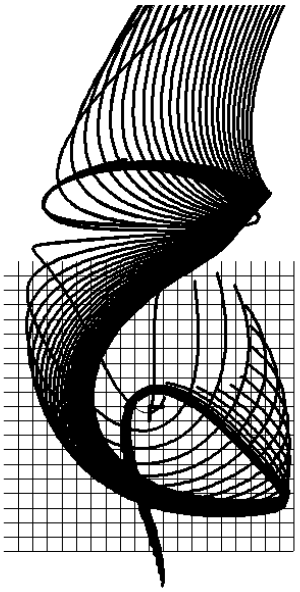

Figure 4.8.12. Transfer evolution starting from near Earth perigee with variations in argument of perigee of 0.05°. The perigee altitude is 500 km and the semi-major axis 575,000 km. The grid is 1 million km from centre to edge, with a sub-grid size of 100,000 km. The axis set is rotating, with the vertical axis in the Earth–Sun direction. The grid lies in the ecliptic. Initial orbit inclination is low.

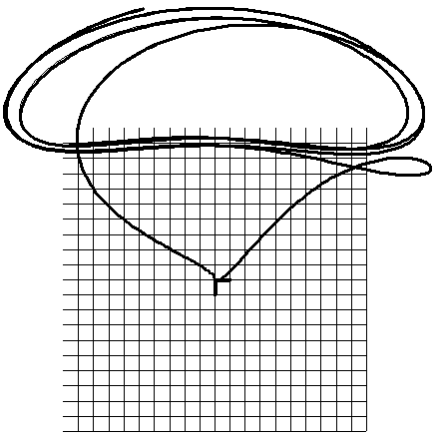

Figure 4.8.13. Transfer evolution of a 775000 semi-major axis initial orbit starting from near-Earth perigee, with variations in right ascension of ascending node of an approximately 110 degrees, reaching free injection Lissajous orbits. In this figure the perigee is rotated through approximately 110 degrees to illustrate two free injection solutions to similar free injection Lissajous orbits. The grid is 1 million km from centre to edge, with a sub-grid of 0.1 AU. The initial apogee/perigee is the same in both cases; only the right ascension of ascending node is changed, which in turn causes a corresponding rotation in the perigee in this low-inclination orbit.

variation in the initial ephemeris can reveal some interesting features of this type of motion. This includes the presence of an alternate 'free injection' transfer route, for a given value of initial apogee and perigee. The only difference in initial orbit ephemeris is the direction of the line of apses, generated for example by a variation in the right ascension of ascending node. This is seen in Figure 4.8.13.

Backwards propagation method If representative simulations of a suitable Lissajous orbit are available, they may be used as the starting point for a backwards propagation. The propagation is continued until the spacecraft passes through perigee. At this point the state can be captured and compared with that available from a suitable launch orbit. This will ultimately determine the manoeuvre requirement.

A possible problem is that the backward propagation from a particular starting point may lead to unacceptable perigees. Reaching a high-perigee orbit either directly with a launch vehicle or by a spacecraft manoeuvre is generally demanding in terms of the manoeuvre ΔV that must be applied. Therefore, a means must be sought that allows an acceptable perigee to be reached (assuming, of course, that the initial Lissajous orbit amplitude is compatible with a low perigee; see the discussion in the previous section).

The backwards trajectory propagation from each of a number of locations around the nominal orbit may be evaluated, after applying a small perturbation to the trajectory at each point. This allows the generation of a range of possible perigee passage states. The back-propagated cases may then be examined and the best match to the initial orbit/injection orbit found. There may also be a concern about the inclination when perigee is reached and the match with possible launcher orbits. This factor can also be included in finding the best match.

Several techniques have been developed for establishing the invariant manifolds associated with such orbits about the Lagrange points, by propagation methods. This area of research has been a source of much recent analysis by several groups (including Lo, Marsden, Ross, Koon *et al.*, and Simo, Cobos, Masdemont *et al.*). Further details are given in the references for this section.

Reaching small-amplitude Lissajous orbits

When lower-amplitude orbits are required, the strategy must be modified. This is because it has been observed that the minimum free injection orbit amplitude is typically over 750,000 km when starting from an initial low Earth perigee (and only considering a single revolution transfer route). A significantly higher perigee is needed to reach lower amplitudes via free injection. This is often expensive to reach in ΔV terms, from an initial injection orbit with a relatively low perigee altitude. When starting from such a low perigee initial state, a dedicated manoeuvre sequence is required to inject into the target orbit when approaching the vicinity of the Lagrange point. This can be accomplished by typically two spacecraft manoeuvres – one approaching the target orbit at the Lagrange point and the other as a final injection manoeuvre into the required orbit.

The total ΔV required for this injection is dependent on the amplitude of the target orbit. Small orbits require higher ΔVs. For in-plane amplitudes of typically

750,000 km and above, a free injection orbit can generally be found. However, for much smaller-amplitude orbits, such as 400,000 km, a typical injection ΔV of 150 m/s would be required.

Generation of transfers to a target Lissjous orbits with high out-of-ecliptic components

The transfer examples discussed so far have concentrated on the motion in the ecliptic. However, Lissajous orbits may be found with significant motions perpendicular to the ecliptic. Section 4.8.3 has discussed the nature of such orbits. It is therefore of some interest to analyze the nature of transfers to such orbits. Previous discussions, regarding linearisations of the motion about the Lagrange point have indicated that the motion perpendicular to the ecliptic dose not cross couple to in-ecliptic motion. This factor may be of use in discovering the nature of the transfer orbits to such target orbits about the Lagrange point.

It has been shown that the manifolds of Lissajous orbits may reach low-perigee conditions that may be used for free injection transfers. Such low-perigee orbits can also be used to achieve transfers to Lissajous orbits with high out-of-ecliptic amplitudes. The orbit at perigee now has an out-of-ecliptic plane velocity component, established through the inclination and argument of perigee.

These transfers are shown in Figures 4.8.14 and 4.8.15, where X is the Sun–Earth direction, Y is the perpendicular in the ecliptic, and Z is perpendicular to the ecliptic.

The figures show two alternative transfers to a Lissajous orbit with a high out-of-ecliptic amplitude. Both final orbits have a similar in-ecliptic amplitude in the rotating Y direction approaching 750,000 km (in this example). Both have a similar out-of-ecliptic component (approximately 400,000 to 600,000 km). However, different transfer orbits are used. Both use the same initial inclination, but one takes a northerly passage and the other a southerly one. This is achieved by using different argument of perigees to determine the declination of the outward traverse of the transfer orbit. An interesting feature of the resulting Lissajous orbit is that although the in-plane motions are similar, the out-of-plane motions are reversed, such that when viewed from the X axis, one moves in a clockwise and the other in an anti-clockwise direction.

Such orbits, with high out-of-ecliptic components, enable efficient communications solutions with Earth, if, for example, a fixed Sun pointing attitude is used for the spacecraft. Such an attitude is typical of an observatory-type mission at the Lagrange points. An example of this type of mission is ESA's planned LISA Pathfinder technology demonstration mission (see references for this section).

4.8.5 Gravity-assisted planetary escape and capture

The discussions in the previous sections have shown that many types of motion are possible when the three-body problem is considered. It has been demonstrated that for typical escape orbit trajectories, where the excess hyperbolic speed is relatively

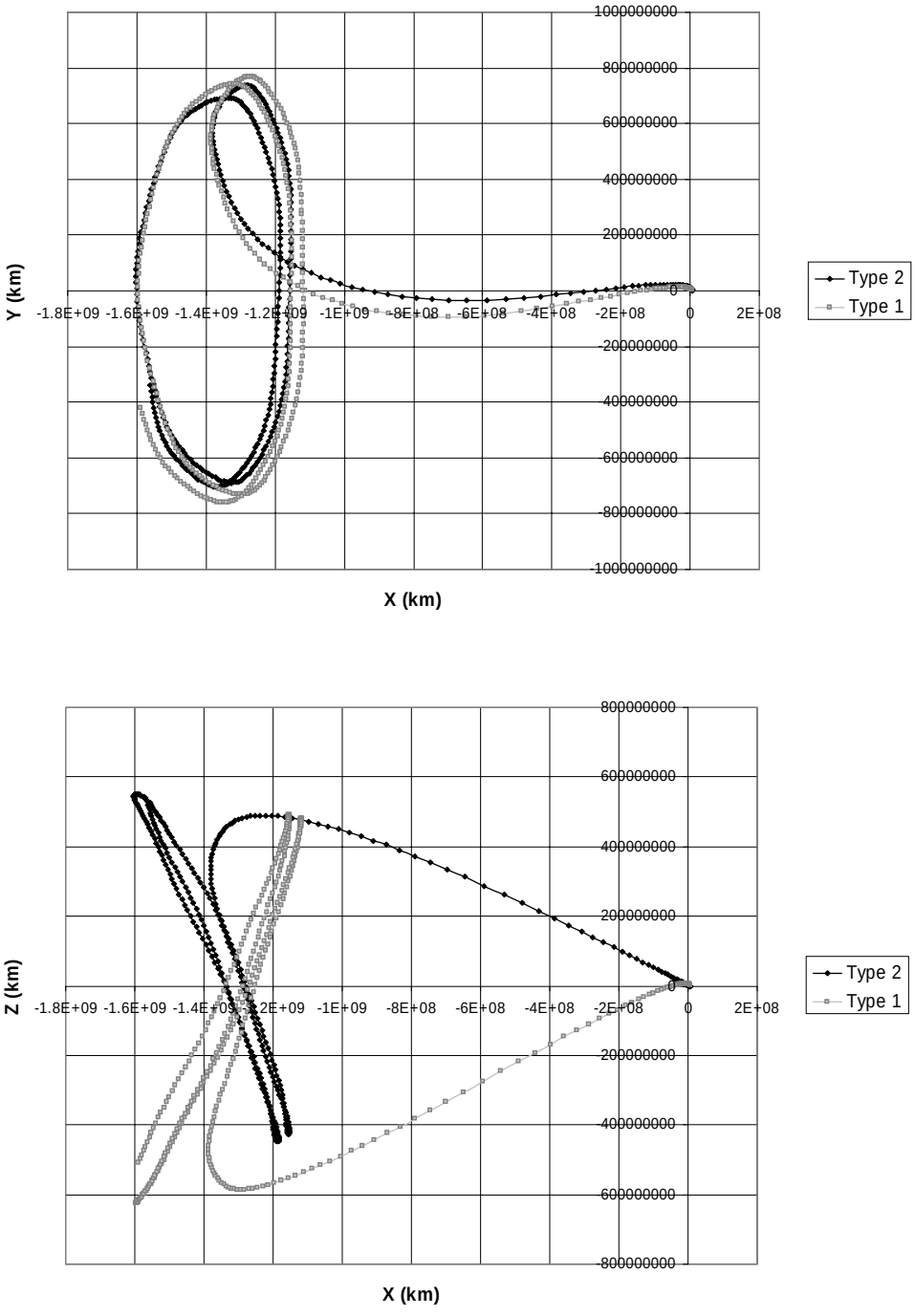

Figure 4.8.14. Transfers from a 500 km perigee orbit to Lissajous orbits about the Earth–Sun L1 point, showing transfers both north and south of the ecliptic. Axes are rotating frame.

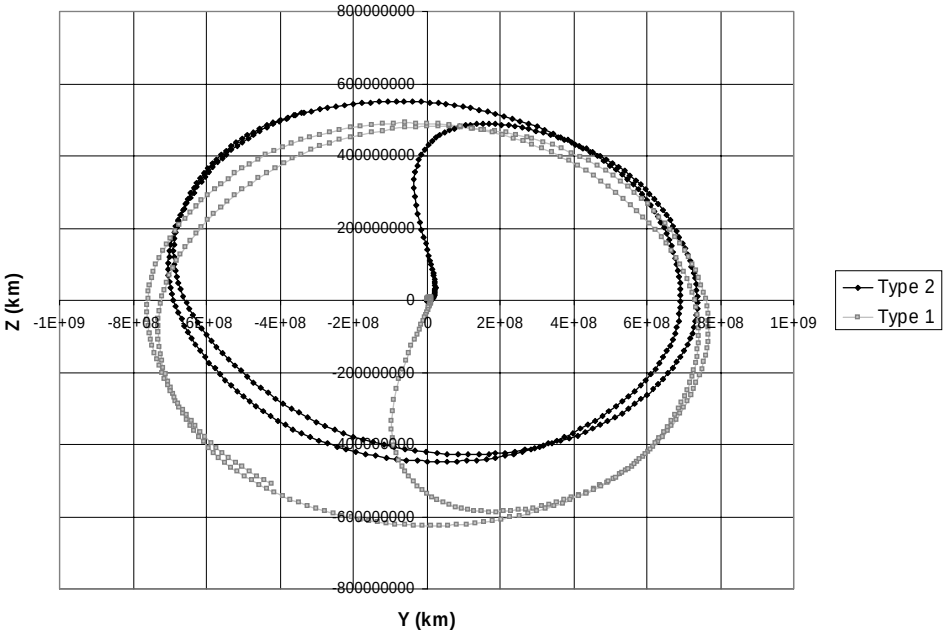

Figure 4.8.15. Transfers from a 500-km perigee orbit to Lissajous orbits about the Earth–Sun L1 point, showing transfers both north and south of the ecliptic and motion in the rotating *YZ* plane.

high and the effects of solar perturbations are limited before the spacecraft leaves the planet's influence, the approximation of the addition of an impulsive velocity vector, equal to the excess hyperbolic velocity vector (derived from the osculating pericentre condition) is a good approximation to the actual resulting motion after leaving the planetary sphere of influence.

However, the preceding analyses of the motions of spacecraft in the vicinity of the Lagrange points has shown that a spacecraft may experience significant changes to key orbit parameters. Energy shows significant variations under the influence of central body gravity perturbations. These changes could potentially allow the spacecraft to escape from the planet, when starting from an initially planet-bound orbit, or conversely, experience capture from an interplanetary orbit approaching the planet.

The problem now is to find a methodology to exploit this motion domain to the advantage of a spacecraft transfer.

Analysis of velocity surfaces

For a spacecraft to experience the significant effects of combined gravity perturbations, the zero-velocity surfaces must allow motion between the Sun and planet.

In the case of the circular, restricted three-body problem, when considering the accessible regions, the range of possible velocities at given locations can be obtained

from the expression of the Jacobi constant, C: $V^2 + 2U = -C$ (as discussed in section 4.8.1), where V is the velocity with respect to the rotating reference frame. This frame rotates with the planet's motion about the central body and is such that X lies along the Sun-to-planet direction and Y lies in the orbit plane of the planet about the central body, perpendicular to X. Z lies normal to the orbit plane.

For motion in the ecliptic (in the case of Earth) the velocity at a given location can be obtained from the following expression, as a function of radial distance from the major body and the X component of that position:

$$V^2 = 2\left(\frac{\mu_1}{(d_1+d_2)\left(1+2\dfrac{r_{2x}}{d_1+d_2}+\dfrac{r_2^2}{(d_1+d_2)^2}\right)^{0.5}}+\frac{\mu_2}{r_2}\right)+\omega^2(d_2^2+r_2^2+2r_{2x}d_2)-C \tag{4.8.45}$$

where subscript 2 denotes the major body or planet, d_1 is the distance from barycentre to the central body, d_2 the distance from barycentre to major body, r_{2x}, r_{2y} and r_{2z} are the components of position with respect to body 2, expressed in the rotating reference frame, and ω is the angular velocity of the rotating reference frame. Also, $r_2^2 = r_{2x}^2 + r_{2y}^2 + r_{2z}^2$, so that if r_{2z} is zero, r_{2x} and r_{2y} define the location.

At a given r_{2x} the variation in V with r_{2y} can be found from the above relationship, until the limiting case is reached where V becomes zero. This analysis will concentrate on cases where the motion lies in the ecliptic, and so r_{2z} is zero.

Note that this is the velocity with respect to the rotating frame. For motion close to the planet the velocity with respect to the rotating frame is similar to the inertial planet relative frame velocity, but diverges at greater distance.

As the value of the constant $-C$ increases, the surfaces of zero velocity change in their nature. From a value where motion is confined either to an Earth-centred or a Sun-centred domain, further increase in $-C$ allows transference from the Earth-centred domain to the Sun-centred domain. The value of the rotating frame velocity may be evaluated over the permissible regions of motion. These are shown in Figures 4.8.16 and 4.8.17 for motion close to Earth. The evaluation here is made in the X, Y rotating reference plane (the plane containing the Earth's motion about the Sun). The X axis lies in the direction from Sun to Earth. The origin of the XY axes is at the centre of the Earth. A locus of the zero velocity values corresponds to the location of the surface of zero velocity discussed in section 4.8.1.

In Figure 4.8.16 the Jacobi constant, C, takes a values that allows a limited degree of motion between geocentric and heliocentric domains. This reference case is used in subsequent comparisons in this section. The value of Jacobi constant used is 2,640,500,000 $(\text{m/s})^2$.

The nature of these surfaces contains several features of interest. The first is the significant change in velocity with distance from Earth in both the X and Y directions. When Jacobi constant values are considered where motion is possible between Earth-centred and Sun-centred orbits, inspection of the evolution of the velocity in the Y direction shows a characteristic initial decrease with distance that is similar in

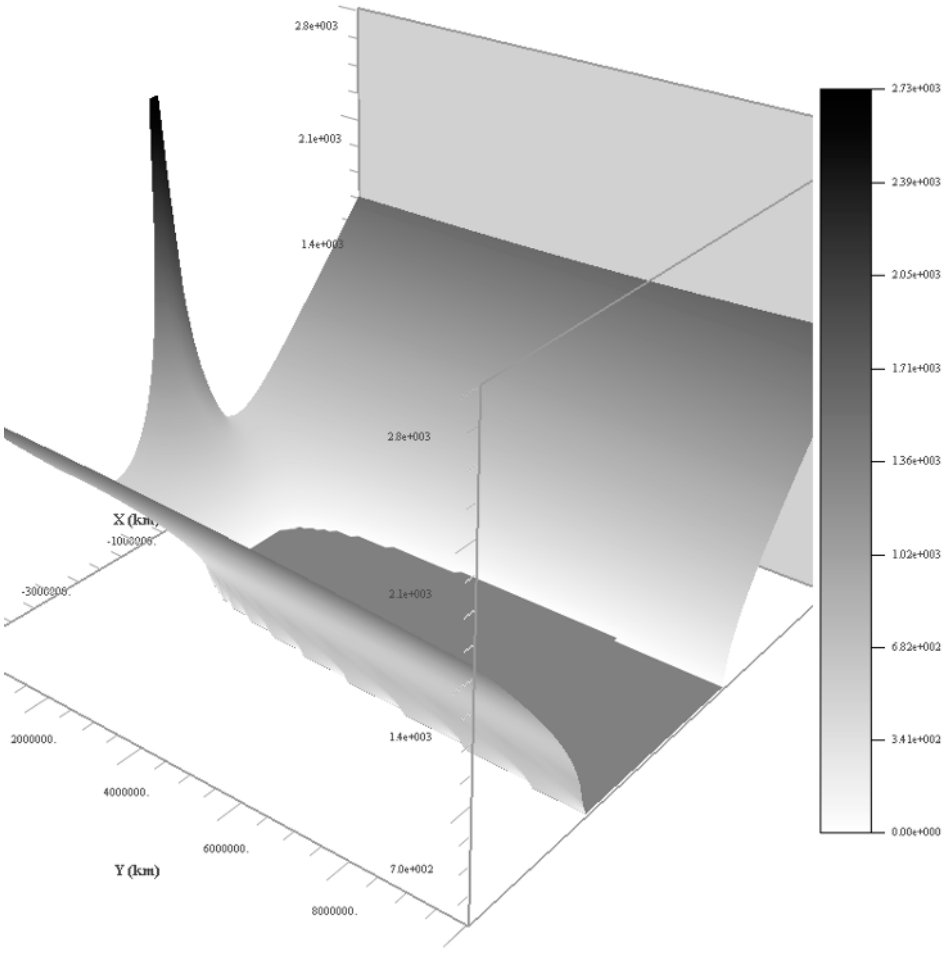

Figure 4.8.16. Variation in rotating frame relative velocity with X and Y displacement in the Earth–Sun system for Jacobi: constant at the reference value.

nature to the behaviour of a classical escape orbit. However, in Figure 4.8.16 this motion in the Y direction is ultimately limited by the zero-velocity surface.

Inspection of the velocity evolution along the X axis shows the presence of a minimum at the co-linear Lagrange points, L1 and L2. Moving along X beyond these points results in an increase in the velocity. A case with an increase in $-C$ can also be examined. This is shown in Figure 4.8.17, in which the zero-velocity surface does not appear. The value of Jacobi constant used here is 2,639,000,000.

The corresponding planet relative velocity can be obtained at any of the above locations in the previous figures for a given Jacobi constant by making assumptions about the direction of motion with respect to the rotating reference plane. In this context, the planet relative velocity is the velocity relative to the planet measured in a

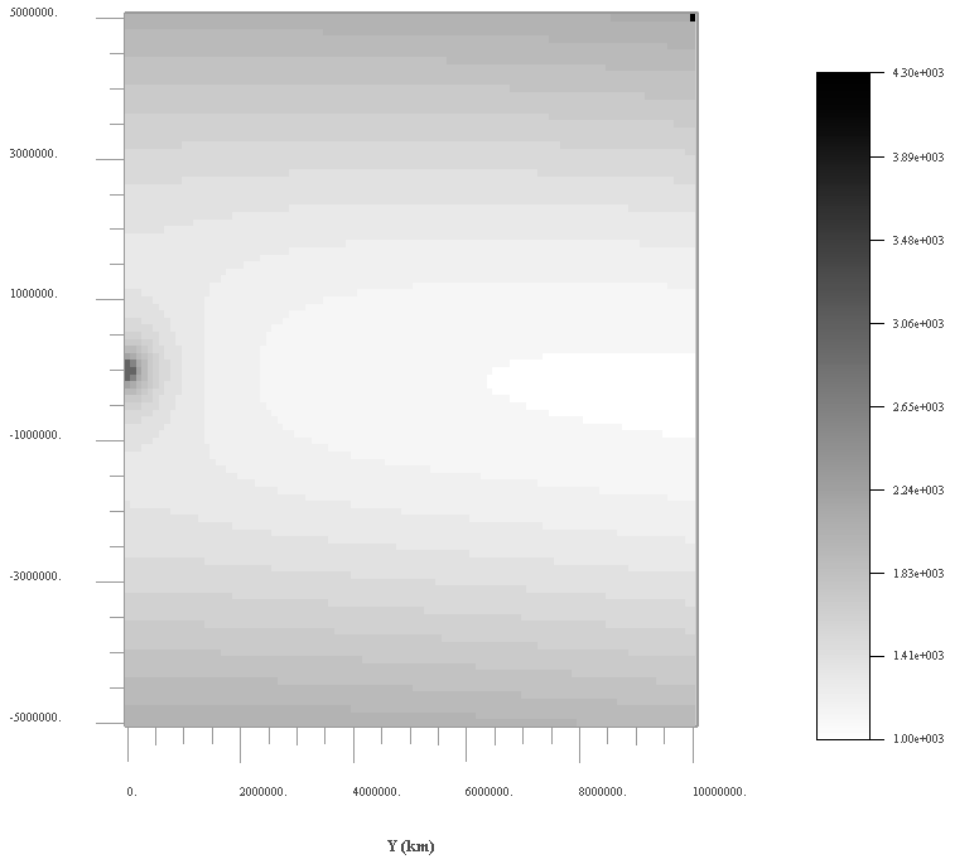

Figure 4.8.17. Variation in rotating frame relative velocity with X and Y displacement in the Earth–Sun system for the case of the incremented Jacobi constant.

frame whose axes directions are inertially fixed (i.e., non-rotating). The preceding analysis gives no information on the rotating frame relative velocity direction, only its magnitude.

The planet relative velocity is obtained by a vector velocity addition, as shown in Figure 4.8.18. The velocity and the corresponding position may be converted into an energy relative to the planet or major body. In Figure 4.8.19, showing this energy, the limits of motion imposed by the surface of zero velocity are arbitrarily assigned a value at $-1e6$. It may be seen that in the vicinity of Earth the energy is negative but rises, reaching escape levels at greater distances from Earth. The plot assumes a rotating reference frame with X again in the Sun–Earth direction. The velocity in the rotating reference frame is assumed to be radial at all points, so defining the planet relative velocity.

This energy value may in turn be converted into an excess hyperbolic speed. In the following plots a zero value is used where the energy remains negative (Earth-

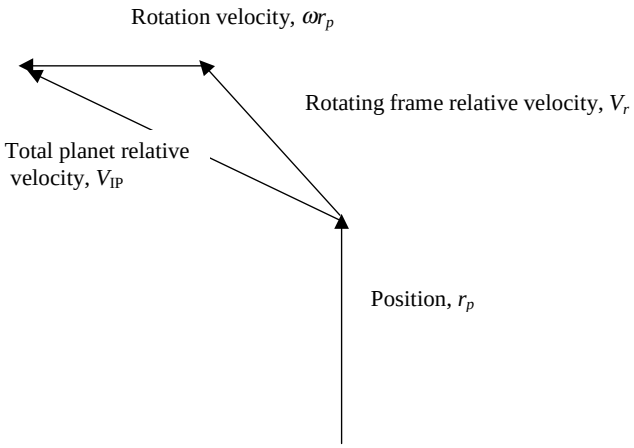

Figure 4.8.18. Planet relative velocity.

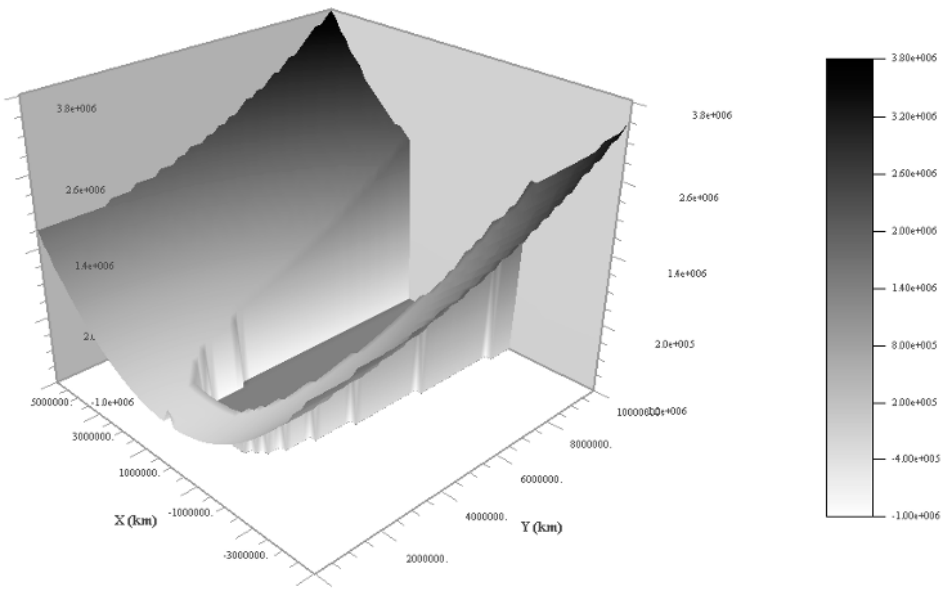

Figure 4.8.19. Variation in Earth relative energy (using rotating frame radial velocity vector direction assumption and reference Jacobi constant value) with rotating frame X and Y displacement.

bound). In these plots the central 'forbidden' zone excluded by the zero-velocity surface is also assigned a zero value.

As examples of some of the possibilities, three cases can be considered to illustrate the energies that are achievable with a given magnitude of Jacobi constant. The first case of Jacobi constant (Figure 4.8.16, the reference value), is used as the basis. The first illustration in Figure 4.8.20 assumes that the velocity with

respect to the rotating frame is always radial. A vector addition of the rotating frame velocity yields the total velocity. The figure therefore shows the variations in energy if the spacecraft were able to maintain such a constant velocity direction in the rotating frame. However, this is clearly not possible, as any spacecraft will experience a continuous variation in the velocity vector direction. The figure therefore provides an indication of the possible variations in energy for a given Jacobi constant, but needs to be considered in conjunction with other admissible velocity vector directions to explore the full range of possibilities regarding energy evolution.

The second illustration in Figure 4.8.20 assumes that the velocity with respect to the rotating frame is in a prograde direction, perpendicular to the radial position vector. Once again a vector addition of the rotating frame velocity yields the total velocity. The third illustration in Figure 4.8.20 assumes that the velocity with respect to the rotating frame is in a retrograde direction, again perpendicular to the radial position vector. These three options span the range of possibilities for the energy at a given location. Prograde and retrograde directions for the rotating frame relative velocity direction yield the maximum and minimum energy.

The energy contours show that at radial distances beyond the Lagrange point distances (1.5 million km) the velocity in the X direction at a given radius is significantly greater than that in the Y direction. The prograde case yields greater velocities at a given XY location, as expected. This set of figures illustrates the total extent of the variation in energy that is possible. Even in the worst-case (i.e., minimum energy) velocity vector direction a transition from bound to escape orbit is achieved with this value of Jacobi constant.

The details of spacecraft trajectory evolution depend on its initial state with respect to the planet and the central body. These initial values will result in a trajectory in the XY plane, and will also provide a given direction of the velocity with respect to the rotating frame at each XY location.

These analyses show that there are significant variations in energy with respect to the major body that are possible for the same value of Jacobi constant. They also indicate that if suitable trajectories can be devised, then there is a possibility for a spacecraft to acquire significant gains in energy with respect to the major body as it moves away from that body. Examples of trajectories that achieve such energy changes are given in the subsequent section.

A qualitative analysis therefore demonstrates the possibilities for the phenomenon of escape or capture at a planet via multi-body gravity perturbations.

Analysis of gravity-assisted escape

When previously discussing the departure of a spacecraft from a planet on a direct escape trajectory, the evolution of the planet relative velocity vector was considered. This enables a comparison of the achieved heliocentric orbit with the predicted orbit by using the osculating excess hyperbolic speed at the pericentre of the departure orbit. This same analysis may be repeated with regard to gravitational escape, but with certain modifications. The following discussion is a qualitative analysis with the objective of identifying the key features that contribute to energy change.

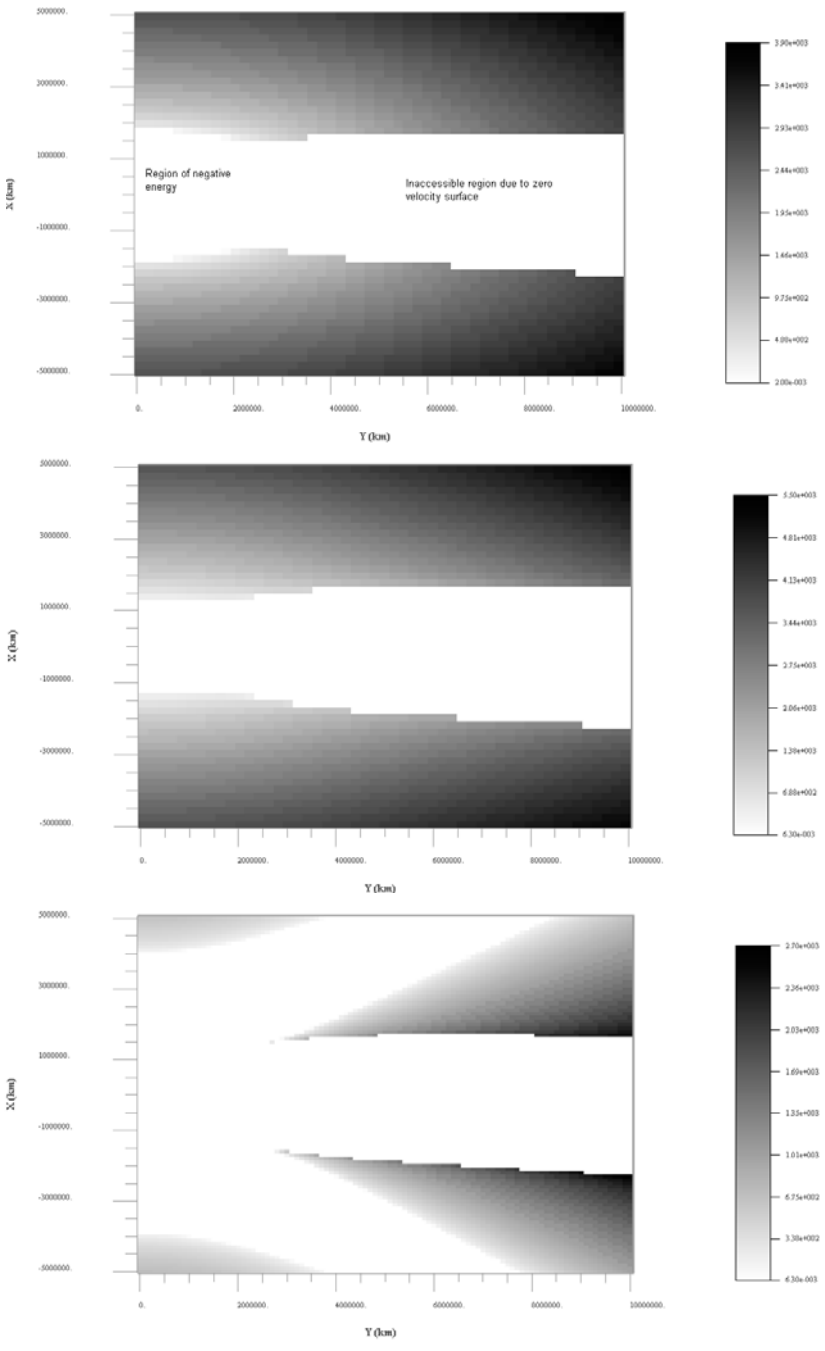

Figure 4.8.20. Variation in Earth relative energy using radial (top) and prograde (middle) and retrograde (bottom) rotating frame velocity vector directions, with X and Y rotating frame displacement and reference Jacobi constant value.

In the case of gravitational escape, then when at the initial pericentre, the spacecraft is in an osculating bound orbit, and there is no directly predicted excess hyperbolic speed, as in a standard escape scenario. However, an analysis may be made regarding the mechanism of the energy increase that may eventually lead to escape.

The gravitational escape trajectory has previously been described as a variation on a transfer orbit from the planet to an orbit about its Lagrange point. The key feature of such a gravitational escape trajectory lies in the solar gravity perturbation of the spacecraft orbit as the spacecraft transfers towards the vicinity of the L1 or L2 Lagrange points.

The initial orbit for this type of escape will initially be a highly elliptical orbit, ideally with a low pericentre. This allows an efficient injection into this orbit directly from a standard launch vehicle. If the apocentre lies beyond the sphere of influence of the planet, it will traverse a domain where solar gravity perturbations have an effect on the orbit that is comparable with the planet's gravity field. During this perturbation period, the spacecraft orbit parameters may be strongly modified due to the effects of the gravity perturbation. The same perturbation will not occur for any initial high-apocentre orbit. The location of the apocentre with respect to the Sun's direction must be such that the effects of solar gravity perturbations strongly influence the orbit. Strong perturbations are found for the 'free injection' class of trajectory in reaching orbits about the Lagrange points, described previously, and also for a range of neighbouring trajectories that do not result in free injection to orbits at the Lagrange points.

Eventually, as the spacecraft gains energy, it may become feasible for the spacecraft to escape from the initial bound planet orbit. It then passes outside of the region of influence of the planet's gravity field, and its motion becomes dominated by solar gravity. If enough energy is gained, the spacecraft enters a heliocentric orbit free from the planet's gravity.

It is possible to perform some qualitative analyses regarding the mechanisms for spacecraft energy increase. The key issue is to examine the energy of the spacecraft as it becomes free of the planet's gravitational influence and enters the domain of the central body. The equivalent excess hyperbolic speed can then be evaluated. The effects of the central body disturbances on the trajectory apply strongly over a range of radial distances, and so the spacecraft state should be assessed when at typically 2–3 times the Lagrange point distance. At this point the state relative to the central body will reveal the equivalent excess hyperbolic speed with which the spacecraft may be said to have departed the planet.

The prediction of the planet relative speed from the conservation of the Jacobi constant was determined in Section 4.2 as:

$$V_p^2 = V_{\infty 0}^2 - 2\underline{\omega}\cdot\underline{h_{p0}} + 2\left(\frac{\mu_c}{r_c} - \frac{\mu_c}{r_{planet}}\right) + 2\underline{\omega}\cdot\underline{h_p} + 2\left(\frac{\mu_p}{r_p}\right)$$

where in this case $V_{\infty 0}$ is the initial osculating excess hyperbolic speed at the initial

pericentre (assumed to lie close to the planet). However, this initial orbit is bound and so no initial escape condition exists. The excess hyperbolic speed term can therefore be replaced by an initial energy term, $2E_0$.

In the above V_p is the speed relative to the planet in an inertially oriented reference frame, h_p is the angular momentum per unit mass (also the subscript 0 denoting the initial value at planet pericentre), r_p is the position relative to the planet, μ_c and μ_p are the gravitational constants for the central body and planet, and ω is the angular velocity of the planet's orbit about the central body.

The energy relative to the major body or planet, evaluated at some later stage in the trajectory after leaving the initial pericentre, is given (using substitutions defined in Section 4.2) by:

$$V_{\infty L0}^2 = 2E_{pL0} = 2E_0 - 2\underline{\omega}\cdot\underline{h_{p0}} + 2(\underline{\omega}\cdot\underline{h_{pL0}}) - \omega^2(r_{PL0}^2) + 3\omega^2(\hat{r}_{planetL0}\cdot\underline{r_{pL0}})^2 \tag{4.8.46}$$

where the subscript $L0$ indicates a state evaluated at a time of passage close to the Lagrange point, assuming that an escape energy is reached at this point. In some situations this may not be the case. Assuming that escape does occur then a later point in the trajectory must be used such that the excess hyperbolic speed becomes real. This expression does not allow a value to be calculated for the escape energy that may be achieved, as the selection of the reference point is not well defined. It does, however, show the dependence of the energy on the evolution of the orbit and so offers an insight into the nature of trajectories that are effective in achieving such an escape.

One of the key terms in equation 4.8.46 in achieving energy gain is the angular momentum. Initially the planet relative energy was negative, but to achieve a positive value for escape, the angular momentum must generally increase. The potential for such an increase can be assessed qualitatively. The rate of change of angular momentum was obtained previously as:

$$\frac{d\underline{h_p}}{dt} = \underline{r_p} \wedge \frac{d\underline{V_p}}{dt} = \frac{-\mu_c}{r_{planet}^3}\left(\left(-3\frac{\underline{r_{planet}}\cdot\underline{r_p}}{r_{planet}^2} - \frac{3}{2}\frac{r_p^2}{r_{planet}^2} + \frac{15}{2}\left(\frac{\underline{r_{planet}}\cdot\underline{r_p}}{r_{planet}^2}\right)^2 + 0\left(\frac{r_p}{r_{planet}}\right)^3\right)\underline{r_p} \wedge \underline{r_{planet}}\right)$$

Then, taking only the dominant term (neglecting terms in r_p^2/r_{planet}^2), this rate becomes:

$$\frac{d\underline{h_p}}{dt} = \frac{\mu_c}{r_{planet}^3}\left(-3\frac{\underline{r_{planet}}\cdot\underline{r_p}}{r_{planet}^2}\right)\underline{r_{planet}} \wedge \underline{r_p} = \frac{-\mu_c}{r_{planet}^3}\frac{3}{2}r_p^2\sin 2\theta \tag{4.8.47}$$

where θ is the angle between the planet position vector and the position relative to the planet. Therefore, the rate is maximised at large r_p and an angle of 45°, reducing as the angle reaches 90°. Integration of this rate along the trajectory is required to obtain the angular momentum change. The spatial regions of a transfer trajectory to the Lagrange point orbit where this rate is highest are the approach phases to the orbit at the Lagrange point.

The second terms contributing to energy change are the radial position dependent terms. The first (in 4.8.36) results in an energy reduction with increasing distance, and the second is dependent on the relationship of the planet relative position vector with respect to the planet position vector. It is maximum when these are parallel or anti-parallel.

This term shows a different behaviour for trajectories that reach a gravitational escape than for those that follow a typical high-energy escape orbit. In this latter case the departure is relatively fast and the angular relationship between planet relative and planet positions does not show significant deviation when distant from pericentre, as the spacecraft escapes the planet's gravitational influence. However, in the classes of trajectories where gravitational escape is achieved, the motion is much slower and the planet relative position vector experiences a significant series of changes in direction. The increase in energy will be maximised when a near radial (or anti-radial) escape passage can be achieved. However, the motion in a classical, higher energy escape orbit in a radial direction also experiences this planet relative energy change due to radial position. Such an escape direction does not by itself result in a significant increase in escape energy. Therefore, the phenomenon of the energy gain in a gravitational escape is primarily related to the combination of angular momentum gain and the position vector evolution.

Designing a gravity-assisted escape or capture

Previous parametric analyses regarding transfers to the Lagrange points (L1 or L2) from initially high elliptical orbits have shown that many of the generated transfers do not enter free injection orbits about the Lagrange points. Some of these return to the planet, and others pass beyond the Lagrange point and move into interplanetary space.

The characteristics of these orbits are such that they have a nominally low initial pericentre and a high apocentre, with a value close to that of the distance Lagrange point. When this is combined with a line of apses such that the spacecraft physically approaches the vicinity of the Lagrange point, the multiplicity of solutions described are encountered. Only small changes in the osculating ephemeris values at the initial pericentre are needed to generate radically different transfer trajectories, which obey the criteria, described in the previous section, for experiencing angular momentum gain.

Therefore, to generate an escape trajectory, shooting methods – such as those used to generate free injection transfer orbits about the Lagrange points – can be used. The key parameters are as follows:

Parameter	*Observations*
Apocentre	Close to or beyond the distance from planet to Lagrange point to enable trajectory perturbation by the central body.
Pericentre	Close to the planet to enable injection directly from a launcher parking orbit or intermediate transfer orbits. Higher pericentre can sometimes be considered, for special cases such as lunar gravity assist related transfers.
Longitude/right ascension of pericentre	Determined by right ascension of ascending node, inclination and argument of pericentre. Should be such as to allow the apocentre passage to pass sufficiently close to the vicinity of free injection orbit transfers about the Lagrange points.
Declination of pericentre	Generally close to ecliptic to ensure that trajectory at apocentre passes sufficiently close to the vicinity of free injection orbits about the Lagrange points. Determined by inclination and argument of pericentre.
Inclination	Often constrained by the launcher under consideration.

If a given apocentre is chosen, of sufficient attitude, then varying the longitude of the pericentre allows a range of escape orbits to be generated, with different degrees of escape energy. This latter quantity is measured effectively by the orbit ephemeris relative to the central body, the spacecraft having left the gravitational influence of the planet. Therefore, a direction for the initial perigee may be found that maximises this energy.

By increasing the apocentre, the maximum energy obtainable may increase, although the apocentre increase is limited if trajectories are to be generated that maintain the characteristic of a passage that moves slowly through the vicinity of an orbit about the Lagrange point. The difference in the initial perigee speed to effect large changes in apogee are only a few metres per second, because the orbit is relatively close to a parabolic orbit state.

The near-infinite number of escape possibilities, due to variations in apocentre altitude and longitude of the line of apses means that the possibility exists for a number of locally minimum solutions that maximise the departure energy.

The options described above have focused on cases where the spacecraft makes a single pass close to a Lagrange point orbit. However, more complex trajectories are possible when the spacecraft makes more than one revolution in this region, or even traverses from the vicinity of one Lagrange point to the other (L1 to L2), and ultimately escapes after passing by the second point. However, an important consideration of such transfers is the additional time that is taken. The spacecraft is relatively slow-moving when traversing these regions (the period of an orbit about a co-linear Lagrange point is close to half of the orbital period of the planet). Therefore, even the use of a single pass adds considerable extra time to the escape process. Multiple revolutions could lead to extremely long transfer durations (especially when such manoeuvres are considered at the outer planets).

Currently, considerable research is taking place in this area (see references for

this chapter particularly Lo *et al.*) to attempt to classify the possible motions in this complex domain and to seek ways to exploit the full potential of this type of motion.

The idealised problem of Earth escape

After the previous discussions regarding the potential for gravitationally assisted planetary escape (or capture), an example is now considered in detail. This concerns an escape from Earth. To ensure conservation of the Jacobi constant, the Earth's orbital eccentricity is set to zero in this example, although in practice, similar effects are also found for the true Earth orbit case.

The initial orbit is: perigee, 500 km; apogee, 3.2 million km; inclination (with respect to the ecliptic. 0°; line of apses, optimised). The escape is generated by starting at perigee of an initially (osculating) high-apogee orbit. The direction of the line of apses is optimised to generate the greatest possible change in heliocentric energy (with respect to Earth's orbit) after escape from Earth.

Figures 4.8.21, 4.8.22 and 4.8.23 show such an example. The motion is plotted both in an Earth–Sun rotating reference frame and an Earth-centred inertial frame. The spacecraft eventually passes close to the L1 Lagrange point before escaping from Earth. It can be seen that this passage close to the Lagrange point lies close to a new raised perigee of a modified Earth-relative orbit.

The changing energy can be compared with the prediction previously obtained:

$$2E_p = 2E_0 - 2\underline{\omega}\cdot\underline{h_{p_0}} + 2(\underline{\omega}\cdot\underline{h_p}) - \omega^2(r_P^2) + 3\omega^2(\hat{r}_{planet}\cdot\underline{r_p})^2$$

where E_p is the orbital energy relative to Earth.

The energy plot (Figure 4.8.22) of predicted and actual energy shows that good agreement is obtained over this range of distances from Earth. The modified excess hyperbolic speed at the raised perigee can therefore be obtained from this previous term (or from the usual expressions for orbital energy depending on current velocity and position) and is approximately 450 m/s.

The sharp increase in the angular momentum term (Figure 4.8.23) occurs as the spacecraft moves first to the apocentre and then remains approximately constant over a radial distance of several million km. The energy has not increased significantly by the time the spacecraft reaches apocentre, but increases and becomes positive as the spacecraft descends to a new, raised pericentre close to the Lagrange point radius. The mechanism for the energy increase after apoocentre now arises from the two radial dependent energy terms: one increases energy because the radius is reduced, and the other increases energy because the position becomes close to parallel with the planet position vector.

The initial Earth bound orbit considered here has a semi-major axis of 1.8 million km and perigee at 500 km altitude. It is therefore a feasible initial injection orbit, in terms of being able to be reached efficiently from an initial launch from Earth, where the initial perigee is typically several hundreds of km, depending on the launcher.

The spacecraft reaches an Earth escape orbit as a result of the gravitational perturbation when moving in the vicinity of the Earth–Sun L1 point. The effect of

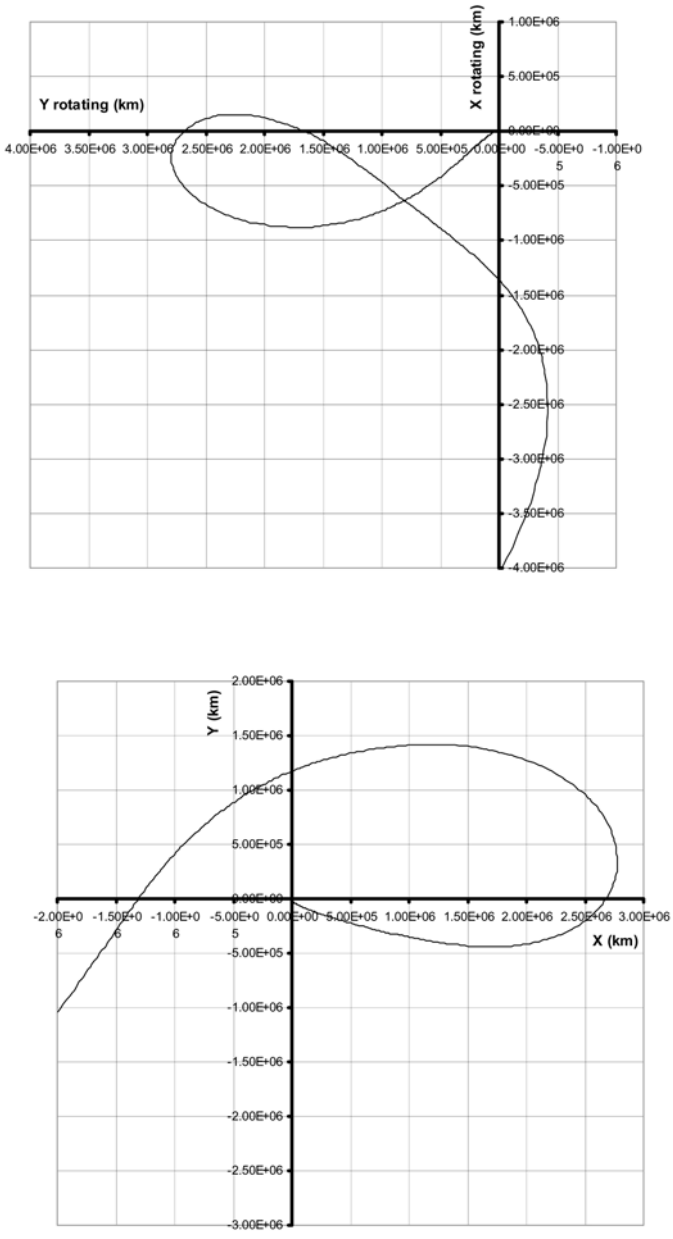

Figure 4.8.21. Escape from an initial Earth-bound orbit with a semi-major axis of 1.8 million km, using gravitational assistance. In the upper figure, motion is in the Earth–Sun rotating reference frame. X lies in the Sun-to-Earth direction, and Y is the perpendicular in the ecliptic. The Earth–Sun L1 Lagrange point lies at $X = -1.5$ million km. In the lower figure, motion is in the Earth centred inertial frame. X and Y are in the ecliptic, and X is defined by first point of Aries.

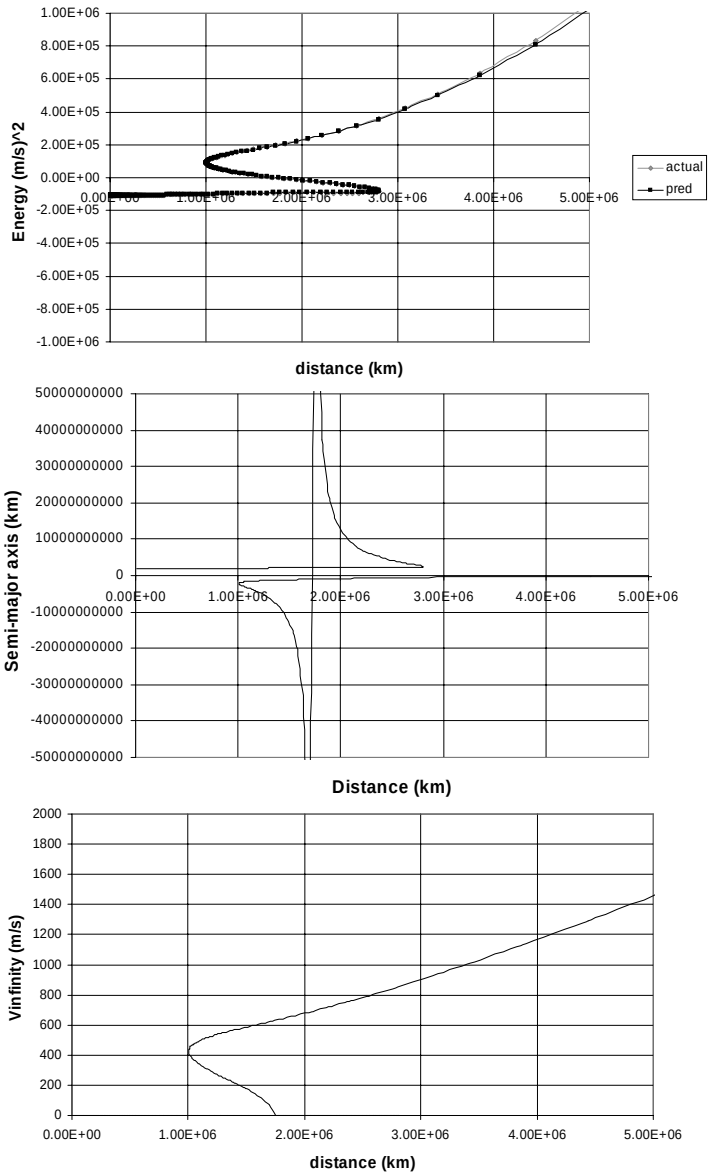

Figure 4.8.22. Evolution of Earth relative semi-major axis and energy from initial bound orbit to escape. In the upper figure, as the spacecraft first moves to apogee and then returns to a modified, high Earth perigee, the solar gravity perturbation increases the orbital energy. The energy becomes positive, in this case, at approximately 1.7 million km from Earth. The actual energy and that predicted by approximation are compared in this plot. In the centre figure, the energy gain results in the semi-major axis asymptotically moving towards positive and negative infinite values before reaching a finite negative value. In the lower figure, the Earth relative osculating excess hyperbolic speed achieves a real value as the Earth relative energy becomes positive.

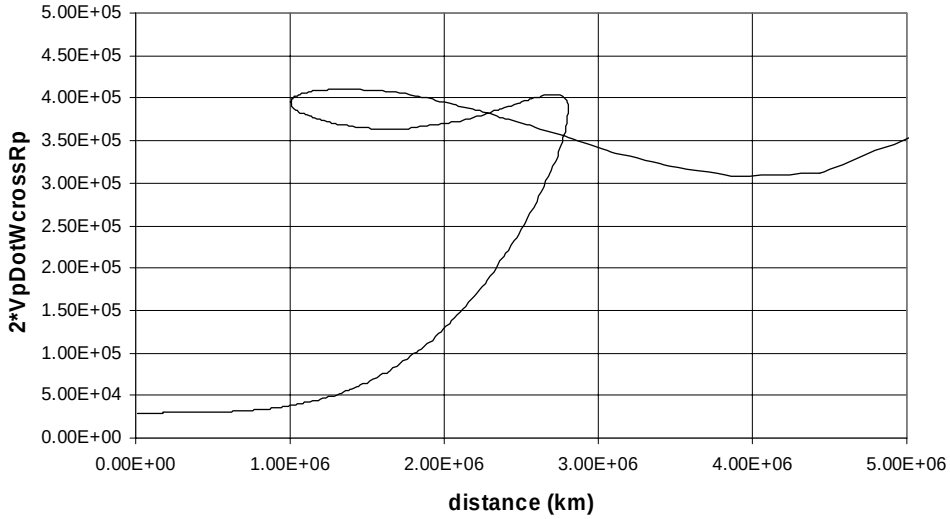

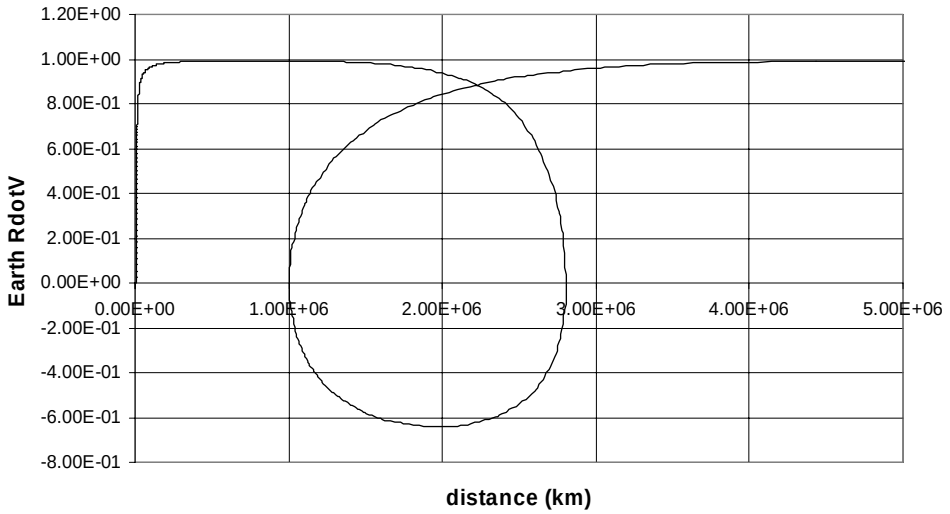

Figure 4.8.23. Evolution of angular momentum and position–velocity angle from the initial bound orbit to escape. The angular momentum (per unit mass) experiences a significant perturbation from the influence of solar gravity. The term plotted here in the upper figure is actually $2\underline{\omega}\cdot(\underline{h_p})$, and would be constant under the two-body Keplerian motion problem. However, as the spacecraft passes close to the Lagrange points a significant increase occurs. This may be contrasted with the conventional hyperbolic escape orbit in Section 4.2.1. The scalar product of Earth, relative position and velocity is shown in the lower figure. As the spacecraft departs perigee in its initially highly elliptical orbit, the directions of r_p and v_p converge. Then, as the spacecraft reaches apogee, r_p and v_p become perpendicular. The return to the new, raised perigee occurs at a radius of 1 million km, where position and velocity vectors again become perpendicular. After the final perigee, the directions converge as the spacecraft departs in a hyperbolic orbit.

this orbital energy on the heliocentric motion must be considered. The escape, in this case takes, place after a passage close to the L1 Lagrange point, and the subsequent heliocentric orbit moves inwards towards the Sun.

Two key parameters of the heliocentric motion are the semi-major axis (or energy) and the angular momentum. The latter term determines the eccentricity and thus the perihelion that may be achieved. The values achieved in this example, when far removed from Earth's sphere of influence, are:

Semi-major axis:	1.402E + 8 km
Eccentricity:	5.596E-02
Aphelion:	1.480E + 8 km
Perihelion:	1.323E + 8 km

The aphelion lies slightly below Earth radius at 1 AU. The most significant effect is the perihelion reduction. The excess hyperbolic speed relative to Earth to reach such a perihelion would be 928 m/s. This impulsive calculation is made for leaving Earth orbital radius directly and reaching the above perihelion. This is considerably higher than the value identified at the raised perigee, but the fact the perigee itself is at nearly 1 million km from Earth (towards the Sun), and that further perturbations apply as the spacecraft leaves the vicinity of the Lagrange point, means that this perigee value of excess speed underestimates the eventual performance.

Figure 4.8.24 shows the evolution of heliocentric semi-major axis and angular momentum as the spacecraft leaves Earth. The heliocentric energy and thus semi-major axis initially show a significant variation as the spacecraft moves from perigee due to its absolute velocity reduction when climbing the Earth's gravity potential. This is a typical feature of any Earth bound orbit.

Reduced energy case

The sensitivity of such an Earth escape to the initial orbit apogee can also be observed. Such a lower energy example is considered (Figure 4.8.25). The initial semi-major axis is now 1 million km and apogee approximately 2 million km. The direction of the line of apses is again rotated to maximise the change in heliocentric orbital energy after escape.

However, although the Earth orbital energy is much lower in this case, the actual manoeuvre ΔV that must be applied at perigee to reach the previous higher orbit is only 8 m/s.

As Earth orbit initial apogee is further reduced, a cut-off point exists where escape is no longer achieved. This occurs when the apogee falls significantly below the Lagrange points. For example, an apogee at 1 million km will not achieve escape. Intermediate values show a high sensitivity of the final orbit to small changes in apogee.

The case of a neighbouring bound Lissajous orbit

The escape orbit described in the previous sections can now be compared with a neighbouring manifold of the three-body problem. Previous discussions have

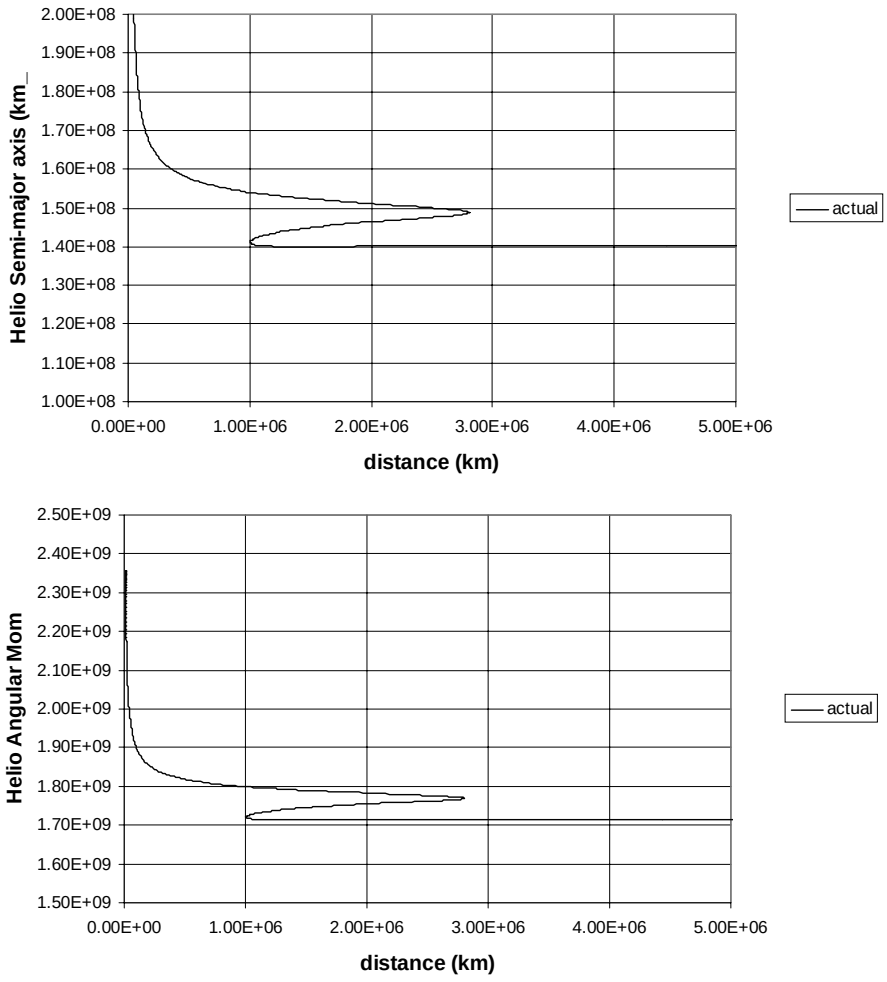

Figure 4.8.24. Evolution of Sun-relative semi-major axis and angular momentum from initial Earth bound orbit to escape. In the upper figure, as the spacecraft passes through apogee and returns towards Earth the heliocentric energy continues to reduce. After the new perigee is passed (at approximately 1 million km) the heliocentric energy reaches a near-constant level. In the lower figure, the angular momentum follows a similar trend to the semi-major axis, almost reaching its asymptotic value as the spacecraft passes through its raised Earth perigee.

indicated the similarity between gravitational escape orbits and free injected transfers to orbits about the Lagrange points.

In this case (Figure 4.8.26), the same apogee and perigee as the previous escape example (osculating values at perigee) are used, but the right ascension (and the azimuth of the line of apses) is rotated by approximately 5°. This can be compared with the escape case in Figure 4.8.21.

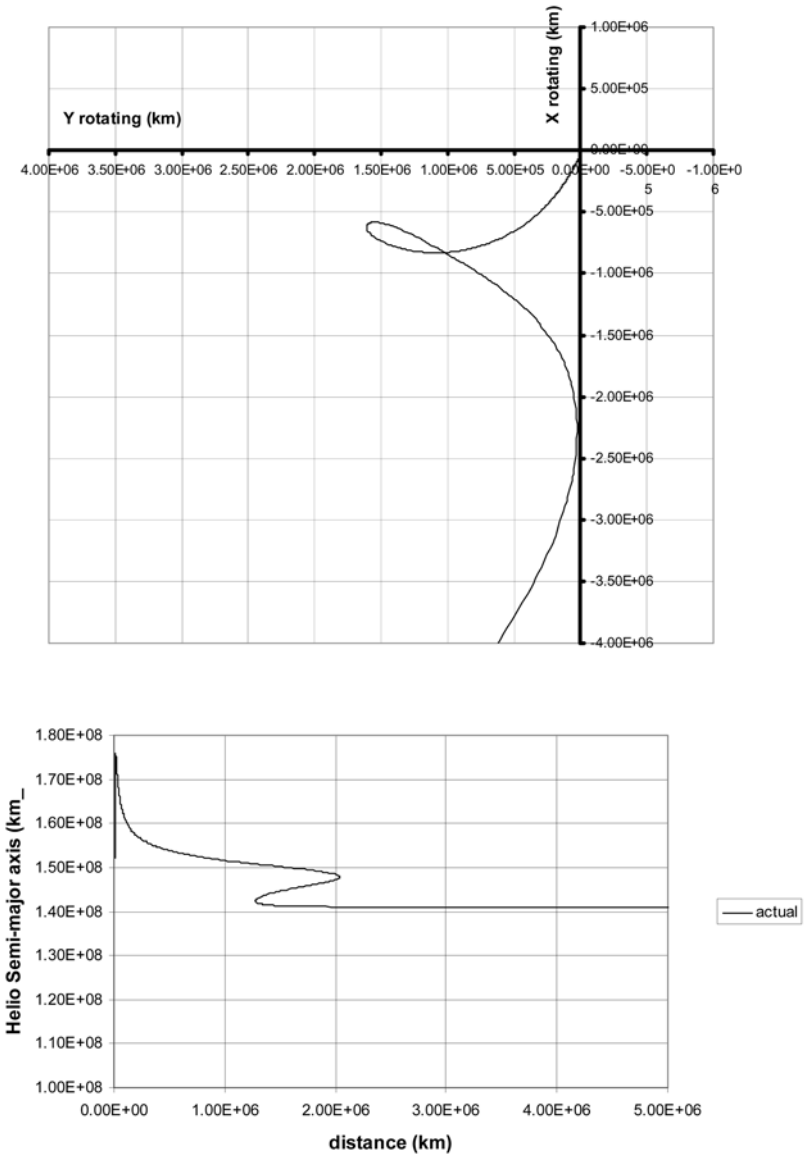

Figure 4.8.25. Escape from lower energy initial Earth bound orbit and evolution of Sun-relative semi-major axis. The upper figure shows motion in the Earth–Sun rotating reference frame. X lies in the Sun-to-Earth direction and Y is the perpendicular in the ecliptic. The Earth–Sun L1 Lagrange point lies at $X = -1.5$ million km. When compared with the previous example, it can be seen that the excursion in the 'Y' direction is reduced in this lower-energy case. The lower figure shows the achieved semi-major axis of 141 million km which results in perihelion at 134 million km. Therefore, a significant reduction in initial Earth orbital energy still leads to similar (although slightly less energy change) heliocentric orbits.

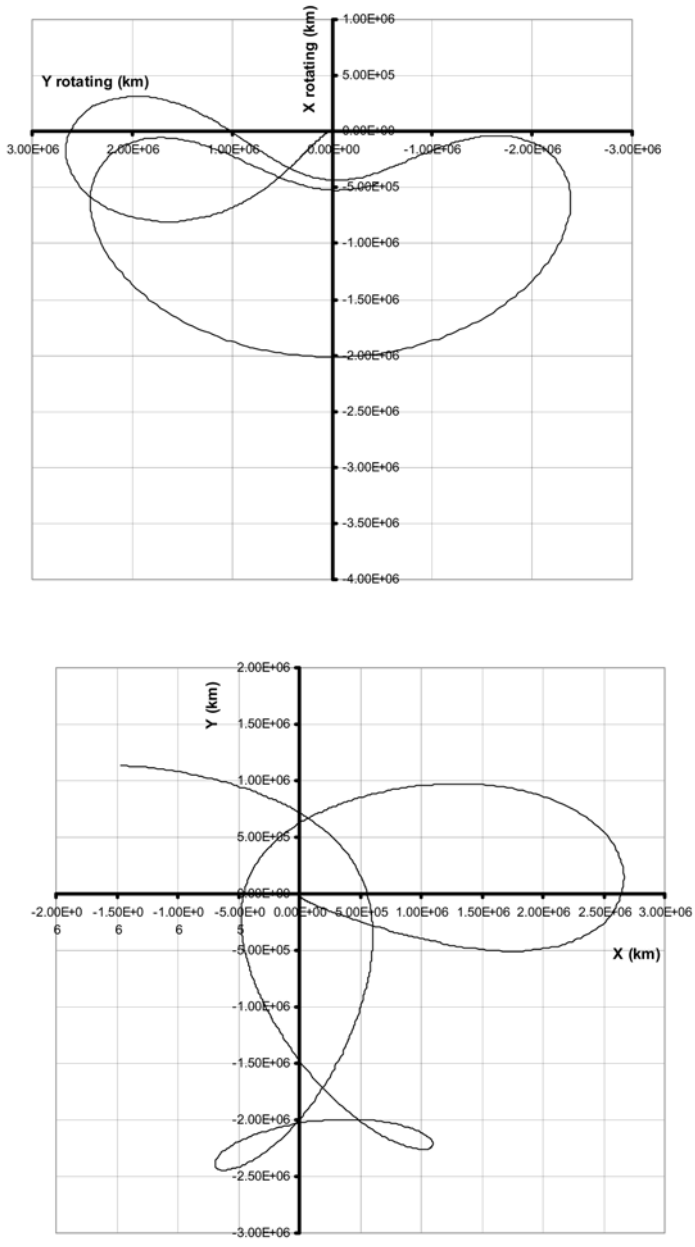

Figure 4.8.26. Transfer to a large-amplitude free injection Lissajous orbit from initial orbit with a semi-major axis of 1.8 million km. The upper figure shows motion in the Earth–Sun rotating reference frame. X lies in the Sun-to-Earth direction, and Y is the perpendicular in the ecliptic. The Earth–Sun L1 Lagrange point lies at $X = -1.5$ million km. The lower figure shows motion in an Earth-centred inertial frame. X and Y are in the ecliptic, and X is defined by the first point of Aries.

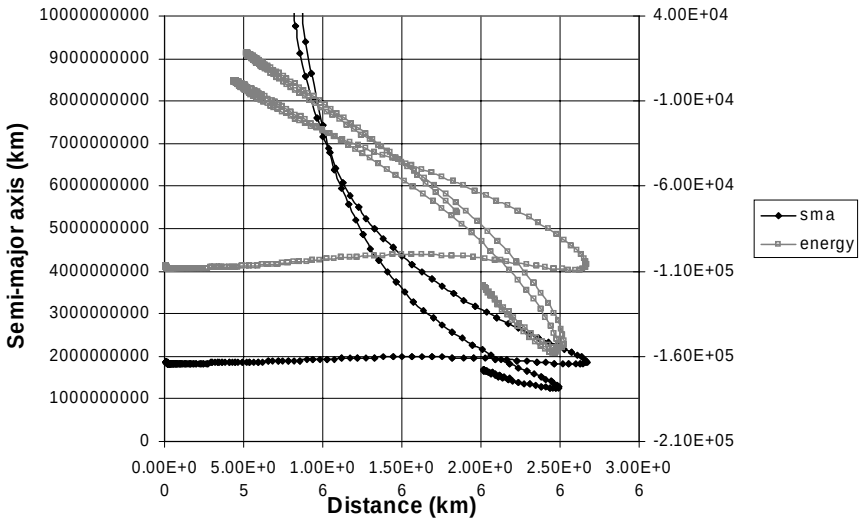

Figure 4.8.27. Evolution of energy and semi-major axis with distance from Earth, for a transfer to a large amplitude free injection Lissajous orbit. The semi-major axis is plotted against the vertical axis on the left, and the energy against the vertical axis on the right.

The resulting motion is a free injection into a large-amplitude Lissajous orbit about the L1 point. The initial evolution of the semi-major axis and Earth relative energy is qualitatively similar to the escape case (Figure 4.8.27). As the spacecraft first moves to apogee and then returns towards Earth, the solar gravity perturbation increases the orbital energy. As the spacecraft approaches the modified, raised Earth perigee, the orbital energy becomes positive. This is achieved at a distance from Earth of approximately 500,000 km. The Earth relative energy then returns to a negative value as the spacecraft moves away from its raised perigee and back towards the modified apogee at over 2.5 million km.

The evolution of the heliocentric energy and angular momentum also follows a similar initial trend as the escape case (Figure 4.8.28). As the spacecraft passes through apogee and returns towards Earth the heliocentric energy (and hence semi-major axis) continues to reduce and reaches a minimum as the new, raised perigee is reached.

The idealised problem of Jupiter escape

Jupiter has the strongest gravity field in the Solar System, after that of the Sun. Therefore, an example of escape from Jupiter is an interesting case to study. The initial Jupiter bound orbit considered here has a semi-major axis of 25 million km and perigee at 1.1 million km altitude. This could be typical of an orbit with pericentre above the radiation belts.

The initial orbit parameters are: pericentre, 1.1 million km; apocentre, 49 million km; line of apses, optimised. The direction of the line of apses is optimised to generate the greatest possible change in heliocentric energy after escape from Jupiter.

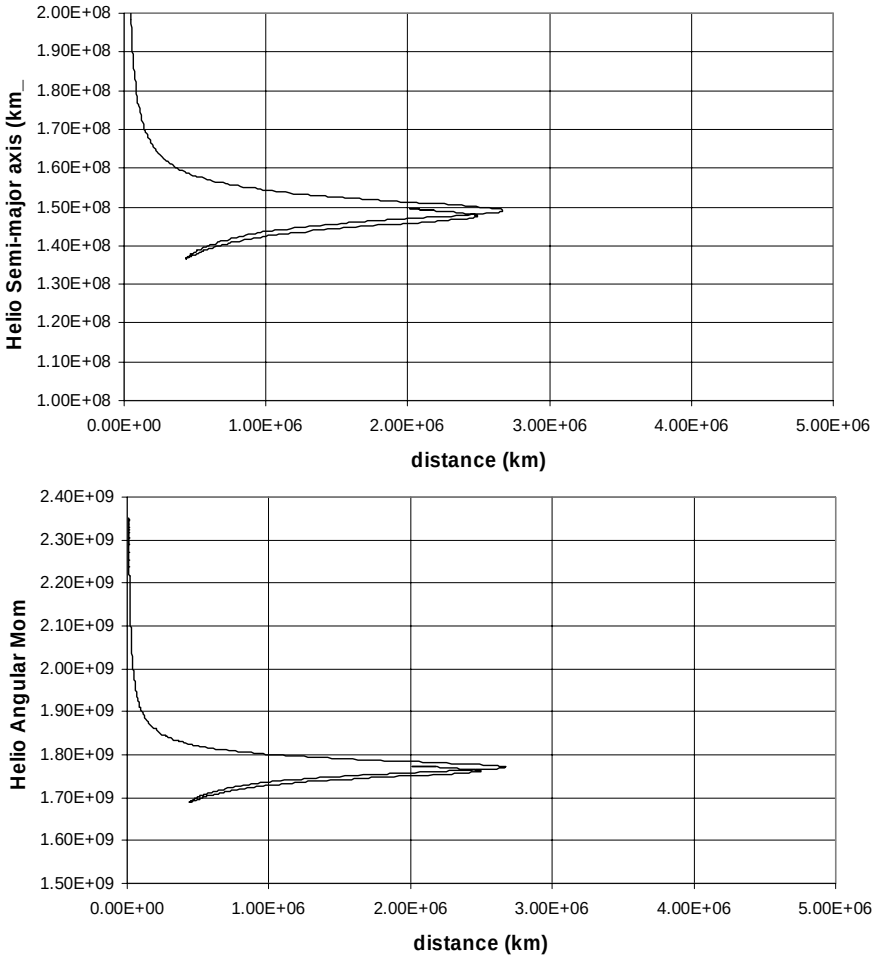

Figure 4.8.28. Evolution of Sun relative semi-major axis and angular momentum from initial perigee to free injection orbit. In contrast with the escape case, the energy rises as the spacecraft moves away from its new, raised perigee back towards apogee. This is because the planet position becomes non-aligned with the planet position vector as it proceeds through the Lissajous orbit. In the lower figure, the angular momentum follows a similar trend to the semi-major axis, reaching its minimum value as the spacecraft passes through its raised Earth perigee.

Figures 4.8.29 and 4.8.30 show an example of gravity-assisted escape from Jupiter. The motion is plotted both in a Jupiter–Sun rotating reference frame and a Jupiter-centred inertial frame. The evolution of energy and semi-major axis are shown in Figure 4.8.30.

After the first apocentre, pericentre is raised significantly by solar gravity perturbation, to approximately 47 million km. The solar gravity perturbation increases

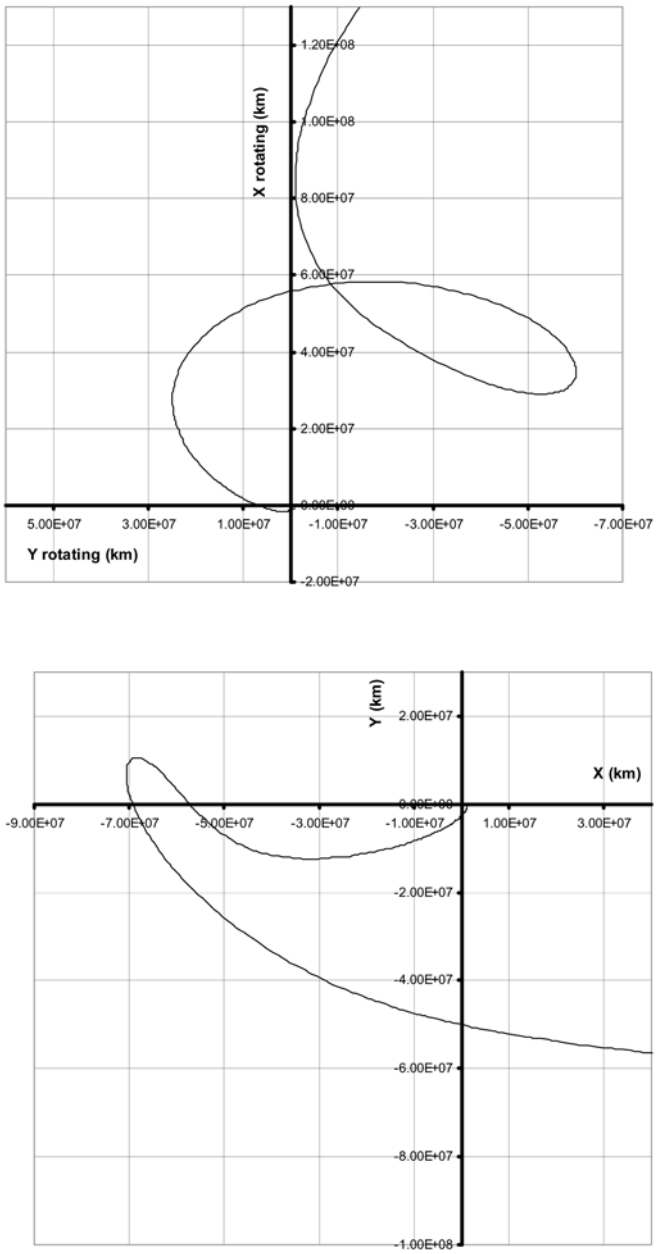

Figure 4.8.29. Escape from an initial Jupiter-bound orbit with semi-major axis of 25 million km, using gravitational assistance. The upper figures shows motion seen in Jupiter–Sun rotating reference frame. X lies in the Sun-to-Jupiter direction, and Y is the perpendicular in the ecliptic. The Jupiter–Sun L2 Lagrange point lies at $X = 50$ million km. The lower figure shows motion in the Jupiter-centred inertial frame. X and Y are in the ecliptic, and X is defined by first point of Aries.

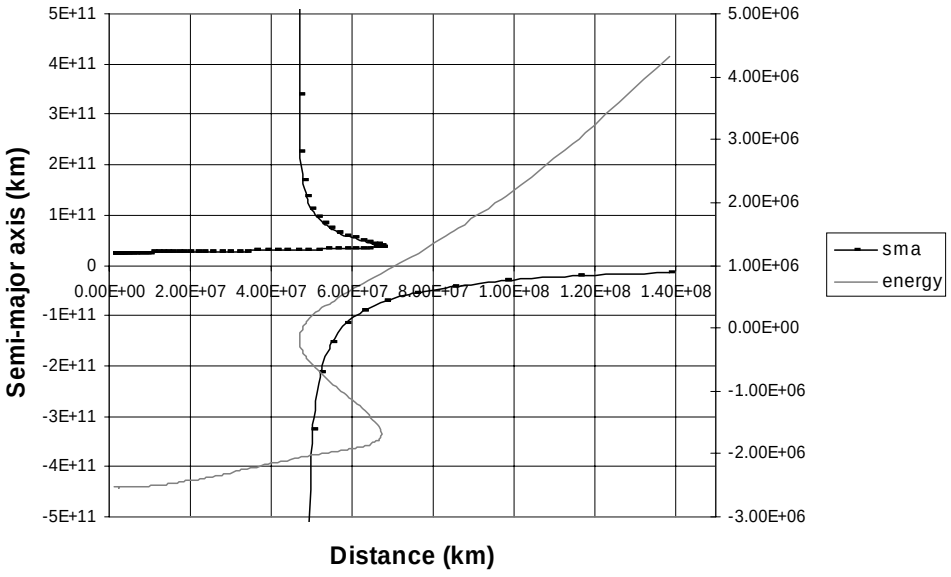

Figure 4.8.30. Evolution of Jupiter relative semi-major axis and energy from initial bound orbit to escape. The energy becomes positive at approximately 49 million km from Jupiter. The semi-major axis is plotted against the vertical axis on the left, and the energy against the vertical axis on the right.

the orbital energy with respect to Jupiter, as the spacecraft moves to apocentre and a further increase on descending to the modified, raised pericentre.

The initial orbit here is similar in nature to that considered in the Earth escape example. Apocentre is at or above the Lagrange point. One difference is that in this case a second type of transfer route is used (Section 4.8.4, Figure 4.8.13)

The spacecraft reaches a Jupiter escape orbit as a result of the gravitational perturbation when moving in the vicinity of the Jupiter–Sun L2 Lagrange point. The escape in this case takes place near the L2 Lagrange point and the subsequent heliocentric orbit moves away from the Sun.

The heliocentric orbit values achieved in this example, when far removed from Jupiter's sphere of influence, are:

Semi-major axis	1.394E + 9 km
Eccentricity	3.878E-01
Aphelion	1.934E + 9 km
Perihelion	8.534E + 8 km

The perihelion lies above Jupiter's orbital radius at 7.785E + 8 km. The most significant effect is the aphelion increase. The excess hyperbolic speed relative to Jupiter that is needed to reach such a aphelion would be 2,530 m/s.

Figure 4.8.31 shows the evolution of heliocentric semi-major axis and angular momentum as the spacecraft leaves Jupiter. As in the Earth escape case, the helio-

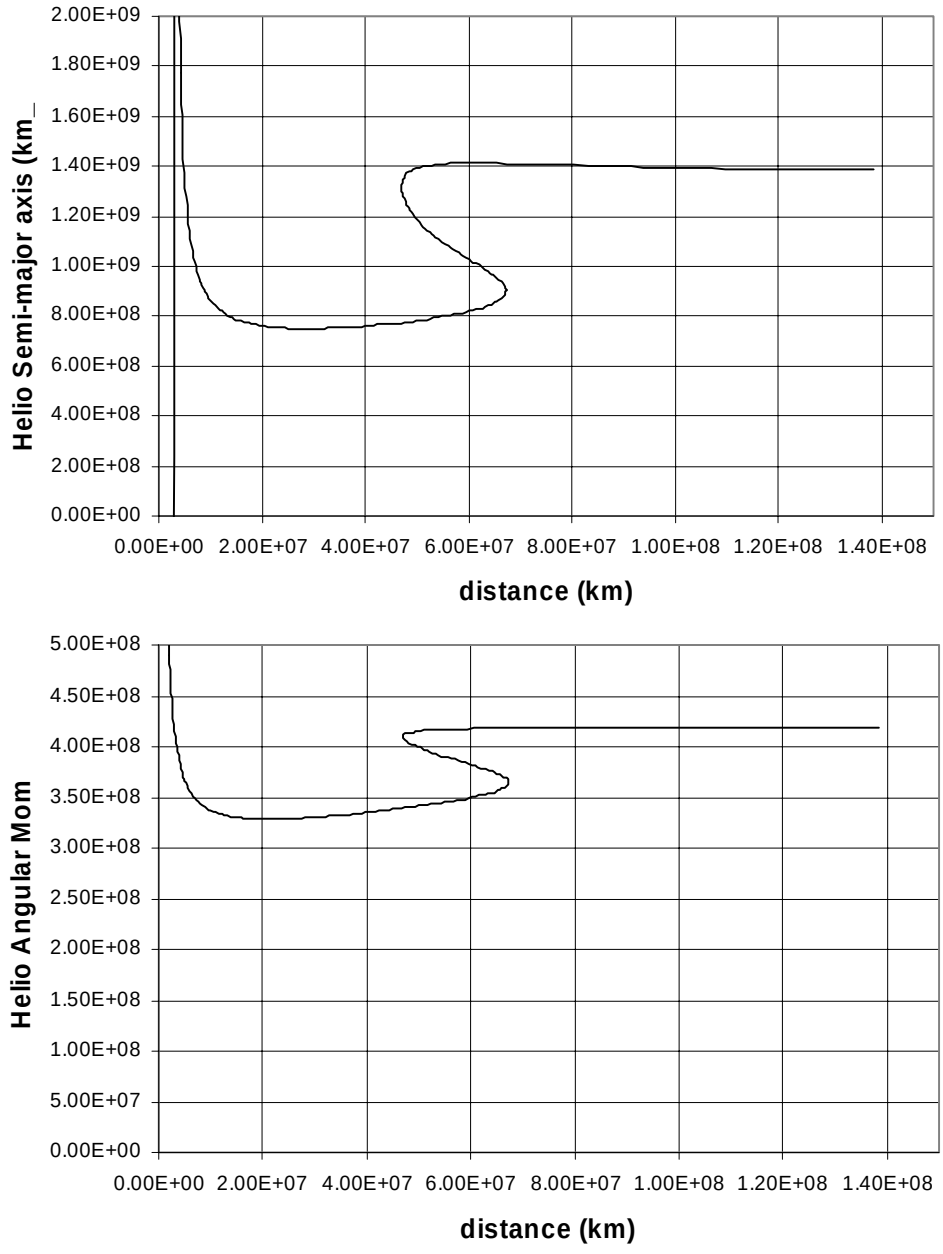

Figure 4.8.31. Evolution of Sun relative semi-major axis and angular momentum from initial Jupiter bound orbit to escape. In the upper figure, after the new pericentre is passed (at approximately 47 million km) the heliocentric energy reaches a near-constant level. This can be compared with Jupiter's semi-major axis at approximately 7.78e8 km. In the lower figure, the angular momentum follows a similar trend to the semi-major axis, almost reaching its asymptotic value as the spacecraft passes through its raised Jupiter pericentre.

centric energy and semi-major axis initially show a significant variation as the spacecraft moves from pericentre. Then, as the spacecraft passes through its initial apocentre and returns towards its raised pericentre the heliocentric energy increases.

This behaviour is a reverse of the Earth escape case, as here the spacecraft is escaping to an orbit with raised aphelion rather than lowered perihelion. Such an escape orbit is suitable to initiate a transfer to the outer planets.

4.8.6 Use of low thrust and gravitational escape

The previous examples have examined the use of gravitational perturbations to assist in escape. In the case of an escape from Earth it is necessary to reach an orbit with apogee at at least 1.2–1.5 million km (close to the Lagrange point). Such an apogee may be reached by direct injection from the launch vehicle or by apogee raising. This second strategy, when executed with a high-thrust chemical system, eventually results in a transfer that is eventually (after a final apogee raising manoeuvre) similar to the direct injection case.

Alternatively, the transfer may be executed with a low-thrust system after injection to a lower-apogee orbit. There will be a transfer duration penalty in achieving such a sequence, but if time constraints are not paramount, then such a strategy is potentially attractive. It could of course be reversed at the target planet.

A strategy is considered that is similar to that discussed in Section 4.6.2, by

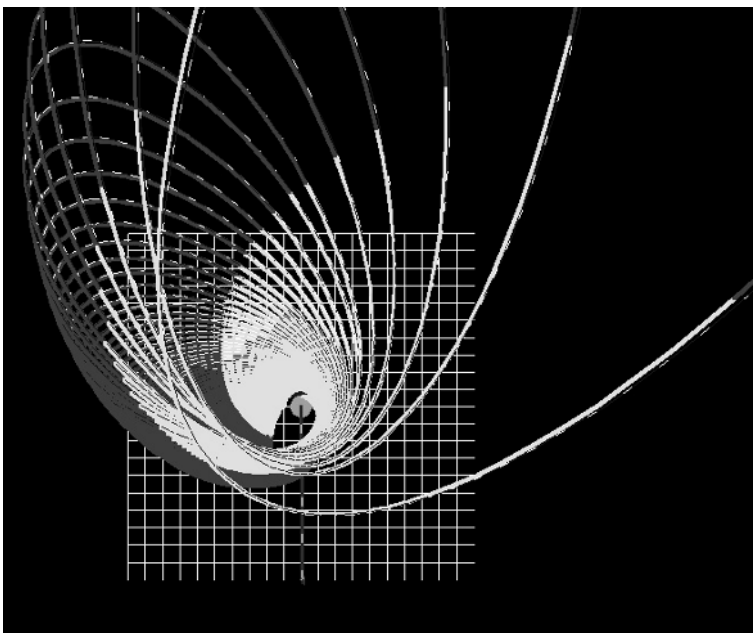

Figure 4.8.32. Using low-thrust apogee-raising for gravitational escape from initial GTO. The trajectory is seen in an Earth centred, rotating reference frame.

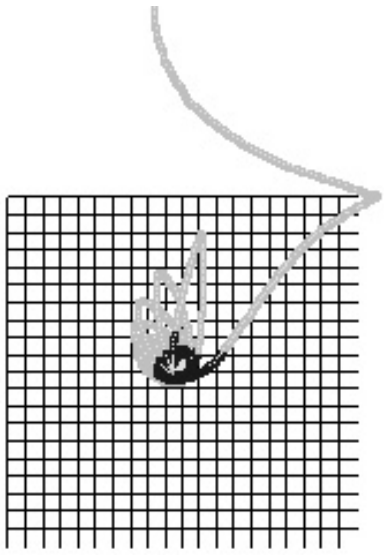

Figure 4.8.33. Gravitational escape after low-thrust apogee-raising. This figure shows the continuation of the previous trajectory, still seen in the same rotating reference frame. The grid is now 1 million km from centre to edge (a sub-grid of 100,000 km), and the thrust arcs are now the dark shaded regions of the trajectory, which passes close to the Earth–Sun Lagrange point and then escapes from Earth, as previously observed in the direct transfer examples.

which a series of alternating thrust and coast arcs is used. Each main thrust arc is an extended manoeuvre around pericentre, and small apocentre arcs may also be applied to increase efficiency by controlling the otherwise rising percentage.

The time taken to raise apogee to the required value will be less than that needed to reach an escape condition (perhaps 2/3 of the time). It will be slightly longer than the time to reach a lunar-crossing orbit, where a lunar gravity assist could be performed. Such a gravity assist would only result in a marginal escape, because the relative velocity at the Moon is reduced due to the raised perigee (that automatically results from such a low thrust transfer). The use of low thrust to reach the region of the Lagrange points also results in a raised perigee. However, this does not penalise the subsequent escape energy after the gravitational perturbation.

Figure 4.8.32 shows such a low-thrust transfer, in which the thrust arcs are the light shaded regions of the trajectory. The transfer is viewed in an Earth–Sun rotating reference frame, with L2 at the top of the figure. The inner grid is 100,000 km from centre to edge. An equivalent Earth escape V_∞ of 900–1000 m/s is achievable in this way.

4.8.7 Summary of gravitational escape and capture techniques

The previous analyses have shown the potential for the use of gravity perturbations to increase the energy of an initially bound orbit, to the extent that a spacecraft

passing along such a trajectory may escape from the planet with a moderate-energy departure orbit. Conversely, capture can occur in the reverse circumstance.

Examples at Earth have shown equivalent escape orbit excess hyperbolic speeds of typically 1 km/sec with a single pass in the vicinity of a Lagrange point. The time penalty is therefore approaching 180 days for such an escape, when compared with a more traditional route. Similar analyses performed at Jupiter show a greater equivalent escape excess hyperbolic speed of over 2.5 km/sec. Only single passes by the Lagrange points have been examined in detail, as these limit the duration spent in these regions to more practical levels for mission design. More complex, longer-duration departure or capture strategies could be considered, with potentially greater energy gain. The shortest extra duration added to a mission for utilising a gravitational escape phenomenon at Jupiter is typically five years. Therefore, when the outer planets are considered, although significant performance gain can be achieved, the time penalties are too great to make this method feasible.

Examples of capture at Venus have shown equivalent approach orbit excess hyperbolic speeds of typically 1 km/sec, subsequently capturing through a single pass in the vicinity of a Lagrange point orbit. The time penalty is therefore approaching 120 days for such a manoeuvre. An analysis of such a transfer is given in the examples of Chapter 5. The excape process is effectively reversed for capture. Capture at Jupiter could be achieved from approach orbits with energies similar to those in the escape cases examined.

Regarding the utilisation of this technique for assisting mission design, it can be seen that it offers the most attractive performance for the inner planets of the Solar System, where the time penalties are limited. Also, when considering such manoeuvres at Jupiter and Saturn, escape and capture manoeuvres can be more efficiently achieved via the use of gravity assist at the moons of those planets. Use of lunar gravity assist at Earth is also more effective than the gravitational methods described here for Earth.

A number of interesting options for mission design using these techniques have been explored for transfers between the moons of Jupiter. Here the escape and capture possibilities principally exploit the combined gravity fields of Jupiter and the moon in question. The four inner moons have significant gravity fields. Details of such mission options can be found in the references listed for this section; much work in this area has notably been performed by Gomez, Koon, Lo *et al.*

The approach described in this section enables the generation of trajectories that experience gravitational escape or capture. Locally optimal trajectories may be obtained by optimisation of the ephemeris at pericentre of the planet or moon under consideration. Further examples of these trajectory types are given in Chapter 5, where interplanetary transfers utilising these techniques are considered.

A number of methods are available for generation of such trajectories. Considerable research has been undertaken on the properties of the invariant manifolds of orbits about the Lagrange points (L1 or L2). These were introduced in the previous section in the context of generating free injection transfers from initial planet pericentre to an orbit about the Lagrange point. The same procedure can be considered to identify those trajectories that result in escape from the planet. This

means that the spacecraft may depart along the unstable manifold. Conversely, on approaching a planet, capture may be achieved by approaching on the stable manifold to an orbit about one of the co-linear L1 or L2 Lagrange points. This area has notably been researched by Lo, Koon *et al.*, and more information may be found in the references for this chapter.

4.9 AEROCAPTURE AND AEROBRAKING

The retarding effect of an atmosphere can be used to assist in insertion to a target orbit about a planet. Most of the planets of the Solar System have an atmosphere that can, in principle, be utilised. The main exceptions are Mercury, with an almost non-existent atmosphere, and Pluto, with an atmosphere that is thought to be extremely rare. Venus, Earth and Mars all have atmospheres that may assist orbit insertion, and the outer four gas giants can also be used for this purpose.

These planets possess atmospheres of very different densities, but all may potentially be effective. There are two major techniques that can be considered to assist in target orbit insertion: aerocapture and aerobraking. A further category of atmospheric assistance (not applicable here), is aerogravity assist, which may be used in conjunction with planetary gravity assist manoeuvres to provide additional retardation or even plane change.

Before these concepts are discussed further, certain key terms must be defined.

Atmospheric drag is the retarding force arising from the density of the atmosphere of the planet:

$$Drag = \tfrac{1}{2}\rho V^2 C_D S$$

where ρ is the atmospheric density, V is the speed of the spacecraft relative to the atmosphere, C_D is the drag coefficient, and S_{REF} is a reference area, typically equal to the area of the spacecraft that is normal to the direction of flight through the atmosphere. The value of C_D depends on the geometrical configuration of the spacecraft.

Dynamic pressure:

$$Q = \tfrac{1}{2}\rho V^2$$

Kinetic heating, caused by passage through the atmosphere:

$$\dot{q} = kp^n V^m$$

where k is a constant related to the local curvature of the surface of the spacecraft, and the values n and m are typically 0.5 and 3 respectively, although vary with the nature of the flow and surface properties.

A detailed discussion on these subjects (hypersonic aerothermodynamics) may be found through the references for this chapter.

4.9.1 Aerocapture

A spacecraft approaching a target planet has a significant excess hyperbolic speed. Insertion to a captured orbit about the planet generally requires a significant pro-

pulsive ΔV applied at perientre. This retards the spacecraft to the extent that the energy reduction ensures that a bound orbit is reached. This will generally be a high elliptical orbit in which the spacecraft may spend some time before subsequent manoeuvres are used to inject it to the final target orbit.

The same effect may, in principle, be achieved by a retarding passage through the planet's atmosphere. The pericentre of the approach orbit is set to an altitude such that the atmospheric drag experienced by the spacecraft is sufficient to retard the spacecraft into an orbit with the desired intermediate apocentre, after emerging from the atmosphere on its new, elliptical orbit. This process is aerocapture. The pericentre must then be raised above the atmosphere (at the subsequent apocentre) in order to ensure that a second atmospheric passage does not occur. Such a passage could result in loss of the spacecraft as its trajectory may be sufficiently retarded to impact the surface of the planet.

The speed reduction required for capture depends on the target planet and the speed with which the spacecraft approaches the planet. However, for example at Venus, Earth and Mars, a speed reduction of typically 700–1,000 m/sec could be required. The spacecraft approach orbit is such that the time spent close to pericentre is relatively short, and so the retardation must be sufficient to achieve this speed change in a short time period (the main period of atmospheric influence may only last for minutes). This means that the atmospheric density must be relatively high in order to ensure that the peak deceleration is high enough to effect capture. The spacecraft could experience peak deceleration loads exceeding 1 g. The corresponding dynamic pressure will also be high. Simultaneously, kinetic heating of the spacecraft will result from the passage through the atmosphere. This combination of factors represents an extreme environment for a typical satellite configuration. Therefore, in many cases aerocapture will require the use of a specialised heat-shield by the spacecraft.

An important consideration with aerocapture is knowledge of the atmosphere before entry occurs. The pericentre is targeted by assuming a particular density profile with respect to altitude above the planet. Variations in the density from that expected at pericentre have a significant effect on the trajectory. These variations could arise either because the local atmospheric conditions are not as expected (for example, local solar weather effects on the atmosphere) or because navigation errors cause dispersion in the achieved pericentre.

If the spacecraft passes through a denser region than expected, it could start to progressively enter the denser regions of the atmosphere and ultimately impact the planet's surface. If the maximum density is less than expected, the spacecraft may exit the atmosphere with less retardation than expected and consequently fail to enter into a captured, bound orbit about the planet.

This spectrum of possibilities is covered by only a few kilometres in pericentre altitude, or the corresponding density variability at the nominal altitude. Therefore, for aerocapture to be feasible, closed loop control systems are generally considered. This allows the spacecraft to monitor its deceleration profile and implement changes to its trajectory to correct deviations from nominal. Such trajectory changes could either be implemented by aerodynamic means or spacecraft propulsion.

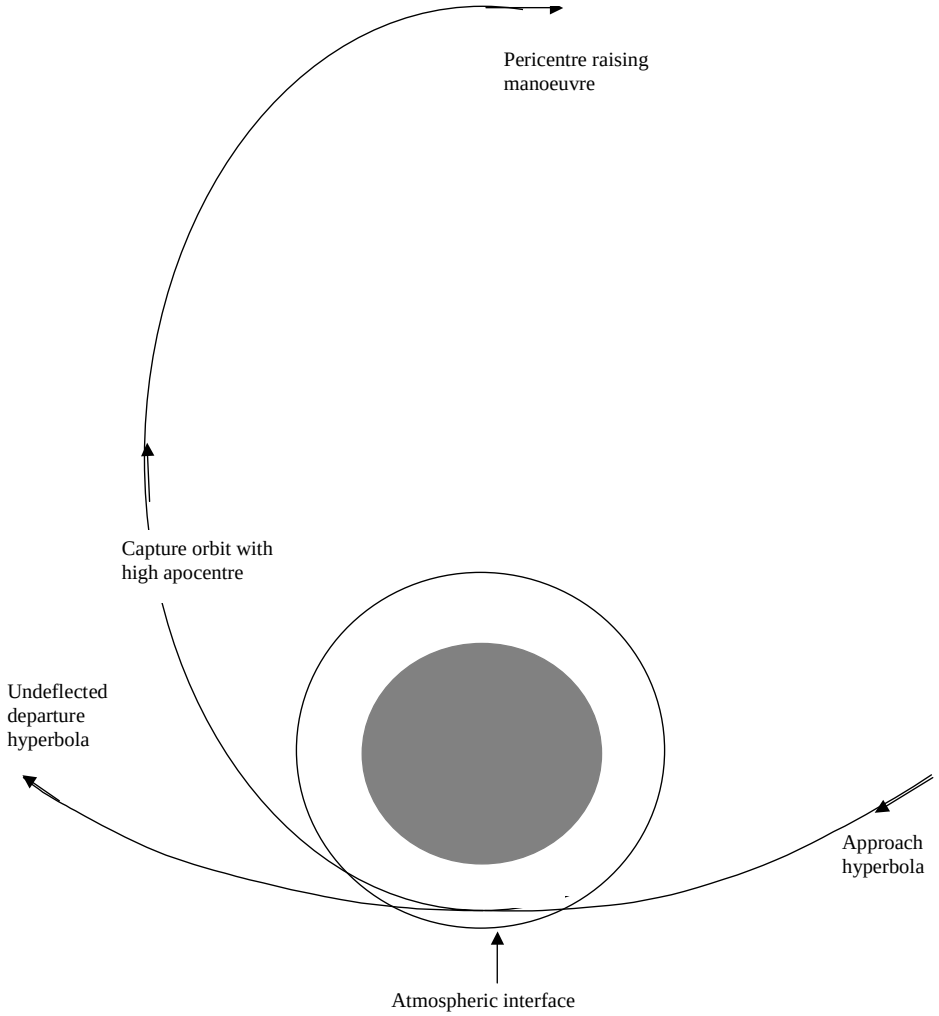

Figure 4.9.1. The principle of aerocapture.

Aerocapture has not as yet been implemented on interplanetary missions, and requires technology developments on the control systems to establish confidence in the technique. The potential gains are high, as large ΔV and hence fuel mass savings are possible.

4.9.2 Aerobraking

Once captured, the spacecraft will generally be in a highly elliptical orbit about the planet. However, the target orbit will have a much lower apocentre, which would normally require one or more retro-burn manoeuvres at pericentre. The ΔV for this process can also be relatively high, depending on the target orbit.

As an alternative to propulsive manoeuvres, aerobraking can be used to apply the required retardation. This requires that the pericentre be lowered into the upper atmosphere, where atmospheric drag will reduce the spacecraft velocity and lower the apocentre. The retardation could, in principle, be accomplished with a single passage through the atmosphere. However, in such a circumstance the spacecraft would encounter all of the problems applicable to aerocapture.

It is therefore possible to perform repeated passes through the atmosphere and slowly, repeatedly, reduce the apocentre. This means that the first passage can be high enough to include a safety margin, in the presence of the expected variability in maximum atmospheric density. Successive passes can adjust the pericentre as greater knowledge regarding the spacecraft and atmospheric state is gained. In this way, the riskier aspects associated with aerocapture are mitigated. The penalty is that the time taken to reach the target orbit is increased, as the spacecraft is now making multiple revolutions in what are initially high-period orbits (of several days). Aerobraking was performed by NASA's Mars Global Surveyor in the Martian atmosphere in 1997, and later by Mars 2001 Odyssey.

An example of an aerobraking sequence would be the following:

(1) Capture to high apocentre orbit (for example, at Mars, 100,000–200,000-km apocentre by 400-km pericentre). This may be propulsive or even by aerocapture.
(2) Lower pericentre to a value that ensures passage through the upper atmosphere (but at an altitude higher than the nominally expected value).
(3) Perform aerobraking to lower apocentre.
(4) Monitor change in orbit and adjust the pericentre via small apocentre manoeuvres, to target the nominal aerodynamic deceleration expected.
(5) Further small pericentre altitude maintenance manoeuvres may be required at apocentre to preserve the pericentre altitude under solar gravity perturbations to the highly elliptical orbit.
(6) Raise the pericentre via a small prograde manoeuvre at apocentre when the apocentre reaches the required altitude.

The time taken for apocentre reduction is dependent on the aero-thermal loads that are allowable. High loads imply the use of a specialised shield, whereas low loads can be experienced without significant modification to the standard spacecraft. A spacecraft can present a large drag surface to the atmosphere by the correct orientation of the solar arrays, as these generally represent the largest surface area of the spacecraft. They can be rotated as the velocity changes direction through the pericentre passage.

In the examples shown in Figures 4.9.2 and 4.9.3, the apocentre is reduced from nearly 200,000 km to almost 39,000 km over a period of 100 days. The peak deceleration is typically 0.02 m/s/s, and so places only modest loads on the spacecraft. The ΔV that would otherwise have been required to implement this apocentre reduction is approximately 150 m/s.

If the aerobraking sequence is continued for another 40 days, the apocentre can be reduced much further, to an altitude below 9,000 km, as shown in Figure 4.9.4.

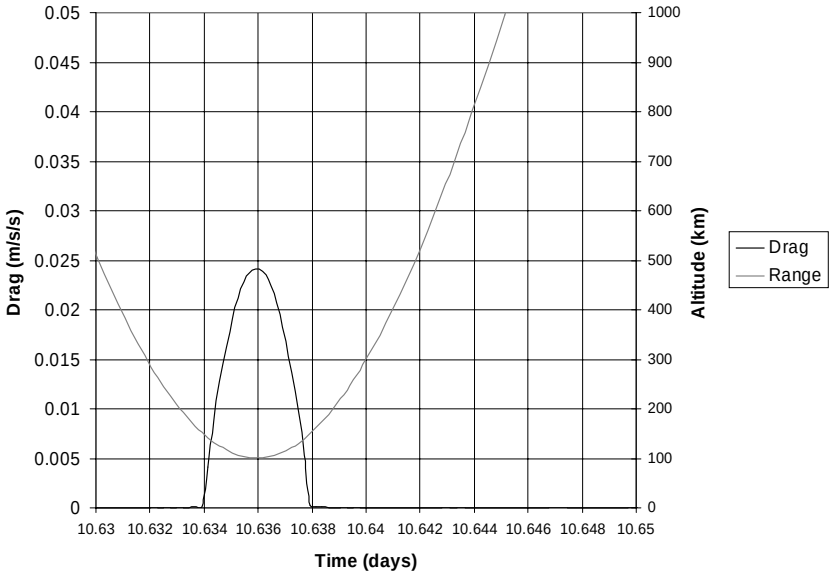

Figure 4.9.2. Aerobraking drag and altitude profile during a typical pericentre passage.

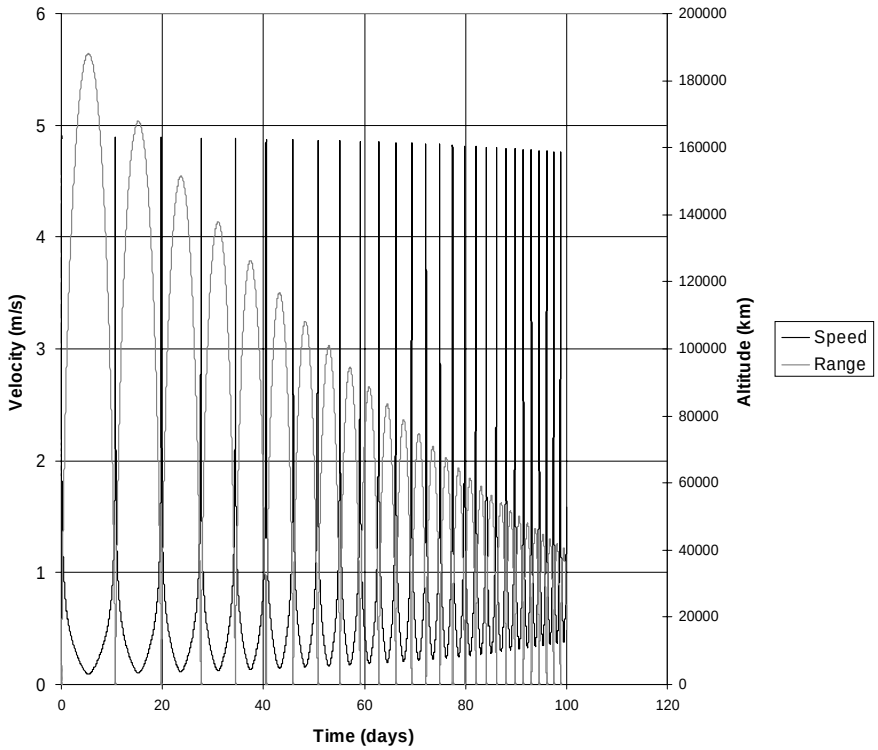

Figure 4.9.3. Aerobraking velocity and altitude profile over a period of 100 days.

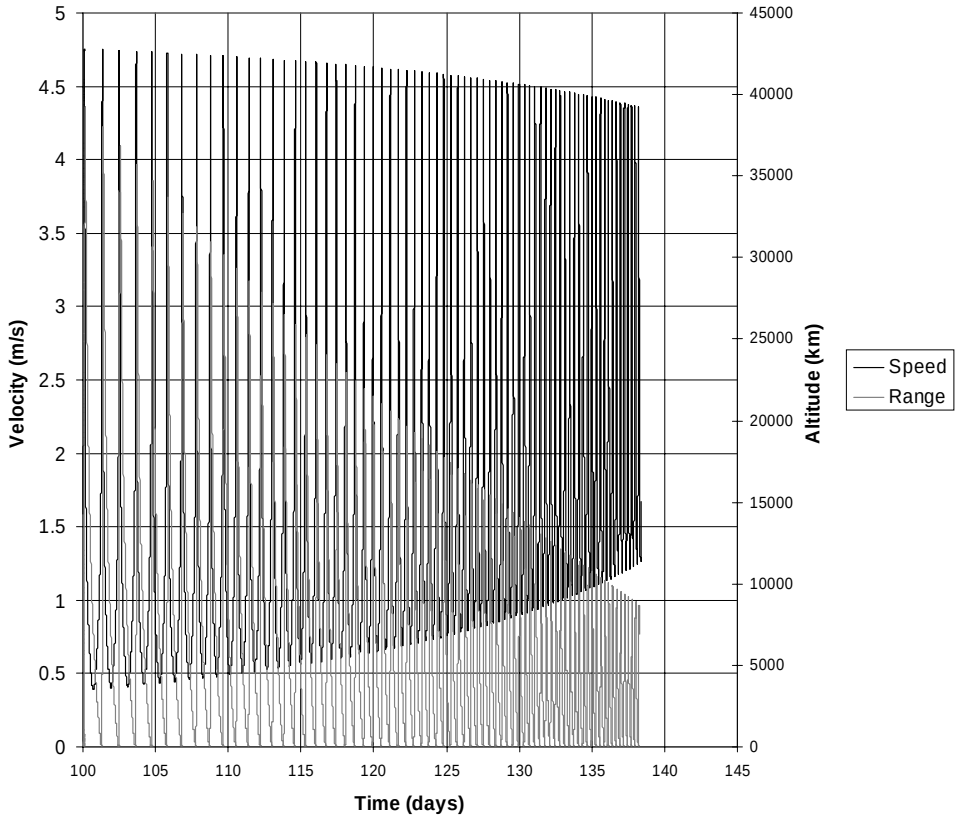

Figure 4.9.4. Aerobraking velocity and altitude profile over a period of 100–140 days.

However, the ΔV needed for this apocentre reduction is approximately 400 m/s. Therefore, if a faster apocentre reduction is required but some ΔV saving needed compared to an all propulsive insertion, a relatively small ΔV can be applied to reduce apocentre until the orbit periods are sufficiently short to make aerobraking much more time-efficient over the remainder of the apocentre reduction that is required.

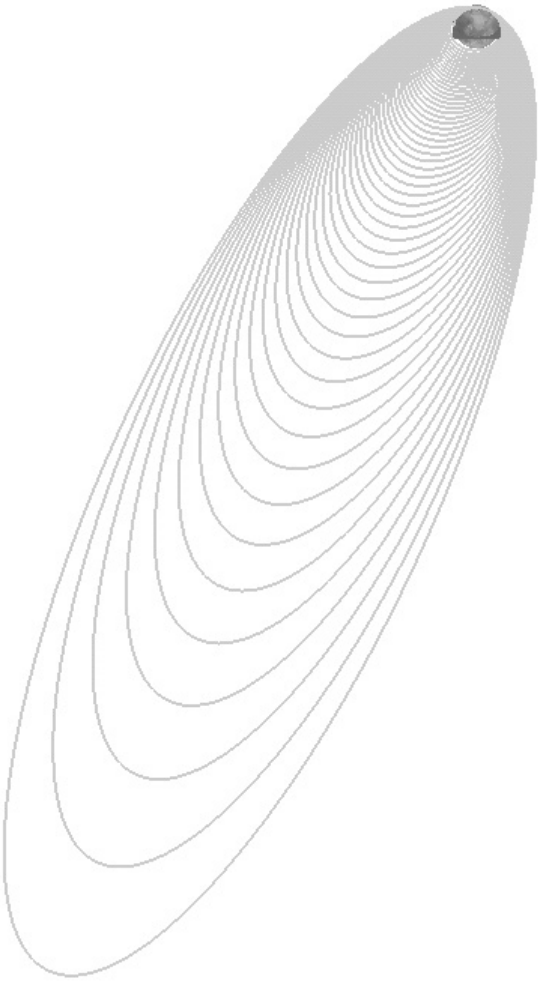

Figure 4.9.5. Aerobraking at Mars from a 100,000-km apocentre insertion orbit over a 100-day period.

5

Missions to the planets

The previous chapters have described a range of techniques that may be applied when designing missions to the planets of our Solar System. In this chapter, a number of such missions are considered. The aim is to demonstrate the application of the methods described. Techniques such as gravity assist and gravity capture are considered, as well as the applications of low-thrust propulsion.

The examples considered include cases of missions to many of the planets of our Solar System, as well as exploration of the Jovian moons. In those cases where particular launch epochs are considered, these often relate to the next decade when future missions may be planned. In some cases, current epochs are considered where the transfers may be related to current missions.

The objective is to find efficient transfers and to show how many of the special transfer techniques previously discussed can assist in this aim. One of the key parameters that indicate the efficiency of a mission is the ΔV, and so this quantity is evaluated for a wide range of missions and transfer types. A mission places requirements on the initial planetary escape and capture, and so the ΔV implications of these phases of the mission must also be included. In many cases, a direct launch into interplanetary transfer orbit may form the basis of the mission design. However, in order to assess the nature of the penalty to the mission implied by a given escape velocity requirement, the ΔV to raise the orbit from an initial reference ellipse to the required escape orbit is considered. The same philosophy may be applied to capture at a planet.

5.1 INTERPLANETARY MISSIONS USING GRAVITY ASSIST

5.1.1 Routes through the inner planets: mission to Mercury

Mercury is in some respects the most difficult planet to reach from Earth, as it requires a greater energy change than a transfer to any other planet. A further

complication is its elliptical orbit and inclination. These are key considerations that influence the mission design.

In order to achieve an efficient transfer to Mercury with traditional propulsion systems, it is mandatory to consider gravity assists. The main possibilities for gravity assist in reaching Mercury include Venus, Mercury and the Earth. As the only intermediate planet, Venus is clearly significant. The launch opportunities therefore tend to be driven by Earth–Venus transfer opportunities. The synodic period is 1.6 years.

The key features of these transfers globally repeat with an eight-year period, as this is the global repeat time for transfers from Earth to Venus. In this context 'global' means that the same transfer geometry applies, in terms of absolute longitudes of the planets. Mercury does not repeat precisely at eight years, but because multiple phasing orbits are generally used between Venus and Mercury, this lesser variation can be accommodated with less overall mission design implications.

A number of preliminary strategies can be assessed by means of simplified, co-planar transfer approximations. This effectively means that the inclinations of Venus and Mercury are not at first considered. As the eccentricity of Earth's and Venus's orbits is low, it will be further assumed that these are circular.

Strategies at Venus

If the first gravity assist occurs at Venus, then the possibilities here must be explored. These can range from using a single VGA to directly rendezvous with Mercury, to using multiple VGAs before rendezvous.

As the transfer is simplified by assuming that the planetary orbits (Earth, Venus and Mercury) are co-planar, then the transfer manoeuvres are dominated by heliocentric orbit raising and lowering operations rather than plane-changing. The simplest strategy that could be considered uses a single gravity assist at Venus. The interplanetary orbit after leaving Earth has the perihelion lower than Venus's orbit. The gravity assist at Venus will further reduce the perihelion so that a rendezvous at Mercury can occur. Mercury's orbit is eccentric, such that aphelion lies at 0.47 AU and perihelion at 0.31 AU. In the case of a direct transfer the optimum rendezvous location is at perihelion, and this is also the target with the gravity-assist transfer.

The V_∞ requirements can be converted to ΔV requirements. To perform this calculation, some reference orbits must be defined:

- The Earth-bound initial reference orbit has a perigee altitude at 200 km and apogee altitude at 35,787 km (GTO standard apogee altitude).
- The Mercury bound reference orbit has a pericentre at 400 km and apocentre at 39,760 km (same apocentre radius as Earth GTO orbit).

Table 5.1.1 shows the transfer details and compares direct with VGA transfers. Rendez-vous at Mercury aphelion and perihelion are compared.

Table 5.1.2 shows the significant ΔV savings that will result from such a transfer

Table 5.1.1. Comparisons of direct and single VGA transfer to Mercury with rendezvous at Mercury aphelion and perihelion. Co-planar planetary orbits are assumed. h is the altitude of the fly-by.

	V_∞ at Earth (m/s)	Intermed Apo (AU)	Intermed Peri (AU)	V_∞ at Venus (m/s)	h fly-by (km)	Intermed Apo (AU)	Intermed Peri (AU)	V_∞ at Mercury (m/s)
Peri RV	9,356	n/a	n/a	n/a	n/a	n/a	n/a	7,453
Apo RV	6,023	n/a	n/a	n/a	n/a	n/a	n/a	12,052
Peri RV + VGA	5,796	1.00	0.48	12,558	400.00	0.80	0.31	5,659
Apo RV + VGA	2,812	1.00	0.70	4,563	400.00	0.73	0.47	9,292

Table 5.1.2. ΔV comparisons of direct and single VGA transfer to Mercury with rendezvous at Mercury aphelion and perihelion.

	ΔV Earth departure (m/s)	ΔV Mercury approach (m/s)	Total ΔV (m/s)
Peri RV	4,208	4,592	8,801
Apo RV	2,310	8,834	11,144
Peri RV + VGA	2,202	3,062	5,264
Apo RV + VGA	1,123	6,251	7,375

strategy using a single VGA. It further confirms the preference for rendezvous at Mercury perihelion for both direct and VGA cases.

A second gravity assist may now be considered, to take place at Venus. In order to facilitate such a second rendezvous, an intermediate resonant orbit will be used. Resonance ensures that no manoeuvres are needed when returning to Venus for the second time.

The first requirement is that the spacecraft must reach a Venus resonant orbit after the first VGA. Two main options that could be considered are 1 : 1 resonance and 4 : 3 resonance. These provide a range of transfer performances but also limit the transfer duration extension to no more than three Venus orbits. A 3 : 2 resonance with Venus can also be considered, but this requires a greater energy change, as the semi-major axis of that orbit is lower.

The maximum perihelion with which a 1 : 1 resonant orbit can be reached with a minimum energy transfer from Earth lies only just lower than Venus's orbit. The aphelion after the gravity assist is then, however, only just above Venus. Consequently, any subsequent gravity assists are limited in the perihelion reduction that can be achieved. Mercury perihelion cannot be reached in this way, because the excess hyperbolic speed at Venus is insufficient to achieve the energy change needed to transfer from the 1 : 1 resonant orbit to one with a perihelion that lies at Mercury.

Table 5.1.3 shows the resonant orbits that may be reached with the minimum excess hyperbolic velocity departing Earth. Greater excess speed implies a lower

Table 5.1.3. 2D patch conic analysis of Earth transfer orbits to reach Venus resonance after VGA. Co-planar planetary orbits are assumed.

Resonant orbit	V_∞ at Earth (m/s)	Apo leaving Earth	Peri leaving Earth	V_∞ at Venus (m/s)	h fly-by (km)	Resonant orbit Apo (AU)	Resonant orbit Peri (AU)
V- 1 : 1	2,531	1.000	0.720	2,978	25,000	0.785	0.662
V- 3 : 4	2,828	1.000	0.694	4,638	400	0.731	0.463
V- 2 : 3	6,934	1.000	0.417	14,649	400	0.827	0.277

Table 5.1.4. 2D patch conic analysis of alternative Earth transfer orbits to reach Venus 1 : 1 resonance after VGA. Co-planar planetary orbits are assumed.

Resonant orbit	V_∞ at Earth (m/s)	Apo leaving Earth	Peri leaving Earth	V_∞ at Venus (m/s)	h fly-by (km)	Resonant orbit Apo (AU)	Resonant orbit Peri (AU)
V- 1 : 1	2,531	1.000	0.720	2,978	25000	0.785	0.662
V- 1 : 1	3,346	1.000	0.650	6,635	31800	0.860	0.587
V- 1 : 1	4,404	1.000	0.570	9,572	39600	0.919	0.527
V- 1 : 1	5,304	1.000	0.510	11,573	67500	0.959	0.488

perihelion and therefore greater excess hyperbolic speed at Venus. V3 : 4 means 3 Venus revolutions and V2 : 3 implies 2 Venus revolutions.

However, many 1 : 1 resonant orbit solutions are available at Venus. These may be reached with increased excess hyperbolic speeds when approaching the planet. Resonance is then achieved in one of two ways:

(1) A gravity assist is used to achieve a significant out-of-ecliptic motion whilst maintaining a semi-major axis at the value needed for resonance. Such techniques are described in the previous section on 3D gravity-assist design.
(2) A higher altitude fly-by is used whilst maintaining the post fly-by orbit close to the ecliptic, such that even with the high V_∞ the semi-major axis can be maintained at the required value. These solutions are shown in Table 5.1.4.

With such higher V_∞ solutions in 1 : 1 resonant orbits, a much lower perihelion can be achieved after the second gravity assist at Venus. However, the price to pay is that the launch V_∞ is also considerable higher to achieve this greater excess speed at Venus. The achievable perihelions after the second gravity assist are shown in Table 5.1.5.

The transfer, using 11.5 km/sec V_∞ at Venus can be converted to ΔV to transfer to Mercury, via a rendezvous after the second VGA (Table 5.1.6).

This case shows that the use of the second VGA in a 1 : 1 resonant orbit results in a gain over the single VGA case. However, more efficient strategies are available when using double VGA. Now the case of a 4 : 3 resonant orbit is considered and shown in Table 5.17.

Table 5.1.5. 2D patch conic analysis of transfer orbits after the second gravity assist from a Venus 1 : 1 resonance.

Resonant orbit	V_∞ at Venus (m/s)	h fly-by (km)	Transfer orbit Apo (AU)	Transfer orbit Peri (AU)
V- 1 : 1	2,978	300	0.728	0.540
V- 1 : 1	6,635	300	0.728	0.367
V- 1 : 1	9,572	300	0.754	0.324
V- 1 : 1	11,573	300	0.781	0.307

Table 5.1.6. ΔV implications for a double VGA transfer to Mercury with a Venus 1 : 1 resonant orbit and V_∞ at Venus of 11.5 km.

ΔV Earth departure (m/s)	ΔV Mercury approach (m/s)	Total ΔV (m/s)

Table 5.1.7. 2D patch conic analysis of Earth transfer orbits to reach Venus 3 : 4 resonance after VGA. Co-planar orbits are assumed.

Resonant orbit	V_∞ at Earth (m/s)	Apo leaving Earth	Peri leaving Earth	V_∞ at Venus (m/s)	h fly-by (km)	Resonant orbit Apo (AU)	Resonant orbit Peri (AU)
V- 3 : 4	2,828	1.000	0.694	4,638	400	0.731	0.463
V- 3 : 4	3,224	1.000	0.660	6,219	2,600	0.749	0.445
V- 3 : 4	3,857	1.000	0.610	8,168	3,150	0.776	0.419

Table 5.1.8. 2D patch conic analysis of transfer orbits after the second gravity assist from a Venus 3 : 4 resonance.

Resonant orbit	V_∞ at Venus (m/s)	h fly-by (km)	Transfer orbit Apo (AU)	Transfer orbit Peri (AU)
V- 3 : 4	6,219	300	0.729	0.387
V- 3 : 4	8,168	300	0.724	0.303

Once again, by using higher V_∞ solutions in 3 : 4 resonant orbits a much lower perihelion can be achieved after the second gravity assist at Venus. The achievable perihelions after the second gravity assist, for the last two cases in Table 5.1.7, are shown in Table 5.1.8.

The table shows that a Mercury rendezvous at perihelion may now be achieved with much lower excess hyperbolic speed departing Earth than the 1 : 1 resonant case. The value here is 3,857 m/s. The energy change between the Venus 4 : 3 resonant orbit and a Mercury rendezvous orbit is less than was the case with the

Table 5.1.9. ΔV implications for a double VGA transfer to Mercury with a Venus 3 : 4 resonant orbit and V_∞ at Venus of 8.2 km/sec.

ΔV Earth departure (m/s)	ΔV Mercury approach (m/s)	Total ΔV (m/s)
1,425	2,228	3,654

Table 5.1.10. Earth to Venus stage with 4 : 3 Venus resonance using full 3D geometry.

	V_∞ at Earth (m/s)	Apo leaving Earth (AU)	Peri leaving Earth (AU)	V_∞ at Venus (m/s)	h fly-by (km)	Resonant orbit Apo (AU)	Resonant orbit Peri (AU)	Inclin (deg)
Earth to VGA1	3,639	1	0.627	7,858	2,890	0.779	0.428	3.39

Table 5.1.11. Venus to Mercury stage with 4 : 3 Venus resonance using full 3D geometry.

	Resonant orbit Apo (AU)	Resonant orbit Peri (AU)	V_∞ at Venus (m/s)	h fly-by (km)	Apo leaving Venus (AU)	Peri leaving Venus (AU)	Inclin (deg)	V_∞ at Mercury (m/s)
VGA2 to Mercury	0.779	0.428	7,858	4,080	0.728	0.327	6.37	5,730

Table 5.1.12. ΔV implications for a double VGA transfer to Mercury with a Venus 4 : 3 resonant orbit including full 3D effects of Mercury's and Venus's orbits.

ΔV Earth departure (m/s)	ΔV Mercury approach (m/s)	Total ΔV (m/s)
1,355	3,120	4,476

Venus 1 : 1 resonant orbit. However, the transfer is longer, as an additional two Venus years are included in the transfer. The ΔV implications are shown in Table 5.1.9.

However, a term so far neglected is the effect of Mercury's orbit inclination. The node lies close to the line of apses, and so an additional speed relative to Mercury exists due to the inclination difference. As Mercury's orbital inclination is 7°, this is a significant term.

The next double VGA strategy considers an intermediate 4 : 3 resonant orbit that achieves inclination change as well as perihelion reduction. The example in Tables 5.1.10 and 5.1.11 are taken from an actual transfer that includes the full orbit ephemeris of the planets. An effect from the relative phasing of the planet's orbits is also present. The transfer can again be converted to ΔV requirements as shown in Table 5.1.12. These results show an increase in ΔV when compared with the

previous 3 : 4 resonant case, but this is due to the effect of accommodating Mercury's inclination and the Earth departure implications for Venus rendez-vous.

Strategies at Mercury

Having lowered the transfer orbit perihelion to Mercury perihelion, it is possible to rendezvous with Mercury. The practical matter of obtaining the correct phasing between orbits is not at first considered. In the following analysis, the transfer is again simplified by assuming that the orbit of Mercury and the spacecraft orbit after the last VGA are co-planar.

After the final VGA the transfer orbit perihelion lies at or close to Mercury perihelion, but the aphelion must lie at or above Venus. The excess hyperbolic speed at Mercury will therefore be high (typically 4–7 km/sec, as seen in the previous section).

The evolution of the orbit via a sequence of gravity assists at Mercury can be obtained. The case of an initial orbit with aphelion at 0.8 AU and perihelion close to Mercury perihelion is considered. The V_∞ at Mercury is then 7.18 km/sec. This is similar to the 1 : 1 resonance case in Table 5.1.5.

Table 5.1.13. Gravity assist sequence at Mercury with constant V_∞ leading to a final 1 : 1 resonant orbit.

	Apo (AU)	Peri (AU)	Semi-major axis (AU)	Duration (days)
	0.8080	0.3049	0.556	
3 : 2	0.8080	0.3049	0.507	395.63
4 : 3	0.7112	0.3029	0.469	469.25
6 : 5	0.6370	0.3010	0.439	634.24
8 : 7	0.5759	0.2991	0.423	804.31
1 : 1	0.5482	0.2981	0.387	87.93

The apohelion and perihelion evolution are seen below.

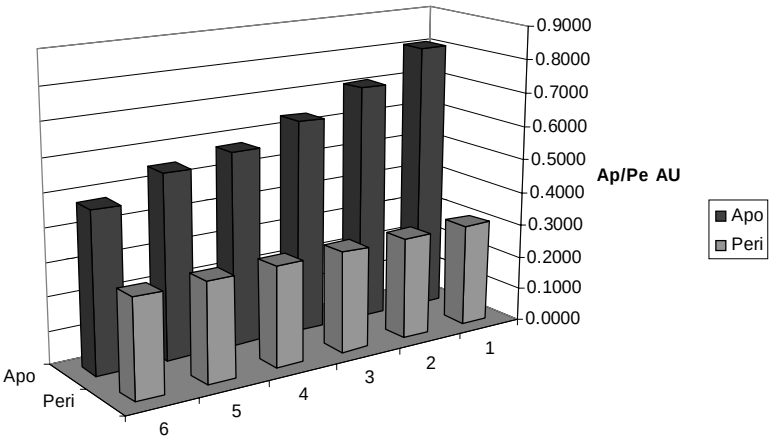

Table 5.1.14. Gravity assist sequence at Mercury with manoeuvres to reduce V_∞ when arriving at final 1 : 1 resonant orbit. Co-planar orbits are assumed for spacecraft and Mercury.

	Apo (AU)	Peri (AU)	Semi-major axis (AU)	Duration (days)	ΔV (m/s)	V_∞ (m/s)
	0.8080	0.3049	0.556			7,184.67
3 : 2	0.7112	0.3070	0.509	395.63	130	4,823.88
4 : 3	0.6337	0.3070	0.470	470.18	50	3,759.83
6 : 5	0.5684	0.3070	0.438	633.30	45	2,701.96
1 : 1	0.4688	0.3070	0.388	88.01	51	1,440.29

Table 5.1.15. Gravity assist sequence at Mercury from lower initial aphelion orbit with manoeuvres to reduce V_∞ when arriving at final 1 : 1 resonant orbit. Co-planar orbits are assumed.

	Apo (AU)	Peri (AU)	Semi-major axis (AU)	Duration (days)	ΔV (m/s)	V_∞ (m/s)
	0.7260	0.3070	0.517			5,044.40
3 : 2	0.7074	0.3070	0.507	395.59	10	4,825.31
4 : 3	0.6337	0.3070	0.470	470.15	50	3,761.77
6 : 5	0.5683	0.3070	0.438	633.19	43	2,760.59
1 : 1	0.4680	0.3070	0.388	87.87	56	1,379.74

The resonance of the orbits must be considered. After the first gravity assist at Mercury, a 3 : 2 resonance can be achieved (3 Mercury revolutions to 2 spacecraft). No manoeuvres are performed nominally, so the V_∞ at Mercury remains constant. In this way, the semi-major axis can be progressively reduced to reach 4 : 3 and then 6 : 5 resonances. However, with this V_∞ at Mercury a 1 : 1 resonance cannot be reached from 6 : 5. An intermediate resonant orbit is required at 7 : 6 or 8 : 7. Such high resonance numbers add considerable extra duration to the transfer. The V_∞ at Mercury remains constant at 7.18 km/sec throughout this sequence. This sequence can be seen in Table 5.1.13.

Strategies can be sought to reduce the V_∞ at Mercury. The principle of a gravity assist 'ladder' (described in the previous chapter) can be adopted. Mercury may now be approached via a series of gravity assists that progressively lower the transfer orbit aphelion. With this new strategy the approach speed to Mercury is also progressively reduced, as intermediate ΔVs are applied to reduce this speed with respect to Mercury. In Table 5.1.14 the perihelion is raised after each gravity assist to 0.307 AU, the Mercury fly-by occurring at 0.3075 AU in this example.

Alternatively, a sequence may be obtained starting from an initial orbit with lower aphelion, as would result from using an intermediate Venus 4 : 3 resonant orbit. This can be seen in Table 5.1.15.

This clearly shows the potential for reduction in the V_∞ at Mercury with such a technique. The sequence can be terminated after any fly-by, and an orbit insertion manoeuvre performed at pericentre. It is an issue of transfer duration trade-off

versus total ΔV. These analyses include the approximation that any pericentre-raising manoeuvres still allow a rendezvous manoeuvre with Mercury at the optimal perihelion location for the next fly-by. This is slightly optimistic, particularly for the 1 : 1 resonant orbit case. However, the principle is clearly demonstrated, and a more detailed sequence for an actual mission design is considered in the next section.

Optimised transfers to Mercury

The previous discussion identified a number of good methods to achieve efficient transfers to Mercury, in terms of minimum ΔV requirement. These can be summarised, in terms of the gravity assist sequences used, as $-$V-V-M^n. The choice of n depends on the ΔV reduction required and the allowable transfer duration. These options all result in an increase in transfer time when compared with a direct, conjunction-type transfer.

It may be assumed that the launch vehicle will inject the spacecraft into the required Earth escape orbit. Alternatively, this escape orbit could be reached after injection to an intermediate Earth-bound orbit, and the spacecraft performs apogee-raising manoeuvres, followed by an escape manoeuvre.

The initial optimisable properties of the Earth departing relative velocity vector are as follows:

Property	*Value*
V_∞ of hyperbolic escape vector	Optimisable
Right Ascension:	Optimisable via selection of launch epoch
Declination:	Optimisable via selection of injection orbit argument of perigee and right ascension

The objective function for this analysis is defined as the sum of impulsive ΔVs:

- Departure ΔV (from a specified Earth-bound reference orbit, to reach the required excess hyperbolic departure speed).
- Approach ΔV (to a specified Mercury orbit, from the approach excess hyperbolic arrival speed).
- Deep-space ΔVs.

The Earth departure ΔV can in practice be supplied either by the launcher or spacecraft, and is the subject of a separate trade-off.

The strategy that is adopted, in terms of the number of gravity assists, has a strong influence on the objective function. In principle, a global optimisation problem may be defined, with a solution that identifies the ideal sequence of gravity assists. This problem could be solved in conjunction with an upper limit on transfer duration. However, the solution of such a global problem is a complex task requiring substantial computational resources. Therefore, in practice the problem is often simplified and a series of parametric solutions are often studied.

The first parameter to be considered is the launch epoch. In practice, there will be a general target launch date for a space mission (or at least a target launch year, typically determined by programmatic considerations). Also, an upper limit on the transfer duration is likely to be considered. However, if this parameter has a strong

bearing on mission ΔV requirements, then a range of transfer durations may be considered and compared; solutions being sought for each duration under consideration.

Now a series of problems reduced in scope is defined for solution. Even so, there may be more than one gravity assist sequence that is compliant with the problem constraints.

In the following examples, several transfers to Mercury are considered. They vary in the upper limit applied to the transfer duration and the strategy. The problem is further constrained by specifying the launch year. In this case, the year 2004 is chosen for a detailed analysis. The reason for choice will become significant in the subsequent discussion on current missions.

Table 5.1.16 shows a series of transfer routes, each leaving Earth in 2004. Each transfer option uses two gravity assists at Venus. Between them, a 4 : 3 resonant orbit with Venus is used (3 Venus years). This gravity assist sequence has been chosen after the previous discussion, illustrating the efficiency of this route in allowing low mission ΔVs. The transfers then vary in the gravity assist sequence that is performed at Mercury. For each transfer the gravity assist sequence is given, together with the excess hyperbolic speeds leaving Earth and arriving at Mercury. Deep-space manoeuvres are also used to reduce the excess hyperbolic speed at Mercury. The total minimised ΔV (making up the objective function) for each transfer is given.

The Earth orbit assumed is a GTO-like orbit with apogee at 42,165 km radius and perigee at 200 km altitude. The Mercury orbit is elliptical, with pericentre at 400 km altitude and apocentre at 12,000 km altitude. A lower limit is placed on the fly-by altitudes during the gravity assist phases. A value of 300 km is used here to allow for potential navigation uncertainties in the pericentre passage.

The shortest sequence uses a single MGA, entering a 2 : 3 resonant orbit with Mercury before rendezvous. This orbit may be reached directly via gravity assist at Mercury from the initial approach orbit from Venus. A deep-space manoeuvre close to aphelion reduces the excess hyperbolic speed at Mercury to minimise the objective function. A longer transfer, that significantly reduces the objective ΔV uses a further MGA. A 3 : 4 Mercury resonant orbit may be reached directly via gravity assist at Mercury from the initial 2 : 3 resonant orbit.

The greatest possible change in orbit period is sought at each fly-by, but is constrained by the need to enter Mercury resonant orbits. Therefore, instead of targeting a 3 : 4 Mercury resonant orbit, a 4 : 5 resonance could be sought. However, this is not achievable directly by the gravity assist and may only be reached if an additional deep-space manoeuvre is performed. Therefore, the objective function value for this sequence is greater than the case using a 3 : 4 resonance.

The sequence may now be extended to further reduce the objective ΔV by seeking even lower-period resonant orbits after further gravity assists. The excess hyperbolic approach speed at Mercury can then be further reduced by the assistance of deep-space manoeuvres. A 4 : 5 resonance at Mercury is considered after the 3 : 4 resonance. However, at this point it is possible to reach a 5 : 6 resonance with a single

Table 5.1.16. ΔV implications of different Mercury gravity assist sequences for launch in 2004.

Route	Earth depart V_∞ (km/s)	Intermediate deep-space ΔV (m/s)	Mercury approach V_∞ (km/s)	Injection to Mercury elliptical orbit (m/s)	Total ΔV after leaving Earth to Mercury elliptical orbit (m/s)	Total ΔV from GTO to Mercury elliptical orbit (m/s)	Transfer time (years)
V-V M3 : 2	3.84	243	4.80	2,594	2,837	4,257	4.07
V-V- M3 : 2 M4 : 3	3.84	304	3.37	1,574	1,878	3,298	5.05
V-V- M3 : 2 M5 : 4	3.84	929	2.77	1,208	2,137	3,557	5.29
V-V- M3 : 2 M4 : 3 M5 : 4	3.84	394	2.64	1,134	1,528	2,948	6.27
V-V- M3 : 2 M4 : 3 M6 : 5	3.84	475	2.17	892	1,367	2,787	6.54
V-V- M3 : 2 M4 : 3 M6 : 5 M1 : 1 M1 : 1	3.84	475	1.50	611	1,086	2,506	6.87
V-V- M3 : 2 M4 : 3 M6 : 5 M8 : 7 M1 : 1 M1 : 1	3.84	540	1.06	477	1,017	2,437	8.80

MGA from the 3 : 4 resonance. These sequences have been extensively evaluated by Yen (see references for this chapter). After 5 : 6, a 1 : 1 resonance with Mercury can be reached after the next gravity assist.

Optionally, a 7 : 8 Mercury resonant phase can be included between the 6 : 5 and 1 : 1 resonances, to explore the possibility for further reduction in the objective. However, it may be seen that although the final Mercury approach excess hyperbolic speed is reduced and so the capture ΔV is less, the additional deep-space manoeuvre

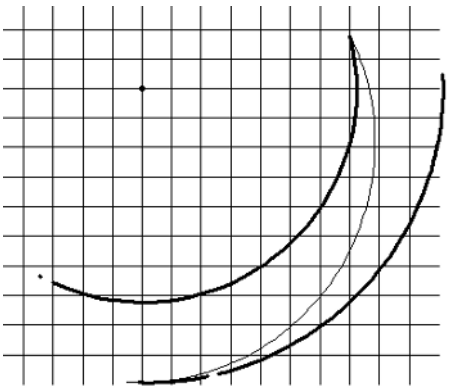

Figure 5.1.1. Transfer to Mercury in 2004: leaving Earth for Venus. The transfers start with a departure from Earth to Venus. In 2004 two conjunction-type transfer opportunities to Venus exist (the 'short' and 'long' transfer options). The 'short' transfer, shown here, forms the basis for this locally optimal transfer. Departure is in March 2004, arriving at Venus in late June 2004. Earth's and Venus's orbits are shown (thick lines). The inner grid segments are 0.1 AU from side to side.

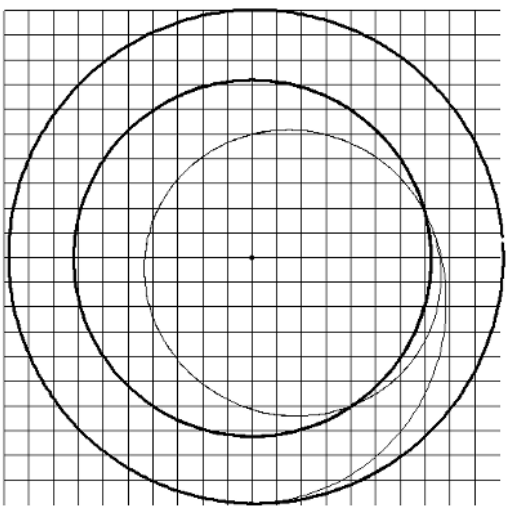

Figure 5.1.2. Transfer to Mercury in 2004: Venus to Venus 4 : 3 resonant orbit. Each transfer option uses two gravity assists at Venus. Between these, a 4 : 3 resonant orbit at Venus is used (3 Venus years). The spacecraft crosses Venus's orbit at two locations. On returning to Venus, the first crossing opportunity is targeted in this particular example, and Venus is reached in slightly less than 3 Venus years. The spacecraft returns to Venus in March 2006. Earth's and Venus's orbits are shown (thick lines). The grid is 1 AU from centre to edge.

needed from the low-aphelion orbit is greater, resulting in only a small net objective function decrease, at the expense of a further two years in transfer.

Some examples of the different phases of such sequences are illustrated in Figures 5.1.1 to 5.1.5.

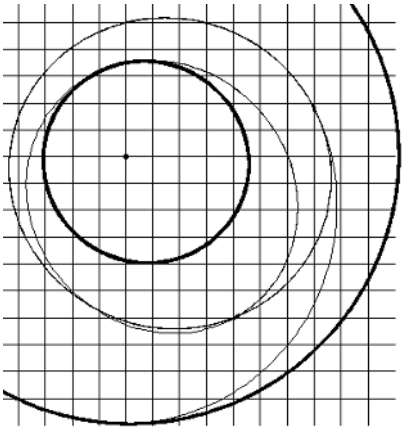

Figure 5.1.3. Transfer to Mercury in 2004: Venus to Mercury rendezvous after 1.5 revolutions. After returning to Venus in March 2006 the spacecraft performs a fly-by resulting in a gravity assist that lowers its perihelion to be located close to that of Mercury. The spacecraft seeks a rendezvous with Mercury, and so the problem of the phasing between Venus and Mercury must be considered. The 4 : 3 Venus resonant orbit crosses the orbit of Venus at two locations. The selection of the first Venus crossing location for the second Venus fly-by is made, as this locates the line of apses of the subsequent heliocentric orbit such that perihelion lies close to the perihelion of Mercury. The spacecraft then makes approximately 3.5 revolutions about the Sun before reaching Mercury close to Mercury perihelion in July 2007. Earth's and Mercury's orbits are shown (thick lines). The inner grid segments are 0.1 AU from side to side.

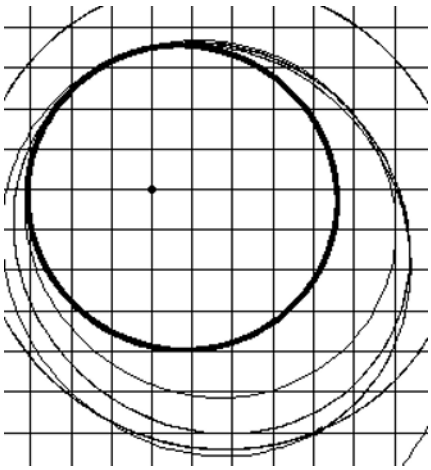

Figure 5.1.4. Transfer to Mercury in 2004: Venus to Mercury and Mercury 2 : 3 and 3 : 4 resonant orbits. On reaching the first Mercury rendezvous the spacecraft executes a gravity assist manoeuvre. This is used to target a 2 : 3 resonant orbit with Mercury. The spacecraft again reaches Mercury in April 2008, and performs a further gravity assist to reach a 3 : 4 Mercury resonant orbit.

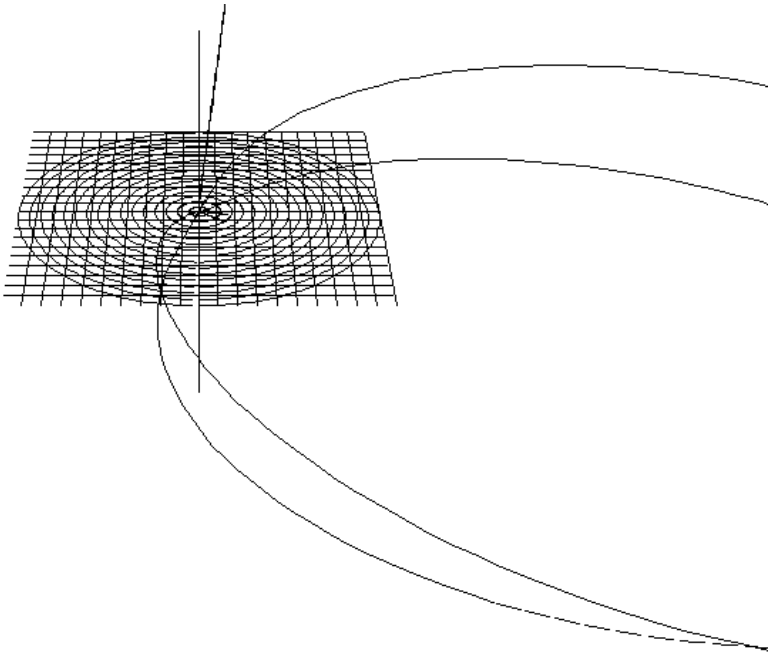

Figure 5.1.5. Transfer to Mercury in 2012: motion relative to Mercury during the last two 1 : 1 resonant orbits. The grid is 1.5 million km from centre to edge and lies parallel to the ecliptic. The trajectory and its projection in the ecliptic (dashed line) are shown. The first 1 : 1 resonant orbit at Mercury returns after one Mercury year after an excursion of several million km. The second resonant orbit returns after approximately 44 days and experiences a relative motion mostly perpendicular to the ecliptic.

Ultimately a 1 : 1 resonance can be achieved. In fact, a second 1 : 1 resonance can be used, as proposed by Langevin (see references for this chapter). This uses the MGA to increase (or reduce) the spacecraft's inclination such that a return to Mercury is achieved after a half heliocentric revolution. The result is that rendezvous is achieved at Mercury aphelion. Here the approach speed is naturally reduced as both Mercury and spacecraft orbits slow towards aphelion.

The details of a complete end-to-end mission are shown in Table 5.1.17.

The table also shows the optimal values of excess hyperbolic speed. These parameters are important in characterising the fly-bys.

The departure ΔV at Earth is calculated relative to an initial GTO-like altitude orbit (200 km perigee altitude). The target orbit at Mercury is now lower than considered in the previous section, taking an altitude of 12,000 km – typical of a science observation orbit about the planet. Pericentre altitude at Mercury is still low; in this example, 400 km. The complete transfer is shown in Figure 5.1.6. The thicker black line shows Earth's orbit. The sub-grid elements are 0.1 AU from edge to edge. The orbit of Mercury is omitted for clarity. The final rendezvous point is close to Mercury aphelion, and the small modifications due to manoeuvres within the Mercury resonant orbit phases, can be seen.

Table 5.1.17. Transfer fly-bys and manoeuvres for Mercury transfer with launch in 2004.

Event	Parameters	Description	ΔV
Launch	$V_\infty = 3.84$ km/s 19 Mar 2004	Transfer orbit to Venus RV after 0.5 revs	1,420 m/sec
GA 1 at Venus to a 4 : 3 resonant orbit	$V_\infty = 8.07$ km/s 25 Jun 2004	Achieve 4 : 3 resonant orbit	
GA 2 at Venus to 3.5 heliocentric revolution transfer to rendezvous with Mercury	$V_\infty = 8.04$ km/s 16 Mar 2006	Transfer orbit to Mercury RV after 3.5 revs	
GA 3 at Mercury to 3 : 2 resonant orbit	$V_\infty = 5.7$ km/s 22 Jul 2007	Achieves 3 : 2 resonant orbit	50 m/s
GA 4 at Mercury to 3 : 4 resonant orbit	$V_\infty = 5.3$ km/s 12 Apr 2008	Achieves 4 : 3 resonant orbit	254 m/s
GA 5 at Mercury to 6 : 5 resonant orbit	$V_\infty = 3.4$ km/s 6 Apr 2009	Achieves 6 : 5 resonant orbit	
GA 6 at Mercury to 1 : 1 resonant orbit	$V_\infty = 2.2$ km/s 21 Sep 2010	Achieves 1 : 1 resonant orbit	172 m/s
GA 7 at Mercury to 1 : 1 resonant orbit over 0.5 revs	$V_\infty = 2.2$ km/s 19 Dec 2010	Achieves 1 : 1 resonant orbit over half rev	
Inject to Mercury elliptical orbit	$V_\infty = 1.5$ km/sec 31 Jan 2011		611 m/s
Total ΔV inc Earth escape from GTO altitude orbit			2,507 m/sec

Previous discussions have shown that Earth-to-Venus transfers show a near-eight-year global repeat period. The initial phases of this transfer are therefore expected to repeat every eight years. For launches in 2012 and 2020, the launch date and first two fly-bys at Venus have very similar characteristics to the 2004 launch. Mercury does not show this eight-year repeat property, and the number of revolutions about the Sun between VGA-2 and MGA-1 differs from the 2004 solution. In 2012, only 1.5 revolutions are needed, but in 2012 4.5 revolutions are required.

Further examples using a Venus 4 : 3 resonant orbit can be considered. In the 2004 example, the Venus resonant phase Venus fly-bys are at different locations (the orbit not quite in 4 : 3 resonance) to control the location of the subsequent longitude of perihelion. This technique is not in general required. The following example is for a launch in 2009, where the two Venus fly-bys occur at the same location.

Figure 5.1.8 and Table 5.1.18 show the features of this mission. It can be seen that many of the characteristics are the same as the 2004 launch case. This example

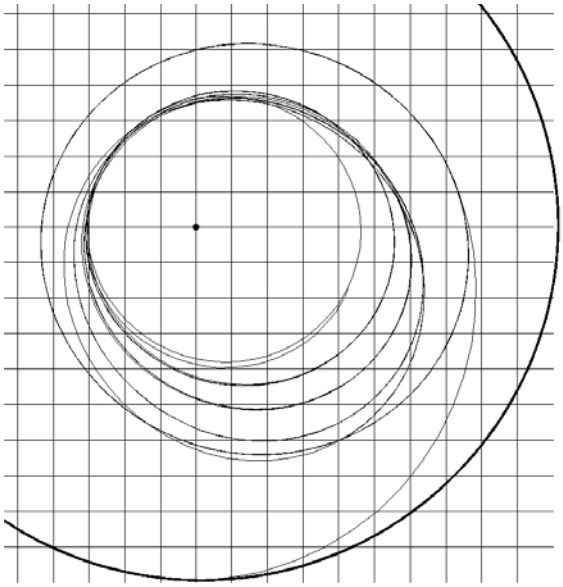

Figure 5.1.6. Transfer with VGA/VGA/MGA/MGA/MGA/MGA/MGA for 2004 case.

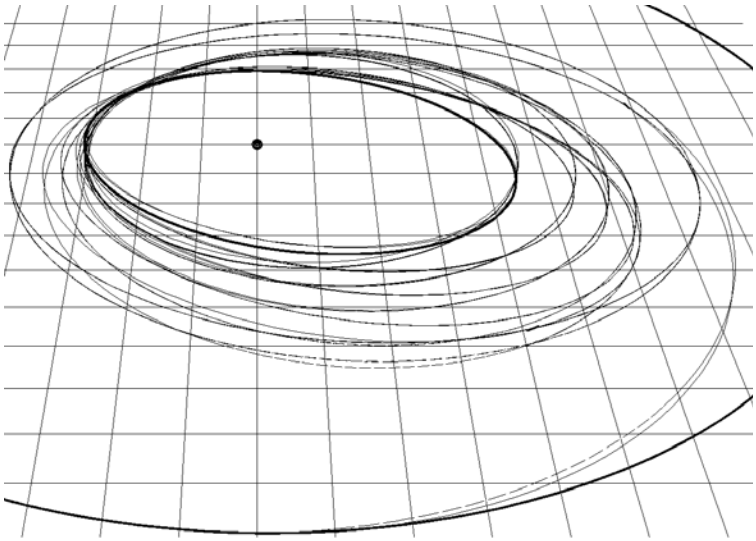

Figure 5.1.7. Transfer with VGA/VGA/MGA/MGA/MGA/MGA/MGA for 2004 case, showing out-of-ecliptic motion. The outer thicker black line shows Earth's orbit, and Mercury's orbit is also shown. The sub-grid elements are 0.1 AU from edge to edge. The dashed lines show the projection of the orbit in the ecliptic. Therefore, the inclination achieved in the 4 : 3 Venus resonant phase can be seen and also that in the Mercury resonant phases.

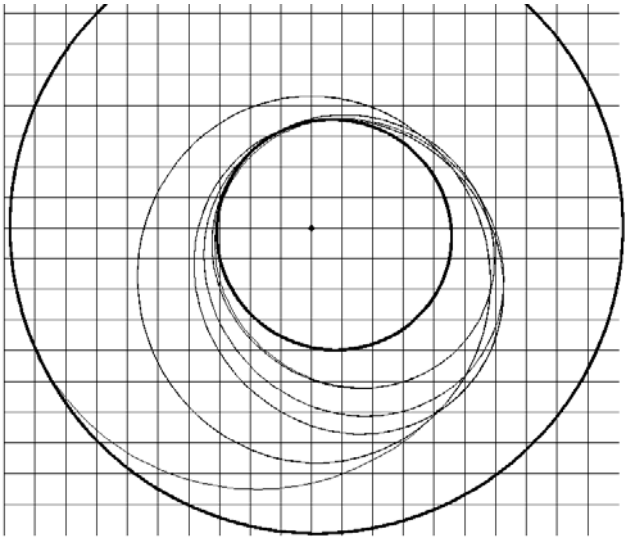

Figure 5.1.8. Transfer with VGA/VGA/MGA/MGA for 2009 launch case. Earth and Mercury orbits are shown as bolder lines. The sub-grid elements are 0.1 AU from edge to edge.

Table 5.1.18. Transfer fly-bys and manoeuvres for short Mercury transfer with launch in 2009.

Event	Parameters	Description	ΔV
Launch	$V_\infty = 3.93$ km/s 9 Jan 2009	Transfer orbit to Venus RV after 0.5 revs	1,450 m/sec
GA 1 at Venus to a 4 : 3 resonant orbit	$V_\infty = 7.47$ km/s 14 Apr 2009	Achieve 4 : 3 resonant orbit	
GA 2 at Venus to 3.5 heliocentric revolution transfer to rendezvous with Mercury	$V_\infty = 7.47$ km/s 17 Feb 2011	Transfer orbit to Mercury RV after 3.5 revs	
GA 3 at Mercury to 3 : 2 resonant orbit	$V_\infty = 5.8$ km/s 7 Nov 2012	Achieves 3 : 2 resonant orbit	20 m/s
GA 4 at Mercury to 3 : 4 resonant orbit	$V_\infty = 5.8$ km/s 28 Jul 2013	Achieves 4 : 3 resonant orbit	340 m/s
Inject to Mercury elliptical orbit	$V_\infty = 3.45$ km/sec 24 Jul 2014		1,627 m/s
Total ΔV inc Earth escape from GTO altitude orbit			3,437 m/sec

only uses two MGAs to achieve a faster transfer but with a greater capture manoeuvre requirement. Consequently, the total ΔV is therefore significantly higher than the 2004 example. It is a truncated version of the 2004 transfer type described previously, but could be extended in the same way with additional gravity assists at Mercury into lower resonant orbits.

The ΔV would then be similar to the 2004 case.

5.1.2 Messenger to Mercury

A second mission to Mercury will now be considered, similar to the NASA Messenger mission design. A launch in March of 2004 is a feasible option. However, Messenger was actually launched in August 2004 and will arrive at Mercury in 2011. The spacecraft will perform a series of gravity assists at Earth, Venus and Mercury, as well as a number of manoeuvres in deep space, before capturing into Mercury orbit. A mission description may be found in the references for this section.

Departure in 2004 is into a 1 : 1 resonant orbit with Earth, so that it returns in August 2005 to perform an Earth gravity assist where it changes its departure declination. The spacecraft therefore finally leaves Earth in 2005 after the gravity assist, with an excess hyperbolic speed of just over 4 km/sec. For a final Earth departure in 2005, two routes to Venus are possible:

- A direct, conjunction-type transfer
- A 1.5-revolution transfer.

This later option is effective in arranging a Venus rendezvous in a favourable location for a subsequent transfer to Mercury. The components of this transfer can now be examined.

Figure 5.1.9 shows a high energy one point five revolution transfer, leaving Earth with a Vinfinity of typically 5.9 km/sec. No deep space manoeuvres are considered at this point, which can in fact be used to reduce this departure speed. The corresponding excess hyperbolic speed at Venus is then approximately 9.5 km/sec.

This sequence forms a key part of the Messenger mission. After reaching its first rendezvous with Mercury, a sequence of gravity assists are performed as in the case described previously for a March 2004 launch. Intermediate orbits have a 2 : 3, 3 : 4 and 5 : 6 resonance with Mercury. Orbit insertion about Mercury then occurs at the next rendezvous.

Figures 5.1.10 and 5.1.11, and Table 5.1.19 show an optimised route to Mercury, finally leaving Earth in August 2005 and using the building blocks just described. This trajectory follows the same type of route to Mercury as Messenger.

Deep-space manoeuvres are included to improve the efficiency of the mission. Firstly, the excess hyperbolic speed leaving Earth can be reduced from 5.9 km/sec, used in the first example, to 4.1 km/sec by including a deep-space manoeuvre close to first perihelion to raise aphelion, before reaching Venus. Then, a sequence of aphelion manoeuvres are included after the final VGA and between the MGAs, to reduce the excess hyperbolic speed at Mercury. The transfer inclination is increased

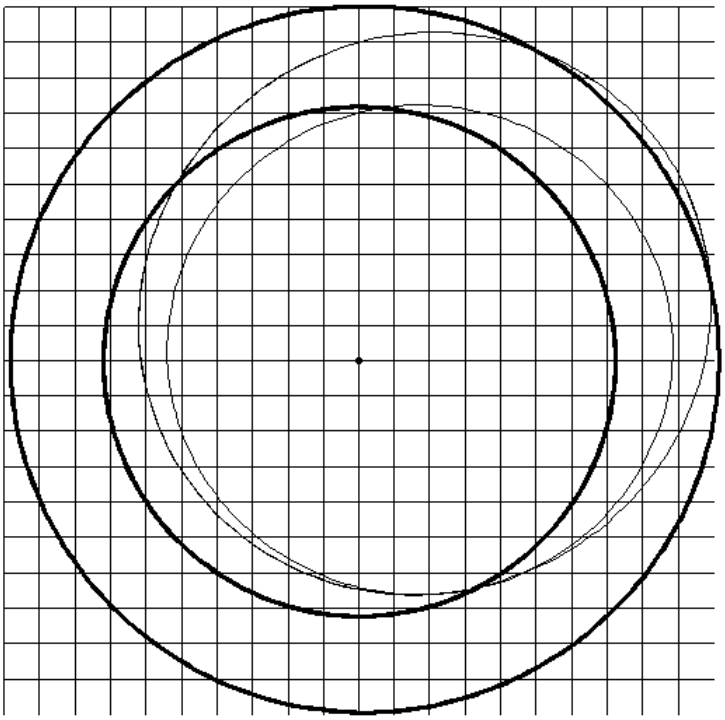

Figure 5.1.9. Messenger type mission: initial Earth to Venus and Venus 1 : 1 resonant phases. The grid is 1 AU from centre to edge with a sub-grid size of 0.1 AU. On reaching Venus a high-altitude fly-by allows a gravity assist to reach a 1 : 1 resonant orbit with Venus. On return to Venus a second gravity assist results in perihelion being lowered to approximately 0.32 AU, which is sufficient to rendezvous with Mercury close to its perihelion. Mercury is reached after a further 1.5 revolutions.

to approximately 7° after the first VGA, which reduces the eventual excess hyperbolic speed when approaching Mercury.

Insertion into Mercury orbit is made from a heliocentric orbit in 5 : 6 resonance with Mercury. A trade-off in the mission design would allow a reduction in the approach speed by using the 1 : 1 resonances described in the previous transfer example. However, if the launcher can inject a spacecraft with sufficient fuel, then there is no requirement for further fuel saving which is associated with an increased duration.

Also, in principle, launch in August 2005 can be considered, omitting the Earth 1 : 1 resonant orbit. The departure declination from Earth in that case must be that required to transfer to Venus. The achievable declinations for a given launch vehicle depend upon its launch site latitude and any path constraints on the launch trajectory.

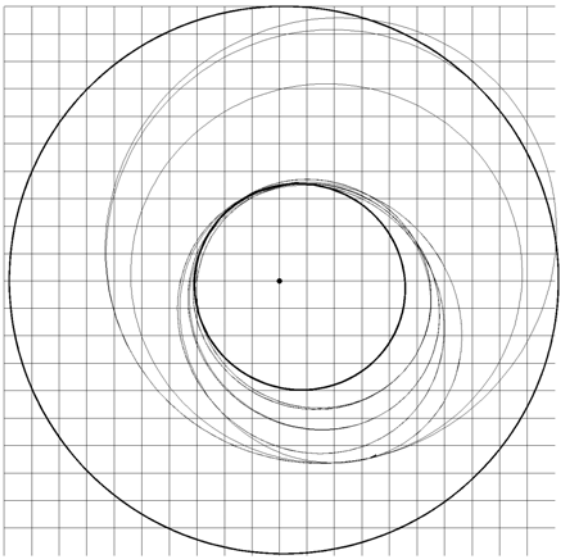

Figure 5.1.10. Messenger type mission. Transfer with VGA/VGA/MGA/MGA/MGA for final Earth departure in August 2005. Earth and Mercury orbits are thick line traces. The grid is 1 AU from centre to edge, with a sub-grid of 0.1 AU.

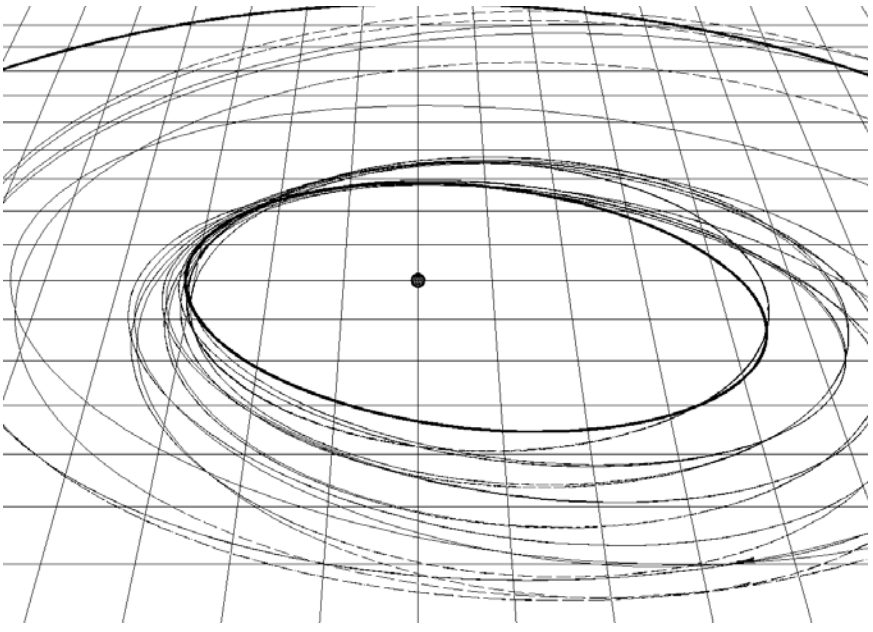

Figure 5.1.11. Messenger type mission. Transfer with VGA/VGA/MGA/MGA/MGA for final Earth departure in August 2005, showing motion out of the ecliptic. The projection of the trajectory in the ecliptic is a dashed line.

Table 5.1.19. Summary of a Messenger type of transfer to Mercury.

Event	Parameters	Description
Earth departure August 2004	$V_\infty = 4.1$ km/s	1 : 1 resonant orbit with Earth
Earth departure August 2005	$V_\infty = 4.1$ km/s	Transfer orbit to Venus RV after 1.5 revs
GA 1 at Venus to a 1 : 1 resonant orbit October 2006	$V_\infty = 9.5$ km/s	Achieve 1 : 1 Venus resonant orbit with 7.5-deg inclination
GA 2 at Venus to 1.5 heliocentric revoluton transfer to rendezvous with Mercury June 2007	$V_\infty = 9.5$ km/s	Transfer orbit to Mercury RV after 1.5 revs
GA 3 at Mercury to 3 : 2 resonant orbit January 2008	$V_\infty = 5.7$ km/s	Achieves Mercury 3 : 2 resonant orbit
GA 4 at Mercury to 4 : 3 resonant orbit September 2008	$V_\infty = 6$ km/s	Achieves Mercury 4 : 3 resonant orbit
GA 5 at Mercury to 6 : 5 resonant orbit September 2009	$V_\infty = 3.7$ km/s	Achieves Mercury 6 : 5 resonant orbit
Inject to Mercury elliptical orbit March 2011	$V_\infty = 2.2$ km/s	

5.1.3 Gravity assist for Mars return missions

A key feature of return missions to Mars is the stay time that is needed before an efficient return to Earth can be arranged. This subject is discussed in Chapter 1. However, the return transfer from Mars to Earth is often subject to stay-time constraints in the vicinity of Mars. As a result, the spacecraft is required to return at non-optimal epochs. This has implications on the mission ΔV and transfer time.

An attractive option is to use a Venus gravity assist manoeuvre on the return route. Such scenarios have a characteristic return time of typically 300 days. This offers an additional transfer opportunity, supporting shorter stay-times at Mars. ΔV is higher than the nominal conjunction case, but for a comparable return time, less than the case without the gravity assist. Such return options are described in Chapter 1.

These options can be found for many launch epochs from Mars to Earth. Alternatively, this option can be used for an outbound Venus gravity assisted transfer, short stay time, and a standard conjunction-type return transfer from Mars to Earth.

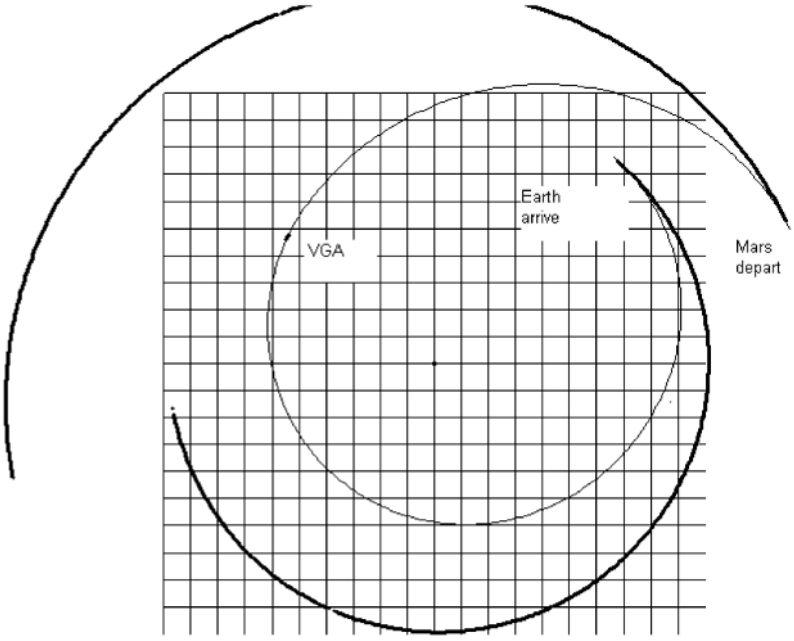

Figure 5.1.12. Return from Mars via Venus gravity assist. Mars departure in September 2014. The grid is 1 AU from centre to edge, with a sub-grid of 0.1 AU. The orbits of Earth and Mars are shown as thicker lines.

The principle is to depart from Mars and transfer to Venus. A gravity assist at Venus then allows a return to Earth. At certain epochs it is possible to generate such a transfer without the need for any deep-space ΔVs. However, deep space manoeuvres are often needed to enable such a transfer at non-optimal launch periods.

Figure 5.1.12 illustrates the characteristics of such a mission option. A higher escape velocity from Mars is required than in a standard conjunction-type return to Earth, as Venus's orbit must be reached. The effect of the Venus gravity assist is to lower the aphelion, such that the arrival excess hyperbolic speed is reduced.

5.1.4 Reaching Jupiter

Previous sections have shown that a direct conjunction-type transfer to Jupiter results in large ΔV requirements on the spacecraft and launcher. However, gravity assist is a well known strategy for alleviating the problems of a transfer to Jupiter. The objective is to reduce the ΔV requirements, whilst still maintaining an acceptable total transfer time.

The basic strategy is to increase the excess hyperbolic speed, at the last gravity assist planet, to a value and direction that allows transfer to Jupiter. At Earth, this would be typically 8 km/sec.

The main options that can be considered are:

Option	*Comment*
Use of EGA or multiple EGA to provide aphelion-raising	Use of EGA potentially provides large ΔV reduction. If used alone, a deep-space manoeuvre is needed to increase the fly-by velocity on returning to Earth. Transfer time will increase because of the requirement for resonance between manoeuvres.
Use of VGA to provide aphelion-raising	Use of VGA in addition to EGA allows increase in the V_∞ on returning to Earth. VGA or multiple VGAs can be considered, in a similar manner to multiple EGAs.
Use of a Jovian moon gravity assist to assist in capture	

Although EGA alone or VGA alone can be considered, substantial deep-space manoeuvres or manoeuvres at the pericentre of the fly-by are needed to reach Jupiter. These are not particularly effective strategies.

A combination of a single VGA and a single EGA can be considered, but the cases offering most ΔV reduction use multiple EGA or VGA. Examples of such missions are the Galileo mission, launched in 1989, reaching Jupiter six years later, and Cassini, launched in 1997. Cassini flew by Jupiter *en route* to Saturn.

Mars can also be used to provide a gravity assist in such transfers. However, as Mars is significantly less massive than Venus, the gains from gravity assist are more limited and so many mission designs focus on Venus and Earth as gravity-assist targets.

Such transfers offer many permutations of transfer routes. Precise repeats of a given route recur very infrequently, because the synodic periods of Earth, Venus and Jupiter must be considered. A given mission will reoccur after 24 years, although the repeat is not exact; but is similar in ΔV magnitude and duration. However, launch possibilities occur much more frequently than this. The synodic period of Earth and Venus is a driving factor, as the first gravity assist in the sequence usually involves Venus.

A number of transfer possibilities will now be discussed, focusing on Venus and Earth gravity assists to aid the transfer.

The V-V-E sequence

This sequence of gravity assists was used by Cassini to reach Jupiter. It then performed a gravity assist at Jupiter to reach Saturn. However, the strategy is easily modified to ensure a lower-speed approach at Jupiter, suitable for capture.

Table 5.1.20 shows the portion of the transfer from Earth to arrival at Jupiter. (The Cassini mission is described more fully in the references for this chapter.) The

total transfer time for this trajectory in reaching Jupiter is approximately 3 years, but the speed relative to Jupiter in this case is high. A deep space ΔV ($\sim$450 m/s) is required to increase the orbital eccentricity prior to the second Venus fly-by. The spacecraft has high energy at Jupiter as it is heading for Saturn and not capture at Jupiter. Initial Earth departure is at an excess hyperbolic speed of approximately 5 km/sec.

A modification to achieve rendezvous at Jupiter results in the sequence shown in Table 5.1.21 and Figure 5.1.13. In this modified transfer the deep-space manoeuvre reduces to approximately 200 m/s. The arrival excess hyperbolic speed at Jupiter is now reduced to just over 6 km/s, but the time taken to reach Jupiter is now longer. The total mission takes just under 5 years to reach a Jupiter rendezvous.

The V-E sequence

With this transfer option only two gravity assists are involved, and it is therefore potentially a faster route to Jupiter than those involving more gravity assists. It is possible to carry out a first gravity assist at Venus and then return directly to Earth for a second gravity assist. A transfer to Venus with perihelion at 0.65 AU results in a Vinfinity at Venus of typically 6.5 km/sec. A close fly-by would result in aphelion being raised to over 1.7 AU, with perihelion just below Venus at 0.72 AU. If phasing between Earth and Venus is neglected (or many intermediate revolutions allowed), then return to Earth would result in an excess hyperbolic speed of approximately 12 km/sec. A gravity assist at Earth would result in aphelion raised to 4.5 AU, with perihelion at 0.9 AU (assuming a close fly-by at 300 km altitude). A ΔV of approximately 500 m/s would result in aphelion being raised to 5.2 AU, so that a rendezvous with Jupiter would be possible.

Table 5.1.20. The Cassini mission to Saturn.

Launch (into low-energy Earth–Venus transfer)	October 1997
First Venus fly-by	April 1998
Deep-space manoeuvre	December 1998
Second Venus fly-by	June, 1999
Earth fly-by	August, 1999
Jupiter fly-by	December 2000
Saturn rendezvous	2004

Table 5.1.21. Adaptation of a Cassini-like mission to rendezvous at Jupiter.

Launch (into low-energy Earth–Venus transfer)	August 1997	$V_\infty = 5.3$ km/s
First Venus fly-by	April 1998	$V_\infty = 6.1$ km/s
Deep-space manoeuvre	October, 1998	0.2 km/s
Second Venus fly-by	July 1999	$V_\infty = 7.9$ km/s
Earth fly-by	August 1999	$V_\infty = 13.8$ km/s
Jupiter arrival	January or July 2002	$V_\infty = 6.2$ km/s

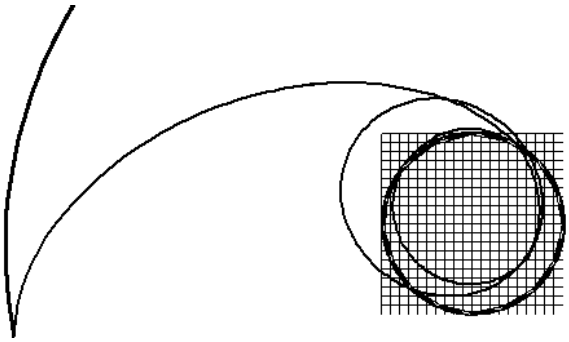

Figure 5.1.13. The V-V-E Cassini mission launched in 1989 and adapted to terminate at Jupiter. The two fly-bys at Venus are separated by a two Venus-year resonant orbit. After finally leaving Venus, the spacecraft flies by Earth before making a rendezvous with Jupiter. Earth and Jupiter orbits are shown. The grid is 1 AU from centre to edge, with a sub-grid of 0.1 AU.

Table 5.1.22. Example of transfer to Jupiter with a V–E sequence. In this case the total deep-space ΔV is approximately 2,100 m/s.

Launch (into low-energy Earth–Venus transfer) April 2012	Vinfinity = 3.2 km/sec
Venus fly-by October 2012	Vinfinity = 6.6 km/sec (fly-by altitude = 16,500 km)
Earth fly-by August 2013	Vinfinity = 9.8 km/sec (fly-by altitude = 5,800 km)
Jupiter arrival July 2016	Vinfinity = 5.5 km/sec

However, with this semi-major axis and orbital period, the phasing of the Earth return is made difficult, and multiple revolutions may be needed before an encounter is possible. The fastest transfer solution can be found by using an aphelion, after the gravity assist at Venus, of typically 1.4 AU. This allows Earth to be re-encountered during the first revolution after VGA. However, in this case the maximum aphelion that may be reached is approximately 3.4 AU (with a fly-by at Earth at 300 km altitude). A deep space ΔV of 1,500–2,000 m/s is required to ensure a Jupiter rendezvous (see Table 5.1.22).

The V-E-E sequence

The previous transfer can be extended by use of a second gravity assist at Venus. Firstly, the case of the Galileo mission will be considered.

Table 5.1.23 shows the Galileo transfer parameters (see references for this section). The total transfer time for this is approximately 6 years. The nature of this particular transfer is such that no deterministic deep space ΔV is required. The excess hyperbolic speed leaving Earth is also low, at approximately 3 km/sec. When

Table 5.1.23. The Galileo transfer to Jupiter.

Launch (into low-energy Earth–Venus transfer)	October 1989
Venus fly-by	February 1990 (fly-by altitude = 19,400 km)
First Earth fly-by	December 1990 (fly-by altitude = 3,700 km)
Second Earth fly-by	December 1992 (fly-by altitude = 300 km)
Jupiter arrival	December 1995

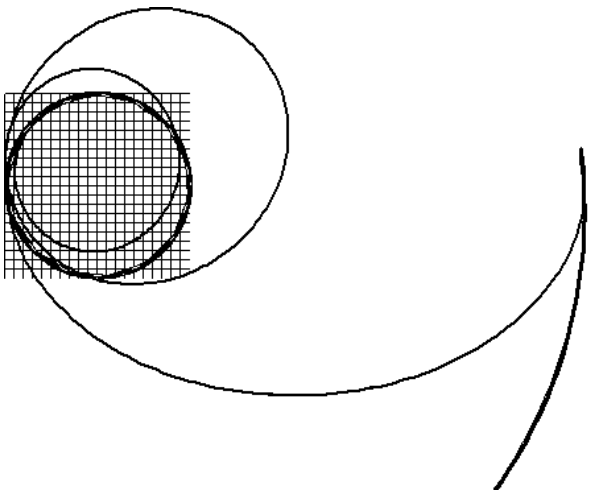

Figure 5.1.14. The V-E-E Galileo mission, launched in 1989. The orbits of Earth and Jupiter are shown. The grid is 1 AU from centre to edge, with a sub-grid of 0.1 AU. The Galileo transfer started in 1989 and first performed a Venus gravity assist. Two Earth gravity assists followed, separated by a two-year Earth resonant orbit. The total transfer took approximately 6.2 years, and required no deterministic deep-space manoeuvres.

compared with the previous Cassini adaptation this is a more efficient route, but takes just over one year longer to reach Jupiter. The transfer is seen in Figure 5.1.14.

A near-identical launch and transfer is possible with a launch in October 2013, following a V-E-E route to arrive at Jupiter in December 2019. This transfer is almost the same as the Galileo transfer of 1989, as it would leave 24 years after Galileo left Earth.

Many future launch opportunities using this strategy are possible. A launch in 2012 is a particularly efficient case (see Table 5.1.24 and Figure 5.1.15).

Table 5.1.24. A V-E-E transfer to Jupiter after launch in 2012.

Launch (into low-energy Earth–Venus transfer)	Vinfinity = 3.4 km/sec April 2012
Venus fly-by	October 2012 (fly-by altitude = 9,000 km)
First Earth fly-by	August 2013 (fly-by altitude = 5,800 km) Vinfinity = 9.8 km/sec
Second Earth fly-by	December, 2015 (fly-by altitude = 300 km) Vinfinity = 9 km/sec
Jupiter arrival	October 2018 Vinfinity = 5.5 km/sec

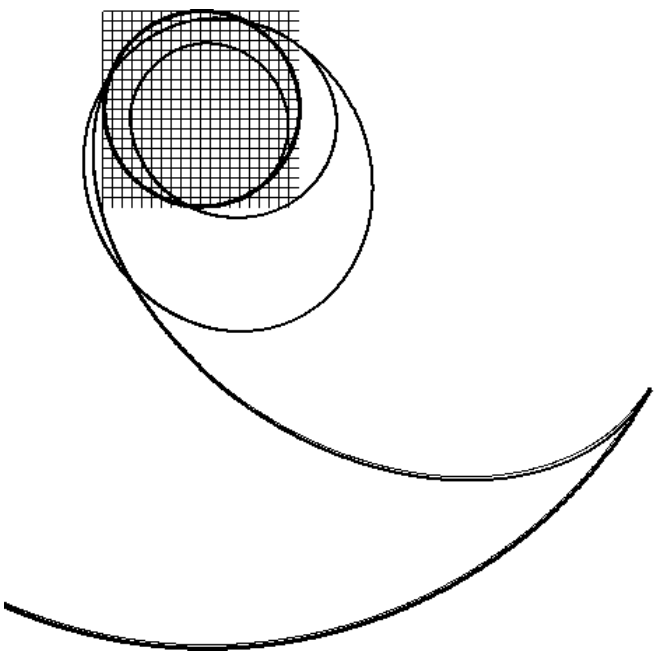

Figure 5.1.15. Multiple gravity assist transfer with a launch in 2012. This uses the efficient strategy of gravity assists at Venus followed by two at Earth, as did Galileo. The orbits of Earth and Jupiter orbits are shown. The grid is 1 AU from centre to edge. The near two-year resonant orbit returns to Earth after 2.3 years, so that rendezvous occurs at the second intersection point of the transfer orbit with Earth's orbit. This strategy allows better phasing between Venus, Earth and Jupiter than a two-year return to Earth at the fixed intersection.

5.1.5 Gravity-assisted tours of Jupiter's moons

The objective of this analysis is to find an efficient way to reach an orbit about the Jovian moon, Europa, from an initial hyperbolic approach orbit to Jupiter. The aims of the transfer are to reach the target in an acceptable period of time and to use low ΔV to reach the final target orbit about Europa.

The assumptions are:

- The initial Jupiter bound orbit is reached after a Ganymede fly-by to reduce energy with respect to Jupiter, followed by application of a retro-ΔV at the subsequent Jovian pericentre.
- The target apocentre after orbit capture (retro-burn) is approximately 20 million km.
- The pericentre after the Ganymede gravity assist is 900,000 km (see discussion in Chapter 4).
- Inclination: ecliptic.

Firstly, an approximated sequence is generated via a 2D patched conic analysis within the jovian system and by examination of loci of the orbit evolution using Tisserand's criterion. All orbits are assumed to be co-planar.

The first problem is to decide on the best route to reach Europa. If a plot of period/pericentre loci for a gravity-assist sequence at the different moons is made, then Ganymede presents a good option for initial orbit energy reduction. Initially, Europa is ineligible because the pericentre lies above the moon's orbital radius (see Figure 5.1.16).

The initial excess hyperbolic speed with respect to Ganymede, for the first Jupiter bound orbit described is approximately 6.5 km/sec. The pericentre becomes lower than Europa when the orbital period is close to 15 days (or apocentre at typically 2.3 million km). At this point, Europa gravity assists may be considered. Numerous examples of mission designs using multiple gravity assists in the Jovian system have been developed. These have been of particular interest for the Galileo mission, and some examples are given in the references for this chapter.

As the ultimate objective is to insert into orbit about Europa, the excess hyperbolic speed there should ultimately be low to reduce orbit injection ΔV requirements. The lowest Europa Vinfinity loci are reached if the first Europa gravity assist in the sequence is initiated when pericentre falls just below Europa's orbital radius. A sequence of gravity assists at Europa would then result in further orbital energy reduction. However, it is desirable to reduce the excess hyperbolic speed at Europa. This can be achieved in a number of ways. Some attractive options are:

(1) A manoeuvre to raise pericentre so that it lies closer to Europa.
(2) Further gravity assists at Ganymede (or even Callisto) to raise pericentre so that it lies closer to Europa (performed after a number of Europa gravity assists are made).

Both options are effective at reducing excess hyperbolic speed at Europa. The second option uses less (or potentially even zero) ΔV in reducing the speed, but intermediate

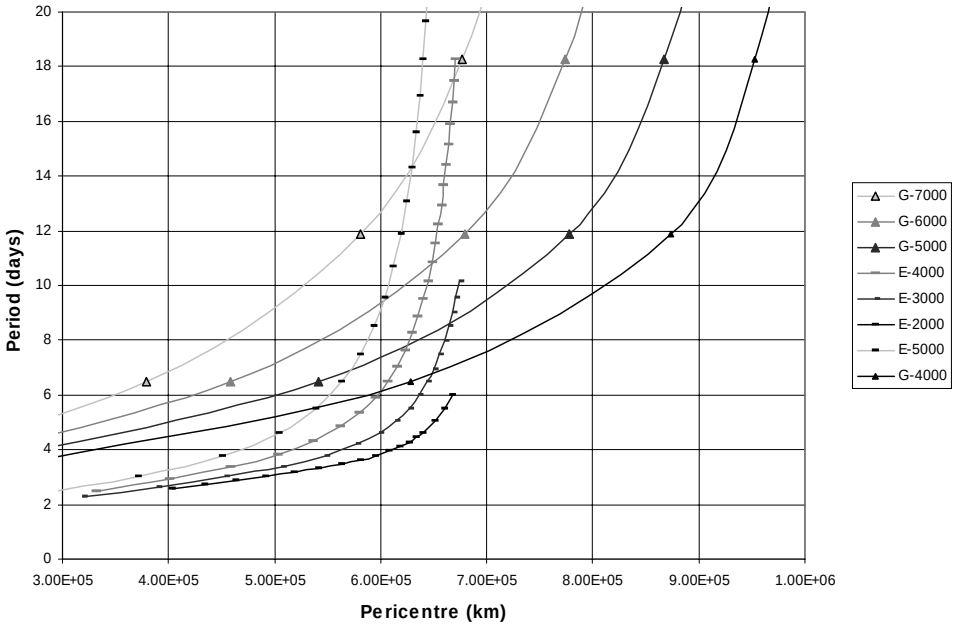

Figure 5.1.16. Period–pericentre loci for a range of Ganymede and Europa Vinfinities. Ganymede Vinfinities from 4,000 to 7,000 m/s are shown and those of Europa from 2,000 to 5,000 m/s.

phasing orbits are needed to accomplish the transfer between rendezvous at the different moons involved. The first option requires no additional phasing orbits, but requires ΔV to execute the reduction. Both routes can be assessed in greater detail.

Both will start with a sequence of gravity assists at Ganymede until pericentre is lowered below Europa. Resonant orbits with Ganymede are generated by selection of the appropriate fly-by distance at Ganymede. No ΔV is needed in this sequence. A key factor here is the Jupiter pericentre radius at the first Europa gravity assist. This should lie as close as possible to Europa's orbital radius to minimise the excess hyperbolic speed at Europa, but the constraints of resonant orbit sequences at Ganymede means that there are limitations as to how closely this condition can be achieved without using excessively long transfer durations. Therefore, a compromise is reached in this example. It is possible to obtain slightly lower ΔV solutions.

Having reached Europa, the manoeuvre option (1, above) is first considered. The sequence used is shown in Table 5.1.25. As apocentre is reduced further by gravity assist at Europa, the excess hyperbolic speed may be reduced by small manoeuvres at the apocentre, raising the pericentre to just below Europa's orbital radius. The first manoeuvre is the largest in the sequence, as the initial pericentre lies quite a way below Europa as a result of the previous resonant orbit required at Ganymede. Resonant orbits with Europa are generated by selecting the fly-by distance to achieve the required semi-major axis.

Table 5.1.25. Gravity assist and manoeuvre sequence in the Jovian system for orbit insertion strategy 1 at Europa.

Event	Apocentre (km)	Pericentre (km)	Period (days)	V_∞ (m/s)	Resonance	ΔV (m/s)
Capture	20,218,103	900,000	221		31 : 1	
Ganymede	7,712,518	847,482	57	6,553	8 : 1	
Ganymede	4,604,948	787,514	29	6,553	4 : 1	
Ganymede	3,223,221	718,692	18	6,553	5 : 2	
Ganymede	2,321,376	618,442	12	6,553		
Europa	2,177,449	613,607	11	4,969	3 : 1	
ΔV	2,177,449	664,000	11	3,383	3 : 1	157
Europa	1,916,281	657,025	9	3,383	8 : 3	
ΔV	1,916,281	664,000	9	3,119	8 : 3	23
Europa	1,696,509	656,797	8	3,119	7 : 3	
ΔV	1,696,509	664,000	8	2,847	7 : 3	25
Europa	1,465,975	654,441	7	2,847	2 : 1	
ΔV	1,465,975	664,000	7	2,495	2 : 1	37
Europa	1,284,558	654,625	6	2,495	7 : 4	
ΔV	1,284,558	664,000	6	2,152	7 : 4	38
Europa	1,094,256	651,110	5	2,152	3 : 2	
ΔV	1,094,256	664,000	5	1,707	3 : 2	57
Europa	893,021	643,557	4	1,707	5 : 4	
ΔV	893,021	664,000	4	1,102	5 : 4	99
Europa	765,826	644,755	4	1,102	11 : 10	
ΔV	765,826	664,000	4	624	11 : 10	98

As the sequence progresses, the accumulated apocentre manoeuvre ΔV increases but the hyperbolic excess velocity with respect to Europa decreases (and so the orbit insertion ΔV from such a hyperbolic approach decreases). After a certain number of fly-bys, a minimum total ΔV is reached (accumulated apocentre plus orbit insertion). The total ΔV is given by:

$$\Delta V_{total} = \sum_i \Delta V_{api} + \sqrt{\frac{2\mu_{Europa}}{r_{EuropaOrbit}} + V^2_{\infty final}} - \sqrt{\frac{\mu}{r_{EuropaOrbit}}} \tag{5.1.1}$$

where ΔV_{api} is the ΔV applied at the apocentre, i to raise the pericentre. $V_{\infty final}$ is the excess hyperbolic speed at Europa from which insertion to Europa orbit is made, and $r_{EuropaOrbit}$ is the radius of the circular orbit about Europa.

The total ΔV for this sequence, including insertion to a 200-km circular orbit at Europa, is approximately 1,100 m/s. Using more gravity assists at Europa increases this ΔV, due to increases in the pericentre raising ΔV eventually outweighing the effect of the excess hyperbolic speed reduction. The period-pericentre laws for this sequence is illustrated in Figure 5.1.17.

The Ganymede gravity assist option is now considered. The sequence used is shown in Table 5.1.26 and Figure 5.1.18, plotted on loci of constant excess hyper-

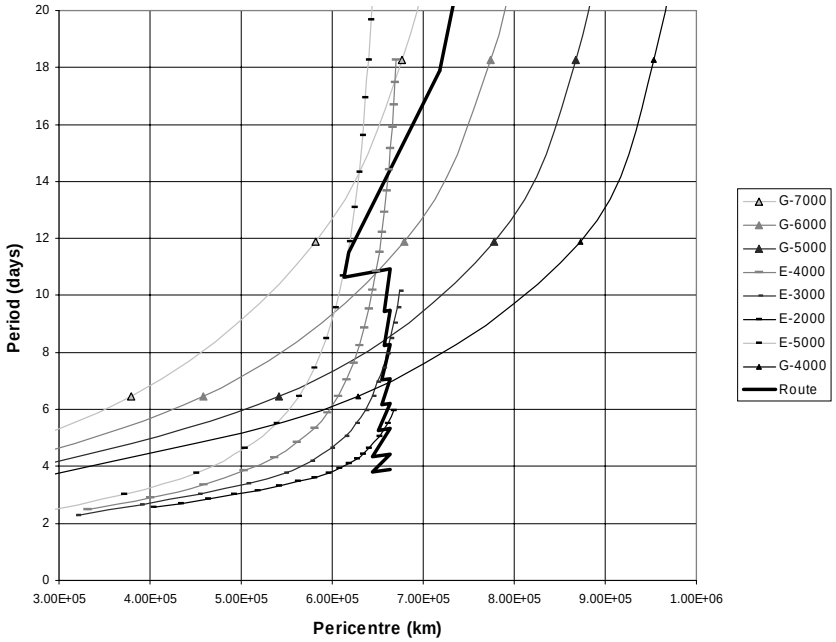

Figure 5.1.17. Gravity assist and manoeuvre sequence in the Jovian system for orbit insertion strategy 1 at Europa plotted over period–pericentre loci at Ganymede and Europa.

Table 5.1.26. Gravity assist and manoeuvre sequence in the Jovian system for orbit insertion strategy 2 at Europa.

Event	Apocentre (km)	Pericentre (km)	Period (days)	V_∞ (m/s)	Resonance	ΔV (m/s)
Capture	20,218,103	900,000	222		31 : 1	
Ganymede	7,712,518	847,482	57	6,553	8 : 1	
Ganymede	4,604,948	787,514	29	6,553	4 : 1	
Ganymede	3,223,221	718,692	18	6,553	5 : 2	
Ganymede	2,321,376	618,442	12	6,553		
Europa	1,873,702	600,456	9	4,969		
Ganymede	2,147,032	664,506	11	5,883		
Europa	1,973,573	660,187	10	3,210	11 : 4	
Europa	1,654,999	648,966	8	3,210	9 : 4	
Europa	1,319,465	629,092	6	3,210		
Ganymede	1,360,010	662,086	6	3,733		
Europa	1,222,197	653,882	6	2,209	5 : 3	
ΔV	1,222,197	664,000	6	1,847		−43
Europa	1,094,256	655,272	5	1,847	3 : 2	
ΔV	1,094,256	664,000	5	1,533		−39
Europa	893,469	644,110	4	1,533	5 : 4	
ΔV	893,469	664,000	4	945		−96
Europa	771,907	648,514	4	945	11 : 10	
ΔV	771,907	664,000	4	479		−78

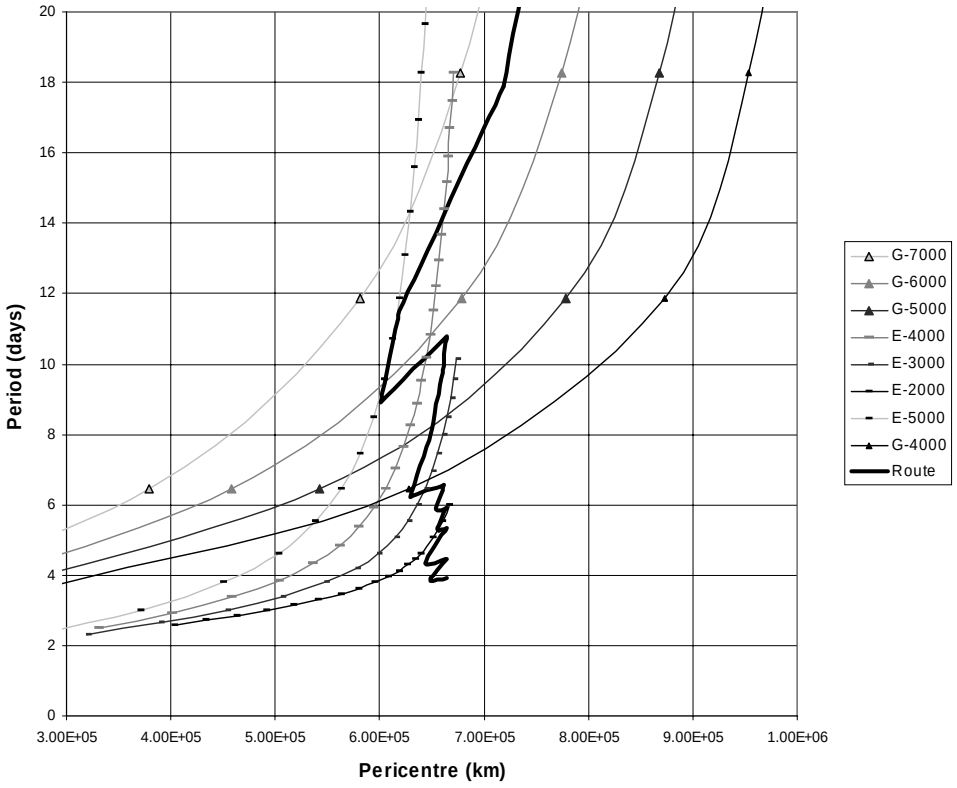

Figure 5.1.18. Gravity assist and manoeuvre sequence in the Jovian system for orbit insertion strategy 2 at Europa plotted over period–pericentre loci at Ganymede and Europa.

bolic speed at Ganymede and Europa. Firstly, the energy-reducing sequence occurs at Ganymede, where excess hyperbolic speed remains constant. The sequence then switches to Europa and then back to Ganymede to raise pericentre. A sequence of three gravity assists at Europa follows, with excess speed reduced following the Ganymede gravity assist. This sequence reduces the apocentre before the pericentre is once again raised by switching back to a Ganymede gravity assist. On returning to Europa the excess speed is reduced further, to approximately 2 km/sec. The next two gravity assists at Europa lower the apocentre to approximately the orbital radius of Ganymede, so further gravity assists there are no longer possible.

Once again, as the apocentre is reduced further by gravity assist at Europa, the excess hyperbolic speed there may be reduced by small manoeuvres at the apocentre, raising the pericentre. The sequence is terminated when the excess hyperbolic speed is again reduced to approximately 500 m/s.

The total ΔV for this sequence, including insertion to a 200-km circular orbit at Europa, is approximately 1,000 m/s. As in the previous example, using more or less gravity assists at Europa increases this ΔV.

This sequence contains approximations, because:

- Only 2D motion is considered.
- The phasing between Ganymede and Europa is not considered. An ideal transfer with no ΔV to assist (or speed up) the phasing is assumed.

Therefore, the use of Ganymede in controlling pericentre results in some significant ΔV reduction, but only a fraction of that needed for final orbit insertion. The durations of the two idealised sequences is similar. However, when the insertion of additional phasing orbits between Ganymede and Europa rendezvous are considered, the Ganymede pericentre raising option will generally become longer. Also, with the manoeuvre option used for pericentre control, the minimum radius remains higher on average throughout the sequence. This can be a significant issue in the presence of Jupiter's radiation belts.

The sequence may be verified by a full 3D simulation and optimisation in the Jovian system. This is shown in Figure 5.1.19 for strategy 1 in the previous examples.

The total ΔV is minimised (the sum of apocentre manoeuvres plus insertion ΔV). The total ΔV is 1,260 m/s, and the total time from first pericentre to Europa orbit insertion is 546 days.

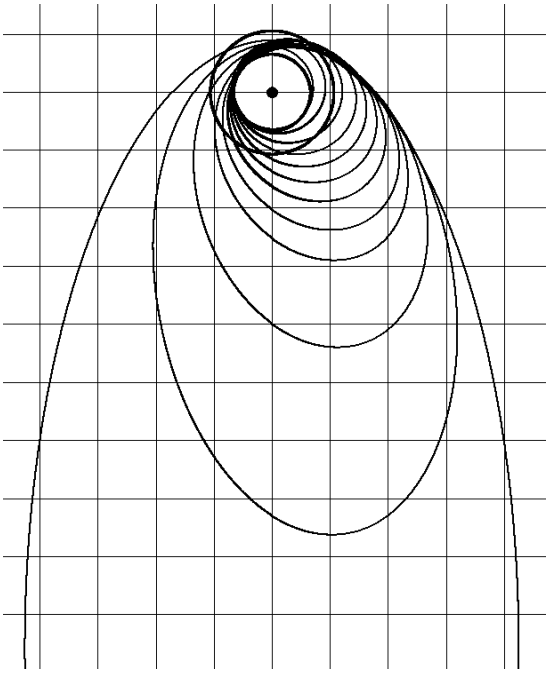

Figure 5.1.19. Sequence of gravity assists at Ganymede and Europa. The unit grid size is 1 million km in width. Jupiter is not to scale. Ganymede's and Europa's near-circular orbits are shown. Eleven gravity assists take place: four at Ganymede, then the pericentre can be seen to pass below Europa such that the sequence of seven gravity assists may begin there.

These results are similar to the approximated 2D analysis. The ΔV is slightly higher because additional manoeuvres to establish phasing and plane-change between Ganymede and Europa sequences are needed (totalling approx 100 m/s).

5.1.6 Transfers to the outer planets

Reaching the outer planets can be a formidable problem, and is often impractical without the use of gravity-assist manoeuvres. For the four planets beyond Jupiter, gravity assist at Jupiter itself is an attractive possibility. Being the most massive planet, considerable orbit modification is possible through a Jupiter gravity assist. A classical example of such a transfer is Voyager. This mission is described more fully in the references.

The objective is to achieve moderate ΔV requirements, whilst still maintaining an acceptable total transfer time. The major options that can be considered are an extension of the Jupiter mission options, and can be summarised as follows:

Strategy	*Observations*
Use of EGA or multiple EGA to provide aphelion-raising	Use of EGA potentially provides a large ΔV reduction. If multiple EGA are used, a deep-space manoeuvre is needed to increase the fly-by velocity on returning to Earth.
Use of VGA to provide aphelion-raising	Use of VGA may provide a ΔV reduction. VGA or multiple VGAs can be considered, in a similar manner to multiple EGAs, and also in conjunction with subsequent EGA to provide further ΔV reduction.
Use of JGA to provide aphelion-raising	Use of JGA is very effective in raising both aphelion and perihelion. This has two benefits: 1. reduces the transfer ΔV to reach the target planet. 2. Reduces the approach V_∞ at the target planet and so reduces the ΔV for orbit insertion. Although Jupiter is very effective in assisting transfers to the outer planets, the synodic period between Jupiter and any planet beyond Jupiter is relatively high. Optimal opportunities arise relatively infrequently.

Although EGA alone or VGA alone can be considered, substantial deep-space manoeuvres or manoeuvres at the pericentre of the fly-by are needed to reach the outer planets. These are not particularly effective strategies. A combination of VGA, EGA and JGA can be considered, but the cases offering most ΔV reduction generally use multiple EGA, VGA and a single JGA.

Such transfers offer many permutations of transfer routes. Repeats of a given route only recur very infrequently, because the combined synodic periods of Earth, Venus, Jupiter and the target planet must be considered.

Some examples of transfers to the outer planets will now be considered, to demonstrate the use of the various strategies.

Mission to Neptune

An effective route for reaching Neptune is first to use the often-considered strategy of V-E-E gravity assists to reach Jupiter. This is followed by a gravity assist at Jupiter, after which Neptune is approached directly. The synodic period of Jupiter and Neptune is 12.8 years, and therefore optimal utilisation of a Jupiter gravity assist arises at this frequency.

The following example (Figures 5.1.20 and 5.1.21) considers a launch in 2013. The first gravity assist is at Venus.

Table 5.1.27 shows the nature of these two transfers. The Injection ΔV is from an initial orbit with GTO-like parameters (apogee radius at 42,165 km and perigee altitude 200 km) and an assumed optimal orbit plane to reach the required declination. The insertion ΔV is to an orbit at Neptune with pericentre at 25,000 km radius (altitude approximately 240 km) and apocentre at 1 million km. Although this orbit has a very high apocentre, it could subsequently be reduced via a series of gravity-assist manoeuvres using Neptune's moon Triton.

The table shows the details of the minimum ΔV case and an accelerated transfer. Fly-by at Jupiter occurs at approximately 400,000 km radius in this accelerated transfer.

The transfers can be further accelerated, the most significant effect being the increased excess hyperbolic speed at Neptune and the consequent increased ΔV for capture. Examples of such highly accelerated transfers are discussed in the subsequent section describing missions to Pluto.

Table 5.1.27. Examples of minimum ΔV and accelerated mission to Neptune.

Launch date	Depart V_∞ (m/s)	Depart ΔV (m/s)	Arrival	Duration (years)	Total deep-space ΔV (m/s)	V_∞ at Neptune (m/s)	Capture ΔV (m/s)	Total ΔV (m/s)
8 Oct 2013	3,910	1,440	5 Oct 2051	38.0	0	2,640	440	1,880
15 Oct 2013	4,230	1,560	19 Dec 2034	21.2	70	6,850	1,270	2,890

V-E-E-J-S mission to Neptune

A variation on this strategy uses a further gravity assist at Saturn. An unusual alignment of the planets is required to enable such a transfer, and as such this opportunity arises infrequently. The synodic period of Saturn and Neptune is 36 years, and the synodic period of Jupiter and Saturn is approximately 20 years. Therefore such a geometry will reoccur at rare intervals, although an opportunity does exists with an extension of the previously described 2013 launch. In fact, a range

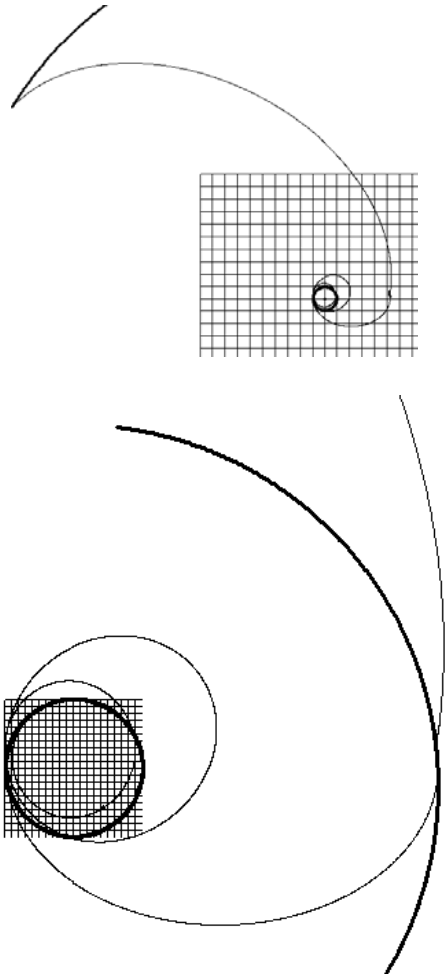

Figure 5.1.20. Minimum ΔV transfer to Neptune with a V-E-E-J sequence after launch in 2013. In the upper figure the transfer trajectory and Earth's and Neptune's orbits are shown. The inner grid is 10 AU from centre to edge, with a sub-grid size of 1 AU. The transfer to Neptune is similar to a Jupiter–Neptune conjunction-class transfer after JGA. This transfer type minimises the ΔV objective at the expense of a long transfer duration, which in this case is approximately 38 years. The minimum allowed fly-by altitudes at Earth and Venus are 300 km. At Jupiter, a lower limit of 500,000 km is initially imposed, to limit the period of exposure to Jupiter's high radiation environment. In the lower figure, the inner part of the transfer trajectory and Earth's and Jupiter's orbits are shown. The grid is 1 AU from centre to edge with a sub-grid of 0.1 AU. The inner transfer follows a conjunction-type transfer from Earth to Venus, where it performs a gravity-assist manoeuvre. The spacecraft then returns to Earth, and after the resulting gravity assist there enters a two-year resonant loop before returning to Earth again for a further gravity assist, allowing the spacecraft to reach Jupiter. The Jupiter gravity assist raises the aphelion to Neptune's orbital radius and also raises the perihelion to 4.9 AU.

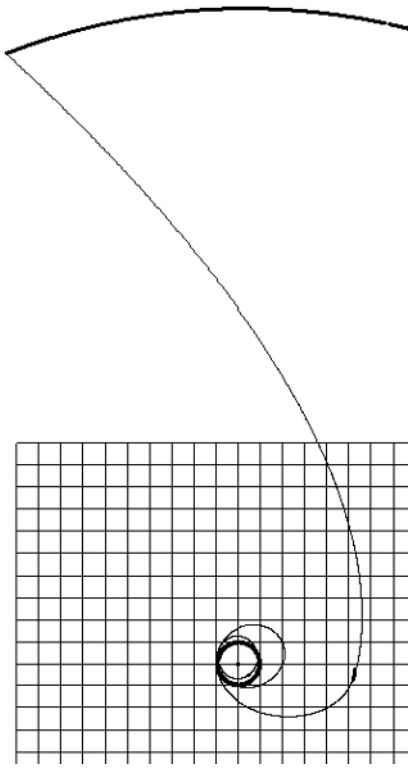

Figure 5.1.21. Minimum ΔV transfer to Neptune with a V-E-E-J sequence after launch in 2013 but with an upper limit on transfer duration. The transfer can be accelerated by constraining this upper limit on duration. The same transfer strategy as the minimum ΔV case is used in this accelerated mission. Although much faster transfers are achieved, the spacecraft meets Neptune with a significantly increased approach speed. Consequently, the capture ΔV is also increased. In this example the upper limit on duration is set to 21 years – almost half of the unconstrained optimal case. The transfer trajectory and Earth's and Neptune's orbits are shown. The inner grid is 10 AU from centre to edge, with a sub grid size of 1 AU.

of launch epochs are possible around 2013 as the geometry of Jupiter, Saturn and Neptune changes relatively slowly over 2–3 years. The Venus–Earth geometry does, however, change relatively quickly and therefore an initial sequence before reaching Jupiter could be restricted to use only Earth gravity assists.

Such a mission using a Saturn fly-by will be expected to take longer for the minimum ΔV solution. However, the opportunity to combine multiple fly-bys in a single mission enhances the scientific interest through the additional observation opportunities. Such a transfer is shown in Figures 5.1.22 and 5.1.23.

Table 5.1.28 summarises the key features of an accelerated transfer example with upper limit on transfer duration. This mission uses approximately the same ΔV as the non-Saturn fly-by case, for a similar transfer duration.

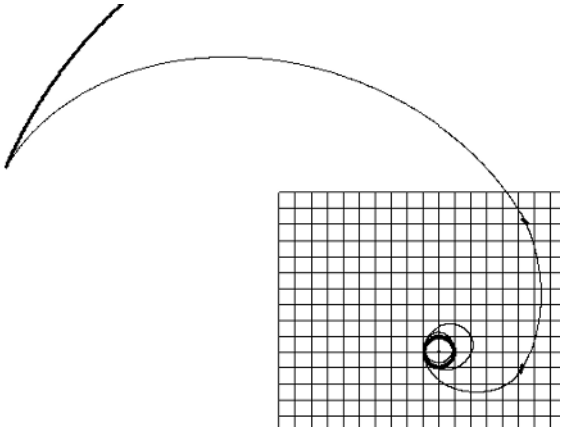

Figure 5.1.22. Multi-gravity assist transfer with Saturn fly-by, approach a 2013 launch and low V_∞ at Neptune. The transfer trajectory and Earth's and Neptune's orbits are shown. The inner grid is 10 AU from centre to edge, with a sub-grid size of 1 AU. This transfer to Neptune is similar to the V-E-E-J route described previously. After the Saturn gravity assist the perihelion is raised to approximately 7 AU, and as a result the approach speed at Neptune may be reduced. The optimum transfer duration is approximately 42 years.

Table 5.1.28. Transfer to Neptune using V-E-E-J-S gravity assist sequence.

Launch date	Depart V_∞ (m/s)	Depart ΔV (m/s)	Arrival	Duration (years)	Total deep-space ΔV (m/s)	V_∞ at Neptune (m/s)	Capture ΔV (m/s)	Total ΔV (m/s)
2 Oct 2013	4,160	1,530	28 Jun 2036	22.75	160	6,350	1,130	2,820

Missions to Pluto

Pluto presents a formidable challenge in mission design, due in part to the large spacecraft-energy change needed to reach the planet, but also due to the vast distance and its implications for transfer duration. A further complication is the Pluto's orbital inclination and eccentricity. The inclination generally requires a considerable plane-change manoeuvre to allow a rendezvous, unless a rendezvous close to the nodes can be arranged. The eccentricity and long orbital period of Pluto imply that at some launch epochs the spacecraft will have to traverse significantly greater distances.

Low-energy transfers to Pluto will be considered, as well as accelerated missions that allow the transfers to be accomplished in acceptable timescales.

Minimum ΔV transfers

Pluto may be reached in a similar manner to Neptune by considering the strategy of V-E-E gravity assists to first reach Jupiter. This is followed by a gravity assist at

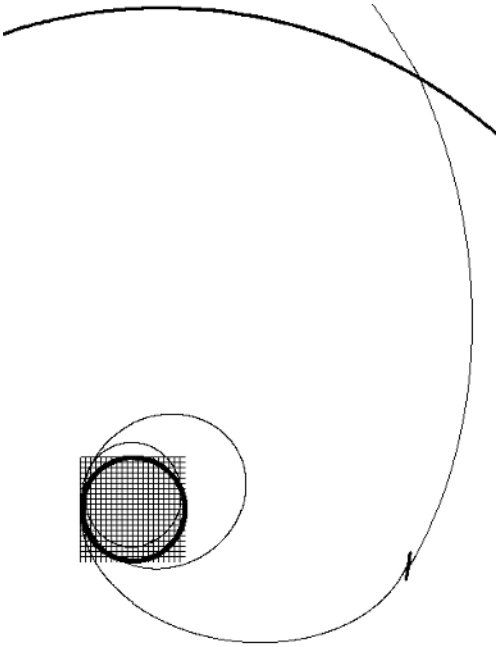

Figure 5.1.23. Inner loop detailed for a multi-gravity assist transfer with Saturn fly-by a 2013 launch and low V_∞ approach at Neptune, showing details of Jupiter and Saturn gravity assist. The inner part of the transfer trajectory and Earth's and Saturn's orbits are shown. The grid is 1 AU from centre to edge, with a sub-grid of 0.1 AU. The portion of Jupiter's orbit at the gravity assist there is also shown. The fly-by at Saturn occurs approximately 3.25 years after the Jupiter fly-by. The minimum allowed fly-by altitudes are as before, with the addition of a minimum radius at Saturn of 100,000 km. However, in this case the inequality constraint is not active, as the fly-by distance is approximately 2 million km at Jupiter and 5 million km at Saturn.

Jupiter, after which Pluto is approached directly. Alternatively, strategies using single or multiple gravity assists at Earth may be considered, and a gravity assist at Mars may also be advantageous. However, the key to the transfer efficiency is Jupiter, which may be used to raise the aphelion of the transfer orbit to Pluto's orbital radius and also to execute a plane change such that a rendezvous with Pluto's inclined orbit may be achieved.

The synodic period of Jupiter with respect to Pluto is approximately 12.5 years, thus defining the main transfer opportunity intervals for such a route. However, this period is calculated on the assumption of circular orbits, and Pluto's orbit has significant eccentricity. In practice, therefore some deviation from this repeat period is expected, depending on the location of Pluto at arrival.

A minimum ΔV transfer is considered, which arrives at Pluto with a low excess hyperbolic speed. The objective is to minimise the total transfer ΔV, being the ΔV needed for Earth escape from a reference, elliptical orbit (GTO-like), deep-space ΔVs and the ΔV needed to capture to an elliptical orbit about Pluto.

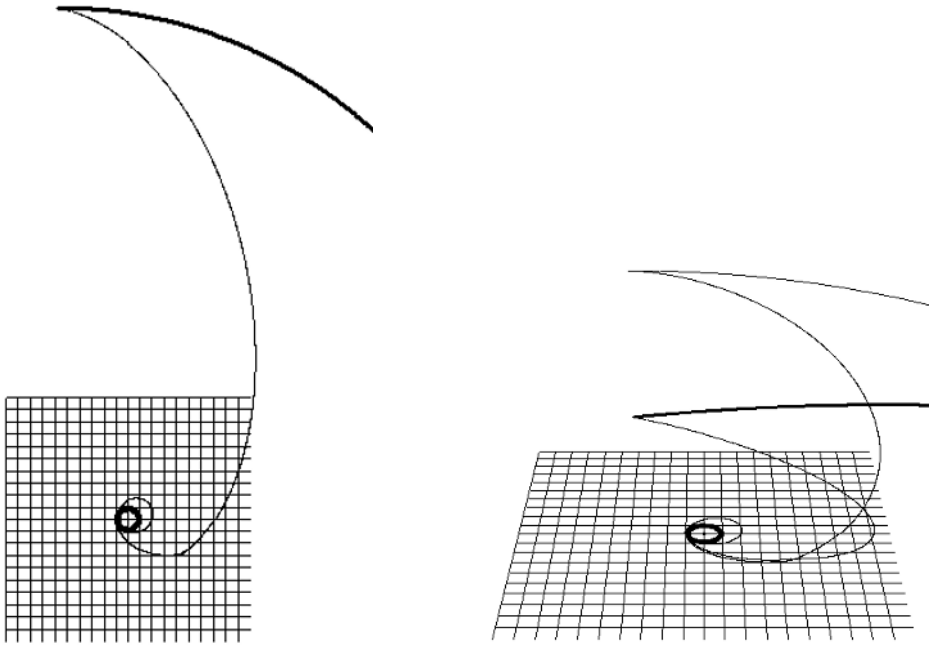

Figure 5.1.24. A high-thrust optimum transfer to Pluto taking 62 years after a 2013 launch using an E-J gravity assist sequence. The transfer trajectory, plus Earth's and Pluto's orbits and Pluto's orbit projection in the ecliptic are shown. The inner grid is 10 AU from centre to edge. The sub-grid size is 1 AU. The gravity assist at Jupiter implements aphelion-raising and plane-change. The transfer inclination after JGA is 4.5°, in this example with a launch in 2013 and JGA in 2018. Rendezvous with Pluto occurs in 2075, with an approach velocity of approximately 2.2 km/sec. The altitude at Jupiter fly-by is approximately 1.4 million km.

This principle is illustrated in the following example (Figure 5.1.24), which uses a single Earth gravity assist before reaching Pluto. The spacecraft is injected into a 3-year Earth resonant orbit. After EGA the aphelion is raised sufficiently high that is crosses Jupiter's orbit with a relative velocity of approximately 9 km/sec. This is one of several possible strategies to reach Jupiter. Routes using only EGA are less constrained in terms of departure epochs, offering opportunities for transfer to Jupiter every year.

The E-J sequence requires an initial V_∞ leaving Earth of nearly 7 km/sec, and a deep-space manoeuvre is performed before returning to Earth to increase the V_∞ to 9.6 km/sec. More efficient alternatives could be considered using, for example, a V-E-E-J sequence with much lower launch V_∞ (typically 3.5 km/sec). This allows a total ΔV reduction at the expense of increased transfer duration.

Faster transfers

The previous example demonstrates the prohibitively long transfer durations associated with a minimum ΔV transfer. However, it is possible to considerably speed up

the transfer, by making a closer fly-by at Jupiter to achieve a greater energy gain. A Solar System escape orbit may be achieved, and in this way the transfer to Pluto may be accomplished much more quickly. The implication is, however, that the approach speed at Pluto is consequently much higher, although, a trade-off may be established relating total mission ΔV to transfer duration. Alternatively, if a fly-by mission at Pluto is considered, no injection manoeuvre is required there.

If the capture at Pluto is no longer required, then an alternative ΔV objective may be considered, being the sum of the Earth departure and deep-space ΔVs.

The transfer to Pluto is unlike transfers to the other planets of the Solar System, in that additional local minimum solutions can be found. In particular, if a faster transfer is sought, a local minimum ΔV trajectory, with unconstrained arrival epoch, exists, offering a fast transfer from Jupiter to Pluto. The presence of these additional local minima arises from the highly inclined and eccentric orbit of Pluto. Even faster transfers may be obtained by constraining the Pluto arrival epoch. The nature of these minima depends on the launch epochs considered. It has been mentioned previously that a key feature of the transfer is driven by the synodic period of Jupiter with respect to Pluto. However, although this period is 12.5 years, launch opportunities in adjacent years with moderate ΔVs can generally be found.

In the subsequent analyses it is assumed that all manoeuvres are impulsive (implying a high-thrust system). It is also possible to allow these manoeuvres to take place either in deep space or at the planet pericentre when a fly-by takes place. This latter option can be particularly effective for Jupiter fly-bys.

In the first analysis, manoeuvres are not performed at planet pericentre (no powered fly-bys). The following example uses an initial injection to a three-year Earth resonant orbit, followed by EGA and then JGA, before the transfer to Pluto. Other options for the transfer to Jupiter will also be considered. A close fly-by occurs at Jupiter. The case of a 14-year transfer is seen in Figure 5.1.25.

The locally optimum transfer duration for this launch epoch was found to be just over 14 years. The previous analysis may be repeated, but with powered fly-bys at Jupiter and Earth allowed instead of using only deep-space manoeuvres. Also, if the same launch year is maintained but the arrival epoch brought forward, the relationship between ΔV and even shorter transfers can be established. The V_∞ at Pluto also rises as the transfer duration is shortened. This is seen in Figure 5.1.26.

The ΔV considered is the ΔV needed for Earth escape from a reference, elliptical orbit (GTO-like) plus the deep-space ΔVs. GTO perigee altitude is 200 km.

It has been assumed that a three-year Earth resonant loop is included in the transfer. This allows a significant change in Earth excess hyperbolic speed, when finally leaving for Jupiter, to be achieved with only a modest deep-space ΔV performed close to aphelion of the three-year orbit. However, other transfer options are possible. A two-year Earth resonant loop can allow shorter transfers to be accommodated with a lesser ΔV penalty. The comparison may be seen in Figure 5.1.27, in which it is assumed that powered fly-bys are allowed.

The two-year resonant orbit case uses a launch in 2013, and the three-year case a launch in 2012. The launch epoch may be delayed in either case for approximately one year (approximately one Earth–Jupiter synodic period). The impact on ΔV is

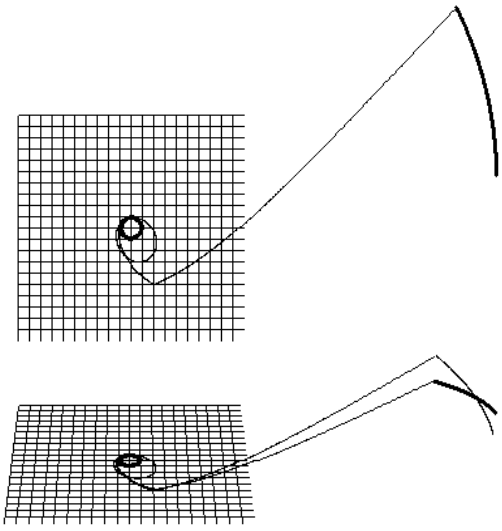

Figure 5.1.25. A high-thrust locally optimum short-duration transfer to Pluto taking 14 years after a 2013 launch, using E-J gravity assist sequence. In the upper figure, the spacecraft leaves Earth, entering a 3-year resonant orbit in 2012. Arrival at Pluto is in 2026, after JGA in 2017. The aphelion after the gravity assist at Earth is now raised further such that the approach speed at Jupiter reaches more than 11 km/sec. When combined with a fly-by at approximately 170,000 km altitude, a heliocentric V_∞ of 15 km/sec is achieved after JGA. The transfer trajectory and Earth and Pluto orbits are shown. The grid is 10 AU from centre to edge, with a sub-grid of 1 AU. In the lower figure, Jupiter gravity assist can be seen to cause a large plane-change, the inclination reaching almost 5.5°. In this plot, the orbit of Pluto (bold line) and its projection in the ecliptic are seen. The spacecraft trajectory and its projection are shown. The spacecraft now reaches Pluto earlier than the minimum ΔV case described previously, and Pluto consequently lies closer to the ecliptic.

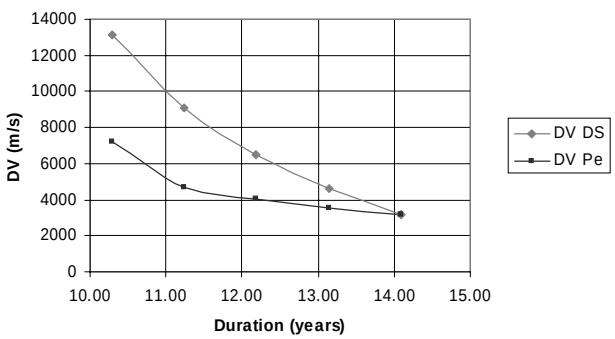

Figure 5.1.26. The ΔV duration relationship for powered and unpowered fly-by cases for a fast transfer type to Pluto, after launch in 2012. The ΔV increases significantly away from the local minimum (at nearly 14 years) for the powered gravity assist and deep-space manoeuvre cases. Powered fly-bys can be seen to give a significant gain for the shorter transfers. This is due to the need for a manoeuvre in the vicinity of Jupiter, which is most efficiently performed in Jupiter's gravity field.

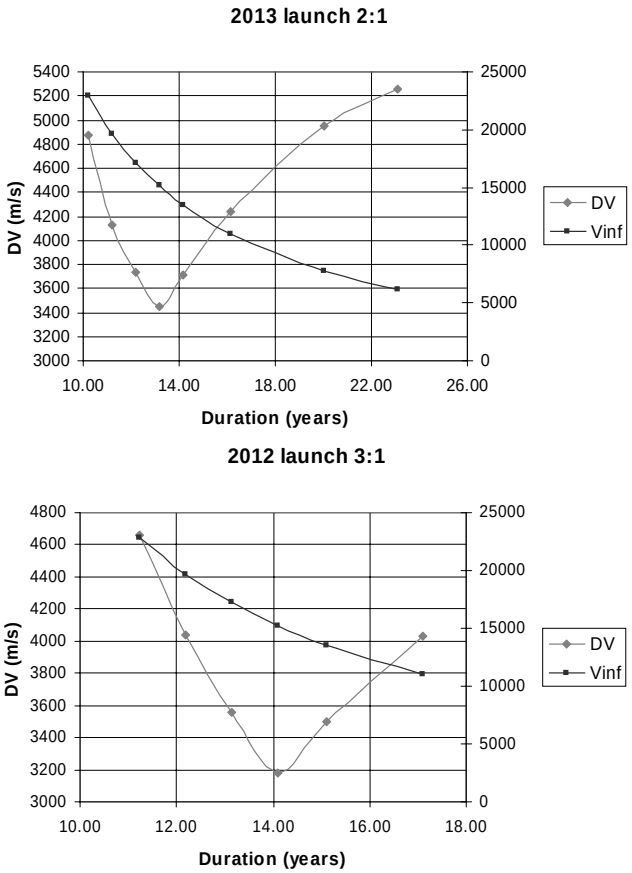

Figure 5.1.27. The ΔV duration relationship for powered fly-bys with two-year and three-year Earth resonant orbits for a fast transfer type to Pluto. Both powered fly-bys and deep-space manoeuvres are allowed. The ΔV required for the shorter transfers increases more quickly with the three-year Earth resonant orbit than in the two-year case. However, the minimum ΔV is less with the three-year orbit. The V_∞ at Pluto is also plotted against the right axis.

typically a few hundreds of m/s, depending on the transfer duration required. However, the minimum ΔV does not change significantly.

A slower but more ΔV-efficient route can be used, involving gravity assist at Venus. The relatively conventional route of Venus–Earth–Earth gravity assists is used to reach Venus. However, it is still possible to achieve relatively fast transfers by using a close Jupiter fly-by. This particular transfer will now be considered in slightly more detail (Table 5.1.29 and Figure 5.1.28). The transfer is qualitatively similar to the case using a single EGA. The details of the transfer can be seen in the figure.

The transfer after the gravity assist at Jupiter is similar to that with the single EGA missions or direct transfer to Jupiter. After leaving Jupiter the spacecraft takes 9.3 years to reach Pluto.

Table 5.1.29. Short duration V-E-E-J transfer to Pluto after 2012 launch. This case does not use any powered fly-bys.

Event	Parameters	Description	ΔV
Launch 17 Apr 2012	$V_\infty = 3.3$ km/s	Transfer orbit to Venus RV after 0.5 revs	1,270 m/s from GTO injection reference orbit
GA 1 at Venus 8 Oct 2012	$V_\infty = 6.89$ km/s	Transfer to an Earth return orbit via aphelion of 1.4 AU	
GA 2 at Earth 22 Aug 2013	$V_\infty = 9.76$ km/s	Transfer to a 2-year Earth resonant orbit; apply ΔV at aphelion to lower perihelion	350 m/s deep-space manoeuvre
GA 3 at Earth 9 Dec 2015	$V_\infty = 11.61$ km/s	Raise aphelion to 9.1 AU for high-speed Jupiter rendezvous	290 m/s deep-space manoeuvre after EGA
GA 4 at Jupiter 15 Jun 2017	$V_\infty = 11.28$ km/s	Jupiter fly-by at 163,000 km to reach Solar System escape velocity	
Rendezvous with Pluto 15 Oct 2026	$V_\infty = 15.4$ km/s	High-speed rendezvous with Pluto	
Total ΔV inc. Earth escape from GTO-altitude orbit to fly-by of Pluto		Total transfer duration 14.5 years	1,910 m/sec

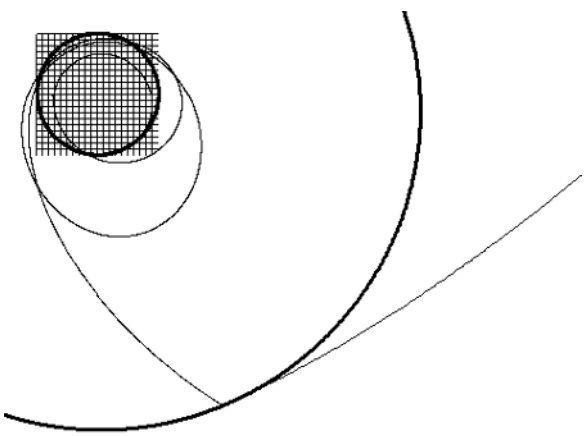

Figure 5.1.28. Inner section of a short duration V-E-E-J transfer to Pluto, after launch in 2012. Earth's and Jupiter's orbits are shown. The inner grid is 1 AU from centre to edge. The inner gravity assist sequence raises aphelion to 1.4 AU after VGA and then to 2.4 AU after EGA. Jupiter rendezvous occurs approximately 5.2 years after launch. The grid is 1 AU from centre to edge.

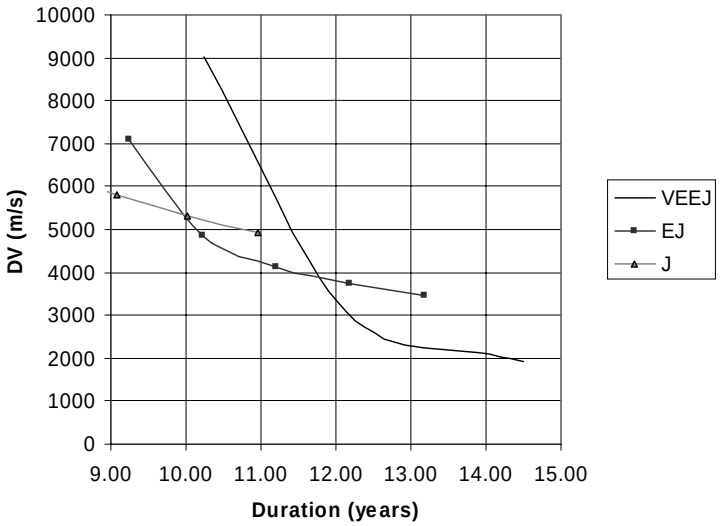

Figure 5.1.29. The ΔV–duration relationship for powered fly-by cases, for a fast transfer type to Pluto, after launch in 2012. Both powered fly-bys and deep space manoeuvres are allowed.

If speed of transfer is to be considered, then the transfer route to Jupiter also has a significant impact, as seen in the previous examples of faster transfers. A direct transfer from Earth to a Jupiter crossing may take typically two years, where an intermediate gravity assist can extend this by two to three years. A V-E-E sequence can take over five years before crossing Jupiter. The ΔV versus transfer duration can be assessed for all of these strategies.

The trade-off considers three transfer routes:

- Jupiter alone.
- Earth (1 : 2 resonant orbit)–Jupiter.
- Venus–Earth–Earth–Jupiter.

The following ΔVs are considered: ΔV from GTO to Earth escape orbit, and ΔV for all deep-space manoeuvres including powered fly-bys.

Figure 5.1.29 shows the relationship between ΔV and transfer duration. The efficiency of a given transfer route depends on the required transfer duration. Fast transfers are best implemented by a direct injection from Earth to Jupiter, whereas slower transfers (greater than 12 years) are best implemented using the V–E–E–J route.

5.1.7 Missions to minor bodies

The missions so far considered have had the objective of reaching other planets or our Solar System. Missions to other bodies such as comets and asteroids present different problems.

The first issue with a mission to a small body is that it does not possess a

significant gravity field, compared with a planet. Orbital speeds about even a large asteroid or comet are only a few m/s. When capturing into an orbit at a planet, the planet's gravity field allows a ΔV for the capture manoeuvre that is in generally much less than the approaching excess hyperbolic speed. At a minor body, the capture manoeuvre requires a ΔV that is almost equal to the approach excess hyperbolic speed.

A second point regarding such a mission is that many of the minor bodies of the Solar System lie in elliptical, inclined orbits. Even in the main asteroid belt between Mars and Jupiter, many asteroids possess eccentricities significantly greater than the planets. This means that in order to execute the transfer most efficiently, the perihelion of the spacecraft approach orbit should lie close to perihelion of the asteroid orbit. In this respect, there are similarities with a mission to Mercury, previously described. This consideration can restrict the number of launch opportunities to a particular target. However, as so many targets exist there is still a good chance of finding a suitable target for a given launch year.

A comet explorer mission: Rosetta

Rosetta is an ambitious rendezvous mission designed to reach one of the distant family of comets that orbit with aphelion close to Jupiter's orbital radius and perihelion close to 1 AU. When the mission was originally designed, Rosetta's target was the Comet 46P/Wirtanen. This was due for launch in January 2003, but the unfortunate circumstances surrounding the first launch of the Ariane 5 meant that it was not feasible to schedule Rosetta for launch at that time.

After studies at ESA, an updated mission was developed for Rosetta. The preferred option was to target the same comet, Wirtanen. However, due to the delayed launch and the motion of the comet in this time, this proved to be too demanding for the original Rosetta spacecraft design, which, to maximise efficiency, had a limited fuel capacity. Therefore, an alternative comet target was selected, with similar properties to Wirtanen: Comet 67P/Churyumov–Gerasimenko. As a result, Rosetta was finally launched on an Ariane 5 in March 2004.

The new mission profile follows a type of transfer similar to that scheduled for the 2003 launch. It includes an additional Earth gravity assist, occurring approximately one year after launch, in March 2004. This is effective in providing a significant out-of-ecliptic component to the Earth relative motion, for the subsequent transfer to Mars. This mission is described more fully in the references to this chapter.

After the first Earth gravity assist, the spacecraft accomplishes approximately 1.25 revolutions about the Sun before a rendezvous with Mars in March 2007. A Mars gravity assist then takes place, such that return to Earth is achieved in approximately half a revolution about the Sun, and this second Earth gravity assist takes place in November 2007. The Mars gravity assist lowers perihelion to below Earth's orbital radius, and so the excess hyperbolic speed at Earth is increased significantly when compared with the departure value. The Earth gravity assist may therefore be used to enter a two-year resonant orbit with Earth. On its return after a further two years, in November 2009, the third gravity assist at Earth raises aphelion to a value

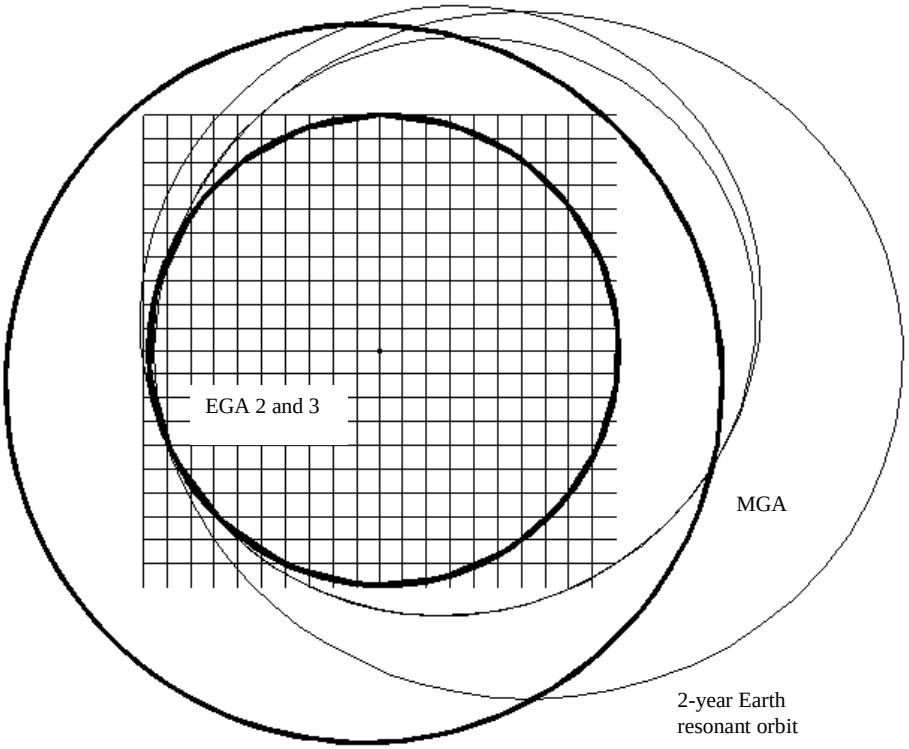

Figure 5.1.30. The early phases of the final Rosetta mission profile, showing transfer to Mars and return to Earth to carry out a further two EGAs. The grid is 1 AU from centre to edge with a sub-grid of 0.1 AU. The orbits of Earth and Mars are shown in addition to the trajectory.

close to the orbital radius of Jupiter, eventually enabling a rendezvous with the target comet, after a series of deep-space burns.

The initial phases of the mission are shown in Figure 5.1.30. This is the sequence after the first Earth gravity assist to the Mars gravity assist and two subsequent Earth gravity assists.

The resulting spacecraft orbit then has a perihelion location that is compatible with the target. Rendezvous with the comet occurs before perihelion is reached. This is to allow an extended period of scientific observations of the comet as it approaches its perihelion passage. The transfer route therefore involves four gravity assist manoeuvres. This strategy allows the final rendezvous manoeuvres with the comet to be limited to a manageable ΔV with a chemical propulsion system.

The basic mission timeline is shown in Table 5.1.26.

Table 5.1.26. The Rosetta transfer to Comet 67P/Churyumov–Gerasimenko.

Event	Epoch
Launch	March 2004
First Earth gravity assist	March 2005
Mars gravity assist	March 2007
Second Earth gravity assist	November 2007
Third Earth gravity assist	November 2009
Rendezvous manoeuvre	May 2014
Global mapping	August 2014
Lander delivery	November 2014
Perihelion passage	August 2015

5.1.8 Escaping the Solar System

Missions have been proposed to explore the region outside our Solar System and beyond, including the interstellar heliopause and in particular its 'nose'. (The interstellar heliopause is described more fully in the references for this section) Such a mission target is a demanding objective for a spacecraft, and requires extraordinary transfer methods.

The nose is located at approximately 200 AU from the Sun, at a longitude of 254° and a declination of 7°. Some tolerance in the precise longitude for a spacecraft exploring this region is possible, as the area of scientific interest covers a large zone.

In considering the design of a mission to reach this objective, a number of key issues will be explored that are generic for such high-energy missions beyond the Solar System.

In practice, transfer durations are to be limited. A typical maximum mission period would be 15–25 years. The longer the transfer may take, the easier is the mission design. In order to achieve a transfer in such periods, the spacecraft must achieve a Solar System escape condition; that is, exceed some minimum excess hyperbolic speed with respect to the Solar System.

The key issue with this mission is how to reach the required Solar System escape velocity. In practice, the spacecraft will need to perform large manoeuvres, which may be in deep space or as powered fly-bys at a large planet. If a high-thrust propulsion system is available, energy-amplifying manoeuvres may be applied efficiently when passing through the pericentre of a fly-by at a major body, or in making a close approach to the Sun and performing a manoeuvre at perihelion.

A number of scenarios will be considered. High-thrust-based transfers can be achieved efficiently in two main scenarios: powered Jupiter gravity assist, or powered solar fly-by. In both of these scenarios, a Jupiter fly-by is used during the early mission phases, either as assistance in reaching the required V_∞ or in lowering perihelion close to the Sun to implement a powered solar fly-by.

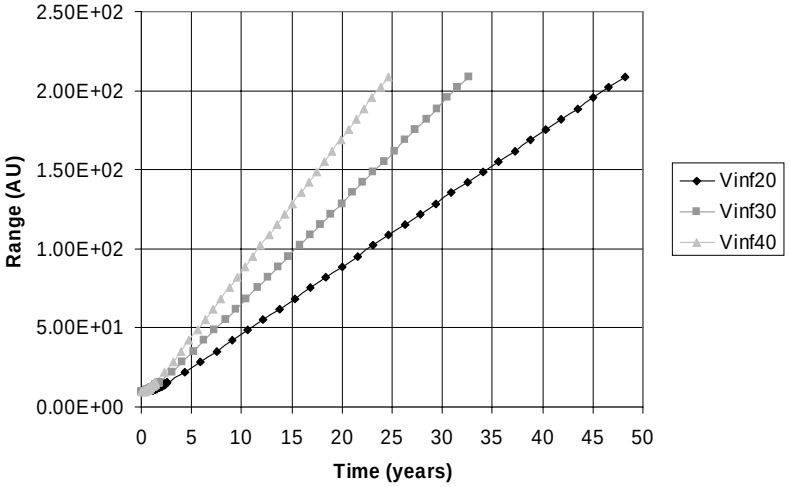

Figure 5.1.31. Heliocentric range versus time for V_∞ between 20 and 40 km/sec, perihelion at 5.2 AU. Such Solar System departure orbits are typical of those that may be achieved with a powered gravity assist at Jupiter.

Basic mission drivers

It is possible to evaluate the characteristics of high-energy orbits to assess their suitability in reaching large heliocentric distances in a short period of time.

Figure 5.1.31 illustrates that with such high-energy departure orbits, the Keplerian orbital motion can be approximated as a linear relationship between position and time. Furthermore, to achieve a transfer in the 20–25-year timescale an excess hyperbolic speed with respect to the Solar System of typically 40 km/sec is required. This may be extrapolated to shorter transfers, such as 15 years, where a speed of 64 km/sec would be required.

Performance available with a powered Jupiter gravity assist

The preceding discussion has assumed that the planetary departure condition can be such that the planet relative departure velocity is tangential to the planet orbit. This requires a particular range of approach directions.

The constraints of optimised approach orbits are often such that this ideal geometry will not be fully realised. A typical approach orbit is the example of a Jupiter crossing orbit, with perihelion close to Earth and a very high aphelion.

This requirement on V_∞ can be compared with the results achievable with such a Jupiter gravity assist manoeuvre. Jupiter is very effective at modifying heliocentric orbits, and it is possible to directly reach a Solar System escape orbit with a single Jupiter gravity assist. The energy that may be gained depends on the approach velocity at Jupiter. For a Jupiter crossing orbit, with typically a perihelion at 1 AU, raising the aphelion of the transfer orbit increases the approach velocity, as seen in Figure 5.1.32.

A means must therefore be found to increase this escape energy. Increasing the

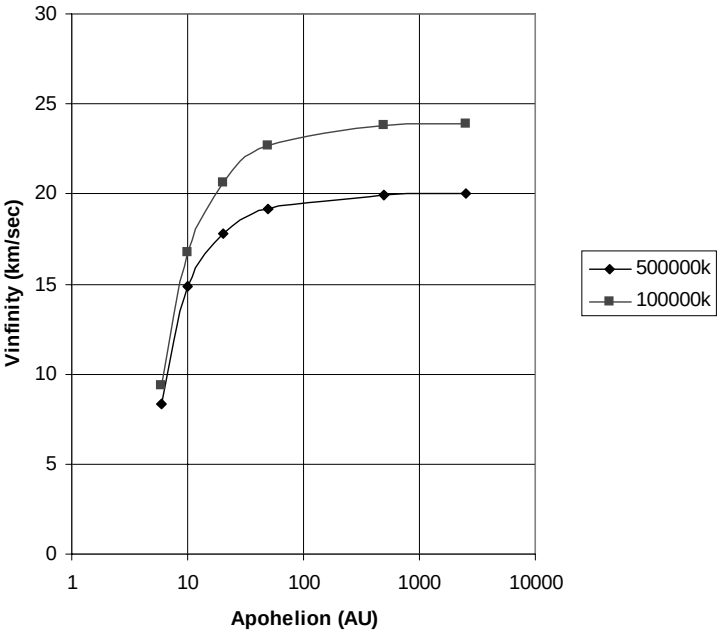

Figure 5.1.32. Solar System relative V_∞ available from Jupiter crossing orbits. A solar system V_∞ approaching 25 km/sec may be achieved from an initially bound Solar System orbit, the value depending on the radius of the fly-by at Jupiter. A gravity assist at Jupiter, from any Solar System bound orbit, is not sufficient to reach the required escape velocities to reach 200 AU in an acceptable timescale. Two fly-by pericentres are considered at Jupiter, the closer fly-by giving a significant gain in achievable Solar System escape energy.

initial energy of the Jupiter crossing orbit could do this, such that the spacecraft already possesses an excess hyperbolic speed relative to the Solar System when Jupiter is reached. This would mean, for example, leaving Earth or the inner Solar System with a very high energy. It could imply either a direct escape from Earth with such energy or alternatively assume that it is achieved after a series of gravity assist manoeuvres in the inner Solar System. Such energies are not achievable by gravity assist alone, and large manoeuvres are implied.

Alternatively, a manoeuvre may be performed at Jupiter pericentre during the fly-by. This enables an increase in the excess hyperbolic speed when leaving the Solar System. Comparing these two strategies it is found that making a manoeuvre at Jupiter pericentre is more efficient than similar manoeuvres at any of the inner planets.

Therefore, in order to reach even moderately acceptable transfer durations to the heliopause (20–25 years), a pericentre ΔV at Jupiter in the region of 8–10 km/sec is required. Such a large manoeuvre has significant implications for the propulsion system, in that sufficient acceleration is needed to prevent excessive ΔV loss arising from the extended duration of the manoeuvre around Jupiter.

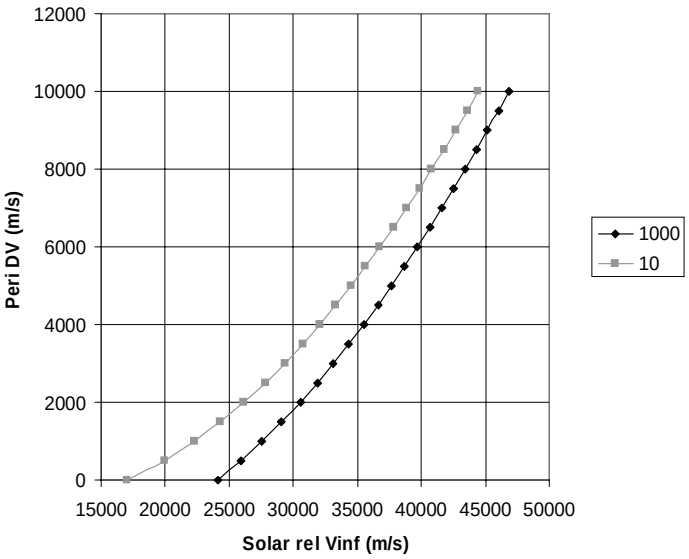

Figure 5.1.33. Jupiter pericentre ΔV versus Solar System V_∞ for Jupiter crossing orbits with aphelion at 10 and 1,000 AU and fly-by distance at 100,000 km. The perihelion is assumed to be initially 1 AU (as an approximation to the properties of such crossing orbits). The resulting Jupiter relative V_∞ (on approach) are -12.2 km/s 10 AU, -17.3 km/s 1,000 AU.

Designing a mission using a powered Jupiter fly-by

The direction of escape from the Solar System is determined by the location of the heliopause. Only one Jupiter longitude for the gravity assist is optimal for a required final V_∞ vector magnitude and direction (some adjustment is possible by changes in perihelion, but these are relatively small). Otherwise, meeting the target V_∞ vector direction requires large ΔV manoeuvres applied after leaving Jupiter.

The choice of the transfer route to Jupiter determines the possible launch epochs to rendezvous with Jupiter at the desired time (and solar longitude). Transfers from Earth to Jupiter have a synodic period of approximately 1.1 years, and these approximately repeat in terms of geometry of arrival at Jupiter after eleven such opportunities, or after almost 12 years.

The transfer routes to Jupiter can include single or double EGAs, VGA–EGA–EGA scenarios, and direct transfer from Earth to Jupiter. The most ΔV efficient route to Jupiter does not necessarily yield the best solution, as this is a longer transfer (5–6 years, using V–E–E) and there will be an upper limit on the total transfer duration. The effect of a long transfer to Jupiter means that a larger solar-relative V_∞ is needed after leaving Jupiter to reach the heliopause in the same time as a case with a direct transfer to Jupiter. This in turn needs a greater ΔV at the powered JGA. The best choice of transfer route depends on the required transfer duration. For the slower transfers (typically 30 years), the best (minimum ΔV) route uses a single EGA and therefore a relatively fast transfer route to Jupiter. For faster transfers, the

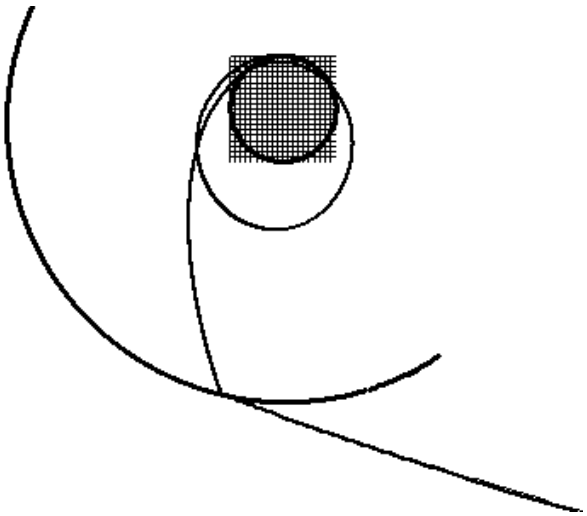

Figure 5.1.34. Transfer using a single EGA followed by a powered JGA with launch in 2011 and 38.3 km/s V_∞ leaving the Solar System. The grid is 1 AU from centre to edge.

overhead of the long transfer phase to Jupiter results in large ΔV requirements at Jupiter fly-by, so that a direct transfer to Jupiter becomes the most efficient route.

An example of a direct transfer route uses Earth departure in August 2012, with JGA in 2016. For a total transfer duration of 30 years, the resulting Solar System escape velocity vector has an error of approximately 1°, compared with the ideal direction to rendezvous with the target longitude. For a faster transfer of 25 years, a 4-degree error in direction is the result. This angular variation arises from the difference in the asymptotic departure direction after JGA due to different departure energies.

Nominally, the optimum departure declination after the Jupiter fly-by (maximising the escape velocity) lies in the ecliptic, The required departure latitude of 7° can be achieved with an additional ΔV penalty of a few hundred m/s.

Figure 5.1.34 shows the inner section of such a transfer using a single EGA. It shows the orbits of Earth and Jupiter, illustrating the ΔV aided gravity assist at Jupiter. The JGA ΔV required reduces with the fly-by radius. Close approaches are needed to obtain an efficient manoeuvre. Therefore, fly-bys at nominally 80,000 km altitude are considered to be the baseline. Jupiter's equatorial radius is over 71,000 km.

Figure 5.1.35 shows a range of transfer ΔVs for alternative mission durations. Each uses the single-EGA route to Jupiter. The orbit after EGA has an aphelion of 12 AU. Most of the ΔV occurs at Jupiter fly-by but other deep-space manoeuvres are also used. In Figure 5.1.36 the EGA and direct transfer routes to Jupiter are compared. As the transfer duration is reduced, the direct transfer becomes progressively more efficient.

Using a transfer route involving Venus gravity assist can improve the efficiency with which Jupiter may be reached, and this can be attractive for the longer allowed

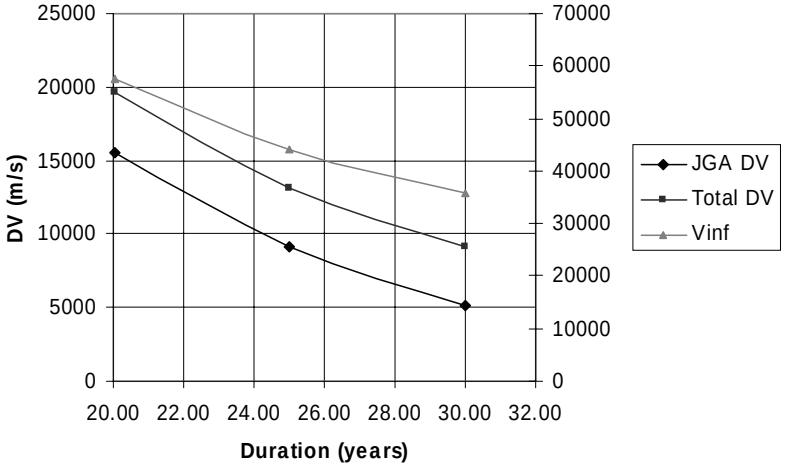

Figure 5.1.35. Results for single-EGA transfer with Jupiter fly-by at 80,000 km for a range of transfer durations. Solar System relative V_∞ is plotted against the right axis.

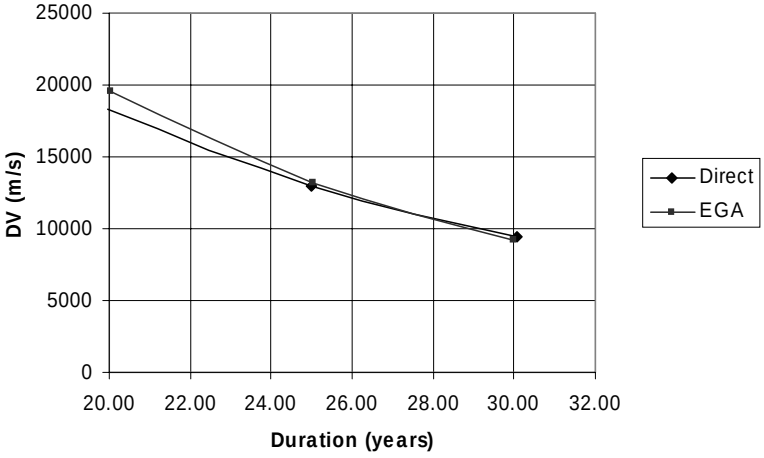

Figure 5.1.36. Results for single-EGA transfer compared with a direct transfer with Jupiter fly-by at 80,000 km for a range of transfer durations.

transfer durations. The number of rendezvous opportunities with Jupiter is reduced in comparison with the previously described routes. This has the consequence of Solar Escape vectors in non-optimal directions.

Using a powered solar fly-by

An alternative to the powered gravity assist missions at Jupiter is to use a powered solar fly-by. This is not a gravity-assist manoeuvre, but simply makes use of a close passage to the Sun as an efficient location to apply a large ΔV. Achieving such a low

Table 5.1.31. Examples of single-EGA transfers with solar fly-by at 0.018 AU for a range of transfer durations.

ΔV at solar fly-by	Total ΔV	Final V_∞	Transfer time post-JGA	Total transfer time
3,000	6,490	39,200	24.27	29.97
4,380	7,860	49,300	19.30	25.00
6,730	10,210	66,500	14.31	20.01

perihelion is in itself a challenge, and is most efficiently accomplished with a gravity assist at Jupiter. Such a mission concept is described in the references for this section.

The solar fly-by mission may use one of several possible routes to achieve the Jupiter crossing orbit. An unpowered JGA is used to lower perihelion close to the Sun. On reaching perihelion, the spacecraft applies a prograde ΔV to reach Solar System escape. The passage from Jupiter to perihelion takes just over 2 years.

For such a fly-by to be effective, the spacecraft must fly close to the Sun at distances less than 0.05 AU, although distances as low as 0.018 AU have been considered. This is approximately 4 solar radii.

As in the Jupiter powered fly-by case, a similar set of options exists in reaching Jupiter. However, because the solar fly-by ΔVs are lower than those at Jupiter, the sensitivity to transfer time to Jupiter is reduced. This means that a V–E–E mission potentially offers good performance for some of the greater allowed transfer durations.

Table 5.1.31 shows some results for a single EGA transfer, assuming that the spacecraft injects directly into a two-year Earth resonant orbit. To enter this orbit requires an excess hyperbolic speed on leaving Earth of approximately 5.5 km/sec (or a ΔV from a GTO-like orbit of 2,180 m/s. A further deep-space ΔV of approximately 1,350 m/s is then used before eventually reaching the solar fly-by.

The transfer for the example of a double EGA is shown in Figure 5.1.37. This example is for a launch in 2015, so that the optimum departure direction lies close to the required longitude, with an error of 13°.

The solar fly-by mission therefore offers considerable ΔV savings over the powered Jupiter fly-by cases, particularly for the shorter transfer durations, providing that a very close approach to the Sun is allowed. Increasing this minimum solar fly-by distance to larger distances reduces the efficiency of the solar fly-by mission. A solar fly-by at 0.054 AU is no more ΔV-efficient than the powered Jupiter fly-by mission for longer transfers at 30 years, but still remains more efficient than the Jupiter option for shorter transfer.

The ΔVs required for these high-thrust transfers are large. The fuel fraction requirements for a conventional chemical propulsion system are extremely high. Alternative technologies can be considered, offering higher specific impulse, such as nuclear thermal propulsion.

Alternatively, different mission scenarios may be considered that use low-thrust propulsion. Powered gravity assists are then no longer possible, but are replaced by extended deep-space manoeuvres. Nuclear electric propulsion systems can be

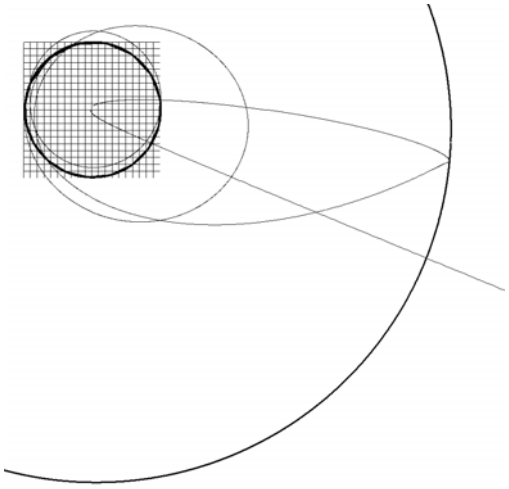

Figure 5.1.37. Transfer with launch in 2015, 38.3 km/s V_∞, and solar fly-by at 0.018 AU. The orbits of Earth and Jupiter are shown. The grid is 1 AU from centre to edge.

considered for such a mission. A variant on a powered solar fly-by mission uses solar sails to accelerate out of the Solar System after a close approach to the Sun. These propulsion systems are discussed in Chapter 2.

5.2 LOW-THRUST MISSIONS

5.2.1 Analysis of a low-thrust, multi-gravity assist mission to Mercury

Missions to Mercury have previously been examined in the previous section in the context of designing a multi-gravity assist mission. In that scenario the use of deep-space manoeuvres was restricted in its scope. Here the transfer possibilities may be expanded by considering the possibilities with much larger manoeuvres. The use of low-thrust systems and the corresponding high specific impulse means that fuel use will still be low.

Firstly, it is useful to consider the nature of a transfer to Mercury using low thrust alone. A scenario may be considered where a continuous low-thrust spiral is used to spiral from Earth orbit to Mercury orbit. As a first approximation, Mercury could be considered to lie in a circular orbit. The ΔV required for such a transfer is given approximately by the difference in circular orbit speeds. This difference between Earth and Mercury is close to 20 km/sec. This would be a large ΔV even for a low-thrust solar electric propulsion system. Furthermore, the transfer duration would depend on the acceleration available from the system, but would be expected to be typically of the order of 100–200 mN/tonne. The transfer duration would therefore be approximately 3–6 years, depending on thrust/mass.

Gravity-assist manoeuvres can be used to significantly reduce the transfer ΔV requirement. The key issues for such a transfer are therefore the total transfer time,

the total ΔV, the system thrust, and therefore the power generation mass requirements.

The main gravity assist options are, as in the 'ballistic' mission option, the Moon, Earth, Venus and Mercury. The previous analyses have shown that Venus is the key target for gravity assist. Therefore, launch opportunities are again driven by Earth–Venus transfer opportunities. The synodic period is 1.6 years.

Gravity-assist sequences that may be expected to be most effective with intermittent low thrust arcs are as follows:

Sequence	*Description*
1) –V–V–M^n	Use a Venus 3:4 resonant orbit to lower perihelion to Mercury. A series of gravity assists at Mercury and low-thrust manoeuvres is then used to reduce approach speed.
2) –V–V–M^n	Use a Venus 1 : 1 resonant orbit to lower perihelion. However, perihelion may be higher than Mercury's perihelion. Therefore, a manoeuvre is required to lower perihelion before rendezvous may take place. Subsequently a series of gravity assists at Mercury and low-thrust manoeuvres are used to reduce approach speed. This scenario uses a greater ΔV than 1), but is potentially faster, as the 1 : 1 Venus resonant phase takes 450 days less than the 3 : 4 resonant phase.
3) L–E–V–V–M^n	This strategy is the same as 2), but the departure from Earth is preceded by a Moon–Earth ΔV 1+year resonant phase (as described in Chapter 4), after which the V_∞ at Earth is amplified sufficiently to achieve a transfer to Venus. This sequence will take approximately 15 months longer than 2), but allows the spacecraft to start its mission from a Lunar crossing orbit, rather than an escape hyperbola to Venus. Consequently, significantly more injection mass is available from the launcher. This strategy is used here to lower aphelion rather than raise it as was shown in the examples of Chapter 4.
4) L–E–V–M^n	This strategy is the same as 3), but uses only a single gravity assist at Venus. The objective is to achieve a high V_∞ at Venus after a high V_∞ departure with the Earth gravity assist.

These options allow ΔVs to be significantly reduced (compared with non-gravity assist routes), and could lie in the 2–8 km/sec range, depending on the upper limit on transfer duration that is allowed. These options allow a compromise between ΔV and transfer time to be found. Use of additional gravity assists at Mercury can reduce ΔV, but at the expense of greater transfer time.

Propulsion assumptions

The key characteristic of the low-thrust propulsion unit for such a mission is thrust/mass. For an SEP system, maximum thrust is dependent on available power, which in turn is dependent on radial distance from the Sun. The exact relationship depends

upon the performance of the solar arrays and power conversion units. Such mission designs may be optimised by using detailed mathematical models of the power and propulsion system performance. For preliminary mission designs, approximations can be considered. In the examples considered here, a fixed value of 200 mN/tonne will be assumed.

The availability of large amounts of power as the spacecraft approaches the Sun makes a mission to Mercury a very good application for an SEP mission.

A further feature of low-thrust propulsion is its specific impulse, which is once again dependent on the type of propulsion used, but could be expected to be several thousands of seconds for a typical gridded ion thruster system. With such high specific impulse the fuel mass usage is generally low, and so the major change in propulsive acceleration over the course of the transfer arises from thrust dependence on available power.

Mercury SEP transfer examples

A series of transfers will now be examined to illustrate effective strategies for such a mission.

The first transfer considered corresponds to option 2. Such a mission has previously been described, notably by Langevin (see the references). The details of the principle of the sequence are as follows:

Event	*Comments*
A direct transfer from Earth to Venus	Excess hyperbolic speed; optimisable. Right ascension of departure vector; optimisable. Declination of departure vector: optimisable. These parameters are targeted by the launcher or through an apogee-raising sequence, as discussed in previous sections.
Venus GA to reach a 1 : 1 resonant orbit with Venus	Use an intermediate resonant orbit to assist in eventual perihelion reduction.
Venus GA to lower perihelion close to Mercury perihelion	
SEP manoeuvre sequence to lower perihelion and lower aphelion	Enables eventual rendezvous with Mercury and reduces approach speed at Mercury. The manoeuvre sequence may be performed over multiple revolutions about the Sun. This allows phasing with Mercury for the eventual rendezvous and the possibility to apply the low-thrust arcs in the most efficient locations rather than experience large ΔV loss.

Event	*Comments*
Mercury GA to a half-revolution resonant orbit with Mercury	This phase is the same as the ballistic mission opportunities described in section 5.1.1. It results in a reduced approach speed to Mercury at aphelion.
Mercury GA to 'propulsive' 1 : 1 resonant orbit with Mercury	This is essentially a reverse implementation of the type of manoeuvre such as the Moon–Earth gravity assist escape loop described previously (i.e., a ΔV-gravity assits loop). The result is to further reduce approach speed at Mercury.
Hyperbolic approach to Mercury	With such a large reduction in approach speed at Mercury, a relatively small (compared with ballistic transfers) capture manoeuvre may be made at Mercury pericentre to inject into an elliptical orbit about the planet.

It is clear that there are a number of parameters that may be traded off in this mission design, with the objective of identifying an optimum solution. In this context this is one that maximises the useful mass in the target orbit at Mercury. Useful mass is used here to refer to the total delivered mass minus any elements of dry mass dedicated to the propulsion system. This concept has been described in Chapter 3.

Examples of mission parameters that may be considered for trade-off are:

- The injection V_∞ from the launcher.
- The capture V_∞ at Mercury.
- The number of revolutions about the Sun before Mercury is first approached.
- The number of MGAs used between VGA and Mercury capture.

The reference thrust/mass assumptions described previously are used. The transfer details are shown in Table 5.2.1.

It is also possible to achieve this transfer with a single gravity assist at Mercury. The half-revolution 1 : 1 resonant phase is omitted. The transfer is approximately 44 days shorter, but uses an additional SEP ΔV of approximately 340 m/s.

Alternatively, additional gravity assists at Mercury may be used to assist in aphelion reduction, rather than relying on propulsion to accomplish this. This would lead to an increase in transfer duration and also a ΔV reduction.

The transfer is shown in Figure 5.2.1. This illustrates the transfer from Earth to a Venus rendezvous, where the spacecraft enters the 1 : 1 Venus resonant orbit. The low-thrust arcs begin after the second Venus gravity assist.

The aspects of the motion out of the ecliptic can be seen in Figure 5.2.2. The significant inclination of the Venus 1 : 1 resonant orbit can be seen and also after the

Table 5.2.1. Low-thrust, multi-gravity assist transfer to Mercury with launch in 2009.

Event	Parameters	Description	ΔV
Launch 20 Jan 2009	$V_\infty = 3.8$ km/s	Transfer orbit to Venus RV after 0.5 revs	
GA 1 at Venus 20 Apr 2009	$V_\infty = 6.78$ km/s	Achieve 1 : 1 resonant orbit Inclination 11.3°	
GA 2 at Venus 1 Dec 2009	$V_\infty = 6.78$ km/s	Lower perihelion to 0.36 AU and inclination of 7°. SEP manoeuvres to achieve Mercury RV after 4.5 revs	SEP ΔV 4,520 m/s
GA 3 at Mercury 5 Jun 2011	$V_\infty = 2.40$ km/s	Achieves 1 : 1 resonant orbit over 0.5 revs Inclination 4.7°	
GA 4 at Mercury 10 Jul 2011	$V_\infty = 1.81$ km/s	Achieves 1 : 1 ΔV resonant orbit	SEP ΔV 450 m/s
Inject to Mercury elliptical orbit 30 Oct 2011	$V_\infty = 0.45$ km/s	Transfer duration 2.8 years	
Total SEP manoeuvres			4,970 m/s

second Venus gravity assist, the achievement of the 7 degrees inclination to match Mercury's orbit plane.

A reduction in the launcher injection V_∞ can be achieved with the use of further SEP ΔV between Earth departure and Venus rendezvous. A reduction to 2.6 km sec V_∞ results in the need for an additional 1.2 km/sec ΔV.

The solution is dependent on the transfer duration. If an additional revolution between Venus and Mercury is inserted, then the duration of the major individual thrust arcs can be expected to reduce due to shorter burn-arc durations per revolution. Adding a further revolution about the Sun will reduce the SEP ΔV by approximately 230 m/s, but increase the transfer duration by 88 days.

Use of lunar and Earth gravity assists

In the previous cases with a launch V_∞ below 3.8 km/sec, the optimal transfer mass solutions utilise thrust arcs in the early phase of the transfer. The higher-energy launch case (V_∞ at 3.8 km/sec) removes the need for these arcs. An alternative means of obtaining a greater V_∞ on leaving Earth is to use an Earth gravity assist manoeuvre after a deep-space manoeuvre. The strategy is that described in Chapter 4 regarding the ΔV gravity assist loop.

In this scenario, launch can be into an initially highly elliptical orbit, followed by a lunar gravity assist to reach a low Earth escape velocity (V_∞ with respect to Earth system typically 1.1 to 1.4 km/sec). The Earth gravity assist manoeuvre then occurs approximately 15 months later, after an intermediate manoeuvre increasing the ec-

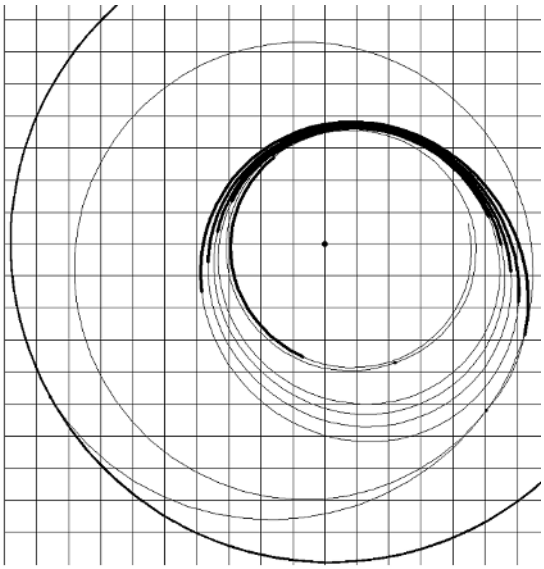

Figure 5.2.1. 2009 low-thrust transfer with Venus–Venus–Mercury–Mercury gravity assist. The orbit of Earth is shown (thick line). The spacecraft coast arcs are depicted by a light line and thrust arcs by a bold line. The grid is 1 AU from centre to edge, with a sub-grid of 0.1 AU. Mercury's orbit is omitted for clarity. Its orbit lies close to that of the final coast phase seen in the transfer trajectory.

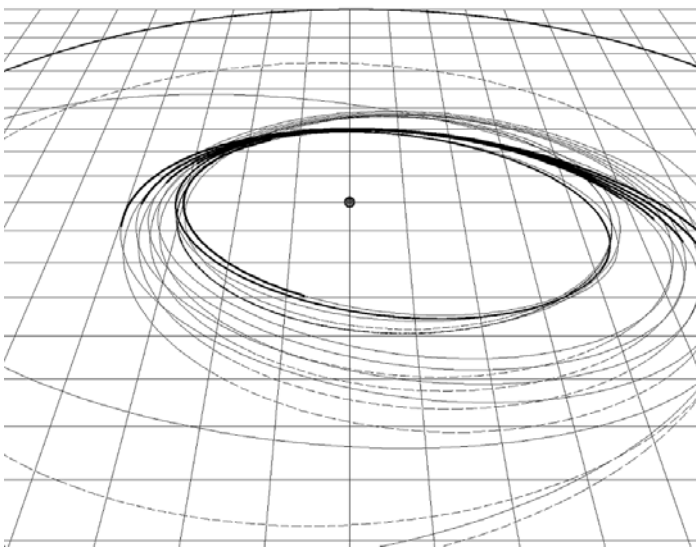

Figure 5.2.2. 2009 low-thrust transfer with Venus–Venus–Mercury–Mercury gravity assist, showing out-of-ecliptic motion. The orbits of Earth and Mercury are shown (thick lines). The spacecraft coast arcs are depicted by a light line and thrust arcs by a bold line. The projection of the motion in the ecliptic is shown by dashed lines. The sub-grid size is 0.1 AU.

centricity of the orbit and therefore the Earth fly-by speed. After the Earth gravity assist, the spacecraft follows a route similar to the previously described case, with two Venus and two Mercury gravity assists. Such a strategy has been proposed for ESA's Bepi-Colombo mission (see references for this section). Table 5.2.2 shows the characteristics of such a transfer. The key features are summarized below.

Event	*Comments*
Injection to trans-lunar elliptical orbit	Apogee altitude typically 410,0000–600,000 km depending on the target V_∞ after gravity assist at the Moon.
Lunar gravity assist to reach low-energy Earth escape	Fly-by altitude 200–300 km, depending on navigation accuracy achievable.
Deep-space burn to increase orbital eccentricity	
Earth gravity assist	Target to achieve $V_\infty > 3$ km/sec on transfer to Venus.
A direct transfer from Earth to Venus	Excess hyperbolic speed optimised by Earth gravity assist; right ascension of departure vector optimised by Earth gravity assist; declination of departure vector optimised by Earth gravity assist.
Venus GA to reach a 1 : 1 resonant orbit with Venus	Use an intermediate resonant orbit to assist in eventual perihelion reduction.

The transfer is shown in Figure 5.2.3. The initial inwards departure is efficient in this case. The transfer trajectory, after the Earth gravity assist, can be seen to be almost identical to the previous case using direct injection. However, between first departing Earth's sphere of influence (after the lunar gravity assist) and the subsequent Earth gravity assist, a large thrust-arc can be seen. The result is that the spacecraft returns to Earth with an excess hyperbolic speed of approximately 3.6 km/sec. The motion out of the ecliptic is shown in Figure 5.2.4. The initial LGA–EGA loop lies close to the ecliptic plane.

Sensitivity of the solution

The LGA–EGA-based solution sensitivity with respect to certain factors may be assessed. Thrust magnitude influences the ΔV. Reducing thrust below 200 mN/tonne penalises ΔV at a rate of typically 6 m/s per mN for the transfer type in Table 5.2.2.

The ΔV solution is less dependent on specific impulse. Its effect is manifest through the thrust/mass variation with variations in fuel usage through the transfer. Reoptimisation shows that (for constant thrust):

$Isp = 3{,}500$ sec $\quad \Delta V$ 5.75 km/sec
$Isp = 4{,}200$ sec $\quad \Delta V$ 5.79 km/sec

Table 5.2.2. Low-thrust multi gravity assist transfer to Mercury with launch in 2007 using EGA.

Event	Parameters	Desctioption	ΔV
Launch 24 Oct 2007	Trans-lunar orbit, apogee at 460,000 km	Transfer orbit to Moon	
GA 1 at Moon 24 Nov 2007	V_∞ wrt Earth system at 1.2 km/s	Achieve 1 : 1 ΔV resonant orbit	SEP ΔV 830 m/s
GA 2 at Earth 12 Jan 2009	$V_\infty = 3.63$ km/s	Transfer orbit to Venus RV after 0.5 revs	
GA 3 at Venus 19 Apr 2009	$V_\infty = 6.70$ km/s	Achieve 1 : 1 resonant orbit Inclination 11.5°	
GA 4 at Venus 30 Nov 2009	$V_\infty = 6.70$ km/s	Lower perihelion then perform SEP perihelion manoeuvres	SEP ΔV 4,470 m/s
GA 5 at Mercury 4 Jun 2011	$V_\infty = 2.46$ km/s	Achieves 1 : 1 resonant orbit over 0.5 revs	
GA 6 at Mercury 10 Jul 2011	$V_\infty = 1.87$ km/s	Achieves 1 : 1 ΔV resonant orbit	SEP ΔV 445 m/s
Inject to Mercury elliptical orbit 30 Oct 2011	$V_\infty = 0.47$ km/s	Transfer duration 3.9 years	
Total SEP manoeuvres			5.75 km/s

Using a single VGA

The previous transfer strategy utilises a given gravity assist sequence during the transfer to Mercury: L–E–V–V–M–M. The V–V phase is a 1 : 1 resonant orbit with Venus, taking 225 days.

Many other transfer variations are possible. Alternative routes may be developed to explore possible ΔV savings and/or thrust reduction possibilities. One option is to maximise the potential of the Moon–Earth phase by achieving a high Earth fly-by speed. This requires a larger ΔV before Earth gravity assist.

There are then implications for the following VGA, as a high Earth departure speed results in potentially higher fly-by speeds at Venus, and it may not be possible or desirable to enter a resonant orbit at Venus. It is possible to directly lower perihelion close to the perihelion of Mercury. Not using a Venus resonant orbit has the advantage of saving time. These factors can be used to achieve a lower ΔV transfer sequence to eventual Mercury rendezvous but a large manoeuvre is required before EGA. An example is shown in Figure 5.2.5.

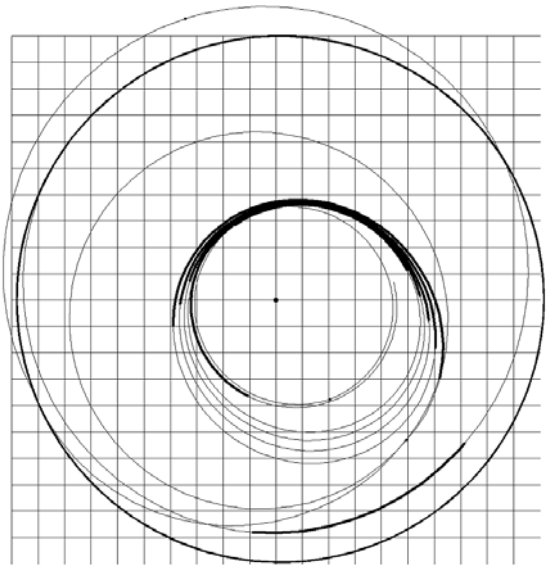

Figure 5.2.3. Low-thrust transfer with LGA/EGA and two Venus GAs for the 2009 case. The grid is 1 AU from centre to edge. Earth's orbit is shown as the thick outer circle, in addition to the spacecraft transfer trajectory. Thrust arcs are bold lines.

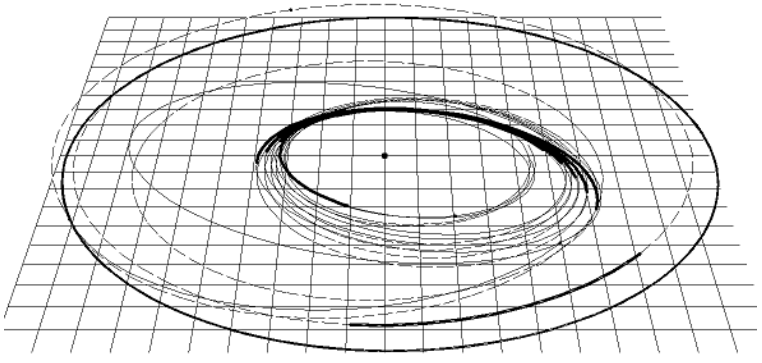

Figure 5.2.4. Low-thrust transfer with LGA–EGA and two Venus GAs for the 2009 case, illustrating out-of-ecliptic motion. Dashed lines show the projection of the transfer in the ecliptic.

5.2.2 Analysis of missions to Jupiter and Saturn using low thrust

Multi-gravity assist transfers to the outer planets typically use gravity assists at Venus and Earth before proceeding to Jupiter or beyond. Therefore, injection must take place into a Venus crossing orbit after leaving Earth. Several such missions are descirbed in Section 5.1. A simple application of low-thrust propulsion

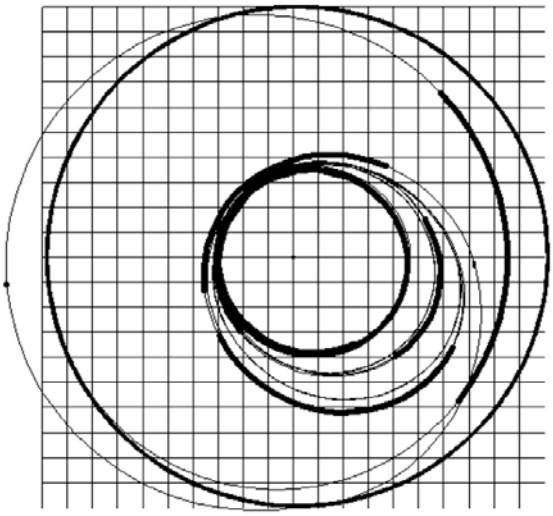

Figure 5.2.5. A single VGA based transfer after launch in 2010. The transfer uses an L-E-V-M-M-M-M sequence and takes 4.75 years. Thrust /mass is constant at 200 mN/tonne and deep space, low-thrust ΔV approximately 5.28 km/sec.

is to use the system to apply the deep-space ΔVs instead of a high-thrust chemical propulsion system. This can result in a significant reduction in fuel mass, but the basic mass of the low-thrust system must also be considered.

A better use of a high specific impulse, low thrust system is to consider the lunar–Earth gravity-assist routes described in the Chapter 4 and referred to in the previous section on transfers to Mercury. This enables the utilisation of an injection to a low-energy lunar crossing orbit. This mechanism, applied to transfers to Jupiter and Saturn, will now be considered.

Reaching Jupiter with LGA and EGA transfer

This strategy starts with utilisation of a lunar gravity-assisted low-energy Earth escape. The spacecraft return to Earth occurs typically 15 months later, after an intermediate deep-space ΔV to increase eccentricity and therefore Earth approach speed.

After the second gravity assist of the mission, taking place at Earth, aphelion is raised considerably, but further thrust arcs are generally needed to optimally raise aphelion to Jupiter radius. Capture at Jupiter can then be implemented by any of a number of techniques (including impulsive pericentre manoeuvres and Jupiter moon gravity assisted capture). Low-thrust propulsion could be considered to assist capture, but the reduction in solar intensity (a factor of more than 25 compared with Earth radius) means that an SEP system would only be able to operate at a much reduced thrust level. However, a nuclear electric propulsion system would be able to apply a constant thrust throughout the mission.

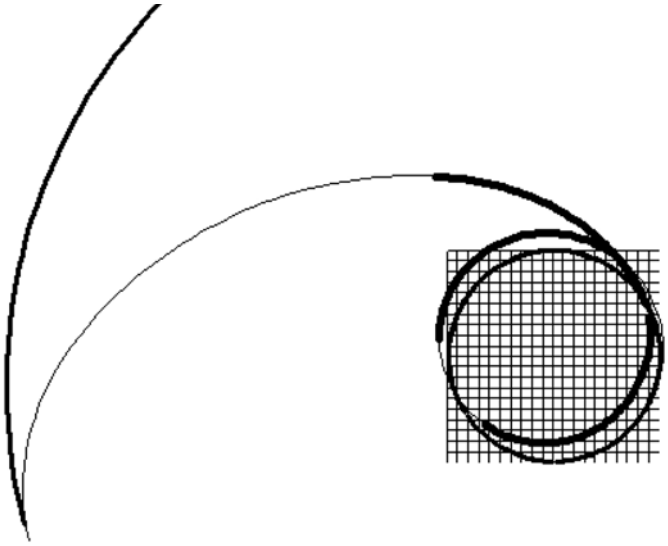

Figure 5.2.6. Transfer to Jupiter with low-thrust plus LGA and single EGA and thrust/mass at 150 mN/tonne. Thick line arcs denote the low thrust manoeuvres. Earth's and Jupiter's orbits are shown. The grid is 1 AU from centre to edge.

The first scenario to be considered is the raising of aphelion to approximately 5.2 AU, via EGA and low thrust, to ensure a rendezvous with Jupiter. Orbit insertion at Jupiter is then achieved with either a direct high-thrust manoeuvre at Jupiter pericentre, or the ΔVs may be reduced by using a gravity assist at one of Jupiter's moons.

In Figure 5.2.6, two thrust arcs prior to EGA are shown, together with a thrust period after EGA. The thrust/mass is 150 mN/tonne. The greatest distance from the Sun at which a thrust arc occurs is approximately 2.5 AU. The initial LGA uses an initial trans-lunar orbit with apogee above the Moon at approximately 500,000 km. After the LGA, the spacecraft escapes from the Earth–Moon system with a V_∞ of approximately 1,200 m/s. An initial outward departure is efficient in this case (after LGA)

Higher apogee trans-lunar orbits are possible, which yield greater Earth departure V_∞. In such cases, the subsequent low-thrust ΔV is reduced, but the mass in the trans-lunar orbit is also reduced.

The trans-lunar orbit is reached either by direct injection by the launcher, or injection into a lower elliptical orbit and the spacecraft performs perigee manoeuvres to raise apogee. In the second case, high-thrust propulsion is implied and thus typical chemical system specific impulses. An optimum apogee, altitude for the trans-lunar orbit can be obtained from these considerations. This is typically in the range 400,000–500,000 km.

The transfer ΔV is dependent on the thrust/mass used. Figure 5.2.7 shows the relationship, based on the assumption that thrust remains constant throughout the transfer. This figure does not include the Jupiter orbit insertion ΔV.

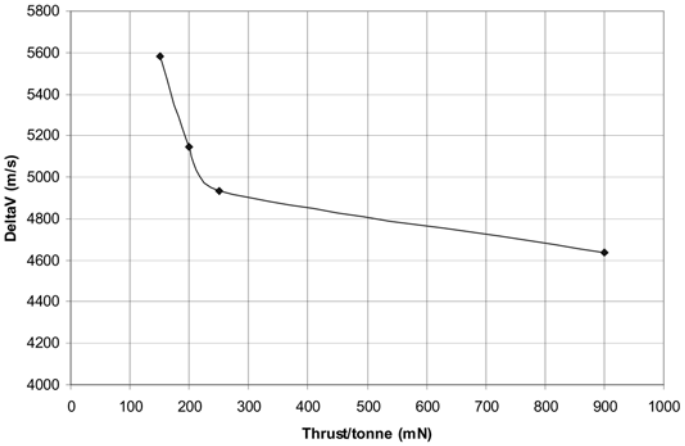

Figure 5.2.7. Transfer ΔV to reach Jupiter with LGA and single EGA thrust. This is the 'low-thrust' ΔV applied after LGA and before Jupiter rendez-vous. The low-thrust ΔV increases sharply as thrust/mass is reduced below 200 mN/tonne. An initial outward departure is assumed (after LGA).

The transfer time is not significantly effected by the thrust within the above range. Transfer times from LGA to the vicinity of Jupiter are 3.7 years. Therefore, although the low-thrust ΔV is quite high, the transfer duration is relatively short.

LGA plus double EGA transfer

It is possible to reduce the low thrust ΔV by introducing a second gravity assist at Earth. This strategy starts with utilisation of a lunar gravity-assisted low-energy Earth escape. Return to Earth once again occurs typically 15 months later after an intermediate deep-space ΔV to increase eccentricity and therefore Earth approach speed.

After the Earth gravity assist, the spacecraft enters a near-resonant orbit with Earth, returning after typically two years. Prior to return, a deep-space manoeuvre is performed near aphelion to reduce perihelion and so increase Earth approach speed.

After the second Earth gravity assist, aphelion is raised to Jupiter radius. As in the single EGA case, capture can be implemented by any of a number of techniques (including impulsive pericentre manoeuvres).

The initial LGA uses an initial trans-lunar orbit with apogee above the Moon at approximately 500,000 km. After the LGA the spacecraft escapes from the Earth–Moon system with a V_∞ of approximately 1,200 m/s. The total low-thrust ΔV is therefore 2,350 m/s. This transfer is illustrated in Figure 5.2.8 and Table 5.2.3. An initial outward departure is assumed.

In Figure 5.2.9 a variable thrust (assuming a $1/r^2$ dependence) increases the low-thrust ΔV slightly. This is a result of the effect of the slightly reduced thrust in some regions of the first Moon-to-Earth loop, as well as the effect of the reduced thrust in

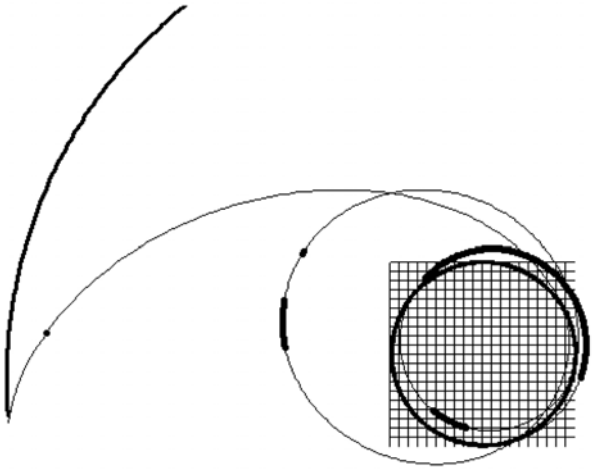

Figure 5.2.8. Double EGA transfer to Jupiter with constant thrust at 100 mN/tonne. Thick line arcs denote the low-thrust manoeuvres. Earth's and Jupiter's orbits are shown. The grid is 1 AU from centre to edge.

Table 5.2.3. Low-thrust transfer to Jupiter using double EGA and constant thrust of 100 mN/tonne. Initial outward departure is assumed (after LGA).

	Epoch	Low-thrust ΔV	V_∞
Launch	March 2008		$V_\infty = 1.2$ km/s after LGA
First EGA	May 2009	1,800 m/s	$V_\infty = 5.4$ km/s
Second EGA	July 2011	550 m/s	$V_\infty = 9.2$ km/s
Jupiter Arrival	Nov 2013		$V_\infty = 5.8$ km/s

the Earth-to-Earth loop. The details of the sequence are shown in Table 5.2.4, illustrating that the V_∞ and epochs do not change significantly. The total low-thrust ΔV is therefore 2,520 m/s. The ΔV/thrust relationship, for a case of constant thrust, is shown in Figure 5.2.10, using double EGA and a two-year resonant orbit. The low-thrust ΔV increases sharply as thrust/mass is reduced below 100 mN/tonne, but is much less sensitive to lower thrust levels than the single EGA case.

The transfer time is not significantly effected by the thrust within the above range. Transfer times from LGA to the vicinity of Jupiter are 5.7 years.

This transfer depends on the relative locations of Earth and Jupiter, and so is dependent on the synodic period of 1.1 years. Optimum launch opportunities therefore arise at this interval. Furthermore, the transfer ΔV will not change significantly between these optimum launch epochs. After 11 such opportunities, the sequence approximately repeats as one Jupiter orbital period is reached.

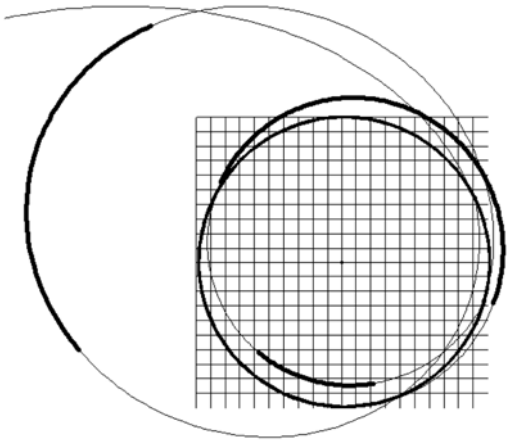

Figure 5.2.9. Inner circuits of two-EGA transfer to Jupiter with 100 mN thrust per tonne at 1 AU and reducing with $1/r^2$.

Table 5.2.4. Low-thrust transfer to Jupiter using double EGA and radially dependent thrust. Initial outward departure is assumed.

	Epoch	Low-thrust ΔV	V_∞
Launch	March 2008		$V_\infty = 1.2$ km/s after LGA
First EGA	May 2009	1,970 m/s	$V_\infty = 5.4$ km/s
Second EGA	July 2011	550 m/s	$V_\infty = 9.2$ km/s
Jupiter arrival	Nov 2013		$V_\infty = 5.8$ km/s

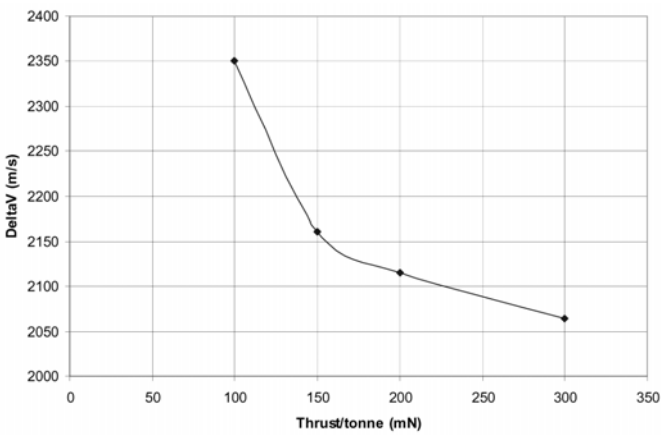

Figure 5.2.10. Transfer ΔV to Jupiter with LGA and double EGA Vs thrust. This is the low-thrust ΔV after LGA and before Jupiter. An initial outward departure is assumed.

Table 5.2.5. Double EGA low-thrust mission to Saturn with constant thrust at 100mN/tonne and initial outward departure after LGA. ΔVs are applied between previous and current events.

	Epoch	Low-thrust ΔV	V_∞
Launch + LGA	Feb 2018		$V_\infty = 1.2$ km/s after LGA
First EGA	April 2019	1,780 m/s	$V_\infty = 5.4$ km/s
Second EGA	March 2021	890 m/s	$V_\infty = 10.9$ km/s
Saturn arrival	Dec 2026	1,330 m/s	$V_\infty = 5.6$ km/s

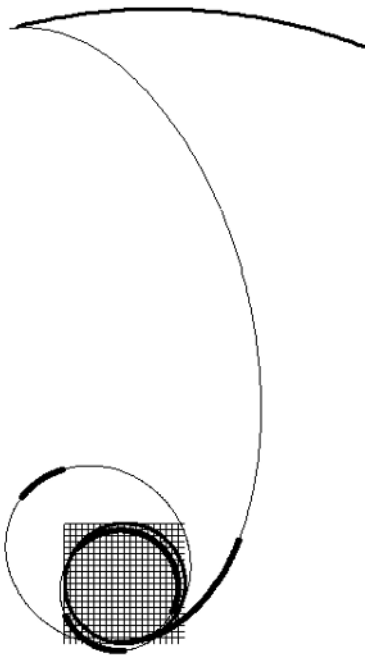

Figure 5.2.11. Two-EGA transfer to Saturn with constant thrust at 100 mN/tonne. Thick line arcs denote low-thrust arcs. The orbits of Earth and Saturn are shown. The grid is 1 AU from center to edge.

Transfers to Saturn with LGA and double EGA

Saturn lies at almost twice the distance from the Sun than Jupiter, and the use of solar-powered propulsion to assist in capture at Saturn can therefore be discounted. However, such a system may still be used to raise aphelion for Saturn rendezvous in the same way as a transfer to Jupiter.

The extra ΔV required now places very large demands on a single EGA strategy, and a double EGA strategy will therefore be considered as the preferred option (see Figure 5.2.11 and Table 5.2.5). The total low thrust ΔV is 4,000 m/s, where an initial outward departure after LGA is adopted.

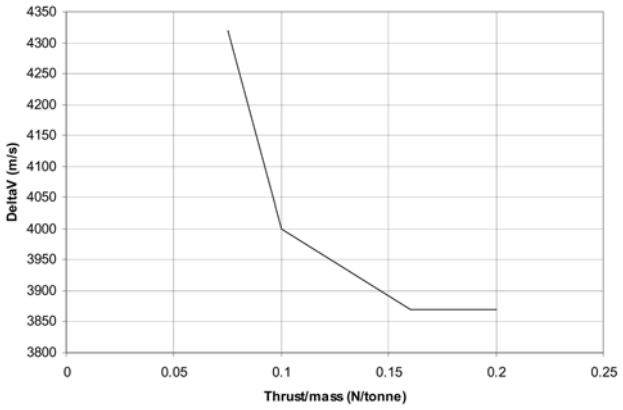

Figure 5.2.12. Transfer ΔV to Saturn with LGA and double EGA Vs thrust for the case of initial outward departure after LGA.

The initial LGA uses an initial trans-lunar orbit with apogee above the Moon at approximately 500,000 km. After the LGA, the spacecraft escapes from the Earth–Moon system with a V_∞ of approximately 1,200 m/s. Two EGAs are used. Thrust is used after the second EGA to boost aphelion to reach Saturn. The excess hyperbolic speed on arriving at Saturn is approximately 5.6 km/sec.

The ΔV/thrust relationship is shown in Figure 5.2.12 using double EGA and a two-year resonant orbit. Thrust is constant over the transfer. The ΔV rises rapidly when below 100 mN/tonne. It is considerably higher than the case of transfer to Jupiter.

The transfer time is not significantly effected by the thrust within the above range. Transfer times from LGA to the vicinity of Saturn are nearly 8.8 years. As in the case of a transfer to Saturn, opportunities arise almost every year; that, is the Earth–Saturn synodic period of 1.1 years.

In Figure 5.2.13, using a $1/r^2$ thrust dependence results in a redistribution of the ΔV profile. There is an increase in the ΔV between EGAs, rather than after the final EGA where thrust is rapidly decreasing as the spacecraft leaves Earth radius. The total ΔV is increased over the constant thrust case, and is similar to the situation in the transfer to Jupiter.

The total low thrust ΔV is 4,310 m/s (Table 5.2.6).

A further option with such transfers is to use low thrust to assist in the insertion at the target planet. The excess hyperbolic speed at Saturn is approximately 5.6 km/sec. This could be substantially reduced by using an accelerating low-thrust manoeuvre when approaching Saturn. However, there are certain consequences.

Firstly, a constant-thrust system must be considered, as a radially dependent system would only achieve very low thrust at Saturn's distance from the Sun. This therefore implies, for example, a nuclear electric system. Secondly, the total ΔV for the electric propulsion system will increase. This may be significant if a near-parabolic approach is required at Saturn. The third point is that the optimal transfer duration will increase slightly over the direct approach cases.

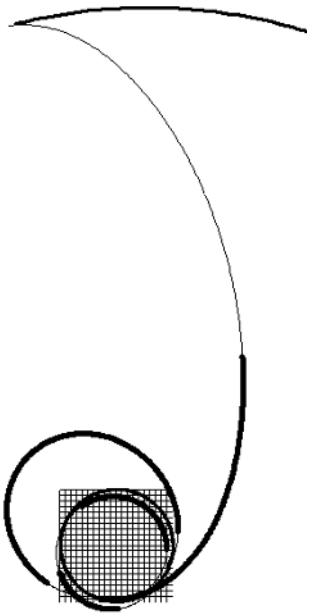

Figure 5.2.13. Two-EGA transfer to Saturn with radial dependent thrust at 100 mN/tonne at 1 AU. Thick line arcs denote low thrust arcs. The orbits of Earth and Saturn are shown. The grid is 1 AU from center to edge.

Table 5.2.6. Double-EGA low-thrust mission to Saturn with radially dependent thrust at 100 mN/tonne at 1 AU. ΔVs are applied between previous and current events. An initial outward departure after LGA is used.

	Epoch	Low-thrust ΔV	V_∞
Launch + LGA	Feb 2018		$V_\infty = 1.2$ km/s after LGA
First EGA	April 2019	2,000 m/s	$V_\infty = 5.4$ km/s
Second EGA	March 2021	1,380 m/s	$V_\infty = 11.4$ km/s
Saturn arrival	Dec 2026	930 m/s	$V_\infty = 5.6$ km/s

In the transfer shown in Figure 5.2.14 and Table 5.2.7, a large accelerating manoeuvre is implemented with the low-thrust system when approaching Saturn. The thrust arc is apparent, as approximately 5 km/sec is applied here. With the thrust/mass used at 100 mN/tonne, this manoeuvre takes approximately 1.3 years. The excess hyperbolic speed (the corresponding insertion manoeuvre) at Saturn is constrained to be just above a parabolic approach condition; that is, 200 m/s. A small capture manoeuvre to a high elliptical orbit may then be performed with a chemical propulsion system.

Therefore, total ΔV is approximately 8,850 m/s. The spacecraft arrives at Saturn one year later than the direct approach case. Such a scenario could be utilised with a minimal chemical propulsion element as the capture manoeuvre is now much

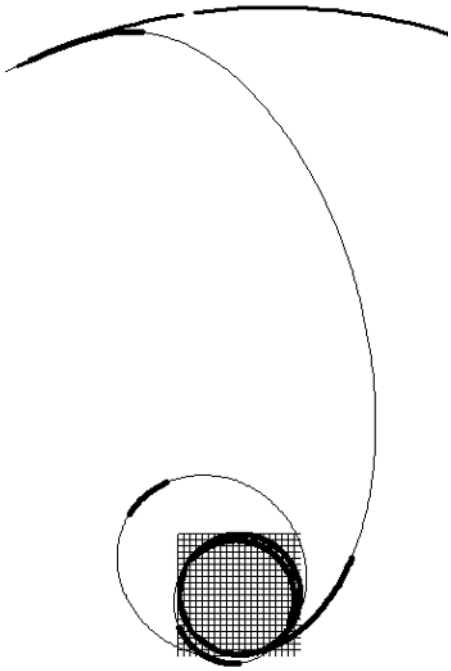

Figure 5.2.14. Two-EGA transfer to Saturn with constant thrust at 100 mN/tonne at 1 AU and low-V_∞ approach at Saturn. Thick line arcs denote low-thrust arcs. The orbits of Earth and Saturn are shown. The grid is 1 AU from center to edge.

Table 5.2.7. Double-EGA low-thrust mission to Saturn with low-speed arrival and using constant thrust at 100 mN/tonne.

	Epoch	Low-thrust ΔV before event	V_∞
Launch	Feb 2018		$V_\infty = 1.2$ km/s after LGA
First EGA	April 2019	1,780 m/s	$V_\infty = 5.4$ km/s
Second EGA	March 2021	850 m/s	$V_\infty = 10.7$ km/s
Saturn arrival	Dec 2027	1,220 m/s leaving Earth 5,000 m/s approaching Saturn	$V_\infty = 0.2$ km/s

reduced. Transfer from the high elliptical capture orbit can be assisted with gravity assists at Saturn's moon Titan. The additional low-thrust ΔV required for the transfer approximates to the change in excess hyperbolic speed at Saturn compared with the previous case.

A range of such approach strategies may be considered. It has been shown previously that a gravity-assisted capture may be performed at Saturn using Titan. A high elliptical capture orbit may be reached with an approach excess hyperbolic speed of typically 3–3.5 km/sec. Therefore, an improved strategy at Saturn would be

to reduce the excess hyperbolic speed to approximately 3 km/sec and then use a Titan-assisted capture. The approach ΔV required for this manoeuvre would be approximately 2.5 km/sec.

If gravity-assisted capture is not used, then a minimum total fuel utilisation capture would also use a higher approach excess hyperbolic speed. In this scenario a more substantial chemical propulsion system is implied. Such optimum approach excess hyperbolic speeds are discussed in Chapter 4.

This strategy, in conjunction with a nuclear powered electric propulsion system, may be repeated at any of the outer planets to reduce the insertion manoeuvre.

5.2.3 Missions to Pluto with low-thrust

A series of options for missions to Pluto have previously been discussed in Chapter 1 and also earlier in this chapter. A number of intermediate-duration transfers were identified, all with relatively high approach velocities at Pluto, consistent with fly-by missions, rather than a Pluto rendezvous. A means of accomplishing a rendezvous is to use a low-thrust propulsion system with high specific impulse, such that the fuel fraction is feasible.

A large manoeuvre is therefore required when approaching Pluto, to reduce the relative velocity. Typical approach velocities for Pluto fly-by-type missions are 10–15 km/sec. An optimal approach velocity, to be followed by a high-thrust pericentre insertion manoeuvre, is only several hundreds of m/s, and a large speed change must be accomplished by low-thrust propulsion.

At Pluto's distance from the Sun, solar-powered electric propulsion is not feasible, and nuclear-powered systems would be required. Therefore, a constant thrust system is implied. A similar mission profile may be considered to that described previously for high thrust missions. The use of a single Earth gravity assist, a Jupiter gravity assist and a 14-year mission constraint can be used. This could also be modified to a double Earth gravity assist scenario, before the transfer to Jupiter is made, in the same way as described for the missions to Jupiter and Saturn.

In this example (see Figure 5.2.15 and Table 5.2.8) an initial three-year Earth resonant orbit is used. Multiple low-thrust arcs are used throughout the mission.

A large decelerating manoeuvre is implemented with the low-thrust system when approaching Pluto. The thrust arc is apparent in the figure; approximately 15 km/sec is applied here. The thrust/mass used is 200 mN/tonne, and the manoeuvre takes approximately 2.7 years. The excess hyperbolic speed at Pluto is constrained to be approximately 100 m/s. On arrival, a small capture manoeuvre to a high elliptical orbit about Pluto may be performed with a chemical propulsion system.

The lower illustration in Figure 5.2.15 shows the out-of-ecliptic rendezvous with Pluto. The in-ecliptic projection is also shown (without thrust arcs added), as is the projection of Pluto's orbit in the ecliptic.

This mission can be modified using a double EGA after an initial LGA. The strategy to instead use a double EGA sequence includes a lower energy launch to a lunar crossing orbit, then perform a gravity assist at the Moon, enter a near-one-year

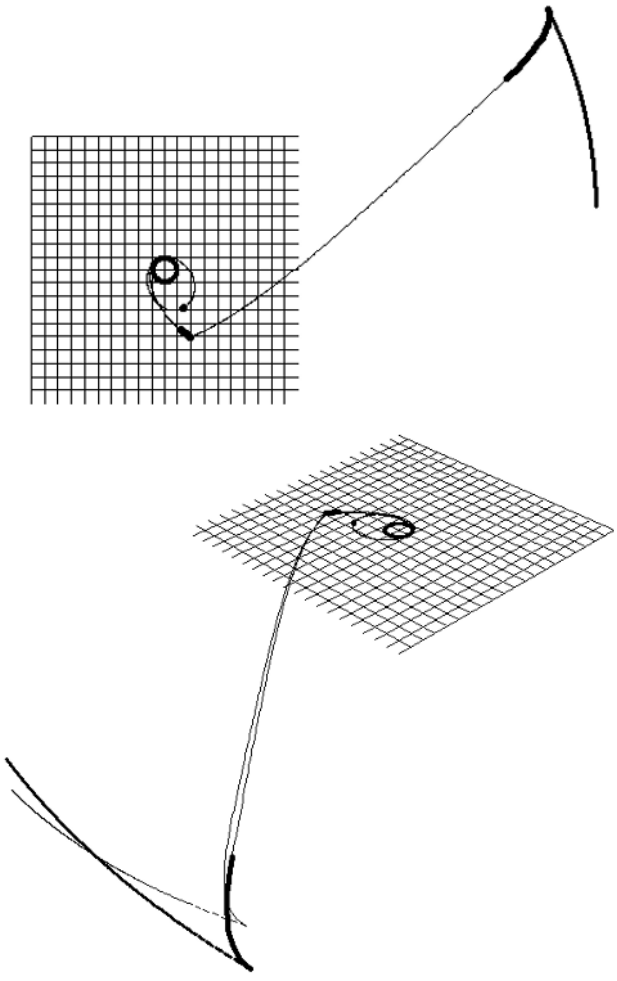

Figure 5.2.15. EGA and JGA transfer to Pluto with constant thrust at 200 mN/tonne and low V_∞ approach at Pluto. The orbits of Earth and part of Pluto's orbit are shown. The grid is 10 AU from centre to edge. In the second plots the projections of motion into the ecliptic are seen.

Table 5.2.8. Single EGA, single JGA low-thrust mission to Pluto with a 14-year transfer and constant thrust at 200 mN/tonne.

	Epoch	Low-thrust ΔV before event	V_∞
Launch	Oct 2012		$V_\infty = 7$ km/s
First EGA	Nov 2015	360 m/s	$V_\infty = 10.4$ km/s
First JGA	June 2017	2,000 m/s	$V_\infty = 13.2$ km/s
Pluto arrival	Nov 2026	15,000 m/s approaching Pluto	$V_\infty = 0.1$ km/s

Table 5.2.9. Double EGA, single JGA low-thrust mission to Pluto with constant thrust at 200 mN/tonne.

	Epoch	Low thrust ΔV before event	V_∞
Launch/post LGA state	Aug 2012		$V_\infty = 1.2$ km/s
First EGA	Nov 2013	2,000 m/s	
Second EGA	Nov 2015	800 m/s	$V_\infty = 10.4$ km/s
First JGA	June 2017	2,000 m/s	$V_\infty = 13.2$ km/s
Pluto arrival	Nov 2026	15,000 m/s approaching Pluto	$V_\infty = 0.1$km/s

Earth resonant orbit with intermediate low-thrust manoeuvres, followed by a two-year resonant orbit with an intermediate low-thrust manoeuvre. After the second EGA, a further low-thrust arc is needed to provide the optimal rendezvous conditions with Jupiter for gravity assist there. This would result in the mission characteristics shown in Table 5.2.9. In this case the low thrust ΔV is further increased, but the launch energy is much less, resulting in a significantly more efficient mission design.

In either scenario this is a large ΔV, even for an electric prolusion system, and high specific impulse would be required to achieve an efficient transfer. If the mission duration constraint is relaxed, then the low-thrust ΔV can be significantly reduced. For example, a 17-year transfer can be achieved with a low-thrust ΔV reduction of approximately 3,000 m/s.

5.3 MISSIONS USING GRAVITY ESCAPE AND CAPTURE

Chapter 4 examined the possibilities of escape and capture by the use of gravitational perturbations, and some examples of escape orbits were shown. These principles can now be used in a complete mission design, and three examples are considered in this section.

The first examples start from Jupiter, which is the most effective planet for utilisation of gravitational escape. The first case considers a transfer to Saturn with capture at Saturn also achieved by gravitational capture. The second case targets Uranus, and gravitational capture is also used there. The missions are optimised from end to end, in terms of ΔV. The optimisation of the departure and arrival phases uses the strategy described in Chapter 4, with regard to the selection of the key orbital parameters at the osculating pericentre.

Finally, an example of a mission to Venus is considered. The missions from Jupiter show good performance in terms of ΔV, but are not feasible as true mission designs due to the long transfer durations required. However, this type of transfer strategy, when used with a mission to Venus, is attractive both in terms of ΔV and transfer duration. A number of options are considered for Venus.

5.3.1 Transfer from Jupiter to Saturn

The two most massive planets in the Solar System are Jupiter and Saturn. In the previous analyses in Chapter 4, it is clear that a moderate energy escape may be obtained from Jupiter using gravitational methods, the aphelion achieved being approximately 13 AU in the examples considered. Therefore, Saturn may be reached, in principle, using such an escape. A gravitational capture at Saturn may then be used to lower the energy of the spacecraft with respect to Saturn and reach a bound orbit.

Intermediate manoeuvres may be used to assist in the link of these two gravity-perturbed phases. In this example, low-thrust manoeuvres are used, although the same effect is achievable with a high-thrust system. The optimisable parameters that define this transfer must be considered. These are summarised as follows:

Parameters at Jupiter pericentre.	
Pericentre: 1 million km	The direction of the line of apses is optimised to generate a change in heliocentric energy required to interface with an approach trajectory to Saturn.
Apocentre: 43 million km	
Inclination (with respect to ecliptic): optimisable	
Argument of pericentre: optimised	The inclination of the initial Jupiter orbit is optimised to generate an out-of-ecliptic component so that the Jupiter escape and Saturn capture arcs may link.
Deep-space electric propulsion manoeuvres.	
Two manoeuvres are possible with intermediate coast arc	Manoeuvre ΔVs and directions are optimised.
Parameters at Saturn pericentre.	
Pericentre: 0.6 million km	The direction of the line of apses (at Saturn pericentre) is optimised to generate a capture from a heliocentre approach orbit, that interfaces with the departure trajectory from Jupiter. The inclination of the final Saturn orbit (at pericentre) is optimised to generate an out-of-ecliptic component so that the Jupiter escape and Saturn capture arcs may link.
Apocentre: 59 million km	
Inclination (with respect to ecliptic): optimisable	
Argument of pericentre: optimised	

The choice of orbits at Jupiter and Saturn both have relatively low pericentres. These are chosen as being practical values that may be used to connect with target orbits of interest, without change being required to the pericentre. Otherwise, such manoeuvres could be expensive in terms of ΔV.

A small deep-space manoeuvre is needed to complete the transfer. When the departure and arrival phases are optimised as described above, this manoeuvre is

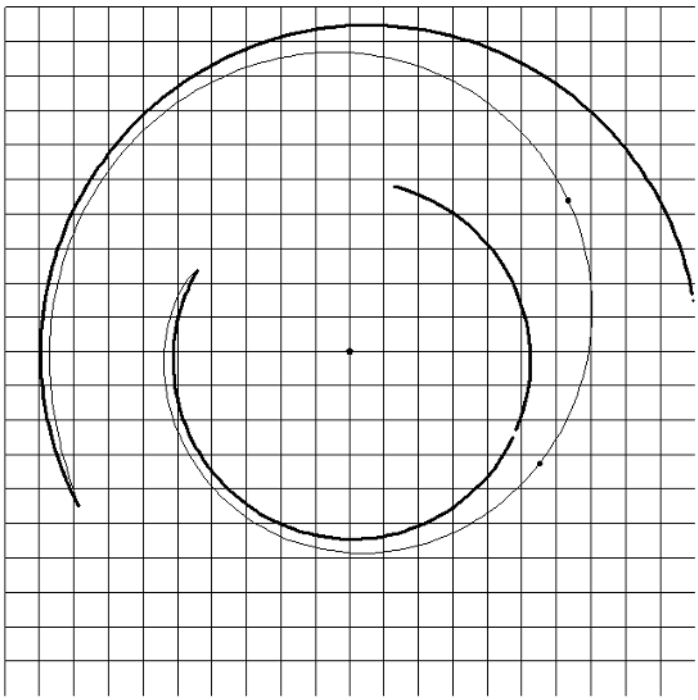

Figure 5.3.1. Transfer from Jupiter to Saturn using gravitational escape and capture. Jupiter's and Saturn's orbits are shown. Grid size is 10 AU from centre to edge with a sub-grid of 1 AU.

approximately 65 m/s for the launch epoch considered in Figure 5.3.1. This is in September 2012.

Such a transfer could potentially be further improved by including the Jupiter and Saturn apocentres as optimisable parameters. The ΔV required for a change in apocentre at Jupiter by 10 million km is 33 m/s. These small ΔVs can be used to further 'tune' the interplanetary transfer orbit. The effect of higher-apocentre orbits (the osculating value defined at planet or major body initial pericentre) on heliocentric orbits was discussed in Chapter 4. The apocentre values chosen here (as being close to the Lagrange points) are typical of values that are suitable for achieving escape trajectories.

This transfer, from Jupiter pericentre to Saturn pericentre, takes approximately 22 years. The aphelion after leaving Jupiter is approximately 1.3 billion km, requiring an excess hyperbolic speed at Jupiter of 1.49 km/sec if gravitational escape methods were not used. The perihelion when approaching Saturn is approximately 930 million km, requiring an excess hyperbolic speed at Saturn of 1.21 km/sec if calculated by velocity vector subtraction. In Figure 5.3.1, the transfer from Jupiter to Saturn is dominated by the gravity perturbed escape and capture phases. A small linking manoeuvre is performed in deep space. The details of the motion relative to Jupiter in the departure phase are shown in Figure 5.3.2.

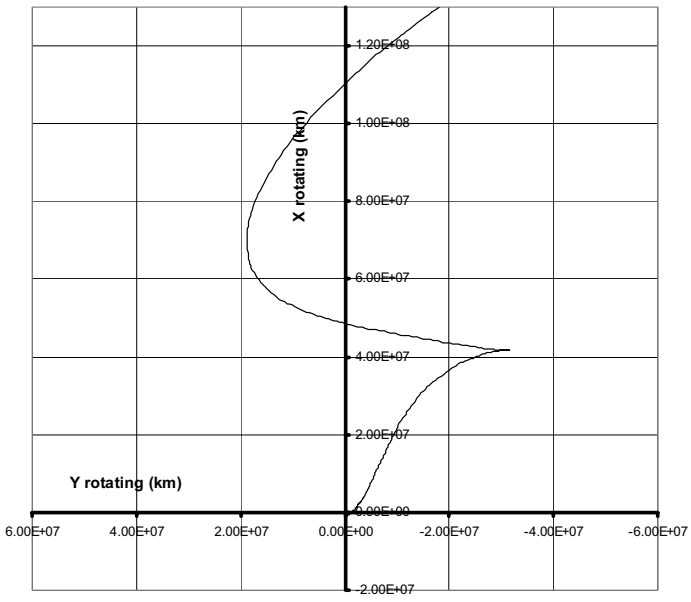

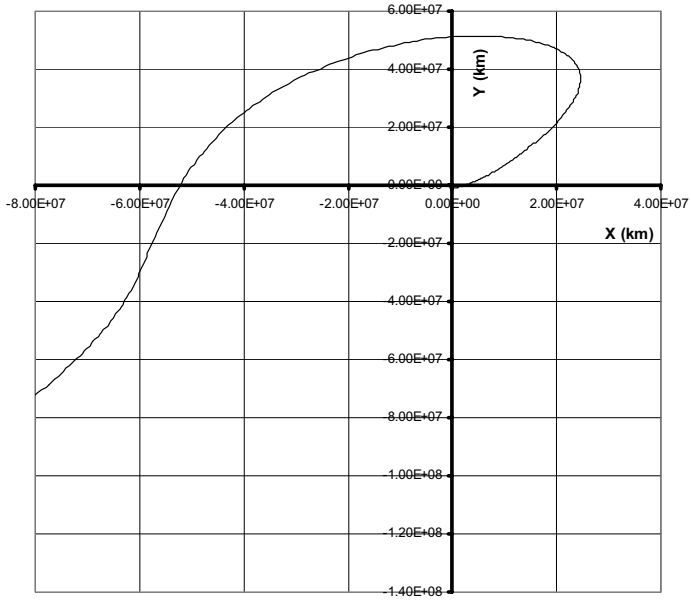

Figure 5.3.2. Escape from a Jupiter bound orbit with a semi-major axis of 22 million km, using gravitational assistance. In the upper figure, the gravitational escape phase from Jupiter is shown here in a Jupiter–Sun rotating reference frame. X is the positive in the Sun–Jupiter direction.In the lower figure the gravitational escape phase shown in a Jupiter-centre inertially oriented reference frame.

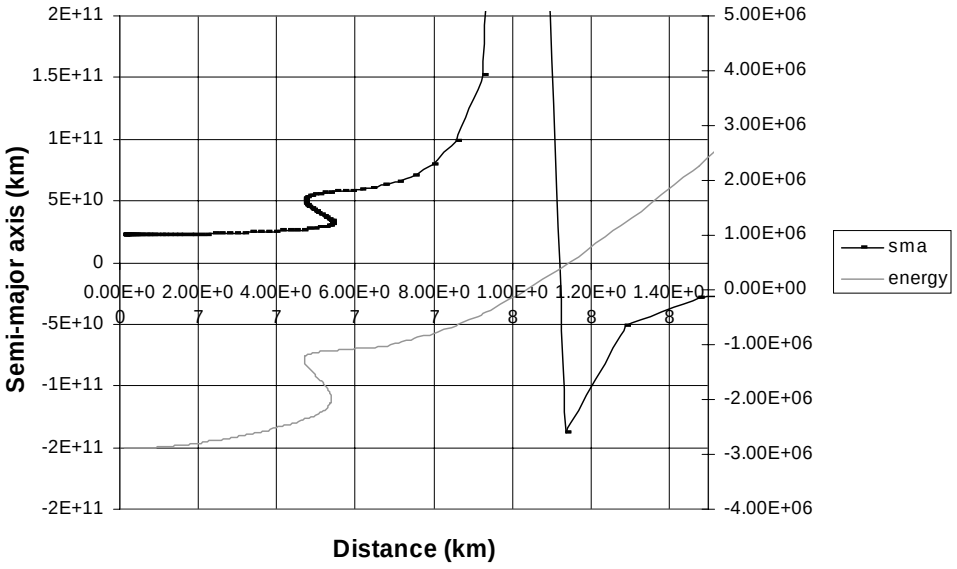

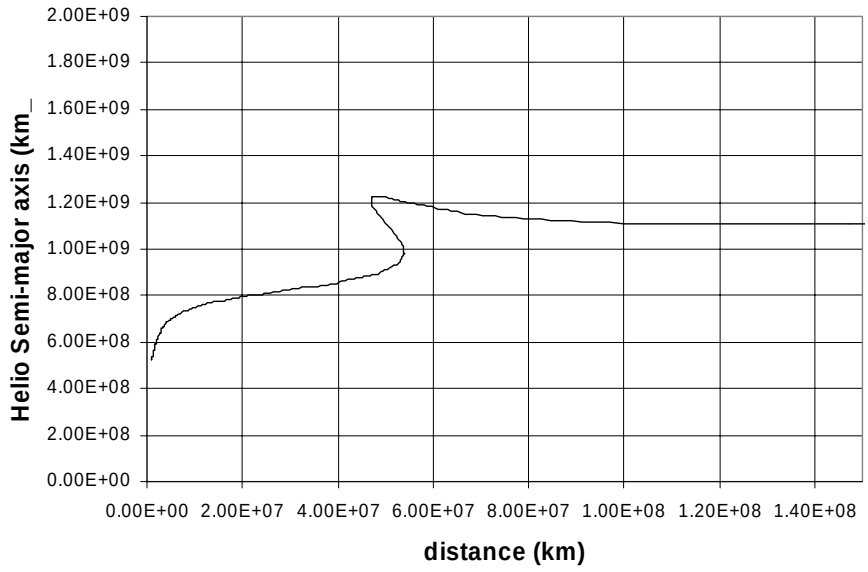

Figure 5.3.3. Energy departing Jupiter for transfer to Saturn. The energy relative to Jupiter is shown in the upper figure. The Jupiter relative energy becomes positive at approximately 110 million km from Jupiter. This is plotted against the right axis. This radius is considerably higher than the gravitationally-raised pericentre of the evolved orbit (at approximately 50 million km). In the lower figure the heliocentric relative semi-major axis achieved is 1,100 million km. This is the value required for the transfer to a Saturn capture orbit.

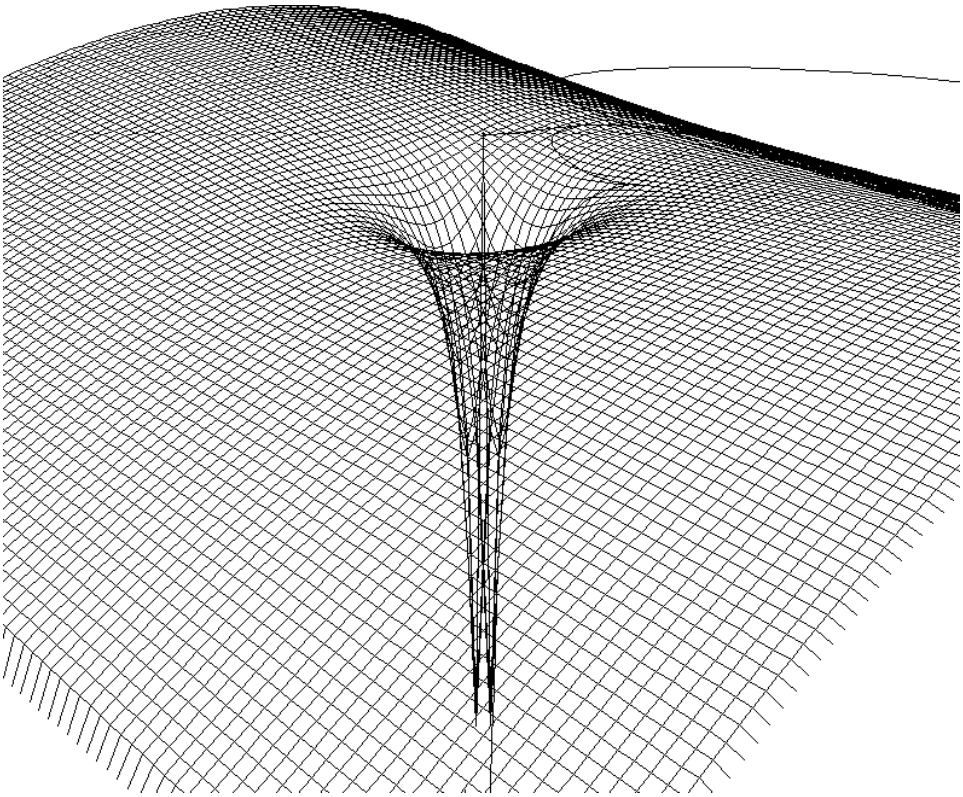

Figure 5.3.4. Gravitational escape from Jupiter plotted in a rotating reference frame over the Jacobi potential surface. The centre of the potential well is Jupiter. The two saddle points are the Sun–Jupiter L1 and L2 points. The spacecraft trajectory is plotted over the potential surface. The spacecraft may be seen close to L2 in reaching an escape trajectory to Saturn. The distance from centre to edge is 500 million km.

The characteristics of such a departure from Jupiter can be seen by examining the trajectory plotted over a potential surface. This is shown in Figure 5.3.4. The potential surface here is that related to the Jacobi constant – the gravitational potentials of Sun and Jupiter plus the angular velocity term arising from Jupiter's orbital velocity. The trajectory is expressed in a Jupiter–Sun rotating reference frame.

The characteristics of the approach and capture at Saturn may now be considered (Figure 5.3.5). Such a process is essentially the reverse of the Jupiter escape trajectory. Although Saturn does not possess such a large gravity field as Jupiter, it still provides a strong gravitational influence at this large solar distance. Its colinear Lagrange points are, in fact, at a slightly greater distance from Saturn than those of Jupiter from the planet, at approximately 65 million km.

In Figure 5.3.6, the gravitational capture at Saturn occurs from an effective approach excess hyperbolic speed of approximately 1,200 m/s.

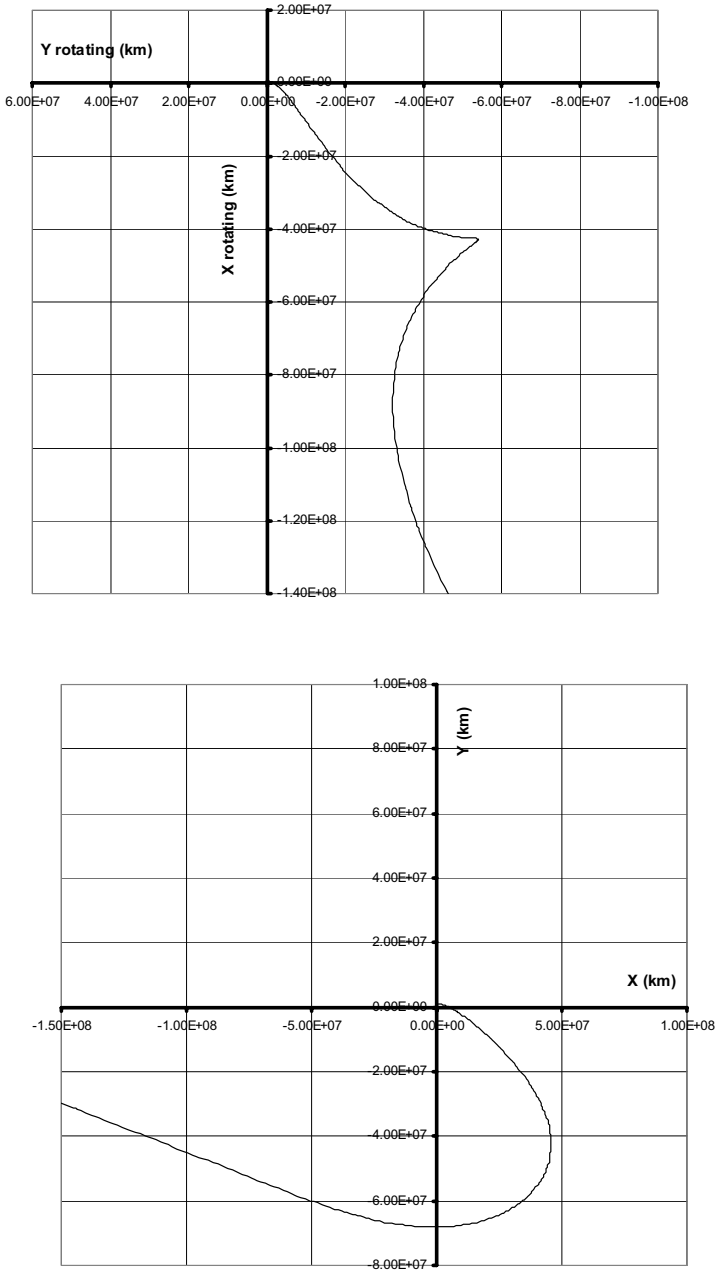

Figure 5.3.5. Capture to a Saturn bound orbit with a semi-major axis of 30 million km, using gravitational assistance. The upper figure shows the gravitational capture phase at Saturn in a Saturn–Sun rotating reference frame. Approach is from the sunward side of Saturn. X is positive in the Sun–Saturn direction. The lower figure shows the gravitational capture phase in a Saturn-centred, inertially oriented reference frame.

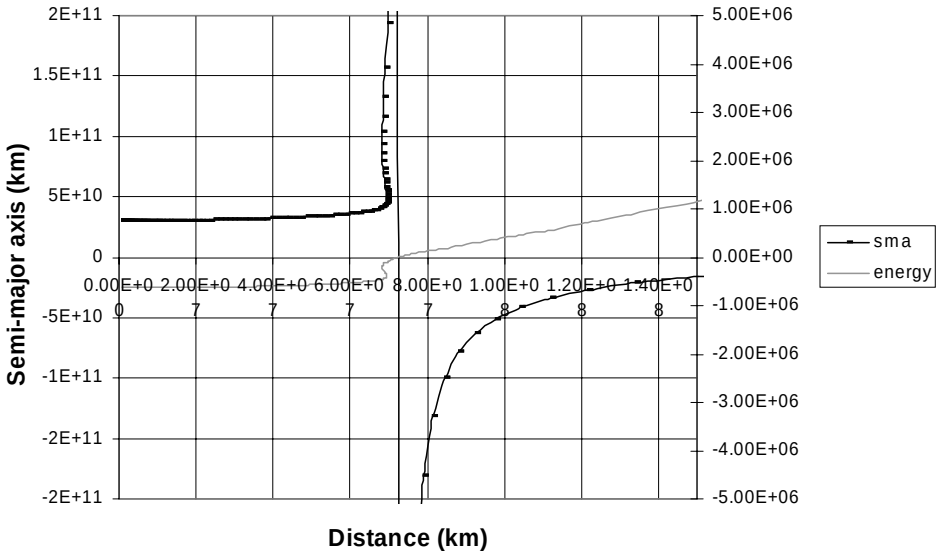

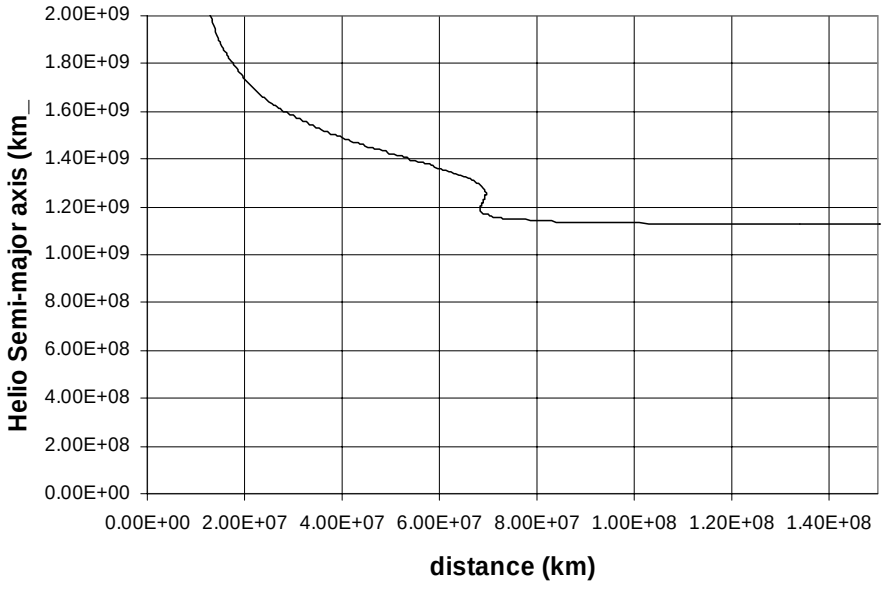

Figure 5.3.6. Energy approaching Saturn after transfer from Jupiter. In the upper figure the energy with respect to Saturn is shown. The Saturn relative energy becomes positive at approximately 70 million km from Saturn. This is slightly higher than the intermediate pericentre of the approaching orbit (before final low pericentre is reached). Energy is plotted against the right axis. The maximum possible energy change at capture is not needed for a transfer required to intersect with the Jupiter escape orbit. In the lower figure the semi-major axis relative to the Sun is shown. The heliocentric semi-major axis approaching Saturn is 1,100 million km. This is the value required to interface with the departure from Jupiter and the small connecting deep-space manoeuvre.

5.3.2 Transfer from Jupiter to Uranus

A more demanding target for a transfer from Jupiter is Uranus, as it has a semi-major axis of 2,860 million km and as such is considerably higher than the aphelion achievable from the high-energy-change escape cases examined in Chapter 4.

Intermediate manoeuvres may be used to assist in the link of these two gravity-perturbed phases. In this example, low-thrust manoeuvres are used, although the same effect is achievable with a high-thrust system. The strategy is described as follows:

Parameters at Jupiter pericentre.	
Pericentre: 1 million km Apoentre: 49 million km Inclination (with respect to ecliptic): optimisable Line of apses: optimised	The direction of the line of apses is optimised to generate the greatest heliocentric energy. The inclination of the Jupiter orbit is optimised to generate an out-of-ecliptic component so that the Jupiter escape and eventual Uranus capture arcs may link with a minimum ΔV requirement for the intermediate transfer section.
Deep-space electric propulsion manoeuvres.	
Two manoeuvres are possible with an intermediate coast arc	Manoeuvre ΔVs and directions are optimised.
Parameters at Uranus pericentre.	
Pericentre: 0.7 million km Apocentre: 69 million km Inclination (with respect to ecliptic): optimisable Line of apses: optimised	The direction of the line of apses is optimised to generate a maximum change in heliocentric energy. The inclination of the final Uranus orbit is optimised to generate an out-of-ecliptic component so that the Jupiter escape and Uranus capture arcs may link with minimum intermediate ΔV.

The departure from Jupiter is very similar to the case discussed in the previous section. The transfer to Uranus demands the greatest possible energy after departure from Jupiter in order to minimise the deep-space manoeuvre requirements. Therefore, a higher apocentre is selected for the initial Jupiter orbit. This enables a higher-energy escape orbit to be reached. As in the Jupiter-to-Saturn case, this transfer could potentially be further improved by including the Jupiter and Uranus apocentres as optimisable parameters. These small ΔVs for apocentre manipulation can once again be used to further 'tune' the interplanetary transfer orbit. In this regard, apocentre can be further raised, although the energy gain is relatively low and transfer period tends to increase. As discussed in Chapter 4, these transfer options have numerous locally minimum solutions. Using a much longer

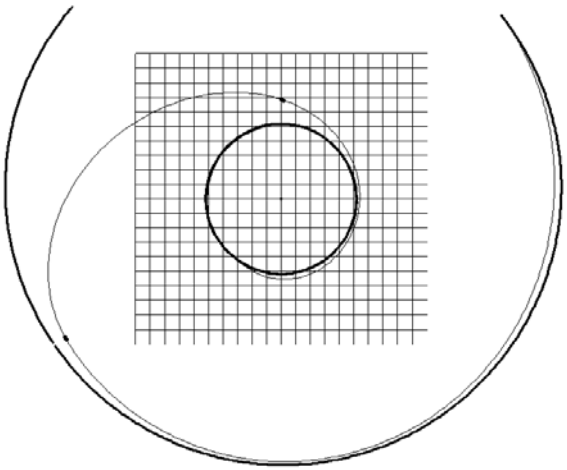

Figure 5.3.7. Transfer from Jupiter to Uranus using gravitational escape and capture. Jupiter's and Uranus's orbits are shown. The deep-space manoeuvres are indicated by bold regions of the transfer trajectory. The grid is 10 AU from centre to edge, with a 1 AU sub-grid.

transfer duration, implying additional revolutions, can potentially further improve the departure energy from Jupiter.

Similarly, the approach to Uranus also demands the greatest possible use of gravitational perturbation in reducing orbital energy. As in the Jupiter escape case, some manipulation of the apocentre at final pericentre can be used to further improve the solution; but, as in the Jupiter escape case, the local minimum solution shows only a limited degree of gain in response to increases in this parameter.

Between the gravity perturbed departure and approach arcs is a coast segment bounded by two low-thrust manoeuvres. These achieve an orbital arc that is almost analogous to a Hohman transfer between the Jupiter and Uranus linked trajectories (i.e., those trajectories that achieve gravitational excape and capture).

The aphelion after leaving Jupiter is approximately 1.93 billion km, requiring an equivalent excess hyperbolic speed at Jupiter of 2.53 km/sec. The perihelion approaching Uranus is approximately 2,240 million km, requiring an equivalent excess hyperbolic speed at Uranus of approximately 0.37 km/sec. Therefore, a pair of deep-space manoeuvre is needed to complete the transfer. When the departure and arrival phases are optimised as described above, this manoeuvre is 2.55 km/sec. The total transfer duration from pericentre to pericentre is approximately 66 years. This transfer leaves Jupiter in July 2015.

The transfer is shown in Figure 5.3.7. The connecting arc bounded by deep-space manoeuvres may be observed. The longest phase of the transfer occurs after the second deep-space manoeuvre, whist the spacecraft experiences gravitational capture in the vicinity of the Uranus–Sun L1 Lagrange point.

The gravitational capture phase at Uranus shown in Figure 5.3.8.

In Figure 5.3.9, the gravitational capture at Uranus occurs from an equivalent approach excess hyperbolic speed approaching 400 m/s.

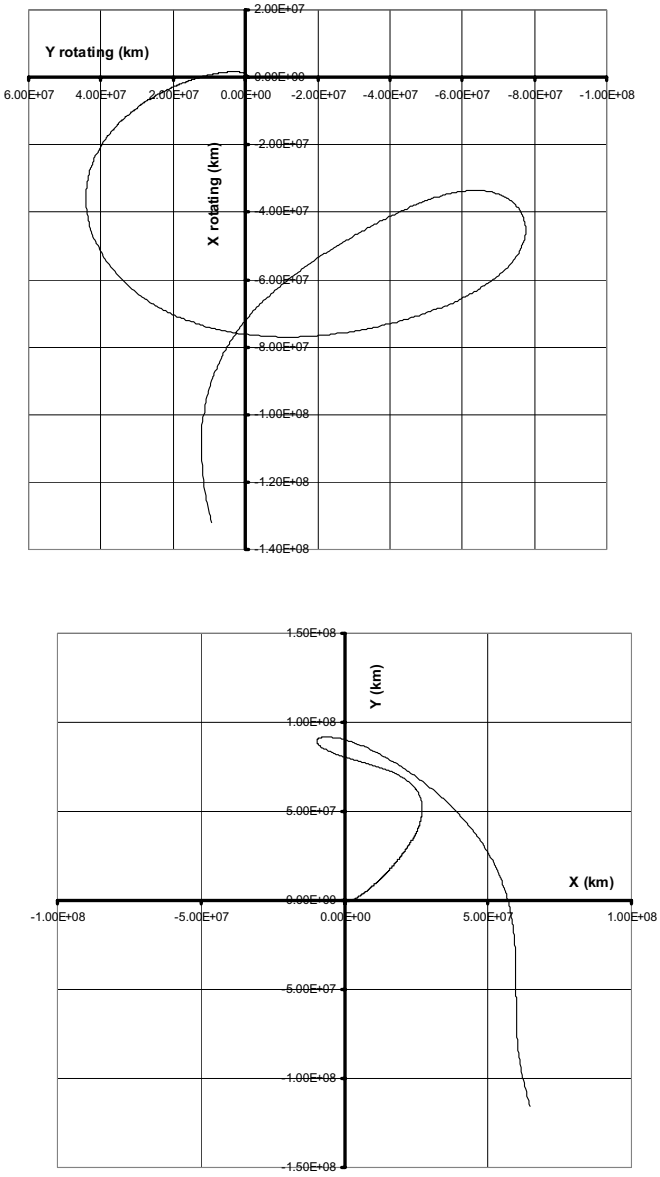

Figure 5.3.8. Gravitational capture to a Uranus bound orbit with a semi-major axis of 35 million km. The upper figure shows the approach to Uranus. Motion is seen in Uranus–Sun rotating reference frame. Approach is via the L1 point. X is in the Sun–Uranus direction. Free capture occurs at an orbit with apocentre at approximately 70 million km. Capture pericentre is less than 1 million km. In the lower figure the approach to Uranus is seen in a Uranus-centred inertial frame. The spacecraft is moving slowly in this phase of the mission, which takes approximately 40 years over the trajectory segment illustrated.

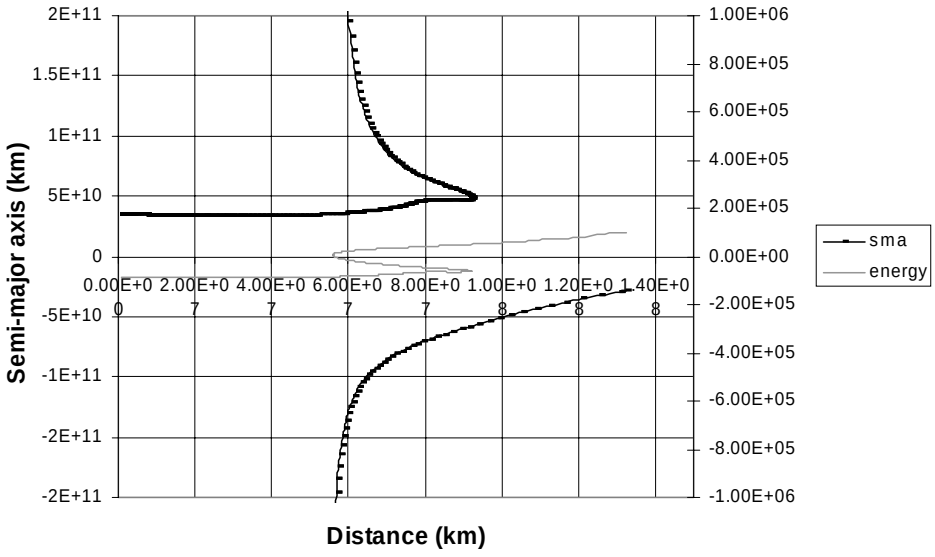

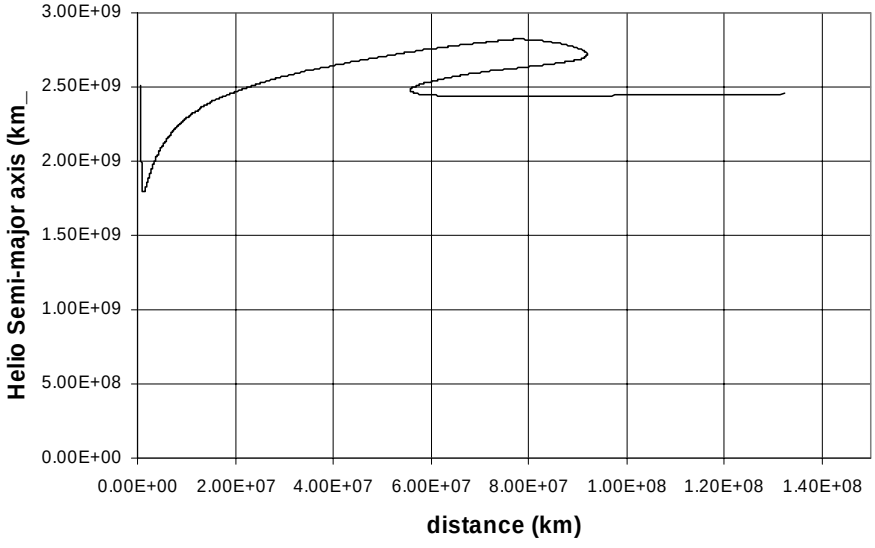

Figure 5.3.9. Energy approaching Uranus after transfer from Jupiter. In the upper figure the energy relative to Uranus is shown. The Uranus-relative energy becomes positive at approximately 57 million km from the planet. Energy is plotted against the right axis. This is at approximately the pericentre of the evolved orbit. In the lower figure the heliocentric-relative semi-major axis approaching Uranus is almost 2,500 million km. This is the greatest energy-change achievable with the initial orbital characteristics described previously.

5.3.3 Analysis of a mission to Venus using capture via the Lagrange points

In the previous sections transfers from Jupiter to the outer planets have been considered. In this section a transfer from Earth to Venus is described. It demonstrates a practical use of gravitational escape and capture. The transfer is built upon a similar strategy to that described previously for the transfer from Jupiter to Uranus; gravitational escape and capture with linking deep-space thrust and coast arcs.

This is considered to be a practical application because it enables a transfer to be achieved in a more reasonable timescale. A further aspect of the mission is that it employs low-thrust, high specific impulse propulsion to provide the deep-space manoeuvres. This mission could be contrasted with a standard, conjunction type transfer using high-thrust, pericentre manoeuvres for escape and capture.

Several transfers can be considered, using variations on the basic transfer theme of gravitational escape and capture. These include:

- Use of a lunar gravity-assisted escape with a Venus gravitational capture. This is one of the shortest low-transfer scenarios.
- Earth gravitational escape with Venus gravitational capture. This scenario is similar to the previous one, but generally takes slightly longer.
- Lunar gravity assist, followed by Earth gravity assist, to start the transfer, with Venus gravitational capture. This allows a significant ΔV saving at the expense of additional transfer time.
- Lunar gravity assist, followed by Earth gravity assist, to start the transfer with Venus gravity assist and Venus gravitational capture. This allows a further significant ΔV saving, but again at the expense of additional transfer time.

Such transfer types may be obtained at approximately 1.6-year launch intervals (the synodic period of Earth and Venus). The key features of these transfers are repeated with an eight-year period; that is, five synodic periods. Some of these are now considered in more detail.

Earth gravitational escape and Venus gravitational capture

This transfer uses two gravitationally perturbed phases. In the initial phase the effect of solar gravity on the initially Earth bound trajectory is used to achieve a low-energy Earth escape, after injection to an initially highly elliptical Earth orbit. Escape V_∞ may typically approach 1 km/sec. The total transfer time is generally increased, because of the additional time taken during the Earth gravitational escape phase.

The key orbit injection parameters that may be chosen, and their relationships, are shown below. The optimum direction of the line of apses will in general lie close to the ecliptic, although this does vary with each launch epoch under consideration. The relationship between these parameters and the launcher injection orbit must be considered, as this effects the feasibility of such a transfer.

Property	*Value*	*Initial orbit implications*
Apogee altitude	Example at 2,000,000 km	Must be sufficiently high to experience gravitational perturbations from Sun (>1.2 million km). Pericentre is low, to be reached by a typical launcher injection orbit.
Right ascension	Optimisable to achieve required direction of the line of nodes with respect to Sun/Lagrange point direction. Choice is cross-coupled with the initial inclination/argument of pericentre in determining the azimuth of the line of apses.	Right ascension of ascending node is primarily determined by launch time epoch and is generally a free launch parameter.
Argument of perigee and inclination	Individually optimisable to achieve the optimal orientation of line of apses with respect to Sun/Lagrange point direction.	Argument of perigee is determined by the upper-stage reignition point, and for many launchers is a freely choosable parameter, with no ΔV/injection mass penalty. Inclination is primarily determined by the launch site and attracts a performance penalty to change this from the optimal value for a particular launcher. High-latitude sites imply high inclination, but, when coupled with the appropriate selection of argument of perigee, allow a wide range of declinations of the line of apses to be achieved without ΔV/injection mass penalty. Inclination and argument of pericentre also contribute to azimuth of the line of apses.

The nature of these transfers is such that often several local minima may be obtained. The example below shows an efficient strategy in terms of both low ΔV and a moderate total transfer duration, and the optimised transfer results for this minimum case. A baseline assumption of 230 mN thrust per tonne is assumed. This transfer takes approximately 1.5 years. The trajectory is seen in Figure 5.3.10.

Table 5.3.1. Earth gravitational escape and Venus gravitational capture with low thrust.

Event	Parameters	Description	ΔV
Launch	Injection apogee = 2,000,000 km, perigee at 200 km. Example launch epoch 16 Apr 2013.	High apogee orbit to achieve strong Solar gravity perturbations.	No deterministic manoeuvre.
Gravitational escape	Equivalent V_∞ achieved after Earth escape: 1 km/sec.	Gravitational escape achieved after passage close to L1 Lagrange point.	No deterministic manoeuvre.
Deep space manoeuvres	Two optimisable low-thrust arcs separated by an optimisable coast arc.	Thrust arc 1: provides further perihelion reduction to achieve a Venus rendez-vous.	Low-thrust ΔV: 3.78 km/sec.
		Thrust arc 2: reduces approach velocity to Venus.	
Gravitational capture at Venus	Reach an elliptical capture orbit: 250 km by 2,400,000 km. Reaches pericentre at 31 Aug 2014.	Gravitational capture from low V_∞ approach to Venus to high-apocentre orbit. Pericentre targeted at 200 km.	No deterministic manoeuvre.
Summary		Transfer duration 502 days.	3.78 km/sec.

One option to speed up such a transfer would be to replace the Earth gravitational escape phase with a lunar gravity assist.

The Earth gravitational escape phase has already been discussed in demonstrating the principle of gravitational escape (Chapter 4).

Figures 5.3.11 and 5.3.12 show the approach phase at Venus, illustrating capture through the Lagrange point. The approach orbit to Venus has an aphelion of 1.2e8 km and an equivalent approach V_∞ at Venus of 850 m/s.

This transfer can be compared with a transfer between parabolic orbits at Earth and Venus (excess hyperbolic speed of zero). The low-thrust ΔV in such a case is approximately 5.5 km/sec. In practice, such a transfer would use an optimised V_∞ at Venus and Earth to minimise total fuel usage, but the gravity-assist case is then compensating for the fuel required for apocentre raising beyond the parabolic case and to a lesser extent the low-thrust system ΔV. The transfer ΔV may be reduced by increasing thrust, but as a result would also increase propulsion mass. The value used here is representative of an achievable system. This transfer can be compared with an idealised case with circular, co-planar planet orbits, where the ΔV reduced to 3.1 km/sec with a thrust at 200 mN/tonne.

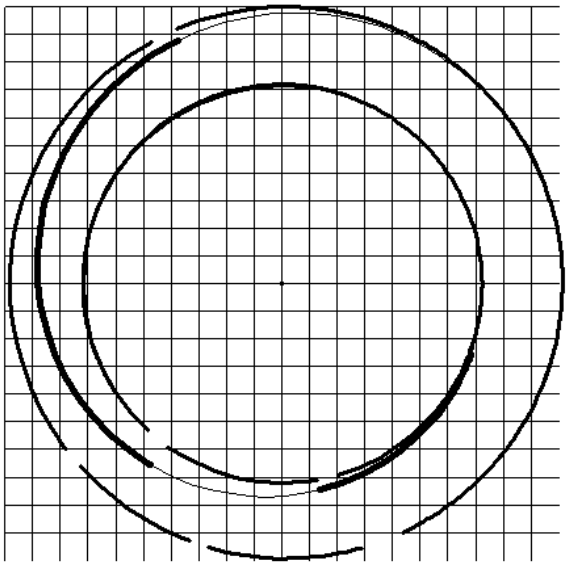

Figure 5.3.10. Transfer using Earth gravitational escape, Venus gravitational capture and two low-thrust arcs. This figure shows the heliocentric transfer and Earth and Venus orbits. The grid is 1 AU from centre to edge, with a sub-grid of 0.1 AU. The thrust arcs are the thick lines. The first thrust arc is considerably longer than the second in this optimised solution. At the end of the second thrust arc the spacecraft enters a gravitational capture approach via the Venus L2 point.

Figure 5.3.11 shows the approach phase at Venus, illustrating capture after a passage close to the Venus–Sun L2 Lagrange point.

Capture to an osculating bound orbit may be achieved at Venus. A further retrograde ΔV is needed to lower the apocentre to reach the final operational orbit. If the manoeuvre does not occur at pericentre (for example, if there is a failure onboard the spacecraft) the spacecraft would subsequently experience an energy increase as it leaves pericentre. In this example it will escape from its temporarily bound Venus orbit. However, using a lower apocentre (1.4 million km) results in a modification of the behaviour after first Venus pericentre. The spacecraft remains in a bound orbit for two complete orbits about Venus and only escapes on the third revolution. The equivalent approach hyperbolic speeds are slightly reduced for capture to the less energetic bound orbit (by approximately 50 m/s). This feature may significantly improve the robustness of planetary capture, offering multiple possibilities for performing an orbit insertion manoeuvre, before final escape from the planet. Such strategies are described in the references for this section (Campagnola *et al.*).

The orbit evolution from approach and after first pericentre is shown in Figure 5.3.12. This shows the approach trajectory, passing close to the Sun–Venus L2 point, and subsequent passage by Venus pericentre. The spacecraft then passes

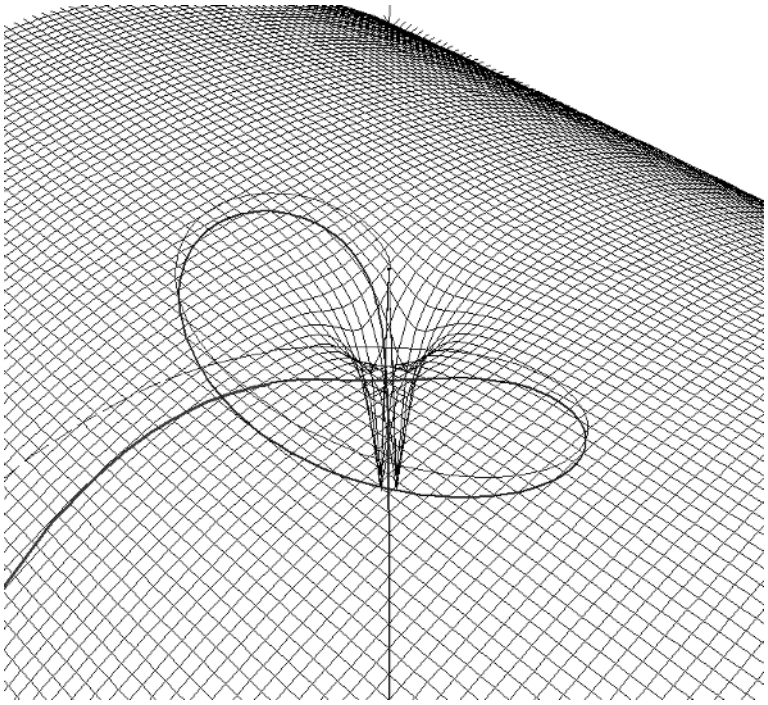

Figure 5.3.11. Approach to Venus, showing capture through the Lagrange point, for short transfer type (2013 launch), plotted on a potential surface. The motion is plotted on a potential surface (gravitational and rotating motion effects), with a rotating frame of reference. This phase is preceded by an approaching thrust phase, which is also shown terminating on this plot. This phase is in a darker line, and Venus is at the centre of this potential function. The Venus–Sun Lagrange points may be seen as the shallow saddle points (in the Venus–Sun direction). These lie at approximately one million km from Venus. The frame rotates with the Venus–Sun system.

into a 'weakly bound' orbit around Venus for two revolution, it eventually escapes from the influence of Venus.

Earth gravity assist, Venus gravity assist and Venus gravitational capture

The possibility of using lunar and Earth gravity assists (as described in previous sections) to increase escape energy from the Earth may be used here. In addition, the benefits obtained from the use of VGA can be considered.

This technique for using Venus gravity assist is essentially the inverse of the lunar and Earth gravity assist sequence. The principle is as follows. On approaching Venus for the first time, use a Venus gravity assist to lower aphelion. A deep-space burn is subsequently applied to reduce the eccentricity of the heliocentric orbit. This

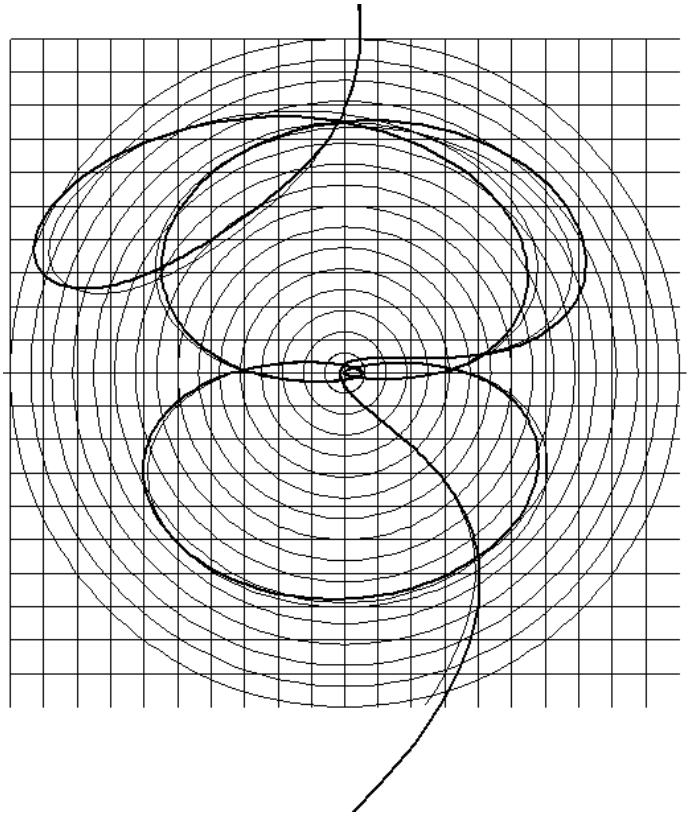

Figure 5.3.12. Approach to Venus showing capture through the Lagrange point, and subsequent motion over a period of one Venus year. The grid is 1.5 million km from centre to edge. The reference frame is rotating with the Venus–Sun direction.

has the effect of reducing the excess hyperbolic speed at Venus to a level where gravitational capture at Venus may be employed (to 800–900 m/s V_∞)

This technique can be compared with the previous cases that use gravitational capture at Venus. Table 5.3.2 shows the optimised transfer results. A baseline assumption of 200 mN thrust per tonne in high elliptical Earth orbit is assumed.

The total low-thrust ΔV is approximately 2.31 km/sec in this example. The heliocentric transfer is shown in Figure 5.3.13.

Table 5.3.2. Transfer from Earth to Venus with EGA, VFA and gravitational capture at Venus.

Event	Parameters	Description
Launch May 2012	Apogee = 600000 km	Trans Lunar orbit
GA1 at Moon June 2012	$V_\infty = 1.4$ km/sec	Transfer to near 1 : 1 resonant orbit with Earth
GA2 at Earth October 2013	$V_\infty = 1.9$ km/sec	Achieve Venus RV Earth departure orbit
GA3 at Venus March 2014	$V_\infty = 3.3$ km/sec	Transfer to near 1 : 1 resonant orbit with Venus
Gravitational capture at Venus. Reaches pericentre at Nov-2014	Elliptical capture orbit 250 km by 2000000 km	Transfer duration 1024 days
Total SEP Manoeuvres		2.3 km/sec

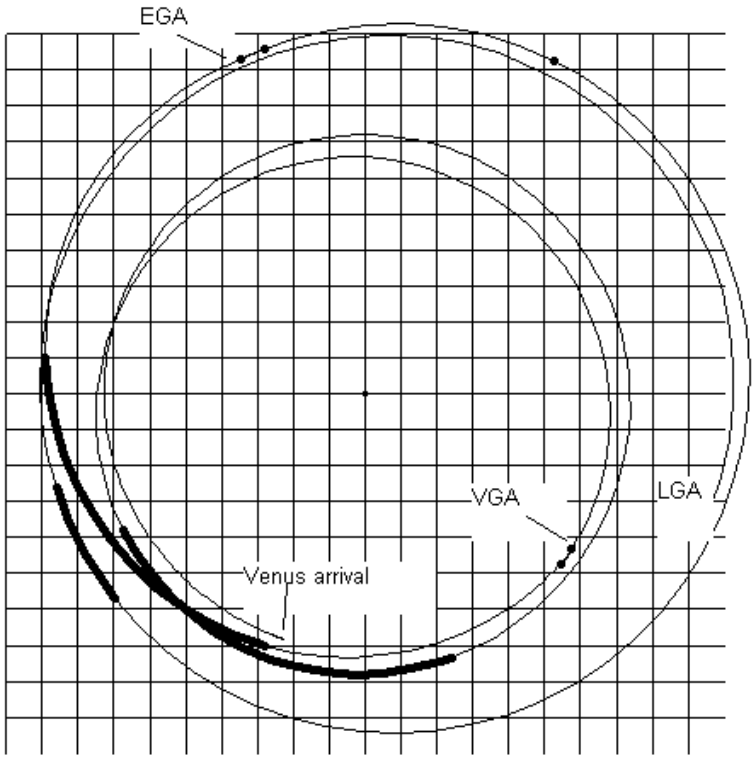

Figure 5.3.13. Launch in 2012 with LGA, EGA escape in 2013 and VGA in 2014; 200 mN per tonne constant thrust. The grid is 1 AU from centre to edge. Low-thrust arcs are bold. Planet orbits are omitted for clarity.

Appendix 1

Keplerian orbits

This appendix reviews the key properties of Keplerian orbits; that is, orbits that result from the solution of the Newtonian equations of motion with a central, attractive, inverse square field. Perturbations to such motion are not considered here.

A1.1 GEOMETRY OF CONIC SECTIONS

Keplerian orbits may be expressed in terms of conic sections. Therefore, the geometry of such entities is of some importance.

The ellipse is shown in Figure A1.1.

The following relationships are used in describing orbits:

- Semi-major axis, a.
- Semi-minor axis, b.
- Semi-minor axis, p.
- Eccentricity, e.

The geometry of an ellipse is such that:

$$\frac{x^2}{a^2} + \frac{y^2}{b^2} = 1$$

It may be seen that $b = a\sqrt{(1 - e^2)}$, and that $p = a(1 - e^2)$.

In the case of an ellipse, the eccentricity is such that $0 \leq e < 1$. In the case of the hyperbola, the geometry is shown in Figure A1.2.

Two solutions are possible for the hyperbola, such that in the figure the mirror image about a vertical axis through the origin gives the second solution.

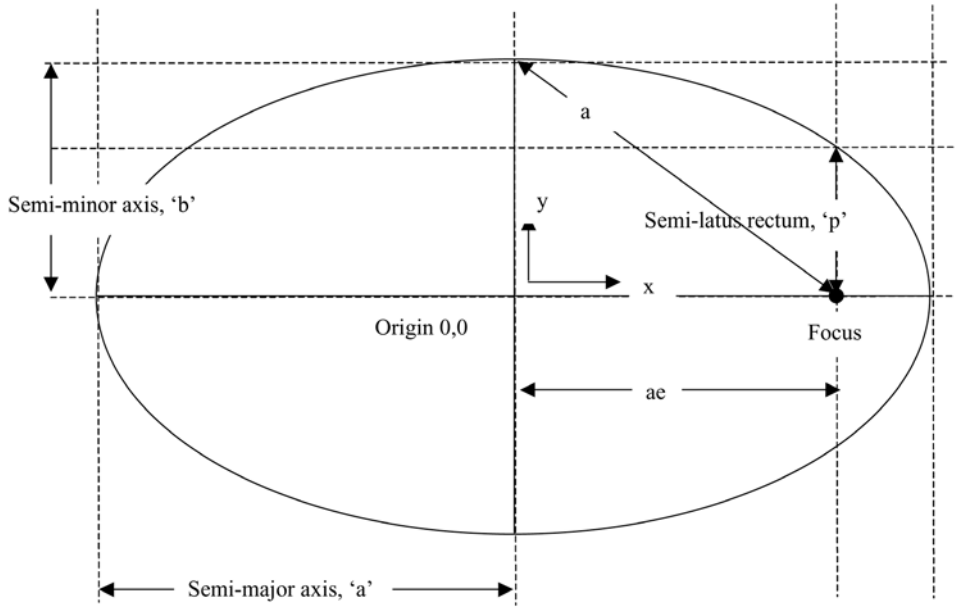

Figure A1.1. Geometry of the ellipse.

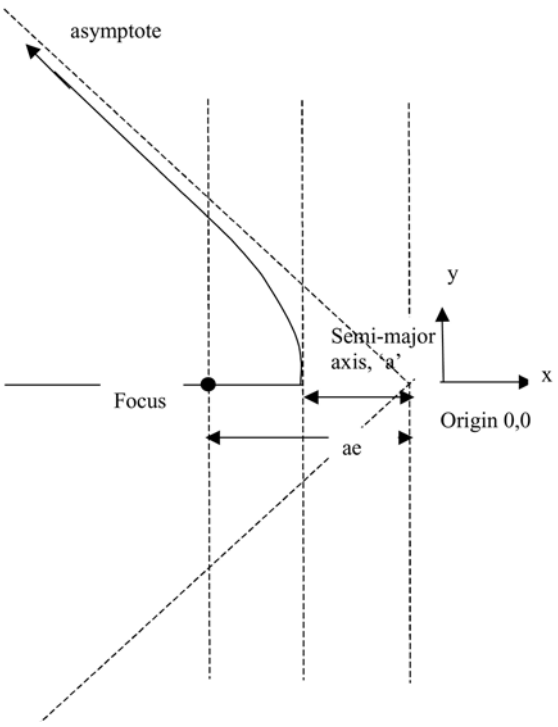

Figure A1.2. Section of a hyperbola.

The geometry of an hyperbola is such that:

$$\frac{x^2}{a^2} - \frac{y^2}{b^2} = 1$$

where $b^2 = a^2(e^2 - 1)$.

The eccentricity is such that: $e > 1$.

A1.2 SUMMARY OF ORBIT NOTATIONS

The following elements are conventionally used to describe the orbit of a spacecraft. The origin of the reference frame is assumed to be the centre of the central body under consideration. A reference plane is assumed. In the case of motion about the Sun, the plane of the ecliptic is taken as the reference. For Earth-relative motion the equator is used. A more detailed discussion on reference systems may be found in Appendix 2.

- a = semi-major axis of the orbit ellipse.
- e = eccentricity of the orbit ($e = 0$ for circular orbits).
- i = inclination of orbit with respect to the equatorial plane or reference plane.
- Ω = right ascension of ascending node.
- ω = argument of perigee.
- θ = true anomaly of satellite.

The central body lies at the focus of the ellipse or hyperbola.

Figure A1.3 illustrates the orbital elements used to describe the plane of a satellite orbit:

The ascending node is defined by the point where the spacecraft passes through the reference plane, in a northerly direction (i.e., positive velocity component in the z or 'polar' direction). It is measured from the reference axis X direction. This is often nominally the 'first point of Aries'. The right ascension is the angle in the reference plane between X and the ascending node. Further definitions related to this idea are the descending node, where the spacecraft moves through the reference plane in a southerly direction, and the anti-node, where the latitude of the spacecraft's motion reaches its maximum or minimum values. Inclination is measured as the rotation about the ascending node from the reference plane to the orbit plane (positive rotation in Figure A1.3). The inclination vector is a vector normal to the orbit plane and a rotation about this vector is in the direction of the orbit of the spacecraft. In Figure A1.3, the projection of the orbit into the reference plane is drawn as the lighter line.

In Figure A1.4 the argument of pericentre is the angle in the orbit plane measured from the ascending node to the pericentre. It is a rotation about the inclination vector (positive rotation in Figure A1.4). In this figure the projection of the orbit into the reference plane is drawn as the lighter line. Pericentre is the point of closest approach, and the apocentre the extreme point in the orbit. The apocentre seen in the figure therefore lies below the reference plane (Earth equatorial plane in

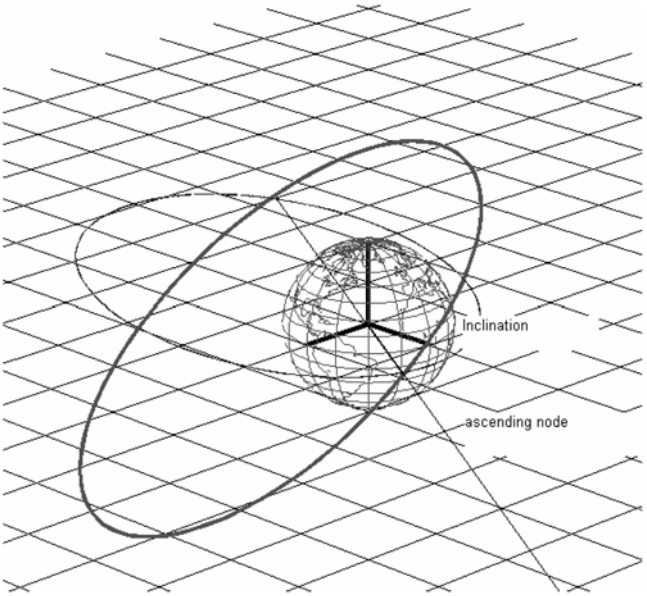

Figure A1.3. Inclination and the ascending node. The light dashed line is the projection of the orbit into the reference plane.

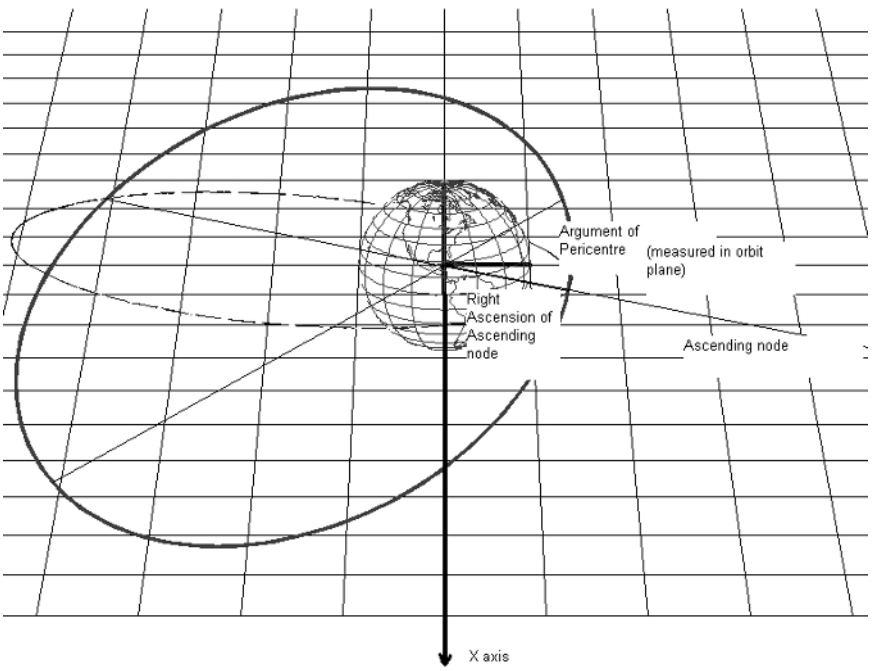

Figure A1.4. Right ascension and argument of pericentre. The light dashed line is the projection of the orbit into the reference plane.

this example). The true anomaly of the orbiting body is the angle, measured in the orbit plane, between the pericentre and its current location. Note that alternative representations of the location in the orbit are possible. In this previous definition, true anomaly is used.

Alternatively, mean anomaly can be used. In the case of a bound orbit, mean anomaly describes the fraction of an orbital period since the subject passed pericentre. It takes values in the range 0 to 2π. One period is completed when mean anomaly is incremented by 2π. A useful quantity associated with mean anomaly is the mean motion, n:

$$n = \sqrt{\frac{\mu}{a^3}} \tag{1.1}$$

such that the orbit period is expressed as:

$$\tau = \frac{2\pi}{n} \tag{1.2}$$

where μ is the gravitational parameter of the central body.

To calculate true anomaly from mean anomaly, when the eccentricity of the orbit is less than 1, an intermediate variable, the eccentric anomaly, is required. This angle is illustrated geometrically in Figure A1.5.

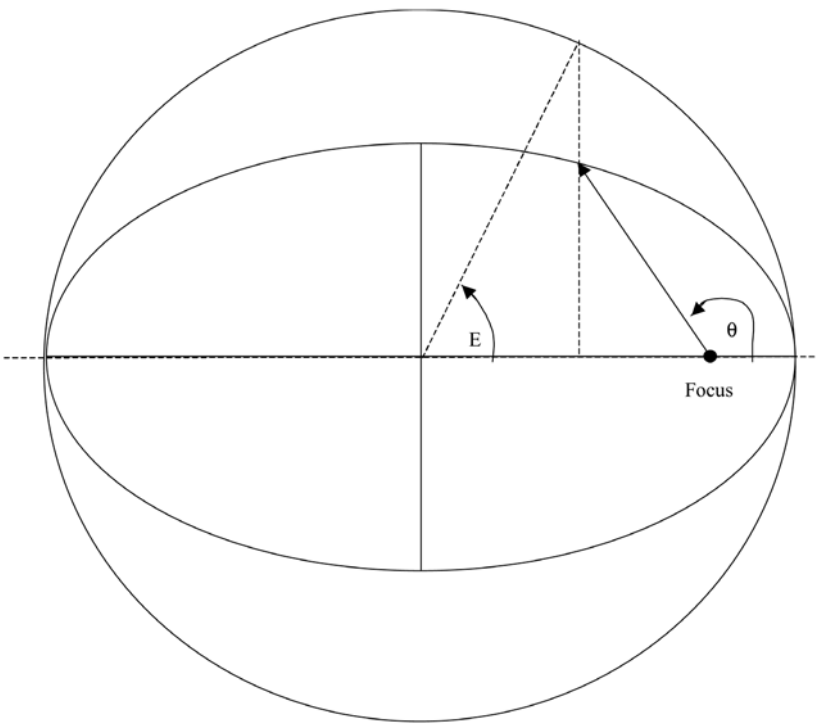

Figure A1.5. Eccentric anomaly.

The relationship between the two quantities is the following:

$$M = E - e\sin E \tag{1.3}$$

where M is mean anomaly and E is eccentric anomaly. This is known as Kepler's equation, which may not be solved analytically for E. An iterative solution is therefore employed. A Newton–Raphson method may be used as follows:

$$M' = E - e\sin E$$

where M' is the current evaluation of mean anomaly given the estimate, E of the eccentric anomaly.

$$E = E + \frac{(M - M')}{\dfrac{\partial M}{\partial E}} \qquad \text{and} \qquad \frac{\partial M}{\partial E} = 1 - e\cos E \tag{1.4}$$

Various schemes have been devised for the solution of the above equation, of which this particular iterative method is only one. The equation may present numerical difficulties when eccentricity approaches 1. A detailed discussion may be found in Battin (see references).

True anomaly is obtained by:

$$\tan\frac{\theta}{2} = \sqrt{\frac{1+e}{1-e}}\tan\frac{E}{2} \tag{1.5}$$

Alternative expressions for the relationship between true and eccentric anomalies are:

$$\cos\theta = \frac{\cos E - e}{1 - e\cos E} \qquad \text{and} \qquad \sin\theta = \frac{\sin E\sqrt{1-e^2}}{1 - e\cos E} \tag{1.6}$$

In the case of a hyperbolic orbit, where the eccentricity exceeds 1, the mean anomaly is converted to true anomaly by use of an intermediate variable known as the hyperbolic anomaly. The relationship between the two quantities is the following:

$$M = e\sinh F - F \tag{1.7}$$

where M is mean anomaly and F is hyperbolic anomaly. An iterative solution is again employed, using the Newton–Raphson method as follows:

$$M' = e\sinh F - F$$

where M' is the current evaluation of mean anomaly given the estimate, F of the hyperbolic anomaly:

$$F = F + \frac{(M - M')}{\dfrac{\partial M}{\partial F}} \qquad \text{and} \qquad \frac{\partial M}{\partial F} = e\cosh F - 1$$

The true anomaly is now obtained from:

$$\tan\frac{\theta}{2} = \sqrt{\frac{e+1}{e-1}}\tanh\frac{F}{2} \tag{1.8}$$

A special case exists for the parabola, where eccentricity is equal to 1. In this situation, Barker's equation gives the relationship between true anomaly and time.

Non-singular elements

It can be seen that the previous expressions are singular. When the inclination is zero, the ascending node is not well defined. When the eccentricity is zero and therefore the orbit circular, the pericentre is not well defined.

To alleviate these problems, non-singular elements may be used to describe the orbit. The elements e, i, ω and Ω are replaced as follows:

$$P_1 = e\sin(\Omega + \omega)$$
$$P_2 = e\cos(\Omega + \omega) \tag{1.9}$$

$$Q_1 = \tan\left(\frac{i}{2}\right)\sin\Omega$$
$$Q_2 = \tan\left(\frac{i}{2}\right)\cos\Omega \tag{1.10}$$

Furthermore, the 'true longitude' can also be used, being defined as:

$$L = \omega + \Omega + \theta \tag{1.11}$$

It should be noted that this is not a 'real' longitude with a physical meaning; the right ascension of the ascending node lies in a different plane to the argument of pericentre and true anomaly. It is a mathematical construction of convenience.

The transformation to conventional elements is given by:

$$e^2 = P_1^2 + P_2^2$$
$$\tan^2\left(\frac{i}{2}\right) = Q_1^2 + Q_2^2$$
$$\tan\Omega = \frac{Q_1}{Q_2}$$
$$\tan(\omega + \Omega) = \frac{P_1}{P_2}$$

Such forms are useful when considering the effects of perturbing forces on orbits close to the singular values. The evolution of the non-singular elements can be monitored in preference to classical elements.

A1.3 MOTION IN AN ATTRACTIVE CENTRAL INVERSE SQUARE FIELD

The motion of a body under the influence of an inverse-square attractive field may be analysed to obtain analytical expressions for the motion. This motion is often referred to as the solution of the two body problem, or Keplerian motion. It is the motion to which Kepler's laws apply.

The gravitational force exerted on a body of mass m_2 by a body of mass, m_1 is given by:

$$m_2\ddot{\underline{r}}_2 = -\frac{Gm_1m_2\underline{r}}{r^3} \tag{1.12}$$

where $\underline{r}$ is the vector from the centre of mass of the body 1 to the centre of mass of the body, 2, and $\underline{r}_2$ is the vector from the centre of mass of the system (i.e., body 1 plus body 2) to body 2. Similarly:

$$m_1\ddot{\underline{r}}_1 = \frac{Gm_1m_2\underline{r}}{r^3} \tag{1.13}$$

where $\underline{r}_1$ is the vector from the centre of mass of the system to body 1.

The acceleration of body 2 relative to body 1 is given by:

$$\ddot{\underline{r}} = -\frac{G(m_1+m_2)\,\underline{r}}{r^3} \tag{1.14}$$

In the following it will now be assumed that body 1 is much more massive than body 2. The gravitational constant for this body is defined as: $\mu = Gm_1$:

$$\ddot{\underline{r}} = -\frac{(m_1+m_2)}{m_1}\frac{\mu\underline{r}}{r^3} \qquad \text{or} \qquad \frac{m_1m_2}{(m_1+m_2)}\,\ddot{\underline{r}} = -m_2\frac{\mu\underline{r}}{r^3} \tag{1.15}$$

where $\dfrac{m_1m_2}{(m_1+m_2)}$ is sometimes referred to as the 'reduced' mass.

If the mass of body 2 can be neglected in comparison with body 1, the subscript 2 will be omitted when referring to the motion of the spacecraft.

Then equation 1.15 becomes the following:

$$\ddot{\underline{r}} = -\frac{\mu\underline{r}}{r^3} \tag{1.16}$$

The force acting only along the separation of the two bodies means that:

$$\underline{r} \wedge m\ddot{\underline{r}} = 0$$

and therefore a constant of motion is the angular momentum of the spacecraft, $\underline{h}$:

$$\underline{r} \wedge m\dot{\underline{r}} = \text{constant} = \underline{h} \tag{1.17}$$

Therefore, the motion remains in the same plane. This conclusion allows a simplification to be made in the description of the motion such that polar co-ordinates (r, θ) can be used. Then:

$$\underline{V} = \dot{\underline{r}} = \dot{r}\hat{r} + r\dot{\theta}\hat{\theta} \tag{1.18}$$

$$V^2 = \dot{r}^2 + r^2\dot{\theta}^2 \tag{1.19}$$

where $\hat{r}$, $\hat{\theta}$ are unit vectors in the radial and transverse directions respectively, and:

$$h = mr^2\dot{\theta} \tag{1.20}$$

The energy of body 2 is given by the sum of potential and kinetic energies:

$$E = \frac{m}{2}(\dot{r}^2 + r^2\dot{\theta}^2) - \frac{Gm_1m}{r} \tag{1.21}$$

Using equation 1.21 it is possible to derive further information regarding the motion of body 2. Substituting for angular momentum gives:

$$E = \frac{m\dot{r}^2}{2} + \frac{h^2}{2mr^2} - \frac{\mu m}{r} \tag{1.22}$$

where $\mu = Gm_1$. Then, using equation 1.20 and equation 1.22

$$\left(\frac{dr}{d\theta}\right)^2 = \frac{r^2}{h^2}(2Emr^2 + 2\mu m^2 r - h^2) \tag{1.23}$$

In the following, the expressions for energy and angular momentum will be used as those relating to unit mass, $m = 1$, or 'specific energy' and 'specific angular momentum':

$$\left(\frac{dr}{d\theta}\right)^2 = \frac{r^2}{h^2}(2Er^2 + 2\mu r - h^2) \qquad \text{and} \qquad h = r^2\dot{\theta}$$

which may be integrated to give:

$$\frac{1}{r} = \frac{\mu}{h^2}\left(1 + \sqrt{1 + \frac{2Eh^2}{\mu^2}}\cos(\theta - \theta_0)\right) \tag{1.24}$$

where θ_0 is a constant. This is the equation of a conic section with eccentricity given by:

$$e = \sqrt{1 + \frac{2Eh^2}{\mu^2}} \tag{1.25}$$

The point of closest approach occurs when $\theta = \theta_0$. This is the pericentre of the orbit, and the true anomaly may be substituted for $\theta - \theta_0$.

The semi-major axis can be shown to be given by:

$$a = -\frac{\mu}{2E} \tag{1.26}$$

The semi-latus rectum is defined geometrically as:

$$p = a(1 - e^2) \tag{1.27}$$

and is therefore:

$$p = \frac{h^2}{\mu} \tag{1.28}$$

such that:

$$r = \frac{p}{(1 + e\cos(\theta))} = \frac{a(1 - e^2)}{(1 + e\cos(\theta))} \tag{1.29}$$

where θ is used to represent the angle measured in the orbit plane from pericentre, previously denoted as $\theta - \theta_0$.

The relationship between velocity and radius is found through the energy per unit mass:

$$E = \frac{V^2}{2} - \frac{\mu}{r}$$

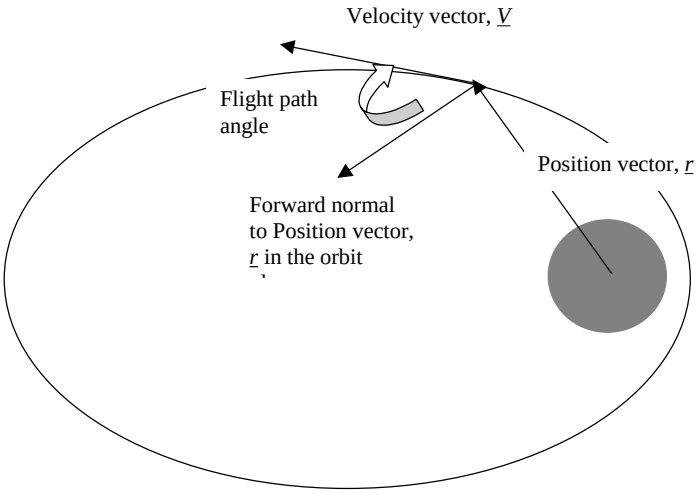

Figure A1.6. Flight path angle geometry.

and therefore

$$V = \sqrt{2\mu\left(\frac{1}{r} - \frac{1}{2a}\right)} \tag{1.30}$$

The direction of the velocity with respect to the forward normal to the radius vector (Figure A1.6) is defined by the flight path angle. This is obtained from the radial velocity component:

$$V \sin \Gamma = \left(e \sin \theta \sqrt{\frac{\mu}{a(1-e^2)}}\right) \tag{1.31}$$

Also, the velocity component V_θ is given by h/r, and an alternative expression for flight path angle is:

$$\tan \Gamma = \frac{V_r}{V_\theta} = \frac{V \sin \Gamma}{V \cos \Gamma} = \frac{e \sin \theta}{1 + e \cos \theta} \tag{1.32}$$

Therefore, the flight path angle depends only on eccentricity and true anomaly. Three cases of eccentricity may be considered.

$0 \leq e < 1$: elliptical orbits
$e = 1$: parabolic orbits
$e > 1$: hyperbolic orbits

If the eccentricity exceeds 1, the energy is positive and the spacecraft will depart from the central body under consideration. Conversely, with an eccentricity of less than 1 the energy is negative and the spacecraft remains in a closed orbit. In the special case of eccentricity being equal to 1, the result is a parabolic orbit and zero energy. The spacecraft reaches zero velocity at infinite distance from the central body.

In the cases of hyperbolic orbits, additional parameters of interest may be

evaluated as follows. The first is the excess hyperbolic speed – the speed remaining when the spacecraft reaches infinite distance from the central body under consideration:

$$V_\infty^2 = -\frac{\mu}{a} = 2E \tag{1.33}$$

The escape velocity may be defined as the speed, when at a given radial distance from the planet, with which the spacecraft achieves a positive energy:

$$V^2 \geq 2\frac{\mu}{r} \tag{1.34}$$

If it is in an initial circular orbit about the planet, then:

$$V^2 \geq 2\frac{\mu}{a}$$

A1.4 GENERATION OF CARTESIAN CO-ORDINATES FROM ORBITAL ELEMENTS

Given an orbit ephemeris, it is possible to derive a set of Cartesian co-ordinates and a velocity vector. The Cartesian position and velocity vector are an alternative representation of the instantaneous state of an orbit (six components are required to represent the state).

Cartesian co-ordinates are illustrated in Figure A1.7.

The procedure for conversion of ephemeris to Cartesian co-ordinates is as follows. The radial distance is given by:

$$r = a\frac{(1-e^2)}{(1+e\cos\theta)}$$

(using the same rotation as the previous section, A1.3)

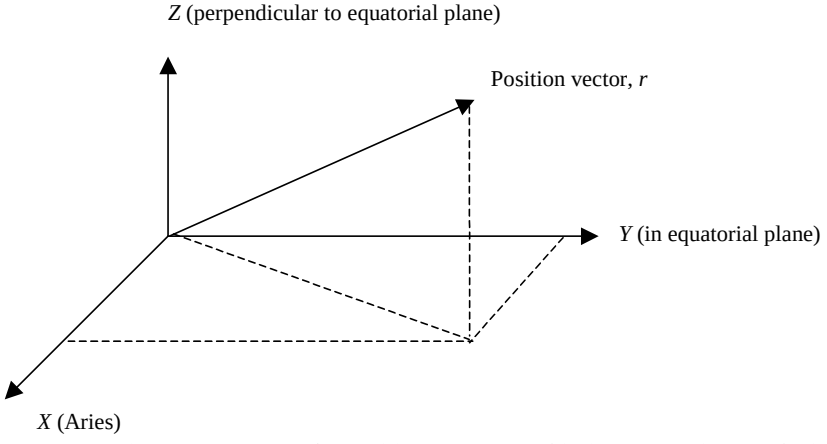

Figure A1.7. Cartesian components of a position vector. In this figure X points to the inertial reference direction.

The speed is given by

$$V = \sqrt{2\mu\left(\frac{1}{r} - \frac{1}{2a}\right)}$$

where μ is the central body gravitational parameter.

X, Y and Z components of the position vector are calculated in an intermediate reference frame (X' lies in the equatorial plane and the orbit plane, along the direction of the ascending node, Y' lies in the equatorial plane, and Z' completes the right-handed set, being perpendicular to the equatorial plane):

$$\begin{aligned} r'_x &= r\cos(\omega + \theta) \\ r'_y &= r\sin(\omega + \theta) * \cos i \\ r'_z &= r\sin(\omega + \theta) * \sin i \end{aligned} \tag{1.35}$$

These co-ordinates are now calculated with respect to an axis set with X pointing to Aries, Y perpendicular to X in the equatorial plane, and Z unchanged:

$$\begin{aligned} r_x &= r'_x\cos(\Omega) - r'_y\sin(\Omega) \\ r_y &= r'_x\sin(\Omega) + r'_y\cos(\Omega) \\ r_z &= r'_z \end{aligned} \tag{1.36}$$

The Cartesian co-ordinates are therefore obtained.

The flight path angle (the angle between the velocity vector and the normal to the radius vector, in the orbit plane) is given by:

$$\Gamma = \sin^{-1}\left(e\frac{\sin\theta}{V}\sqrt{\frac{\mu}{a(1-e^2)}}\right) \qquad \text{or} \qquad \Gamma = \tan^{-1}\left(\frac{e\sin\theta}{1 + e\cos\theta}\right) \tag{1.37}$$

The velocity vector components calculated in the intermediate reference frame are:

$$\begin{aligned} V'_x &= V\cos\left(\omega + \theta + \frac{\pi}{2} - \Gamma\right) \\ V'_y &= V\sin\left(\omega + \theta + \frac{\pi}{2} - \Gamma\right)\sin i \\ V'_z &= V\sin\left(\omega + \theta + \frac{\pi}{2} - \Gamma\right)\cos i \end{aligned} \tag{1.38}$$

These components are now calculated with respect to an axis set with X pointing to Aries, Y perpendicular to X in the equatorial plane, and Z unchanged:

$$\begin{aligned} V_x &= V'_x\cos(\Omega) - V'_y\sin(\Omega) \\ V_y &= V'_x\sin(\Omega) + V'_y\cos(\Omega) \\ V_z &= V'_z \end{aligned} \tag{1.39}$$

A1.5 GENERATION OF ORBITAL ELEMENTS FROM CARTESIAN COMPONENTS

The six orbital elements can be derived from the Cartesian state vector (three position and three velocity vector components). Firstly, the angular momentum is calculated (assuming unit mass) from the relationship:

$$\underline{h} = \underline{r} \wedge \underline{V} \tag{1.40}$$

where $\underline{r}$ and $\underline{V}$ are the position and velocity vectors and therefore $h^2 = h_x^2 + h_y^2 + h_Z^2$, where h_x, h_y and h_z are the components in x, y, and z directions.

This is used to find the inclination and right ascension of ascending node. The location of the ascending node is given by:

$$\Omega = \tan^{-1}\left(\frac{h_x}{-h_y}\right) \tag{1.41}$$

and the inclination is given by:

$$i = \tan^{-1}\left(\frac{\sqrt{h_x^2 + h_y^2}}{h_z}\right) \tag{1.42}$$

The Laplace–Range–Lenz vector may now be obtained as follows:

$$\underline{E} = \underline{V} \wedge \underline{h} - \frac{\mu \underline{r}}{r} \tag{1.43}$$

and $E = \sqrt{E_x^2 + E_y^2 + E_z^2} = \mu e$.

The Laplace–Range–Lenz vector allows the calculation of the argument of pericentre, which is now calculated from:

$$\sin\omega = \frac{E_z}{E \sin i} \quad \text{for } i \neq 0 \tag{1.44}$$

$$\cos\omega = \frac{E_x + E \sin\omega \cos i \sin\Omega}{E \cos\Omega} \tag{1.45}$$

$$\omega = \tan^{-1}\left(\frac{\sin\omega}{\cos\omega}\right) \tag{1.46}$$

This formulation allows the pericentre to be located correctly over a 360-degree range.

The semi-major axis is calculated from the orbital energy. Then,

$$Energy = \frac{V^2}{2} - \frac{\mu}{r}$$

giving

$$a = \frac{-\mu}{2Energy} \tag{1.47}$$

The eccentricity is now obtained by:

$$e = \sqrt{1 + 2Energy\left(\frac{h}{\mu}\right)^2} \tag{1.48}$$

Having obtained the main orbital parameters, the location within the orbit is given by the true anomaly, which may be obtained geometrically by using an intermediate transformation:

$$r'_x = r_x \cos\Omega + r_y \sin\Omega$$
$$r'_y = r_y \cos\Omega - r_x \sin\Omega$$
$$r''_y = r'_y \cos i + r_z \sin i \tag{1.49}$$

Then

$$\sin\theta = \frac{r''_y \cos\omega - r'_x \sin\omega}{r} \tag{1.50}$$

$$\cos\theta = \frac{r''_y \sin\omega + r'_x \cos\omega}{r} \tag{1.51}$$

and $\theta = \tan^{-1}\left(\dfrac{\sin\theta}{\cos\theta}\right)$. This formulation allows the true anomaly to be located correctly over a 360-degree range.

If $e < 1$, the mean anomaly is calculated using the eccentric anomaly:

$$\cos E = \frac{e + \cos\theta}{1 + e\cos\theta} \tag{1.52}$$

and

$$\sin E = \frac{\sin\theta(1 - e\cos E)}{\sqrt{1 - e^2}} \tag{1.53}$$

then $E = \tan^{-1}\left(\dfrac{\sin E}{\cos E}\right)$ and $M = E - e\sin E$.

If $e > 1$, the mean anomaly is calculated via the hyperbolic anomaly, F:

$$F = 2\tan^{-1}\left(\tan\left(\frac{\theta}{2}\right)\sqrt{\frac{e-1}{e+1}}\right) \tag{1.54}$$

and

$$M = -F + e\sinh F \tag{1.55}$$

Appendix 2

Frames of reference

Our Galaxy is one of many in a rapidly expanding Universe. Within our Galaxy the Sun moves at a velocity of approximately 250 km/sec with respect to the Galactic centre. However, when considering the motion of spacecraft executing interplanetary transfers, these velocities are not considered, as the key reference point for motion is the Sun. The gravitational forces exerted by distant objects outside the Solar System are small, and usually need not be considered. Furthermore, because of their great distances they impart a near-constant acceleration on all of the bodies within our Solar System; that is, the gravity gradient is so small that differential acceleration terms are negligible.

A2.1 REFERENCE AXES

The usual origin considered for motion within the Solar System is referenced to the centre of the Sun. An inertially oriented axis set is used. A reference plane is defined, being the ecliptic. This plane contains the Sun and the Earth's orbit. However, as the Earth's orbital plane is perturbed by the other planets of the Solar System, such a plane would very slowly change its orientation with time. Therefore, the ecliptic is often referred to that pertaining at a particular reference epoch.

Within the ecliptic plane exists a reference direction, nominally aligned with the direction of a distant star, the first point in the constellation of Aries. Such a celestial alignment is chosen as it defines a near fixed, inertial direction. This direction defines the X axis direction of a reference frame, and is chosen as it lies very close to the direction of the Sun, as seen from Earth, at the northern hemisphere Spring or Vernal Equinox (21 March). It therefore lies along the intersection of the Earth's equatorial plane with the ecliptic. However, this direction also shows a small drift over time and is again referenced to a particular epoch (discussed subsequently). The second, Y, axis is chosen to lie in the ecliptic plane, and is orthogonal to X. This

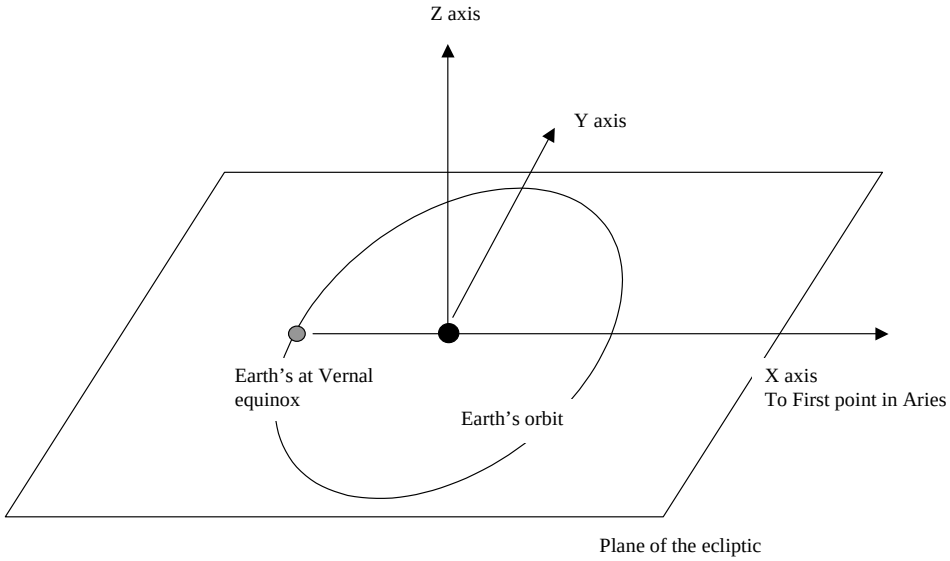

Figure A2.1. Reference axes in the ecliptic plane.

means that the right-handed axis set is completed by Z, which is perpendicular to the ecliptic. The ambiguity of this choice is removed by relating this direction to the direction of a celestial pole. Also, the choice of X and Y axes (as a rotation about the Z axis from X to Y) is consistent with the direction of the rotation of the planets about the Sun. This is sometimes considered to be an 'inertial' reference set. It is inertial in the sense that its direction is fixed inertially, although its origin in this case moves with the centre of the Sun, which is accelerated by the other planets of the Solar System and (as discussed previously) by bodies outside the Solar System. The axis set is illustrated in Figure A2.1.

Further frames of reference are used when motion with respect to a particular planet is considered. The natural choice for the X–Y plane is the planet's equatorial plane. In Earth's case, the X axis again lies in the direction of Aries, which is contained both within the ecliptic plane and Earth's equatorial plane. As in the case of the ecliptic plane, Earth's equatorial plane does not remain fixed, but experiences a small motion over long periods of time. Therefore, as in the ecliptic case, its orientation may be defined at a reference epoch.

The relationship between equatorial and ecliptic axes is defined by the inclination of the ecliptic with respect to the Earth's equatorial plane, otherwise known as the obliquity of the ecliptic. This is illustrated in Figure A2.2.

Drift in the reference directions

The X direction has been chosen to correspond to the intersection of the ecliptic and equatorial planes. This corresponded to the direction of the first point of Aries approximately 2,000 years ago. The intersection of the two planes slowly changes

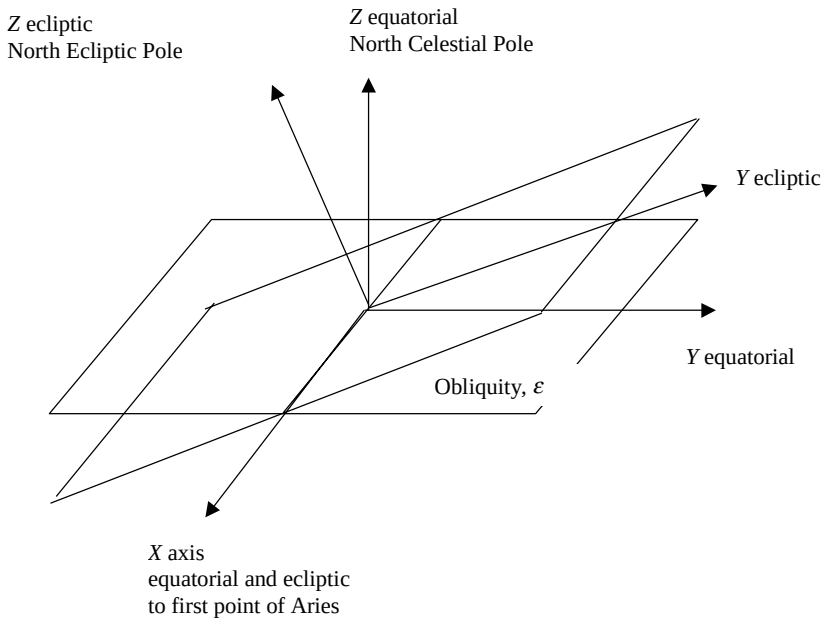

Figure A2.2. Relationship between ecliptic and Earth equatorial planes.

because of a precession and nutation of the Earth's axis of rotation, and also because of a slow change in the orientation of the plane of the ecliptic.

An axis set may therefore be referred to a particular epoch, which defines the orientations of the two planes. The 'mean' equinox, ecliptic and equatorial planes, at a particular date, are the orientations obtained by neglecting the local effect of the short-period nutation of the Earth's axis of rotation. The date chosen may be either a commonly adopted epoch or the current epoch. A reference epoch given by 1 January 1950 is sometimes adopted. The frames are then defined as 'mean of 1950' or 'mean of date'. In more recent years a reference epoch of 1 Jan 2000 is generally chosen. The reference epochs are actually at noon (Universal time) on these dates. The year 2000 case is sometimes denoted 'J2000'.

A2.2 ROTATING REFERENCE FRAMES

A commonly used axis is that of a planet's rotating reference frame. The X axis is defined by the instantaneous direction from the Sun to the planet. The Y axis is in the plane of the planets orbit (which is usually close to the ecliptic), and the Z axis lies close to the ecliptic pole and completes the right-handed set. The origin is usually considered to be the centre of the planet, or could alternatively be the Sun. Such a set is shown in Figure A2.3.

A standard transformation may be obtained to transform from 'inertial' to 'rotating' axes.

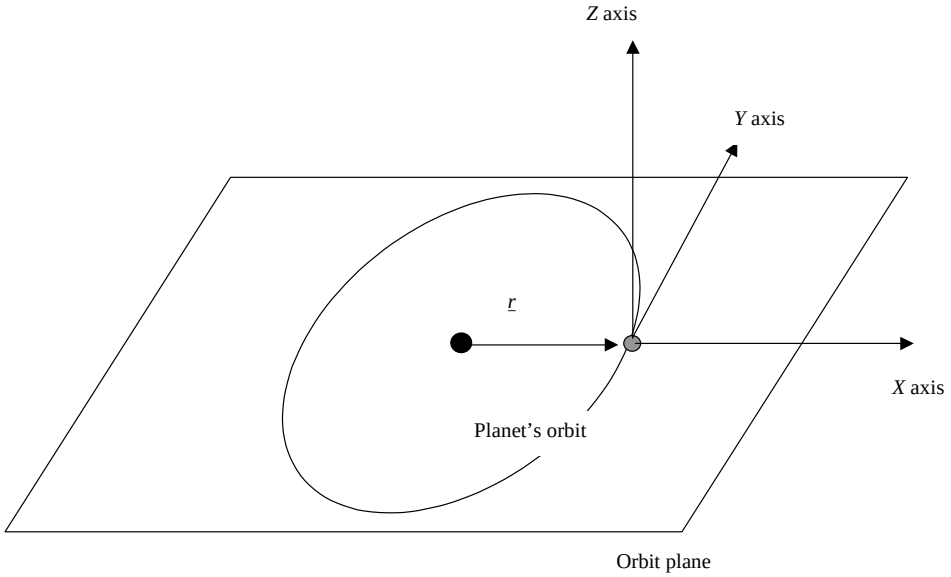

Figure A2.3. Illustration of a rotating reference plane.

The unit vector triad is obtained by:

$$\hat{x} = \frac{\underline{r}}{|\underline{r}|}, \quad \hat{y} = \frac{\underline{V} - (\hat{x} \cdot \underline{V})\,\hat{x}}{|\underline{V} - (\hat{x} \cdot \underline{V})\,\hat{x}|}, \quad \hat{z} = \hat{x} \wedge \hat{y}$$

where $\underline{r}$ and $\underline{V}$ are the Cartesian states for the position and velocity of the planet with respect to the Sun. The transformation matrix between inertial and rotating axes is so obtained:

$$[A]_I^R = [\hat{x}\hat{y}\hat{z}]$$

where A_I^R is the transformation matrix from rotating to inertial reference frames and $\hat{x}$, $\hat{y}$ $\hat{z}$ are the above triad expressed in the inertial frame.

A2.3 TIME REFERENCES

The standard unit of time is the SI unit the second. This is based on a definition based upon the time kept by atomic clocks. However, other time intervals are defined in different ways. The passage of sidereal time is defined by the hour angle of the Vernal equinox. When the meridian of the Vernal equinox is directly overhead at a point on the Earth's surface, the local sidereal time is 00:00. Greenwich sidereal time is the hour angle of the Vernal equinox with respect to the Greenwich Meridian, which is the 'prime' meridian on Earth. However, the Vernal equinox itself has alternative orientations as described in Section A2.1. Therefore, the 'true' equinox

defines the passage of 'apparent' sidereal time. The 'mean' equinox defines the passage of 'mean' sidereal time.

There are two main types of 'day'; the solar day and the sidereal day.

A sidereal day, measured by an observer on the surface of the Earth, is the interval between two successive passages of the Vernal equinox across the observer's meridian. It is a measure of the true period of the Earth's rotation about its axis, with respect to a fixed inertial reference attitude system. As in the definitions of sidereal time, both apparent and mean sidereal days are defined by the respective definitions of the equinox. The mean sidereal day is currently 86164.09054 seconds. A steady increase of approximately 0.0015 seconds per century exists. This variation is due to the steady reduction in the Earth's angular rotation rate.

The passage of solar time is defined by the hour angle of the Sun. When the Sun reaches its highest elevation seen from a point on the Earth's surface (i.e., local 'noon') the local solar time is 12:00.

A solar day, measured by an observer on the surface of the Earth, is the interval between two successive passages of the Sun's direction across the observer's meridian. However, the direction of the Sun varies by approximately one degree per day. Therefore, a solar day is slightly longer than a sidereal day. The Earth's orbit is slightly eccentric (0.0167), therefore does not travel around the Sun at a constant angular rate. Therefore, the solar day, as defined here, varies with the location of the Earth with respect to this perihelion. Therefore, an average may be taken, known as the mean solar day, being $86400 + 0.0015^{*}(\text{Year} - 1900)/100$ seconds. This steady variation in mean solar day is due to the steady state reduction in the Earth's angular rotation rate. A constant reference time is taken as the Julian day, namely 86400 seconds.

An abosolute time reference is needed. The system used is that of the Julian Date (JD). This is the number of mean solar days elapsed since noon at Greenwich on 1 Jan 4713 BC. A second absolute reference system is also used: the Modified Julian Date (MJD), which is used to allow the use of small numbers to describe current epochs.

$$\text{MJD} = \text{JD} - 2400000.5$$

Therefore, MJDs start at midnight (Greenwich local time).

The year

There are several definitions of a year. The tropical year is the period between two successive crossings of the Sun through the Vernal equinox and is 365.2422 days. This year varies from the sidereal year because of the precession of the equinoxes. A sidereal year is defined by the directions of the fixed stars and is 365.2564 days. A calendar year is 365 days except for 'leap' years with 366 days, every 4 years. This is the Julian calendar and the average length of this year is 365.25 years. The Gregorian calendar introduces an additional modification to the occurrence of leap years; one is skipped when the year is a century and is not divisible by 400. This then defines the average length of the Gregorian year as 365.2425 days (i.e., closer to othe true period of the tropical year).

Appendix 3

The planets

The nine planets of the Solar System have a spectacularly diverse set of properties. As well as inspiring scientific exploration, many of these properties influence the possibilities for mission to the planets.

The following constants and units are used:

Astronomical Unit (AU)	$1.49597870691 \times 10^{11}$ (± 3) m
Julian day (day)	86,400 secs
Julian year (year)	365.25 days
Mean Sidereal day	86,164.09054 secs = 23:56:04.09054 hours:min:sec
Sidereal year	365.25636 days
Gravitational constant	$6.67259\ (\pm 0.00030) \times 10^{-11}\,\mathrm{kg}^{-1}\,\mathrm{m}^3\,\mathrm{s}^{-2}$

(courtesy NASA)

A3.1 PROPERTIES OF THE PLANETS

The properties are given in Tables A3.1 to A3.4. These include the key physical properties of the planets and also the orbital data.

A3.1.1 Inner planets

Table A3.1. Physical properties of the inner planets.

	Mercury	Venus	Earth	Mars
Mass (10^{24} kg)	0.3302	4.869	5.9736	0.6419
Volume (10^{10} km^3)	6.085	92.843	108.321	16.318
Equatorial radius (km)	2,440	6,052	6,378	3,397
Polar radius (km)	2,440	6,052	6,356	3,375
Volumetric mean radius	2,440	6,052	6,371	3,390
Ellipticity	0	0	0.0034	0.0065
Mean density (kg/m^3)	5,427	5,204	5,520	3,933
Surface gravity (equatorial) (m/s^2)	3.7	8.87	9.78	3.69
Escape velocity (km/s)	4.3	10.36	11.2	5.03
GM ($\times 10^6$ km^3/s^2)	0.02203	0.3249	0.3986	0.04283
Bond albedo	0.056	0.72	0.385	0.16
Visual geometric albedo	0.11	0.65	0.367	0.15
Solar irradiance (W/m^2)	9,214	2,660	1,380	595
Black-body temperature (K)	442.5	238.9	247.3	216.6
Moment of inertia (I/MR2)	0.33	0.33	0.3308	0.366
J2 ($\times 10^{-6}$)	60	4.458	1,082.63	1,960.45

Table A3.2. Orbital data of the inner planets.

	Mercury	Venus	Earth	Mars
Semi-major axis (10^6 km)	57.9	108.2	149.6	227.9
Sidereal orbit period (days)	87.969	224.701	365.257	686.960
Perihelion (10^6 km)	46.0013	107.4760	147.0981	206.6446
Aphelion (10^6 km)	69.8171	108.9419	152.0977	249.2288
Synodic period (days)	115.88	583.92	—	779.94
Mean orbital velocity (km/s)	47.87	35.02	29.79	24.13
Sidereal rotation period (hrs)	1407.6	5832.5	23.9345	24.6229
Obliquity to orbit (deg)	~0.1	177.3	23.45	25.19
Semi-major axis (AU)	0.38709893	0.72333199	1.00000011	1.52366231
Semi-major axis rate (AU/century)	0.00000066	0.00000092	−0.00000005	−0.00007221
Orbital eccentricity	0.20563069	0.00677323	0.01671022	0.09341233
Orbital eccentricity rate (″/century)	0.00002527	−0.00004938	−0.00003804	0.00011902
Orbital inclination (deg)	7.00487	3.39471	0.00005	1.85061
Orbital inclination rate (″/century)	−23.51	−2.86	−46.94	−25.47
Longitude of ascending node (deg)	48.33167	76.68069	−11.26064	49.57854
Longitude of ascending node rate (″/century)	−446.3	−996.89	−18228.25	−1020.19
Longitude of perihelion (deg)	77.45645	131.53298	102.94719	336.04084
Longitude of perihelion rate (″/century)	573.57	−108.8	1198.28	1560.78
Mean Longitude (deg)	252.25084	181.97973	100.46435	355.45332
Mean Longitude rate (″/century)	538,101,628	210,664,136	129,597,741	68,905,103.8

A3.1.2 The outer planets

Table A3.3. Physical properties of the outer planets.

	Jupiter	Saturn	Uranus	Neptune	Pluto
Mass (10^{24} kg)	1,898.60	568.46	86.83	102.43	0.0125
Volume (10^{10} km^3)	143,128	82,713	6,833	6,254	0.616
Equatorial radius (km)	71,492	60,268	25,559	24,766	
Polar radius (km)	66,854	54,364	24,973	24,342	
Volumetric mean radius	69,911	58,232	25,362	24,624	1137
Ellipticity	0.0649	0.098	0.023	0.0171	
Mean density (kg/m^3)	1,326	687	1,318	1,638	2050
Surface gravity (equatorial) (m/s^2)	23.12	8.96	8.69	11	0.66
Escape velocity (km/s)	59.5	35.5	21.3	23.5	1.1
GM ($\times 10^6$ km^3/s^2)	126.686	37.931	5.794	6.8351	0.00083
Bond albedo	0.7	0.75	0.9	0.82	0.145
Visual geometric albedo	0.52	0.47	0.51	0.41	0.3
Solar irradiance (W/m^2)	51	15	3.71	1.47	0.9
Black-body temperature (K)	90.6	63.9	35.9	33.2	42.7
Moment of inertia (I/MR2)	0.254	0.21	0.225		
J2 ($\times 10^{-6}$)	14,736	16,298.00	3,343.43	3411	

Table A3.4. Orbital data of the outer planets.

	Jupiter	Saturn	Uranus	Neptune	Pluto
Semi-major axis (10^6 km)	778.4122	1,426.7257	2,870.9728	4,498.2538	5,906.3774
Sidereal orbit period (days)	4,335.3558	10,757.739	30,708.169	60,224.921	90,613.3324
Perihelion (10^6 km)	740.7427	1,349.4676	2,735.5556	4,459.6324	4,436.8255
Aphelion (10^6 km)	816.0816	1,503.9837	3,006.3900	4,536.8752	7,375.9294
Synodic period (days)	398.88	378.09	369.66	367.49	366.73
Mean orbital velocity (km/s)	13.07	9.66	6.82	5.48	4.75
Sidereal rotation period (hrs)	9.9250	10.500	17.24	16.11	153.2928
Obliquity to orbit (deg)	3.12	26.73	97.86	29.56	122.46
Semimajor axis (AU)	5.203363	9.53707	19.19126	30.06896	39.48169
Semimajor axis rate (AU/century)	0.000607	−0.00302	0.00152	−0.001252	−0.0007691
Orbital eccentricity	0.048393	0.054151	0.047168	0.008586	0.248808
Orbital eccentricity rate (/century)	−0.00013	−0.00037	−0.00019	0.0000251	0.00006465
Orbital inclination (deg)	1.3053	2.48446	0.76986	1.76917	17.14175
Orbital inclination rate (″/century)	−4.15	6.11	−2.09	−3.64	11.07
Longitude of ascending node (deg)	100.5562	113.715	74.22988	131.7217	110.3035
Longitude of ascending node rate (″/century)	1217.17	−1591.05	−1681.4	−151.25	−37.33
Longitude of perihelion (deg)	14.75385	92.43194	170.9642	44.97135	224.0668
Longitude of perihelion rate (″/century)	839.93	−1948.89	1312.56	−844.43	−132.25
Mean Longitude (deg)	34.40438	49.94432	313.2322	304.88	238.9288
Mean Longitude rate (″/century)	10,925078	4,401,053	1,542,548	786,449.21	522,747

The reference data commonly adopted for high-accuracy models of the ephemeris of the planets is NASA's JPL ephemeris model (courtesy NASA), available for download at http://ssd.jpl.nasa.gov/eph_info.html. These files allow the Cartesian components of planetary positions to be obtained at a given epoch, via the use of a program supplied with the model.

Less accurate data, used typically in the preliminary phases of mission design, can also be obtained from NASA. These are included in Tables A3.2 and A3.4, which contain mean orbit solutions from a 250-year least-squares fit of the NASA DE 200 planetary ephemeris to a Keplerian orbit where each element is allowed to vary linearly with time. This solution fits the terrestrial planet orbits to $\sim 25''$ or better, but achieves only $\sim 600''$ for Saturn. Elements are referenced to mean ecliptic and equinox of J2000 at the J2000 epoch (2451545.0JD = 51544.5MJD).

A3.1.3 The Sun

The key property of the Sun required in mission design is the gravitational constant:

$$1.32712440018 \times 10^{20} (\pm 8 \times 10^{9})\,\mathrm{m^3\,s^{-2}}$$

A3.2 GUIDE TO THE PLANETS

A short description of each of the planets of the Solar System is now presented, including some of the key properties of each planet and a brief history of its exploration.

A3.2.1 Mercury

Mercury is the smallest planet in the Solar System and is closest to the Sun. It has been known since prehistoric times. It is not significantly larger than Earth's Moon. The rotational period is approximately two thirds of its year, which results in extremes of surface temperatures between local noon and midnight. Temperatures reach a maximum of approximately 450°C. It has a very thin atmosphere, with a surface pressure of 10^{-15} bar (0.001 picobar), and its equator is not far removed from the ecliptic (approximately 7°).

Exploration

Mercury was explored by Mariner 10, launched by NASA in 1973. Following a Venus gravity assist to help reach Mercury, the spacecraft performed a series of three gravity assists at Mercury, affording multiple observational opportunities. NASA's Messenger is planned to reach Mercury in 2011.

A3.2.2 Venus

Venus is almost the same size as the Earth. It is often visible in the evening or early dawn. It has been known since prehistoric times. It possesses a dense atmosphere – predominantly carbon dioxide, which acts as a 'greenhouse' gas. The dense atmo-

sphere of Venus results in surface temperatures exceeding 450°C. The surface pressure is also very high, at typically 92 bar.

Venus's day is longer than its year, lasting approximately 243 days. Furthermore, its rotation is opposite to that of Earth (it is reversed when compared to the direction of its orbital motion). The obliquity of the equatorial plane to the planet's orbit is approximately 177° (compared with 23° for Earth).

Exploration

Venus has been visited several times. NASA's Mariner 2 arrived there in 1962, followed by Mariner 5 in 1967. It was then explored in greater detail by further NASA missions: Pioneer Venus and Magellan. The Pioneer Venus mission had an orbiter and also probes to enter the Venusian atmosphere. Both orbiter and probes arrived there in 1978. The probes were carried by a second spacecraft, arriving at Venus approximately five months after the orbiter's arrival, which remained in orbit until 1992, before entering the planet's atmosphere. Magellan reached Venus in 1990 and carried out a four-year mission orbiting the planet. The satellite generated radar maps of approximately 98% of the surface. The Soviet Venera series of missions visited Venus. Venera 14 deployed a lander and Venera 16 orbited in 1983. In late 2005, ESA's Venus Express mission left for Venus and plans to enter Venus orbit in the spring of 2006.

A3.2.3 Earth

Earth is the third innermost planet of the Solar System and the fifth largest. It possesses many unique features when compared with the other planets. These include the substantial presence of water on the surface, and an atmosphere with large oxygen content. No other planet is known to possess life. The obliquity of the equatorial plane to Earth's orbit is approximately 23.4°. The moon orbits Earth with a semi-major axis of approximately 384,000 km and an inclination to the ecliptic of 5°.

A3.2.4 Mars

Mars has been known since prehistoric times. The planet is relatively small, its mass being only roughly one tenth that of Earth. However, its smaller radius means that the surface gravitational acceleration is approximately one third that of Earth, giving rise to extensive speculation regarding the development of a future manned presence on Mars.

The Martian atmosphere is much thinner than that of Earth, with a surface pressure of typically 6–10 mbar. The main component of the atmosphere is carbon dioxide, at over 95%. The atmosphere does, however, extend to approximately 120 km. It can therefore be used to brake the approach of landers heading for the planet's surface. The angle between the Martian equatorial plane and the ecliptic is

similar to that of Earth. The obliquity of the equatorial plane to the planet's orbit is approximately 25°.

Exploration

Mars has attracted considerable interest as the subject of interplanetary missions. Many spacecraft have orbited the planet, and several landers have successfully reached the surface. A similar number of landers have also failed to successfully reach the surface, as planetary landing is a difficult and risk-prone task. A series of missions is planned over the next decade, and so martian exploration is set to continue.

Mars was first visited by NASA's Mariner 4, which flew by the planet in 1965. It was subsequently visited by Mariners 6, 7 and 9. The NASA Viking missions landed on the surface: Viking 1 and Viking 2 were launched within a small time interval (approximately two weeks). Each launch carried an orbiter with a lander attached. They arrived in 1976, and the landers were deployed after the landing sites were selected. The orbiter continued operations until 1980 and the landers until 1983.

The NASA Pathfinder mission was launched in 1996 and landed on Mars in 1997. The lander directly entered the atmosphere from its interplanetary approach trajectory. It also deployed a rover to explore the vicinity of the landing site. NASA later followed with two further rover missions, Spirit and Opportunity, both arriving in 2004 and with the capability to carry out long excursions across the Martian surface.

NASA used an aerobraking technique to reach the target orbit about Mars for both Mars Global Surveyor and Mars 2001 Odyssey. Surveyor arrive at Mars in 1997, and Odyssey in 2001.

Several Soviet probes have visited Mars. Phobos 2 orbited the planet in 1988.

In 2003 ESA launched Mars Express, which successfully entered orbit about Mars at the end of 2003. This mission also carried a lander named Beagle 2, but contact was lost after separation from the mother-ship.

The moons of Mars

Mars has two small moons: Phobos and Deimos, each of which is the size of a large asteroid. Both of them were discovered by Asaph Hall in 1877.

Table A3.5. The moons of Mars.

	Semi-major axis (km)	Eccentricity	Inclination (deg)	Radius (median axis) (km)	Mass (10^{15}kg)	Orbital period (days)
Phobos	9,380	0.0151	1.075	11.2	10.6	0.319
Deimos	23,460	0.0002	1.793	6.1	2.4	1.262

A3.2.5 Jupiter

Jupiter is the fifth and most massive planet in the Solar System. It has been known since prehistoric times. It is the first of the family of the outer gas giants. Its radius at a pressure of 1 bar exceeds 70,000 km. Below this radius the pressure rises rapidly. The major constituent of the Jovian atmosphere is hydrogen (90%), with significant helium content. Its equator lies close to the ecliptic, the obliquity being 3° with respect to the orbital plane. Jupiter also possesses a vast magnetosphere, which extends far into the outer Solar System. Its gravity field is so intense that orbital velocities around the planet are particularly high. This has significant implications for exploration of the atmosphere.

The major moons of Jupiter

So far, 63 Jovian moons have been discovered. The outer objects were probably asteroids captured by the Jovian gravity field. The inner moons are massive. Table A3.6 shows the four large moons orbiting within approximately 2 million km of the planet. They each have interesting individual characteristics. Io, the innermost of these moons, is volcanically active. Europa is the subject of much debate, perhaps in part inspired by science fiction novels of the last century. It is thought to possess an icy surface with an ocean below. Ganymede is the largest moon in our Solar System.

Exploration

Jupiter has been explored by several spacecraft. It was first visited by NASA's Pioneer 10, launched in 1972, which performed a gravity assist at Jupiter *en route* to the outer Solar System and beyond. Pioneer 10 has now left the Solar System and is travelling in a direction opposite to that of the Sun through the Milky Way. This probe was followed by Pioneer 11, launched in 1973. This spacecraft also performed a gravity assist at Jupiter, *en route* to Saturn and beyond.

NASA's Voyager 1 and Voyager 2 were both launched in 1977, with 1 leaving 16 days later than 2. However, Voyager 1 reached Jupiter first, in March 1979. It flew by *en route* to Saturn, and is now heading beyond the Solar System. Voyager 2 flew by Jupiter in September 1979, and continued to perform a 'grand tour' of the outer planets, passing Saturn, Uranus and Neptune.

Table A3.6. The major moons of Jupiter.

	Semi-major axis (km)	Eccentricity	Inclination (deg)	Radius (km)	Gravitational parameter ($m^3\,s^{-2}$)	Orbital period (days)
Io	421,600	0.0041	0.04	1,821	$5.960 * 10^{12}$	1.77
Europa	670,900	0.0101	0.47	1,560	$3.203 * 10^{12}$	3.55
Ganymede	1,070,000	0.0015	0.195	2,634	$9.887 * 10^{12}$	7.15
Callisto	1,883,000	0.007	0.281	2,400	$7.180 * 10^{12}$	16.69

NASA's Galileo mission was launched in 1989, reaching Jupiter after a longer transfer than the Voyagers, by performing gravity assists at Venus and Earth. It was particularly successful in exploring the planet and also its system of moons. A probe was deployed into Jupiter's atmosphere. Galileo was eventually deliberately crashed into Jupiter to avoid any potential contamination of Europa after accidental collision. Recently, Cassini flew by Jupiter on its way to Saturn.

A3.2.6 Saturn

Saturn is the sixth planet in the Solar System and the second most massive (after Jupiter). It is sometimes described as the 'jewel of the Solar System' because of its spectacular ring system. Like Jupiter, it is predominantly composed of hydrogen and helium. The equator of Saturn lies at approximately 27° from its orbital plane. Its largest moon is Titan (Table A3.7).

Exploration

The recent NASA–ESA Cassini-Huygens mission has explored the planet, its rings, and also Titan. This is the first spacecraft to orbit Saturn, as earlier visitors only flew by *en route* to the outer Solar System. The spacecraft arrived at Christmas 2004, and deployed the atmospheric probe, Huygens, which eventually descended through Titan's atmosphere.

Table A3.7. Saturn's largest moon, Titan.

	Semi-major axis (km)	Eccentricity	Inclination (deg)	Radius (km)	Gravitational parameter ($m^3\,s^{-2}$)	Orbital period (days)
Titan	1,221,800	0.0292	0.33	2,575	$8.978 * 10^{12}$	15.945

A3.2.7 Uranus

Far beyond Saturn lies Uranus, the seventh planet of the Solar System. Unlike the planets orbiting closer to the Sun, Uranus was discovered only relatively recently, by William Herschel in 1781. Uranus is another gas giant, composed of hydrogen with helium and methane as minor constituents. However, it is far less massive than Jupiter and Saturn, being approximately fifteen times the mass of Earth. One of the most unusual features of Uranus is that its equatorial plane lies at 98° from its orbital plane, and it is effectively toppled onto its side.

Exploration

Uranus was visited by Voyager 2 during its tour of the outer Solar System. The spacecraft flew by in 1986, at a distance of approximately 100,000 km

A3.2.8 Neptune

Neptune lies in the outer reaches of the Solar System. It was discovered in 1846 by Johann Gottfried Galle (based on the orbital predictions made by John Couch Adams and Urbain Leverrier). It is slightly more massive than Uranus, with a composition similar to the other gas giants. Its equator has a more conventional orientation than Uranus, lying at approximately 29° from its orbital plane. Its largest moon, Triton, is of significant interest. Several smaller moons are also present.

Exploration

Voyager 2 flew by Neptune in 1989. It is the only spacecraft to visit the planet to date.

A3.2.9 Pluto

Pluto is, on average, the most distant planet, but because of its elliptical orbit, it sometimes moves inside the orbit of Neptune. Pluto was discovered by Clyde Tombaugh in 1930. It is the smallest planet in the Solar System. It may also be the largest of a group of objects known as Kuiper belt objects. This region consists of thousands of small icy objects with diameters reaching over 1,000 km. An interesting feature of Pluto is that its orbital inclination (at 17°) is significantly higher than that of any other planet in the Solar System. This, combined with its extreme distance, makes it a difficult target for spacecraft exploration, and it has not yet been visited.

Pluto's equator also lies in an unusual attitude, at approximately 122° from its orbital plane. The planet has a very thin atmosphere composed of methane and nitrogen. It is orbited by its moon, Charon, which is more than 1,000 km in diameter and has an orbital inclination of approximately 97°.

Appendix 4

Optimising launcher injection

A4.1 LAUNCHER PERFORMANCE

Recalling Chapter 1, the maximum spacecraft mass than can be injected directly by the launcher upper stage is:

$$m_{SC} = m_0 - m_{fuel} - m_{LDry} = m_{0\max} \exp\left(\frac{-\Delta V}{Isp_L * g_0}\right) - m_{LDry}$$

where the initial mass, m_0, is always the maximum mass for the upper stage, $m_{0\max}$, if the mass of the spacecraft is to be maximised. Also m_{LDry} is the dry mass of the launcher upper stage (the mass after fuel is burnt to depletion), m_{SC} is the total mass of the spacecraft, m_0 is the initial total mass of the upper stage, and Isp_L is the specific impulse of the launcher propulsion system.

The maximum fuel tank capacity imposes a restriction on the above described performance. On reaching this limit, the required ΔV can be achieved only by reducing the mass injected in parking orbit, with implications for the achievable spacecraft mass injected into the final orbit. When the launcher upper stage is fully fuelled:

$$m_0 = \frac{m_{fuel\max}}{\left(1 - \exp\left(\frac{-\Delta V}{Isp_L * g_0}\right)\right)}$$

and therefore

$$m_{SC} = \frac{m_{fuel\max} \exp\left(\frac{-\Delta V}{Isp_L * g_0}\right)}{\left(1 - \exp\left(\frac{-\Delta V}{Isp_L * g_0}\right)\right)} - m_{LDry}$$

or $m_{SC} = m_0 - m_{fuel\max} - m_{LDry}$.

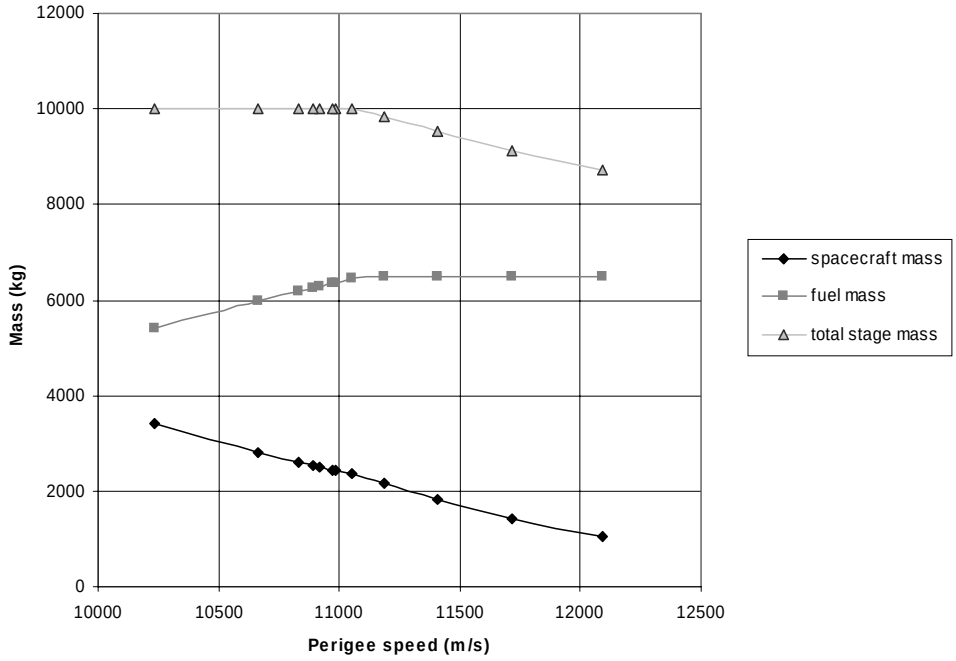

Figure A4.1. Launcher injection performance versus injection perigee speed for a tank mass capacity at 65% of upper-stage mass.

In Chapter 1 examples were given using typical intermediate launcher characteristics. This and other examples will now be considered.

In the first case, the maximum upper-stage mass that can be injected into a defined parking orbit is 10 tonnes. The parking orbit is a 200 km-altitude circular orbit. The fuel tank limit of the upper stage is assumed to be 6.5 tonnes. The dry mass of the launcher is assumed to be 1.2 tonnes.

Figure A4.1 then shows the spacecraft mass that the launcher may inject, as a function of the target perigee speed. Evaluating performance as a function of perigee speed enables a continuous plot to be achieved over the transition from bound to escape orbits. The transition occurs in this perigee altitude case at a perigee speed of approximately 11,008 m/s.

Figure A4.1 shows that the maximum upper stage mass of 10 tonnes can be fully utilised for this range of target, high-elliptical orbits (perigee speeds less than 11,000 m/s). However, at a speed of just over 11,000 m/s, the fuel-tank limit of the launcher is reached.

In the second case to be considered, the maximum upper stage mass that can be injected into a defined parking orbit is again 10 tonnes. The parking orbit is a 200-km-altitude circular orbit. The fuel tank limit of the upper stage is assumed to be 6 tonnes. The dry mass of the launcher is assumed to be 1.108 tonnes. This maintains the same dry mass-to-fuel mass ratio for the launcher. Although not a precise relationship, this is a first estimate of the dry mass dependence for such a stage.

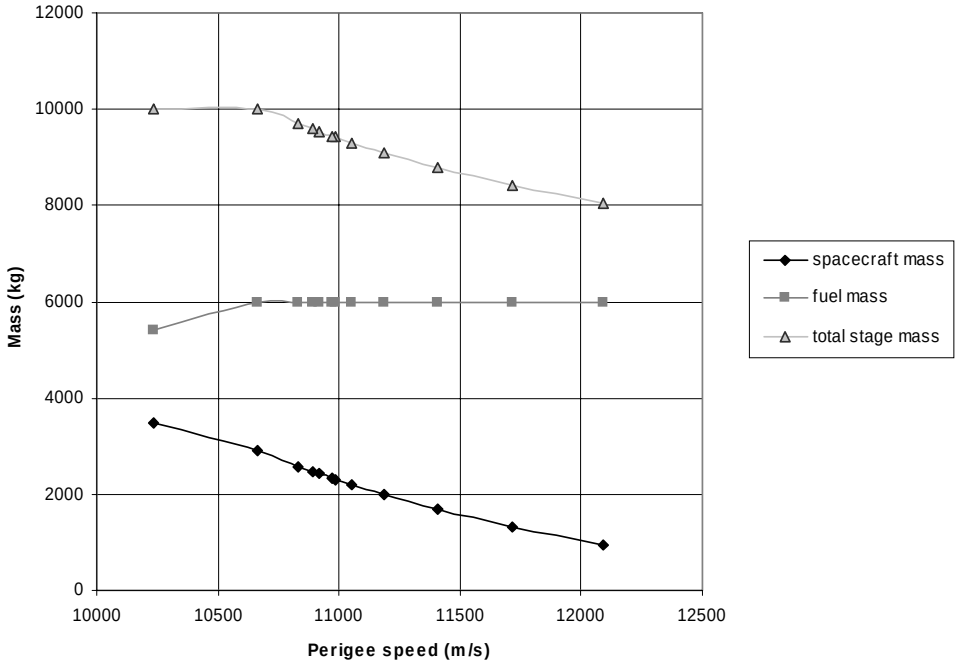

Figure A4.2. Launcher injection performance versus injection perigee speed for a tank mass capacity at 60% of upper-stage mass.

Figure A4.2 shows that the maximum upper stage mass of ten tonnes can again be fully utilised for a range of target, high apogee elliptical orbits. However, at a speed of just over 10,600 m/s, the fuel tank limit of the launcher is reached. This is lower than the case with greater fuel capacity, as it corresponds to an apogee in the region of 100,000 km.

The result is that at low-injection speeds, the spacecraft mass injected is greater than the previous case, because of the lower launcher-stage dry mass. However, at greater target speeds, the mass is lower because of the fuel mass limitations.

The procedure may be repeated for a higher fuel fraction, at 70%. The fuel tank limit of the upper stage is assumed to be 7 tonnes. The dry mass of the launcher is assumed to be 1.29 tonnes. This again maintains the same dry mass-to-fuel mass ratio for the launcher.

The result now is that at low injection speeds, the spacecraft mass injected is less than in the first case, because of the higher launcher-stage dry mass. However, at greater target speeds, the injection mass is higher. The spacecraft masses for all these cases are compared in Figure A4.4.

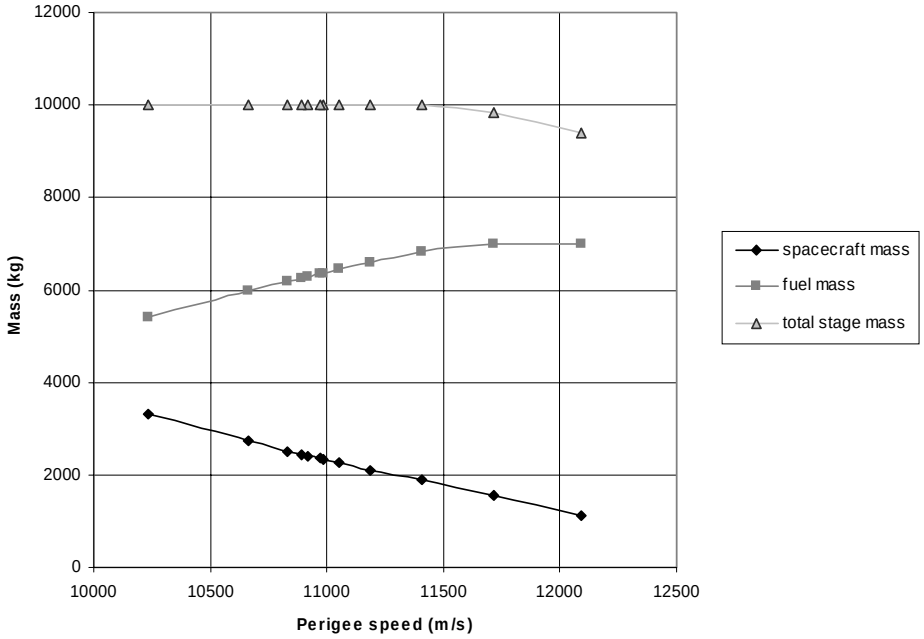

Figure A4.3. Launcher injection performance versus injection perigee speed for a tank mass capacity at 70% of upper-stage mass.

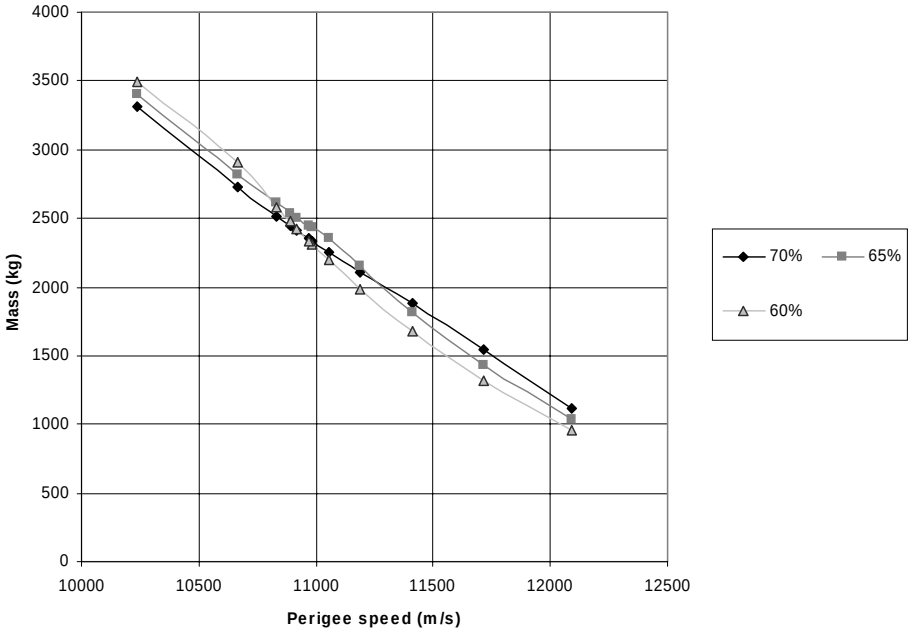

Figure A4.4. Comparative launcher injection performance versus injection perigee speed for a tank mass capacity at 60% to 70% of upper-stage mass.

A4.2 OPTIMUM INJECTION PERFORMANCE

In the case of using an intermediate injection orbit, the 'useful spacecraft mass' may be expressed by the relationships from Chapter 1 as:

$$m_{SCpay} = \left(m_0 \exp\left(\frac{-\Delta V_a}{Isp_L * g_0} \right) - m_{LDry} \right) \exp\left(\frac{-\Delta V_b}{Isp_{SC} * g_0} \right) - m_{SCprop}$$

where Isp_{SC} is the specific impulse of the spacecraft propulsion system, ΔV_a is the ΔV applied by the upper stage propulsion, and ΔV_b is the ΔV applied by the spacecraft. Each of these ΔV terms will consist of a speed change plus a loss term.

The constraint on total ΔV must apply:

$$\Delta V + \Delta V_{aLoss} + \Delta V_{bLoss} = \Delta V_a + \Delta V_b$$

The launcher injection capability for the spacecraft is then shown in Figure A4.5, for the 65% fuel capacity case. This is an extension of the previous figure (A4.1), to include lower injection perigee speeds that could be chosen for intermediate orbit injection.

This figure also shows injection at speeds beyond 11 km/sec, where escape takes place. It would not be practical to use such a launcher injection condition (i.e., escape) to an intermediate orbit, as the spacecraft manoeuvre, to reach the target escape orbit, would have to take place immediately after separation from the launch vehicle. Although possible in principle, current spacecraft design and operation

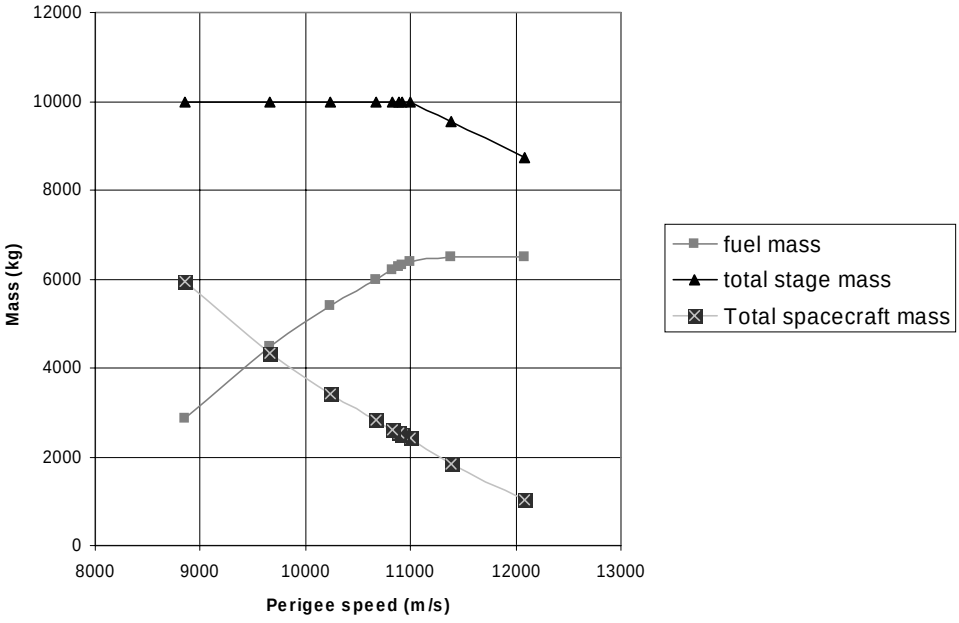

Figure A4.5. Launcher injection performance versus injection perigee speed for a tank mass capacity at 65% of upper stage mass, for use as an intermediate injection orbit.

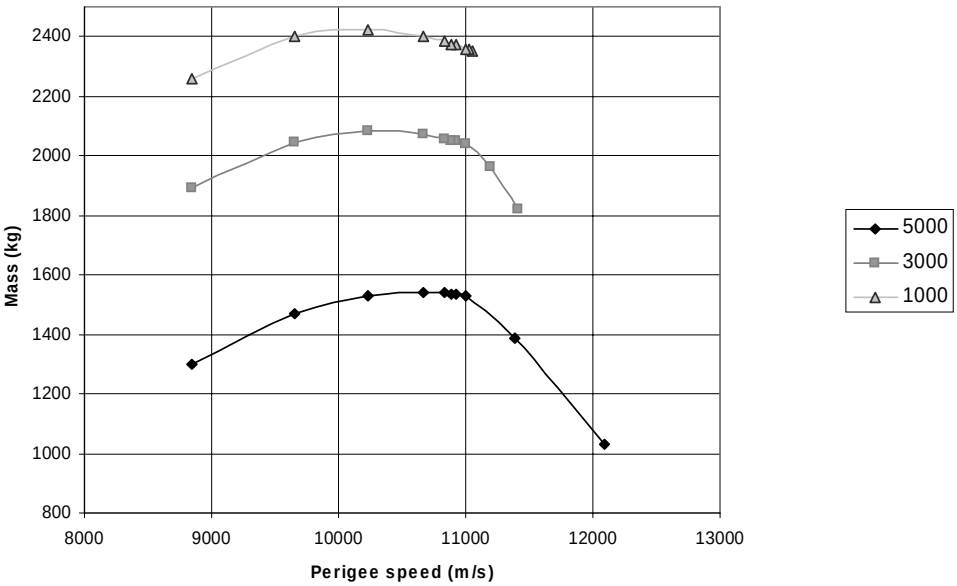

Figure A4.6. Spacecraft useful mass performance versus injection perigee speed for a launcher upper-stage tank mass capacity at 65% of upper stage mass, for three target excess hyperbolic speeds.

methods eliminate these options. However, their inclusion shows the principle of this method more clearly.

Figure A4.6 shows the useful spacecraft mass that is obtained, versus the injection perigee speed. In the following examples, the specific impulse of the spacecraft propulsion system is assumed to be lower than that of the upper stage, at 320 sec. The spacecraft propulsion mass fraction considered is 0.15. The ΔV loss assumed here is 10% in the apogee raising by the spacecraft, as this includes the escape manoeuvre that must be performed in a single burn. This manoeuvre would generally be a combination of smaller manoeuvres to raise apogee to a high elliptical orbit and then a final, larger escape manoeuvre. The 10% in this case can be regarded as average over these manoeuvres. The performance is evaluated for three target excess hyperbolic speeds, between 1 and 5 km/sec.

The figure clearly shows that the optimum injection perigee speed increases with the target excess hyperbolic speed. In the 5 km/sec case, the optimum corresponds to an intermediate orbit apogee at approximately 100,000 km (perigee speed at 10,660 m/s). The performance then falls off significantly as the injection perigee speed increases beyond the escape velocity (at 11,008 m/s). The maximum perigee speed shown in the figure, for each excess hyperbolic speed target, corresponds to a direct injection to that orbit.

The effects of variations in the launcher design should also be considered. The effects are shown in Figures A4.7 and A4.8.

When considering a given target excess hyperbolic speed, using a smaller fuel

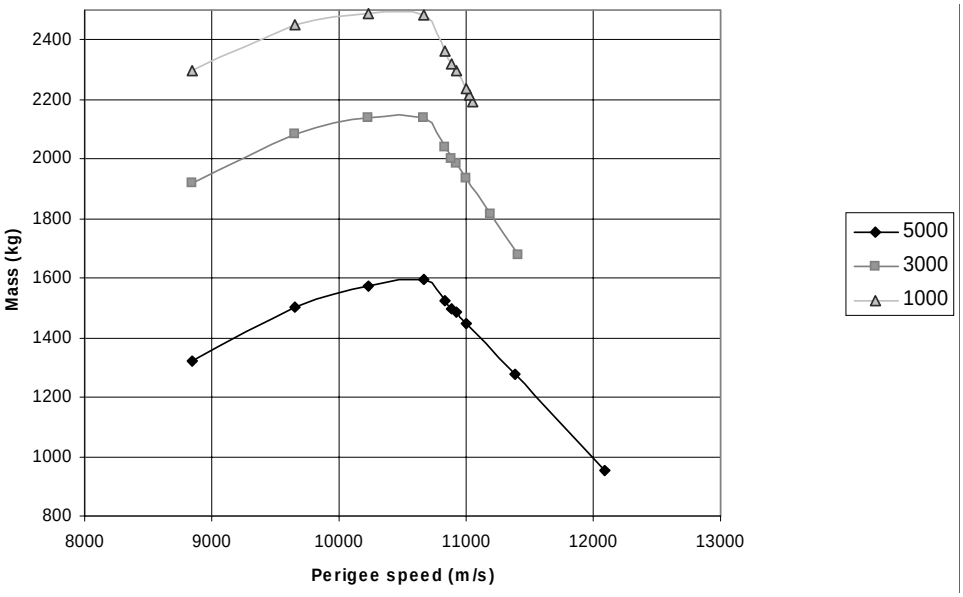

Figure A4.7. Spacecraft useful mass performance versus injection perigee speed for a launcher upper stage tank mass capacity at 60% of upper stage mass, for three target excess hyperbolic speeds.

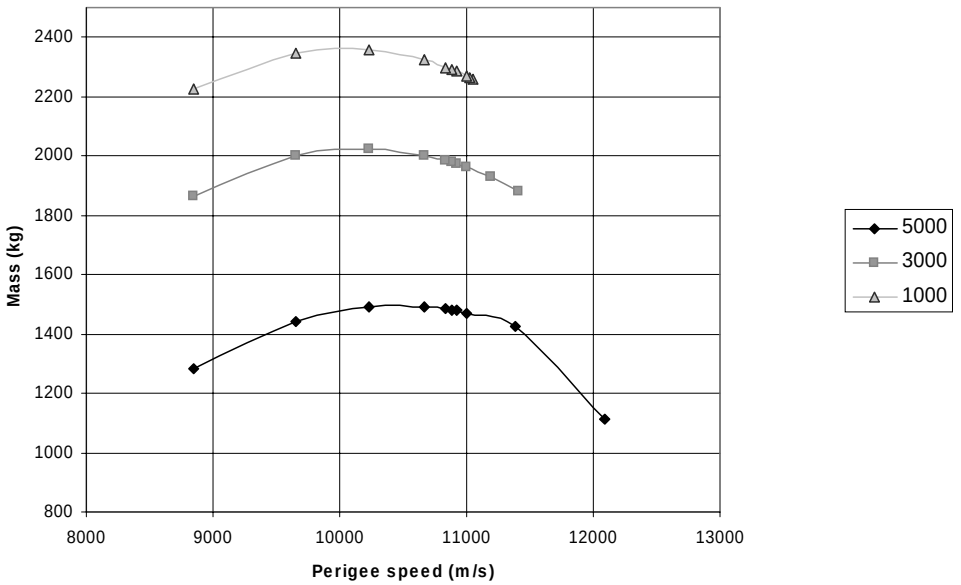

Figure A4.8. Spacecraft useful mass performance versus injection perigee speed for a launcher upper stage tank mass capacity at 70% of upper-stage mass, for three target excess hyperbolic speeds.

mass fraction in the upper stage not only penalises the direct injection performance (the performance at maximum perigee speed) but also moves the optimum injection apogee. The optimal performance capability at lower fuel fractions exceeds that at the higher fuel fraction case, because of the reduced dry mass of the upper-stage fuel tanks.

Therefore, a launcher design that enables a reduced upper-stage mass dependence on fuel mass could allow the optimal performance to switch to the higher fuel fraction case.

All cases demonstrate a significant improvement when using intermediate orbit injection, compared with a direct injection.

References and further reading

The following references provide material that is relevant to the text and that also may be read to obtain detailed information on the subjects discussed. They are divided into those that are applicable to each chapter and further sub-divided into particular subject areas within each chapter.

General

1. R.H. Battin, *An Introduction to the Mathematics and Methods of Astrodynamics* (AIAA Education series). AIAA, New York, 1987.
2. D. Brouwer, G.M. Clemence, *Methods of Celestial Methanics*. Academic Press, New York, 1961.
3. A.E. Bryson and Y.C. Ho, *Applied Optimal Control*. Hemisphere publishing corporation, 1975.
4. J.W. Cornelisse, H.F.R. Schoyer and K.F. Wakker, *Rocket Propulsion and Spaceflight Dynamics*. Pitman, London, 1979.
5. H. Goldstein, *Classical Mechanics*. Addison-Wesley, Reading, MA, 1980.
6. D.F. Lawden, *Optimal Trajectories for Space Navigation*. Butterworths, London, 1963.
7. A.E. Roy, *Orbital Motion*. Adam Hilger Co., Bristol, UK, 1982.

Orbital dynamics and data

8. R.A. Broucke and P.J.Cefola, On the equinoctial orbital elements, *Celestial Mechanics*, **5**(3), 303–310, 1972.
9. W. Donat and A. Boksenberg, *The Astronomical Almanac* (Annual publication). HMSO, London.
10. P.K. Seidelmann, *Explanatory Supplement to the Astronomical Almanac*. University Science Books, CA, 1992.
11. NASA JPL ephemeris data: *http://ssd.jpl.nasa.gov/eph_info.html*

Chapter 1

Lamberts problem

1.1. R.H. Battin, *An Introduction to the Mathematics and Methods of Astrodynamics* (AIAA Education series). AIAA, New York, 1987, pp. 276–343.
1.2. H. Shen and P. Tsiotras, Optimal two impulse rendez-vous between two circular orbits using multiple revolution Lambert's solutions. *AAS/AIAA Astrodynamics Specialist Conference, August, 1999*.
1.3. J.E. Prussing, Geometrical interpretation of angles α and β in Lambert's problem. *Journal of Guidance, Control and Dynamics*, **2**(5), 442–443, 1979.

Interplanetary missions

1.4. J.V. Breakwell, R.W. Gillespie and S.Ross, Researches in interplanetary transfer. *A.R.S.J.*, **31**, 201–208, 1961.
1.5. J. Graf, R. Zurek, R. Jones, H. Eisen, M. Johnson and B.Jai, An overview of the Mars Reconnaissance Orbiter Mission. *2002 IEEE Aerospace Conference Proceedings, Big Sky, Montana, March 11–15, 2002*.
1.6. M. Hechler and A. Yanez, *Mars Express Orbit Design*, IAC, Houston, 2002, IAC-02-A.2.09.
1.7. R.S. Saunders and G.H. Pettengill, Magellan mission summary. *Science*, **252**(5003), 247–249, April 1991.
1.8. Venus Express: *http://www.esa.int/SPECIALS/Venus_Express*

Sample return missions

1.9. R.H. Battin, The determination of round-trip planetary reconnaissance trajectories. *Journal of Aeronautical and Space sciences*, **26**, 545–567, 1959.
1.10. A.L. Friedlander, J.C. Niehoff, D.V. Byrnes and J.M. Longuski, Circulating transportation orbits between Earth and Mars. *AIAA/AAS Astrodynamics Conference, August, 1986* (AIAA 86-2009-CP).
1.11. S.J. Hoffman, J.V. McAdams and J.C. Niehoff, Round trip trajectory options for human exploration of Mars. *Greenbelt, April 1989* (AAS 89-201).
1.12. R.C. Parkinson and S. Kemble, Mars Sample Return as a Micromission. *54th IAC, Bremen, Germany, 2003* (IAC-03-Q.3.b.08).
1.13. J.R.Wertz, Interplanetary round trip mission design. *IAC, Bremen, 2003* (IAC-03-Q.4.06).
1.14. J.R. Wertz, Rapid Interplanetary round trips at moderate energy. *IAC Vancouver, 2004* (IAC-04-Q.2.a.11).

Launch vehicle performnce

1.15. Ariane V, VEGA: *http://www.arianespace.com/site/launcher/future_sub_index.htm*
1.16. Atlas, Proton: *http://www.ilslaunch.com/*
1.17. Delta2, Delta 4: *http://www.boeing.com/defense-space/space/delta/*
1.18. Dnepr: *http://www.kosmotras.ru/*
1.19. NASDA H-II: *http://www.nasda.go.jp/projects/rockets/h2a/index_e.html*
1.20. Rockot: *http://www.eurockot.com/*
1.21. Soyuz–Fregat: *http://www.starsem.com/*

Chapter 2

2.1. A. Bond, A.R. Martin, R.A. Buckland, T.J. Grant, A.T. Lawton, H.R. Mattison, J.A. Parfitt, R.C. Parkinson, G.R. Richards, J.G. Strong, G.W.Webb, A.G.A. White and P.P. Wright, Project Daedalus. *Journal of the British Interplanetary Society,* Interstellar studies, Supplement (A.R. Martin, ed.), 1978.

2.2. J.R. Brophy and M. Noca, Electric propulsion for Solar System exploration. *Journal of Propulsion and Power*, **14**(5), 700–707, 1998.

2.3. J.W. Cornelisse and H.F.R. Schoyer, K.F. Wakker, *Rocket Propulsion and Spaceflight Dynamics* (Chapter 5, pp. 85–111), Pitman, London, 1979.

2.4. D. Fearn and P. Smith, A review of UK ion propulsion a maturing technology. *IAC, Melbourne, 1998* (IAF-98-S-4.01).

2.5. R.G. Jahn, *Physics of Electric Propulsion*. McGraw Hill, New York, 1968.

2.6. J. Kawaguchi and T. Uesugi, Technology development status of the Muses C sample and return project. *IAC, Amsterdam, 1999* (IAF-99-IAA.11.2.02).

2.7. M. Leipold, M. Eiden, C.E. Garnerd, L. Herbeck, D. Kassing, T. Niederstadt, T. Krüger, G. Pagel, M. Rezazad, H. Rozemeijer, W. Seboldt, C. Schöppinger, C. Sickinger and W. Unckenbold, Solar sail technology development and demonstration. *Acta Astronautica*, **52**, 317–326, 2003.

2.8. A.E. Marini, G.D. Racca and B.H. Foing, SMART-1 Technology preparation for future planetary missions. *Advanced Space Research*, **30**(8), 1985–2000, 2002.

2.9. C.R. McInnes, *Solar Sailing: Technology, Dynamics and Mission Applications*. Springer–Praxis, Chichester, UK, 1999.

2.10. R.C. Parkinson, M. Bernasconi, P. Bravais and F. Corberand, Solar Thermal Orbit Transfer System (STOTS), *52nd IAC, Toulouse, France, Oct 2001*.

2.11. D. Poston, Nuclear design of the SAFE-400 space fission reactor. *Nuclear news*, December, 28–35, 2002.

2.12. M. Rayman, P. Varghese, D. Lehman, L. Livesay, Results from the Deep-Space 1 technology validation mission. *Acta Astronautica*, **47**, 475, 2000.

2.13. G. Saccoccia and D. Estublier, SMART-1. A technology demonstration mission for science using electric propulsion, 1998 (AIAA 98-3330).

2.14. S.S. Voss, TOPAZ II System description. *Engineering, Construction and Operations in Space IV*. Albuquerque, 1994.

2.15. H.J. Willenberg, Nuclear electric propulsion vehicle architectures, *IAC Bremen, 2003* (IAC-03.IAA.13.1.07).

Chapter 3

Optimisation methods

3.1. M.C. Bartholomew-Biggs, Recursive quadratic programming based on penalty functions for constrained minimisation, non-linear optimisation, theory and algorithms. In: L.C.W. Dixon, E. Spedicato and G.P.Szego (eds), *Numerical Optimisation Theory and Algorithms*. Birkhauser, Boston, 1980.

3.2. M.C. Bartholomew-Biggs, *Non-linear Optimisation with Financial Applications*. Boston, Kluwer, 2005.

3.3. J.T. Betts, Survey of numerical methods for trajectory optimisation. *Journal of the Astronautical Sciences*, **42**(3), 247–268, 1994.

3.4. J.T. Betts, Optimal interplanetary orbit transfer by direct transcription. *The Journal of the Astronautical Sciences*, **42**(3), 247–268, 1994.
3.5. J.T. Betts, Trajectory optimisation using sparse sequential quadratic programming. In: , R. Bulirsch, A. Miele, J. Stoer, K.H. Well (eds), *Optimal Control* (Vol 111 International series of numerical mathematics), pp 115–128. Berkhauser-Verlag, Bassel, 1993.
3.6. A.E. Bryson, Y.C. Ho, *Applied Optimal Control*. Hemisphere publishing corporation, 1975.
3.7. R. Fletcher, *Practical Methods of Optimisation,* Volume 2: *Constrained Optimisation. John Wiley and Sons, New York, 1985.*
3.8. P.E. Gill, W. Murray and M.A. Wright, *Practical Optimisation* Academic Press, New York, 1981.
3.9. T. Goodson, J. Chuang and J. Hanson, Optimal finite thrust orbit transfers with large numbers of burns. *Journal of Guidance, Control and Dynamics*, **22**(1), 139–147, 1999.
3.10. C.R. Hargraves and S.W. Paris, Direct trajectory optimisation using nonlinear programming and collocation. *Journal of Guidance, Control and Dynamics*, **10**(4), 338–342, 1987.
3.11. A.L. Herman and B.A. Conway, Direct optimisation using collocation based on high order Gauss Lobatto quadrature rules. *Journal of Guidance, Control and Dynamics*, **19**(3), 592–599, 1996.
3.12. C. Jansch, K. Schnepper and K.H Well, Ascent and Descent Trajectory Optimisation of Ariane V/Hermes. *AGARD conference proceedings No. 489, Space Vehicle Flight Mechanics*, 1989.
3.13. M. Noton, *Modern Control Engineering*. Pergamon Press, New York, 1972.
3.14. L.S. Pontryagin, V.G. Boltyanskii, R.V. Gamkrelidze and E.F. Mishchenko, *The Mathematical Theory of Optimal Processes*. Interscience, New York, 1962.
3.15. R.D. Russell and L.F. Shampine, A Collocation method for boundary value problems. *Numerical Mathematics,* **19**, 1–28, 1972.
3.16. C.G. Sauer, MIDAS: Mission Design and Analysis Software for the optimisation of ballistic interplanetary trajectories. *The Journal of the Astronautical Sciences*, **37**(3), 251–259, 1989.
3.17. W.A. Scheel and B.A. Conway, Optimisation of very low thrust multi-revolution spacecraft trajectories. *Journal of Guidance, Control and Dynamics*, **17**(6), 1265–1282, 1994.
3.18. M.Vasile, A global approach to optimal space trajectory design. *13th AAS/AIAA Space Flight Mechanics meeting, Puerto Rico, 2003* (AAS 03-141).
3.19. K.H. Well and S.R. Tandon, Rocket ascent trajectory optimisation via recursive quadratic programming. *Journal of the Astronautical Sciences*, **30**(2), 101–115, 1982.

Propulsion system optimisation

3.20. M. Auweter-Kurtz, H.L. Kurtz and H.O. Schrade, Optimisation of electric propulsion systems considering specific power as a function of specific impulse. *Journal of Propulsion*, **4**(6), 512–519, 1988.
3.21. G. Colasurdo and L. Casalino, Characteristics of electric propulsion systems for optimal interplanetary trajectories. *IAC 2003, Bremen* (IAC-03-A.7.08).
3.22. G. Fedotov, V. Kim, M. Konstantinov, V. Petukhov, G. Popov and F. Scortecci. Estimation of optimum combination of chemical upper stage and solar stationary plasma propulsion for the geostationary transfer. *IAC 1996, Beijing* (IAF96S.3.09).

3.23. L.W. Hobbs and J.P.W. Stark, Optimisation of electric propulsion for GEO missions, AIAA 1989.

Chapter 4

Motion about the Lagrange libration points and the three body problem

4.1. J.W. Cornelisse, H.F.R. Schoyer and K.F. Wakker, In: *Rocket Propulsion and Spaceflight Dynamics*. pp. 337–354. Pitman, London, 1979.
4.2. G. Gomez, J. Masdemont and C. Simo, Quasihalo orbits associated with Libration points. *The Journal of the Astronautical Sciences*, **46**(2), 135–176, 1998.
4.3. G. Gomez, A. Jorba, J.J. Masdemont and C. Simo, *Dynamics and Mission Design Near Libration Point Orbits*, Volume 4: *Advanced Methods for Collinear Points*. World Scientific, River Edge, NJ, 2001.
4.4. G. Gomez, A. Jorba, J.J. Masdemont and C. Simo, *Dynamics and Mission Design Near Libration Point Orbits*, *Advanced Methods for Triangular points*, World Scientific, River Edge, NJ, 2001.
4.5. G. Gomez, W.S. Koon, M.W. Lo, J.E. Marsden, J.J. Masdemont and S.D. Ross, Invariant manifolds, the spatial three-body problem and space mission design. *Advances in the Astronautical Sciences*, **109**, 3–22, 2001.
4.6. M. Hechler, J. Corbos and M. Bello-Mora, Orbits around L2 for First, Planck and GAIA Astronomy missions. *IAC 1999, Amsterdam* (IAF-99-A.2.02).
4.7. M. Hechler and A. Yanez, Orbits around L2 with non-gravitational perturbations. *IAC 2004, Vancouver* (IAC-04-A.7.01).
4.8. K.C. Howell, B.T. Barden and M.W. Lo, Application of dynamical system theory to trajectory design for a libration point mission. *Journal of Astronautical Sciences*, **45**(2), 161–178, 1997.
4.9. K.C. Howell and H.J. Pernicka, Station keeping for libration point trajectories. *Journal of Guidance, Control and Dynamics*, **16**(1), 151–159, 1993.
4.10. K.C. Howell and L.A. Hinday-Johnston, Time free transfers between libration-point orbits in the elliptic restricted three body problem. *Acta Astronautica*, **32**, 245–254, 1994.
4.11. A. Jorba and J. Masdemont, Dynamics of the centre manifold of the collinear points in the restricted three body problem. *Physics D*, **132**, 189–213, 1999.
4.12. W.S. Koon, M.W. Lo, J.E. Marsden and S.D. Ross, Heteroclinic connections between periodic orbits and resonant transitions. *Chaos*, **10**(2) 427–469, 2000.
4.13. W.S. Koon, M.W. Lo, J.E. Marsden and S.D. Ross, Dynamical systems, the three body problem and space mission design. In: B. Fielder, K. Groger and J. Sprekels (eds), *International Conference on Differential Equations, Berlin, 1999*, pp. 1167–1181. World Scientific, River Edge, NJ, 2000.
4.14. D.L. Richardson, A note on a Lagrangian formulation for motion about the Collinear points. *Celestial Mechanics*, **22**, 231–236, 1980.
4.15. D.L. Richardson, Analytical construction of periodic orbits about the collinear points. *Celestial Mechanics*, **22**(3), 241–253, 1980.
4.16. C. Simo, G. Gomez, J. Llibre, R. Martinez and R. Rodriquez, On the optimal station keeping control of Halo orbits. *Acta Astronautica*, **15**(6), 391–397, 1987.
4.17. C. Simo, Dynamical systems methods for space missions on a vicinity of collinear libration points. In: C. Simo (ed.), *Hamiltonian Systems with Three or More Degrees of Freedom*, pp. 223–241. Kluwer Academic Publishers, 1999.

4.18. A.E. Roy, The many body problem. In: *Orbital Motion*, pp. 111–163. Adam Hilger Co., Bristol, 1982.
4.19. G. Gómez, M.W. Lo, J.J. Masdemont (eds), Libration point orbits and applications. In: *Proceedings of the Conference Aiguablava, Spain 10–14 June, 2002*. World Scientific, River Edge, NJ, 2002.

Missions to the Lagrange libration points

4.20. R.W. Farquhar, D.P. Muhonen, C.R. Newman and H.S. Heuberger, Trajectories and orbital manoeuvres for the first Libration point satellite. *Journal of Guidance and Control*, **3**, 549–554, 1980.
4.21. R.W. Farquhar, D.P Muhonen, C.R. Newman and H.S. Heuberger, The first Libration point satellite. *AAS/AIAA Astrodynamics specialist conference*, 1979.
4.22. R.W. Farquhar and D.P. Muhonen, Mission Design for a Halo Orbiter of the Earth. *Journal of Spacecraft*, **14**(3), 170, 1977.
4.23. M. Hechler and J. Corbos, *Herschel, Plank and Gaia Orbit Design, Libration Point Orbits and Applications*. Girona, Spain, 2002.
4.24 S. Kemble, M. Landgraf and C. Tirabassi, The design of the SMART-2/LISA-Pathfinder mission, *IAC-2004*, *Vancouver* (IAC.04.A.207).
4.25. M. Landgraf, M. Hechler, and S. Kemble, Mission design for LISA Pathfinder. *Classical Quantum Gravity*, **22**, S487–S492, 2005.
4.26. M.W. Lo, B.G. Williams, W.E. Bollman, D. Han, Y. Hahn, J.L. Bell, E.A. Hirst, R.A. Corwin, P.E. Hong, K.C. Howell, B.T. Barden and R.S. Wilson, Genesis mission design. *AIAA Space Flight Mechanics* (AIAA 96-4468 1998).

Gravitational capture

4.27. E.A. Belbruno, Examples of the nonlinear dynamics of ballistic capture and escape in the Earth-Moon system. *AIAA Astrodynamics conference, Portland, August, 1990* (AIAA-90-2896).
4.28. M. Bello-Mora, F. Graziani, P. Teofilatto, C. Circi, M. Porfilio, M. Hechler, A systematic analysis on Weak Stability Boundary transfers to the Moon. *IAC 2000, Rio de Janiero* (IAF-00-A.6.03).
4.29. A. Castillo, M. Bello-Mora, J. Gonzalez, G. Janin, F. Graziani, P. Teofilatto and C. Circi, Use of Weak Stability Boundary trajectories for planetary capture. *IAC-2003, Bremen* (IAF-03-A.P.31).
4.30. K.C. Howell, B.G. Marchand and M.W. Lo, Temporary Satellite capture of short period Jupiter family comets from the perspective of dynamical systems. *AAS/AIAA Space Flight Mechanics Meeting* (AAS 00-155, 2000).
4.31. R. Jehn, S. Campagnola, D. Garcia and S. Kemble, Low-thrust approach and gravitational capture at Mercury. *18th Int. Symposium on Space Flight Dynamics, Munich, Germany, Oct, 2004*.
4.32. S. Kemble, Interplanetary missions utilising capture and escape through the Lagrange points. *IAC 2003, Bremen* (IAC-03-A.1.01).
4.33. W.S. Koon, W.S., Lo, M.W., Marsden, J.E. and S.D. Ross, Resonance and capture of Jupiter comets. *Celestial Mechanics and Dynamical Astronomy*, **81**(1–2), 27–38, 2001.
4.34. M.W. Lo and S.D. Ross, Low-energy interplanetary transfers using the invariant manifolds of L1,L2 and Halo orbits. *AAS/AIAA Space Flight Mechanics meeting, Monterey, 1998* (AAS-98-136).

4.35. S.D. Ross, Statistical theory of interior-exterior transition and collision probabilities for minor bodies on the solar system. In: G. Gomez, M.W. Lo and J.J. Masdemont (eds), *Libration Point Orbits and Applications*, pp. 637–652. World Scientific, River Edge, NJ, 2003.
4.36. F. Topputo, M. Vasile and A.E. Finzi, Combining two and three body dynamics for low-energy transfer trajectories of practical interest. *IAC 2004, Vancouver* (IAC-04-A.7.02).

Interplanetary missions with gravity assist

4.37. R.H. Battin, *An introduction to the mathematics and methods of Astrodynamics* (AIAA Education series, pp. 419–437). AIAA, New York, 1987.
4.38. S. Campagnola, R. Jehn and C. Corral, Design of Lunar Gravity Assist for the BepiColombo Mission to Mercury. *AAS 04-130, 14th AAS/AIAA Space Flight Mechanics Conference, Maui, Hawaii, Feb, 2004*.
4.39. J.M. Deerwester, Jupiter swingby missions to the Outer Planets. *Journal of Spacecraft and Rockets*, **3**(10), 1564–1567, 1966.
4.40. A.F. Heaton, N.J. Strange, J.M. Longuski and E.P. Bonfiglio, Automated design of the Europa orbiter tour (AIAA 2000-4034).
4.41. M. Lavagna, A. Povoleri and A.E. Finzi, Interplanetary mission design manoeuvre multi-objective evolutive optimisation. *IAC 2004, Vancouver* (IAC-04-A.1.02).
4.42. J.R. Johannesen and L.A. D'Amario, Europa Orbiter mission trajectory design. *AAS/AIAA Astrodynamics specialist conference, Girdwood, August, 1999* (AAS 99-360).
4.43. J.M. Longuski and S.N. Williams, Automated design of gravity assist trajectories to Mars and the outer planets. *Celestial Mechanics and Dynamical Astronomy*, **52**(3), 207–220, 1991.
4.44. J.V. McAdams and R.L. McNutt, Ballistic Jupiter gravity assist perihelion DV trajectories for an Interstellar explorer. *Journal of Astronautical Sciences*, **51**(2), 179–193, 2003.
4.45. M.A. Minovitch, Gravity thrust Jupiter orbiter trajectories generated by encountering the Galilean satellites. *Journal of Spacecraft and Rockets*, **9**, 751–756, 1972.
4.46. J.C. Niehoff, Gravity assisted trajectories to Solar System targets. *Journal of Spacecraft and Rockets*, **3**(9), 1351–1356, 1966.

Low thrust

4.47. R.H. Battin, *An introduction to the mathematics and methods of Astrodynamics* (AIAA Education series, pp. 471–490). AIAA, New York, 1987.
4.48. D. Fearn, The use of Ion thrusters for orbit raising. *Journal of British Interplanetary Society*, **33**, 129–137, 1980.
4.49. A.E. Roy, *Orbital Motion*, pp. 179–205. Adam Hilger Co., Bristol, 1982.

Low-thrust departure optimisation

4.50. M. Hechler, AGORA: asteroid rendezvous low thrust mission basic trajectory data for S/C design. European Space Operations Centre, 1983. M.A.O. working paper No. 186.
4.51. J.B. Serrano-Martinez and M. Hechler, Low-thrust asteroid rendezvous tours with Vesta. European Space Operations Centre, 1985. M.A.O. working paper No. 223.

Interplanetary missions with low thrust

4.52. L.K. Atkins, C.G. Sauer and G.A. Flandro, Solar electric propulsion combined with Earth gravity assist: A new potential for planetary exploration. *AAS/AIAA Astrodynamics specialist conference, San Diego, August, 1976* (AAS 76-807).
4.53. L. Casalino, G. Colasurdo and D. Pastrone, Optimal low-thrust escape trajectories using fly-by. *Journal of Guidance, Control and Dynamics*, **22**(5), 637–642, 1999.
4.54. L. Casalino, G. Colasurdo, D. Pastrone, Optimisation low-DV Earth gravity assist trajectories. *Journal of Guidance, Control and Dynamics*, **21**(6), 991–995, 1998.
4.55. G. Colasurdo and L. Casalino, A new mission concept to reach near Earth planets, (AIAA 2000-4137).
4.56. J. Kawaguchi, Solar electric propulsion leverage, Electric Delta-VEGA (EDVEGA) scheme and its applications. *AAS/AIAA Space Flight Mechanics meeting, Santa Barbara, CA, Feb, 2001* (AAS 01-213).
4.57. S. Kemble, Optimised Transfers to Mercury. *IAC Toulouse, 2001* (IAF-01-A.5.03).
4.58. S. Kemble and M.J. Taylor, Mission design options for a small satellite mission to Jupiter. *IAC Bremen, 2003* (IAF-03-A.09).
4.59. M. MacDonald and C.R. McInnes, Analytical control laws for near optimal geocentric solar sail transfers. *American Astronautical Society*, AAS 01-472.
4.60. H.F. Meissinger, Earth Swingby, a novel approach to interplanetary missions using electric propulsion. *AIAA 8th Electric Propulsion conference, Stanford, 1970*.
4.61. A.E. Petropoulos and J.M. Longuski, A shape based algorithm for the automated design of low-thrust, gravity assist trajectories. *AAS/AIAA Astrodynamics specialist conference, Quebec, Jul–August, 2001* (AAS 01-467).
4.62. A.E. Petropoulos, J.M. Longuski, N.X. Vinh, Shape based analytic representation of low thrust trajectories for gravity assist application. *AAS/AIAA Astrodynamics specialist conference, Girdwood, August, 1999* (AAS 99-337).
4.63. J.A. Sims, J.M. Longuski and A.J. Staugler, Vinfinity leveraging for interplanetary missions: Multiple revolution orbit techniques. *Journal of Guidance, Control and Dynamics*, **20**(3), 409–415, 1997.

Aerobraking and aerocapture

4.64. J. Beerer, R. Brooks, P. Esposito, D Lyons, W. Sidney, H. Curtis and W. Willcockson, Aerobraking at Mars: The MGS Mission. *AIAA 34th Aerospace Sciences Meeting, Reno, NV, Jan, 1996* (AIAA 96-0334).
4.65. J. R. French, Aerobraking and Aerocapture for Mars Missions, AAS 81-246.
4.66. M.Vasile, Robustness optimisation of aerocapture trajectory design using a hybrid co-evolutionary approach. *18th International Symposium on Space Flight Dynamics, October 2004, Munich*.

Chapter 5

Mission descriptions

5.1. A. Atzei, G. Schwehm, M. Coradini, M. Hechler, J. De Lafontaine and M. Eiden, Rosetta/CNSRESA's Planetary Cornerstone Mission. *ESA Bulletin*, **59**, 18–29, 1989.
5.2. A. Atzei, P. Falkner and T. Peacock, The Jovian minisat explorer: The challenge of studying Europa. *IAC Fukuoka, 2005* (IAC.05.A.3.2.A.05).

5.3. Galileo: The tour guide at: *http://www2.jpl.nasa.gov/galileo/tour*
5.4. J. Kawaguchi, Muses-C launch and early operations report. *AAS/AIAA Astrodynamics Specialists Conference, Big Sky, August, 2003* (AAS-03-662).
5.5. D. Kolbe and R. Best, The ROSETTA mission. *IAC Turin, 1997* (IAF-97-Q.5.01).
5.6. A. Lyngvi, P. Falkner, S. Kemble, M. Leipold and A. Peacock, The Interstellar Heliopause probe. *IAC Vancouver, 2004*.
5.7. A. Lyngvi, N. Rando, R. Marsden, A. Jeanes, A. Owens, L. Gerlach, G. Janin and A. Peacock. The Solar Orbiter. *IAC Fukuoka, 2005* (IAC-05-A3.2.B.07).
5.8. R T. Mitchell, The Cassini/Huygens Mission to Saturn and Titan. *Houston, October, 2002* (IAC-02-Q.2-02).
5.9. R. T. Mitchell, Cassini/Huygens at Saturn and Titan. *Fukuoka, October, 2005* (IAC-05-A3.2.A.01).
5.10. P. Renard, C. Koeck, S. Kemble, A. Atzei and P. Falkner, System concepts and enabling technologies for an ESA low-cost mission to Jupiter/Europa. *IAC Vancouver, 2004* (IAC-04-Q.2.a.02).
5.11. G. Schwehm, M. Hechler, 'Rosetta' – ESA's Planetary Cornerstone Mission. *ESA Bulletin*, **77**, 7–18, 1994.
5.12. G.D. Racca, G.P. Whitcomb and B.H. Foing, The SMART-1 Mission. *ESA Bulletin,* **95**, 72–81, 1998.
5.13. K. Uesugi, Space Odyssey of an Angel—Summary of the Hiten's Three Year Mission (AAS 93-292).
5.14. J. Van Casteren, J. Benkhoff, R. Carli, B. Gramkow, M. Novara, M. Ranne, R. Schulz, R. Jehn, BEPI COLOMBO: A mission to Mercury. *IAC Fukuoka, 2005* (IAC-05-A3.2.B.05).

Gravity assist missions

5.15. S. Cornara, M. Belló-Mora, M. Hechler, Study on Recovery of Escape Missions (AAS 03-246).
5.16. Y. Guo, R.W. Farquhar, Current design of the Solar Probe mission. *IAC Bremen, 2003,* (IAC-03-Q.2.05).
5.17. Y. Guo and R.W. Farquhar, New horizons Pluto-Kuiper belt mission: Design and simulation of the Pluto-Charon encounter. *IAC Houston, 2002* (IAC-02-Q.2.07).
5.18. Y. Langevin, Chemical and Solar electric propulsion options for a cornerstone mission to Mercury. *Acta Astronautica*, **47**(2–9), 443–452, 2000.
5.19. J.V. McAdams, Discovery class Mercury orbiter trajectory design for the 2005 launch opportunity. *AAS/AIAA Astrodynamics specialist conference, Boston, August, 1998* (AIAA 98-4283).
5.20. *http://messenger.jhuapl.edu/*
5.21. R.A. Mewaldt, J. Kangas, S.J. Kerridge and M. Neugebauer, A small probe to the heliospheric boundary and interstellar space. *Acta Astronautica*, **34**, 267–276, 1995.
5.22. SOLO: *http://www.esa.int/science/solarorbiter*
5.23. C.L. Yen, Ballistic Mercury orbiter mission via Venus and Mercury gravity assist. *Journal of the Astronautical Sciences*, **37**(3), July–Sept, 417–432, 1989.
5.24. C.L. Yen, New trajectory options for ballistic Mercury Orbiter missions (AAS 01-158).
5.25. G.J. Whiffen, An investigation of a Jupiter Galilean moon orbiter trajectory. *AAS/AIAA Astrodynamics Specialist Conference, Big Sky, August, 2003* (AAS 03-554).

Low-thrust missions

5.26. T.S. Balint, G.J. Whiffen and T.R. Spilker, Mixing moons and atmospheric entry probes: Challenges and limitations of a multi-objective science mission to Jupiter. *IAC Bremen, 2003* (IAC-03-Q.2.04).
5.27. Bepi-Colombo: *http://www.esa.int/science/bepicolombo*
5.28. G.G. Fedotov, M.S. Konstantinov and V.G. Petukhov, Electric propulsion mission to Jupiter. *47th IAC, Beijing, 1996*.
5.29. G.W. Hughes and C.R. McInnes, Mercury Sample return and small body encounters using solar sail propulsion. *IAC Houston, 2002* (IAC-02-W.2.08).
5.30. M. Katzkowski and R. Jehn, Optimum trajectories to Mercury combining low-thrust with gravity assists. *IAC Toulouse, 2001* (IAF-01-Q.2.05).
5.31. Y. Langevin, Chemical and Solar electric propulsion options for a Mercury cornerstone mission. *50th IAC, Amsterdam, 1999* (IAF-00-A.2.04).
5.32. M.Vasile, R. Biesbroek, L. Summerer, A. Galvez and G. Kminek, Options for a mission to Pluto and beyond. *AAS/AIAA Space Flight Mechanics meeting, Puerto Rico, Feb, 2003* (AAS 03-210).
5.33. M.Vasile, F. Bernelli Zazzera, R. Jehn and G. Janin, Optimal interplanetary trajectories using a combination of low-thrust and gravity assist manoeuvres. *IAC Rio de Janeiro, 2000* (IAF-00-A.5.07).

Gravitational capture

5.34. E.A. Belbruno and J. Miller, Sun-perturbed Earth to Moon transfers wilt ballistic capture. *Journal of Guidance, Control and Dynamics*, **16**, 770–775, 1993.
5.35. W.S. Koon, M.W. Lo, J.E. Marsden and S.D. Ross, Resonance and capture of Jupiter comets. *Celestial Mechanics and Dynamical Astronomy*, **81**(1), 63–73, 2001.
5.36. A. Carusi and G. Valsecchi, Numerical simulation of close encounters between Jupiter and minor bodies. In: *Asteroids*, pp. 391–416. Univ. Az. Press, Tucson, 1979.
5.37. H. Yamakawa, J. Kawaguchi, N. Ishii and H. Matsuo, A numerical study of gravitational capture orbit in the Earth-Moon system. *AAS/AIAA Spaceflight Mechanics, Colarado Springs, 1992* (AAS 92-186).

Index

Printing: Mercedes-Druck, Berlin
Binding: Stein+Lehmann, Berlin